FINITE ELEMENT INVESTIGATION OF THE INCREMENTAL DEFORMATION OF COMPONENTS.

by

BARKAWI BIN SAHARI. B.Sc.(Hons.)

Thesis submitted to the University of Nottingham for the degree of Doctor of Philosophy, September 1984.

To

Sahari, Salamah, Zurina and Ashraff.

SUMMARY.

Many components in conventional and nuclear power plants and chemical plants are likely to be subjected to 'severe' loading conditions, i.e. loads which would cause cyclic plastic straining and/or incremental deformation (i.e. ratchetting). For operating temperatures above the creep threshold, creep strain also occurs, which may exacerbate the ratchetting of components. If ratchetting occurs, the components may fail either due to excessive deformation so that the components cannot function properly or due to incremental collapse.

For simple component geometries, loadings and material behaviour models, the mechanism of ratchetting and the behaviour of components are well understood and analytical solutions (closed form or simplified model) are available. However, for components with complicated stress distributions, loading and material behaviour, the mechanisms of ratchetting are not fully understood and closed form solutions , in general, cannot be obtained. An understanding of the mechanisms of ratchetting is important as an aid to the design process and to apply bounding techniques. Also information on the effect of the material ratchetting phenomena on the ratchetting of components is still scarce.

Components with different geometries and loading conditions have been analysed by using the finite element method. The results have been used to investigate ratchetting mechanisms and to obtain ratchet strain data. The effects of complete

stress redistributions due to creep have also been investigated. The effects of material ratchetting on the behaviour of components were also investigated.

Comparison between experimental results, for a component made of lead alloy material, and finite element predictions, using simple and sophisticated material behaviour models, is also presented. The results show the improvement in accuracy which is possible if more realistic material behaviour models are used.

CONTENTS.

NOTATION AND ABBREVIATION.

A, A_1, A_2	Constants in creep law
D	plate stiffness
E	Young's modulus
FC	First compressive
FT	First tensile
LMFBR	Liquid Metal Fast Breeder Reactor
R	Boltzmann's constant
T	temperature
UTS	Ultimate Tensile Strength
Δ, d	increments, beam depth
h	hardening modulus (equation 2.16), tube thickness
r, q_o, q, t	constants for Goodman and Goodall model (Chapter 2, Chapter 5 and Appendix III)
t	time in creep law
t'	local thickness for the eccentric tube
u	plate deflection
E_{ijkl}	fourth order tensor which contains the elastic constants
S_{ij}	stress deviator tensor
α	(without subscripts) coefficient of linear expansion
α	(with subscripts) position of the centre of the yield surface
δ_{ij}	Kronecker delta
R_o	Outer radius
R_i	Inner radius

ε, γ	strain
σ, τ	stress
ν	Poisson's ratio
θ	angle, circumferential direction

Superscripts

c	creep
e	elastic
p	plastic
R	ratchet
T,t	total

Subscripts

ave	average
eff	effective
eq	equivalent
o	yield
R	range
s	saturation
t	thermal
xx, yy, zz	direct
xy	shear
r	radial
θ	hoop
rθ	shear

All other symbols are defined in the text where used.

CHAPTER 1

INTRODUCTION

Many components in chemical plant, conventional and nuclear power plants and aero engines are subjected to combinations of steady and cyclic mechanical and thermal loads. Under these conditions, the response of the components depends upon the severity of the loading. Under moderate loads, components may either behave elastically, or shakedown after a few cycles, having experienced permanent inelastic deformation. Under severe loading conditions, reverse plastic straining and/or incremental deformation (i.e. ratchetting) may occur. When the operating temperatures are high enough creep may also occur, which may exacerbate the ratchetting process.

The failure modes for components under the above loading conditions can be divided into three classifications (e.g. 1) namely:-

i) failure due to excessive deformation (usually as a result of ratchetting or creep) such that the component cannot function properly,

ii) failure due to buckling and

iii) failure due to rupture (caused by creep or fatigue or a combination of both creep and fatigue)

This thesis is mainly concerned with the analyses associated

with the first type of failure. In particular, ratchetting which can be the major contributor to the deformation of components subjected to severe loading, is studied. Failure due to ratchetting is a gradual process but if ratchetting is not restricted, incremental collapse will eventually occur. However, prior to incremental collapse, the component may fail due to excessive deformation. There are two ways of designing such components. Firstly, the components may be designed to operate within the shakedown region, i.e. ratchetting is avoided altogether. This type of design procedure prevents the possibility of incremental collapse. However, some inelastic deformation may be accumulated before shakedown occurs. In some cases this accumulated inelastic deformation may be too large for the components to function properly. Hence, design for shakedown is not necessarily an entirely satisfactory procedure. Also, cyclic plastic straining may occur and this may result in failure due to fatigue. Alternatively, components may be designed so that the deformation accumulated throughout the design life of the component is within a specified safe limit. This method is the more realistic, but the possibility of fatigue failure due to cyclic plastic straining must also be taken into account.

If the first option is adopted, the problem becomes that of determining the shakedown limit of the component. The assesment of deformation at the design stage is usually not necessary provided a sufficiently large factor of safety with respect to shakedown is imposed to ensure that the design is safe. The second option, on the other hand, requires that the

deformations (strains, curvature and/or deflections) are estimated or predicted at the initial design stage.

Whichever design route is taken, there are three main methods available to the designer. Firstly, experiments can be performed on either prototype or model components subjected to the loading conditions which would be experienced by the service component (e.g. 2,3 and 4). The components geometry and its loading need to be accurately modelled if this procedure is adopted. Experimentation and model testing are usually expensive. Secondly, design codes (1) can be used. However, the procedures are often restricted to simple components and loadings and their interpretation is not always unambiguous. Thirdly, analytical or computational methods can be used. For simple component geometries and loadings, closed form analytical solutions are available (see 5,6,7,8,9,10 and 11). Also, approximate bounding techniques are available for predicting the behaviour of components under cyclic loading conditions (i.e. 7,12 and 13). These techniques are based upon simple material behaviour model and sometimes, the mechanism of deformation needs to be assumed. These analytical and bounding techniques can sometimes produce unnecessarily conservative designs. For components with a more complicated geometries (such as those with stress raisers, imperfections etc.), complicated loading conditions (e.g. combination of steady and cyclic loading and operation above the creep threshold temperature) and complex material behaviour (real materials exhibit cyclic hardening, softening, relaxation and material ratchetting) closed form and

bounding techniques are difficult to perform. As an alternative, more sophisticated prediction methods such as the finite element method (e.g. 14,15,16 and 17) can be used. The finite element method is adopted here. Even though, in principle, it is possible to use the finite element method to predict the elastic-plastic-creep behaviour of any component subjected to any general loading conditions, major difficulties do arise.

Some of these are:-

i) The details of the loading histories are often unknown at the design stage. This problem could be overcome by considering the worst possible case.

ii) A relatively large number of elements may be required to model some component geometries. The computer storage and time requirements may therefore be prohibitive. However, with the current rate of development of computers, this problem will become less significant in the future.

iii) Accurate constitutive equations, for predicting the elastic-plastic-creep behaviour of materials, subjected to complex stress-strain-temperature-time histories do not exist. Unfortunately this is likely to be the situation for the forseeable future.

The main objectives of this project are:-

i) To identify and quantify the parameters which influence ratchetting and to determine the shakedown/ratchetting boundaries of some components,

ii) To study and classify the mechanism of ratchetting of components subjected to combined steady and cyclic, mechanical and thermal loads, with and without dwell periods during which creep occurs.

iii) To incorporate a more complex constitutive equations (18,19) into the finite element programs so that the effects of material ratchetting can be assessed by comparing predictions with experimental data.

In order to achieve objectives (i) and (ii), three components were used. The components used are concentric and eccentric tubes subjected to a steady internal pressure and cyclic linear through thickness temperature gradients and a circular plate clamped at its edges and subjected to steady transverse pressure and cyclic linear radial temperature distribution. The effects of creep on the behaviour of eccentric tubes and clamped circular plates are bounded by the 'no-creep' and 'complete redistribution' conditions.

Objective (iii) was achieved by using a uniform beam subjected to a steady axial mechanical load. Cyclic loading was applied to the beam by either applying linear through the depth

temperature variations or by applying fully reversed cyclic bending moments. The latter results were compared directly with experimental results (3).

A lot of time and effort was also devoted to developing the constitutive equations and the associated computer coding to allow the Goodman and Goodall (18,19) material ratchetting model to be used under multi-axial conditions. An entirely new subroutine for this model was written and existing relevant subroutines needed to be significantly modified. A detailed description of the model and its equations are given in Chapter 2 section 2.2.2.1 (B) (for the uniaxial case) and in Appendix III (for the multi-axial case). The program modifications are also described in detail in Appendix III.

The thesis is divided into 7 Chapters. Chapter 2 reviews the literature, with particular attention given to the material behaviour as observed experimentally and various models proposed to describe the experimental observations. The behaviour of components and prediction methods are also reviewed in Chapter 2. Chapters 3 and 4 present the finite element results obtained for the concentric and eccentric tubes and clamped circular plate with particular attention given to the mechanism of ratchetting. An elastic-perfectly-plastic material model was used in the analyses presented in Chapters 3 and 4. In Chapter 5 the behaviour of a uniform beam subjected to a steady axial load and cyclic fully reversed bending moment is described. The Goodman and Goodall (18) material ratchetting model was used in the calculations. The

necessary material constants for lead alloy were used. This allowed a direct comparison between experimental and finite element result to be made. Also in Chapter 5, results obtained for the behaviour of a uniform beam subjected to a steady axial load and cyclic linear through the depth temperature gradient are presented. The results for a linear kinematic hardening and Goodman and Goodall (18,19) material ratchetting model applicable to stainless steel, are compared. A general discussion and conclusion are given in Chapters 6 and 7 respectively.

CHAPTER 2

LITERATURE REVIEW

2.1 Introduction

As stated in Chapter 1, this thesis is concerned with methods of predicting failure of components due to excessive deformation. The review is, therefore restricted to literature directly related to this method of failure. The predictions accuracy depends on the accuracy with which the real material is modelled. For this reason, a great deal of attention is given to describing the experimentally observed material behaviour and the method by which it is modelled. This is described in section 2.2. In the remainder of this chapter, literature relating to the experimental observations of component behaviour and the methods of predicting component behaviour is reviewed.

2.2 Material Behaviour

All materials, including metals and metallic alloys, deform when subjected to stress. At low stress and temperature, the behaviour is elastic and the deformation is recoverable. When the stress is high, plastic deformation occurs in addition to the elastic deformation. The plastic deformation is not recoverable. Time dependent creep deformation may also occur when the temperature is high. For metals, creep may occur when the temperature is above about 0.3 of the absolute melting temperature. Generally creep and plastic deformation interact.

2.2.1 Experimental Observations.

2.2.1.1 Elastic-Plastic Behaviour.

(i) Monotonic Loading.

The behaviour of metals under monotonic loading has been extensively studied (20,18,21,22). The simplest, most common and important test is the tensile test in which a specimen having a uniform cross section is subjected to either increasing load or increasing deformation. A typical load/extension or stress/strain curve is shown in Fig 2.1. In the region OA, elastic deformation occurs and if the load is reduced to zero, the line AO is traced. The line OA is the elastic line with the modulus of elasticity E. When the stress is increased further, the strain is no longer linearly related to the stress. The curve AB is traced which departs from the elastic line OA. The point of departure is called the elastic limit and the stress at the point of departure is the yield stress of the material. Along AB the strain is increasing with increasing stress until point B is reached. From B to C, the stress decreases with increasing strain due to necking prior to failure at C. The maximum stress reached at B is called the ultimate tensile strength, UTS. The shape of the curve, the values of E, the yield stress and the UTS are the parameters which distinguish, in an engineering sense, one material from another. For the same material, the yield stress and UTS also depend on the temperature and the strain rate (22,23).

In the plastic range, the total strain is the sum of elastic strain and plastic strain. That is

$$\varepsilon^t = \varepsilon^e + \varepsilon^p \qquad 2.1$$

where elastic strain, ε^e , is given by Hooke's Law, σ/E (σ is the stress) and plastic strain, ε^p, is a function of stress $f(\sigma)$.

The stress strain curve with a smooth elastic plastic transition can be represented by

$$\varepsilon = \sigma/E + f(\sigma) \qquad 2.2$$

Ramberg and Osgood approximate the function $f(\sigma)$ by

$$f(\sigma) = K(\sigma/E)^n \qquad 2.3$$

where K and n are constants. Voce (24) used the concept of saturation stress and $f(\sigma)$ is approximated by

$$f(\sigma) = K\left(\frac{\sigma - \sigma_o}{\sigma_s - \sigma_o}\right)^n \qquad 2.4$$

where σ_s is the saturation stress

σ_o is the yield stress

K and n are constants.

Equation 2.4 fitted very well with the experimental data for copper alloy as shown in (24). More recently, Swindeman (21) applied Voce's (24) equation to describe large strain behaviour of 304 Stainless Steel. The results in reference (21) show that for 304 Stainless Steel, Voce's (24) equation fitted the data well for strain about .001 to the strain at failure.

Since engineering components are most likely to be subjected to a multi-axial stress state, tests using monotonic multi-axial stress systems are of practical relevance. However, it is necessary to define a relationship for multi-axial stress systems which is equivalent to the uniaxial state of stress. In multi-axial stress systems, stress,σ becomes stress tensor,σ_{ij}; and strain, ε, becomes strain tensor, ε_{ij}.

Equation 2.1 becomes

$$\varepsilon_{ij}^{T} = \varepsilon_{ij}^{e} + \varepsilon_{ij}^{p} \qquad 2.5$$

and elastic strain tensor is related to stress tensor by the generalized Hooke's Law:-

$$\varepsilon_{ij}^{e} = E_{ijkl}\,\sigma_{kl} \qquad 2.6$$

It is also often convenient to use the deviatoric stress tensor $S_{ij} = \sigma_{ij} - \frac{1}{3}\delta_{ij}\sigma_{kk}$ rather than the actual stress tensor. It is also necessary to define the yield conditions so that elastic-plastic analyses can be performed. Various theories were proposed and the most widely used are those due to Tresca and von-Mises. The von-Mises yield criterion which is used throughout this work, can be written as,

$$\sigma_{eq} = \sqrt{1.5 S_{ij} S_{ij}} \qquad 2.7$$

Equation2.7 defines the equivalent stress. The increment of the equivalent plastic strain can be defined in terms of the plastic strain increments.

That is

$$\Delta\varepsilon^{p}_{eq} = \sqrt{\frac{2}{3}\Delta\varepsilon^{p}_{ij}\Delta\varepsilon^{p}_{ij}} \qquad 2.8$$

Some tests on lead alloy material subjected to a monotonic and cyclic biaxial stresses were performed (e.g.in 20 and 25). When the equivalent stress is plotted against the equivalent plastic strain, the curves for different biaxiality ratios 1:1 and 2:1 show that the shapes of the curves are similar to the uniaxial case except that the effective yield stress reduces for the biaxial stress system. The equivalent stress versus equivalent plastic strain curves are shown here in Fig.2.2(i).

(ii) Cyclic Loading.

The response of material subjected to cyclic loading differs considerably from that obtained with monotonic loading. Cyclic loading can cause reverse plastic flow in the material and fatigue failure may occur. The behaviour of material subjected to cyclic loading is usually investigated by considering either strain or stress cycling. Different materials react differently when subjected to cyclic loading. In general, the yield stress of material reduces during reverse loading after an initial plastic deformation. Also, during stress reversal, an elastic range exists within which Hooke's Law can be applied. Fig.2.2(ii) shows the stress-strain behaviour during a load reversal. The yield stress during reversal, generally occurs at a point such as C which is in between σ_1 $-2\sigma_o$ and $-\sigma_o$ (see Fig.2.2(ii) for notation). The lower yield stress obtained during load reversal is due to the anisotropy induced during

previous plastic loading. This effect is called the Bauschinger effect. This behaviour is important in cyclic plasticity. Since the Bauschinger effect causes complications in the analysis of structural problems, it is often ignored or simplified in the developments of material behaviour models and constitutive equations for cyclic plasticity. Some tests on materials subjected to cyclic loading had been performed (e.g. in 20,18,3,26). At this stage, it is appropriate to describe certain phenomena such as cyclic hardening, cyclic softening, cyclic relaxation and material ratchetting, which are observed in materials subjected to cyclic loading.

(a) Cyclic Hardening and Cyclic Softening.

In a cyclically hardening material the resistance to deformation in the material increases with cycles. This means that the increment of strain reduces for the same stress increment. For stress and strain controlled cycling, the behaviours are shown in Figs.2.3(i) and 2.3(ii) respectively. The reverse occurs if the material cyclically softens. In this case, the resistance to deformation decreases with cycles and hence the increment of strain increases for the same increment of stress. Figs.2.4(i) and (ii) show the stress-strain curves for material that cyclically softens for stress and strain controlled cycling respectively. In real material, these are transient phenomena and usually stabilize.

(b) Cyclic Relaxation and Material Ratchetting.

If a material is cycled between two fixed strains with an offset mean strain, it is often observed that the peak stress reduces until a stable hysteresis loop, about a zero mean stress, is obtained. This is called cyclic relaxation. If the material cyclically hardens at the same time, the amount of the reduction of peak stress decreases and vice-versa.

If the material is cycled between two fixed stress levels, about a non-zero mean stress, it is often observed that there is an increment of strain with cycle. This is called material ratchetting or cyclic creep. For a non-cyclically hardening material, a steady increment of strain occurs. For a cyclically hardening material there is a reduction in ratchet strain before a steady ratchet strain per cycle is achieved.

The behaviour is illustrated, schematically, in Figs.2.5(i) and (ii) for cyclic relaxation and material ratchetting respectively.

These definitions of cyclic hardening and softening, cyclic relaxation and material ratchetting will be used throughout the rest of this thesis without further explanations.

Yahiaoui (3) performed a number of cyclic reverse plastic uniaxial tests on a lead alloy material. His tests included stress controlled cycling, strain controlled cycling with an enforced ratchet strain. Yahiaoui (3) observed that for a

strain range cycling about a zero mean strain, a stable loop was reached after the first cycle of loading. For cycling about a positive non-zero mean strain, it was also observed that the loop shifted downwards towards zero mean stress. A small softening effect occurs in the material. The stress strain loops obtained in a typical test are shown in Figs.2.6(i) and 2.6(ii). In stress controlled cycling tests, with non-zero mean stress, the results show that material ratchetting occurs. The ratchet strain reduces in the first cycle and after this a practically constant ratchet strain occurs. This is shown by the results in Fig.2.6(iii), these results are typical of those obtained from all of the lead alloy tests.

Hyde (20) performed cyclic plastic tests on lead alloy material similar to that used by Yahaioui (3) under biaxial loading. Biaxiality ratios of 1:1 and 2:1 were used. Most tests were performed with strain controlled cycling. The results were plotted using effective stress and effective plastic strain, taking into account the sign of the stresses. The shape of the curves were similar to those obtained for the uniaxial case. Hyde (20) also observed that stable loops occurred after the first cycle. In addition he also observed that the biaxial stress 'caused a reduction in the effective stress range compared with uniaxial data having the same effective stress range'. There was a small change in elastic strain range with cycle which has also been observed by Jhansale (27) for other materials.

The cyclic plastic behaviour of Type 316 Stainless Steel have been reported in reference (28). Cyclic hardening is significant in stainless steel. In the test conducted by Goodall (28), however, cyclic hardening was stabilized first by strain controlled cycling, without strain accumulation, before enforced ratchet strains were applied. The subsequent results obtained indicate that kinematic hardening occurs and the displacement of the hysteresis loops indicate that cyclic relaxation also occurs. For stress controlled cycling, material ratchetting would occur.

2.2.1.2 Creep Behaviour.

It is generally known that for temperatures above about $0.3\ T_m$ (where T_m is the absolute melting point of metals), time dependent creep behaviour occurs. When creep occurs, a structure continues to deform even under constant load. For many years the creep phenomenon has been investigated under both steady and variable loading conditions.

(i) Creep Under Steady Load.

Creep data is usually obtained from constant load or stress, uniaxial tests under constant temperature conditions. A typical creep curve is shown in Fig.2.7(i) where the total strain or deformation is plotted against time. Initially, there is a strain, ε_1 , obtained from the initial loading. If the stress is below the yield stress of the material, ε_1 consists of elastic strains. For stress above the yield stress

ε_1 is composed of elastic and plastic strains. After this, the strain continues to increase with time. The shape of the curve can be divided into three regions, as shown in Fig.2.7(i). These regions are:-

a) Primary creep. In this region the strain rate decreases.

b) Secondary creep. In this region the strain rate is constant.

c) Tertiary creep. In this region the strain rate increases until creep rupture occurs.

The amount of creep deformation obtained depends on both the stress and temperature at which the tests are conducted. Generally, creep strains are increased by increasing either stress levels or temperatures.

The creep curves obtained under isothermal condition but different stress levels are shown in Fig.2.7(ii). Fig.2.7(iii) shows the creep curves obtained at constant stress but at different temperatures. Experimental data for creep in metals under steady loads are reported in many papers and books (e.g. in 3,11,29).

(ii) Creep Under Variable Load.

As in the case of elastic plastic behaviour, the behaviour of creep under variable load is different from the behaviour under steady load. When the load is removed after creep has occurred, a phenomena known as creep recovery occurs (11,30).

On the other hand, when creep occurs at a constant strain, stress relaxation occurs (11,30). To illustrate these two behaviours, consider first, a material which is subjected to a stress σ_1 and allowed to creep for some time t_1 when creep strain ε^c was attained. The stress is then removed completely and the resulting strain is observed. Fig.2.8(i) shows the response of the material. From OAB, creep under steady load occurs. When the stress is removed at B, the elastic strains due to the stress σ_1 is recovered instantaneously. After this, the strain continues to drop in a time dependent manner until a steady value ε^{∞} is obtained as shown in Fig.2.8(i). The time dependent drop in strain is a result of the creep recovery which has occurred and ε^{∞} consists of plastic strain and non-recoverable creep strain. The second phenomenon occurs when the material is subjected to a stress σ and is then allowed to creep at a constant strain. Fig.2.8(ii) shows the response of the material. The stress reduces with time to a steady value. This phenomenon is referred to as a creep relaxation.

2.2.1.3 Creep/Plasticity Interaction.

Experiments have been conducted to investigate the effects of plastic strain on the creep behaviour (31,32,33,28). A number of tests were reported by Fessler, Hyde and Webster (31) on lead alloy models in which the specimens were loaded plastically before creep occurs. However, in some cases, part of the load was removed so that creep occurs at a stress which is below the yield stress. The creep curve was compared to the creep curve of the virgin material, without pre-plastic

straining, at the same stress level. The results show that at stress levels below the yield stress, the creep strain is reduced when plastic pre-strain occurs. Reverse creep may also occur for some period before forward creep reappears. When creep occurs at a stress level above yield, the creep strain rate was increased due to plastic pre-strain and the fracture times were reduced. Tests were also carried out (31) in which intermittent plastic strains were applied to a specimen under creep conditions. This is particularly relevant to power plant components during starting-up and shutting-down and under emergency conditions. Experiments to investigate creep/plasticity interaction in 316 Stainless Steel at high temperatures (at temperatures of 550^{o}C) are also in progress at Nottingham University (32). Early results indicate that when creep is interrupted by plastic strain, the creep strains are reduced compared to the creep strains under constant load creep test at the same stress levels. The tests are still in progress at the present time.

2.2.2 Material Behaviour Models.

2.2.2.1 Elastic Plastic Models.

A) Simple Models

a) Elastic-Perfectly-Plastic.

The most commonly used model for elastic plastic analysis is the elastic-perfectly-plastic model. The model assumes that there is no hardening at all. The model will predict an indefinite plastic strain whenever the applied stress is above

the yield stress. For strain controlled cycling, the model cannot describe hardening or softening, see Fig.2.9(i). Though it is simple and does not usually describe real material behaviour very accurately, the model can be used to accurately predict the load bearing capacity of some structures (34,35). The model is used here to analyse the mechanisms of ratchetting of components.

b) Isotropic Hardening.

In this model, hardening of the material is included. It is assumed that the yield range varies during plastic deformation. For a uniaxial stress case, the behaviour of a linear isotropic hardening model under strain controlled cycling is illustrated by Fig.2.9(ii). OAB represents the monotonic stress-strain curve with the initial yield stress at A. Reverse loading from B is represented by BCD and yield occurs at C. If the stress at B is σ_B and at C is σ_C, the model is based on the assumptions that

$$|\sigma_C| = |\sigma_B| \ .$$

Reloading from D will yield at E such that $|\sigma_E| = |\sigma_D|$ and so on. For continued cycling, an elastic behaviour will eventually be reached. Fig.2.9(iii) shows the behaviour under stress controlled conditions; elastic behaviour is reached after a reloading from the first plastic reversal. In the multi-axial case, the yield surface expands during plastic deformation without any translations in the stress space. For a von-Mises yield criterion, the changes in the yield surface, in the π -plane, are shown in Fig.2.9(iv). The points A and B in Fig.2.9(iv) corresponds to the points A and B in Figs.2.9(ii)

and 2.9(iii). The model does not describe the Bauschinger effect. The non-linearity in the plastic behaviour can be approximated by a number of linear segments. It does not show any softening behaviour and cannot predict material ratchetting.

c) Kinematic Hardening.

To include the Bauschinger effect with the hardening model, Prager (36) used the kinematic hardening model. In this model, the yield range remains constant at twice the yield stress of the material. For strain controlled cycling the uniaxial behaviour is shown in Fig.2.9(v). A steady state cyclic plastic loop is obtained after the first cycle. Fig.2.9(vi) shows the effect of stress controlled cycling for the model. Again a steady state loop is obtained after the first cycle. The phenomena of cyclic hardening, softening and material ratchetting cannot be represented using this model. In a multi-axial state, the yield surface translateS in stress space during plastic deformation, with the size of the surface remaining constant. For von-Mises yield criterion, the movement of the yield surface in the π-plane is shown in Fig.2.9(vii) and is denoted by the parameter $d\alpha_{ij}$. The direction of $d\alpha_{ij}$ is in the direction of the plastic strain increment during plastic deformation, which is normal to the yield surface. This rule has been modified by Ziegler (37). Ziegler (37) specified that the movement of the yield surface should be in the direction of the vector joining the centre of the yield surface and the current stress in the stress space.

Experimental data for the subsequent yield surfaces of annealed mild steel, obtained by Michno and Findley(38), indicate that the Ziegler model is more accurate than the Prager model.

So far, only the situation in which the plastic modulus remains constant during plastic deformation has been considered. To describe non-linear kinematic hardening model, Zienkiewicz et al (39) proposed the overlay model, which uses simple constitutive equations to describe complex material behaviour. In this model, the component is divided into a number of sub-elements having identical deformation but different material behaviour. This technique offers an unlimited material behaviour laws. The main difficulty is perhaps in choosing the number of sub-layers and their corresponding material behaviour to give the desired material behaviour. However, material ratchetting phenomena cannot be described.

B) Complex Models.

Since the simple models cannot describe material ratchetting, more complex models are required. To formulate constitutive equations for complex models, two basic ingredients are necessary. Firstly, the flow rule which relates the increments of plastic strains to the increments of stress. Secondly, the hardening rule which defines the movement of the loading surface during plastic deformation. The development of complex models (usually non-linear models) can be based on allowing the plastic modulus to change during plastic deformation. This

approach was followed by several investigators such as Mroz (40,41), Mroz et al (42), Eisenberg and Phillips (43), Green and Naghdi (44), Dafalias and Popov (45) and Goodman and Goodall (18). Mroz (40,41) and Mroz et al (42) used the concept of fields of work hardening. In the uniaxial case, the monotonic stress-strain curve is approximated by a number of linear segments as shown in Fig.2.10(i). The discontinuities of the uniaxial monotonic stress-strain curve are represented for convenience, by circles in multi-axial stress space, initially centred at the origin as shown in Fig.2.10(ii). The inner circle corresponds to the initial yield surface so that elastic changes only takes place in this circle. The yield surface is given by (40):-

$$f_o = f(\sigma_{ij}-\alpha_{ij}) - \sigma_o = 0 \qquad 2.9$$

where α_{ij} is the position of the centre of f_o with respect to the origin; initially, $\alpha_{ij} = 0$.

Other surfaces f_l and f_{l+1} (where l =1,2 etc.) are given by:-

$$f_l = f(\sigma_{ij} - \alpha^l_{ij}) - (\sigma^l_o) = 0 \qquad 2.10$$

and

$$f_{l+1} = f(\sigma_{ij} - \alpha^{l+1}_{ij}) - \sigma^{l+1}_o = 0 \qquad 2.11$$

with centres α^l_{ij} and α^{l+1}_{ij} respectively and radii σ^l_o and σ^{l+1}_o respectively. Also, initially α^l_{ij} and α^{l+1}_{ij} are zero.

For a loading path OABC of Fig.2.10(i) elastic changes occur along the path OA until the stress point is at A. From A to B,

the yield surface f_o moves together with the stress point until point B is reached on the surface, f_1. The plastic modulus during this process is given by the gradient of the line AB. From B to C, both surfaces f_o and f_1 move together with the stress point until point C is reached. The plastic modulus is now the gradient of the line BC. The surfaces are not allowed to intersect but only touch one another. When the stress point is at D the positions of the surfaces are shown in Fig.2.10(iii). For non-proportional loading histories such as PHK of Fig.2.10(iii), the motion of the yield surface $d\alpha_{ij}$ is in the direction PR until the stress point reaches H. The lines O_oP and O_1R are parallel where O_o and O_1 are the positions of the centre of surfaces f_o and f_1, respectively. O_oP is normal to f_o at P. The translation of the surface $d\alpha_{ij}$ is given mathematically by:-

$$d\alpha_{ij} = \frac{d\mu}{\sigma_o} \quad (\sigma_o^1 - \sigma_o)\sigma_{ij} - (\alpha_{ij}\sigma_o^1 - \alpha_{ij}^1 \sigma_o) \qquad 2.12$$

where $d\mu$ is a scalar determined from the condition that the stress point always lies on the yield surface. That is

$$(d\alpha_{ij} - d\sigma_{ij})\frac{\partial f_o}{\partial \sigma_{ij}} = 0 \qquad 2.13$$

The simultaneous translation, $d\alpha_{ij}^1$, of two surfaces, e.g. f_1 and f_{1+1}, can be generalised from equation 2.12 to give

$$d\alpha_{ij}^1 = \frac{d\mu}{\sigma_o^1} \quad ((\sigma_o^{1+1} - \sigma_o^1)\ \sigma_{ij}^1 - (\alpha_{ij}^1 \sigma_o^{1+1} - \alpha_{ij}^{1+1}\ \sigma_o^1)) \qquad 2.14$$

similarly, equation 2.13 can be written as:-

$$(d\alpha_{ij}^{1} - d\sigma_{ij})\frac{\partial f}{\partial \sigma_{ij}} = 0 \qquad 2.15$$

Equations 2.14 and 2.15 give the generalised translation rule. When the stress point reaches K, the relative positions of the surfaces are shown in Fig.2.10(iv). The hardening rule proposed by Mroz (40,41) is different from that of Prager (36) and Ziegler (37). In another paper Mroz et al (42) proposes a non-linear model in which the hardening modulus depends on the vector joining the stress point and the centre of the yield surface and plastic strain vector,

$$h = c(\varepsilon^{p}) - d(\varepsilon^{p})\frac{(S_{ij} - \alpha_{ij}).\varepsilon_{ij}^{p}}{\sigma_{o}} + \frac{2}{3}\sigma_{o} \qquad 2.16$$

where c and d are functions of total plastic strain ε^{p}. It was shown in reference (42) that the phenomena of material ratchetting can be qualitatively described by this model. The hardening rule (Equation 2.14) is different from that proposed by Prager (36) which is

$$d\alpha_{ij} = a d\varepsilon_{ij}^{p} \qquad 2.17$$

where a is a constant and from that due to Ziegler (37) which is

$$d\alpha_{ij} = (\sigma_{ij} - \alpha_{ij})d\phi \qquad 2.18$$

where $d\phi$ is a scalar constant determined also using equation 2.13 .

To describe the cyclic hardening, cyclic softening and material ratchetting phenomena, Jhansale (27,46) proposed a model based on the change of 'elastic' part of the stress-strain curve called the Yield Range Increment (YRI). In this model, during constant stress amplitude or strain amplitude cycling, the non-linear (plastic) part of the curve does not change in shape during consecutive cycles. Using this model, cyclic hardening and softening are associated with either an increase or decrease in the yield range. Experimental data for aluminium and steel are used to support the model in the uniaxial case (46). However, the model has not been extended to multi-axial stress cases. Material ratchetting can be predicted by using this model.

The concept of bounding surface in the stress space to describe cyclic behaviour of metals, was proposed by Dafalias and Popov (45) and Dafalias (47). In this model, the loading surface is enclosed by the bounding surface. When the loading surface touches (surfaces are not allowed to intersect) both surfaces move simultaneously. The plastic modulus depends on the relative positions of the two surfaces. On the bounding surface, the plastic modulus is a constant value. Fig.2.10(v) shows the uniaxial stress-strain curve. The bounding surfaces become line bounds X'X in the tensile direction and Y'Y in the compressive direction. The gradient of X'X and Y'Y are equal and the tangent modulus of the stress-strain curve approaches this value during loading. The model proposed in (45) was also generalised to multi-axial stress cases. The model is capable of describing cyclic

relaxation, cyclic hardening and material ratchetting for strain controlled and stress controlled cycling due to the changes in plastic moduli.

Goodman and Goodall (18) proposed a saturation stress model. The concept of saturation stress has also been used by Voce (24) and Swindeman (21). The model describes a non-linear kinematic hardening. It predicts a steady ratchet for cycling between a fixed stress level and non-zero mean stress. It is assumed that both hardening and softening mechanisms exist. The model incorporates both these mechanisms whereby the softening mechanism opposes the hardening mechanism. At a saturation stress, σ_s, the two mechanisms balance one another. The model was developed by Goodman and Goodall to describe the behaviour of 316 Stainless Steel.

Two functions U and V are used to describe hardening and softening mechanisms respectively so that monotonic and cyclic stress-strain curves can be described. The plastic strain during a monotonic loading is given, empirically, as:-

$$\varepsilon^p = (rU)^q V^t \qquad 2.19$$

where

$$U = \frac{\sigma - \sigma_o}{\sigma_s - \sigma_o} \qquad 2.20$$

$$V = \frac{\sigma_s - \sigma_o}{\sigma_s - \sigma} \qquad 2.21$$

In equation (2.19), r and t are material constants, but q is treated as a quasi -steady parameter for the purpose of differentation. Goodman and Goodall allows q to increase to

describe cyclic hardening. By differentiating equations (2.19) with respect to σ, the tangent plastic modulus, E^p, is obtained and

$$E^p = \frac{d\sigma}{d\varepsilon^p} = \frac{(\sigma_s - \sigma_o)\, U}{(rU)^q V^t (q + tUV)} \qquad 2.22$$

In modelling for a cyclic plasticity, it is required that the plastic modulus at a stress $\sigma=\sigma_m$ is equal to the plastic modulus at $\sigma=-\sigma_m$. That is symmetry of the stress-strain curve is preserved for cycling with a zero mean stress. σ_m is the maximum stress reached during the previous loading history. This condition could be written as

$$E^p)_{\sigma=\sigma_m} = E^p)_{\sigma=-\sigma_m} \qquad 2.23$$

For cyclic loading, it is necessary to define a parameter, n, such that

$$n = +1 \quad \text{for} \quad \delta\varepsilon^T \geqslant 0 \text{ (forward loading)} \qquad 2.24$$

$$\text{and} \quad n = -1 \quad \text{for} \quad \delta\varepsilon^T < 0 \text{ (reverse loading)} \qquad 2.25$$

where $\delta\varepsilon^T$ is the change in total strain during the current increment. Equations 2.24 and 2.25 imply that forward loading occurs if n is positive, reverse loading if n is less than zero and neutral loading for n=0. The functions U and V depends on whether the current stress, σ , is greater or less than the maximum stress σ_m . The following expressions are used:-

$$U = \frac{\sigma - n\sigma_o}{\sigma_s - \sigma_o} \qquad \text{for} \quad n\sigma \geqslant \sigma_m \qquad 2.26$$

or

$$U = \frac{1}{2}\left|\frac{\sigma - n\sigma_o - \alpha_k}{\sigma_s - \sigma_o}\right| \quad \text{for} \quad n\sigma < \sigma_m \qquad 2.27$$

and

$$V = \left|\frac{\sigma_s - \sigma_o}{n\sigma_s - \sigma}\right| \qquad \text{for} \quad n\sigma \geqslant 0 \qquad 2.28$$

or

$$V = \left|\frac{\sigma_s - \sigma_o}{\sigma_s - \sigma}\right| \qquad \text{for } n\sigma < 0 \qquad 2.29$$

A factor of 1/2 is introduced in equation 2.27 to satisfy the condition given by equation 2.23. The quantity α_k is only updated whenever a reversal of plastic straining occurs and is given by

$$\alpha_k = \sigma - n\sigma_o \qquad 2.30$$

The subsequent yield condition during cyclic loading become

$$|\sigma - \alpha_k| = \sigma_o \qquad 2.31$$

since a kinematic hardening is assumed. The maximum stress reached during the previous loading history, σ_m, is updated when the current stress is above σ_m, that is

$$\sigma_m = |\sigma| \quad \text{for} \quad |\sigma| \geqslant \sigma_m \qquad 2.32$$

These formulations indicate that the previous loading history influences the evolution of the cyclic plastic stress-strain curves of the material. The significance of σ_m will become

important in the development of the model in multi-axial stress space given in Appendix III.

The effect of cycling between two stress levels, σ_1 and σ_2, with a non-zero mean stress is shown in Fig.2.10(vi). A previous loading brought the material to a state at P_o. From P_o, unloading occurs to a stress σ_2 followed by reloading to a stress level at σ_1. With respect to σ_s, the loop is not symmetric. The compressive branch of the plastic stress strain curve is steeper than the tensile branch. Reloading from P_1 to the same strain as at P_o results in a reduction in stress by an amount $\delta\sigma$ as shown in Fig.2.10(vi). For a strain controlled cycling with a fixed strain range and a strain offset, this represents a stress relaxation. If reloading to the same stress σ_1, occurs, the stress-strain curve continues to the point P_3 giving a ratchet strain ε^R. For cycling about a non-zero mean stress and a fixed stress range, σ_R, this corresponds to material ratchetting.

The plastic strain increment $\Delta\varepsilon^p$ for this special case is simply given by:-

$$\Delta\varepsilon^p = \frac{\Delta\sigma}{E^p} \qquad 2.33$$

where E^p is the plastic modulus from equation 2.22 calculated using the value of stress at the beginning of the current increment. Cyclic hardening is denoted by an increase in q from an initial value of q_o. Goodman and Goodall (18) suggested that the variation of q depends on the cyclic plastic

strain path, P*, according to the relation

$$q = q_o \lg(10 + H \lg(1 + 100p^*)) \qquad 2.34$$

where

$$p^* = \Sigma \left|d\epsilon^p\right| - \left|\epsilon^p\right| \qquad 2.35$$

and H is the material hardening constant.

Goodman and Goodall (18) described the model in the uniaxial stress case. An attempt has also been made to extend the model for use in the multi-axial stress systems and non-proportional loading (19). However, in practice there were problems associated with this multi-axial formulation and further developments were necessary. The development of the model equations for multi-axial stress systems and general loading conditions are described in Appendix III. Also included in Appendix III is a method for determining the necessary material constants and illustrative results obtained for simple, non-proportional, biaxial stress case.

2.2.2.2 Creep.

Uniaxial creep curves, obtained under constant load conditions, as shown in Fig.2.7(i), can be represented by an equation of the form

$$\epsilon^c = F(\sigma, T, t) \qquad 2.36$$

where σ is the stress

T is the absolute temperature and

t is the time

If the effects of stress, temperature and time are assumed to be separable, then Equation 2.36 can be expressed in the form

$$\varepsilon^c = F_1(\sigma)F_2(T)F_3(t) \qquad 2.37$$

and $F_1(\sigma)$ is a function of stress only.

$F_2(T)$ is a function of temperature only and

$F_3(t)$ is only a function of time.

A number of different functions of stress, temperature and time have been suggested (e.g. 11,30). The most commonly used creep law is the combination of Norton's stress function and Bailey's time function (11,30). The Norton-Bailey creep law can be expressed as

$$\varepsilon^c = A_1\sigma^n t^m \qquad 2.38$$

where A_1, n and m are material constants.

To include the effect of temperature, Dorn (30) suggested a separate temperature function of the form

$$F_2(T) = A_2 e^{(-Q/RT)} \qquad 2.39$$

Hence combining equations 2.38 and 2.39 gives the Norton-Bailey-Dorn creep law which can be expressed as

$$\varepsilon^c = A\sigma^n t^m e^{(-Q/RT)} \qquad 2.40$$

and A,n,m and Q are material constants. An alternative to Norton stress function is a 'sinh law' proposed by

McVetty (30). This could be combined with Bailey's time function to give the following creep law:-

$$\varepsilon^c = A_3 \sinh(\sigma/\sigma_o) t^m \qquad 2.41$$

where A_3, σ_o and m are constants. The values of m can be used to model the different parts of the creep curve, namely,

m < 1 primary creep

m = 1 secondary creep and

m > 1 tertiary creep.

Most creep curves are obtained at constant load. However, during creep, the stresses in the structure often change. To cope with the resulting changes in stress, three laws are usually used (22,11,30). Firstly, the time hardening law which assumes that the creep rate of the material depends on the current stress and the time. Secondly, the strain hardening law which assumes that the creep rate depends on the current stress and the current creep strain. Finally, a law which is intermediate between the time hardening and strain hardening laws. This is known as the combined law (30) or the life-fraction law (22). Overall, the strain hardening law appears to give the best fit to experimental data.

2.2.2.3 Creep-Plasticity Interaction Model.

The effects of plastic strains on the subsequent creep behaviour as observed experimentally, were reviewed in section 2.2.1.3. The results indicate that creep behaviour can be

affected by either prior plastic strain or intermittant plastic strain, i.e. some form of interaction exists between creep and plasticity. The present commonly used constitutive equations do not include such interaction effects. Modelling the interaction between creep and plasticity has, however, been the subject of recent research by a small number of investigators (48,49,50).

Since creep is time dependent, Krempl (51) argued that equation of state approach is not particularly suitable. In particular equations of state cannot hold if during loading there is a change in material structure (51). During loading, unloading and reloading or cyclic loading, changes in material structure due to slip processes during deformation, do occur. Krempl (52) and Liu (48) have proposed that strain rates can be obtained from a non-linear differential equation of the form

$$m(\sigma-\sigma_n,\varepsilon-\varepsilon_n,M_\alpha,M_o)\frac{d\varepsilon}{dt} + g(\varepsilon-\varepsilon_n,M_\alpha,M_o) =$$

$$\sigma-\sigma_n + k(\sigma-\sigma_n,\varepsilon-\varepsilon_n,M_\alpha,M_o)\frac{d\sigma}{dt} \qquad 2.42$$

where σ, ε, and t are the stress, strain and time respectively. σ_n, ε_n, M_α and M_o are the values stored for history dependence. By choosing suitable functions for m, g and k, the equation could be used to model creep and plasticity behaviour without decomposing the total strain into elastic and inelastic components. The results indicated that an accurate prediction was obtained. The procedure was not applied to situations where creep occurs. Miller (49,50) developed the creep-plasticity interaction model from a unified standpoint. Miller (49) proposed the rate of inelastic strain (plastic plus

creep), $\dot{\varepsilon}$, in the unified model of the form:-

$$\dot{\varepsilon} = f\left[\frac{\sigma-R}{D}\right] \qquad 2.43$$

In equation 2.43,σ is the applied stress. D is the variable which represent the isotropic hardening properties. Miller (49), describes D as the characteristic drag stress and R as the 'rest stress'. The development of the model involved the determination of a suitable function, f, and the form of variables D and R so that the behaviour of creep and plasticity could be predicted. D and R depend on the entire previous deformation history. The model has been used to simulate tensile tests, strain sensitivity tests, creep, strain controlled cycling and creep-fatigue interaction (50). The qualitative agreements was generally good and Miller (50) recommended that quantitative improvements should be pursued.

The development of creep/plasticity interaction models is at an early stage and research such as that described above, particularly the unified approach, is of significance and needs to be explored further.

2.3 Component Behaviour.

The behaviour of components subjected to applied load depends on the nature of loading (e.g. monotonic, cyclic or combination of steady and cyclic) and the operating conditions (e.g. at temperatures below and above the creep threshold).

Under monotonic loading, the behaviour is elastic if the stresses everywhere in the component are below the yield stress of the material and if temperatures are below the creep range. At temperatures above the creep threshold, elastic-creep behaviour occurs which could lead to creep rupture. For stresses above the yield stress, elastic, plastic and creep deformation may occur. Under monotonically increasing load, plastic collapse will eventually occur. This problem has been exhaustively studied (e.g. in 53,54,34 and 35).

The loadings which are most likely to be encountered in practical situations are the combination of steady and cyclic load. Under these conditions, the following response could occur:-

a) Elastic.

In this case, the stresses at every point in the structure are below the yield stress at any instant. A recoverable elastic deformation is obtained.

b) Shakedown.

The stresses in some parts of the structure are above the yield stress during the transient cycles. Increments of inelastic deformation occur during these transient cycles and at the same time, residual stresses develop in the structure. After the transient behaviour, a situation arises when in the subsequent cycles of loading, only elastic changes of stress occurs. When this happens, there is no increment of deformation in the structure and complete shakedown occurs.

c) Cyclic Plasticity.

In this case, plastic yielding occurs in the structure which produces an increment of plastic strain in one half cycle and an equal but opposite plastic strain in the other half cycle. The net increment of plastic strain over a cycle is zero. Consequently, the structure does not suffer incremental deformation but in some parts of the structure, the material undergoes cyclic plastic straining. The behaviour could lead to failure by fatigue.

d) Ratchetting.

In this situation, the structure deforms incrementally in each cycle of applied load. This results in an increment of inelastic deformation during each cycle. If this is allowed to continue indefinitely, collapse will occur. However, in the process, the structure may cease to function properly due to excessive deformation.

2.3.1 Experimental Observation.

2.3.1.1 Below the Creep Threshold.

A number of investigators have obtained experimental data for the behaviour of components subjected to combined steady and cyclic loads below the creep range (e.g. 3,4,55). The loads applied to the components should be such that either the mean operating temperatures are below those which would cause creep

or the mean sustained stresses are below yield stress so that cold creep does not occur. Most of the experiments however, have been performed such that the dwell periods between each cycle of load were 'short' (i.e. rapid cycling), so that the effects of creep are insignificant (4).

The behaviour of a two bar structure such as that shown in Fig.2.11(i) has been the subject of interest of a number of investigators (56,57,5,58,7,10). Some workers extended the structure to a 3 and multi-bar structures (59,9). In terms of structural behaviour the behaviour of 2-bar structure is not significantly different from the behaviour of a 3-bar structure. For this reason only the behaviour of a two-bar structure investigated by Ponter (7) is described here.

In Ponter's work (7), the structure shown in Fig.2.11(i) was made of copper; the bars were of different lengths. The structure was subjected to a steady axial load and cyclic temperature variations were applied to one of the bars. Both bars suffered incremental deformation in the direction of the mechanical load (incremental elongation for tensile mechanical load). The rate of accumulation was found to decrease with cycles during the first few cycles. Afterwards, a steady ratchet state was achieved. Ponter (7) argued that the steady state ratchet strains were entirely due to material ratchetting. The effects of the magnitude of the mechanical and thermal load combinations were also investigated by Ponter (7). The effect of a stress concentration was simulated by having bars of unequal lengths and cross-sectional areas.

In general, the ratchet strains increased with increasing mechanical load. Elastic shakedown and ratchetting behaviours were also observed depending on the magnitudes of the applied loads.

The behaviour of thin and thick tubes subjected to a steady mechanical load such as axial load or an internal pressure, and cyclic thermal loads has also recieved considerable attention (8,60,61,10,16,3,4,62,63,64,65,66,67).

Yahiaoui (3) and Hyde (4) performed ratchetting tests on a flanged tube component made of a lead alloy. The components contains a plain tube section and a fillet (stress concentration region). The ratchetting behaviour of the component when subjected to a steady axial load and cyclic transient thermal loading was studied. The thermal load was applied by varying the temperature of water flowing through the bore. Results were obtained for different values of mean axial stress. The results indicate that the ratchet strains in the plain section and in the fillet increase with an increase in either the axial or the thermal load. The ratchet strains in the fillet region (i.e. region of stress concentration) and in the plain tube region reduced with cycle number and reached a steady value after 15 to 20 cycles.

Yahiaoui (3) and Megahed et al (55) peformed tests on beams subjected to a steady axial load and cyclic bending moment. In (3), the beam contains a uniform section (shank) and a stress concentration region (a fillet). A load controlled cyclic

mechanical bending moment was applied. The beam was made of lead alloy material. This test is of particular relevance in the present work when the effect of material ratchetting on the finite element prediction is investigated. A number of load combinations were used. In general, increasing any of the loads results in an increase in ratchet strains. Megahed et al (55) on the other hand investigated the behaviour of a uniform beam, made of copper; cyclic curvature controlled tests were performed. The material used in (3) and (55) exhibit material ratchetting but cyclic hardening is less significant in the lead alloy (3) compared to the copper (55). The results also indicated that increasing the magnitude of the applied load causes an increase in the steady state ratchet strain. For the case of the lead alloy beam (3) a steady ratchet strain was achieved after about ten cycles of bending moment but for copper (55) about one hundred cycles were required. Megahed (55) argued that the transient ratchetting was due to structural ratchetting and the steady state ratchetting was caused by material ratchetting.

2.3.1.2 Above the Creep Threshold.

Practical engineering components often operate at high temperatures, typically above the creep threshold. Also the time between thermal cycles is usually long. Therefore, significant creep strains are inevitable, particularly because these long dwell periods often occur when the plant is under operating conditions. Experiments to simulate rapid cycle conditions in reality require finite cycle times and

consequently they may include small creep strains. It is therefore difficult to exclude completely creep from experimental ratchetting tests. The most practical way of interpretting the experimental results is to try to quantify the effects of the creep dwell period on the component behaviour. The effect of creep on the behaviour of components has been studied by a number of workers (e.g. 2,68,3,69,4,23,62,63,70,65,66,67).

Experimental investigation of 2 and 3 bar structures has received considerable attention (2,23,69). Creep ratchetting tests on a 2-bar structure made of aluminium specimen was investigated by Ponter et al (69). The structure shown in Fig.2.11(i) was subjected to a steady mechanical load P and cyclic temperature variations. The results were compared with the theoretical predictions using various constitutive relationship. In another paper, Megahed and Ponter (71) reported tests on a 2-bar structure made of copper. The tests were conducted such that bar 1 (see Fig.2.11(i) for notation) was heated and cooled during a cycle whereas bar 2 remained at a constant temperature. Dwell periods were allowed both during isothermal and non-isothermal conditions. The mechanical load, area ratio and dwell period were the test parameters. The results showed that the stress amplitude in bar 2 increased initially and subsequently reached a constant value. The strain increment reduced with cycle number to a steady value. The steady state ratchet strains increased with increasing dwell period. Following the same approach as in (69), Megahed et al (23) studied the behaviour of a 2-bar structure

made of 316 Stainless Steel. Apart from the numerical values obtained, the observed behaviour was similar to that for aluminium (69). The load condition imposed in the 316 Stainless Steel tests (23) however allowed the interactions between creep and plasticity to be studied. Ainsworth (2) investigated the behaviour of a 316 Stainless Steel 3-bar structure subjected to a steady axial load and cyclic thermal load in the creep range. The effect of creep is similar to those observed by Ponter (69) and Megahed (23).

Many authors (3,4,62,63,65,66) have investigated the effect of creep on the behaviour of tubes subjected to a steady mechanical and cyclic thermal loads. Yahiaoui (3), Hyde et al (4,65,66) have reported tests on ratchetting of tubes. The component geometry and loading has already been described in the previous section. In the experimental investigation of shouldered tube component (66), the effect of creep dwell period is to increase the ratchet strains at low mean axial stresses. However, for the load combination considered in the experimental study of flanged tube component (3,4), the effect of increasing the creep dwell period, reduced the ratchet strains.

Corum et al (62) performed tests on a stainless steel pipe subjected to a steady internal pressure and cyclic thermal loading. The thermal loading was induced by intermittently flowing liquid sodium through the bore. Dwell periods were allowed to occur at high temperature to simulate creep during on-power conditions. The response of the pipe indicates that

substantial ratchetting due to creep and plastic strains occurs but the incremental deformation decreases with increasing cycles.

Yamamoto et al (63) performed tests on a tube made of 304 Stainless Steel subjected to a steady mechanical axial load and cyclic thermal load. The thermal load was applied using liquid sodium flowing through the bore.

Some tests were also performed for which both the steady and cyclic loads were mechanical. Yahiaoui (3) investigated the behaviour of beams subjected to steady tension and cyclic mechanical bending moment. Cousseran et al (70) investigated the behaviour of a thin tube subjected to a steady axial load and cyclic torsion. Creep was allowed to occur between each of the cycles. Cousseran et al (70) devised a technique whereby the creep ratchetting data from various tests for different materials could be correlated. The method involved defining two parameters called the efficiency index,V, and secondary stress ratio, SR. When the data, obtained from various experiments and different materials, were plotted on an SR-V diagram (called the efficiency diagram) the points lie within a narrow band as shown in Fig.2.11(ii). On this diagram the data is relatively insensitive to the detail of the material behaviour. The secondary stress ratio SR is defined as follows

$$SR = \Delta Q/(P+\Delta Q) \qquad 2.44$$

where ΔQ is the secondary stress range and P is the primary stress.

The efficiency index V is defined by

$$V = P/P_{eff} \qquad 2.45$$

where P_{eff} is the effective stress defined as the equivalent primary stress that give the same inelastic strain as the combined primary and secondary stresses for a ratchetting test over the same duration of test.

2.3.2 Prediction Methods.

2.3.2.1 Below the Creep Range.

In the study of ratchetting in engineering components it is first necessary to have a method of predicting the combinations of load which would cause ratchetting to occur. The normal approach is, initially, to assume that the material is elastic-perfectly-plastic and the effects of creep are ignored. For simple structures, such as 2 or 3-bar structures, subjected to axial load and temperature variation and uniform beam subjected to axial load and through the depth temperature distribution, complete analytical solutions can be obtained. Some components, such as plain tubes subjected to an internal pressure and through thickness temperature distribution, can be simplified to a beam so that a complete analysis could be made. From these analyses the effects of hardening could also be assessed. For more complicated structures, complete analytical solutions cannot be performed and other techniques and numerical methods (e.g.the finite element method) had to be used.

Due to its simplicity, the behaviour of a 2-bar structure has recieved a considerable attention by several authors (56,57,5,58,66). Parkes (56) used a 2-bar structure to analyse the incremental deformation of an aircraft wing. In another paper Parkes (57) investigated the effect of the variations of yield stress with temperature on the behaviour of a 2 bar structure subjected to thermal loadings only. It was found that ratchetting could occur even though there was no applied mechanical load (57). Burgreen (5) investigated the behaviour of a 2-bar structure subjected to a steady axial load and cyclic thermal load. A perfectly plastic material with the yield stress independent of temperature was used. Depending on the magnitudes of the loads, the structure may behave either purely elastically, shakedown to an elastic behaviour after an increment of plastic deformation, cyclic plasticity on one bar without structural incremental deformation or suffer incremental deformation. Megahed (6) and Ponter (7) also observed similar behaviour. These different behaviours could be distinguished by using an interaction diagram such as Fig.2.12(i) for a perfectly plastic material and bars with identical sizes. Similar diagrams can be obtained when the bars have different lengths and areas. Miller (59), Mulcahy (58) and Megahed (6), investigated the effects of material hardening on the structural behaviour. Both linear kinematic hardening and linear isotropic hardening models give bounded ratchet strains. For a linear kinematic hardening model, the steady state behaviour is either elastic shakedown or cyclic plasticity without ratchetting. For a linear isotropic hardening model, the steady state behaviour is always elastic after transient ratchetting behaviour.

A significant contribution in this field is that due to Bree (8) who predicted the behaviour of a nuclear fuel can subjected to steady internal pressure and cyclic through thickness temperature distribution. The can is modelled using an element subjected to a uniaxial stress, σ_p , and cyclic linear through thickness temperature gradient such that the maximum elastic thermal stress in the element is σ_t. The material was assumed to be elastic-perfectly-plastic with the yield stress initially independent of temperature. Fig.2.12(ii) shows the 'Bree' diagram for the behaviour of the fuel can. The diagram subdivides into several regions. Purely elastic response occurs in the E (see Fig.2.12(ii) for notation) region, in the S_1 and S_2 regions, elastic shakedown occurs, cyclic plastic straining occurs on P region and ratchetting occurs in the R_1 and R_2 regions. These regions are separated by boundaries which are also shown in Fig.2.12(ii). Also only tensile yielding occurs in the regions with suffix 1 and tensile and compressive yielding occurs in regions with suffix 2. In the ratchetting regions, the ratchet strain per cycle ε^R can be calculated. In the R_1 region,

$$\varepsilon^R = \frac{2\sigma_t}{E} \left(1 - 2\sqrt{(\sigma_o/\sigma_t - \sigma_p/\sigma_t)} \right) \qquad 2.46$$

where E is the Young's modulus

and in the R_2 region

$$\varepsilon^R = \frac{2\sigma_t}{E} \left(\sigma_p/\sigma_o - \sigma_o/\sigma_t \right) \qquad 2.47$$

The effects of changes of yield stress with temperatures and

the effects of a linear kinematic hardening model were also investigated by Bree (8). The shakedown ratchetting boundaries are given by

$$\sigma_p / \sigma_o + \frac{1}{4} \sigma_t / \sigma_o = 1 \text{ for } \sigma_t / \sigma_o \leqslant 2.0 \qquad 2.48$$

$$\frac{\sigma_p}{\sigma_o} \cdot \frac{\sigma_t}{\sigma_o} = 1 \quad \text{for} \quad \sigma_t / \sigma_o > 2.0 \qquad 2.49$$

Burgreen (5) obtained analytical solutions for a beam subjected to a steady axial load and a cyclic bending moment. An elastic-perfectly-plastic material behaviour model was used. The general behaviour is similar to that of a 2-bar structure and the Bree tube described above, namely, depending on the applied load, elastic, shakedown, ratchetting and collapse can occur. The equivalent Bree diagram is shown in Fig.2.12(iii) known as the Burgreen diagram. Unlike the Bree diagram of Fig.2.12(ii), the ratchetting/collapse boundary is closed because both the axial load and the bending moment, by themselves can cause the component to collapse. The narrowness of the ratchetting regime indicate that the behaviour is very sensitive to changes in the applied loads.

Knowledge of the shakedown/ratchetting boundary is particularly important during the initial design stage of components, in which the possibility of ratchetting exists. Several methods are used to determine shakedown/ratchetting boundaries. The solutions for the 2-bar structure (shown in Fig.2.12(i)), for the simplified model for the fuel can (shown in Fig.2.12(ii)) and for the beam shown in Fig.2.12(iii) are exact solutions. Many other components are, however, too complicated for exact solutions to be obtained and approximate methods are sometimes

a possible alternative. Melan (72) proposed the Lower Bound Shakedown Theorem. Symonds (73) later applied the Melan's (72) theorems to obtain the boundary for a circular bar subjected to an axial force and cyclic torsional moment between given limits. Melan's theorem (72) generally gives a boundary which is conservative and gives a safe boundary against ratchetting. The apparent setback is that it can be too conservative and hence the material is not exploited to its full advantage. The attention is now focussed on the Upper Bound Shakedown Theorem proposed by Koiter (12) based on the principle of virtual work. Ponter (7) recently extended the theorem to include cases where cyclic plasticity occur. This was used to determine the shakedown/ratchetting boundary for a number of components. For a 2-bar structure and Bree tube, the boundary obtained by Ponter (7) is identical to the boundary obtained from the closed form analytical solutions. In solving the problem of a simply supported circular plate subjected to a steady transverse pressure and cyclic linear radial temperature gradient, Ponter (7) states that the mechanism of ratchetting at low thermal load is different from the mechanism at high thermal load. From the assumed mechanism of ratchetting deformations shown in Fig.2.12(iv) and 2.12.(v) the Upper Bound Shakedown Theorem were applied. The shakedown/ratchetting boundaries are shown in Fig.2.12(vi).

For structures with complicated shapes and stress distributions, e.g. structures with stress concentrations, closed form analytical solutions and bounding techniques can be difficult or impossible to apply. The alternative is to use a

numerical computer method. Dwivedi et al (17), Hyde (15), Hardy (16) and Hyde et al (33,65,67) used the finite element method. Hyde (15) investigated the behaviour of a circular plate with a radially movable, direction fixed edge, subjected to a combination of membrane stress, transverse pressure and cyclic through thickness temperature variations. Hyde (15) found that for no transverse pressure, a Bree (8) type of mechanism exists and the ratchet strain per cycle is approximately twice that predicted by Bree's equation for a tube. A perfectly-plastic material behaviour model was assumed by Hyde (15). When a transverse pressure is applied the behaviour differed. The mechanism of ratchetting for the plate used by Hyde (15) but without the membrane stress was investigated by Hardy (16).

Dawson et al (61) and Hardy (16) investigated the elasto-plastic behaviour of shouldered and flanged tubes subjected to an axial load and cyclic transient through thickness temperatures. Due to the changes in section a region of stress concentration occurs. In reference (61), the finite element results were compared directly to the experimental result on lead alloy material. The material data for a lead alloy was used in (61) and (16). A linear hardening model was used by Dawson et al (61) whilst Hardy (16) assumed elastic-perfectly-plastic, linear kinematic hardening and linear isotropic hardening models. The results were also compared to the experimental values. A detailed analysis of a uniform beam subjected to an axial load and cyclic bending moment by Hardy (16) is of particular relevance to the present

work. Here, a direct detailed comparison was made between finite element predictions using elastic-perfectly-plastic, linear kinematic hardening and linear isotropic hardening assumption. For the load combinations considered, perfectly plastic material behaviour gave an overestimate of the ratchet strains whilst the other models gave underestimates. Hardy (16) argued that the poor prediction was due to the inability of the material models used to predict the material ratchetting phenomenon which is a characteristic of the lead alloy material.

Several general points have emerged from the review of the methods of predicting component ratchetting behaviour. Firstly, the exact solutions can be obtained only for simple component geometries and loadings. Secondly, the bounding techniques can be used for some components assuming an idealised material behaviour model. The results however can sometimes be too conservative if the Lower Bound Theorem is used. The Upper Bound Theorem can give the'exact' ratchetting boundary, if the mechanism of ratchetting deformation is accurately assumed. Finally, the finite element method is unlimited in its application. Provided the material behaviour model resembles the true material behaviour, and sufficient computing capacity exists, good predictions are obtained.

2.3.2.2 Above the Creep Threshold.

The effects of creep on the ratchetting behaviour of components have been considered by some authors

(e.g. 8,10,11,16,30,23,74,75,33,70,55,65,71,69). The behaviour, in general, is time dependent even though at complete stress redistribution state, the behaviour is independent of time. As a result, a time history analysis is required which could be both time consuming and expensive. Therefore there is a need for approximate, but reasonably accurate methods of analysis. This section is mainly concerned with both the approximate and complete time history analyses.

Ainsworth (76) derived upper bounds for the work, displacements and creep energy dissipation of structures subjected to cyclic loading and creep. The analysis was restricted to a stationary cyclic state. In a further paper (77) the bounds were applied to structures subjected to steady mechanical loads and cyclic strains. A beam subjected to a steady axial load and cyclic curvature, a thin walled tube subjected to a steady axial stress and internal pressure and cyclic through thickness temperature and a 2-bar structure subjected to a steady axial load and cyclic variation in temperatures were analysed. The results were compared with those obtained from more detailed calculations; generally good agreement was obtained. The bounding solutions in (76) were later extended to include the behaviour which occurs before the cyclic stationary state is achieved (78) and the bound was subsequently applied to predict the deformation bounds for components subjected to a steady and cyclic loads.

An upper bound for the accumulation of creep and plastic strains for the Bree problem (8) was obtained by O'Donnell and

Porowski (79). The load conditions covered (79) correspond to S_1 and S_2 and P regions of Fig.2.12(ii). In these regions, some parts of the material near the tube mid-thickness, does not experience plastic straining (i.e. a so-called elastic core exists). The maximum stress in the elastic core was used to bound the accumulated strains. This was possible because the stresses in the elastic core is uniform through the thickness and also for the present problem the total strain is uniform through the whole thickness. Hence, any point can be taken as being representative of the creep deformation of the whole section.

An excellent review of bounding techniques used in shakedown and ratchetting analysis at elevated temperatures is given by Leckie (80). Shakedown and ratchetting theorems below and above the creep threshold were discussed. In particular, for the case of variable loading it was deduced that the effects of plasticity can be considered small for load combination within n/(n+1) of the shakedown load (80); n is the creep stress index. For loads in excess of this value, the effects of plasticity could be significant.

Hardy (16) and Hyde et al (75,33,65,67) obtained solutions for creeping structures using the finite element method. Results of the prediction were compared to experimental values. In the finite element analysis an idealised material behaviour model was used and no creep/plasticity interaction was assumed. The effect of stress concentration was also assessed. Reasonably good agreement between experimental and finite element results

was obtained considering that very simple material behaviour models were assumed.

2.4 Conclusion.

Literature relating to the ratchetting behaviour and ratchetting mechanisms for components with complicated loadings and/or geometries, particularly components with stress concentrations, and the effects of creep on ratchetting is scarce. Current material behaviour models do not adequately describe material behaviour, particularly cyclic hardening, cyclic relaxation, material ratchetting and plasticity/creep interaction are not well described.

The results contained in this thesis are intended to fill some of the gaps in the literature and to assist with the understanding of the ratchetting mechanisms. Also, more specifically, the effect of creep on ratchetting is illustrated (for the complete redistribution case) by use of the eccentric tube and clamped circular plate and the effect of material ratchetting on the predicted ratchet strains is illustrated for a simple beam component. The beam is subjected to a steady, axial mechanical load and cyclic, fully reversed bending moments. The results obtained for a tube subjected to a steady, axial, mechanical load and cyclic torsion are also presented to show that material ratchetting can be included for components with non-proportional, multi-axial stress systems.

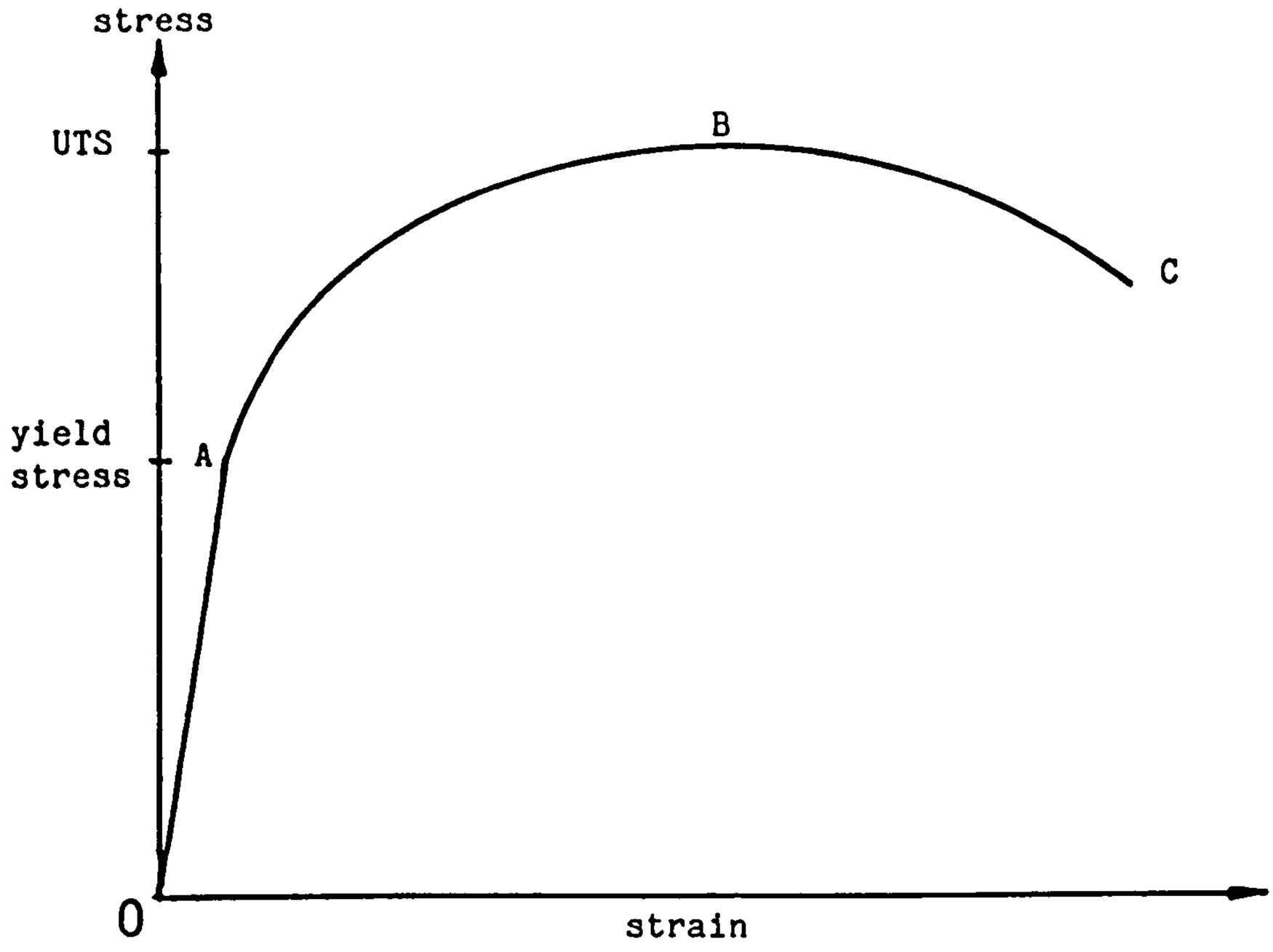

Fig. 2.1. Typical uniaxial stress-strain curve

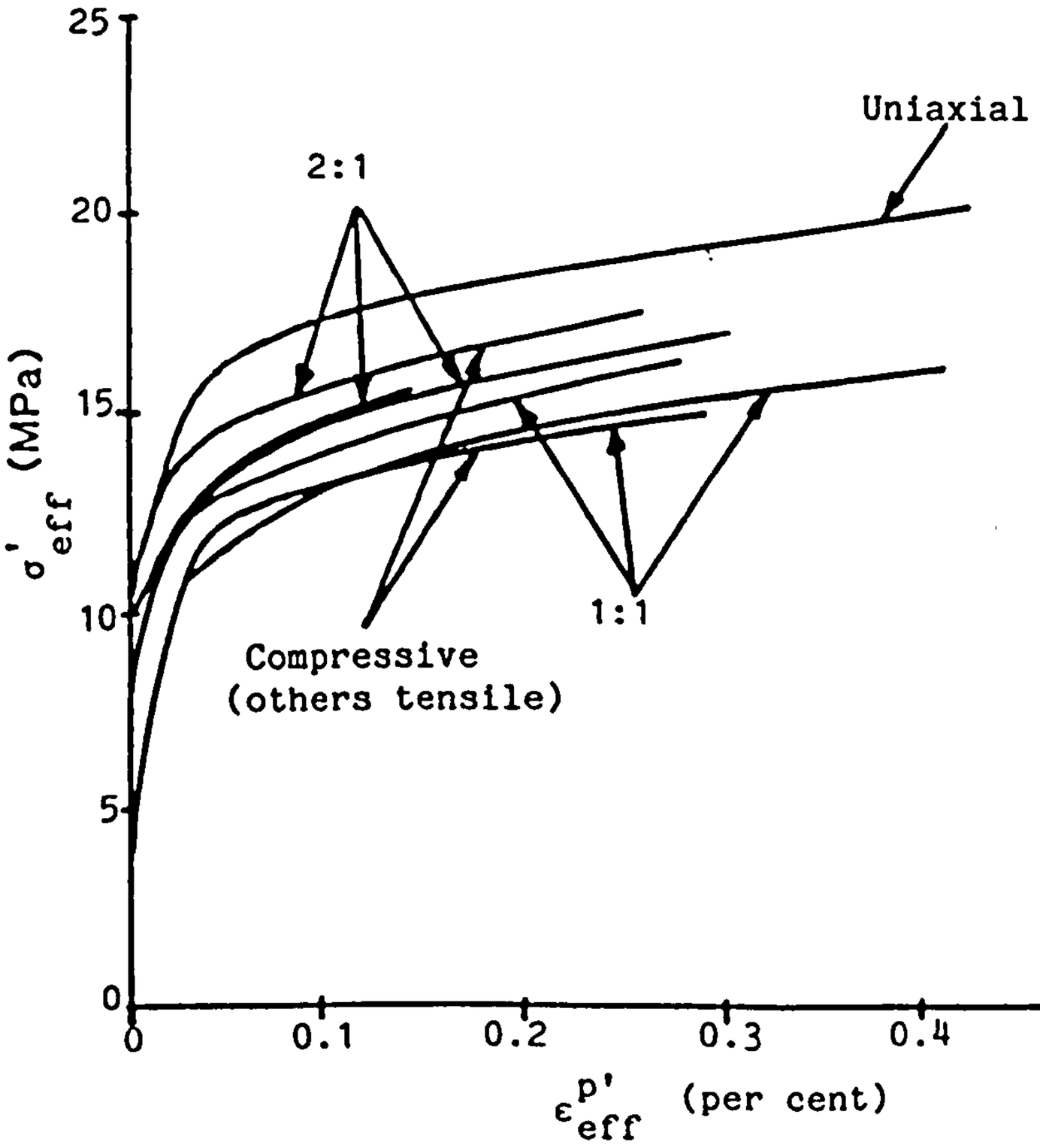

Fig.2.2(i).Effective stress-effective strain data from the initial monotonic loading part of the uniaxial and biaxial tests for lead alloy (from ref. 20)

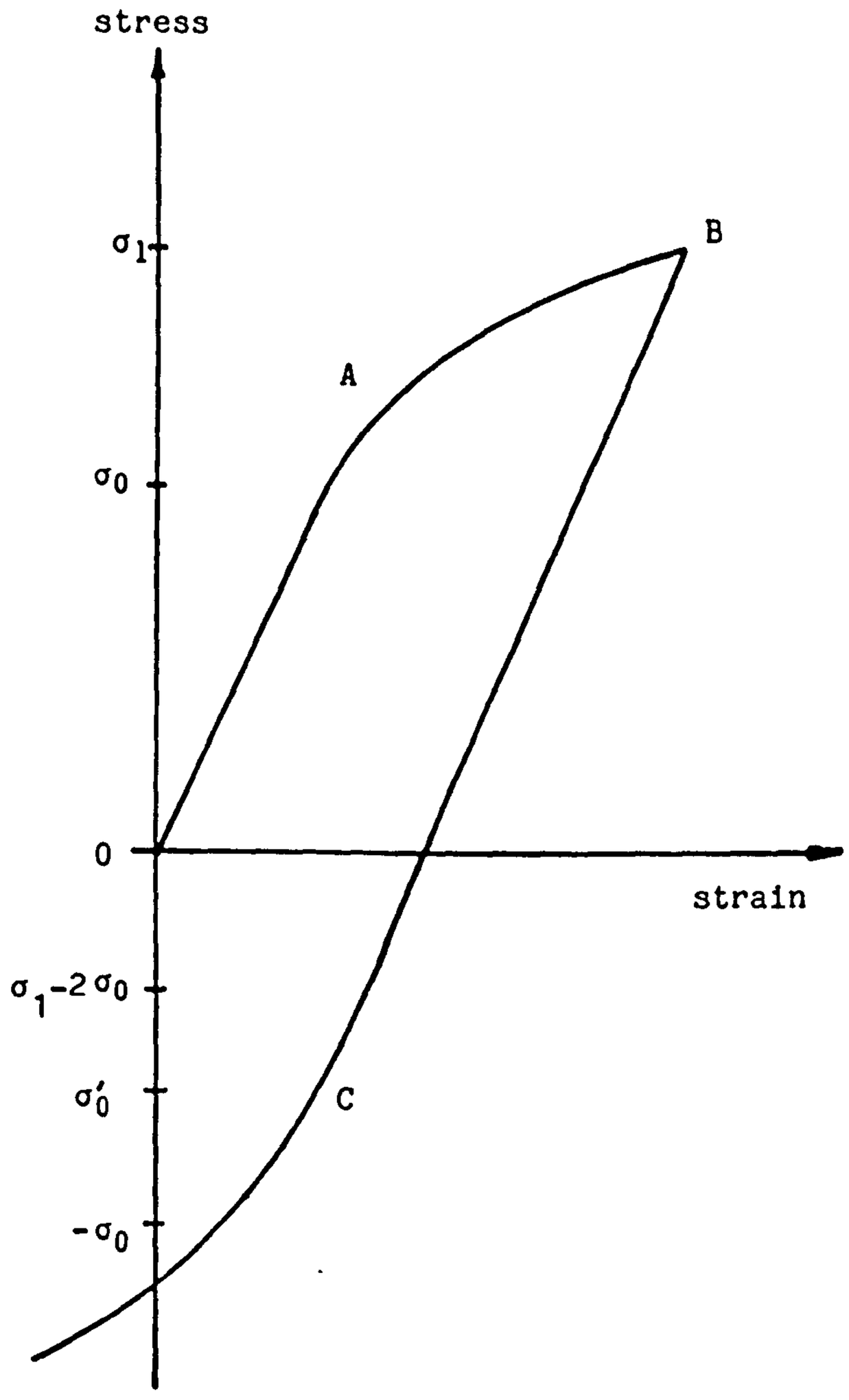

Fig.2.2(ii) Bauschinger Effect
σ'_0 -the yield stress during reverse loading

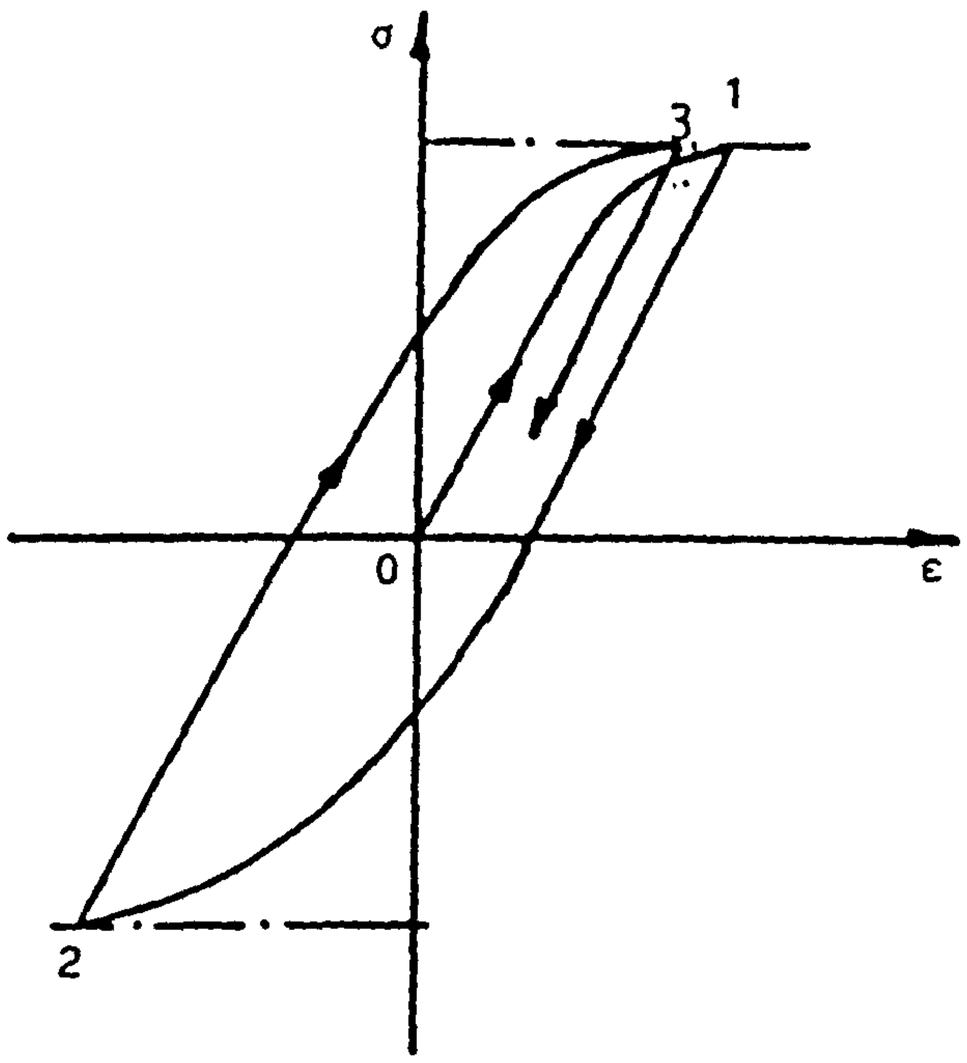

Fig.2.3(i) Cyclic hardening.
Stress controlled cycling.

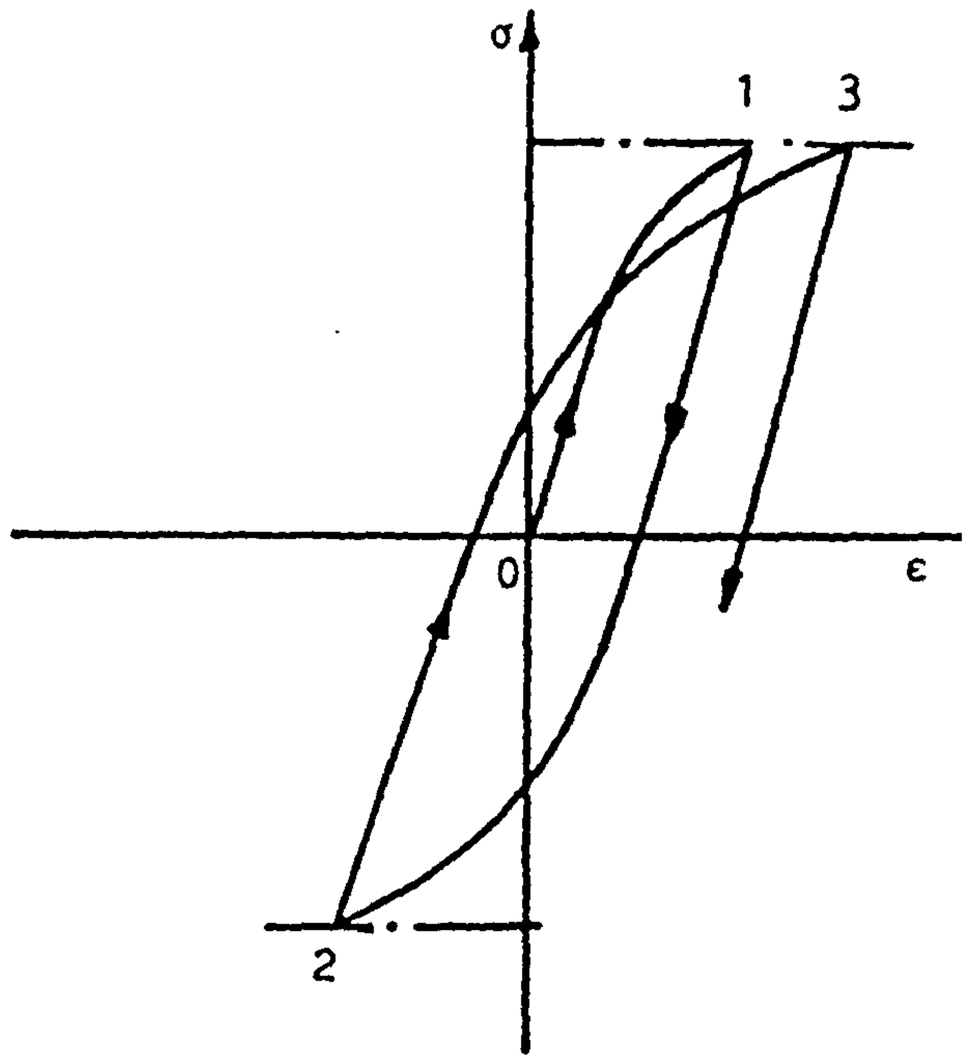

Fig.2.4(i) Cyclic softening.
Strain controlled cycling.

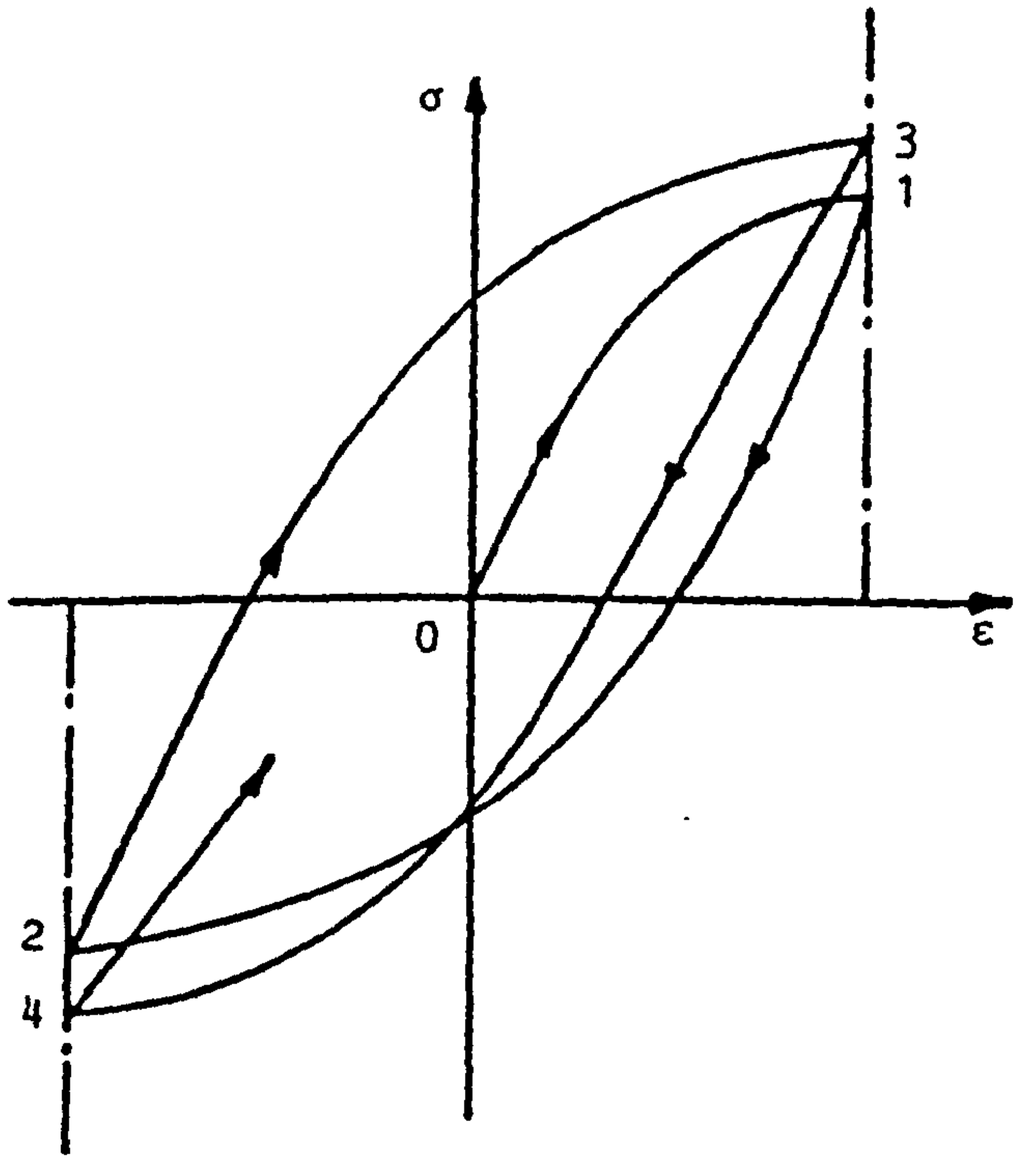

Fig.2.3(ii) Cyclic hardening.
Strain controlled cycling.

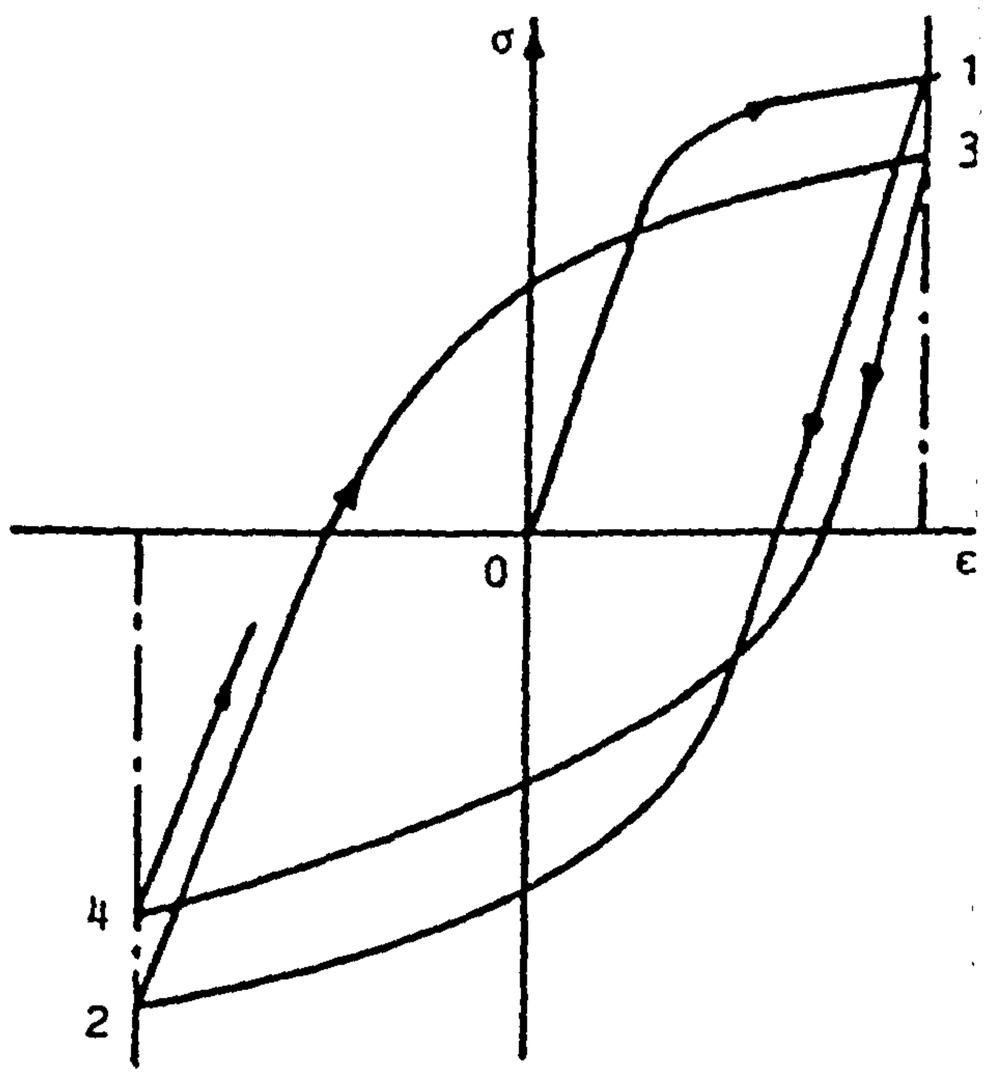

Fig.2.4(ii) Cyclic softening.
Strain controlled cycling.

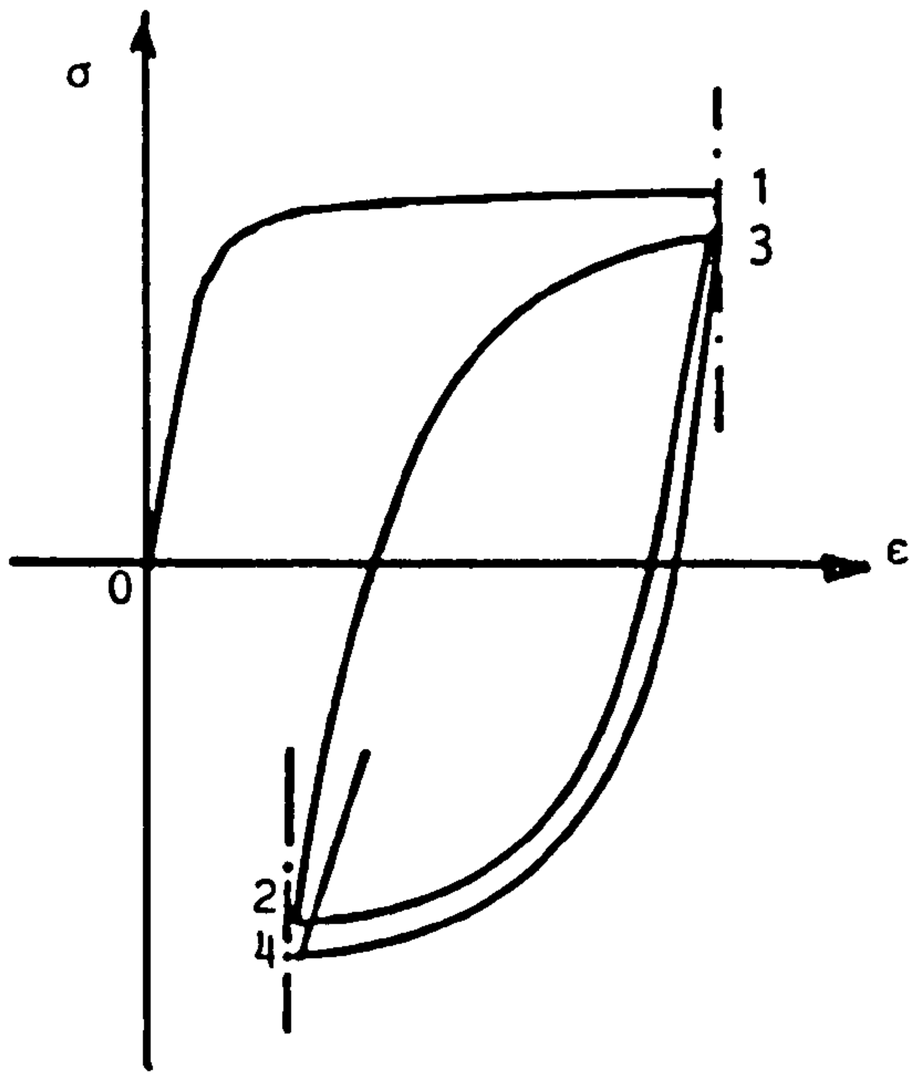

Fig.2.5(i) Cyclic relaxation.

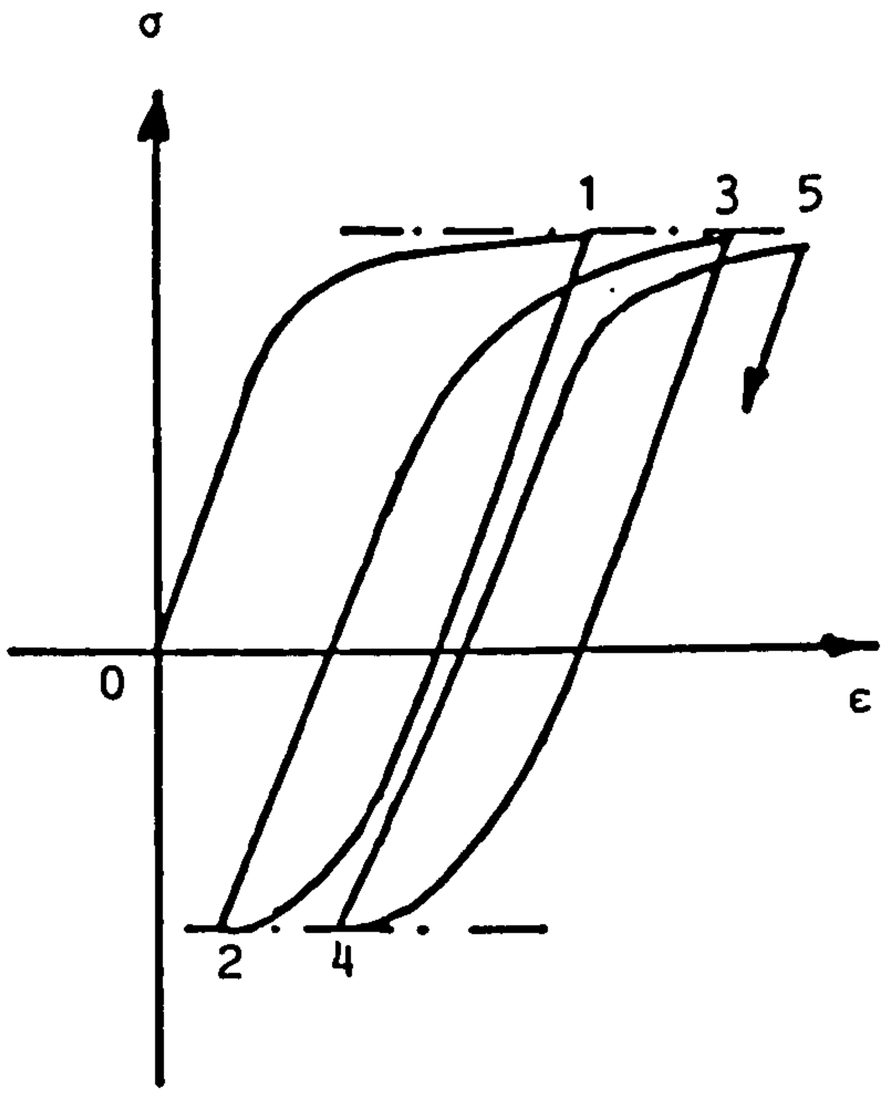

Fig.2.5(ii) Material ratchetting.

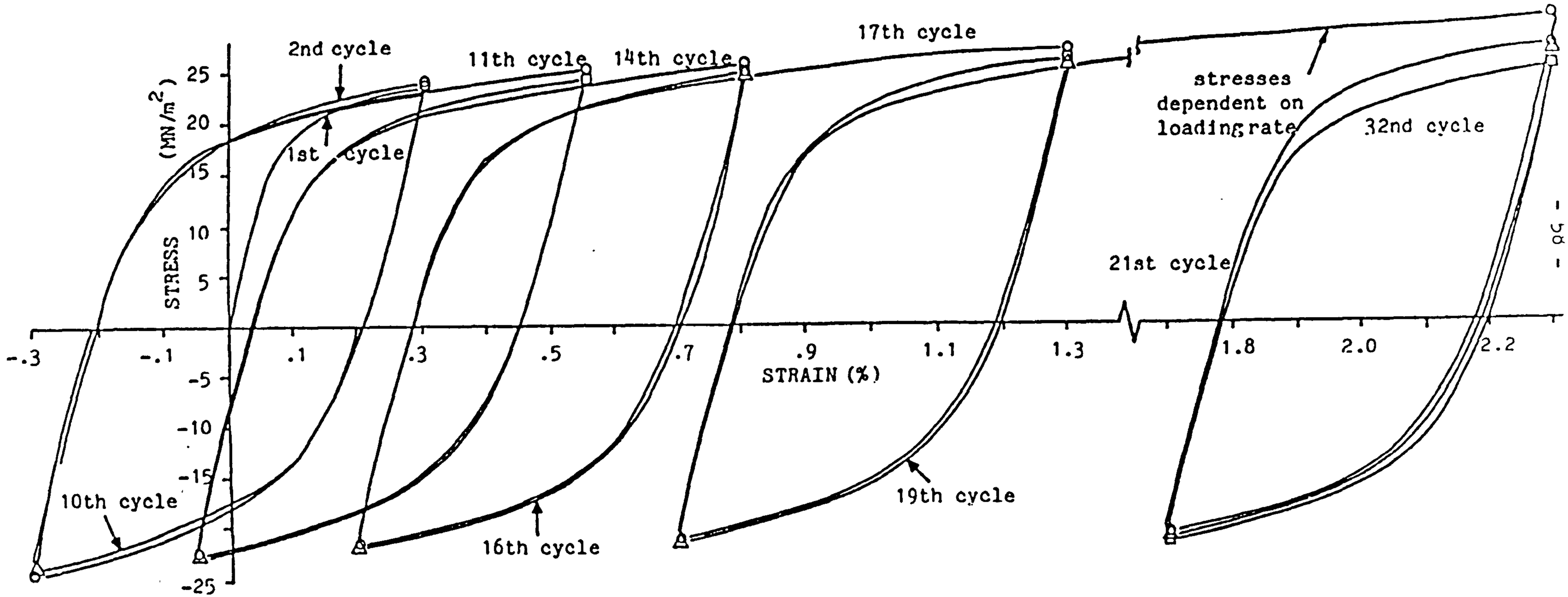

Fig.2.6(i) Reverse plasticity test on lead alloy: stability of the material. (from ref. 3)

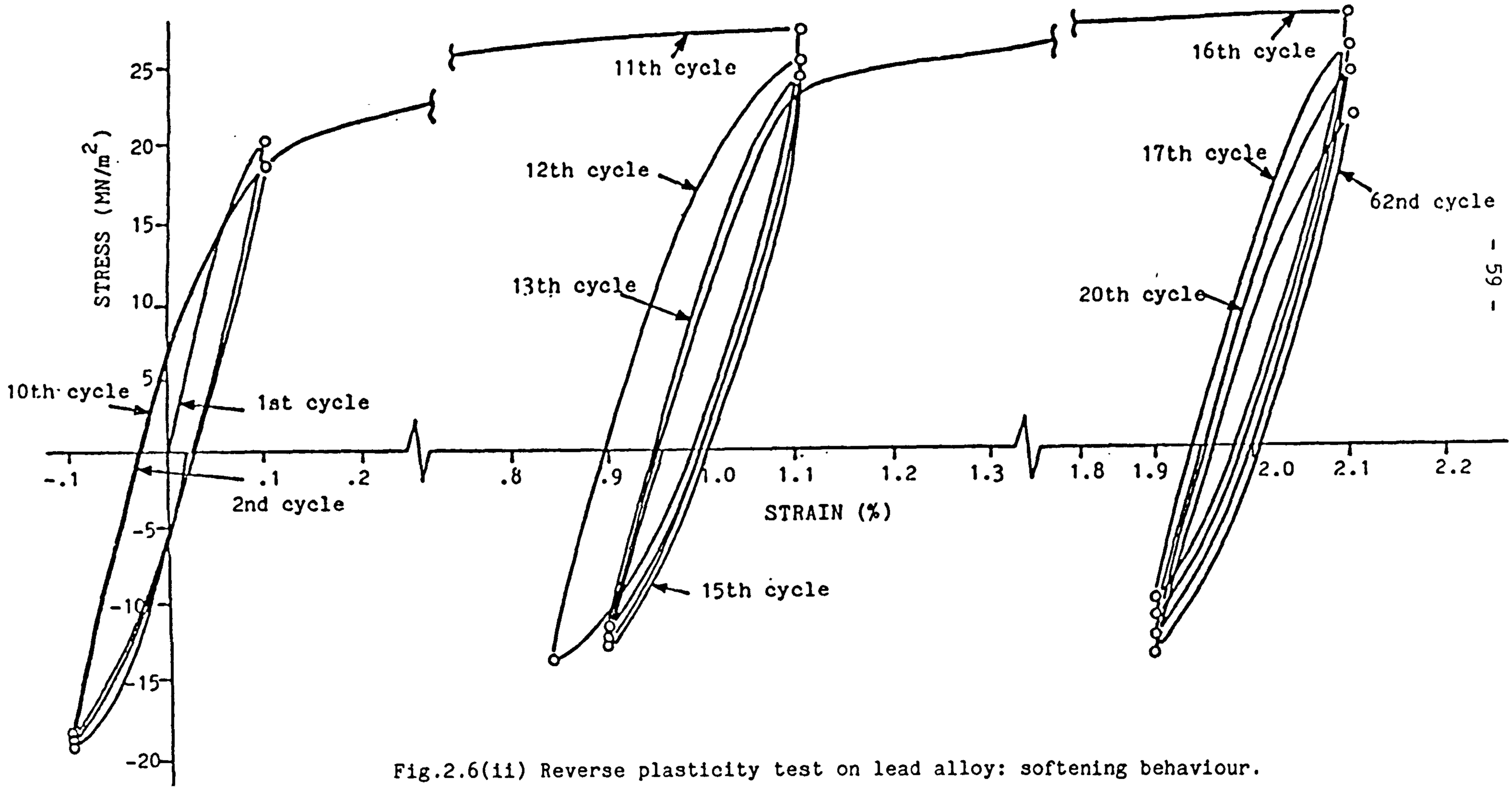

Fig.2.6(ii) Reverse plasticity test on lead alloy: softening behaviour.

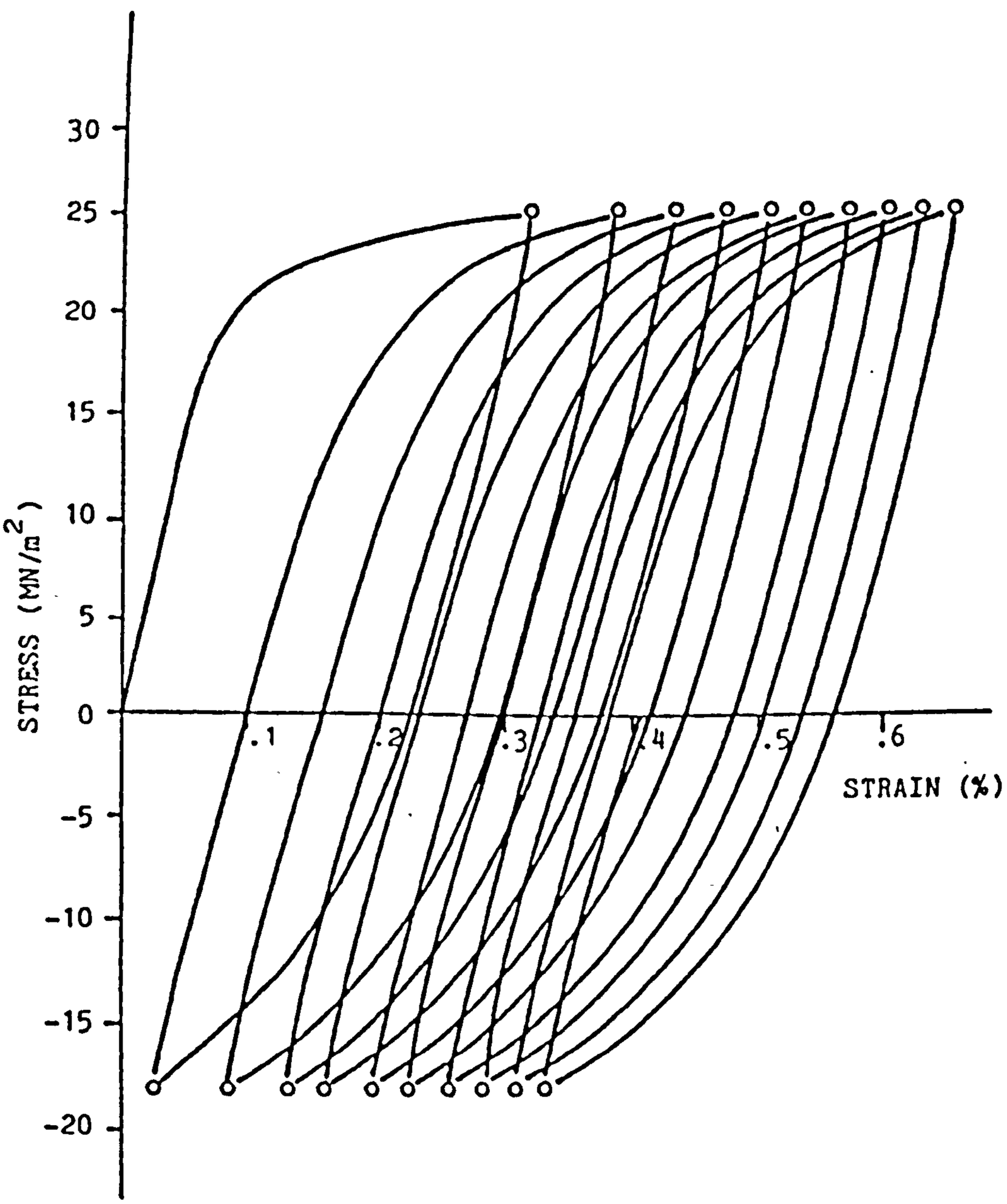

Fig.2.6(iii) Reverse plasticity test on lead alloy: Material ratchetting.

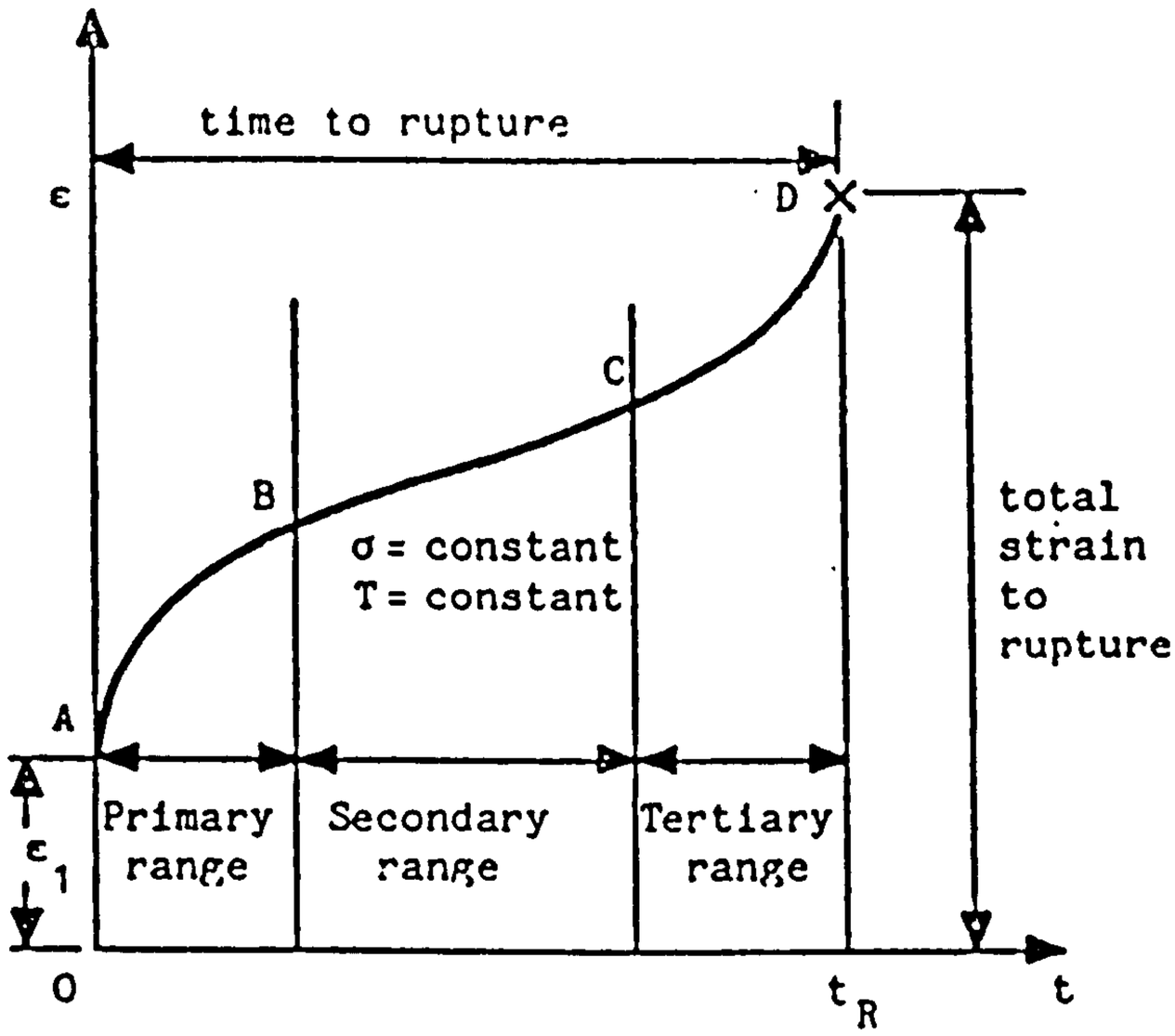

Fig.2.7(i) Typical creep curve.

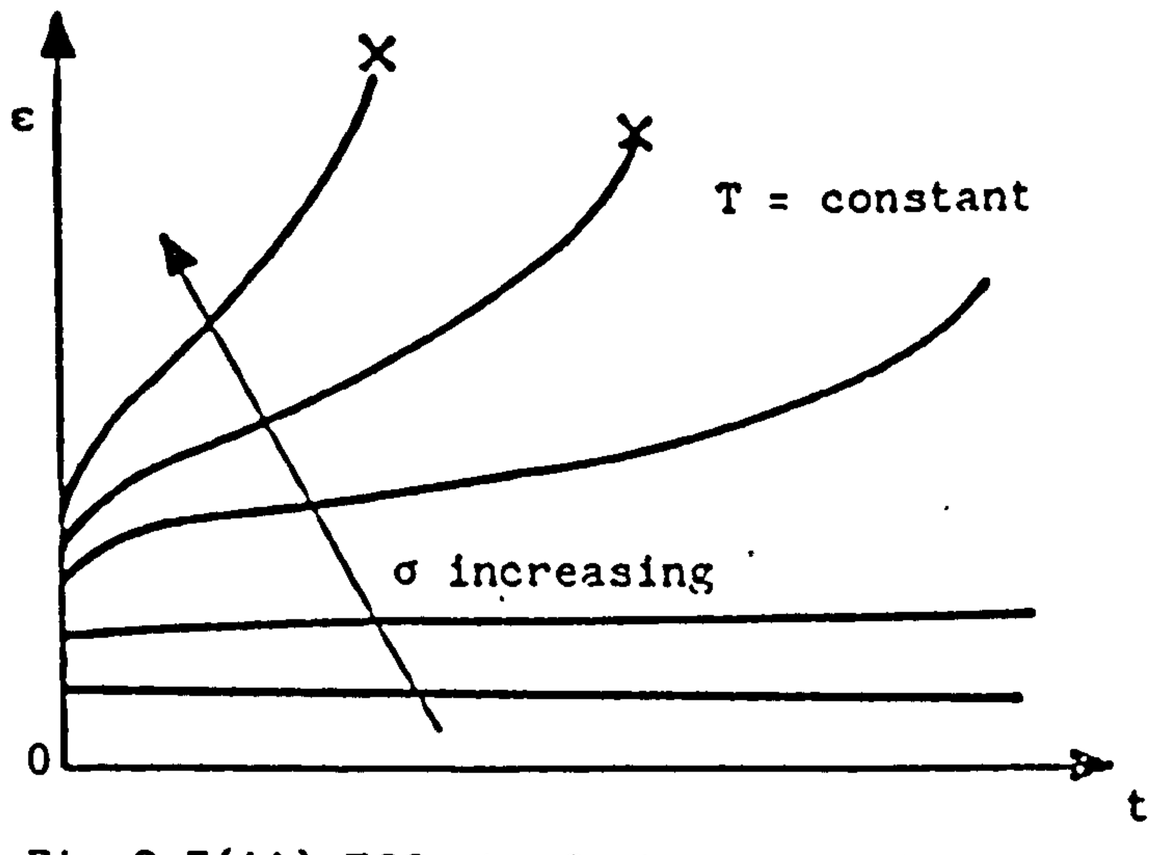

Fig.2.7(ii) Effect of stress on the creep curve at constant temperature.

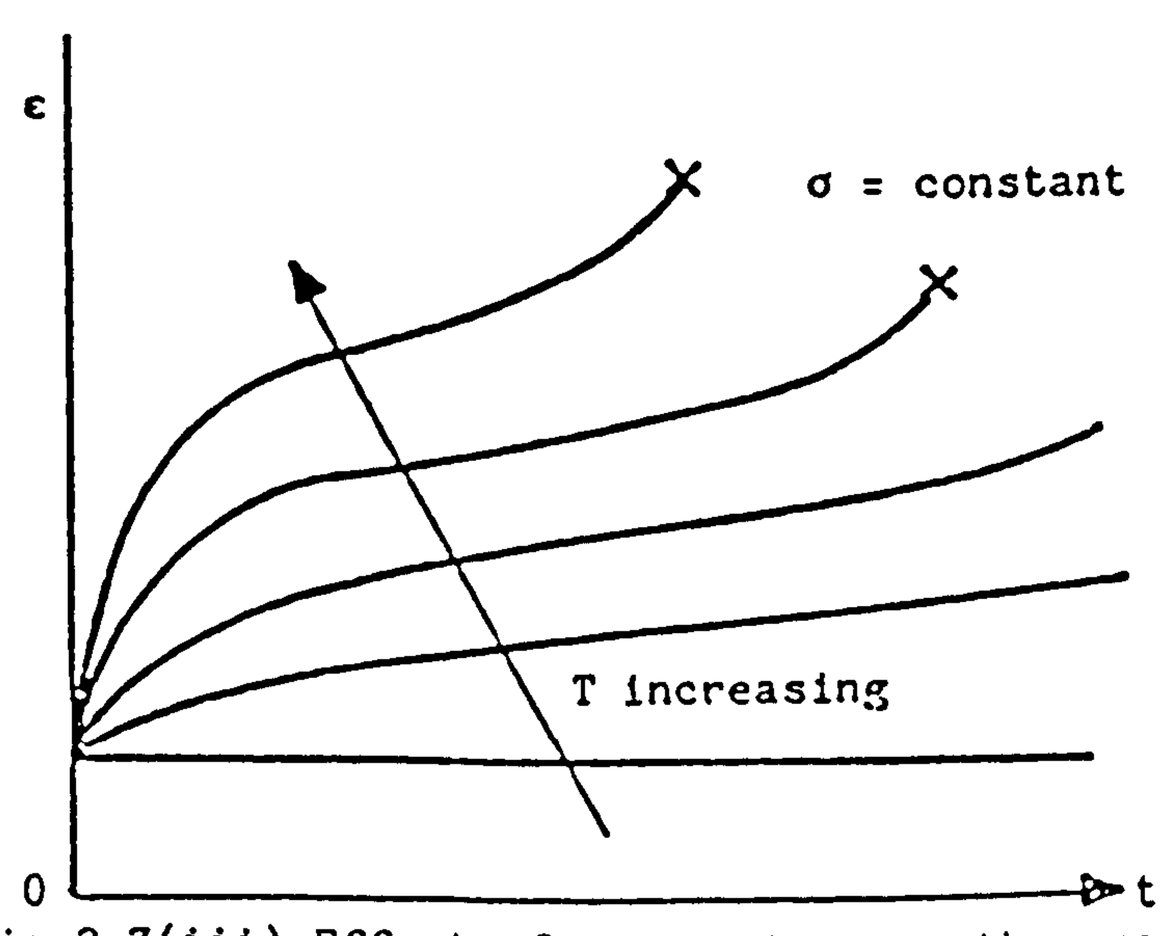

Fig.2.7(iii) Effect of temperature on the creep curve at constant stress.

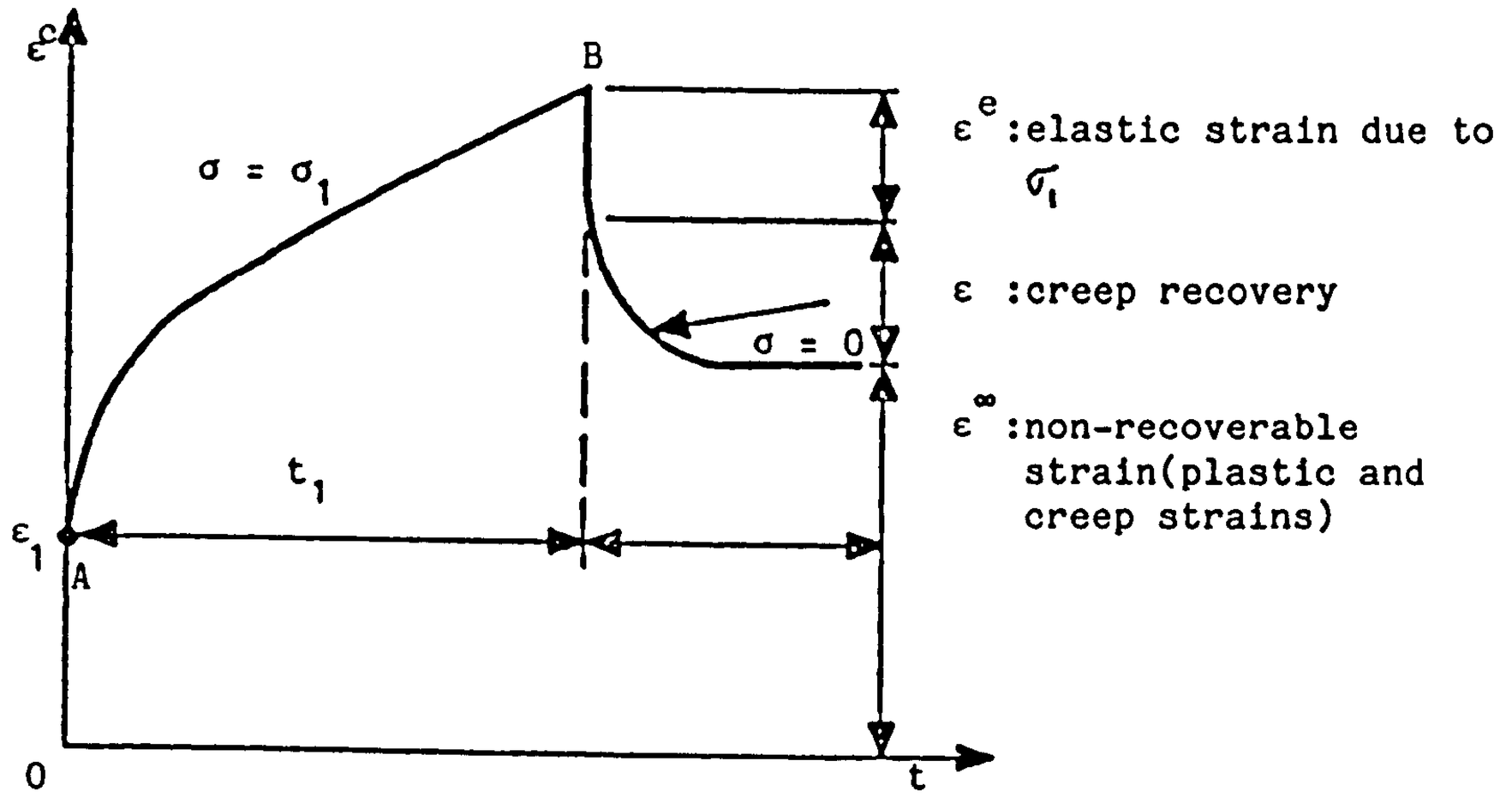

Fig.2.8(i) Creep and creep recovery.

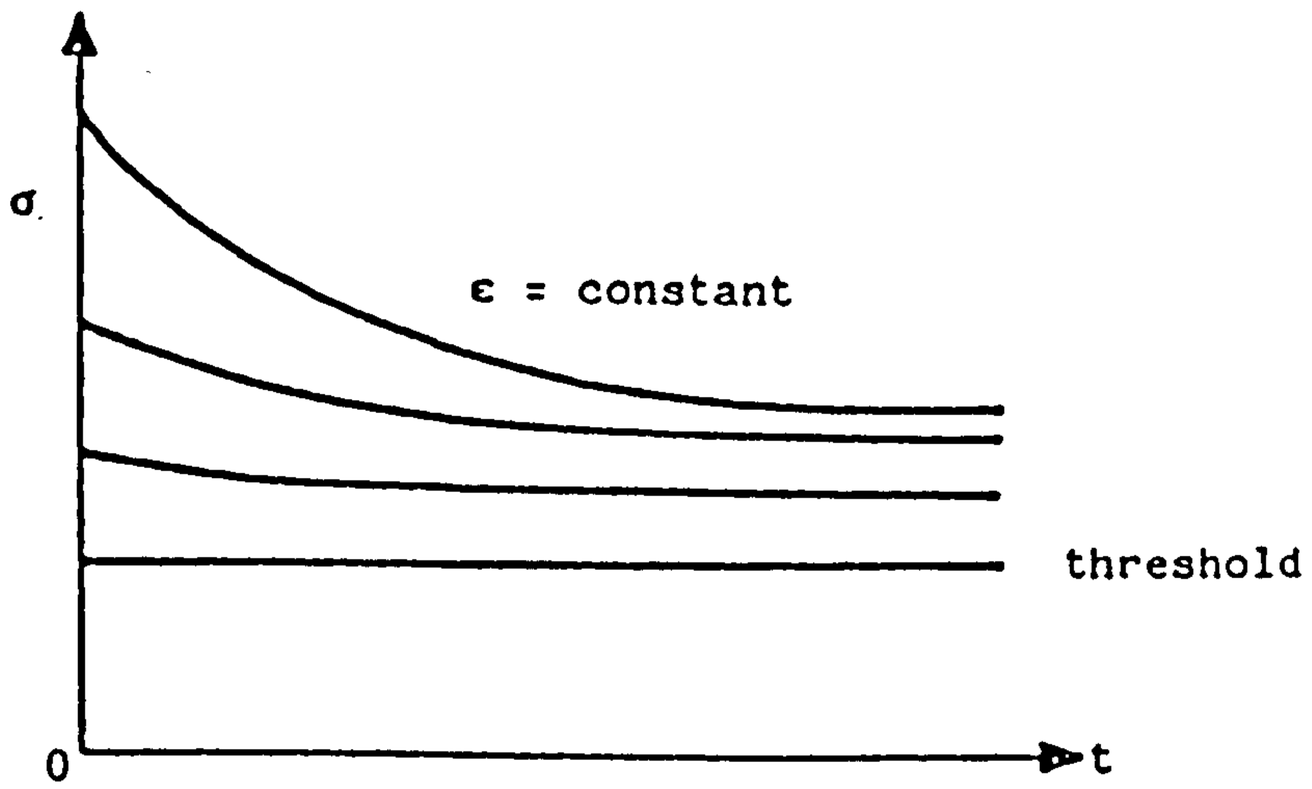

Fig.2.8(ii) Effect of stress level on creep relaxation at constant temperature.

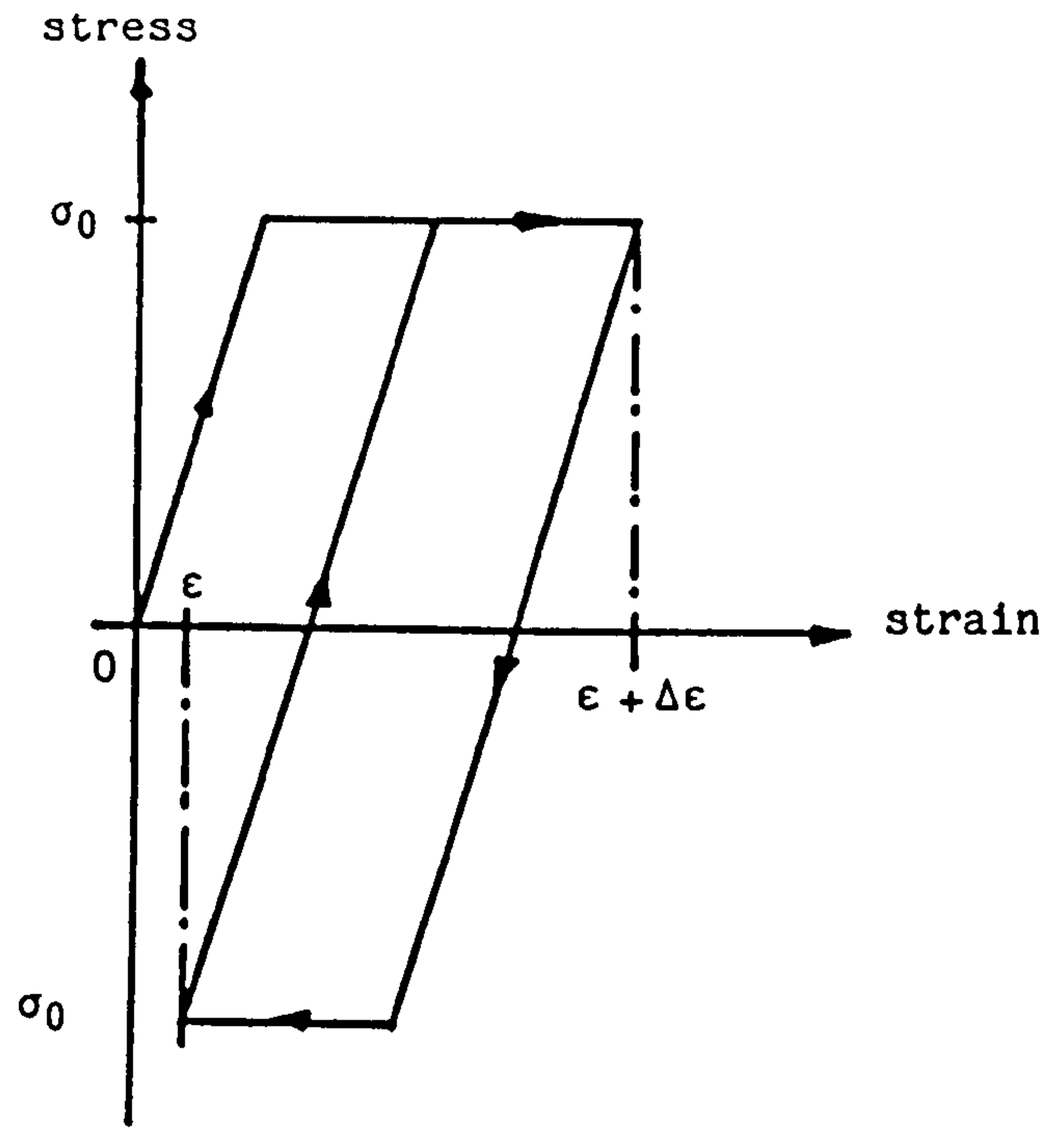

Fig.2.9(i) Elastic-perfectly plastic model.

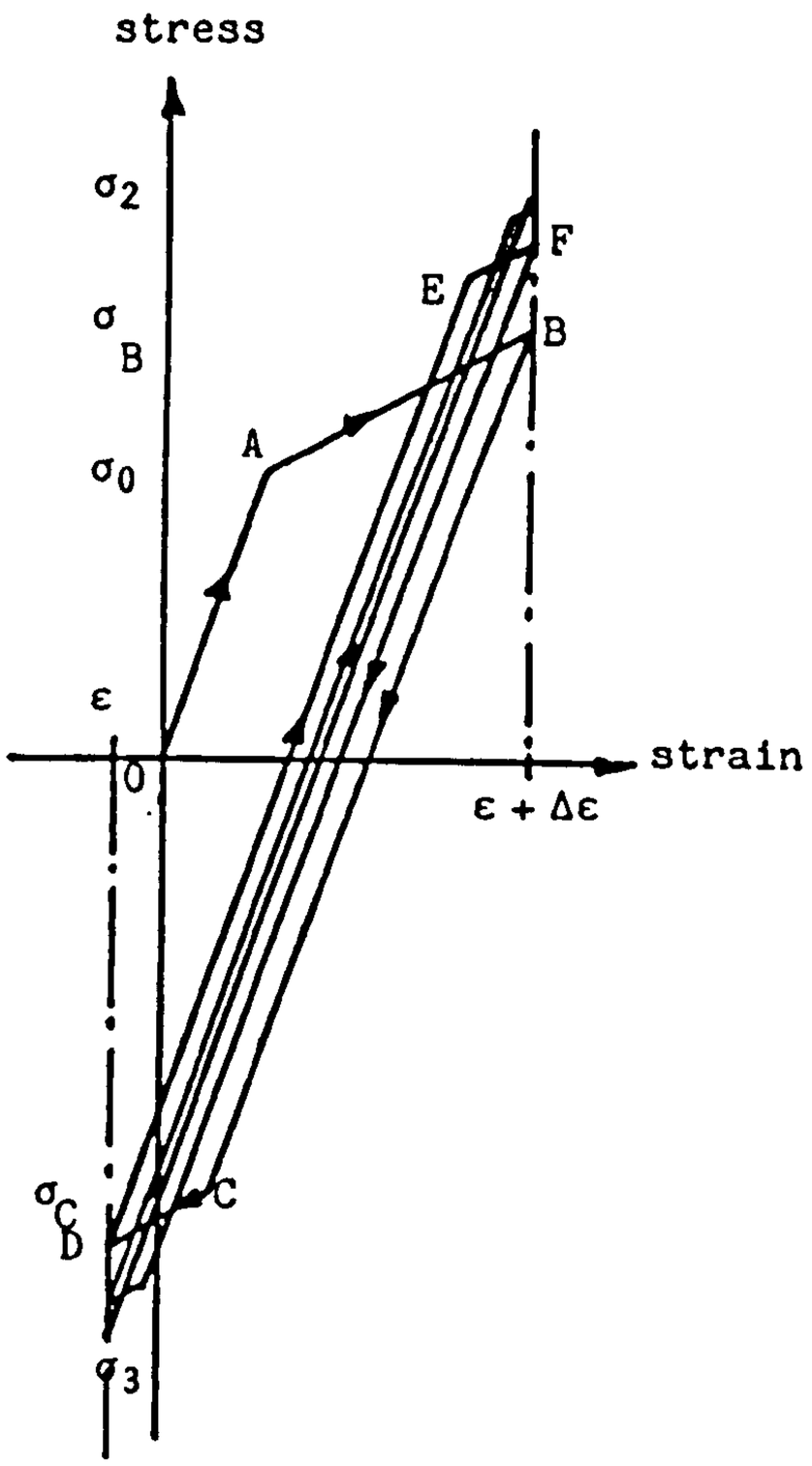

Fig.2.9(ii) Isotropic hardening. Strain controlled cycling.

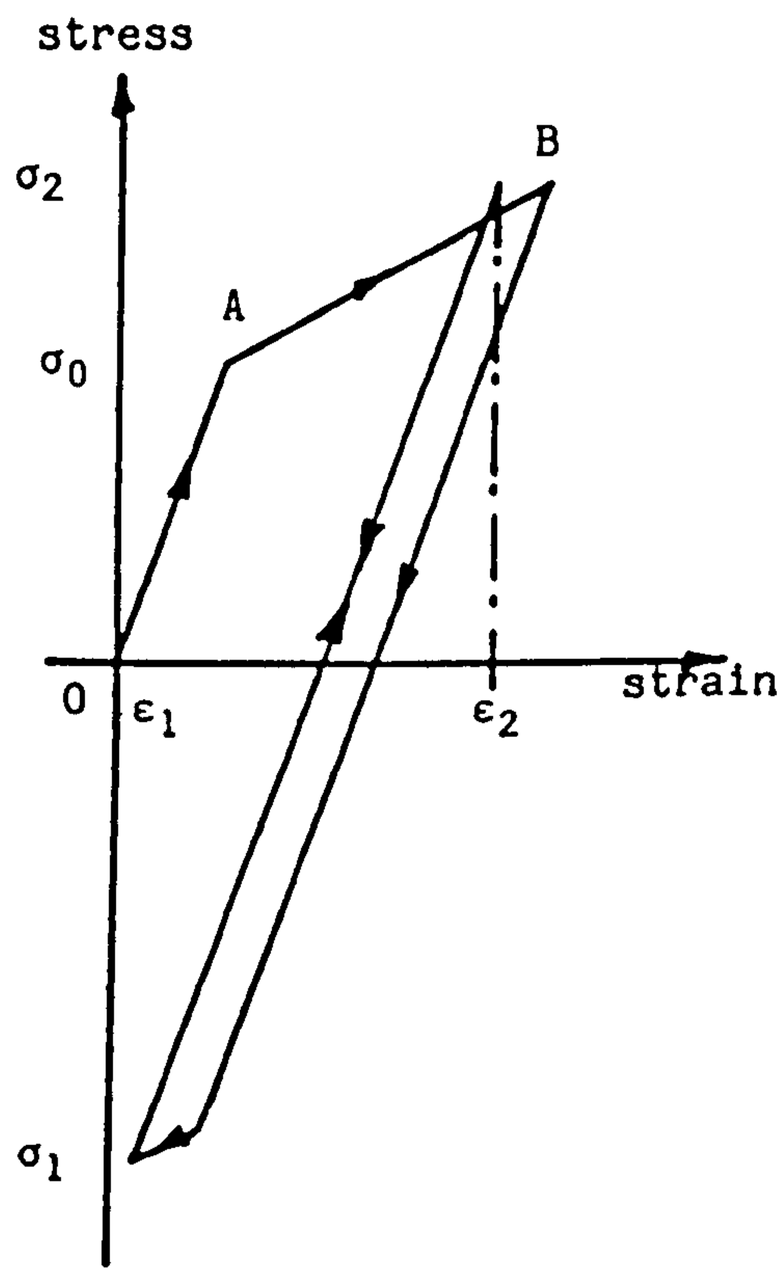

Fig.2.9(iii) Isotropic hardening Stress controlled cycling.

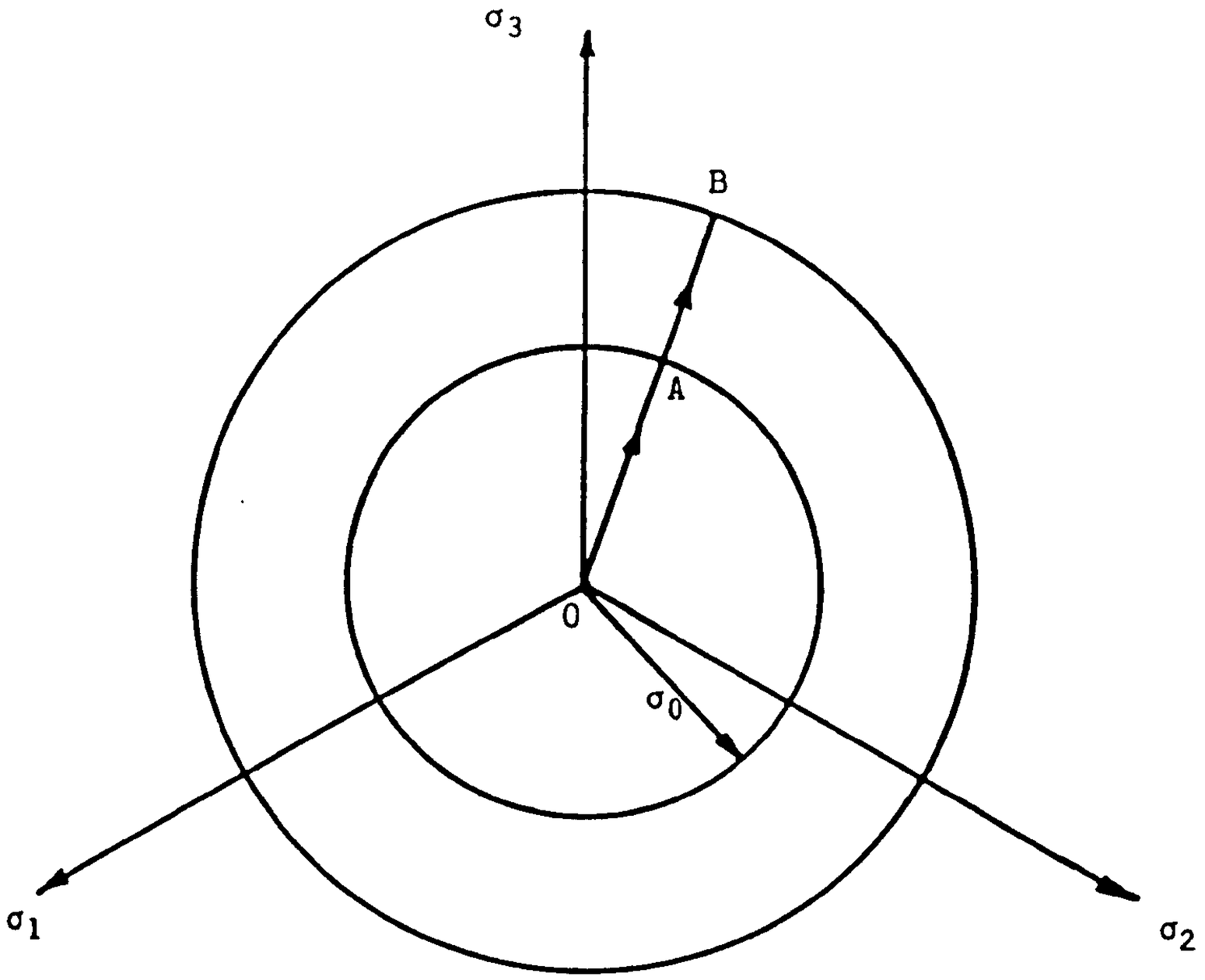

Fig.2.9(iv) Isotropic hardening model in the π-plane.

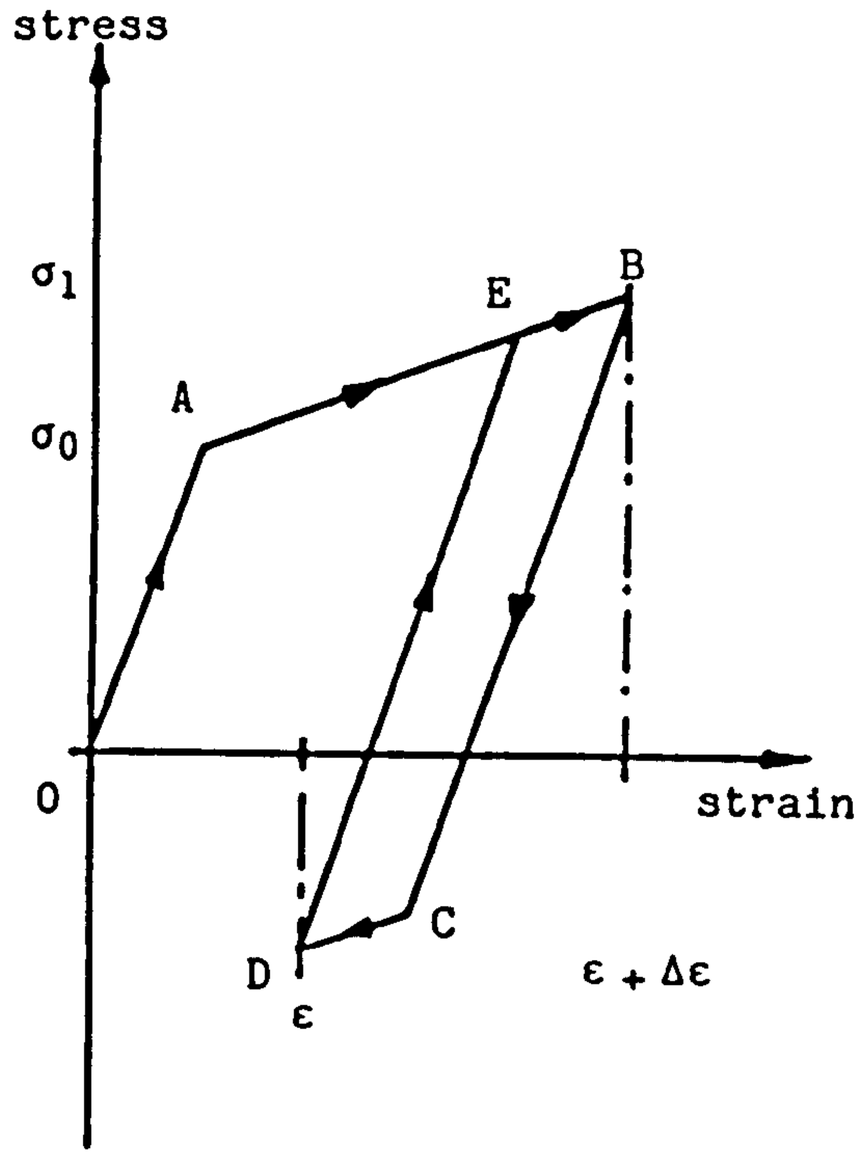

Fig.2.9(v) Kinematic hardening.
Strain controlled cycling.

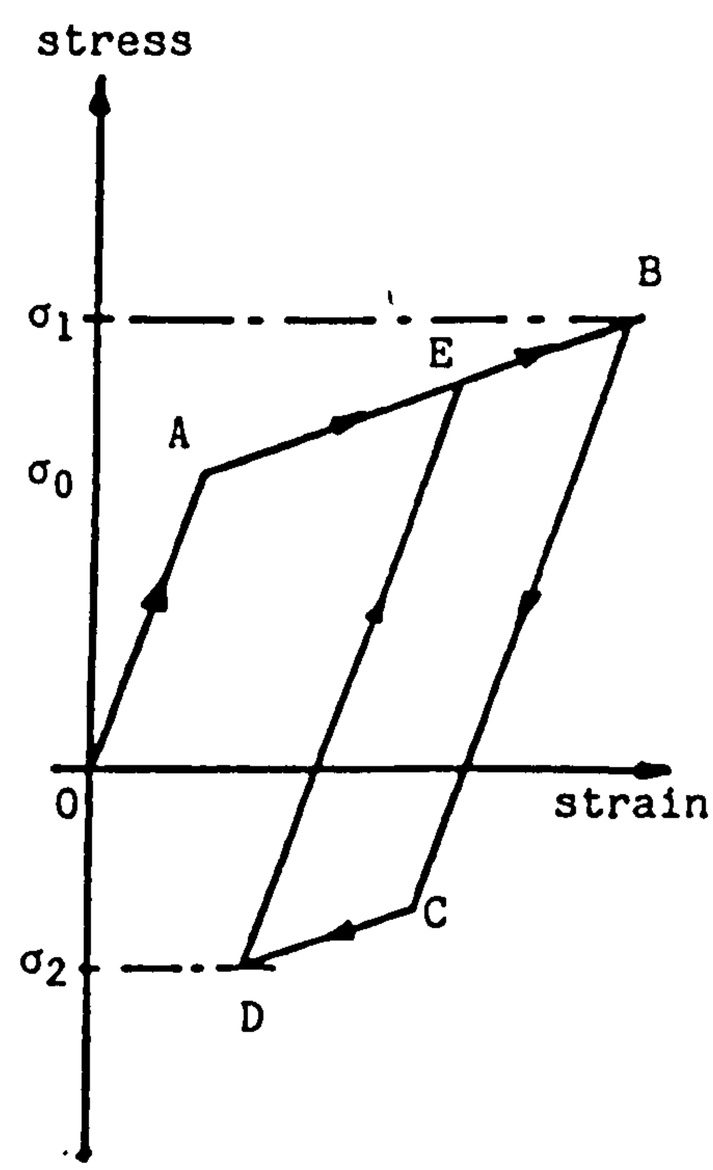

Fig.2.9(vi) Kinematic hardening.
Stress controlled cycling.

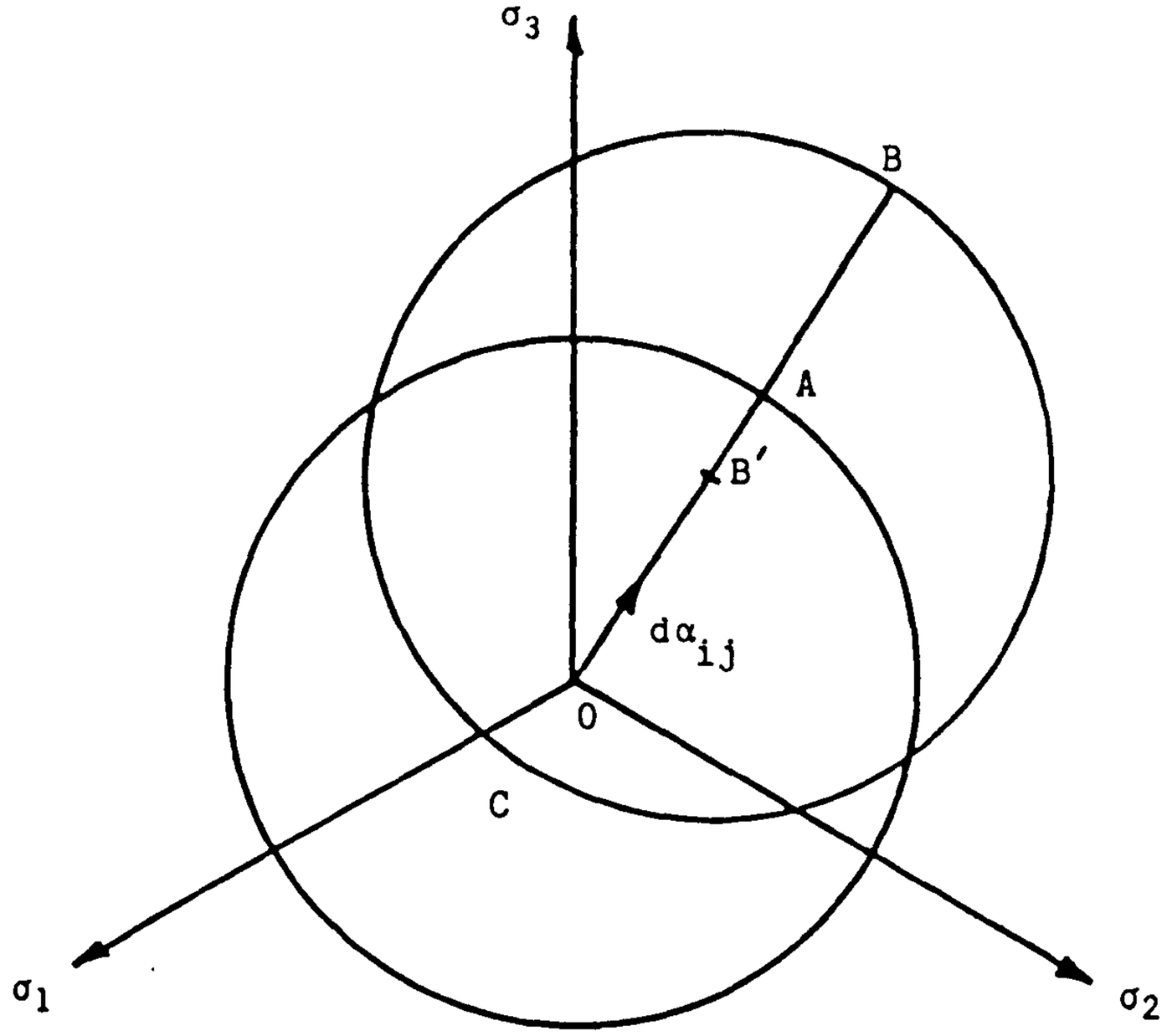

Fig.2.9(vii) Kinematic hardening model in the π-plane.

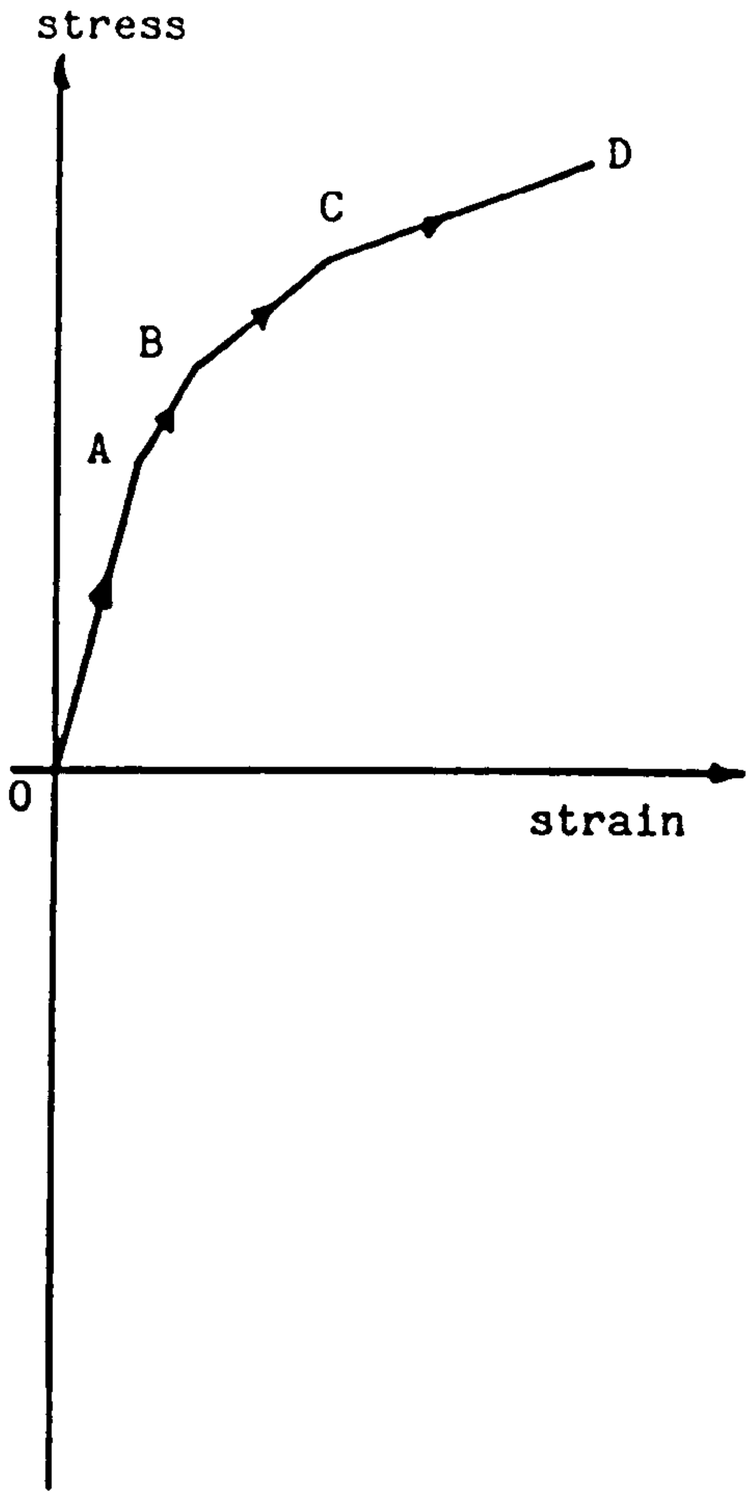

Fig.2.10(i) Mroz`s model. Monotonic stress-strain curve.

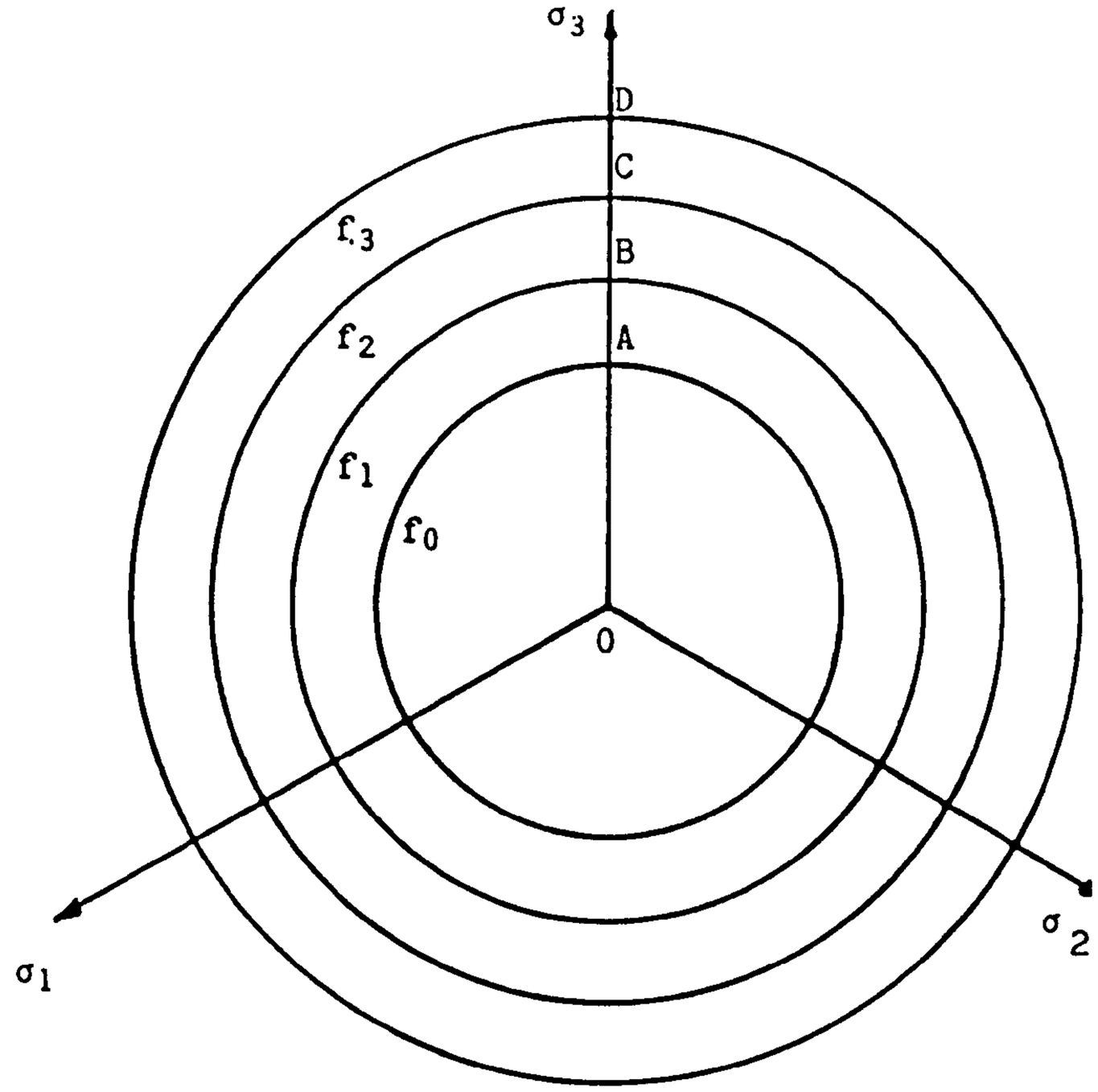

Fig.2.10(ii) Mroz`s model. Virgin material in the π-plane.

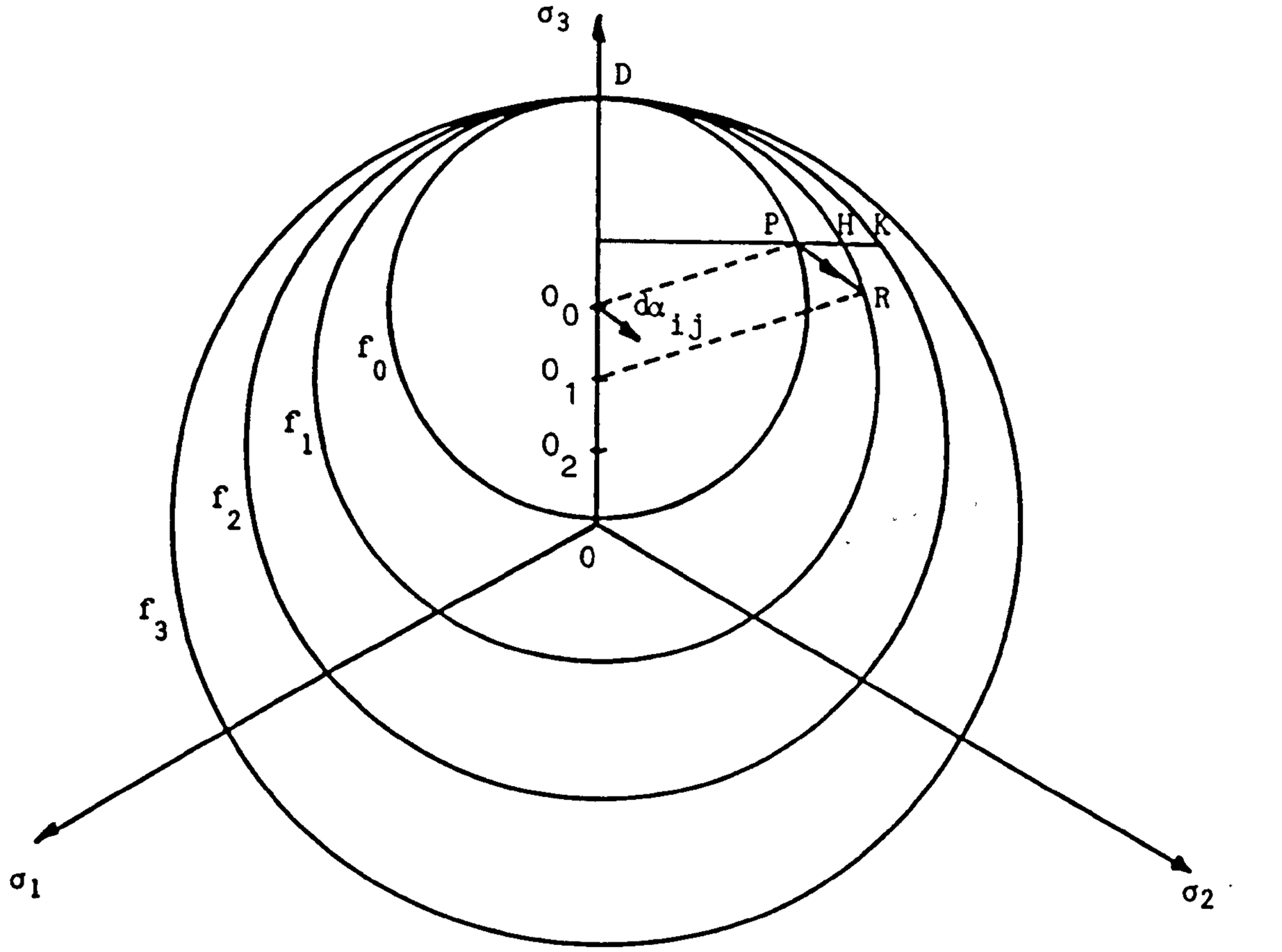

Fig.2.10(iii) Position of the surfaces at the end of loading path OABCD in Fig.2.10(1) for Mroz`s model.

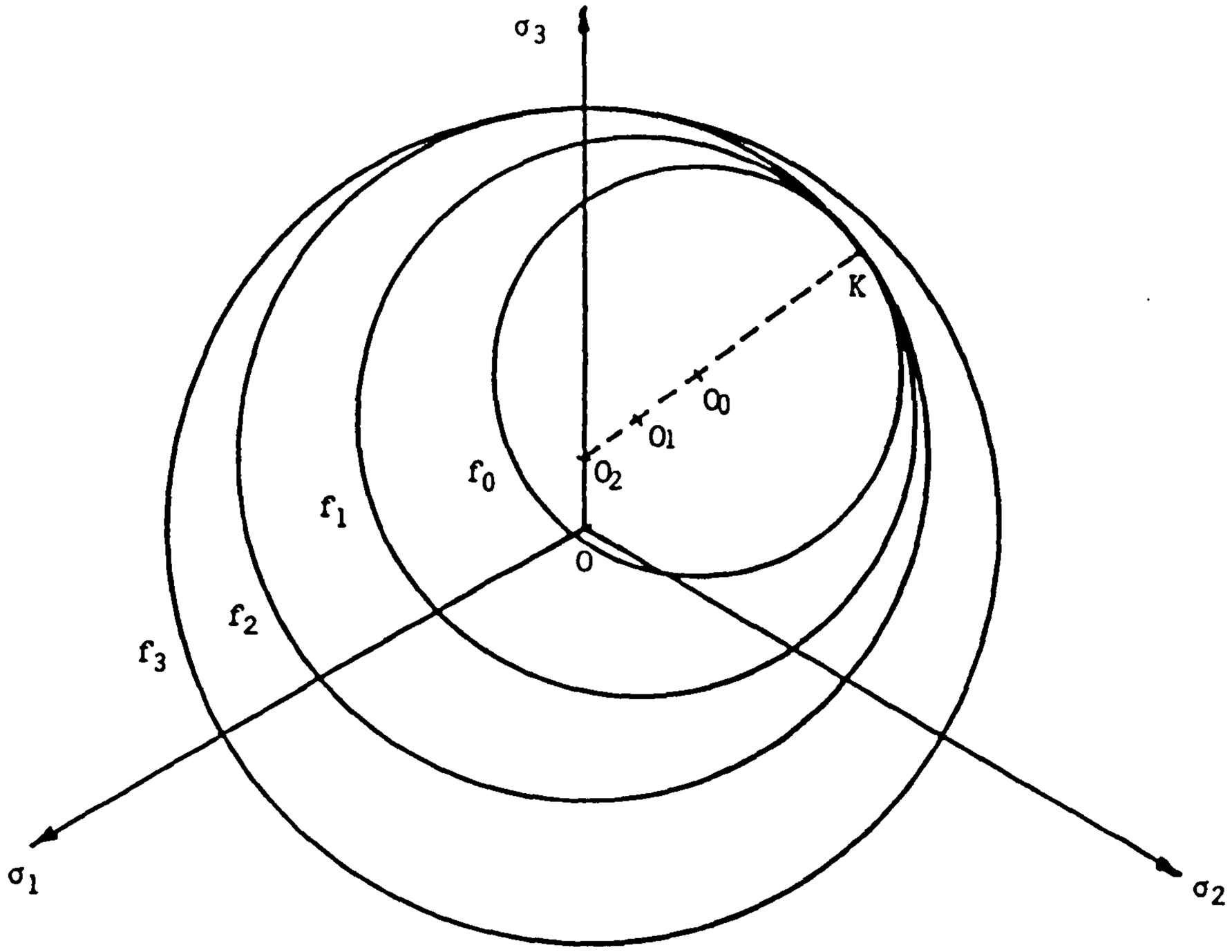

Fig.2.10(iv) Mroz`s model. Position of the work hardening surfaces at the end of non-propotional loading path PHK of Fig.2.10(iii).

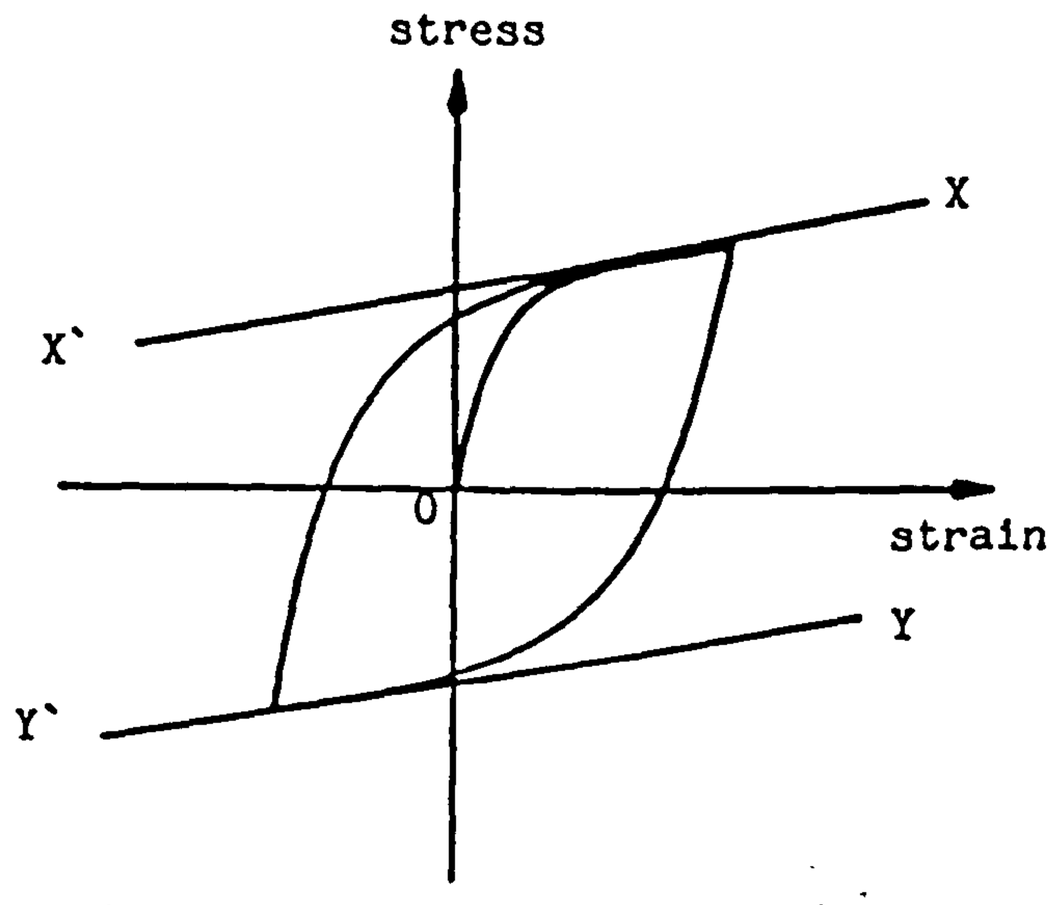

Fig.2.10(v) Dafalias and Popov model(45). Uniaxial bounding surface.

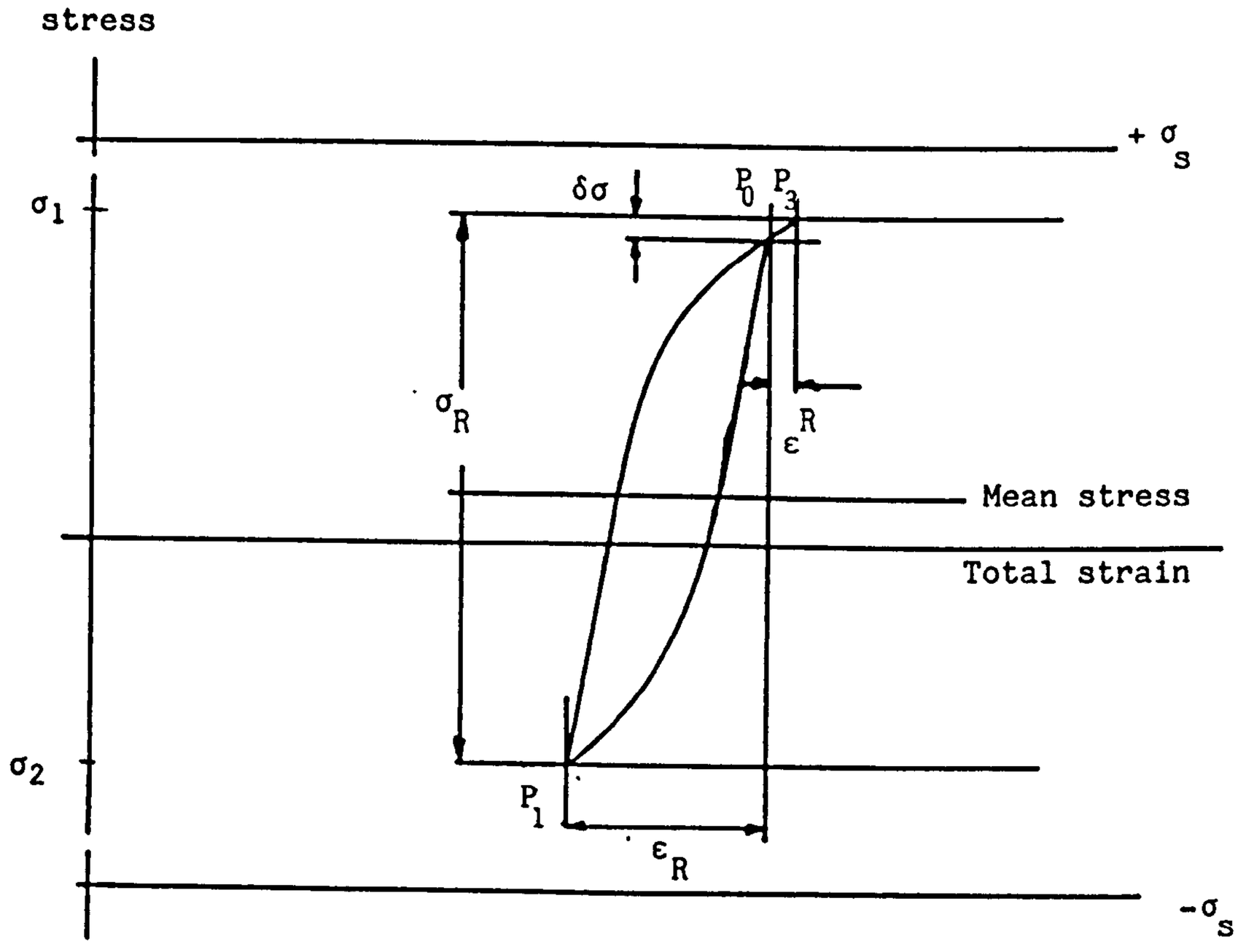

Fig.2.10(vi) Goodman and Goodall model. Loop with offset mean stress.

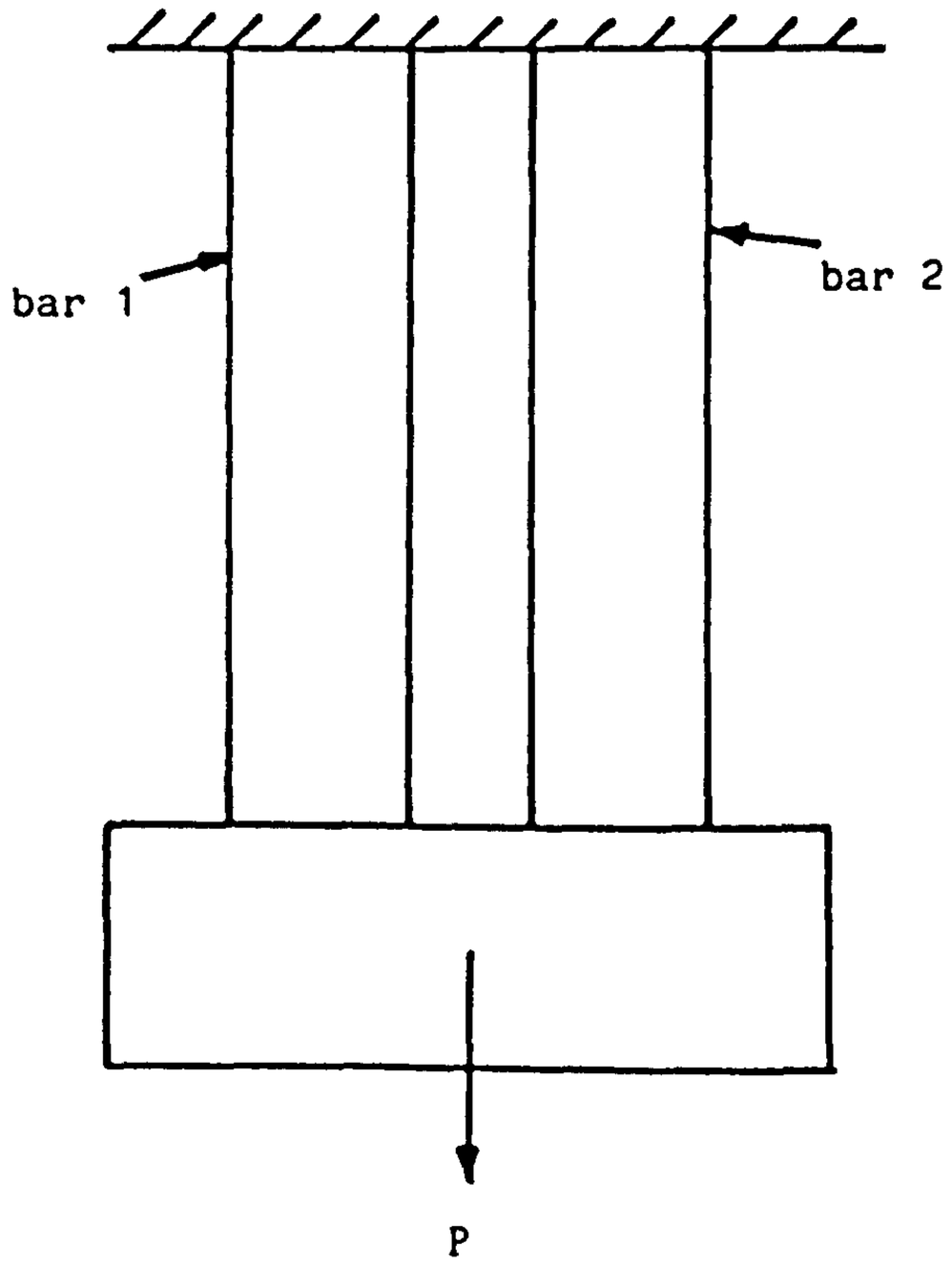

Fig.2.11(i) Two-bar structure.

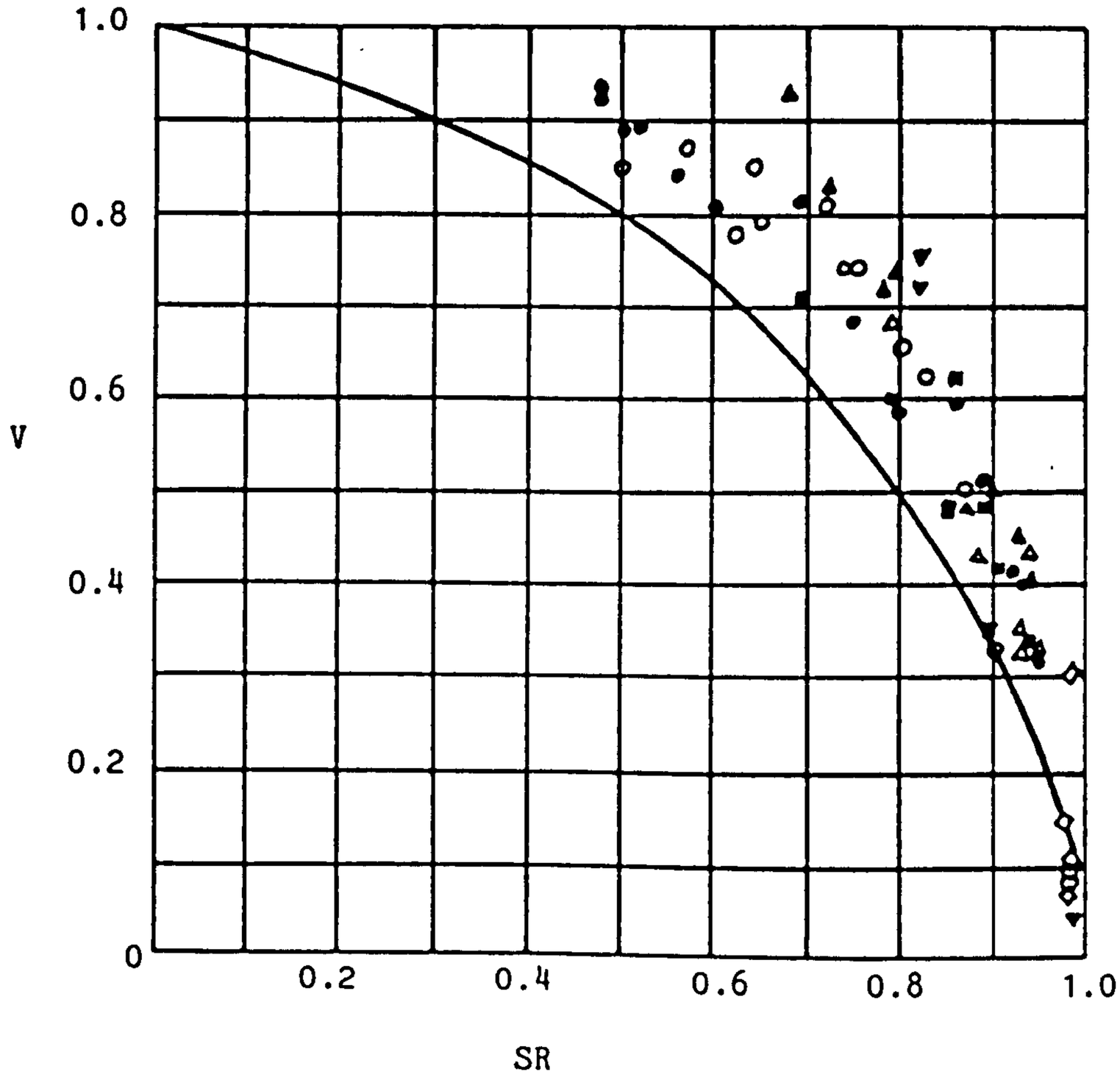

Fig.2.11(ii) Cousseran Efficiency Diagram. Results of different tests.

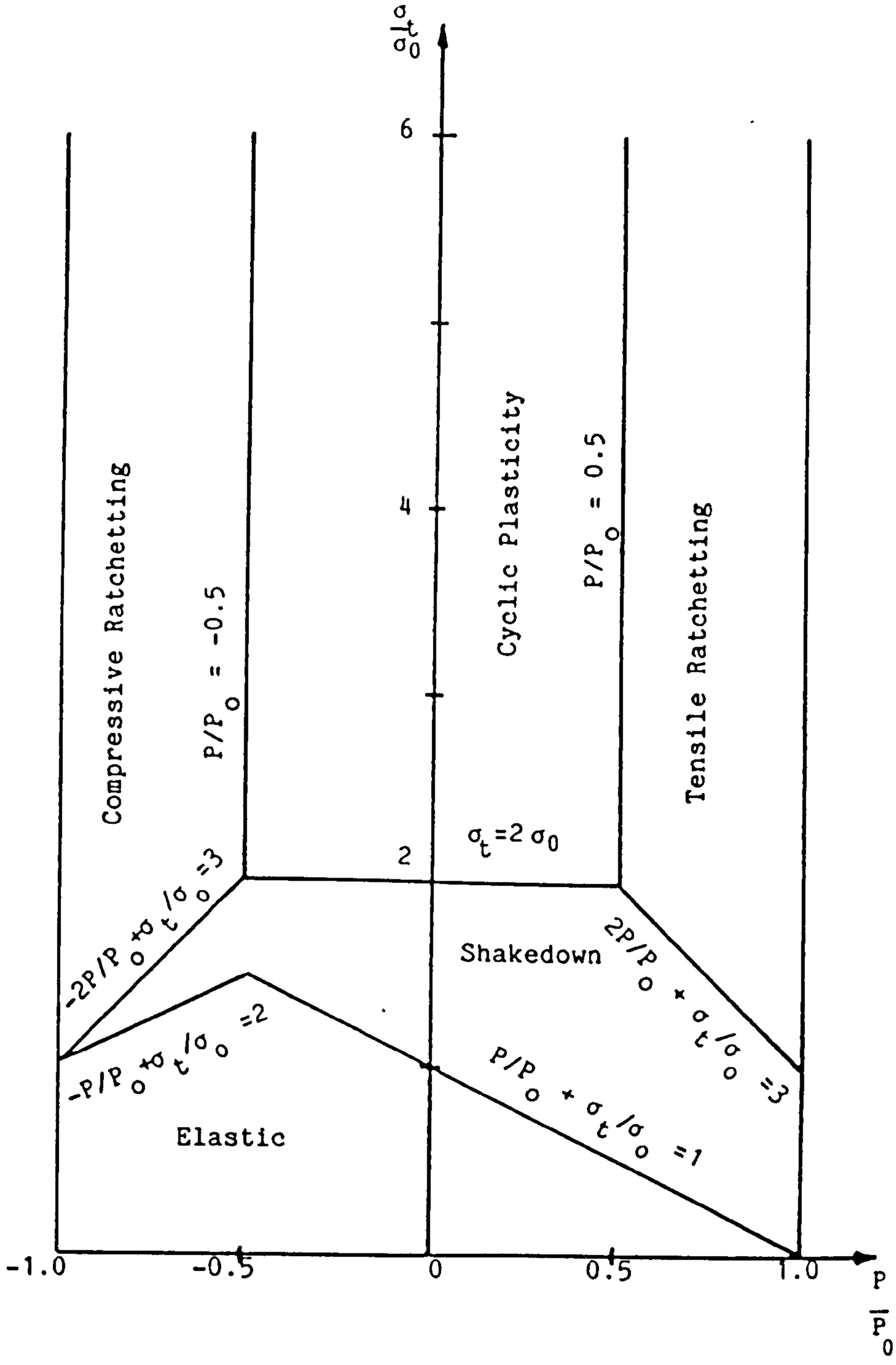

Fig.2.12(i) Interaction diagram for two-bar structure.
Perfectly-plastic material model. Bars with equal size.

$P_o = \sigma_0 X$ total area of bar

$\sigma_t = E\alpha\Delta T/2$

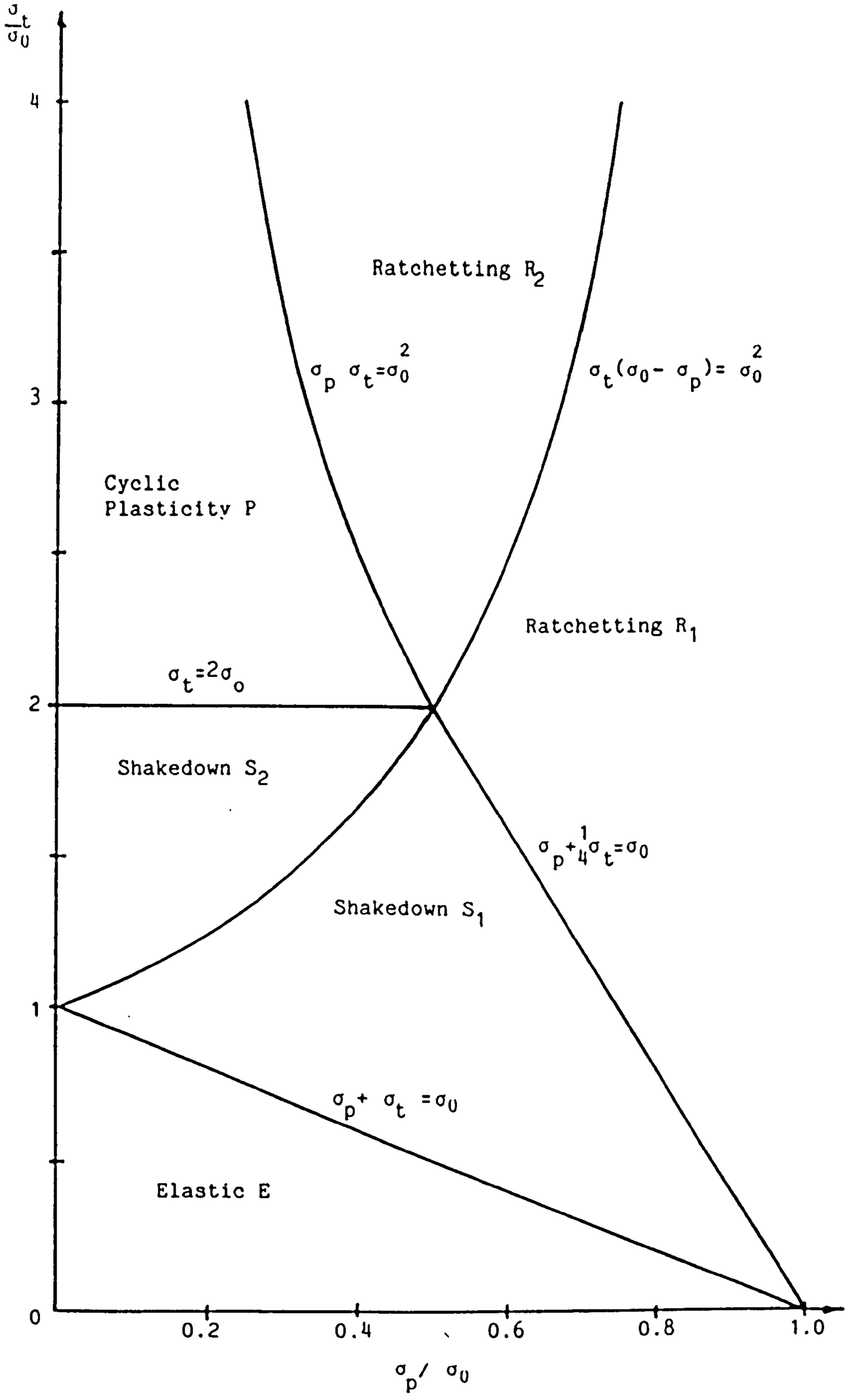

Fig.2.12(ii) Bree diagram for a tube subjected to steady internal pressure and cyclic linear through thickness temperature gradient.

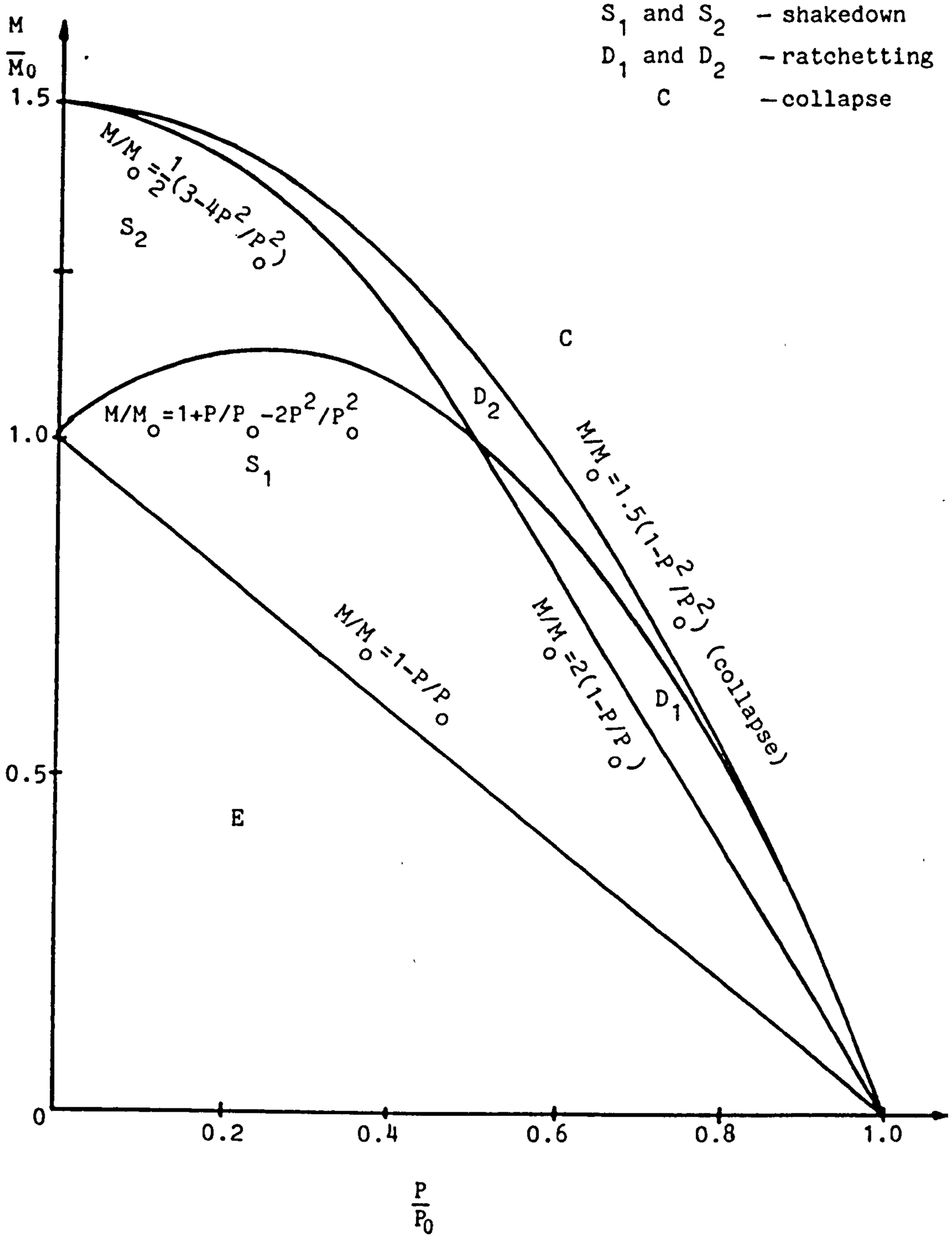

Fig.2.12(iii)Burgreen diagram for a beam subjected to a steady axial load and cyclic bending moment.

$$M_0 = \frac{h^2}{12}\sigma_0$$

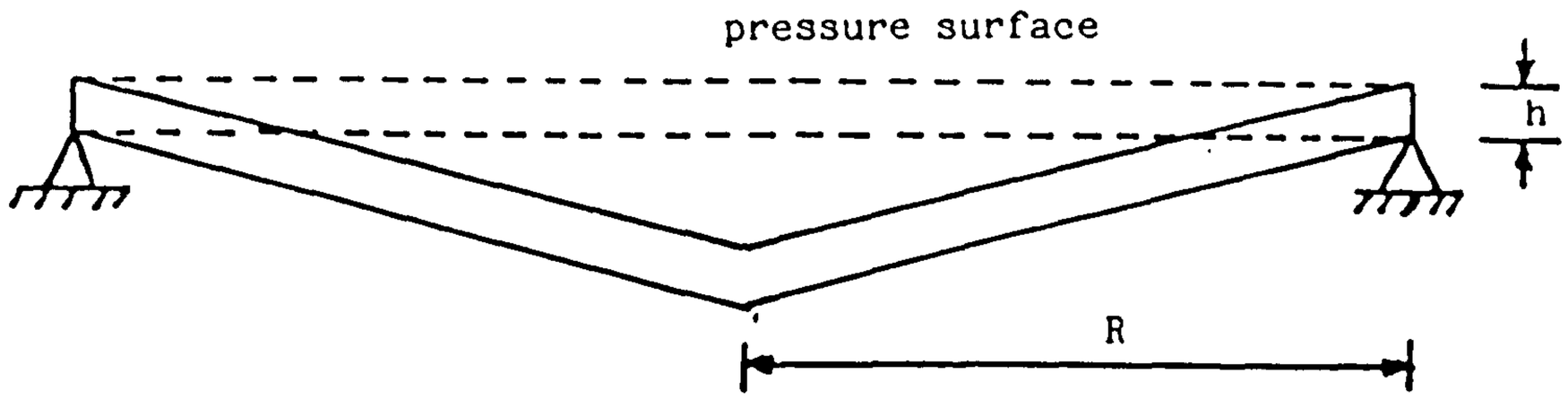

Fig.2.12(iv) Conical deformation of collapse.
$(\frac{E\alpha\Delta T}{3\sigma_0} < 2.0)$

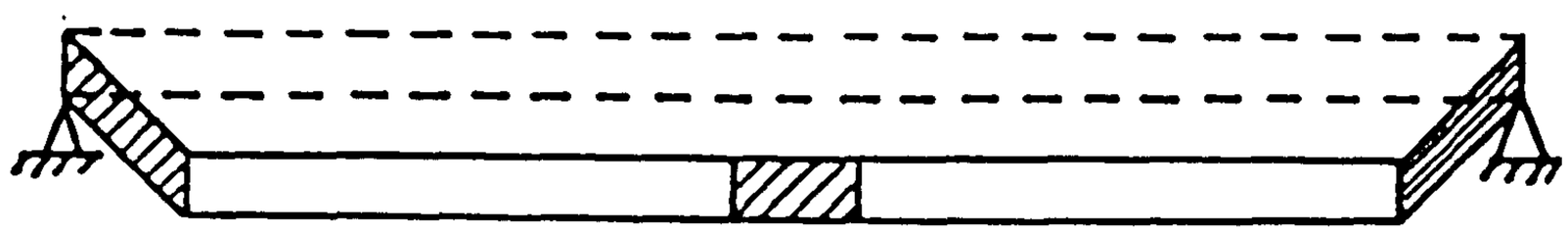

Fig.2.12(v) Shear mechanism of collapse.
$(\frac{E\alpha\Delta T}{3\sigma_0} > 2.0)$

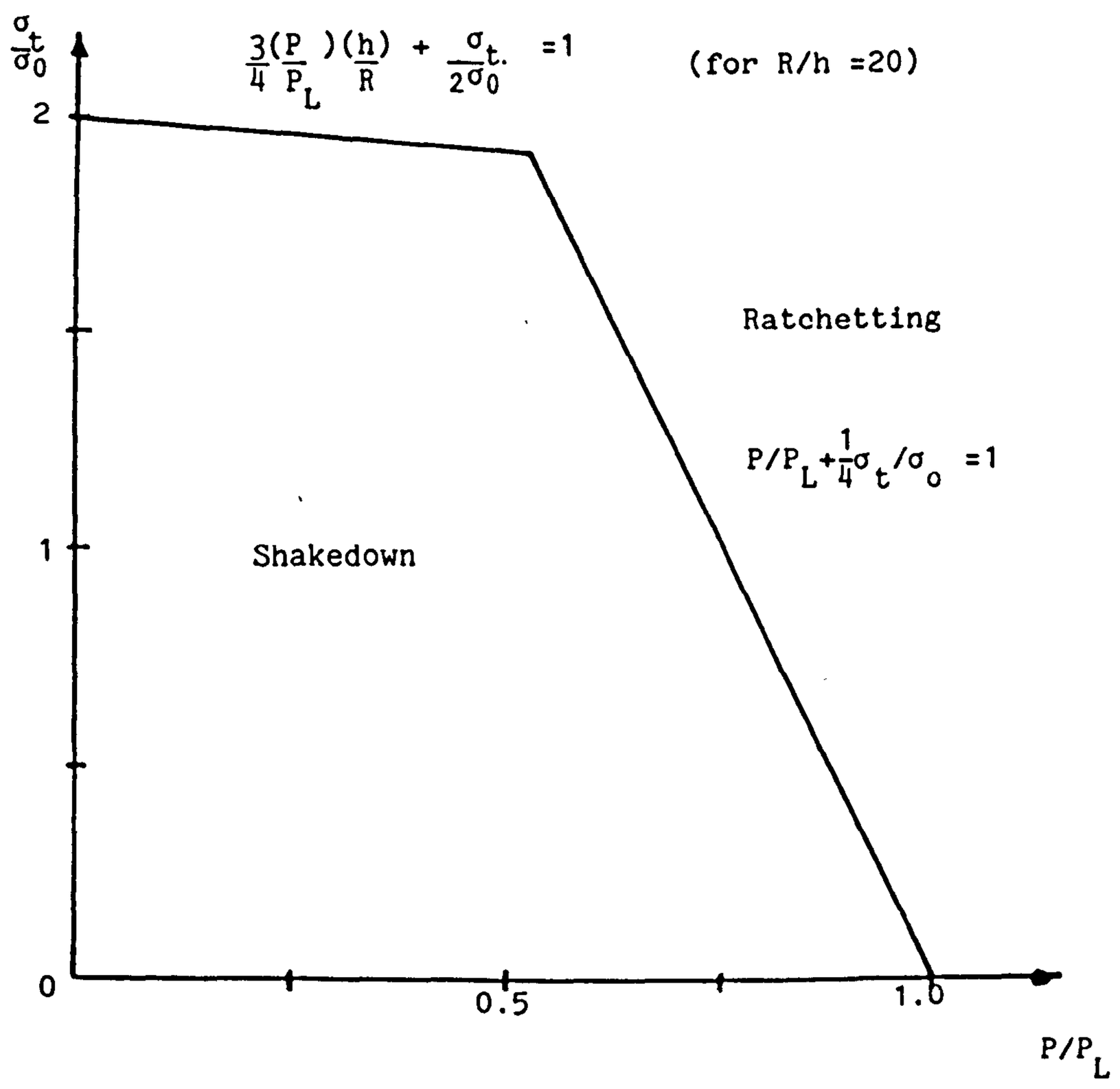

Fig.2.12(vi) Shakedown/ratchetting boundary for the plate solved by Ponter (7). $P_L = 1.5h^2\sigma_0/R^2$, $\sigma_t = E\alpha\Delta T/3$

CHAPTER 3.

RATCHETTING OF THIN TUBES.

3.1 Introduction.

Tubes are used in many industrial applications. Often they are subjected to internal pressure and cyclic, through-thickness, temperature variations. When the resulting thermal strains and pressures are large enough, ratchetting will occur. Bree (8) obtained analytical solutions to predict shakedown/ratchetting boundaries and ratchet strains for a uniaxial simplification of the problem. In order to obtain the analytical solutions, Bree (8) assumed that the axial stress was zero and he neglected the radial stresses.

In many practical situations, axial loading (e.g.due to pressurized end closures on components), axial restraint (e.g.due to end restraints on pipework systems) or non-uniformity of wall thickness (e.g.resulting from initial manufacture or due to corrosion) may be present. In this chapter the effects of each of the above deviations from the problem analysed by Bree, for the shakedown/ratchetting boundary and the ratchet strains are investigated.

The effect of 'complete' stress redistribution due to creep which occurs during 'long' dwell periods between thermal cycles is also investigated.

3.2 Tube Geometries and Finite Element Meshes.

For the uniform wall thickness analyses, a tube with an outside diameter to thickness ratio of 20 was used. Since the component and loadings (see section 3.4) were axisymmetric, the mesh simply consisted of four elements (four elements through the thickness by one element along the length). Eight-noded, axisymmetric, isoparametric elements with 4 'gauss integration' points per element were used.

For the non-uniform wall thickness analyses, a tube with an outside diameter to mean wall thickness ratio of 20 was chosen, so that the results could be compared with those from the uniform thickness tube analyses. The eccentricity of the centre of the bore with respect to the centre of the outside diameter was chosen to be 0.2 x the mean wall thickness. This eccentricity was considered to be the absolute maximum that was likely to occur in practice. Since the geometry was not axisymmetric, simple axisymmetric finite element mesh could not be used. The mesh, consisting of 48, 8-noded, isoparametric, plane stress elements, with four 'gauss integration' points per element, is shown in Fig.3.1.

3.3 Material Properties.

The elastic-plastic material properties were chosen to approximate those of 316 Stainless Steel at elevated temperature (i.e.400 to 600^{o}C). An elastic-perfectly-plastic material (with E/σ_0=1000), having a Poisson's ratio, ν , of

0.3, was used. All the mechanical and thermal properties were assumed to be independent of temperature, the actual properties used are given in Table 3.1.

During the dwell periods, a steady-state power-law creep (Norton Creep) formulation was used (i.e. $\dot{\varepsilon}^c = A\sigma^n$). Since complete stress redistribution was allowed in all cases, the actual values of the constants in the creep law do not have an effect on the subsequent ratchet strains for the uniform wall thickness tubes. For the non-uniform wall thickness tubes, only the stress index,n, can have an effect on the subsequent ratchet strains; results were obtained for stress exponents of 3,5 and 7. The constants in the creep law were assumed to be temperature independent.

The von-Mises effective stress criterion and the Prandtl-Reuss flow rule were used to relate the multi-axial behaviour to uniaxial behaviour for both the plasticity and creep calculations.

3.4 Loading Conditions and Boundary Conditions.

Pressure loading was applied to the bore of the tubes in all cases (for both uniform and non-uniform wall thickness). Calculations were then carried out for both the uniform and the non-uniform wall thickness tubes with a zero axial stress condition imposed. These calculations were performed so that direct comparisons with the Bree solution (8) could be made. Further calculations were carried out for the uniform wall

thickness tube in which

i) a uniform axial strain, with an axial load (corresponding to a long, closed ended cylinder conditions), was imposed and

ii) a zero total axial strain was imposed

The first of these simulates a more realistic condition than that assumed by Bree (8). The second simulates a pipe which has its ends constrained from moving. This condition sometimes occurs when a pipe (without bellows) is used to carry fluid between two relatively stiff components.

In all cases (for both uniform and non-uniform wall thickness tubes), the thermal load was applied by incrementally imposing through thickness temperature distributions to the tubes. During a complete thermal loading cycle, the temperature of the external surfaces were maintained constant at temperature, T, while the temperatures of the internal surfaces were increased from T to T+ΔT and then reduced back to T, linear through thickness temperature distributions being maintained at every stage during the thermal loading.

3.5 Results and Discussion.

3.5.1 Effect of the Pressure on the Bore.

In order to obtain simple analytical solutions, Bree (8) neglected the variation of radial stress (-P at the bore and

zero at outside) and the consequent variations in the hoop stress. In this section the effect of the radial pressure, in the absence of axial stress (as assumed by Bree (8)) is investigated. The load combinations for which the finite element results were obtained are given in Table 3.2. Applying Lame's equations, the elastic radial stress and hoop stress, σ_r^p and σ_θ^p respectively, due to pressure, P, are given by

$$\sigma_r^p = \frac{PR_i^2}{(R_o^2-R_i^2)} \left(1 - \left[\frac{R_o}{r}\right]^2 \right) \qquad 3.1$$

and

$$\sigma_\theta^p = \frac{PR_i^2}{(R_o^2-R_i^2)} \left(1 + \left[\frac{R_o}{r}\right]^2 \right) \qquad 3.2$$

Although the hoop stress is not uniform through the thickness (see Fig.3.2) when the pressure is applied, the mechanical load is still conveniently characterised by the mean hoop stress i.e.

$$\sigma_p = PR_i/h \qquad 3.3$$

Under zero axial stress conditions, the maximum elastically calculated thermal stress is given by:-

$$\sigma_t = E\alpha\Delta T/2 \qquad 3.4$$

3.5.1.1 Ratchetting Mechanisms.

For this type of component, two ratchetting regimes can be identified, these were defined as R_1 and R_2 by Bree (8), see Fig.2.12(ii). Detailed finite element results are presented for one load combination in each regime.

a) The R_1 Regime.

For a load combination of $\sigma_p/\sigma_o=0.758$ and $\sigma_t/\sigma_o=1.376$, the distributions of radial and hoop stresses, after the applications of the internal pressure, are shown in Fig.3.2. Fig.3.3(i) shows the through thickness distribution of the hoop stress at the end of the first half cycle and the hoop stress at the end of the second half cycle.

It can be seen that tensile yielding occurs over more than half the thickness of the tube at the end of each half cycle. There exists a volume of material, near the centre, in which tensile yielding occurs during each half cycle, this gives rise to the ratchetting behaviour. The increments of plastic hoop strain at the end of each half cycle are shown in Fig.3.3(ii). The ratchet strain during the cycle, in this case, is the sum of these plastic strain increments. It is observed that the through thickness variations of plastic hoop strain increment over a cycle are not uniform. This is due to the non-uniform distribution of the radial stress through the thickness. The variation of total strain at the mid-thickness with cycle number is included in Fig.3.4(i). Fig.3.4(ii) includes the

variation of ratchet strain at the tube mid-thickness with cycle number. A large ratchet strain occurs in the first cycle and is constant for each cycle after the first. The mechanism is very similar to that described by Bree (8). However, in the Bree's analysis, the stress distributions during the first and second half cycles of each thermal shock are mirror images of each other. When the radial pressure is included in the analysis, the stress distributions are no longer mirror images.

b) The R_2 Regime.

For a load combination of $\sigma_p/\sigma_o=0.379$ and $\sigma_t/\sigma_o=3.0$, the through thickness distribution of the hoop stress at the end of first and second half cycles are shown in Fig.3.5(i). Both compressive and tensile yielding occurs at the end of each half cycle. The volume of material at the tube mid-thickness yields in tension at the end of each half cycle whilst the material at the surfaces, exhibit cyclic plasticity over a cycle. The through thickness variation of the increment of plastic hoop strain at the end of each half cycle is shown in Fig.3.5(ii).

The variations of the total hoop strains and hoop ratchet strain with cycle number are included in Figs.3.4(i) and (ii) respectively. Again, a large ratchet strain was obtained in the first cycle. A constant ratchet strain was obtained for the second and subsequent cycles.

As was the case in the R_1 regime, the 'mirror image' stress distributions predicted by the Bree's analysis were not

obtained. However, the ratchetting mechanism was found to be essentially the same as that predicted by Bree (8).

3.5.1.2 Effect of Mechanical and Thermal Load Magnitudes on Ratchet Strains.

For each load combination given in Table 3.2, five cycles of thermal loads were imposed. Steady state ratchetting was achieved in each case. The steady state ratchet strain per cycle at the tube mid-thickness for each load combination is given in Table 3.2.

The variations of the steady state ratchet hoop strains with σ_p/σ_o for constant σ_t/σ_o values are shown in Fig.3.6. From Fig.3.6, the shakedown/ratchetting boundary (i.e. the boundary above which ratchetting occurs) was determined by linearly extrapolating the result to zero ratchet strain. The amount of extrapolation is small. The extrapolated values are given in Table 3.2 and in Fig.3.7 which shows the shakedown and ratchetting regions on a 'Bree-diagram'. The contours of constant ratchet strains, linearly interpolated from Fig.3.6 are also shown in Fig.3.7. The shakedown/ratchetting boundary and the constant ratchet strain contours obtained from the finite element results are very accurately predicted by the Bree's analysis(8). It is therefore concluded that the effect of the variations in the hoop and radial stress distributions, caused by the pressure applied to the bore, have a very small effect on the ratchetting behaviour.

3.5.2 Effect of Pressurised Closed Ends.

As well as ignoring the radial stress variations and the consequent hoop stress variations, Bree (8) also assumed that axial stresses are zero in order to obtain a simple analytical solution. In this section the effect of axial stress, caused by pressurised end closures, on a long cylinder is investigated. The elastic axial stress due to pressure, σ_z^p is given by:-

$$\sigma_z^p = PR_i^2/(R_o^2 - R_i^2) \qquad 3.5$$

The radial and hoop stresses are also given by Equations 3.1 and 3.2 respectively. Again, for convenience, the mechanical load is characterised by the mean hoop stress (Equation 3.3). However, because uniform axial strain conditions were imposed, the maximum, elastically calculated thermal stress is given by:-

$$\sigma_t = E\alpha\Delta T/2(1-\nu) \qquad 3.6$$

In the following description of the results, Equation 3.6 is used to characterise the thermal loading. The load combinations for which the finite element results were obtained are given in Table 3.3.

3.5.2.1 Ratchetting Mechanisms.

As in the case where zero axial stress conditions are imposed (section 3.5.1), ratchetting regimes R_1 and R_2 can be identified. Typical behaviour in both regimes is illustrated by Figs 3.8 to 3.10.

a) The R_1 Regime.

The distribution of axial and hoop stresses through the thickness for a load combination of σ_p/σ_o=0.853 and σ_t/σ_o=1.5 are shown in Fig.3.8(i). Due to the pressure loading, the axial stress is uniform through the thickness, whereas the hoop stress varies slightly across the thickness. When thermal loading is applied, both the axial and hoop stresses change. In the first half of each cycle, at the steady ratchet state, the through-thickness distribution of the axial and hoop stresses are also shown in Fig.3.8(i). Yielding occurs in the tensile-tensile quadrant of the yield surface (in the σ_z-σ_θ plane) over more than half the tube thickness. In the second half of each cycle, at the steady ratchet state, yielding also occurs in the tensile-tensile quadrant of the yield surface over more than half the tube thickness. The material near the mid-thickness position yields during each half cycle. Also, due to the non-uniform distribution of through-thickness radial stress, the stress distribution during each of the first half cycles, Fig.3.8(i) are not a mirror image of that in the second half cycle. Fig.3.8(ii) shows the increments of the plastic axial and hoop strain components over

each half cycle in the steady ratchet state. Also in this case, the sum of each of the half cycle plastic strain increments gives the ratchet strain. As expected, the axial ratchet strain is uniform through the thickness because 'plane sections remain plane'. However, the ratchet hoop strain is not uniform through the thickness. Also, the magnitude of the axial ratchet strain is lower than the magnitude of the hoop ratchet strain.

The variation of total axial and mid-thickness total hoop strains with cycle number are shown in Fig.3.9(i). The corresponding variation of ratchet strains with cycle number are shown in Fig.3.9(ii). A steady ratchet occurs after the first cycle. The mechanism is similar to the Bree's analysis (8), that is, yielding of material near the centre during each half cycle is necessary to cause ratchetting in the tube.

b) <u>The R_2 Regime.</u>

A load combination of $\sigma_p/\sigma_o=0.568$ and $\sigma_t/\sigma_o=2.5$ is chosen to illustrate the behaviour in the R_2 regime. For this load, the through thickness distribution of the axial and hoop stresses are shown in Fig.3.10(i). In the first half of each cycle, in the steady cyclic state, yielding in the compression-compression quadrant of the yield surface in the σ_θ-σ_z space occurs near the inner surface. Yielding in the tensile-tensile quadrant occurs at the outer surface of the tube and extends to more than half the tube thickness. The

reverse occurs during the second half of each cycle. As in the R_1 regime, the material near the centre yields in tensile-tensile quadrant during each half cycle. This was also observed for the tube with zero axial load described in section 3.5.1. Also, as for load combinations in the R_1 regime and for the tube with zero axial stress, the distribution of stresses through the thickness in the first half of each cycle is not a mirror image of the distribution in the second half of each cycle. The variation of the plastic axial and hoop strain increments through the thickness during each half cycle, at the steady ratchet state are shown in Figs.3.10(ii) and (iii) respectively. As expected, the ratchet axial strain is uniform through the thickness whereas the ratchet hoop strain varies through the thickness; the maximum ratchet hoop strain occurs at the inner surface.

3.5.2.2 Effect of Mechanical and Thermal Load Magnitudes on Ratchet Strains.

Similar linear extrapolations and interpolations of plots of ratchet strain versus σ_p/σ_o, under constant σ_t/σ_o values, were used to obtain the shakedown/ratchetting boundary and contours of constant ratchet strain. The shakedown/ratchetting boundary is shown in Fig.3.11 (numerical values are given in Table 3.3) together with the contours of constant ratchet strains. Also shown in Fig.3.11 is the shakedown/ratchetting boundary obtained from the simplified Bree's analysis (8). The presence of the axial stress has a significant effect on the shakedown/ratchetting boundary. It is seen that the axial

stress, which is not included in Bree's analysis (8), significantly increase the loads which are required to cause ratchetting. The axial stress reduces the effective stress in the tube. The equivalent stress at the mid-thickness, due to pressure only, $\bar{\sigma}^{p}_{eq}$, from Equations 3.1, 3.2 and 3.5, can be expressed by:-

$$\bar{\sigma}^{p}_{eq} = 0.9091\sigma_{p} \qquad 3.7$$

for the present tube geometry.

Fig.3.12 shows the shakedown/ratchetting boundary obtained from the method outlined above, plotted as σ_{t}/σ_{o} versus $\bar{\sigma}^{p}_{eq}/\sigma_{o}$. Also shown in Fig.3.12 is the boundary obtained from Bree's analysis (8). The two boundaries are practically the same. Therefore Bree's solution could be used provided the mechanical load is characterised by the equivalent stress at the mid-thickness. If the Bree's solution (8) is used in this manner a safe boundary against ratchetting is obtained.

When the axial stress is not zero, the behaviour differs slighty from the zero axial stress case. For the case considered, which modelled the pressurised closed ends, a biaxiality ratio of 2:1 was applied; i.e. the ratio of the hoop stress to axial stress is 2. As pointed out earlier, the effective stress is reduced for this biaxiality ratio and the pressure required to cause ratchetting is increased compared to the zero axial stress case. Hence the shakedown/ratchetting boundary as shown in Fig.3.11 does not correlate with the

simplified Bree's analytical boundary (8). This is different from the component analysed by Hyde (15) which has a biaxiality ratio of 1:1. In (15) the shakedown ratchetting boundary practically coincided with Bree's boundary. However, for the present case, if the equivalent stress at the tube mid-thickness is taken as the mechanical load parameter, a better correlation is obtained as shown in Fig.3.12. The Bree's boundary is conservative.

3.5.3 Effect of Complete Axial Restraint.

In sections 3.5.1 and 3.5.2, slight deviations from the Bree's analysis (8) were investigated. In this section a somewhat extreme, but practically relevant deviation from the Bree's analysis is investigated; complete axial restraint, i.e. no strain in the axial direction, is imposed.

The radial and hoop stresses due to pressure are also given by Equations 3.1 and 3.2 respectively. Again, the mechanical load is characterised by the mean hoop stress (Equation 3.3). Due to the axial restraint, the component of axial stress σ_z^p is given by:-

$$\sigma_z^p = \nu(\sigma_r^p + \sigma_\theta^p)$$

$$= 2\nu PR_i^2/(R_o^2 - R_i^2) \qquad 3.8$$

Equations 3.1, 3.2 and 3.8, give the equivalent stress due to pressure;

$$\sigma^{p}_{eq} = \frac{1}{2} \frac{PR_i^2}{(R_o^2 - R_i^2)} \left[6\left(\frac{R_o}{r}\right)^2 + 2(1-2\nu)^2 \right]^{1/2} \qquad 3.9$$

From equation 3.9, the equivalent stress due to pressure at the outer surface $\overset{v}{\sigma}{}^{p}_{eq}$ is given by

$$\overset{v}{\sigma}{}^{p}_{eq} = 0.8420PR_i/h \qquad 3.10$$

for the present tube geometry and dimension.

The expression 3.10 will be used later.

The linear through-thickness temperature distribution, T', is given by:-

$$T' = -\frac{\Delta T}{2}\left(\frac{2x}{h} - 1\right) + \bar{T} \qquad 3.11$$

where x is measured from the tube mid-thickness. When the temperature distribution, T', is applied, assuming the tube is very thin, the hoop stress, σ^{T}_{θ}, and the axial stress, σ^{T}_{z}, are given by:-

$$\sigma_\theta^T = 2\sigma_t x/h \qquad 3.12$$

and

$$\sigma_z^T = \nu\sigma_\theta^T - E\alpha'(T' - T)$$

$$= -\sigma_t(1 - \nu - 2x/h) \qquad 3.13$$

where

$$\sigma_t = \frac{E\alpha\Delta T}{2(1-\nu)} \qquad 3.14$$

Equation 3.14 is used to characterise the thermal load. The maximum values for both σ_θ^T and σ_z^T occurs at x=-h/2 and hence the maximum equivalent thermal stress ($\hat{\sigma}_{eq}^T$) can be determined This is given by

$$\hat{\sigma}_{eq}^T = 1.48\sigma_t \qquad 3.15$$

The effect of using Expressions 3.10 and 3.15 as the mechanical and thermal load characteristics will be assessed. The elastic thermal stresses for σ_t/σ_o=.61 are shown in Fig.3.13(ii).

3.5.3.1 Ratchetting Mechanism.

In this case, R_1 and R_2 regimes are not clearly identifiable, although, at high mechanical load and low thermal load, the behaviour is similar to that in the R_1 regime. The axial restraint produces axial stresses which depend on both the mechanical and thermal loads; these axial stresses affect the behaviour considerably. The behaviour is illustrated by results for the load conditions of $\sigma_p/\sigma_o=0.995$ and $\sigma_t/\sigma_o=0.688$ and for $\sigma_p/\sigma_o=0.284$ and $\sigma_t/\sigma_o=3.5$.

a) Mechanisms for a High Mechanical Load and Low Thermal Loads.

When a load combination of $\sigma_p/\sigma_o=0.995$ and $\sigma_t/\sigma_o=0.688$, was applied, the through thickness variation of the stresses during a cycle, at the steady ratchet state, are shown in Fig.3.14. The radial stresses are practically unaffected by the thermal load. The distribution of stresses due to pressure only, are not uniform through the thickness.

At the end of the thermal loading, yielding occurs over more than half the thickness near the outer surface. Neglecting the radial stress, yielding occurs in the tensile-tensile quadrant of the yield surface in the σ_θ-σ_z space. At the end of the thermal unloading (second half cycle) yielding also occurs in the tensile-tensile quadrant of the yield surface to more than half the tube thickness. Over a cycle, in the steady ratchet state, there is an 'overlap' of the plastic zone in the region

of the tube mid-thickness. The increment of the plastic axial strains through the thickness are shown in Fig.3.15(i). A compressive increment is obtained in the first half cycle whereas in the second half of each cycle, a tensile increment is obtained. In a cycle, the ratchet axial strain, which is also given by the sum of the plastic strain increments during each half cycle, is zero. The increment of the plastic hoop strain through the thickness in the first and second half of each cycle are shown in Fig.3.15(ii). A tensile increment occurs during each half cycle which gives a non-zero ratchet strain. The variation of ratchet hoop strain through the thickness is also shown in Fig.3.15(ii). The non-uniform through thickness stress distribution result in a non-uniform through thickness ratchet hoop strain. The variations of total hoop strain and ratchet hoop strain, at the mid-thickness, with cycle number are shown in Fig.3.16(i) and (ii). It can be seen that a steady ratchet occurs after the second cycle.

b) Mechanism of Ratchetting for σ_p/σ_o=0.284 and σ_t/σ_o=3.5.

In this case, the thermal loading is much more severe. The most severe loading occurs at the end of each thermal upshock (first half cycle) and at the end of each thermal downshock (second half cycle). The through-thickness distributions of axial stress, at the ends of each thermal upshock and thermal downshock, at the steady ratchet state, are shown in Fig.3.17(i). Fig.3.17(ii) shows the through-thickness distributions of the hoop stress at the end of each thermal upshock and thermal downshock. The thermal load is so severe

that it is possible for yielding to occur throughout the tube material at the end of each half cycle. In the first half cycle, the yield zone can be divided into the following:-

a) for $-0.5<x/h<-0.0875$ yielding occurs in the compressive-compressive quadrant of the yield surface,

b) for $-0.0875< x/h < 0.1875$ yielding occurs in the compressive (axial)-tensile (hoop) quadrant of the yield surface and

c) for $0.1875 < x/h < 0.5$ yielding occurs in the tensile-tensile quadrant of the yield surface.

Due to the severity of the thermal load, it is also possible for yielding to occur throughout the material in the second half cycle. The following zones are obtained:

a') $-0.5 < x/h < 0.2375$ yielding occurs in the tensile-tensile quadrant,

b') for $0.2375 < x/h < 0.425$ yielding occurs in the compressive (hoop)- tensile (axial) quadrant of the yield surface and

c') for $.425 < x/h < 0.5$ yielding occurs in the compressive-compressive quadrant of the yield surface.

Again, the radial stresses are negligible. The through-thickness distribution of the axial and hoop stress in the first half cycle are not mirror images of the distributions in the second half cycle. The mechanism is different from that described in sections 3.5.1 and 3.5.2.

The distributions of plastic axial strain increment through the thickness, at the steady ratchet state, is shown in Fig.3.18(i). A compressive increment occurs in the first half

of each cycle and an equal tensile increment occurs in the second half of each cycle; the axial ratchet strain is zero. Fig.3.18(ii) shows the through-thickness distribution of plastic hoop strain increment. The distribution of the ratchet hoop strain is also shown in Fig.3.18(ii). The ratchet hoop strain is not uniform across the thickness. The variation of the total hoop and ratchet hoop strains at the mid-thickness with cycle number are shown in Fig.3.16. Steady state ratchetting occurs after the second cycle of thermal loads.

3.5.3.2 Effects of Mechanical and Thermal Load Magnitudes on Ratchet Strains.

Table 3.4 shows the load combinations for which the finite element results were obtained. For each load, six thermal cycles were imposed. A steady ratchet state has been achieved in each case.

The steady state maximum ratchet hoop strains and ratchet hoop strains at the mid-thickness for each load combination are also given in Table 3.4. By linearly extrapolating the results to zero ratchet strains, the shakedown/ratchetting boundary is determined. The boundary (denoted as 'computed boundary') is shown in Fig.3.19. Contours of constant mid-thickness ratchet hoop strains and the Bree's boundary (8) are also shown in Fig.3.19. For $\sigma_t/\sigma_o < 1.38$, the Bree's boundary (8) is conservative and for $\sigma_t/\sigma_o > 1.38$, the Bree boundary (8) is unsafe. Fig.3.20 shows the shakedown/ratchetting boundary plotted using the maximum equivalent thermal stress ($\tilde{\sigma}^T_{eq}$) and

the equivalent stress due to pressure at the tube outer surface ($\check{\sigma}^{p}_{eq}$) as the loading characteristics. The correlation of the boundaries is 'improved' slightly. In this case, the Bree boundary is conservative for $\hat{\sigma}^{T}_{eq} < 3.35\sigma_{o}$. Other methods of characterising the loads were attempted but these did not give better correlations.

3.5.4 Effect of Non-uniform Wall Thickness.

In order to investigate the effect of non-uniformity of wall thickness, a zero axial stress condition was imposed so that the results could be compared with Bree's solution (8). The mechanical load was characterised by the mean hoop stress (Equation 3.3) and the thermal loading was characterised by the maximum thermal stress (Equation 3.4).

Jeffrey (81) has obtained an analytical solution for the elastic stresses in a tube with an eccentric bore. For the present geometry (Fig.3.1), the analytical solutions are compared with the finite element predictions (obtained with the mesh shown in Fig.3.1) in Fig.3.21. The comparison indicates that the finite element mesh is adequate.

The load combinations used in the finite element analyses are given in Table 3.5.

3.5.4.1 Ratchetting Mechanisms.

Unlike the uniform wall thickness tubes, for a given

combination of loads, in general, there is not a single mechanism which characterises the behaviour of the non-uniform wall thickness tube. However, at any particular circumferential position, the mechanism can be identified as lying in either the shakedown, S, cyclic plasticity, P, or ratchetting, R_1 or R_2, regimes. The results obtained for two load combinations will be used to illustrate the behaviour of the 'tube'.

a) Behaviour with $\sigma_p/\sigma_o = .568$ and $\sigma_t/\sigma_o = 1.72$.

The variation of the hoop stress with θ at the inner and outer surfaces due to the applications of the pressure is shown in Fig. 3.21. The radial and shear stresses are small and have an insignificant effect on the behaviour of the component. Prior to the thermal loading, the stress distribution is entirely elastic. When the thermal loading is applied, a large plastic zone develops during the first and second halves of the first cycle. The distributions of plastic zone at the ends of the first and second half cycles are shown in Fig.3.22. A large increment of strain is obtained during the first cycle of thermal load. During the subsequent cycles, the growth of the plastic zones are shown in Figs.3.23(i) to (viii). During the thermal loading, i.e. in the first halves of the cycles, the plastic zones emanate from the mid-thickness position, at the thinnest section of the tube (i.e. $\theta = 0^0$) as shown in Fig.3.23(i). After this, the plastic zone spreads in the hoop and radial direction towards the outer surface. The extent of the plastic zone at the 17th of 21 increments and at the end of

the thermal loading (21st of 21 increments) are shown in Figs.3.23(ii) and 3.23(iii) respectively. Fig.3.23(iv) shows the regions which experience plastic straining during the first half cycle. During the thermal unloading, i.e. in the second half cycle, the plastic zone again emanates from the mid-position of the thinnest section, as shown in Fig.3.2 3(v). During the thermal unloading, the plastic zone spreads in the hoop and radial directions towards the inner surface. Figs.3.23(vi) and 3.23(vii) show the plastic zones at the 17th of 21 increments of the second half cycle and at the end of the second half cycle. Fig.3.23(viii) shows all of the regions which experience plastic straining during the thermal unloading. It is observed that, there is a zone which experiences plastic straining over both the first and second halves of a thermal cycle. However, this zone does not extend over the whole circumference of the tube. The region of particular interest is that which experiences plastic straining in the region close to the thinnest section, i.e. at $\theta=0^{o}$. The variation of the stresses at $\theta=3^{o}$, at the inner surface and at the mid-thickness position, with cycle number are shown in Fig.3.24(i). It can be seen that a steady cyclic state is achieved after about 7 cycles. The corresponding variation of the total strain with cycle number is shown in Fig.3.24(ii). The large changes in the total strain at the inner surface, during the thermal loading, is due to the thermal expansion which is insignificant at the mid-thickness. Fig.3.25 shows the variation of the ratchet strains at the mid-thickness position with θ, it can be seen that ratchetting is confined to the region $0^{o} < \theta < 94^{o}$ with the maximum value occuring at $\theta=0^{o}$.

The variations of ratchet strains with cycle number, at $\theta=3^{o}$, at the inner surface and mid-thickness positions, are shown in Fig.3.26. Apart from the small variations due to the accuracy criterion of 0.5% (see Appendix III section AIII.4.1.) used in the plasticity calculations, steady state ratchetting occurred after about the 7th cycle.

The variations of stress, through the thickness , at $\theta=3^{o}$ and at $\theta=27^{o}$, are shown in Figs.3.27(i) and (ii) respectively. The behaviour is similar except that the 'overlap' region at the mid-thickness position is smaller at $\theta=27^{o}$ compared to that at $\theta=3^{o}$. In fact, this 'overlap' region reduces to zero at $\theta= 94^{o}$. The variation of increment of plastic strain, through the thickness, at $\theta=3^{o}$ and at $\theta=27^{o}$ are shown in Fig.3.28(i) and Fig.3.28(ii) respectively. The distribution of the ratchet strain through the thickness, at $\theta=3^{o}$ and at $\theta=27^{o}$, are shown in Fig.3.28(iii). Although the distribution is not uniform through the thickness, the behaviour is essentially the same as that described by Bree (8).

Figs.3.29(i) and 3.29(ii) show the displacements at the 10th cycle and the ratchet displacement at the steady ratchet state for the tube, respectively.

b) Behaviour with $\sigma_p/\sigma_o= 0.379$ and $\sigma_t/\sigma_o= 2.5$

This load combination represents a low mechanical and high thermal load which is common in LMFBR components. Prior to the thermal loading, the stress distribution is also entirely

elastic. When the thermal loading is applied, in the first half cycle, compressive yielding occurs at the inner surface and tensile yielding occurs at the outer surface. In the second half cycle, plastic tensile yielding occurs at the inner surface and compressive yielding occurs at the outer surface. The distribution of the plastic zone during the first thermal loading and thermal unloading are shown in Figs.3.30(i) and 3.30(ii) respectively. Due to the residual stresses developed during the first cycle, in the subsequent cycles, the plastic zones reduce in size. At the steady cyclic state (achieved after 6 cycles) the developement of the plastic zones during a cycle are shown in Figs.3.31(i) to 3.31(vi). At the steady ratchet state, in the first half cycle, tensile yielding emanates from the mid-thickness position at the thinnest section and spreads in the hoop and radial directions towards the outer surface. Towards the end of the first half cycle, compressive yield starts to develop at the inner surface. The distribution of the plastic zone at the end of the first half of each cycle, at the steady ratchet state, is shown in Fig.3.31(iii). In the second half of each cycle, tensile yielding also emanates from the mid-thickness positions at the thinnest section and spreads around the tube. Near the end of the second half of each cycle, compressive yield zones develop at the outer surface. The distribution of the plastic zones at the end of the second half of each cycle is shown in Fig.3.31(vi). A large plastic zone occurs over a region close to the thinnest section as observed in section 3.5.4.1(a) above.

The distribution of the ratchet strain with θ at the mid-thickness is shown in Fig.3.32. It can be seen that ratchetting also occurs over only a part of the 'tube' and not the whole component. The variations of stresses at $\theta=3^{o}$, at the inner surface and at mid-thickness position, with cycle number are shown in Fig.3.33(i). The corresponding variations of total strain with cycle number are shown in Fig.3.33(ii). It is observed that a steady cyclic state (from Fig.3.33(i)) is achieved after 6 cycles. The ratchet strains at $\theta=3^{o}$ at the mid-thickness and at the inner surface with cycle number are shown in Fig.3.34.

The distribution of the hoop stress through the thickness at $\theta=3^{o}$, $\theta=42^{o}$ and at $\theta=177^{o}$ at the end of each half cycle, at the steady ratchet state, are shown in Figs.3.35(i), 3.35(ii) and 3.35(iii) respectively. The corresponding distributions of plastic strain increments, through the thickness, at $\theta=3^{o}$, $\theta=42^{o}$ and $\theta=177^{o}$, at the end of each half cycle, are shown in Figs 3.35(iv), 3.35(v) and 3.35(vi) respectively. At $\theta=3^{o}$, tensile yielding spreads over more than half the tube thickness at the end of each half cycle. At $\theta=42^{o}$, both tensile and compressive yielding occurs in each half cycle with a non-zero net increment of plastic strain over a cycle. At the mid-thickness position, tensile yielding occurs during each half cycle. This is a characteristic of ratchetting in the R_2 regime of the Bree diagram. At $\theta=177^{o}$, shakedown occurs with cyclic plasticity. For this particular load combination it is possible to obtain both types of behaviour described by Bree (8). However, at the lower values of σ_p/σ_o, ratchetting

in the R_2 region at the thinnest section, with shakedown in the rest of the tube with a cyclic plasticity would occur. The ratchet strains are shown in Fig.3.35(vii).

The displacement of the tube at the 10th cycle is shown in Fig.3.36(i) and Fig.3.36(ii) shows the region of the 'tube' which suffer incremental deformation.

3.5.4.2 Effects of the Thermal and Mechanical Load Magnitudes on Ratchet Strains.

From the results presented in section 3.5.4.1, it is apparent that the shakedown or ratchetting behaviour, at any circumferential position in the non-uniform wall thickness tube, can be identified as similar to that described by Bree in the uniform tube. However, more than one regime can be present within the non-uniform wall thickness tube.

The normalised average ratchet strains at $\theta=3^{o}$(i.e. nearest 'gauss point' plane to the thinnest section) are plotted against σ_p/σ_o, for given values of σ_t/σ_o, in Fig.3.37. By extrapolation and interpolation, the shakedown/ratchetting boundary and contours of constant ratchet strains in Fig.3.38 were obtained. Also shown in Fig.3.38 is the shakedown/ratchetting boundary obtained by Bree (8). It can be seen that the shakedown/ratchetting boundary is non-conservatively predicted by Bree's analytical solution. However, if instead of using the average hoop stress, σ_p, to represent the mechanical loading characteristics, the maximum hoop stress (i.e. the hoop stress at $\theta=0^{o}$, see Fig.3.21) is

used, the correlation is much better (see Fig 3.39). For thin cylinders the maximum hoop stress can be simply obtained by scaling up the mean hoop stress, σ_p, by the ratio of the mean wall thickness to the minimum wall thickness ϕ, i.e.

$$\hat{\sigma}_p = \phi\sigma_p .$$

It is therefore concluded that for design purposes, the ratchetting results for uniform wall thickness thin tubes can be applied to non-uniform wall thickness tubes, provided the minimum wall thickness is considered.

3.5.5 The Effect of Complete Stress Redistribution Due to Creep.

When complete stress redistribution, due to steady load creep between each thermal cycle occurs, the shakedown/ratchetting boundary is coincident with the elastic boundary (see Fig.2.12(ii) for example).

For the uniform wall thickness tubes, the ratchet strain per cycle under complete redistribution conditions is the same as the first cycle ratchet strain. This is because the stationary state stress distribution, i.e. uniform stress, is independent of the creep stress index, n. The contours of constant ratchet strain per cycle, under complete redistribution conditions, for the uniform wall thickness tubes, are given in Fig.3.40(i) to 3.40(iii).

For the non-uniform wall thickness tube, the stationary state stress distributions are not independent of the creep stress index, n; for the particular geometry chosen, the differences are, however, very small, see Fig.3.41(i) to 3.41(iii). To illustrate the behaviour of the non-uniform wall thickness tube when creep occurs, the results for a load combination of σ_p/σ_o=0.379 and σ_t/σ_o=1.376 will be used.

Under no-creep conditions, the variations of hoop stress at the inner and outer surfaces with θ due to the pressure as shown in Fig.3.42 and is purely elastic. The variation of hoop stress due to pressure (indicated as initial), at the end of thermal loading (first half cycle) and at the end of thermal unloading (second half cycle) at $\theta=3^o,42^o,72^o,108^o$, $153^o$and $177^o$are shown in Figs.3.43(i) to (vi). In the first half cycle, tensile yielding occurs at the outer surface. Since the loads correspond to the shakedown region elastic behaviour occurs in the subsequent cycles. The distribution of increment of total strain during the first cycle is shown in Fig.3.44, the maximum occurs at the inner surface for $\theta=0^o$. The variations of maximum total hoop strain and maximum hoop ratchet strain with number of cycles are shown in Fig.3.45(i) and (ii). Shakedown occurs after the first cycle.

When redistribution is allowed to occur, the initial distribution of hoop stress shown in Fig.3.42 changes until the distributions of hoop stress shown in Figs.3.41(i),(ii) and (iii), for n values of 3,5 and 7 respectively, are obtained. For the n values considered the effect of creep is to

redistribute the stresses so that a more uniform distribution, through the thickness, occurs.

The distribution of stress through the thickness, for various values of θ, at the end of first and second half cycles, for n=3,5,and 7, are shown in Fig.3.46(i) to (vi), Figs.3.47(i) to (vi) and Figs.3.48(i) to (vi) respectively. The stress distribution prior to each thermal cycles are also given in Figs.3.46,3.47 and 3.48. For each value of n considered, during the first half cycle, plastic yielding occurs in the region close to the outer surface and elastic behaviour occurs during the second half cycle. The behaviour is similar to the first cycle behaviour of the tube in the 'no-creep' case. The variation of strain increment with θ at various surfaces, through the thickness, for n=3,5 and 7, are shown in Figs.3.49(i), 3.49(ii) and 3.49(iii) respectively. The distribution is very similar to the first cycle behaviour in the 'no-creep' condition as shown in Fig.3.44. Since a stationary state of stress occurs prior to thermal load, the behaviour at successive cycles will be identical to the behaviour just described. At each cycle, an increment of strain as shown in Figs.3.49(i) to (iii) is obtained during each cycle and is practically independent of n. The maximum value occurs at the thinnest section. Table 3.6 shows the values of the maximum ratchet strains and ratchet strains at mid-thickness position, at $\theta=3^{o}$, for the values of n considered. The first cycle ratchet strain for the 'no-creep' case and the predicted value using Bree's analysis (8) are also given. It can be seen that Bree's solution (8) accurately

predicts the mid-thickness ratchet strain of the tube in the presence of creep. The first cycle ratchet strains in the 'no-creep' case are lower than those obtained when creep occurs.

Young's Modulus, E	160 GNm^{-2}
Yield stress, σ_0	160 MNm^{-2}
Poisson's ratio, ν	0.3
Coefficient of expansion, α	20 X 10^{-6} K^{-1}

Table 3.1 Materials data for the elastic-plastic analysis of the tubes.

σ_t/σ_o	σ_p/σ_o	Mid-thickness normalised ratchet hoop strains $\bar{\varepsilon}^R_\theta/\varepsilon_o$			Maximum normalised ratchet hoop strain $\hat{\varepsilon}^R_\theta/\varepsilon_o$	
		first cycle	steady state	shakedown boundary	first cycle	steady state
0.688	0.758	0.0975	0		0.1034	0
	0.853	0.2429	0.166	0.815	0.2597	0.180
	0.947	0.8023	0.557		0.867	0.600
1.204	0.663	0.2584	0		0.2647	0
	0.758	0.5115	0.335	0.696	0.5493	0.363
	0.853	0.9151	0.812		0.9957	0.880
1.376	0.568	0.2475	0		0.2593	0
	0.663	0.3955	0.100	0.639	0.4089	0.108
	0.758	0.7093	0.528		0.7633	0.571
1.720	0.474	0.3258	0		0.3393	0
	0.568	0.455	0.048	0.559	0.4634	0.053
	0.663	0.7374	0.4210		0.7919	0.459
2.064	0.474	0.519	0		0.524	0
	0 568	0.7789	0.368	0.507	0.8304	0.402
	0.663	1.1602	0.889		1.2489	0.958
2.752	0.379	0.7156	0.097	0.351	0.7316	0.107
	0.474	1.1168	0.442		1.199	0.483
3.0	0.379	0.8849	0.274	0.317	0.9246	0.301
	0.474	1.3437	0.666		1.449	0.727
3.5	0.284	0.8128	0.0716	0.275	0.8212	0.080
	0.379	1.2348	0.5779		1.3216	0.634
4.0	0.284	1.0511	0.3084	0.226	1.0862	0.344
	0.379	1.6589	0.8421		1.7976	0.880

Table 3.2 Ratchet strains and shakedown/ratchetting boundary for a uniform tube under plane stress condition.

σ_t/σ_o	σ_p/σ_o	Mid-thickness normalised ratchet hoop strains $\bar{\varepsilon}^R_\theta/\varepsilon_o$			Normalised ratchet axial strains $\varepsilon^R_z/\varepsilon_o$		Maximum normalised ratchet hoop strains $\varepsilon^R_\theta/\varepsilon_o$	
		first cycle	steady state	boundary	first cycle	steady state	first cycle	steady state
0.5	0.947	0.01859	0		0.01067	0	0.0581	0
	0.995	0.1254	0.0721	0.976	0.0137	0.0045	0.1371	0.080
	1.042	0.3054	0.2667		0.0143	0.010	0.3395	0.294
1.0	0.758	0.0069	0		0.0494	0	0.1373	0
	0.853	0.2087	0.0231	0.846	0.0625	0.0037	0.2258	0.026
	0.947	0.5229	0.4114		0.0732	0.04067	0.5817	0.455
1.5	0.663	0.2467	0		0.1266	0	0.2666	0
	0.758	0.4078	0.1468	0.723	0.1488	0.0284	0.4449	0.142
	0.853	0.7456	0.5488		0.1741	0.09	0.8208	0.609
2.0	0.568	0.3728	0		0.2279	0	0.4038	0
	0.663	0.6073	0.2573	0.604	0.2669	0.0753	0.666	0.287
	0.758	0.9389	0.6665		0.3091	0.156	1.0359	0.742
2.5	0.379	0.3566	0		0.2290	0	0.385	0
	0.474	0.4712	0.0150	0.470	0.2826	0.0022	0.5102	0.016
	0.568	0.7626	0.3596		0.3757	0.1187	0.8382	0.402
3.0	0.379	0.5068	0		0.323	0	0.5488	0
	0.474	0.7867	0.3067	0.410	0.4193	0.1093	0.8633	0.343
	0.568	1.151	0.7636		0.5278	0.246	1.2732	0.854
3.5	0.379	0.6772	0.1936		0.3961	0.0791	0.7385	0.217
	0.474	1.120	0.6383	0.338	0.5805	0.2387	1.2383	0.715
4.0	0.284	0.5877	0		0.3581	0	0.6354	0
	0.332	0.6841	0.141	0.309	0.3929	0.0501	0.744	0.157
	0.379	0.9879	0.4377		0.5485	0.1627	1.0875	0.490

Table 3.3 Results for pressurised closed ends tube

σ_t/σ_o	σ_p/σ_o	Mid-thickness normalised ratchet hoop strains $\bar{\varepsilon}^R_\theta/\varepsilon_o$			Maximum normalised ratchet hoop strains $\hat{\varepsilon}^R_\theta/\varepsilon_o$	
		First cycle	steady state	Shakedown boundary	First cycle	Steady state
0.688	0.947	0.5461	0.110	0.923	0.5929	0.111
	0.995	0.890	0.330		0.972	0.363
1.376	0.663	0.567	0.016	0.656	0.6064	0.017
	0.758	0.874	0.221		0.9449	0.244
1.720	0.568	0.7118	0.103	0.531	0.7609	0.114
	0.663	1.0204	0.364		1.1024	0.40
2.064	0.474	0.7957	0.153	0.426	0.8514	0.203
	0.568	1.1127	0.454		1.2009	0.500
2.752	0.284	0.7708	0.144	0.234	0.8185	0.158
	0.379	1.1039	0.415		1.1869	0.457
3.0	0.189	0.5929	0.08	0.1488	0.6207	0.088
	0.284	0.9251	0.269		0.9875	0.297
3.5	0.189	0.8045	0.264	0.107	0.853	0.291
	0.284	1.248	0.568		1.3434	0.625
4.0	0.189	1.0046	0.454	0.0912	1.095	0.556
	0.284	1.557	0.895		1.6834	0.986

Table 3.4 Ratchet hoop strains and shakedown/ratchetting boundary for a tube with uniform thickness subjected to a steady internal pressure and cyclic linear through thickness temperature variation and zero axial strain.

σ_t/σ_o	Peak $\hat{\sigma}_p/\sigma_o$	Mid-thickness ratchet hoop strains at $\theta=3^o$ $(\bar{\varepsilon}^R_\theta/\varepsilon_o)$			Maximum ratchet hoop strains at $\theta = 3^o$ $(\hat{\varepsilon}^R_\theta/\varepsilon_o)$	
		first cycle	steady state	boundary	first cycle	steady state
0.688	0.875	0.3601	0.230		0.5075	0.290
	1.0	3.460	2.81	0.8639	4.451	3.22
1.204	0.750	0.4446	0.196		0.6897	0.280
	0.875	1.240	1.240	0.727	1.799	1.35
1.376	0.750	0.7176	0.535		1.138	0.585
	0.875	1.240	1.41	0.674	1.848	1.460
1.720	0.625	0.5002	0.185		0.7844	0.260
	0.750	1.0426	0.920	0.588	1.544	0.970
	0.875	1.332	1.75		1.868	1.780
2.064	0.625	0.8102	0.581		1.161	0.660
	0.750	1.1726	1.235	0.514	1.604	1.265
2.50	0.375	0.3948	0		0.6874	0
	0.50	0.8437	0.390	0.411	1.216	0.417
	0.625	1.097	0.940		1.313	0.960
3.0	0.250	0.3917	0		0.693	0
	0.375	0.6168	0.070	0.358	1.176	0.123
	0.50	0.9417	0.579		1.225	0.580
3.5	0.250	0.4419	0		0.9226	0
	0.375	0.8033	0.252	0.301	1.3044	0.270
	0.500	0.9637	0.680		1.338	0.733

Table 3.5 Ratchet strains for a tube with an eccentric bore

Cases	Normalised ratchet strain $E\varepsilon_\theta^R/\sigma_o$		
	Computed		Bree's solution*
	Maximum	mid-thickness	
n=3	0.258	0.190	0.204 (all n)
n=5	0.254	0.200	
n=7	0.250	0.198	
first cycle 'no-creep'	0.243	0.174	

Table 3.6 Normalised ratchet strains for elastic-plastic-creep computation.

* The Bree's solution(8) is calculated from the equations

$$\varepsilon^R/\varepsilon_o = (1-\sigma_p'/\sigma_o) + (\sigma_t/\sigma_o)(1-2((\sigma_o/\sigma_t)(1-\sigma_p'/\sigma_o)))^{1/2}$$

by taking $\theta = 0^o$,

$$\sigma_p'/\sigma_o = \frac{\text{stress due to pressure at mid-thickness}}{\text{yield stress}}$$

$$= 77.0/160.0 = 0.48$$

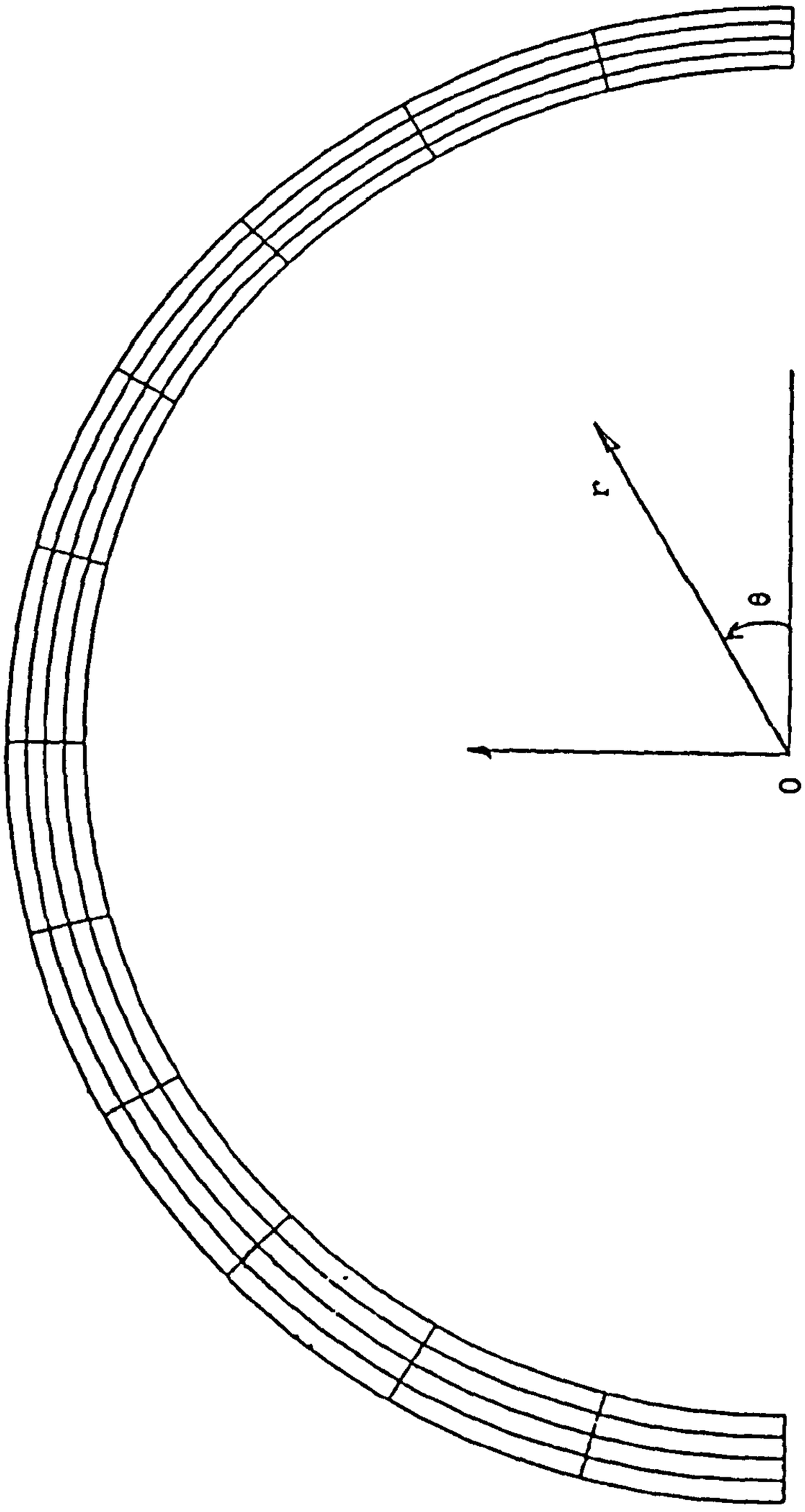

Fig.3.1 Finite element mesh for a tube with an eccentric bore.

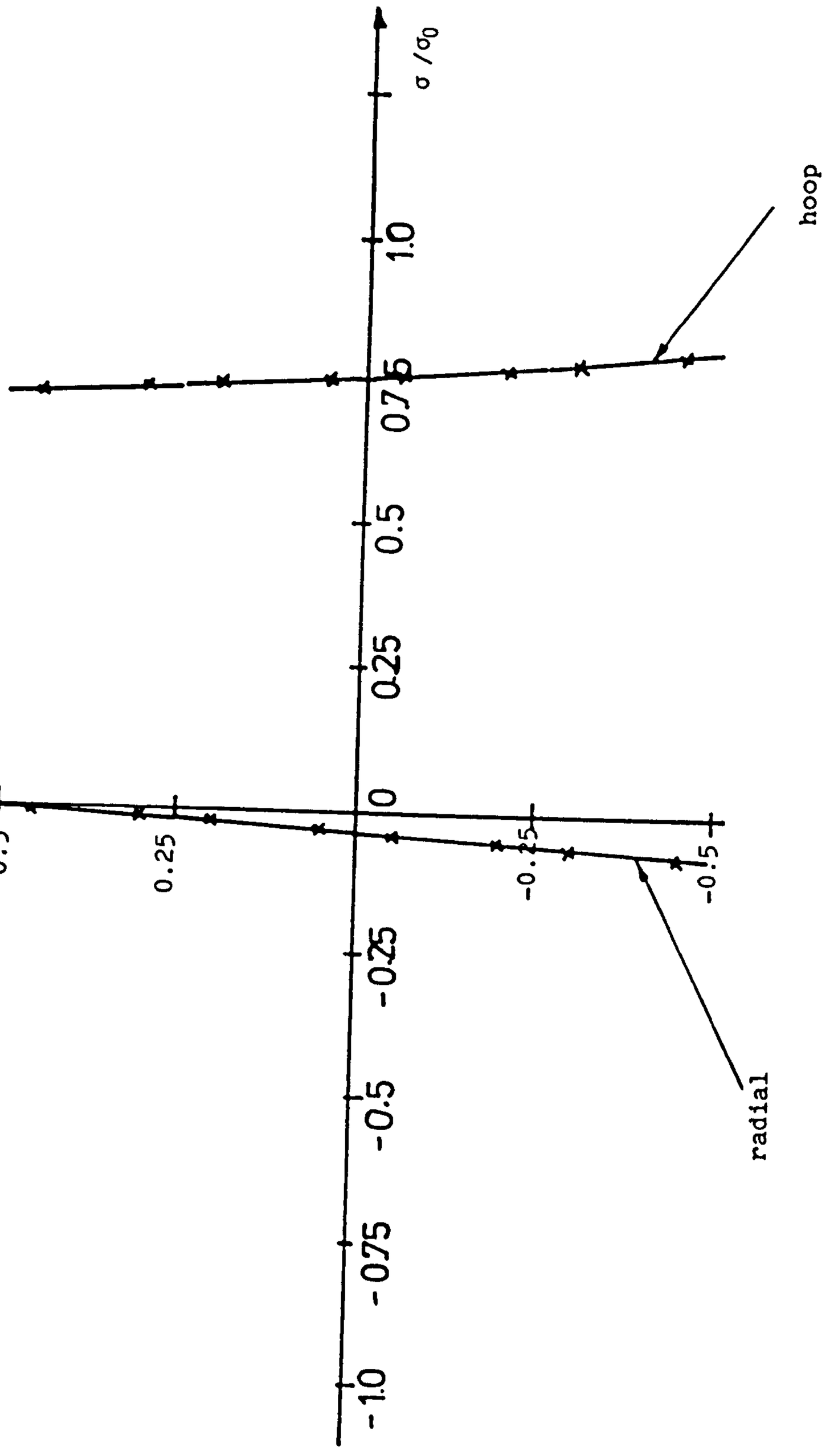

Fig.3.2 Variation of radial and hoop stresses through the thickness for σ_p/σ_0 =0.758.

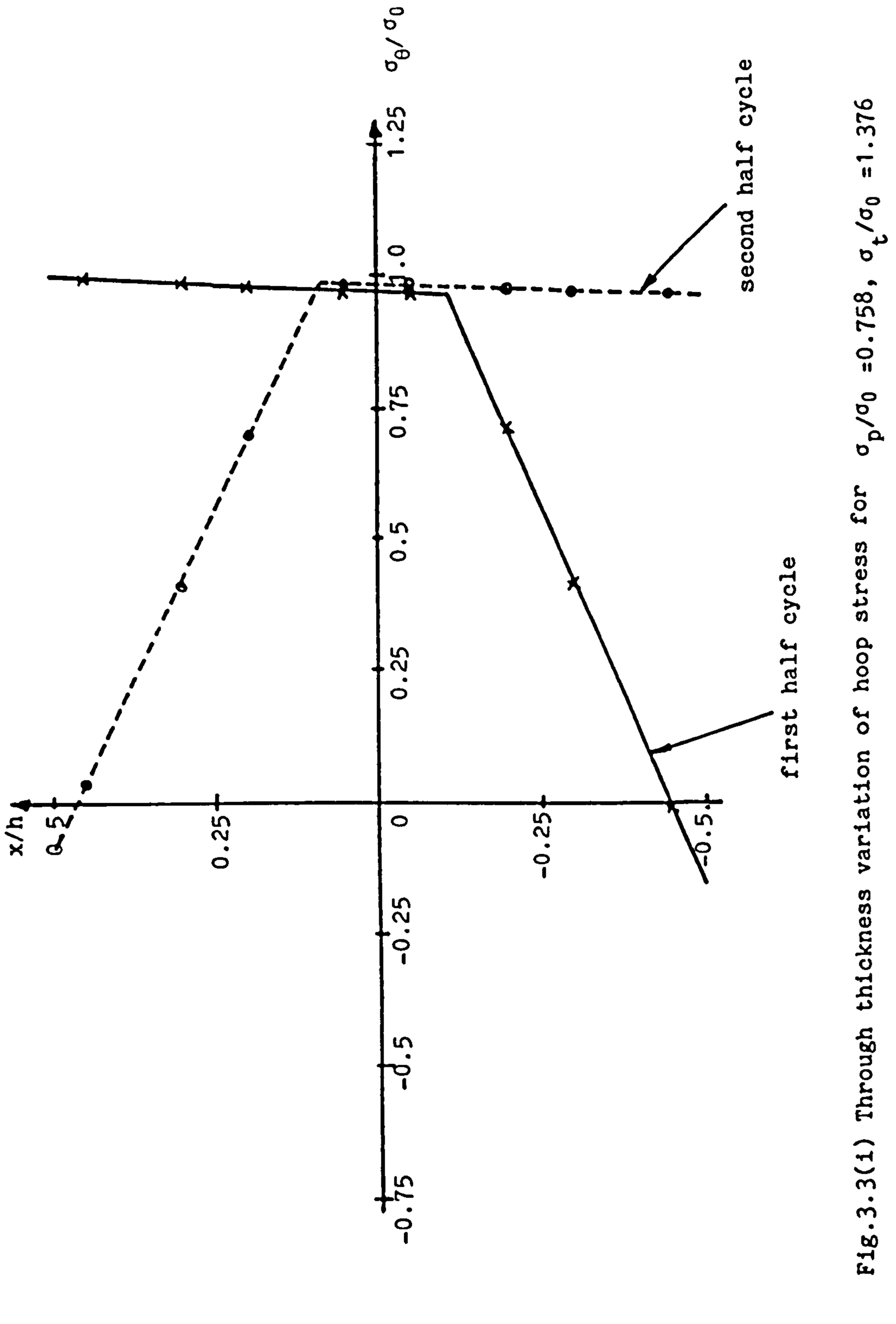

Fig.3.3(1) Through thickness variation of hoop stress for

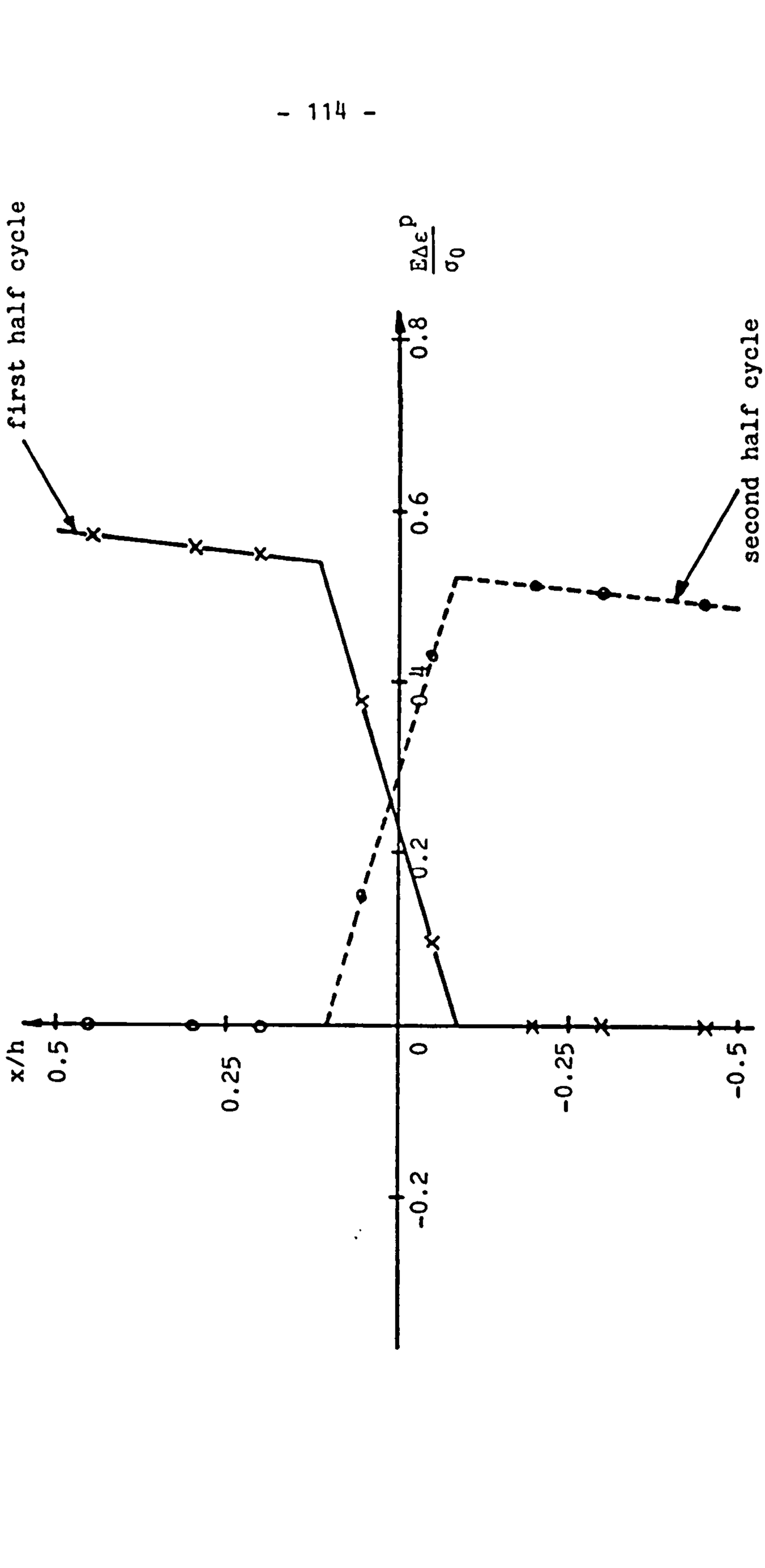

Fig.3.3(11) Through thickness variation of plastic hoop strain increment for σ_p/σ_0 =0.758, σ_t/σ_0 = 1.376

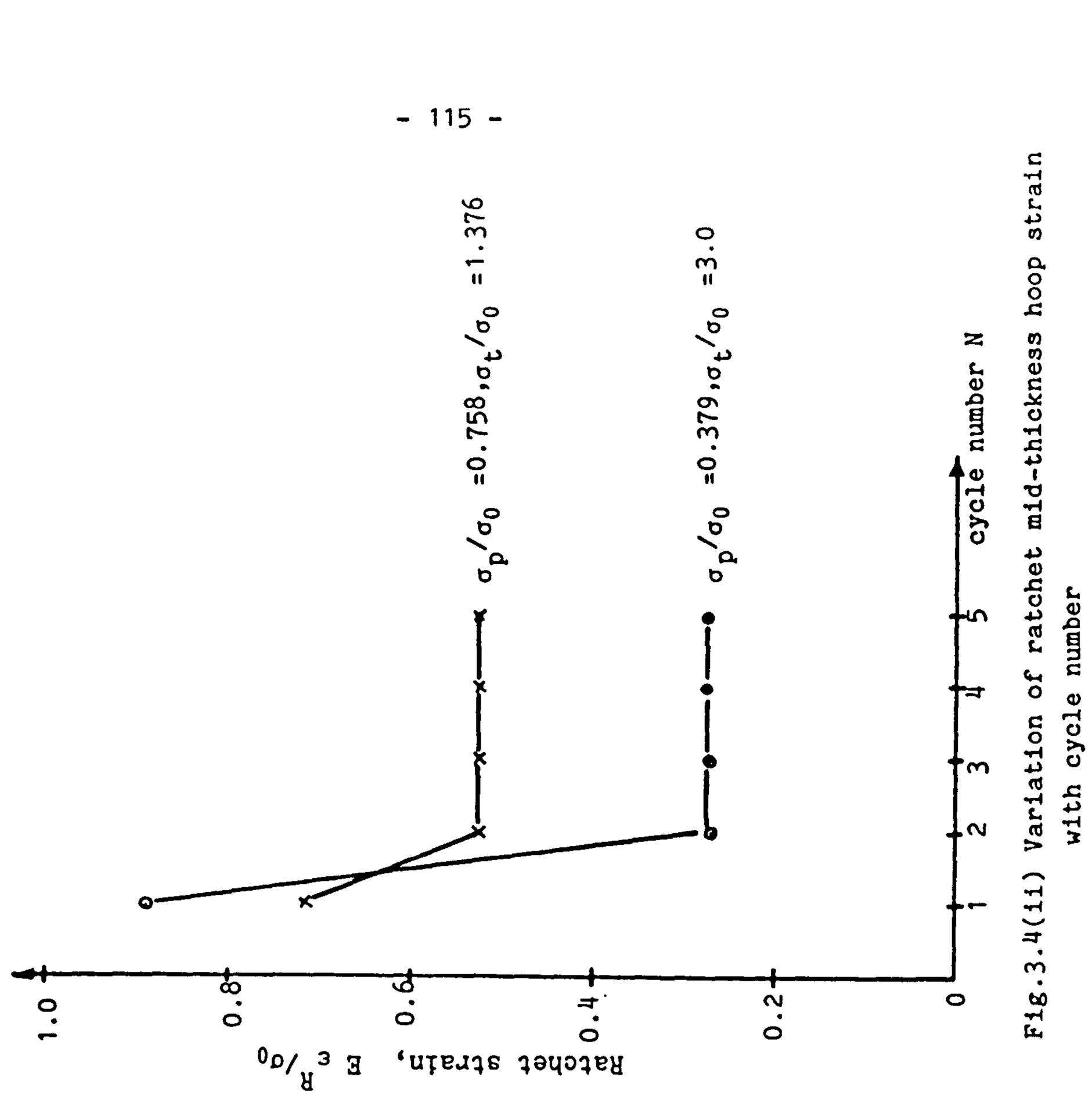

Fig.3.4(ii) Variation of ratchet mid-thickness hoop strain with cycle number

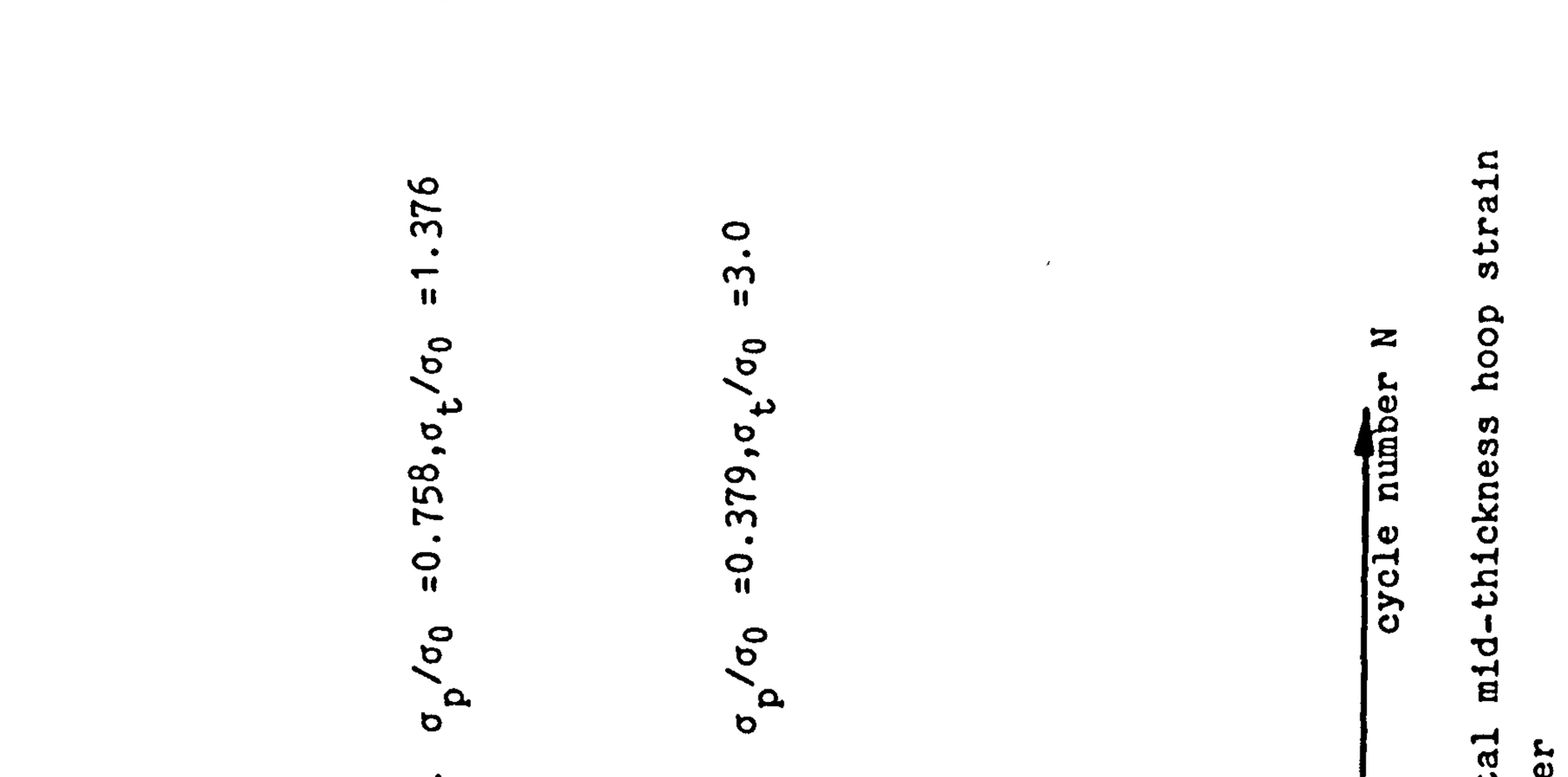

Fig.3.4(i) Variation of total mid-thickness hoop strain with cycle number

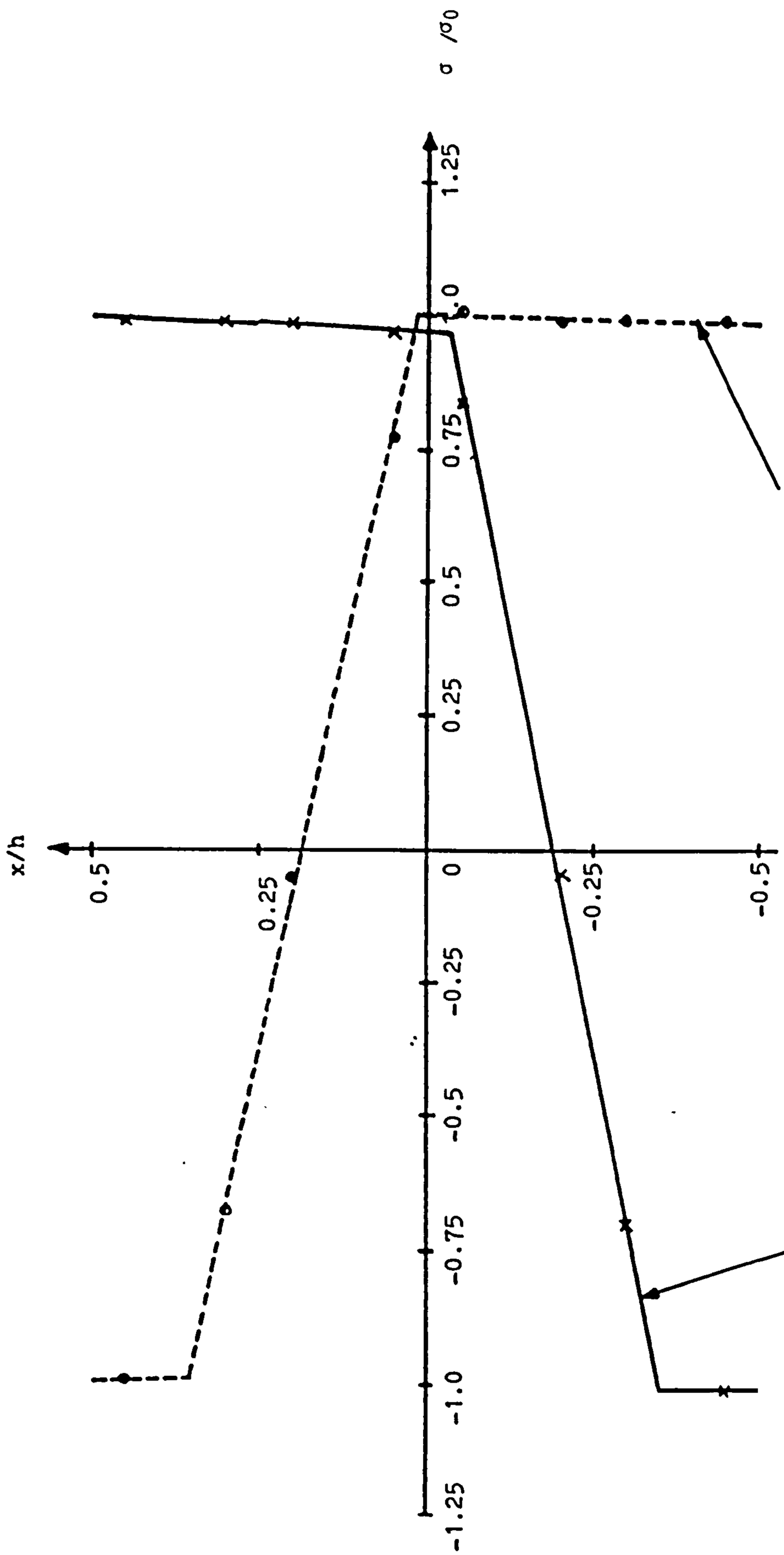

Fig.3.5(1) Through thickness variation of hoop stress. σ_p/σ_0 =0.379, σ_t/σ_0 =3.0

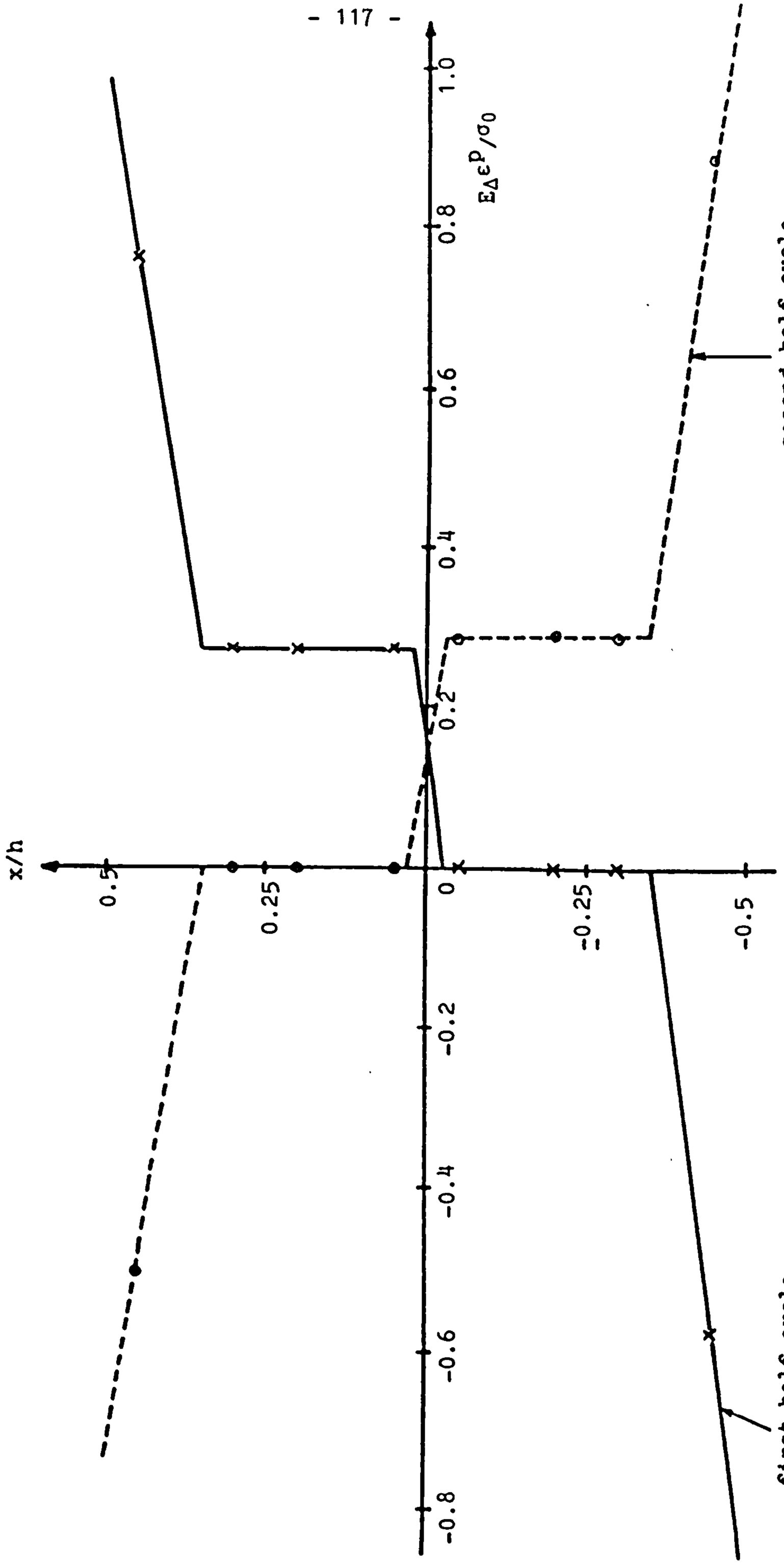

Fig.3.5(11) Through thickness variation of plastic hoop strain increment. σ_p/σ_0 =0.379, σ_t/σ_0 =3.0

Fig.3.6 Variation of ratchet strain at mid-thickness with σ_p/σ_0 at constant σ_t/σ_0 for a tube with uniform thickness.. $\sigma_t = E\alpha\Delta T/2$

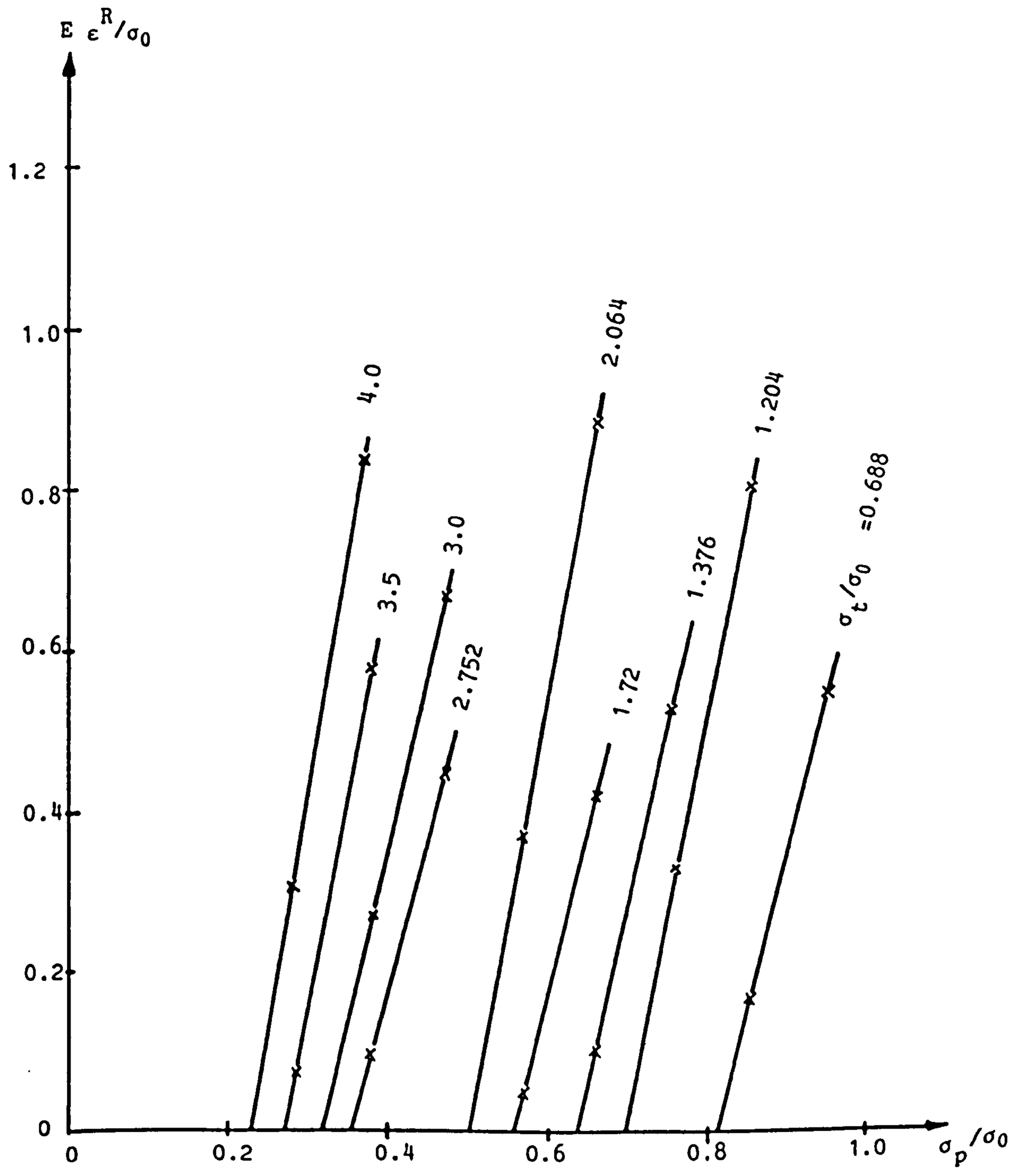

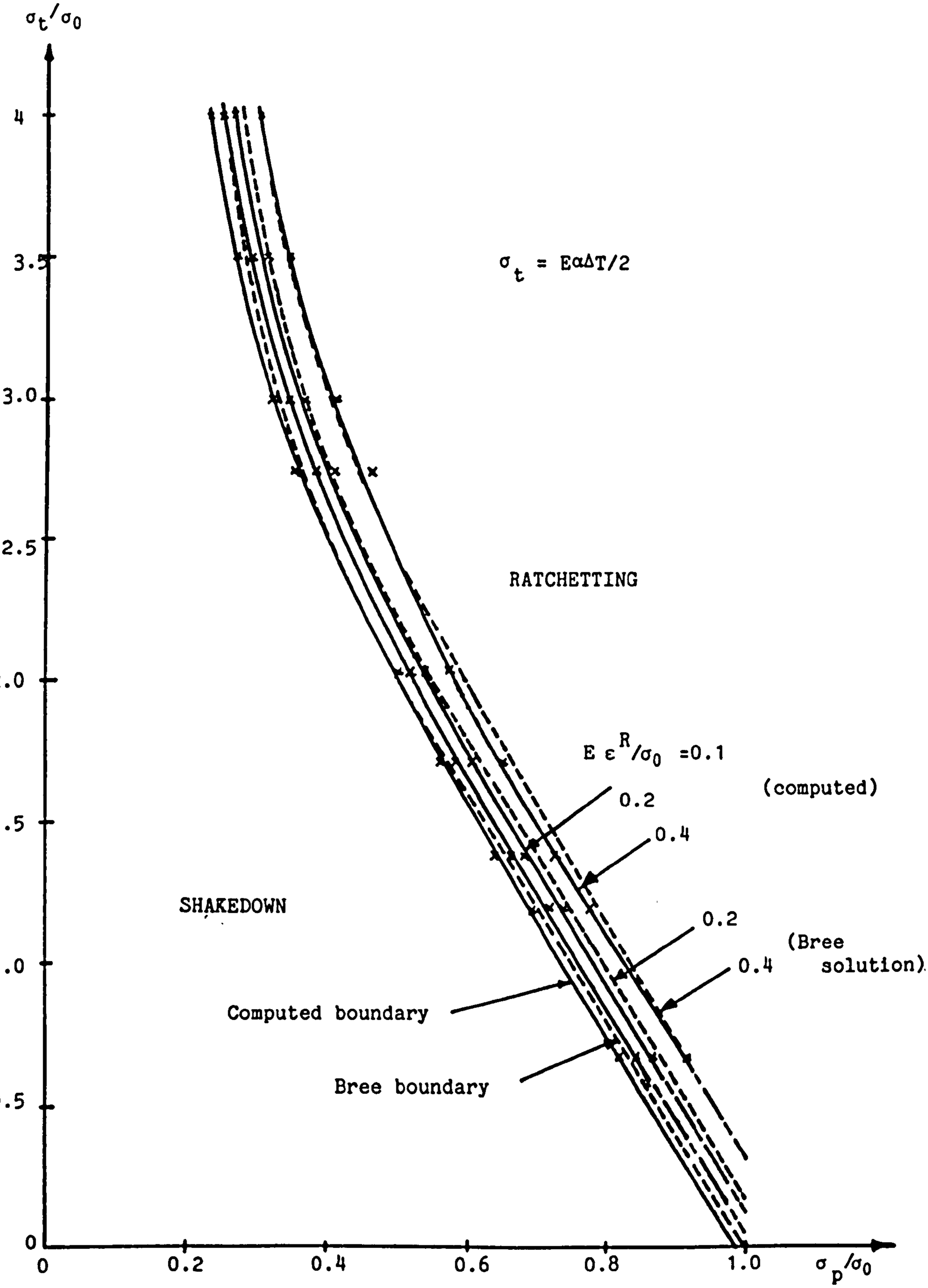

Fig.3.7 Shakedown/ratchetting regimes of a tube with a uniform thickness and comparison with Bree`s simplified solution

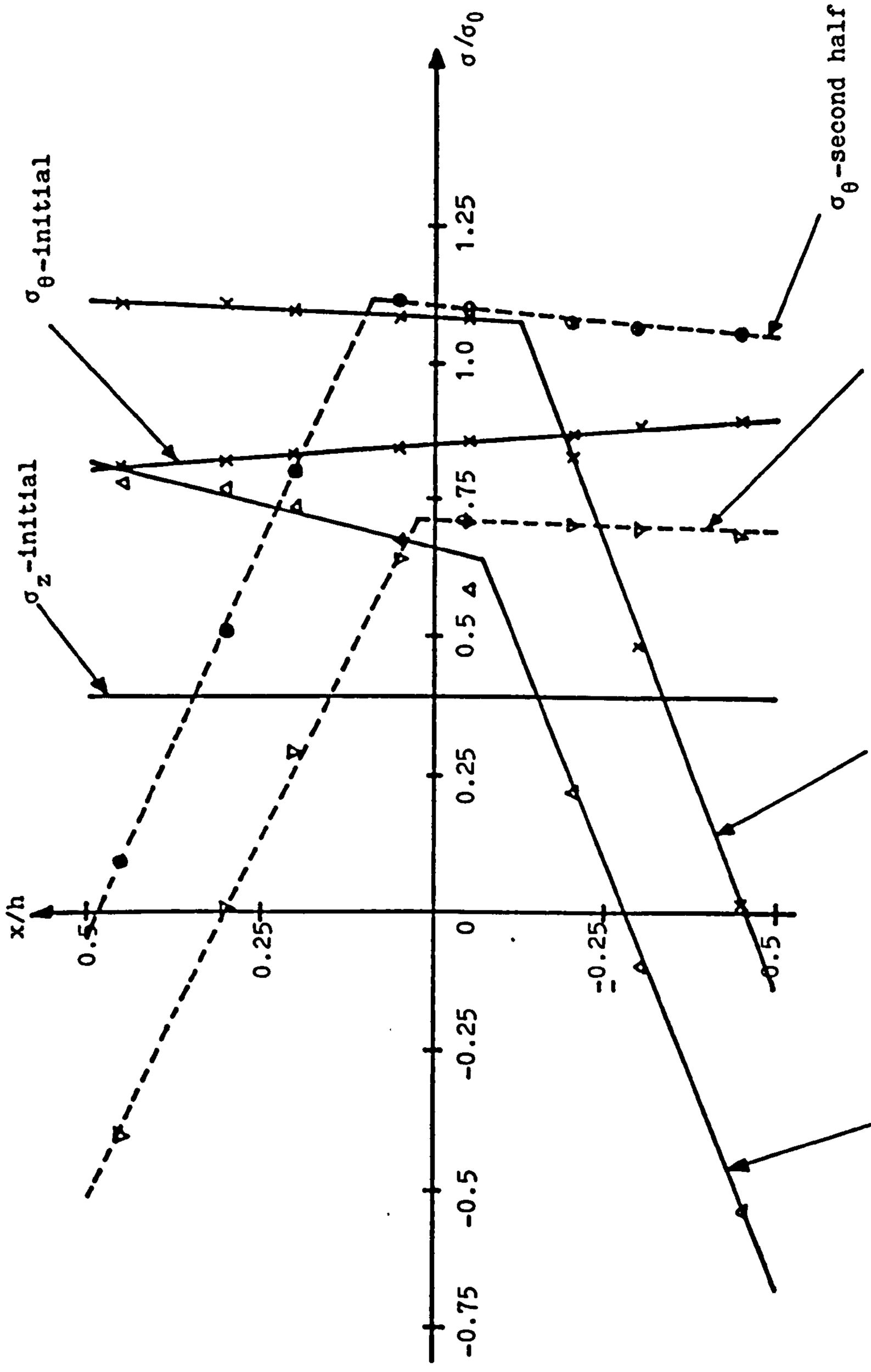

Fig.3.8(i) Through thickness stress distribution for a tube with pressurised closed ends.

σ_p/σ_0 =0.853, σ_t/σ_0 =1.5

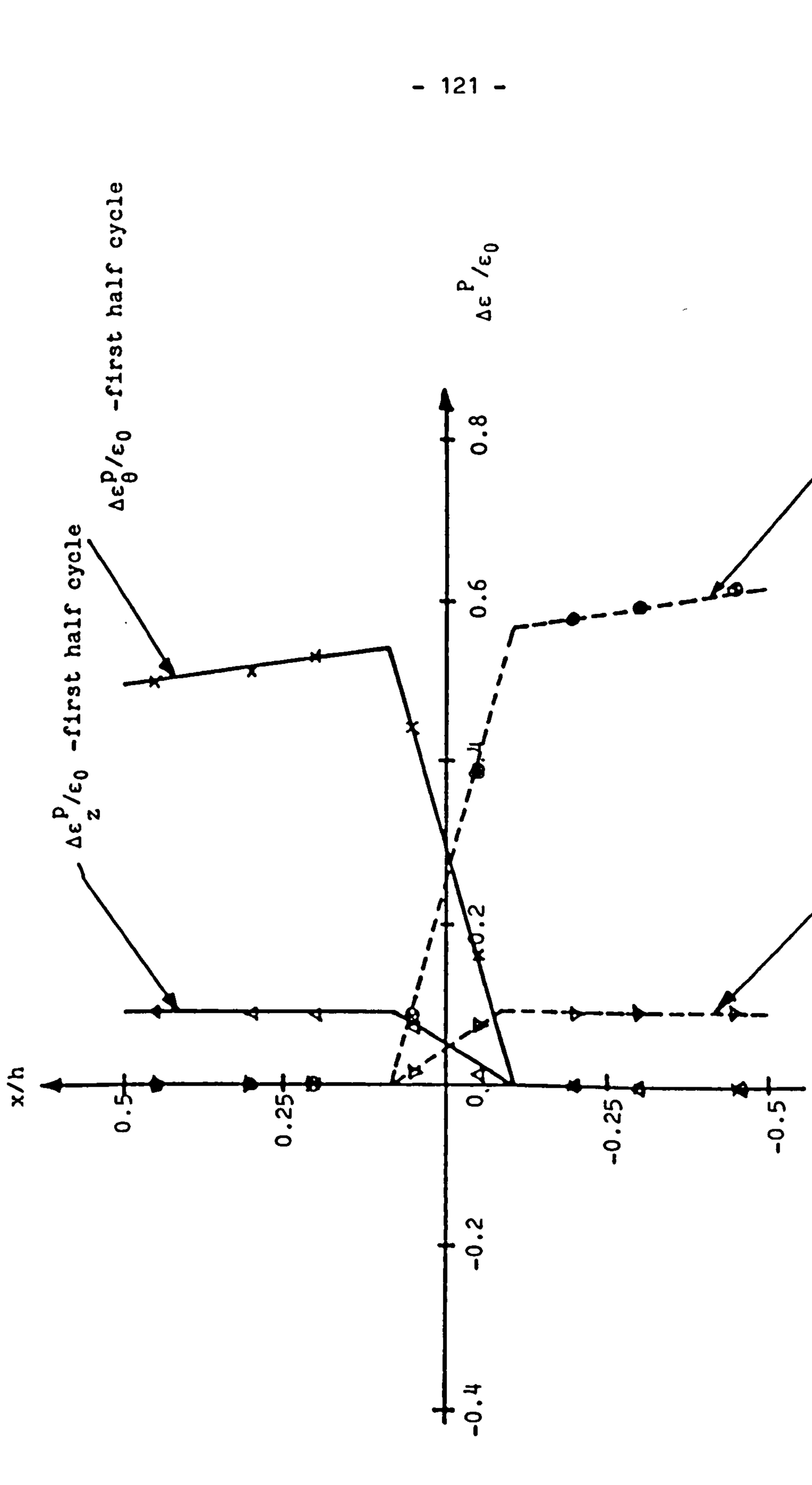

Fig.3.8(ii) Through thickness variation of plastic hoop and axial strain increment over cycle at the steady state, for a tube closed at both ends. σ_p/σ_0 =0.853, σ_t/σ_0 = 1.5

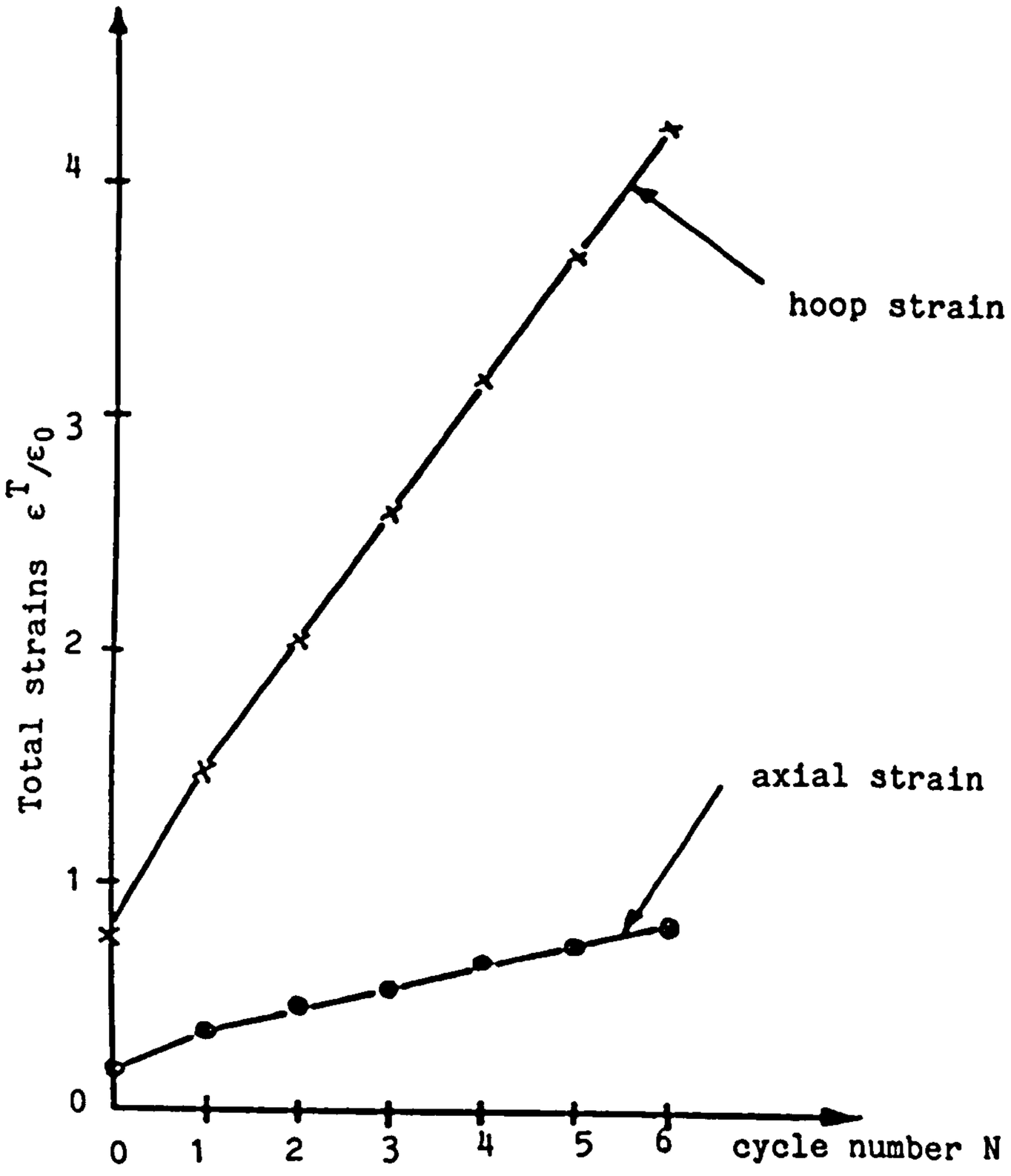

Fig.3.9(i) Variation of mid-thickness total strains with cycle number. Pressurised closed end tube.
σ_p/σ_0 =0.853, σ_t/σ_0= 1.5

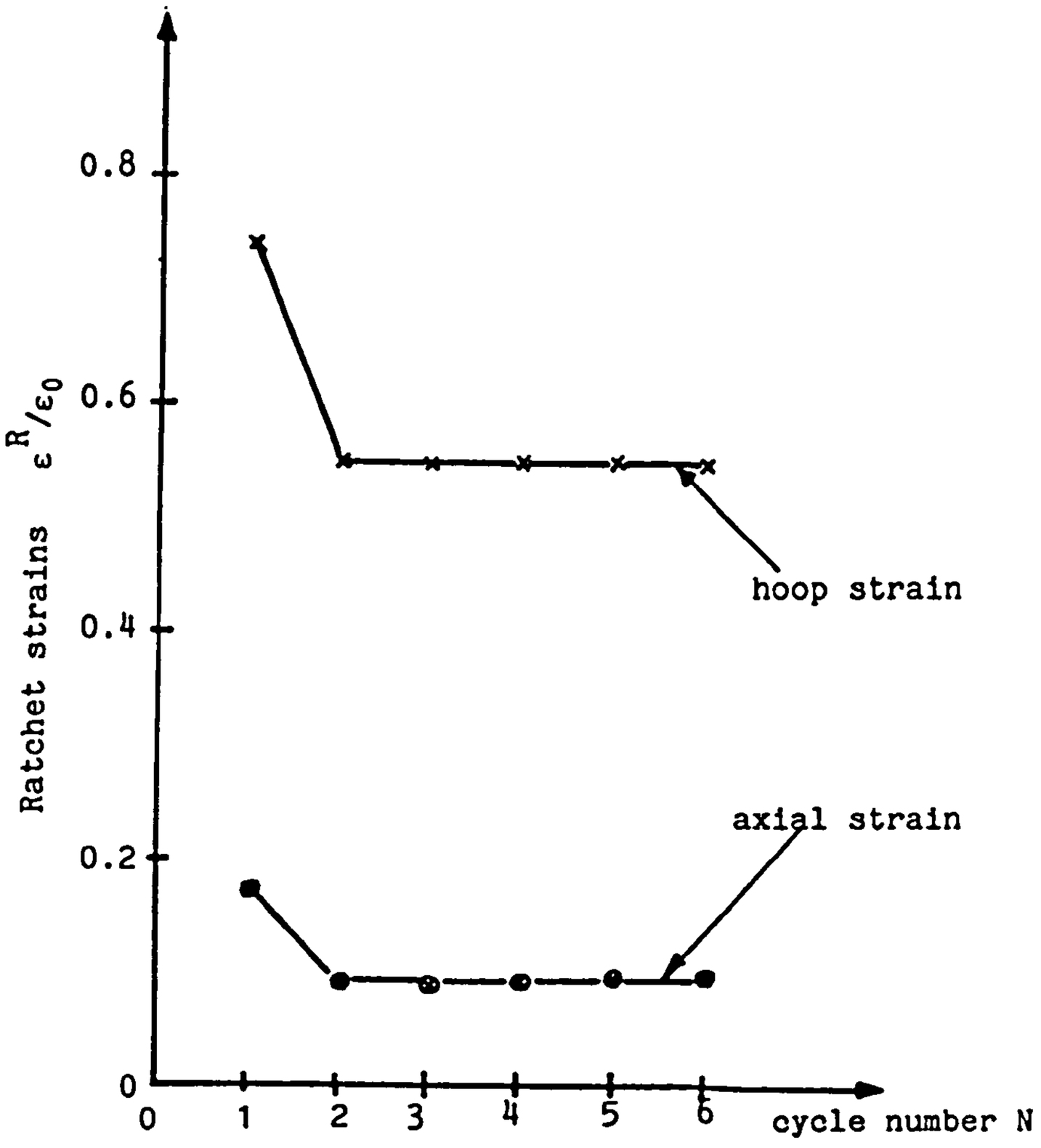

Fig.3.9(ii) Variation of mid-thickness ratchet strains with cycle number. Pressurised closed end tube.
σ_p/σ_0 = 0.853, σ_t/σ_0 = 1.5

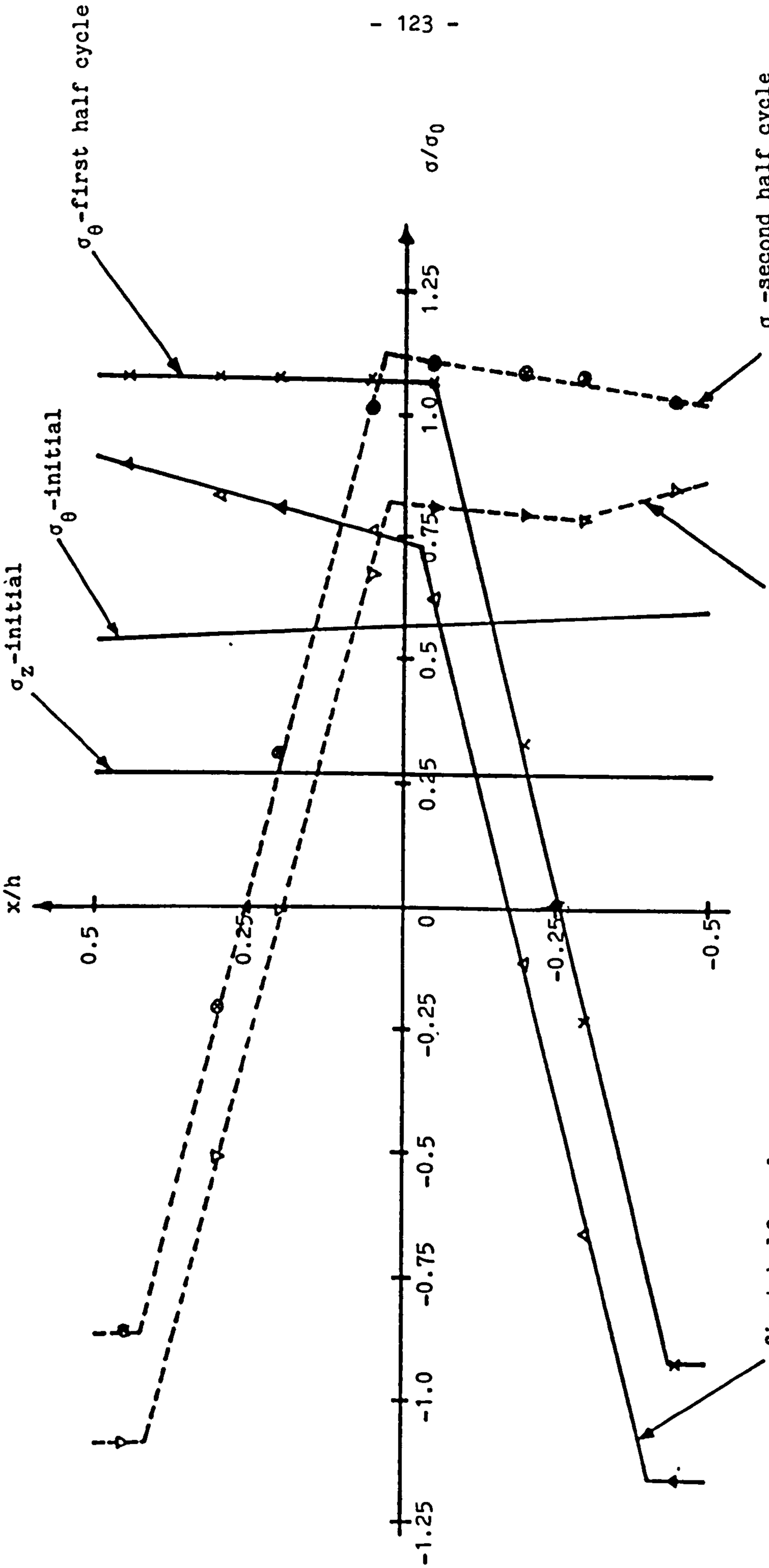

Fig.3.10(1) Through thickness variation of hoop and axial stresses for pressurised closed end tube.
Steady state cycle. σ_p/σ_0 =0.568, σ_t/σ_0 = 2.5.

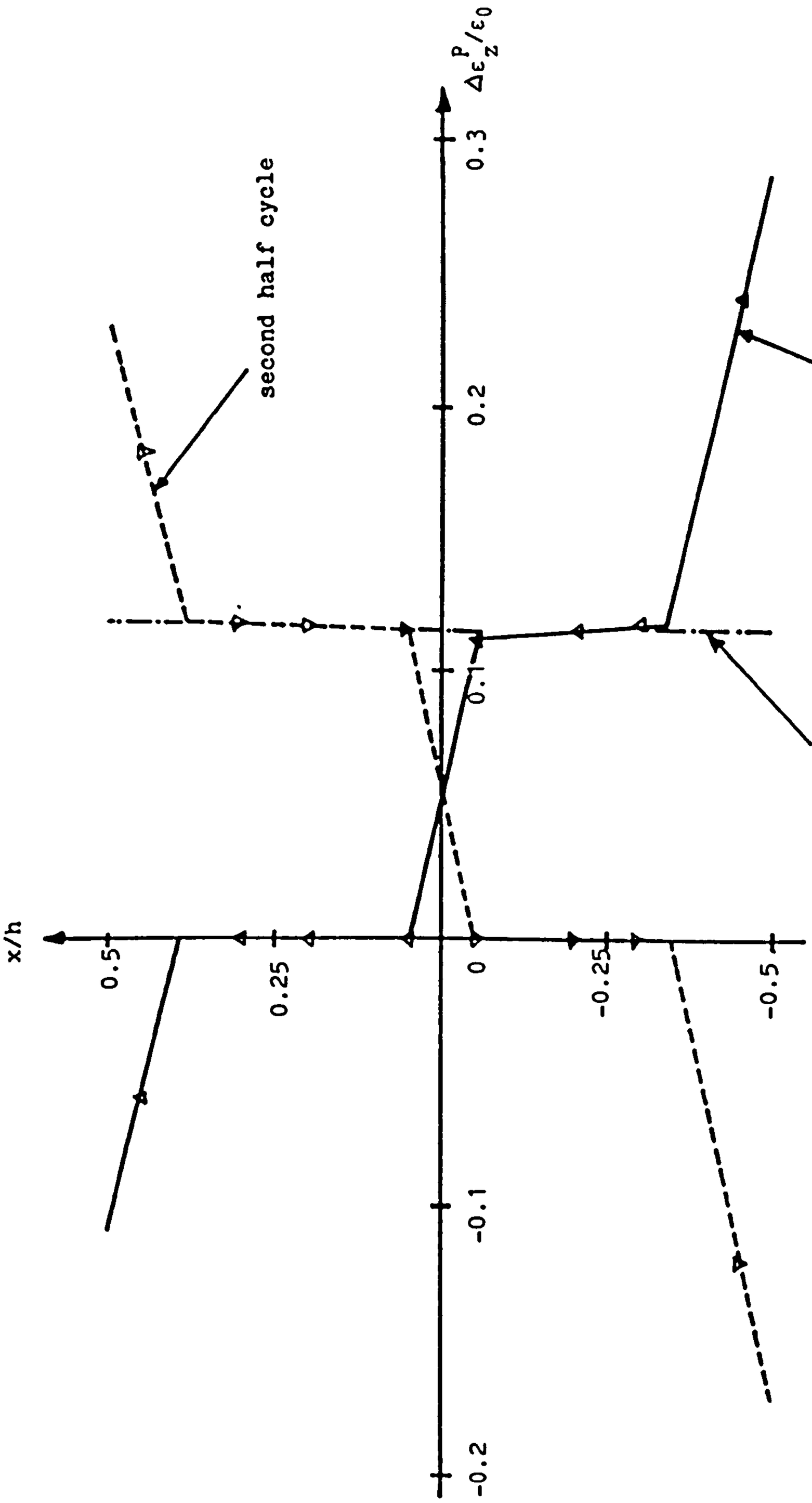

Fig.3.10(11) Variation of increment of plastic axial strain through the thickness at a steady ratchet state foa a pressurised closed end tube. σ_p/σ_0 =0.568, σ_t/σ_0 = 2.5

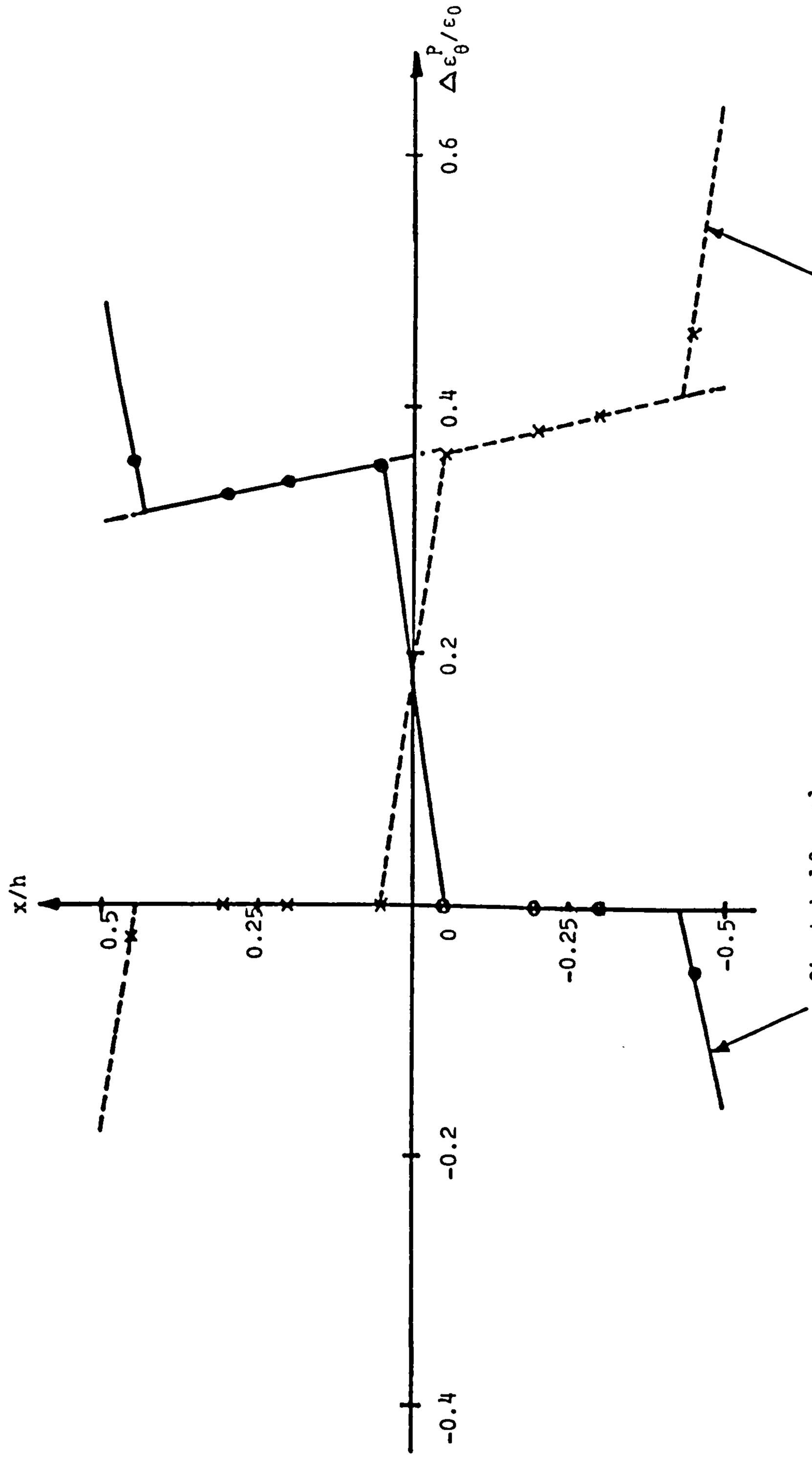

Fig.3.10(iii) Through thickness variation of plastic hoop strain increment at the steady ratchet state for a pressurised closed end tube. $\sigma_p/\sigma_0 = 0.568$, $\sigma_t/\sigma_0 = 2.5$

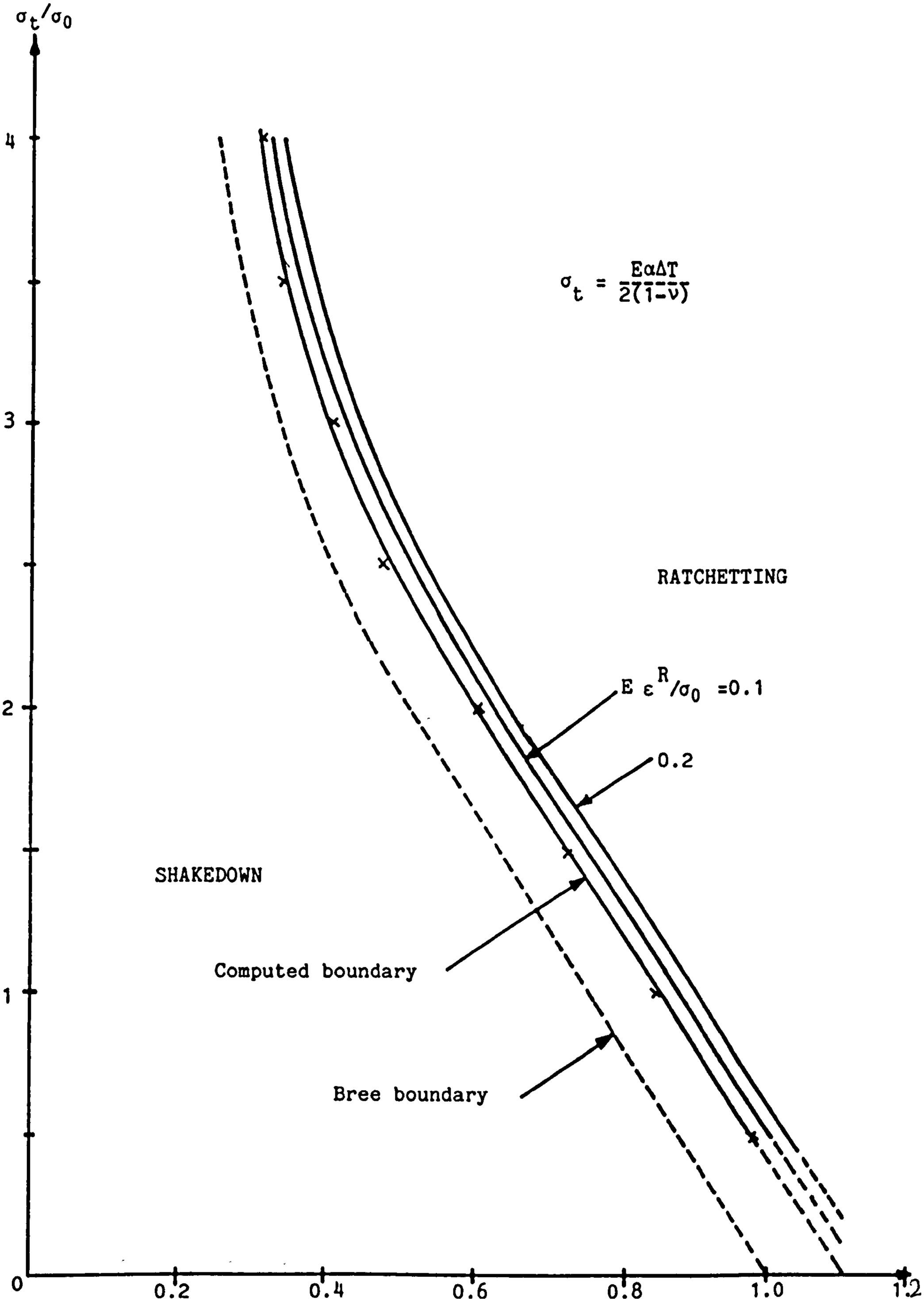

Fig.3.11 Shakedown/ratchetting regimes for a pressurised closed ends tube.

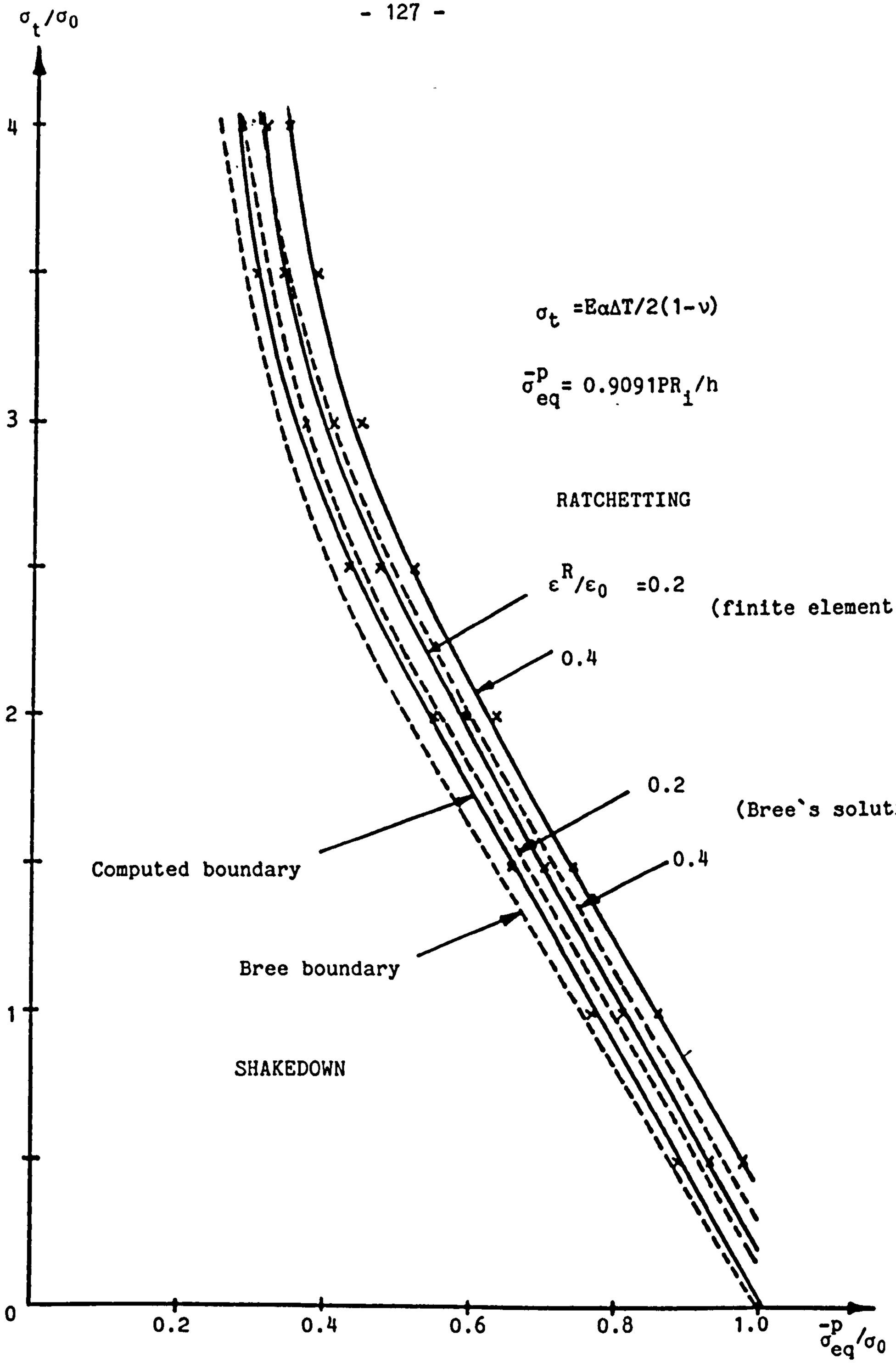

Fig.3.12 Shakedown/ratchetting regimes for pressurised closed ends tube. Correlation between finite element and Bree`s solution.

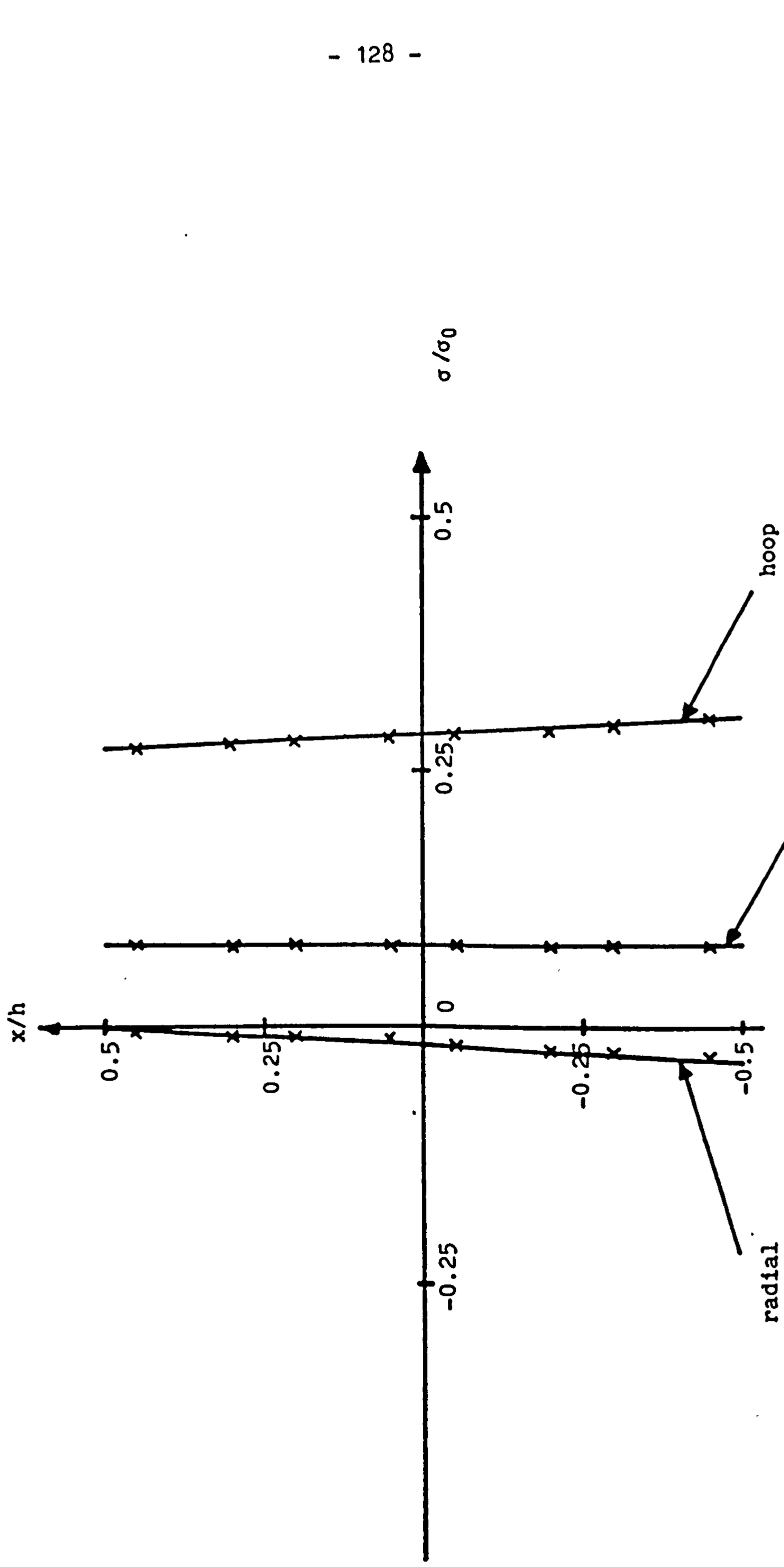

Fig.3.13(i) Through thickness variation of stresses for a tube with axial restraint. $\sigma_p/\sigma_0 = 0.284$

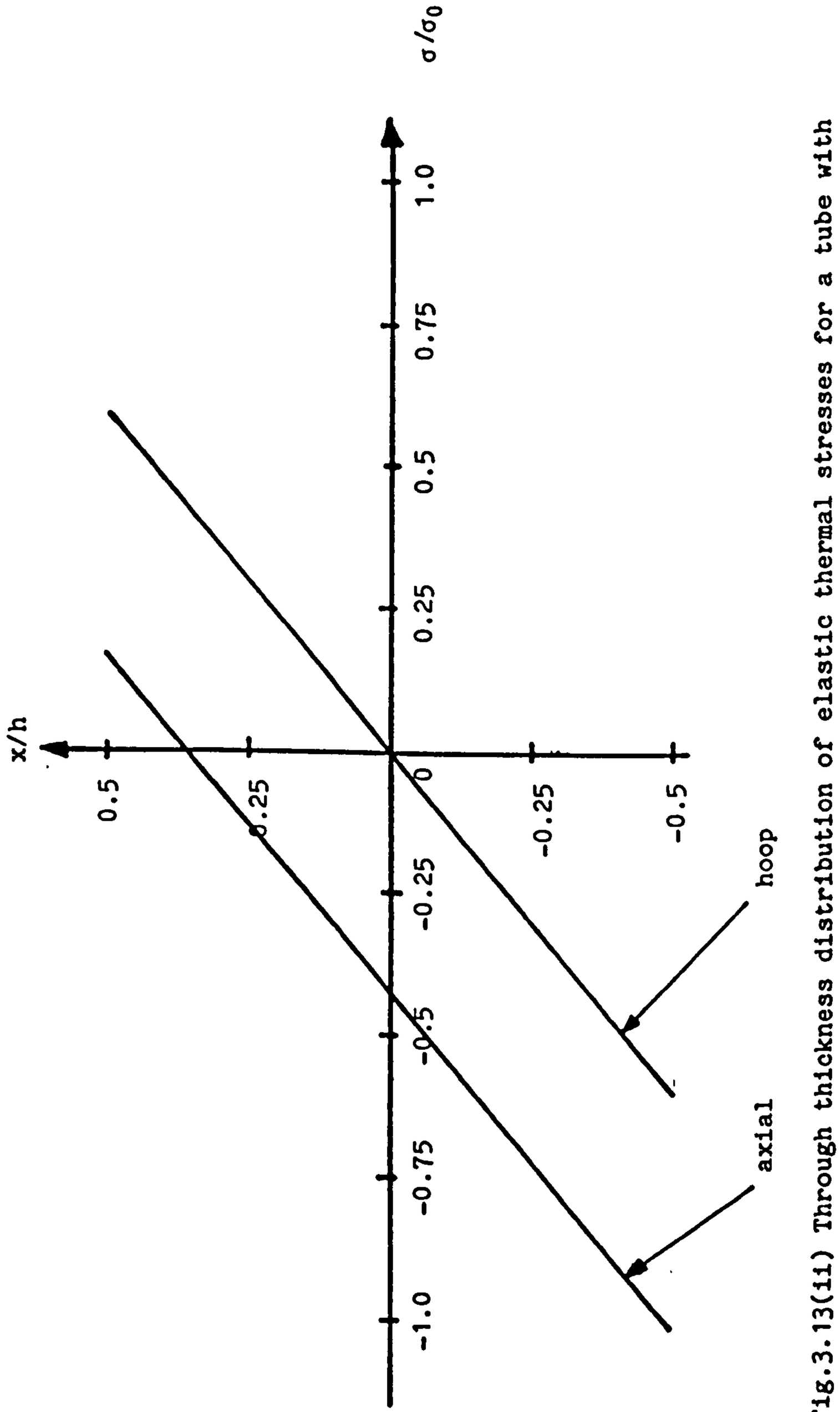

Fig.3.13(ii) Through thickness distribution of elastic thermal stresses for a tube with axial restraint. $\sigma_t/\sigma_0 = 0.61$

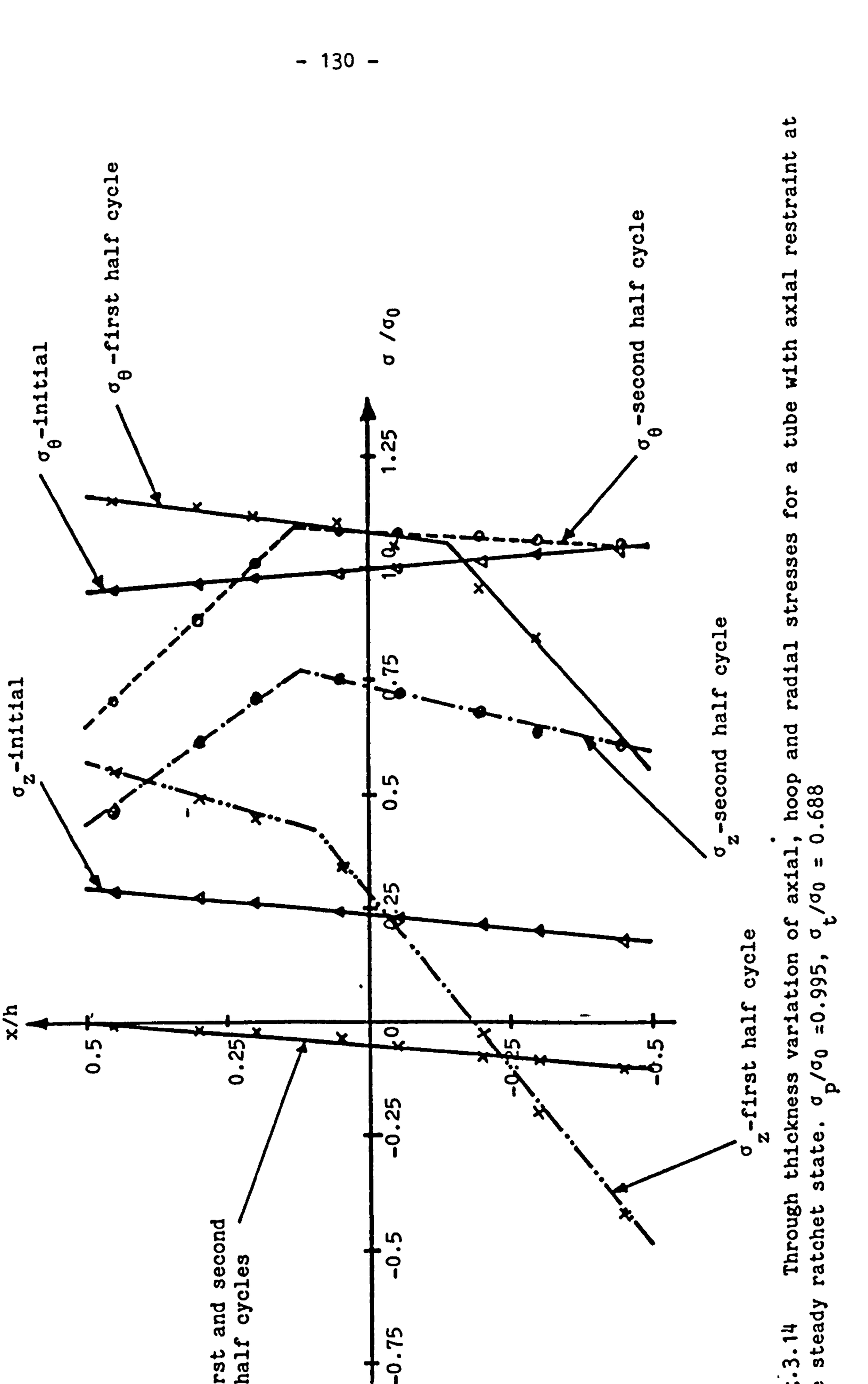

Fig.3.14 Through thickness variation of axial, hoop and radial stresses for a tube with axial restraint at the steady ratchet state. σ_p/σ_0 =0.995, σ_t/σ_0 = 0.688

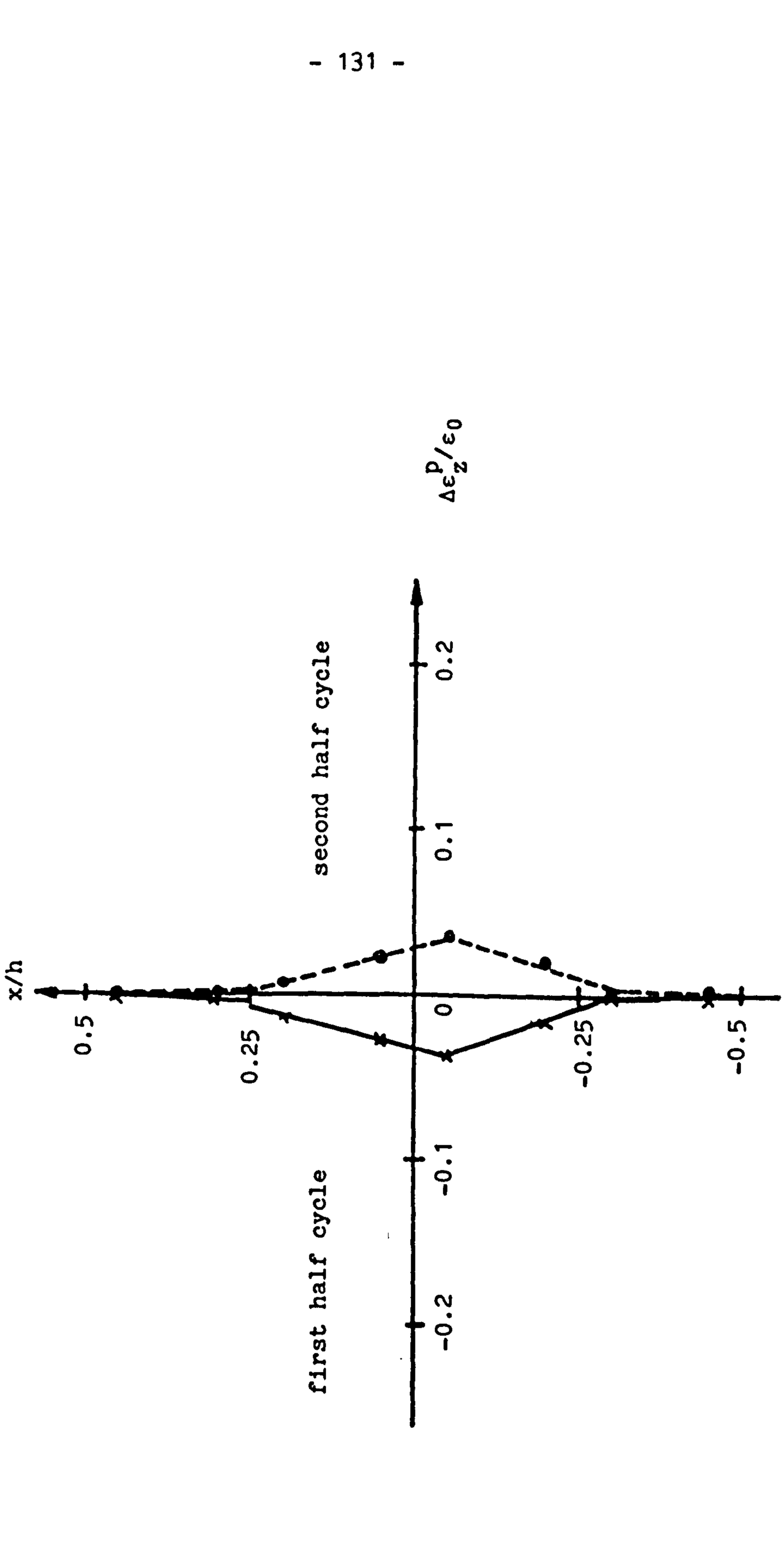

Fig.3.15 (i) Through thickness variation of plastic axial strain increment at the steady ratchet state for a tube with axial restraint. σ_p/σ_0 =0.995, σ_t/σ_0 =0.688

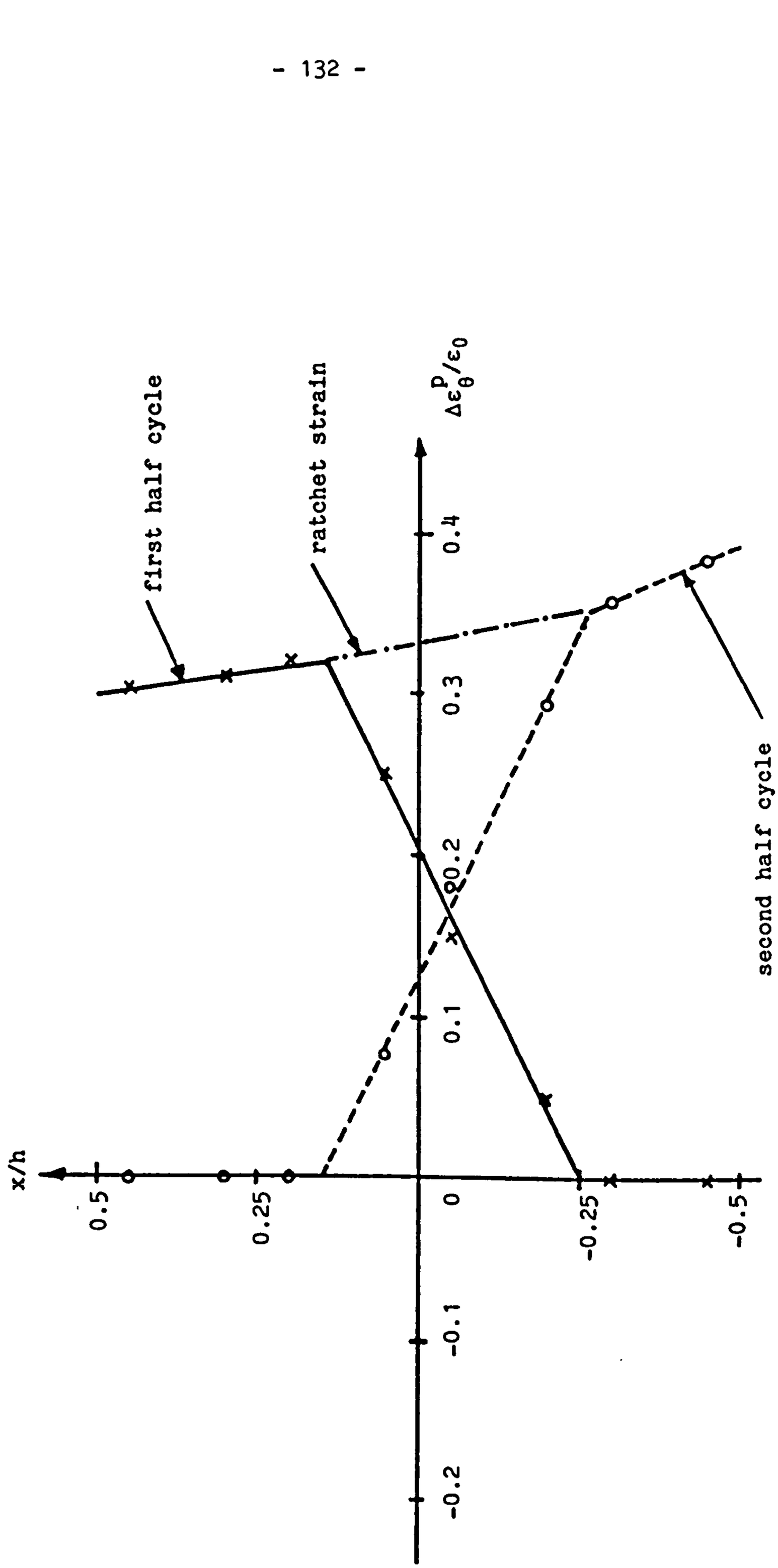

Fig.3.15(ii) Through thickness variation of plastic hoop strain increment at the steady ratchet state for a tube with axial restraint. $\sigma_p/\sigma_0 = 0.995$, $\sigma_t/\sigma_0 = 0.688$

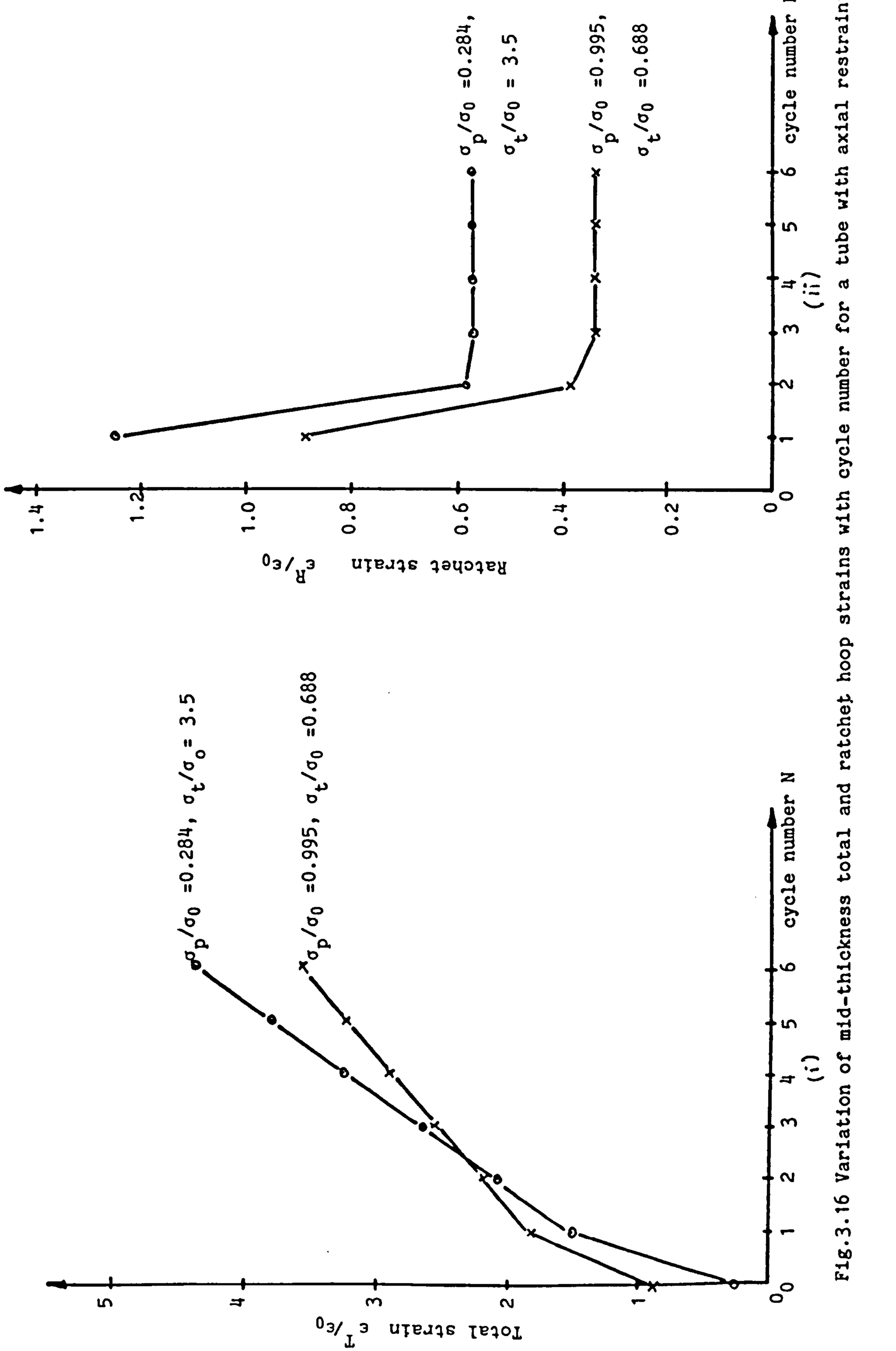

Fig.3.16 Variation of mid-thickness total and ratchet hoop strains with cycle number for a tube with axial restraint

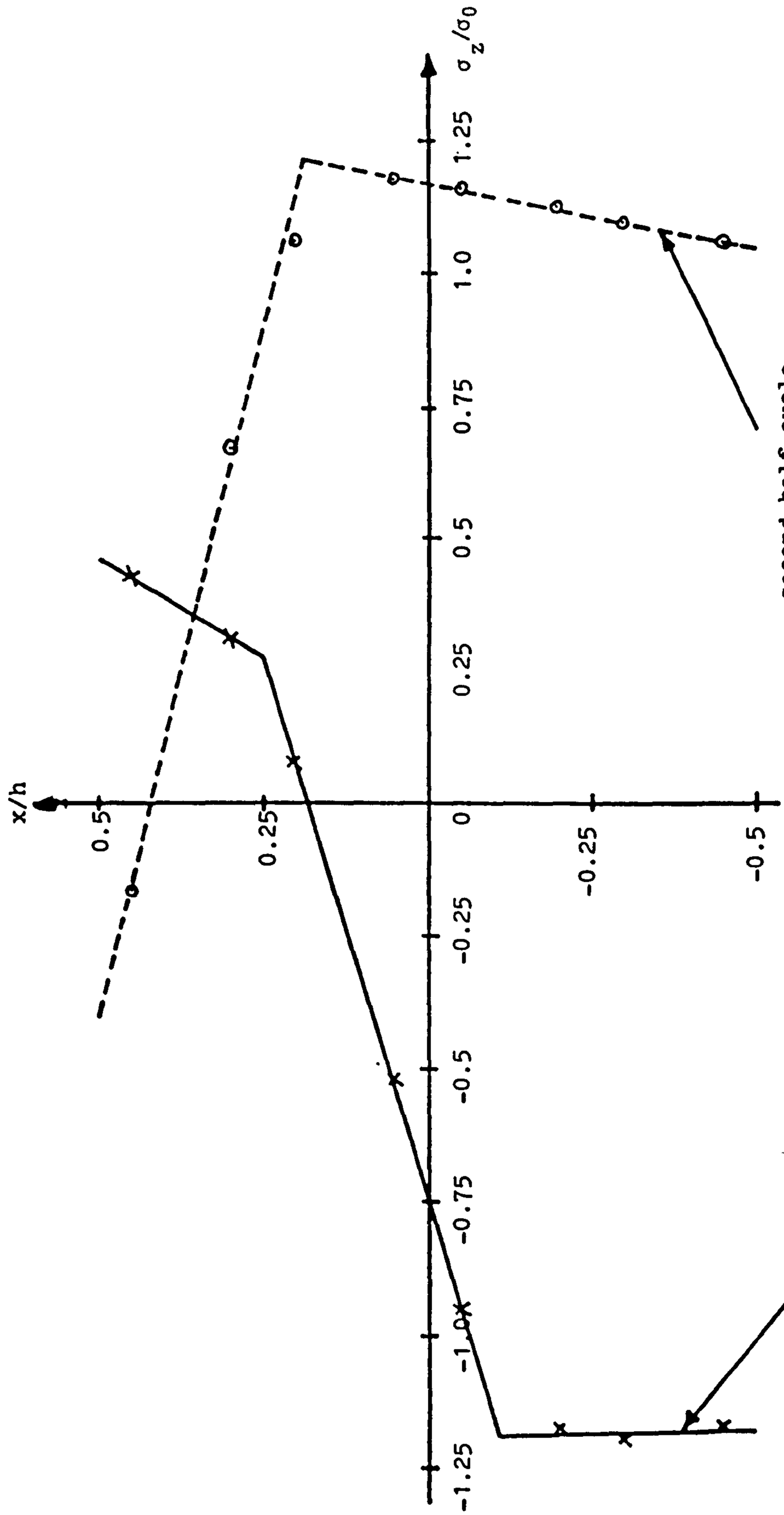

Fig.3.17(1) Through thickness variation of axial stress at the steady ratchet state for a tube with axial restraint. $\sigma_p/\sigma_0 = 0.284$, $\sigma_t/\sigma_0 = 3.5$

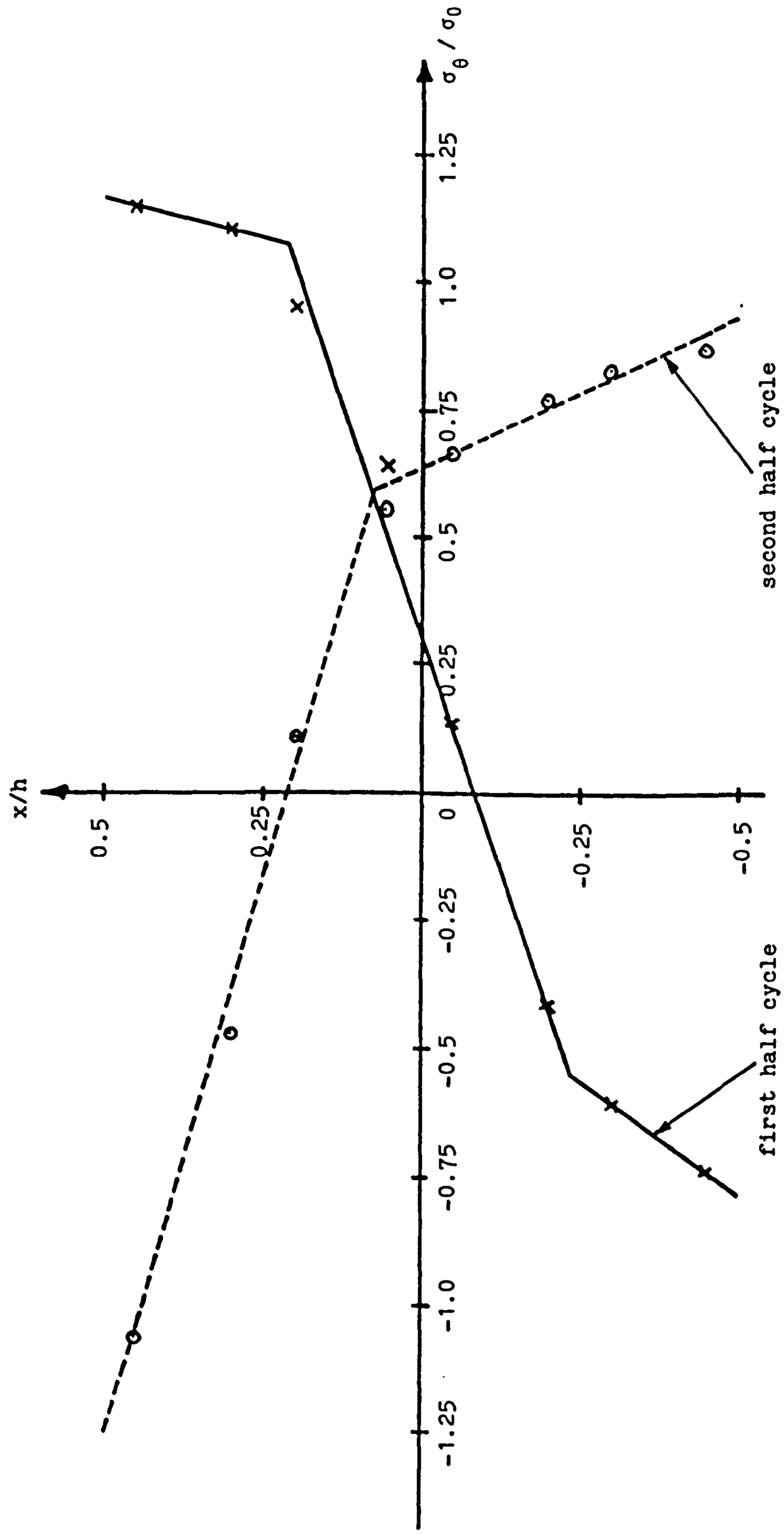

Fig.3.17(ii) Through thickness variation of hoop stress at the steady ratchet state for a tube with axial restraint. $\sigma_p/\sigma_0 = 0.284$, $\sigma_t/\sigma_0 = 3.5$

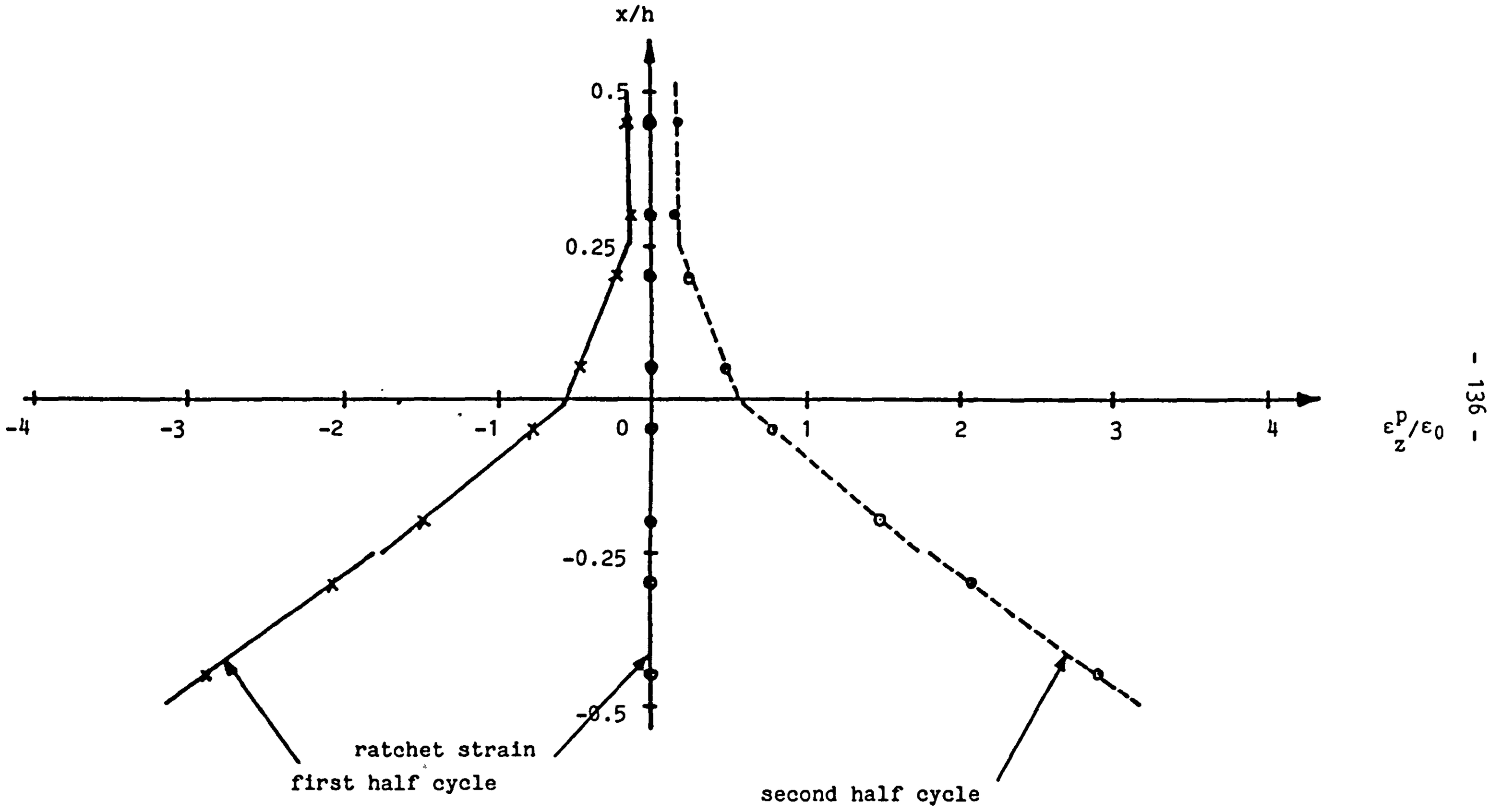

Fig.3.18(i) Through thickness variation of plastic axial strain increment at the steady ratchet state for a tube with axial restraint. $\sigma_p/\sigma_0 = 0.284$, $\sigma_t/\sigma_0 = 3.5$

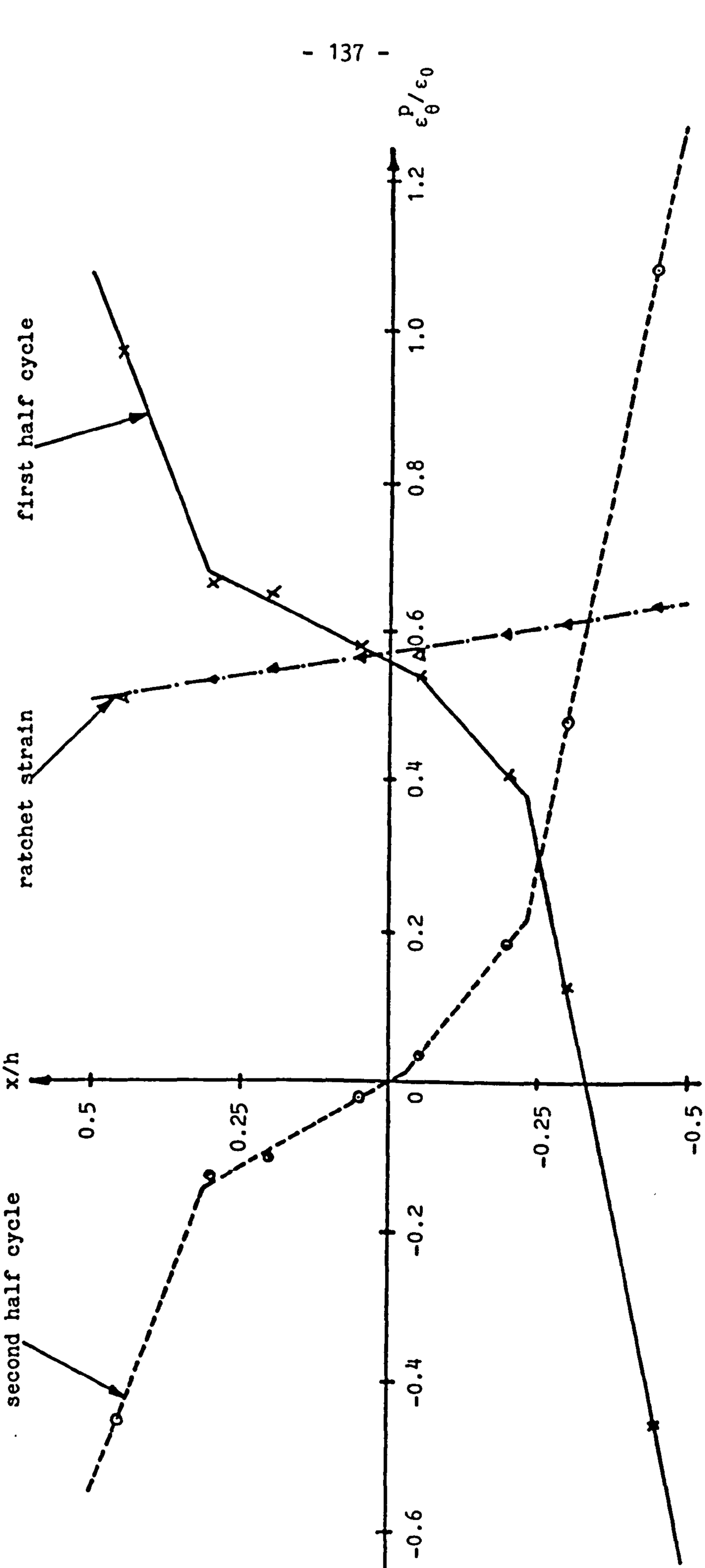

Fig.3.18(11) Through thickness variation of plastic hoop strain increment at the steady ratchet state for a tube with axial restraint. $\sigma_p/\sigma_0 = 0.284$, $\sigma_t/\sigma_0 = 3.5$

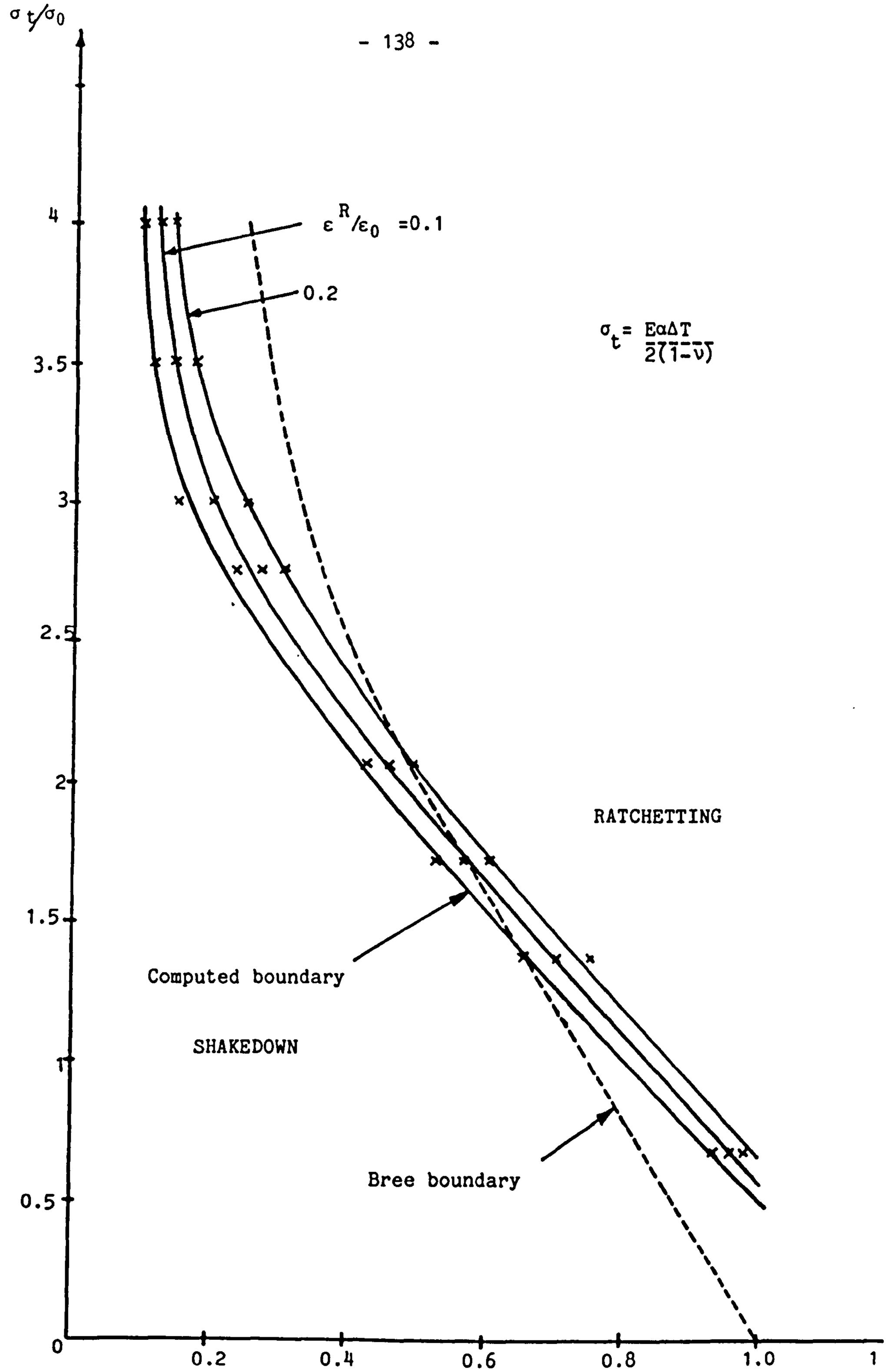

$$\sigma_t = \frac{E\alpha\Delta T}{2(1-\nu)}$$

Fig.3.19 Shakedown/ratchetting regimes for a tube with axial restraint

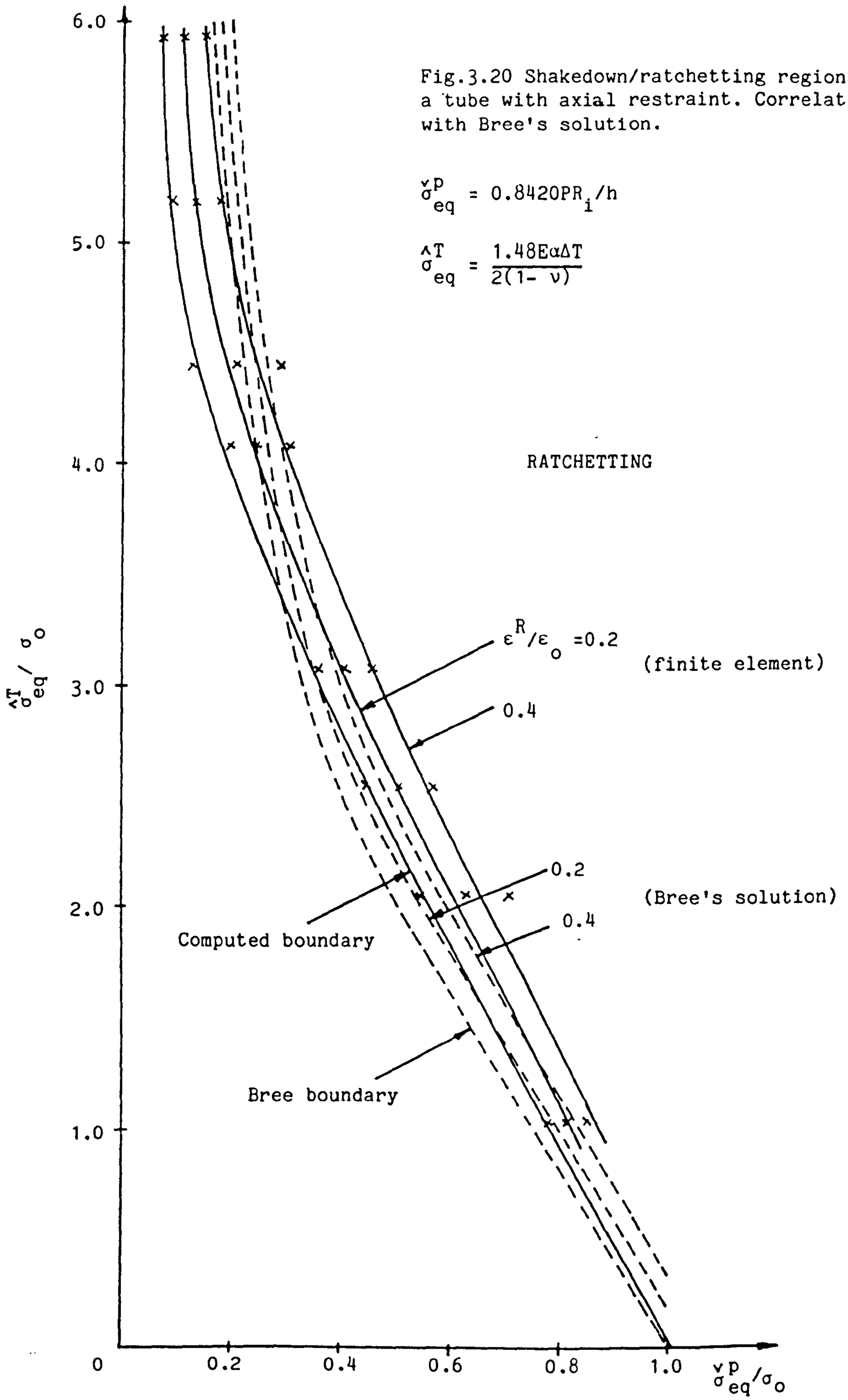

Fig.3.20 Shakedown/ratchetting region for a tube with axial restraint. Correlation with Bree's solution.

$$\check{\sigma}^p_{eq} = 0.8420PR_i/h$$

$$\hat{\sigma}^T_{eq} = \frac{1.48E\alpha\Delta T}{2(1-\nu)}$$

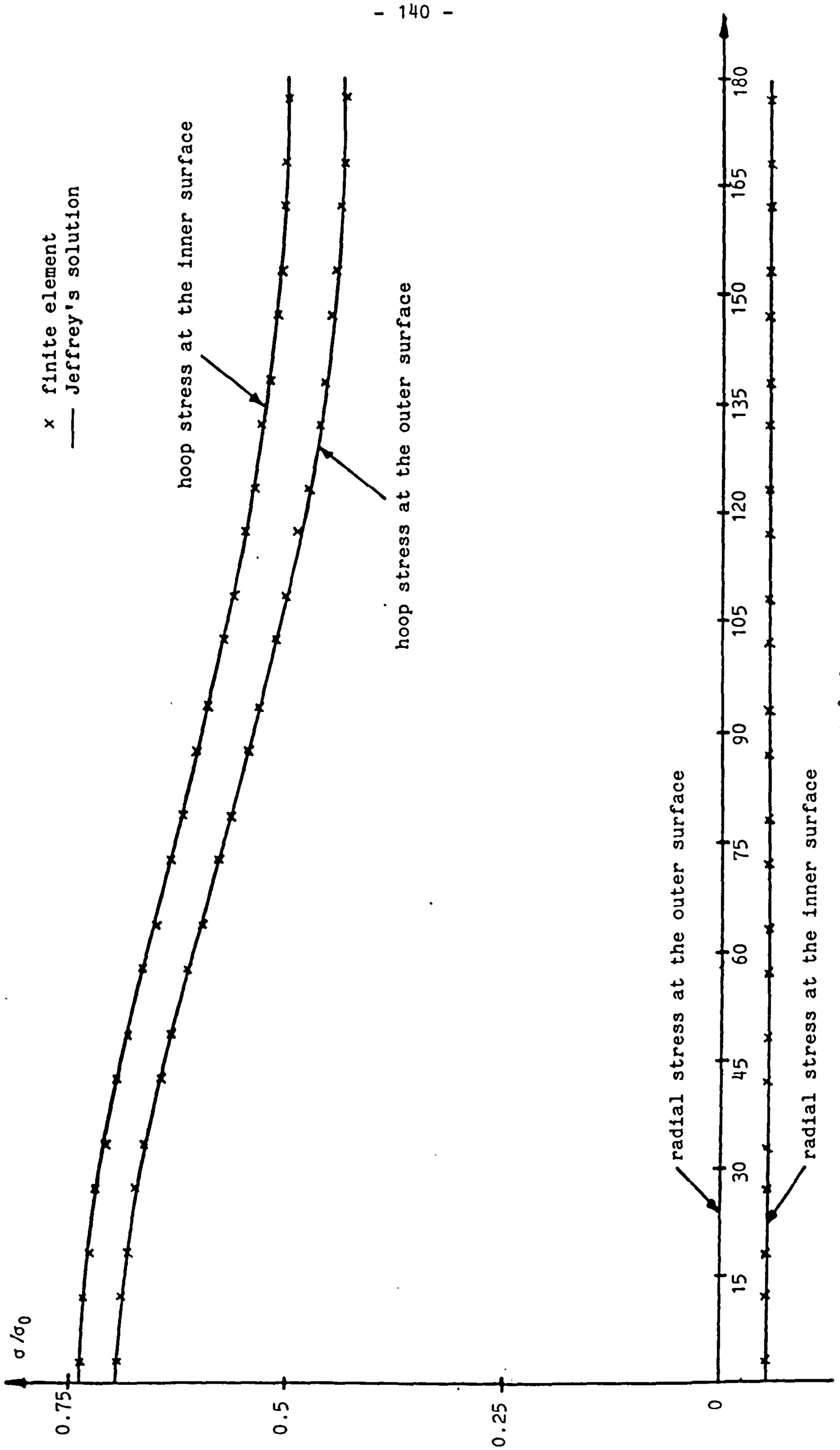

Fig.3.21 Variation of hoop and radial stresses with θ for σ_p/σ_0 =0.568. Comparison between finite element and Jeffrey's(81) solution. Plane stress case.

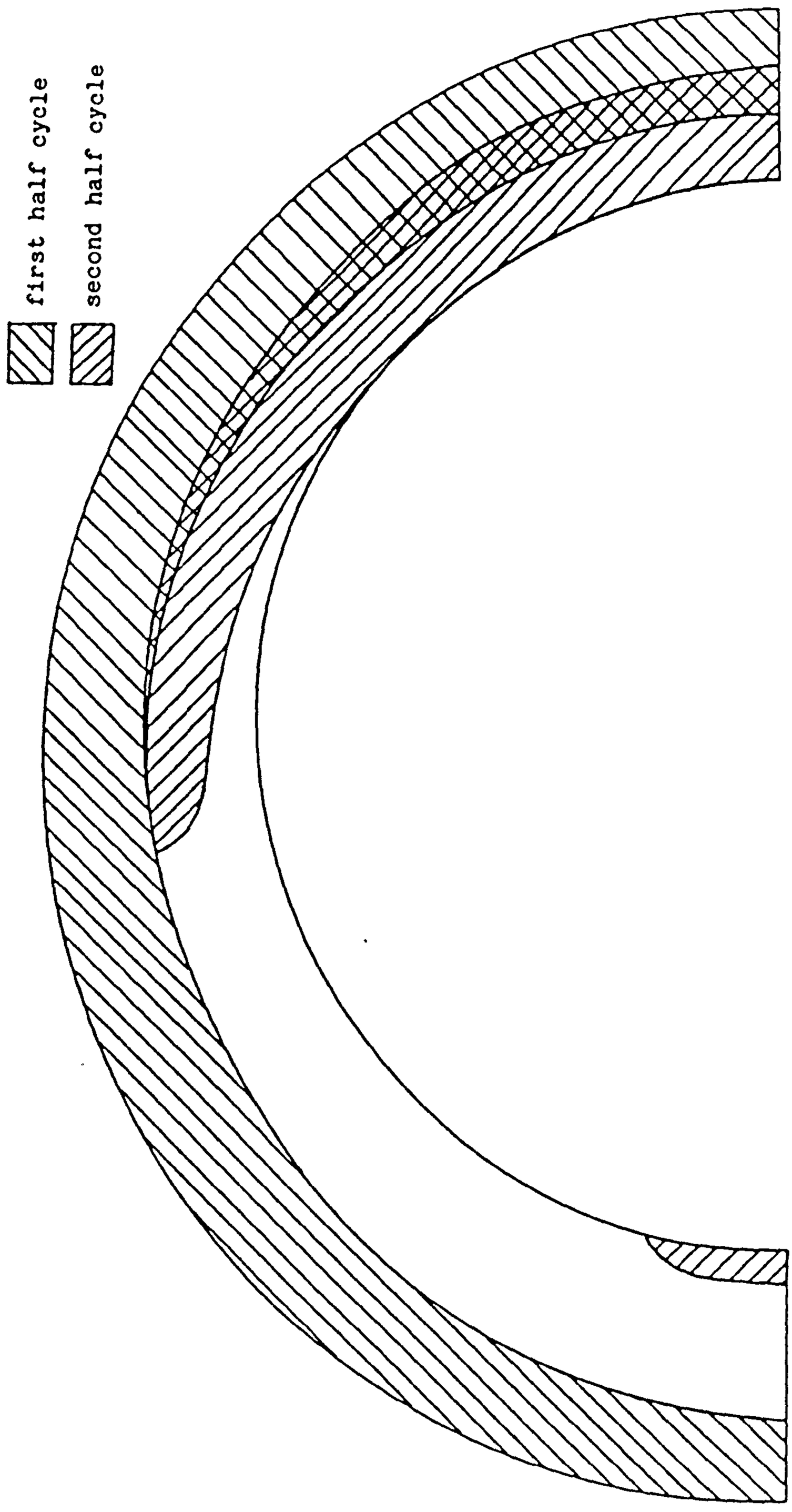

Fig.3.22 Extent of plastic zone in the first cycle. σ_p/σ_0 =0.568, σ_t/σ_0 =1.72. (The thickness is exaggerated)

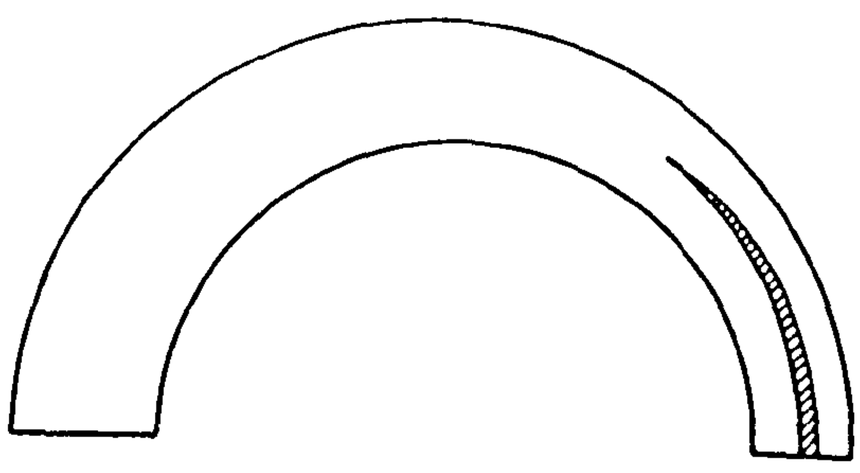

(i) 3/21 σ_t

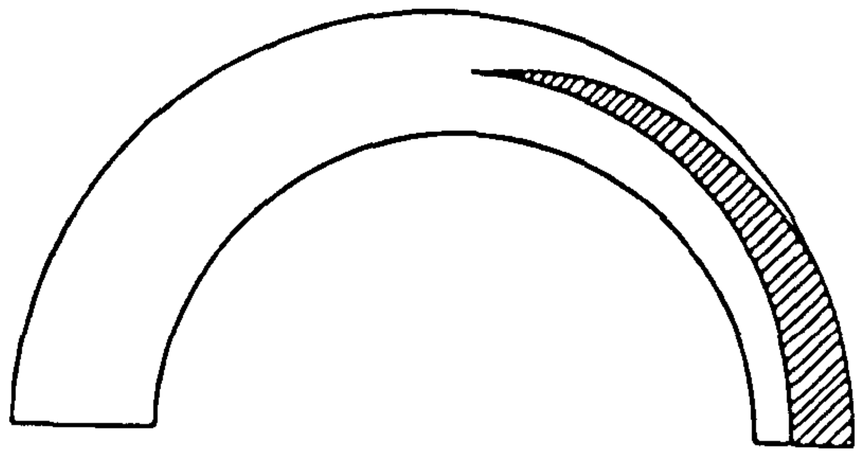

(ii) 17/21 σ_t

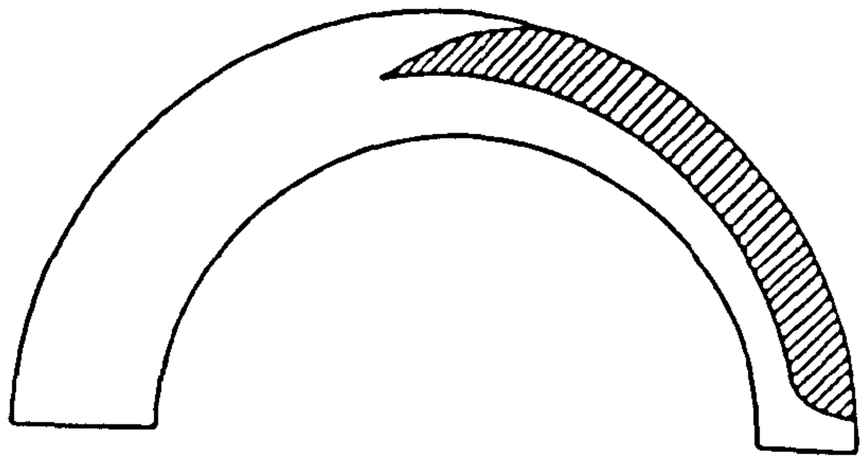

(iii) 21/21 σ_t

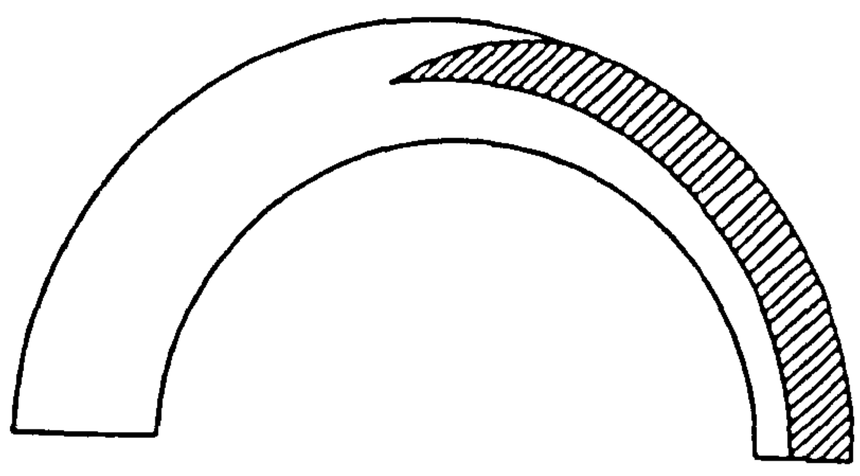

(iv) over the first half cycle

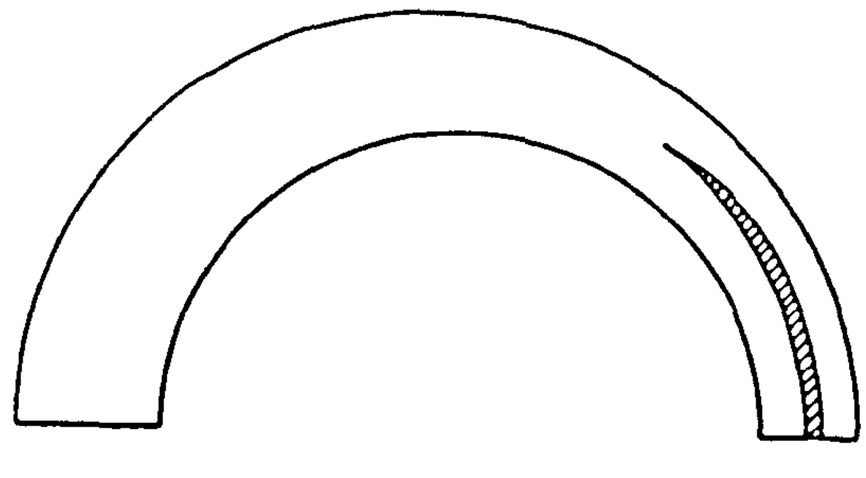

(v) 3/21 σ_t

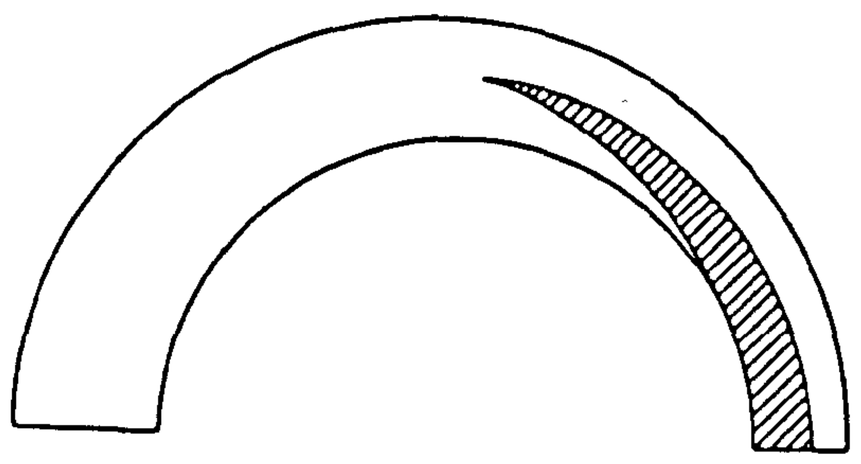

(vi) 17/21 σ_t

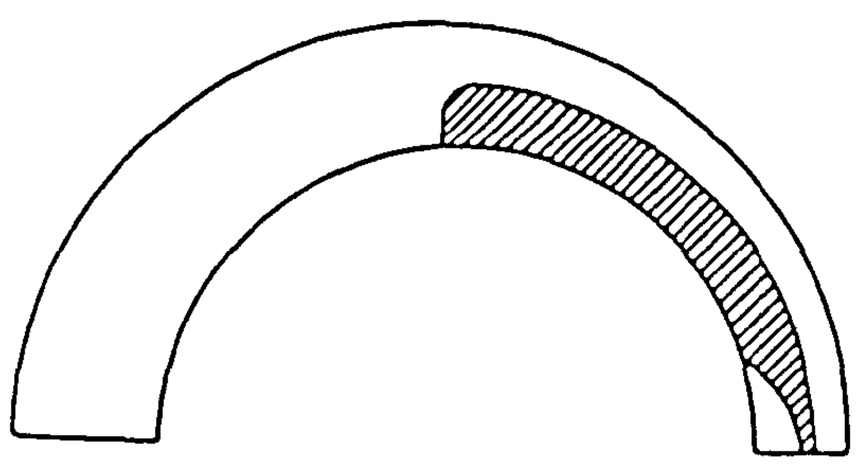

(vii) 21/21 σ_t

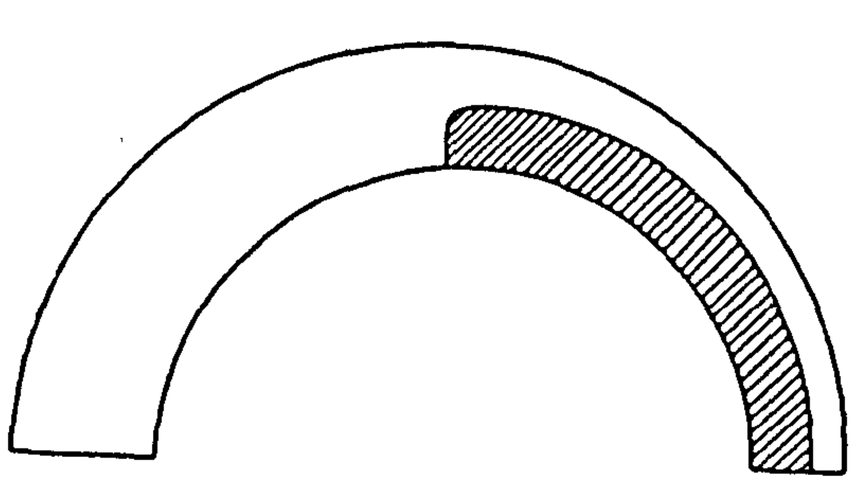

(viii) over the second half cycle

first half cycle

second half cycle

Fig.3.23 Development of plastic zone during a steady state cycle for a tube with an eccentric bore. $\sigma_p/\sigma_o = 0.568$ $\sigma_t/\sigma_o = 1.72$

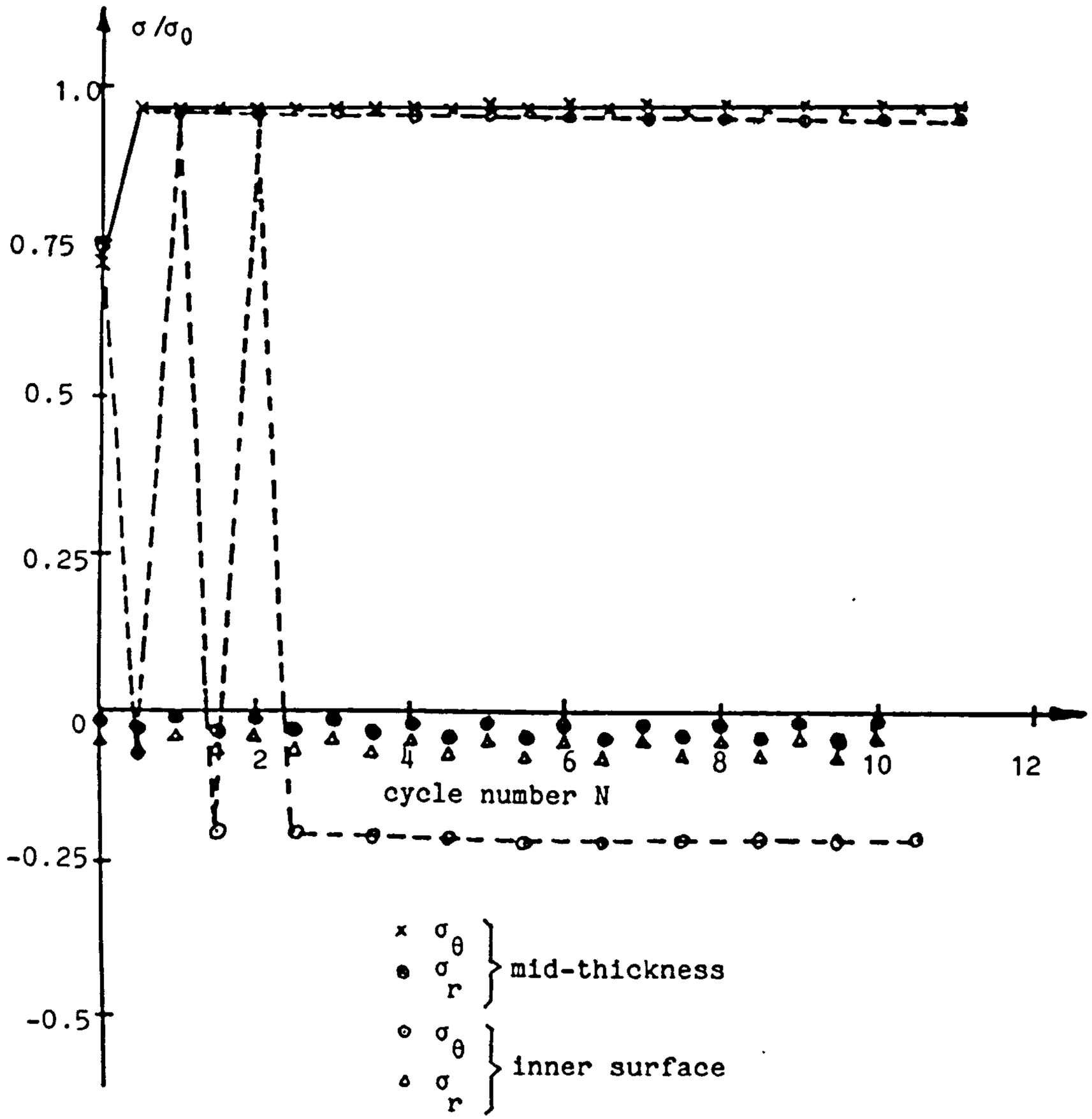

Fig.3.24(i) Variation of stresses with cycle nnumber for tube with an eccentric bore. σ_p/σ_0 =0.568, σ_t/σ_0 =1.72

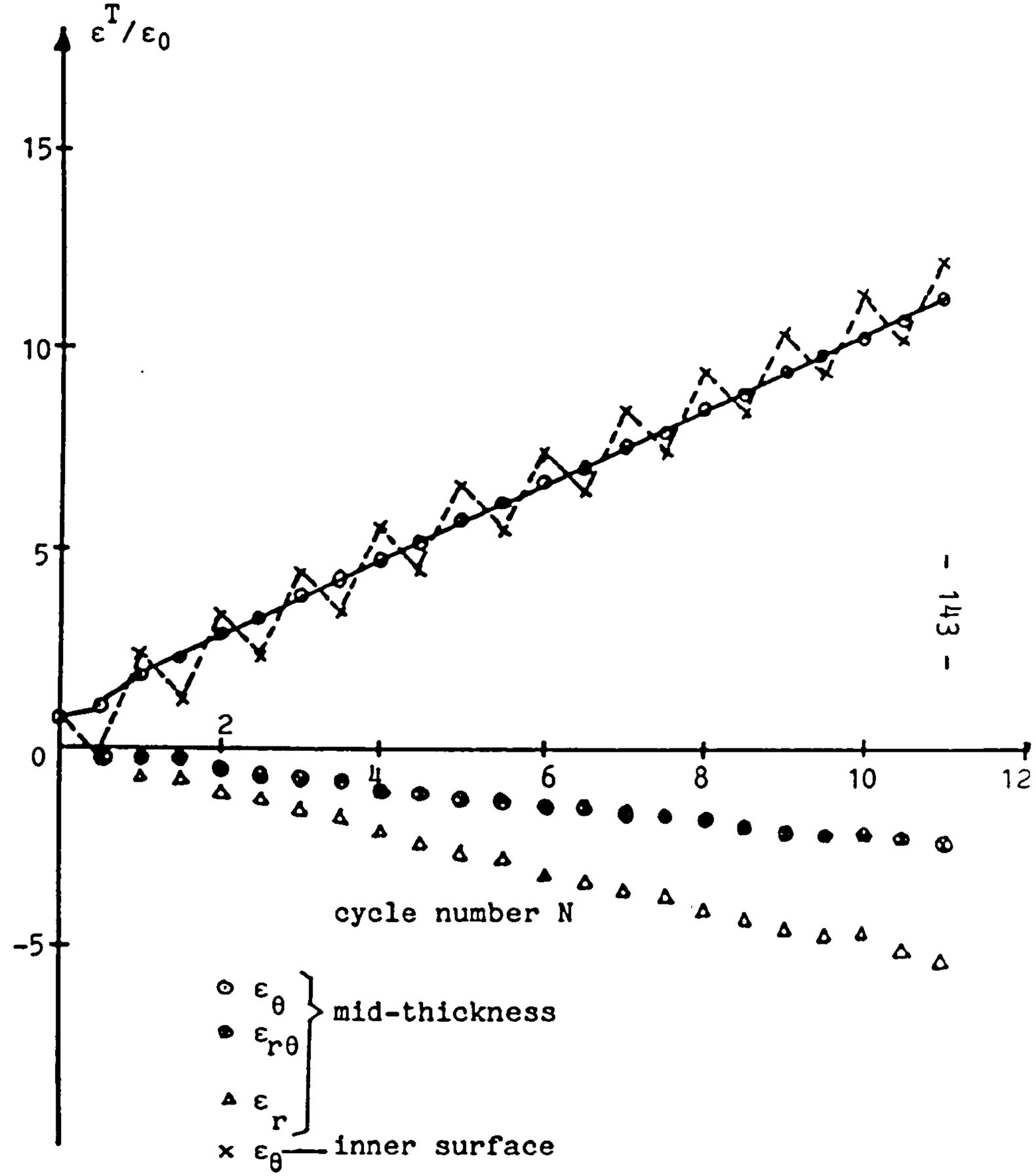

Fig.3.24(ii) Variation of total strains with cycle number for a tube with an eccentric bore. σ_p/σ_0 =0.568, σ_t/σ_0 =1.72

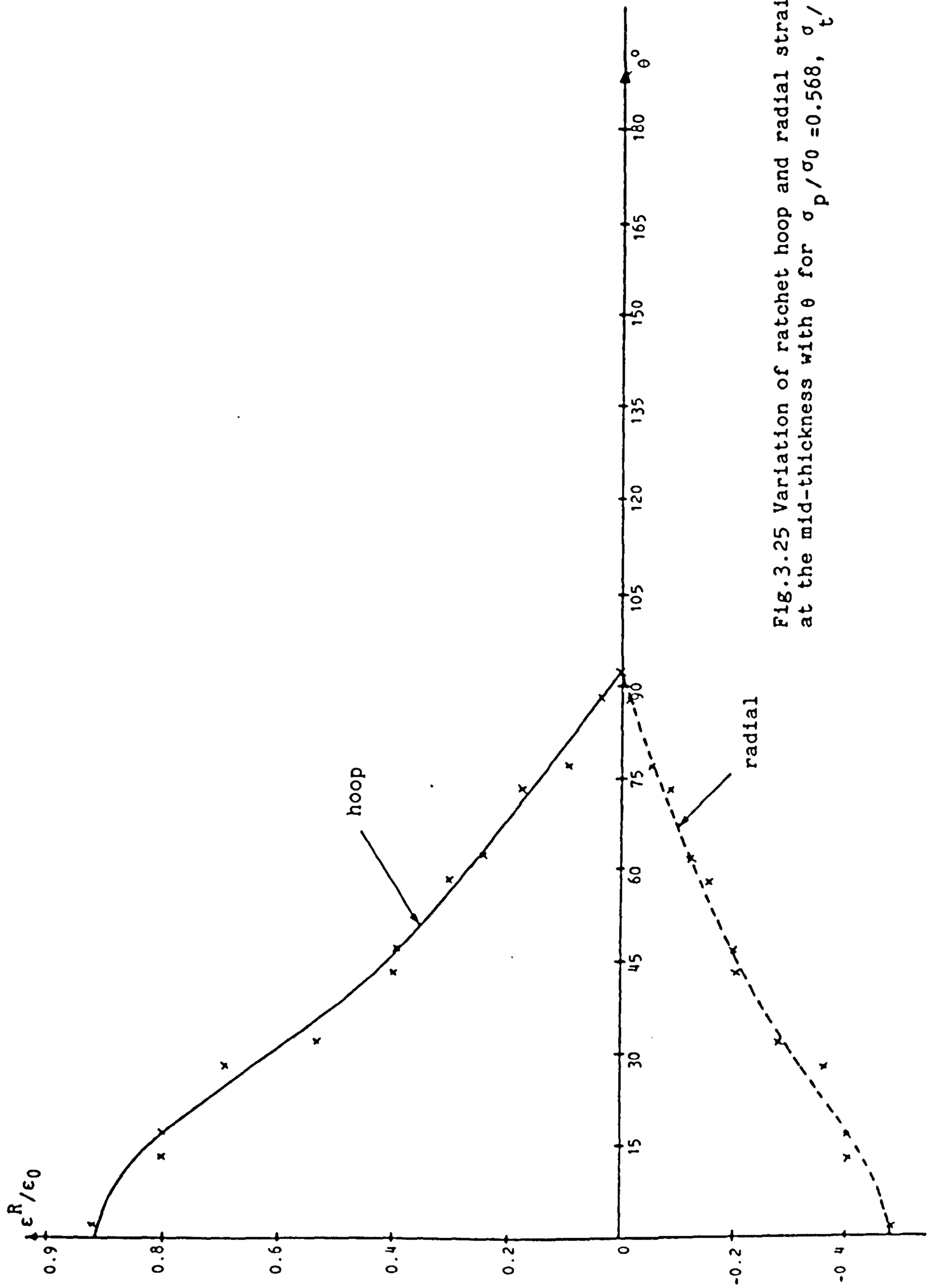

Fig.3.25 Variation of ratchet hoop and radial strains at the mid-thickness with θ for σ_p/σ_0 =0.568, σ_t/σ_0 =1.72

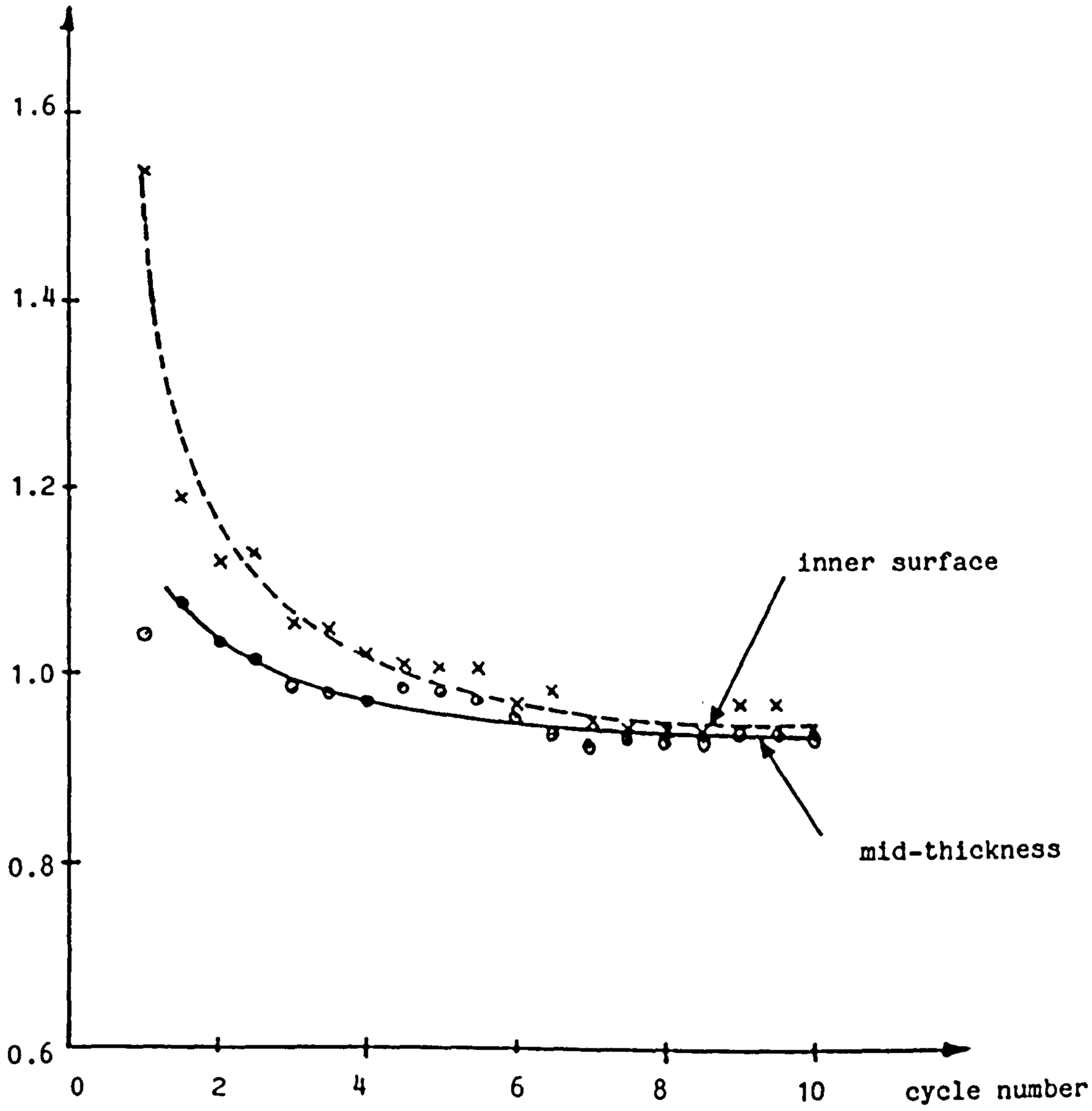

Fig.3.26 Variation of ratchet hoop strain with cycle number for a tube with an eccentric bore. σ_p/σ_0 =0.568, σ_t/σ_0 1.72, $\theta=3^0$

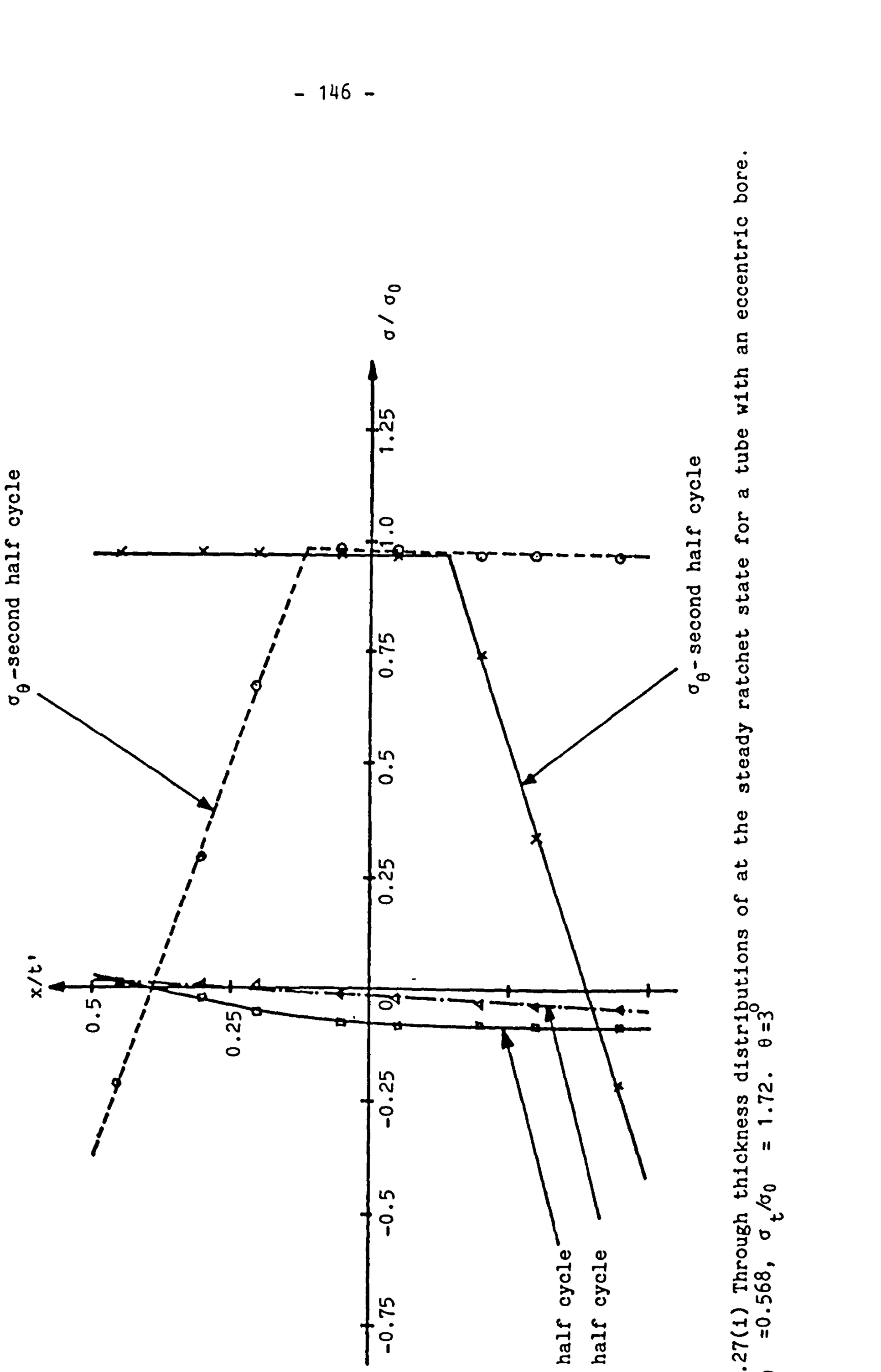

Fig.3.27(1) Through thickness distributions of at the steady ratchet state for a tube with an eccentric bore.
σ_t/σ_0 = 1.72. $\theta = 3^0$
σ_p/σ_0 =0.568, σ_e

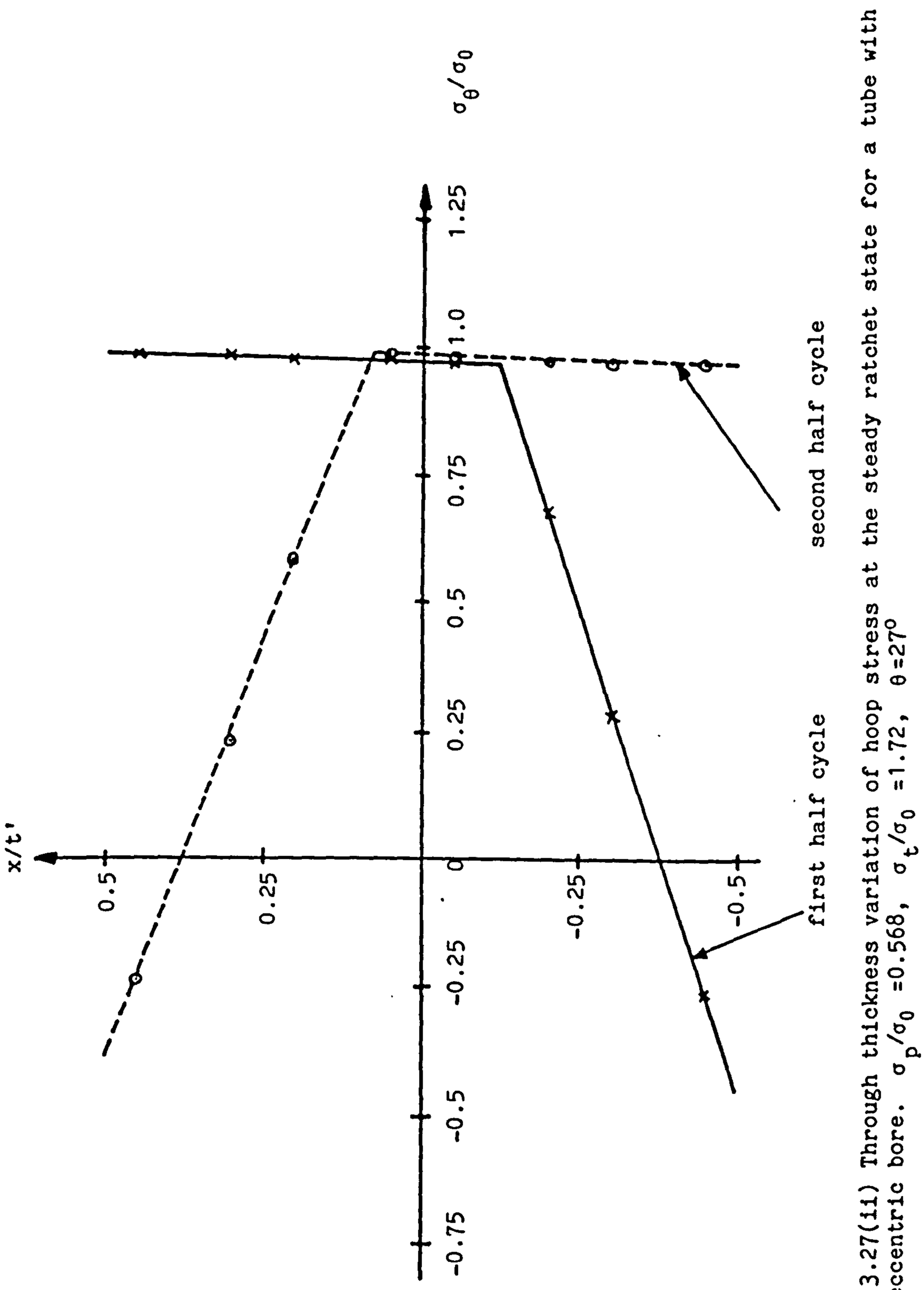

Fig.3.27(ii) Through thickness variation of hoop stress at the steady ratchet state for a tube with an eccentric bore. σ_p/σ_0 =0.568, σ_t/σ_0 =1.72, θ=27°

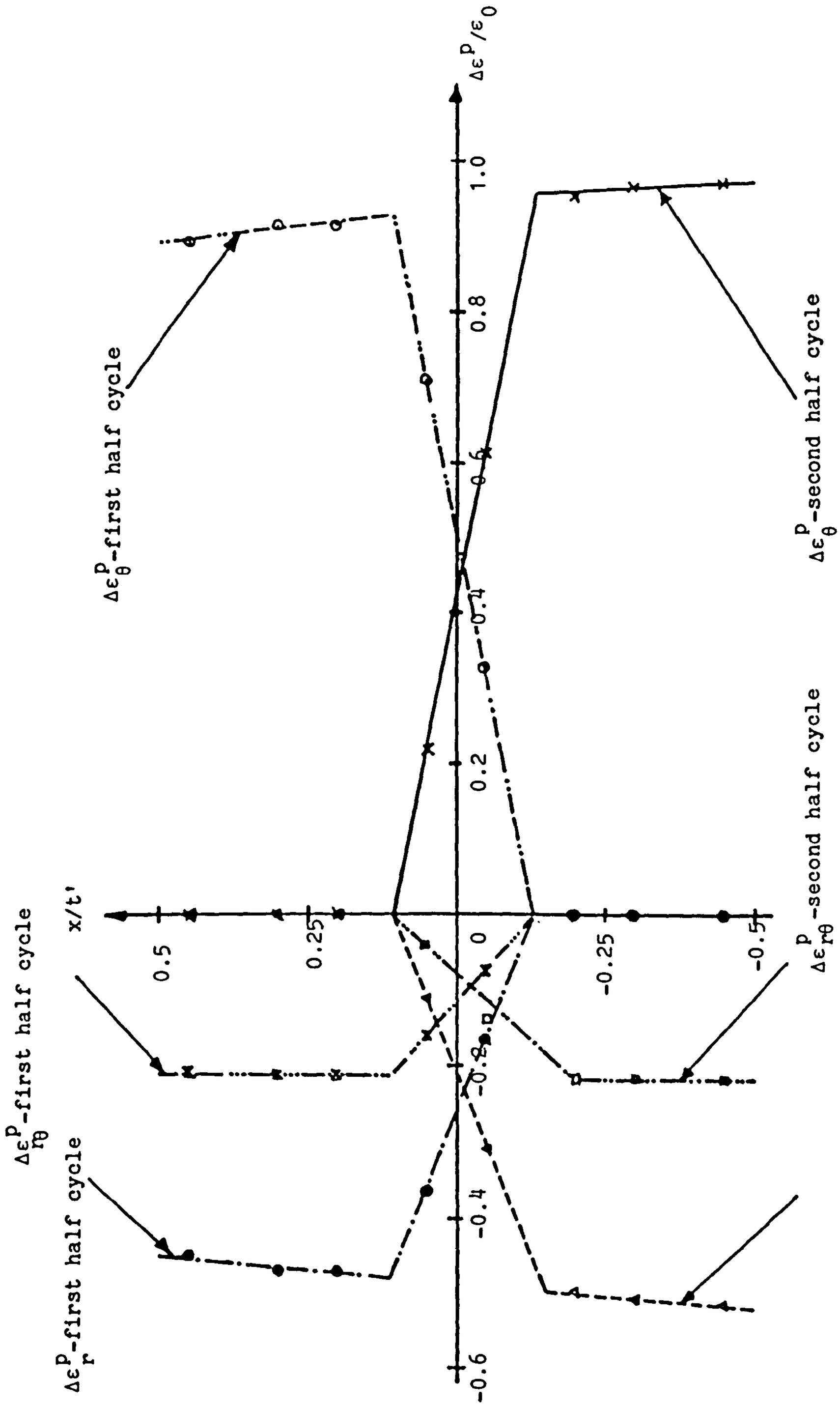

Fig.3.28(i) Through thickness distribution of plastic strain increment at the steady ratchet state. Tube with eccentric bore. σ_p/σ_0 =0.568, σ_t/σ_0 = 1.72, $\theta=3^0$

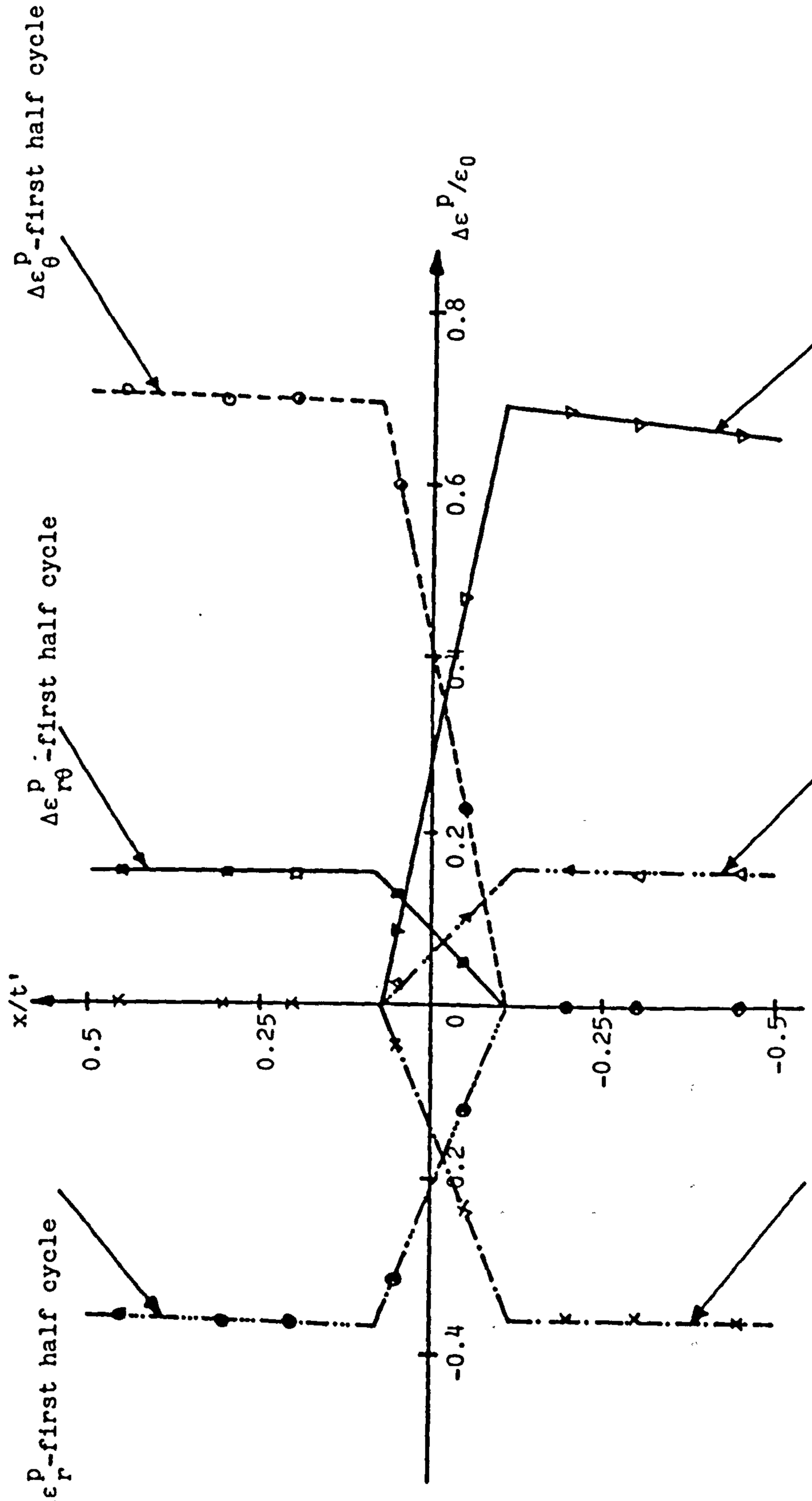

Fig.3.28(ii) Through thickness variation of plastic strain increments at the steady ratchet state. Tube with an eccentric bore. σ_p/σ_0 =0.568, σ_t/σ_0 =1.72, θ= 27°.

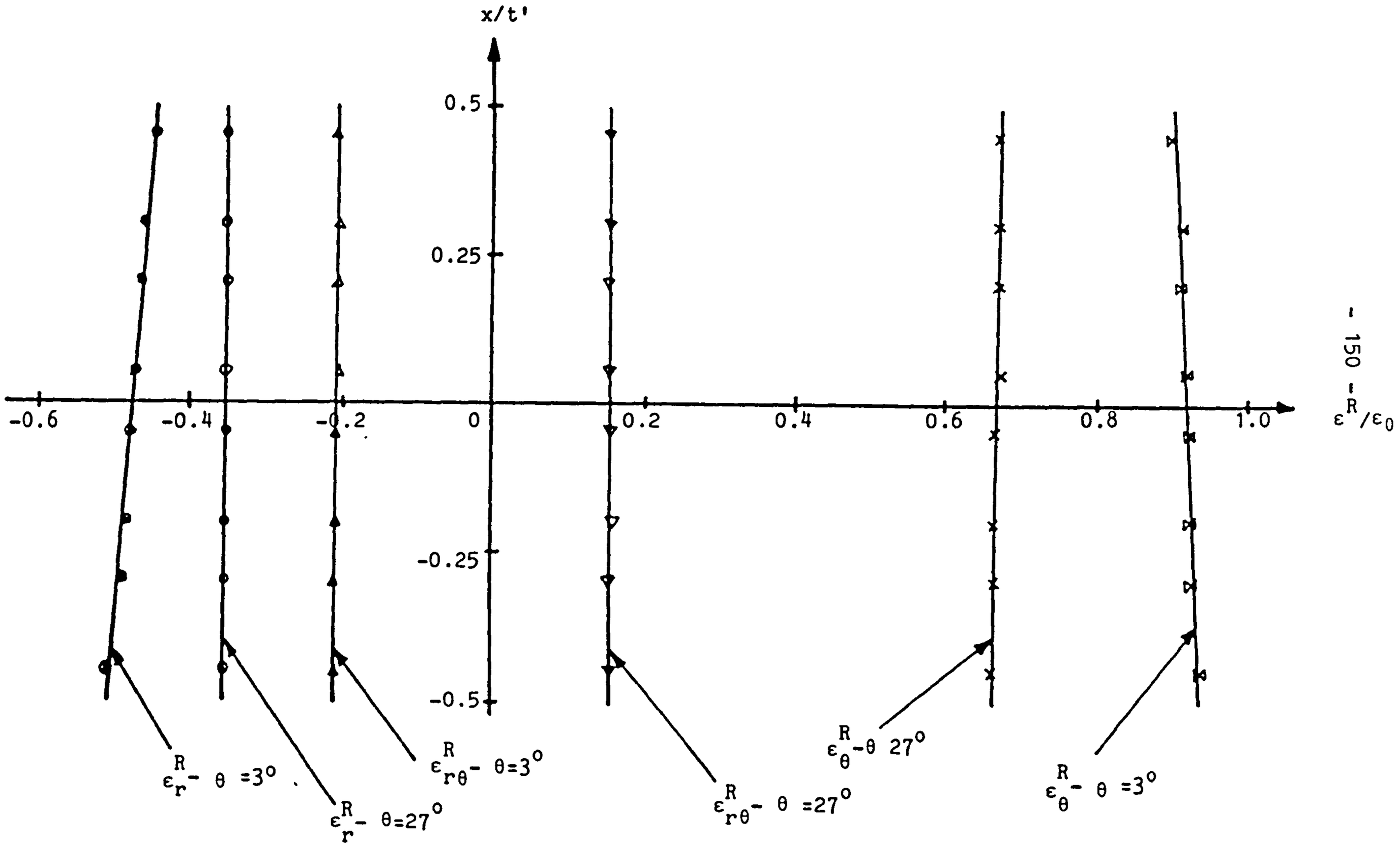

Fig.3.28(iii) Through thickness variation of ratchet strains at the steady ratchet state. Tube with an eccentric bore. σ_p/σ_o =0.568, σ_t/σ_o =1.72, for $\theta = 3^o$ and $\theta = 27^o$.

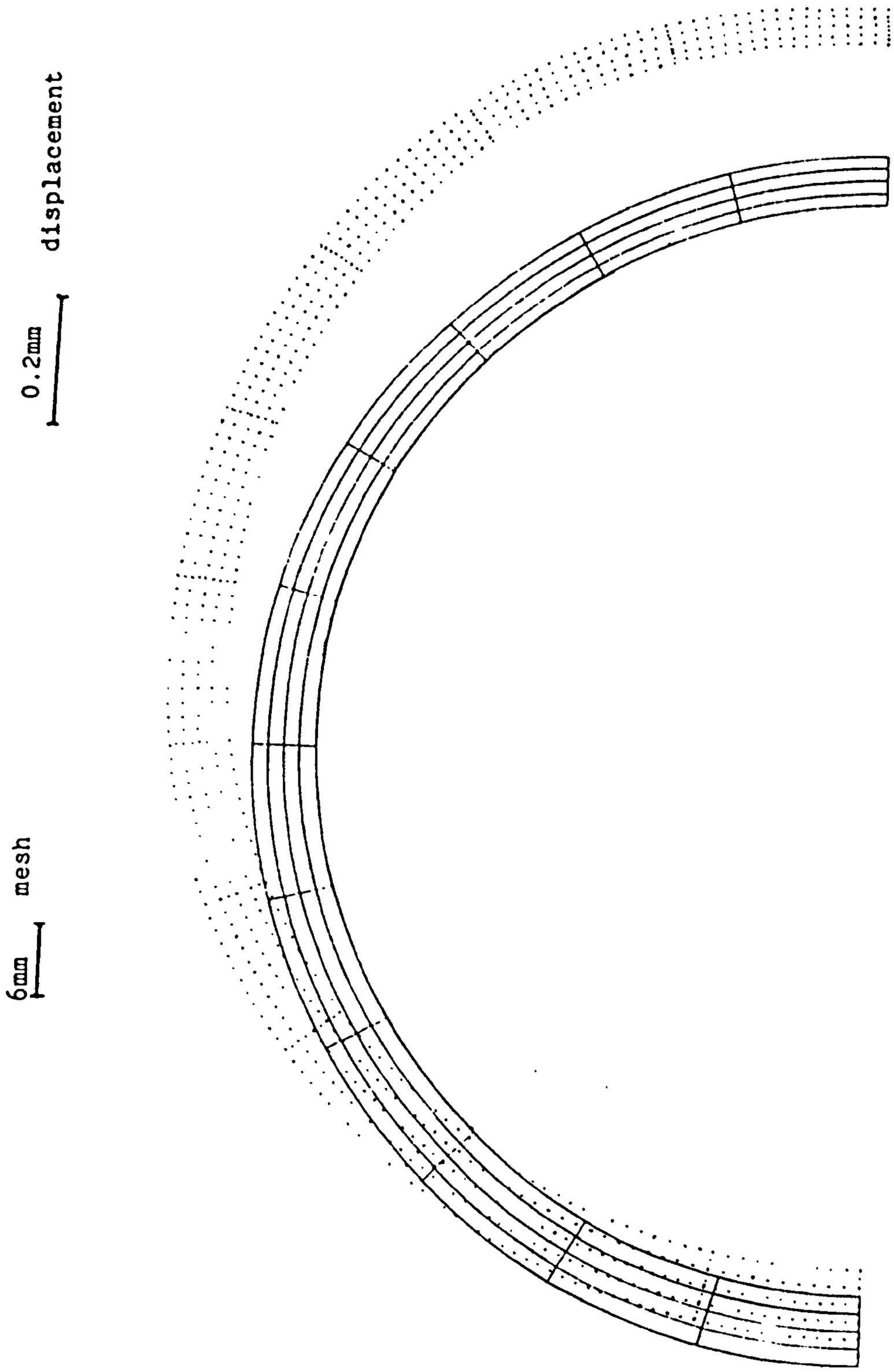

Fig.3.29(1) Displacement at the 10th cycle for σ_p/σ_o = 0.568, σ_t/σ_o =1.72

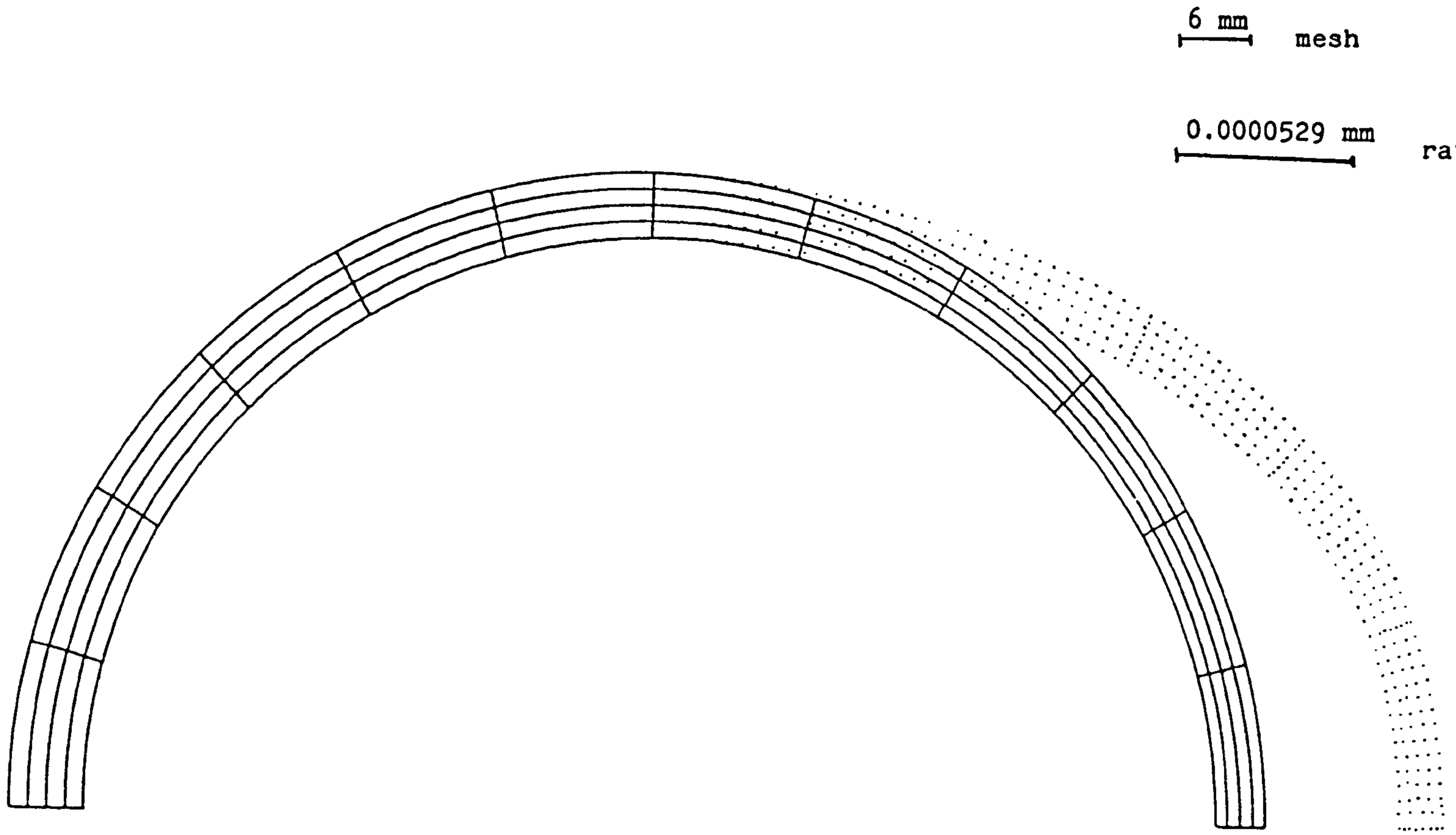

Fig.3.29(ii) Ratchet displacement fo σ_p/σ_o =0.568, σ_t/σ_o =1.72

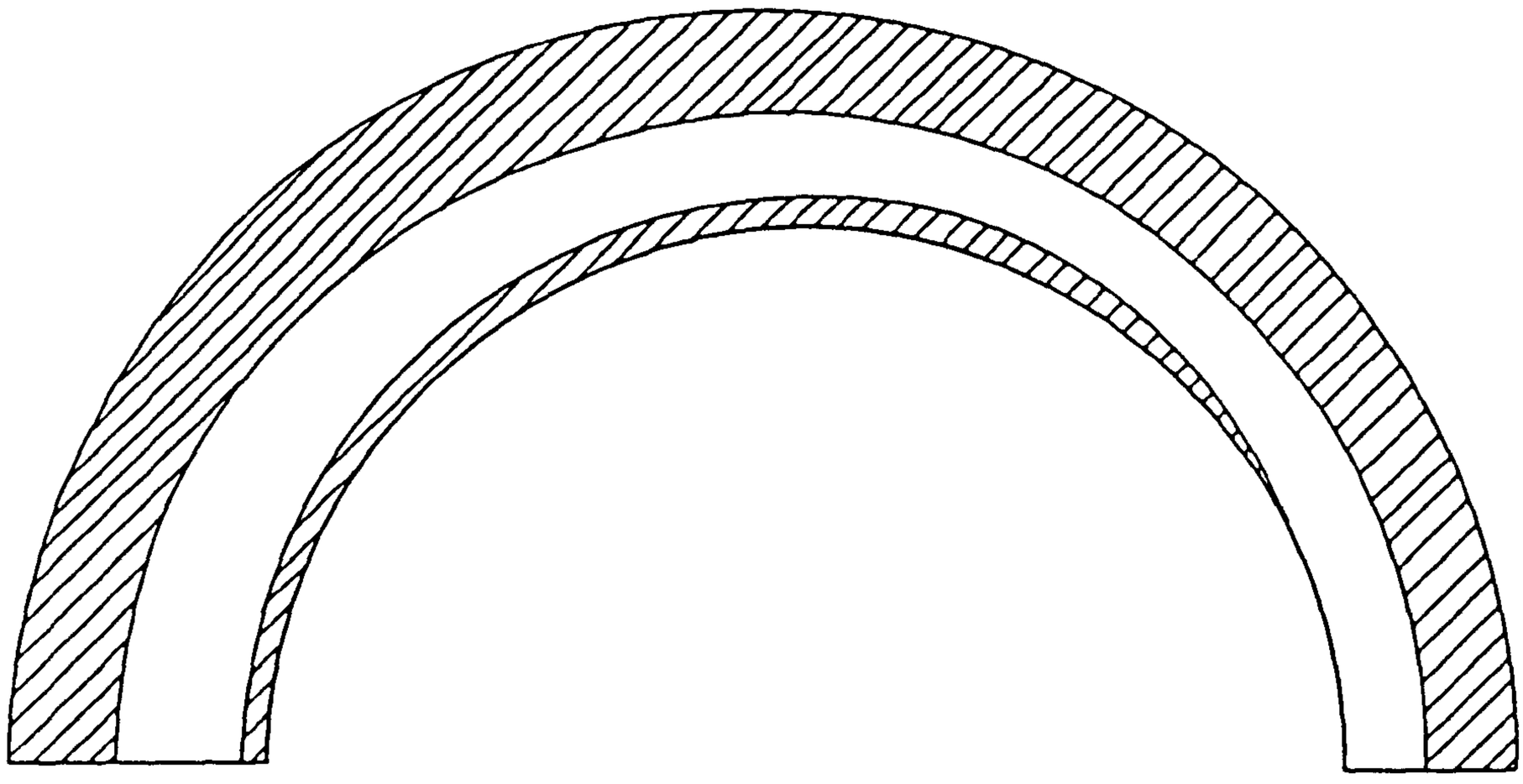

(i) First half cycle

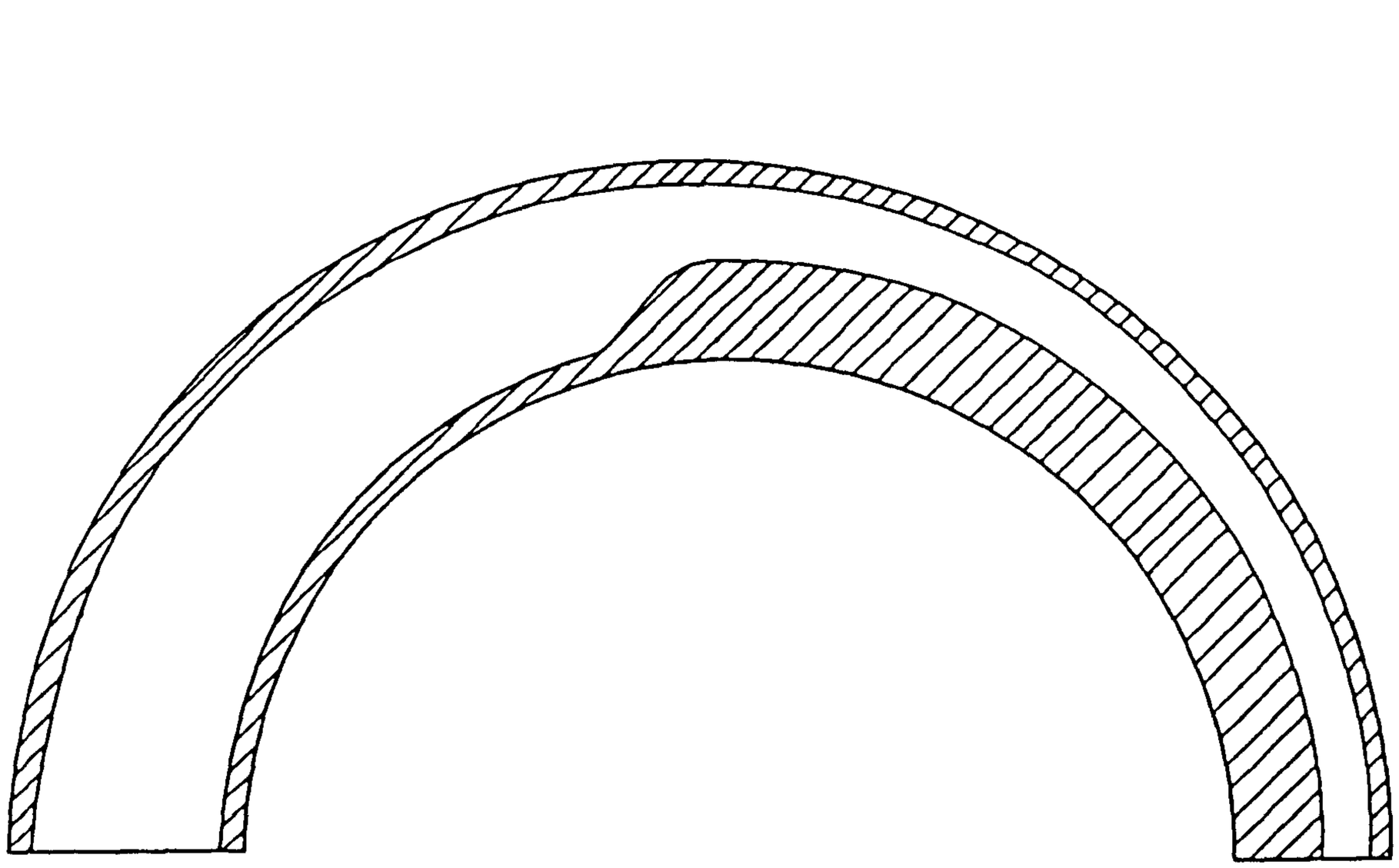

(ii) Second half cycle

Fig. 3.30 Extent of plastic zone at the end of each half cycle for a tube with an eccentric bore $\sigma_p/\sigma_o = 0.379$, $\sigma_t/\sigma_o = 2.5$

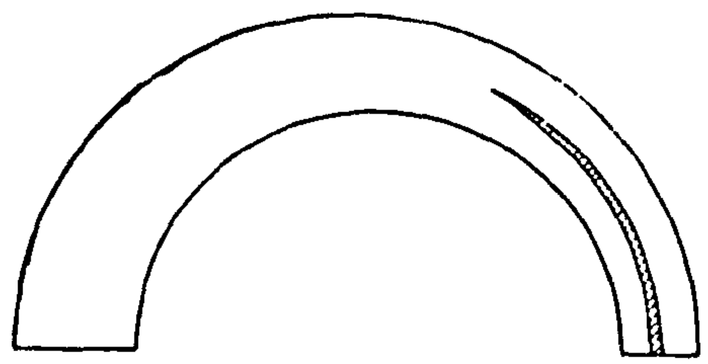

(i) 11/21 σ_t

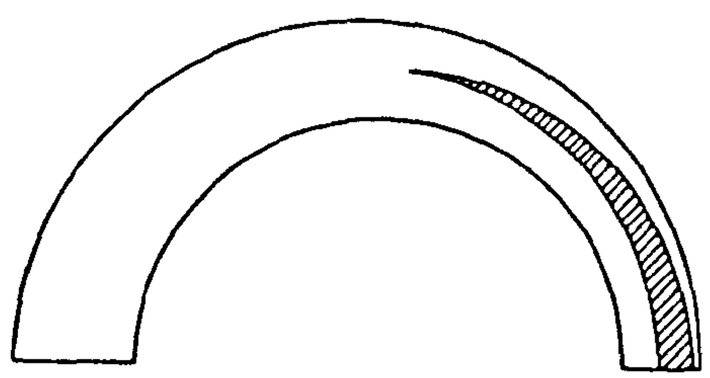

(ii) 17/21 σ_t

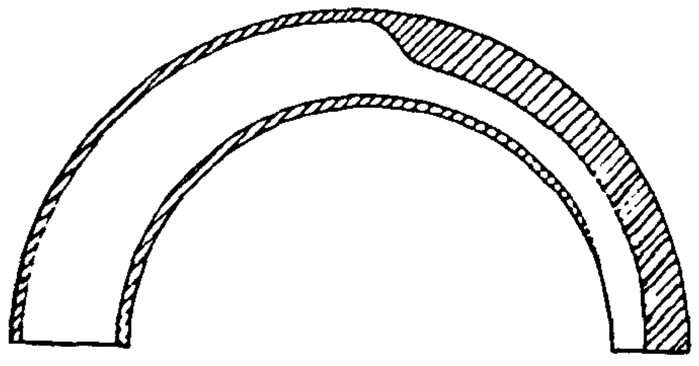

(iii) 21/21 σ_t

First half cycle

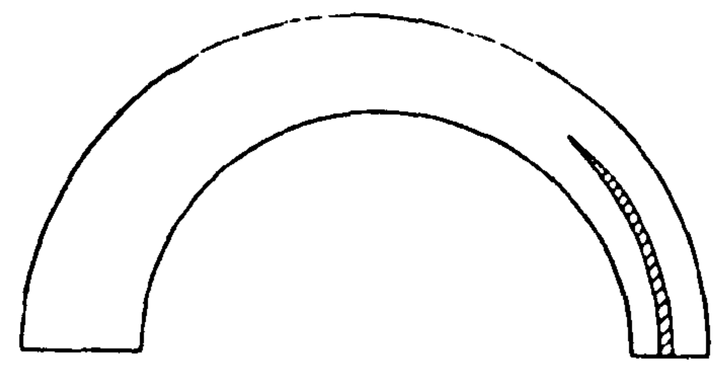

(iv) 9/21 σ_t

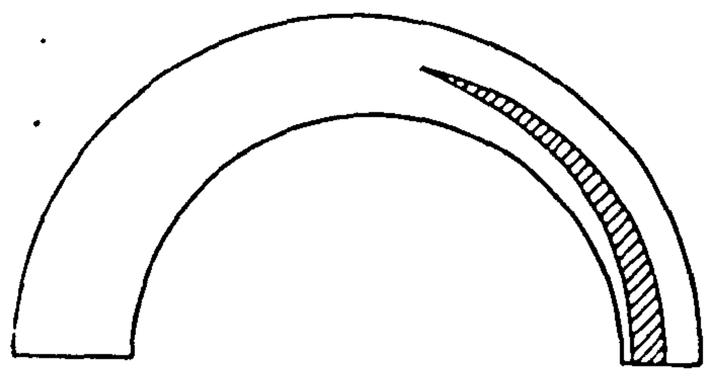

(v) 18/21 σ_t

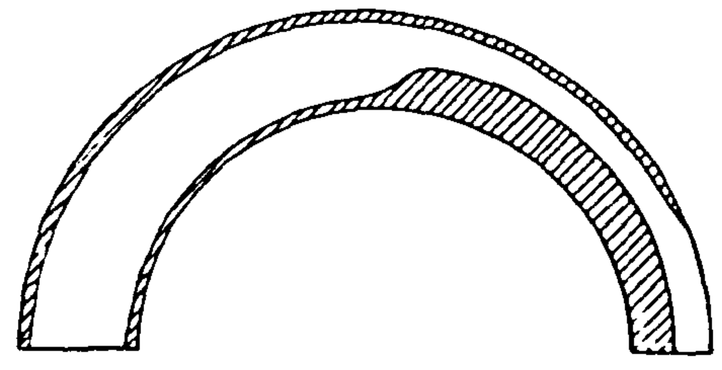

(vi) 21/21 σ_t

Second half cycle

Fig. 3.3 1 Development of plastic zone during a steady state cycle for a tube with an eccentric bore $\sigma_p/\sigma_o = 0.379$, $\sigma_t/\sigma_o = 2.5$

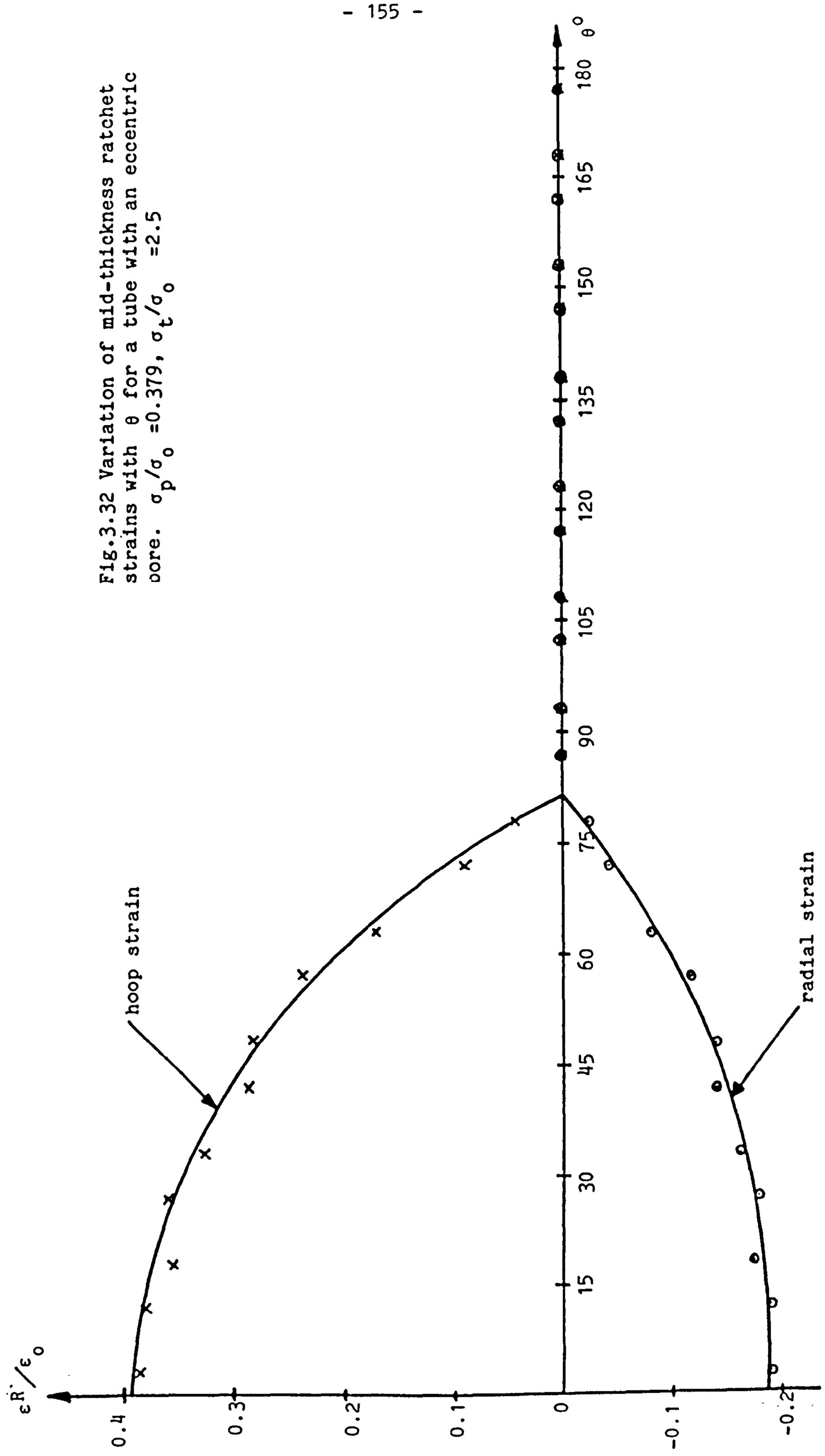

Fig.3.32 Variation of mid-thickness ratchet strains with θ for a tube with an eccentric bore. σ_p/σ_o =0.379, σ_t/σ_o =2.5

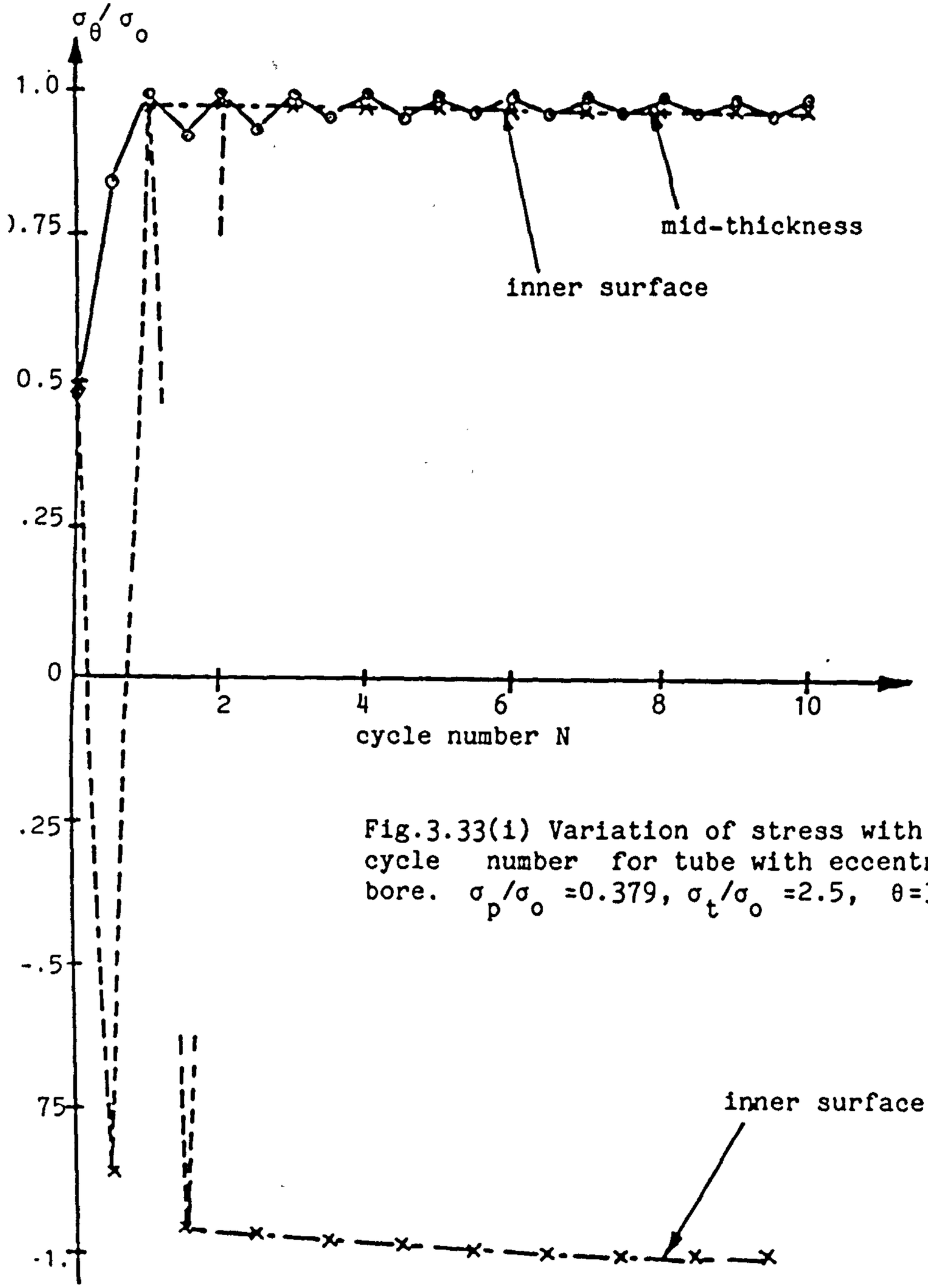

Fig.3.33(i) Variation of stress with cycle number for tube with eccentric bore. σ_p/σ_o =0.379, σ_t/σ_o =2.5, $\theta=3^o$

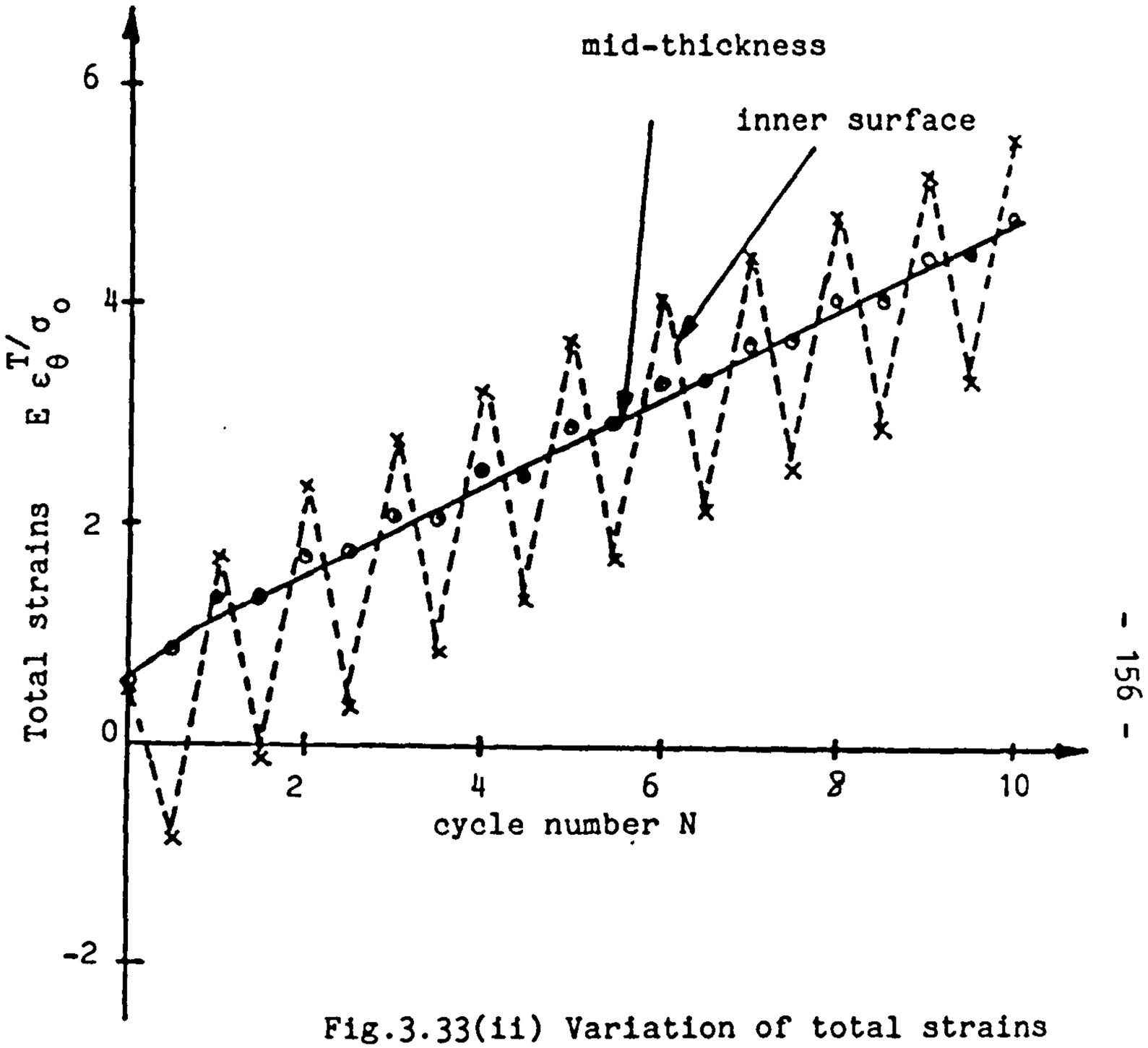

Fig.3.33(ii) Variation of total strains with cycle number for tube with eccentric bore. σ_p/σ_o =0.379, σ_t/σ_o =2.5, $\theta=3^o$

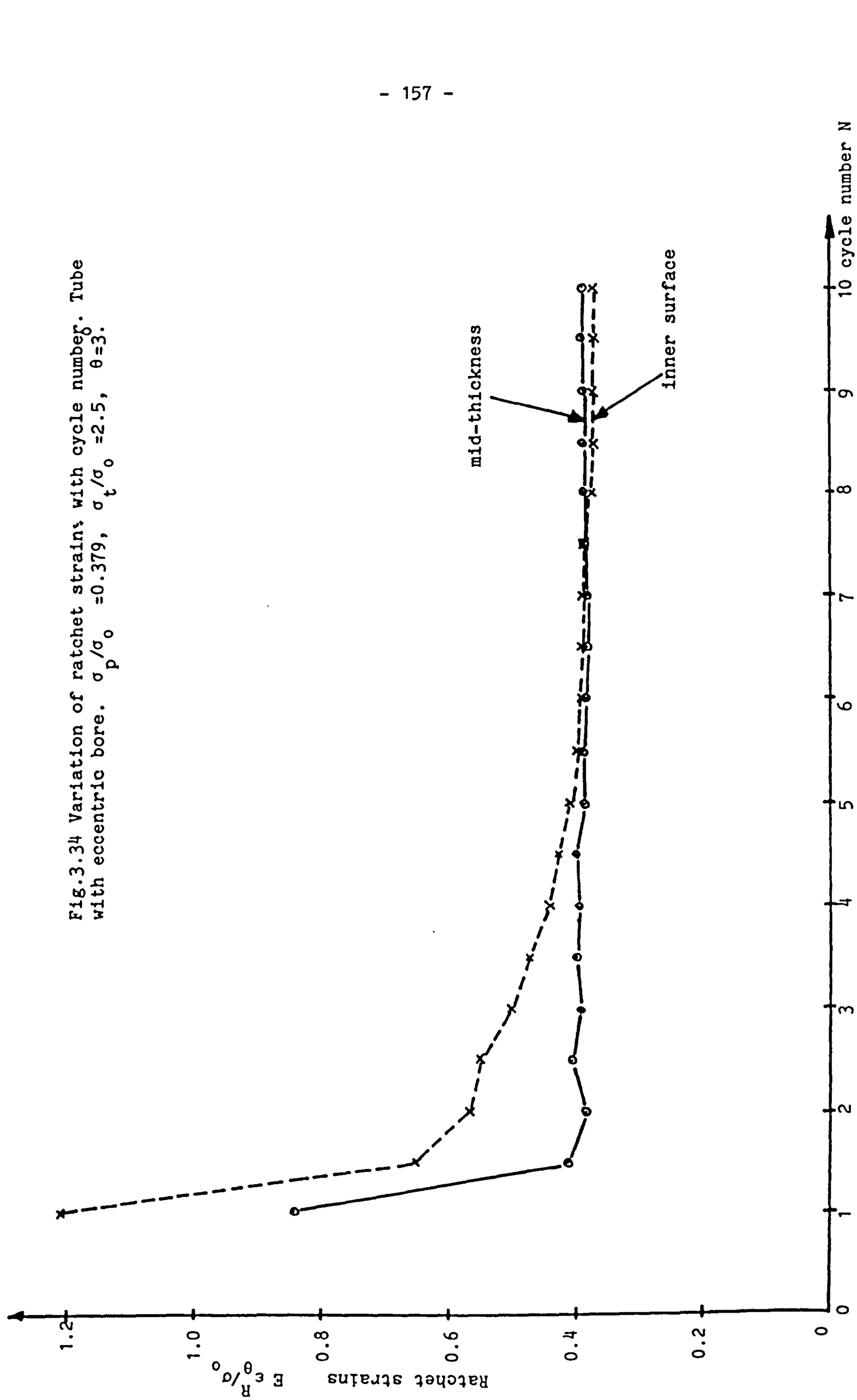

Fig.3.34 Variation of ratchet strain with cycle number. Tube with eccentric bore. σ_p/σ_o =0.379, σ_t/σ_o =2.5, θ=3.

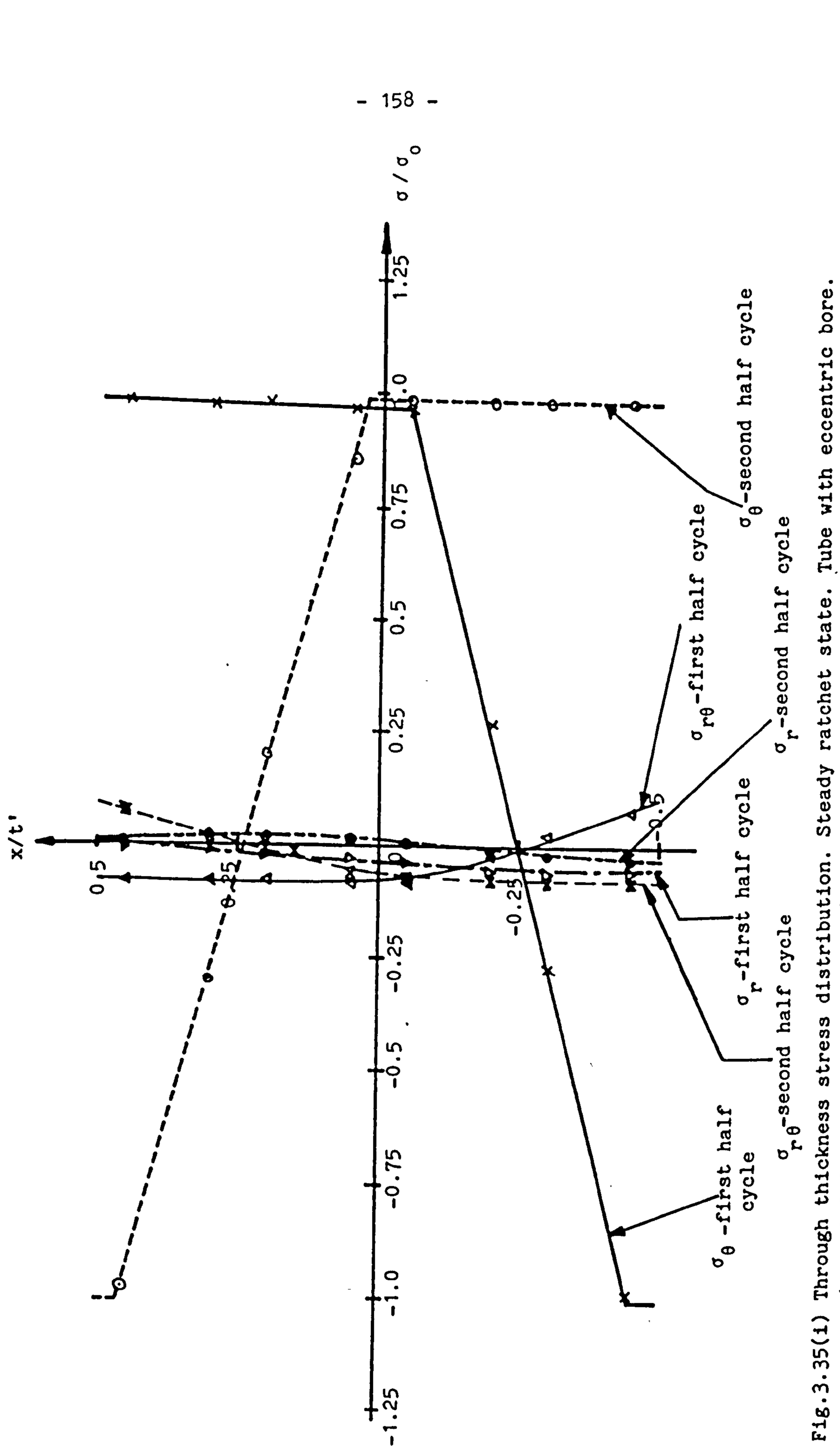

Fig.3.35(1) Through thickness stress distribution. Steady ratchet state. Tube with eccentric bore.
σ_p/σ_o =0.379, σ_t/σ_o =2.5, θ=3°

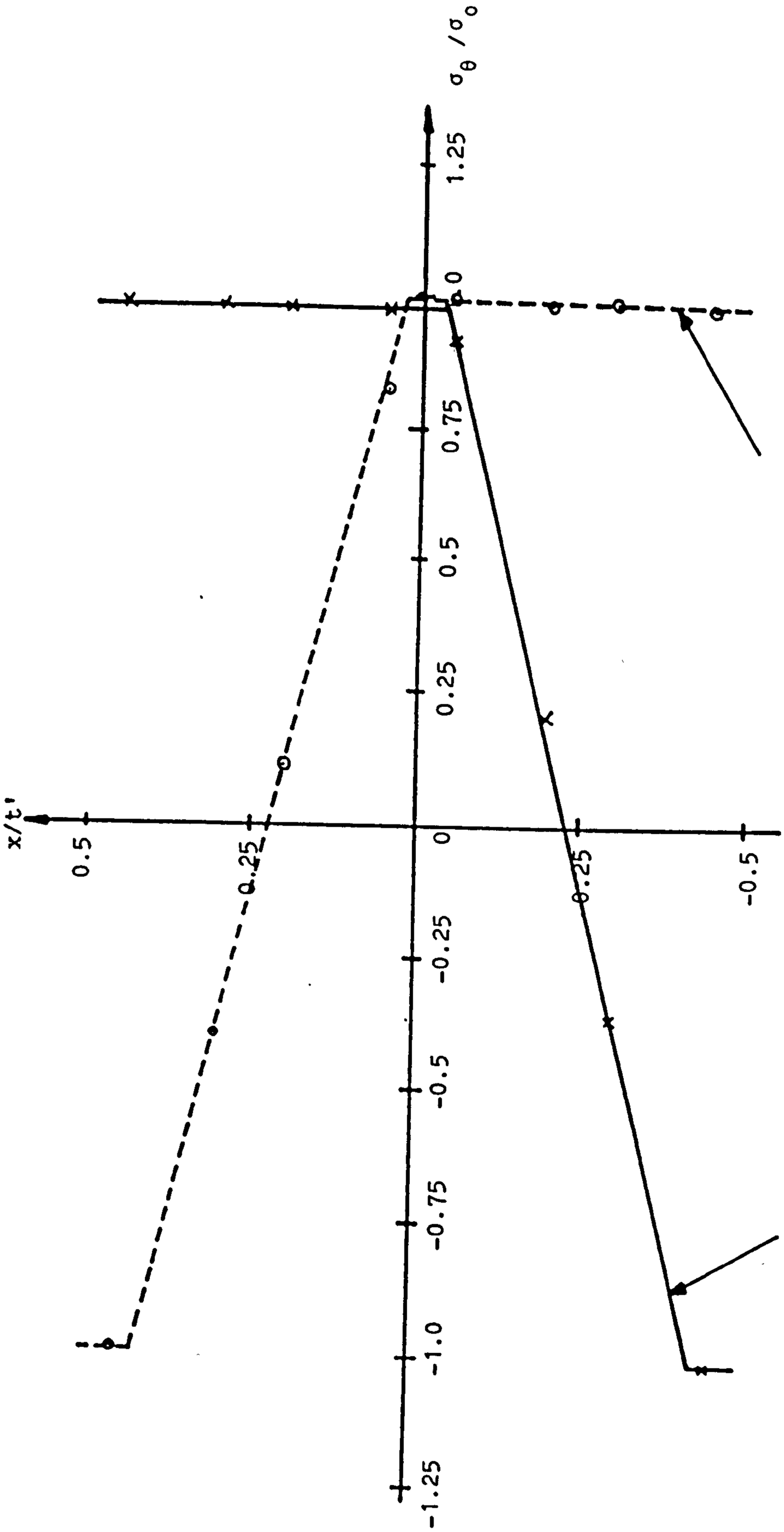

Fig.3.35(11) Through thickness distribution of hoop stress. Tube with eccentric bore at the steady ratchet state.
σ_p/σ_o =0.379, σ_t/σ_o =2.5, $\theta=42^o$

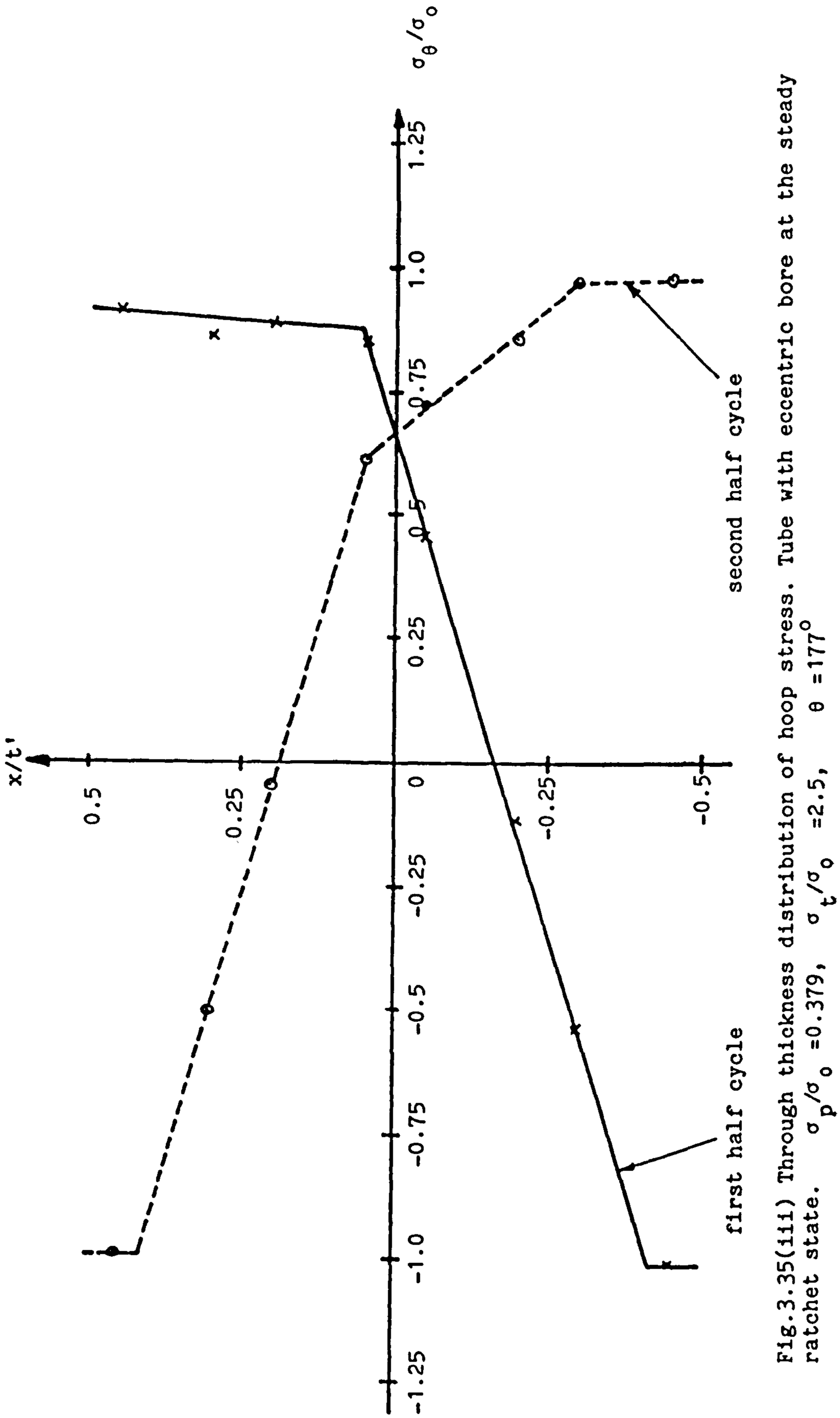

Fig.3.35(111) Through thickness distribution of hoop stress. Tube with eccentric bore at the steady ratchet state. σ_p/σ_o =0.379, σ_t/σ_o =2.5, θ =177°

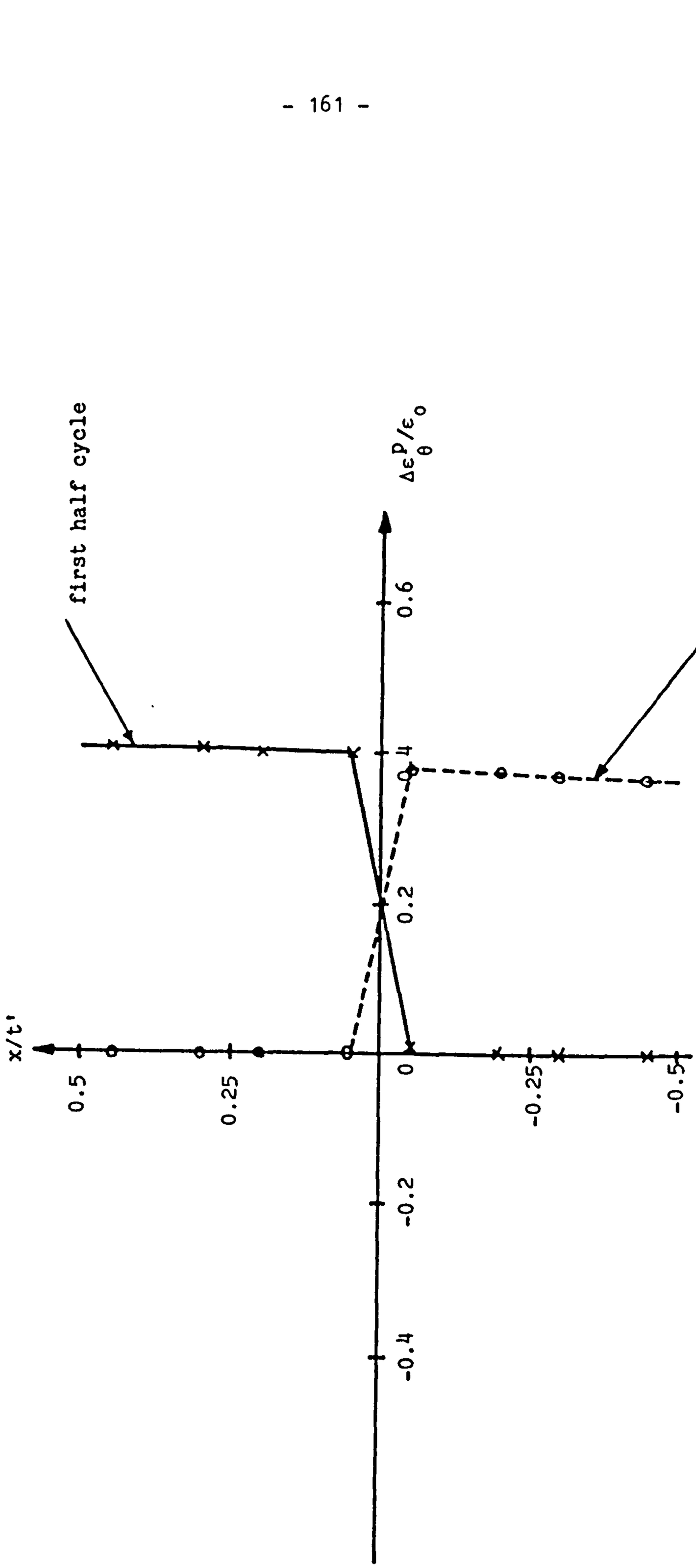

Fig.3.35(iv) Through thickness distribution of plastic hoop strain increment. Tube bore at the steady ratchet state. σ_p/σ_o =0.379, σ_t/σ_o =2.5, $\theta=3^o$

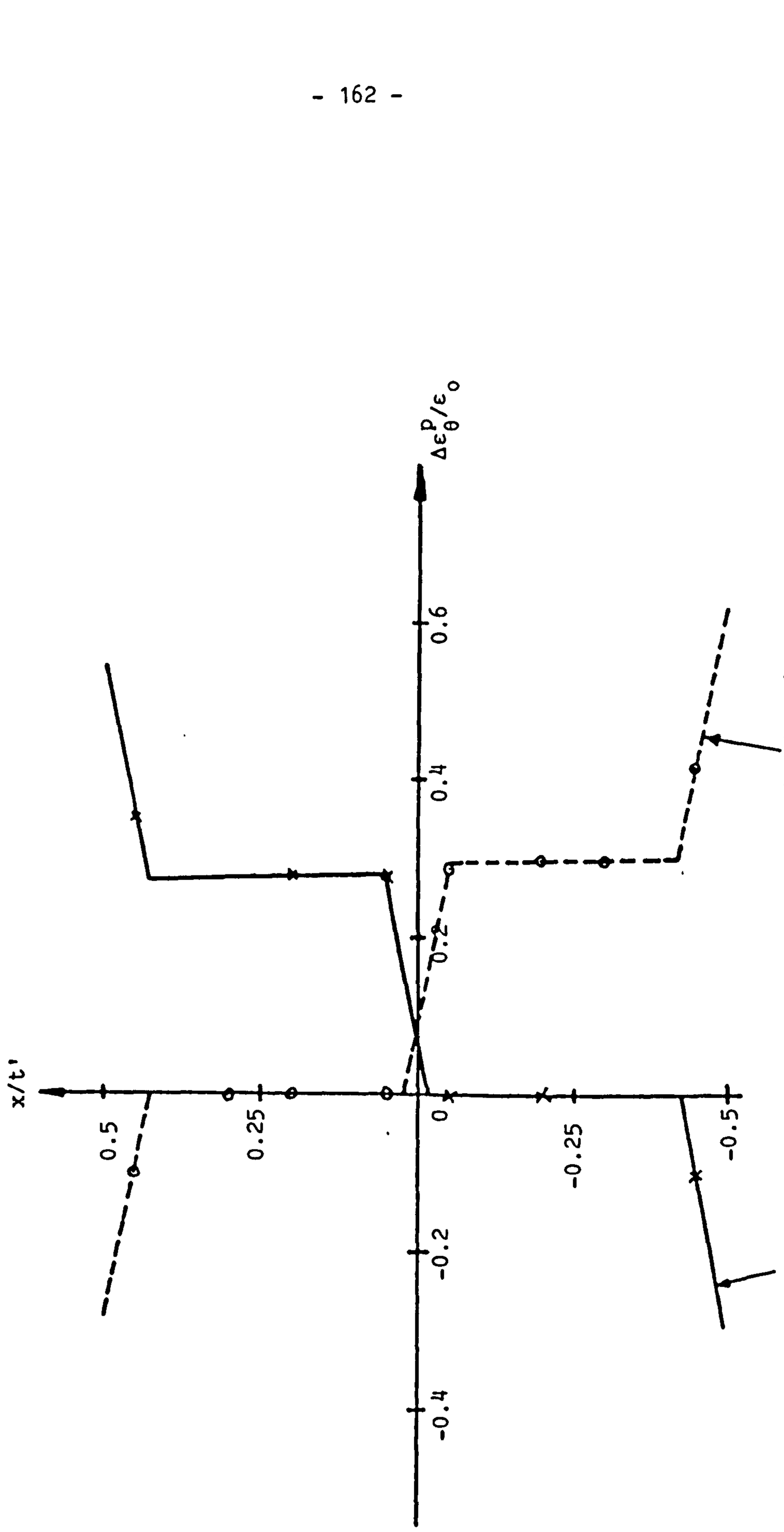

Fig.3.35(v) Through thickness distribution of plastic hoop strain increment. Tube with eccentric bore at the steady ratchet state. σ_p/σ_o =0.379, σ_t/σ_o =2.5, θ =42°

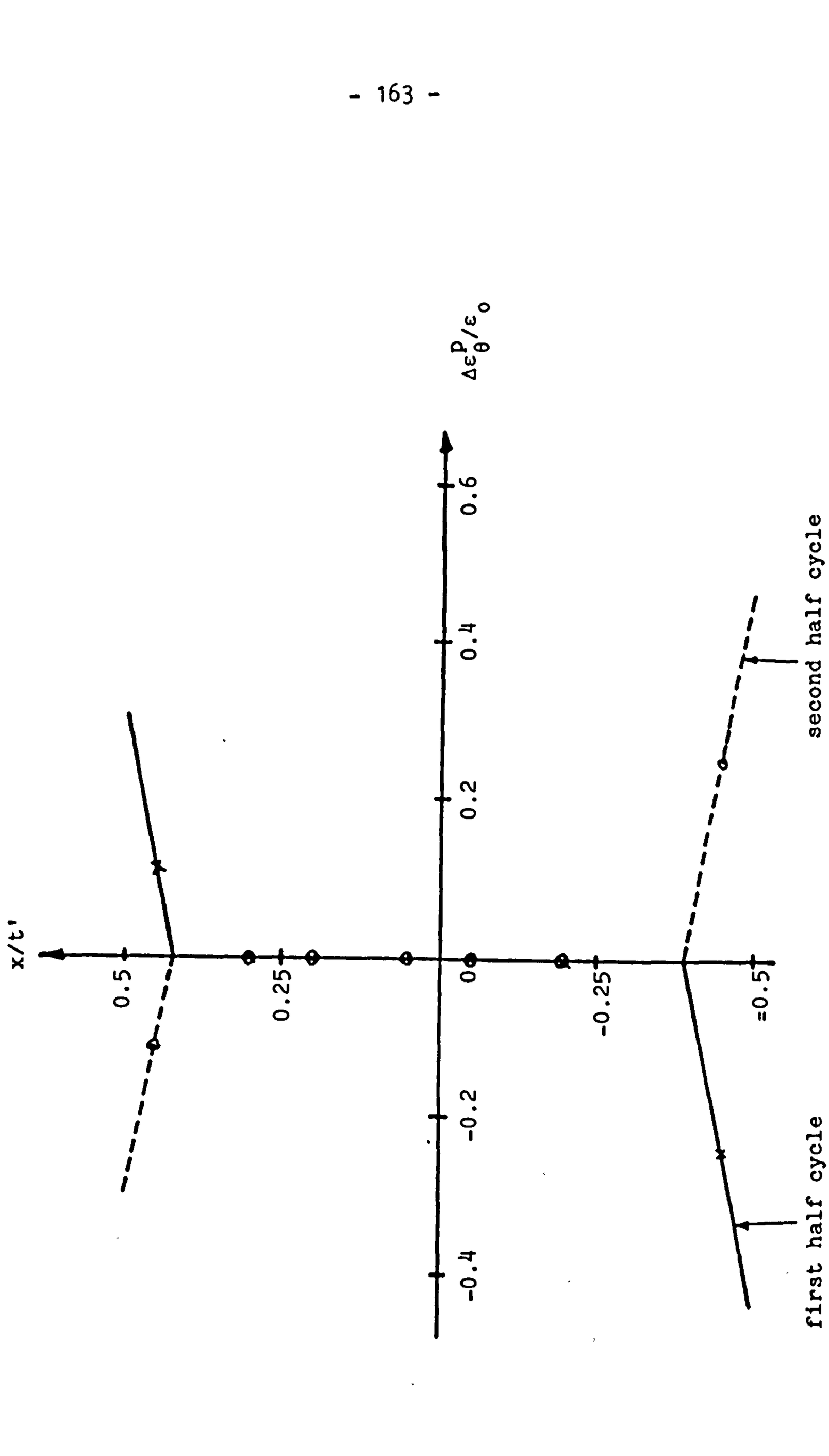

Fig.3.35(vi) Through thickness distribution of plastic hoop strain increment. Tube with eccentric bore at the steady ratchet state. σ_p/σ_o =0.379, σ_t/σ_o =2.5, θ=177°

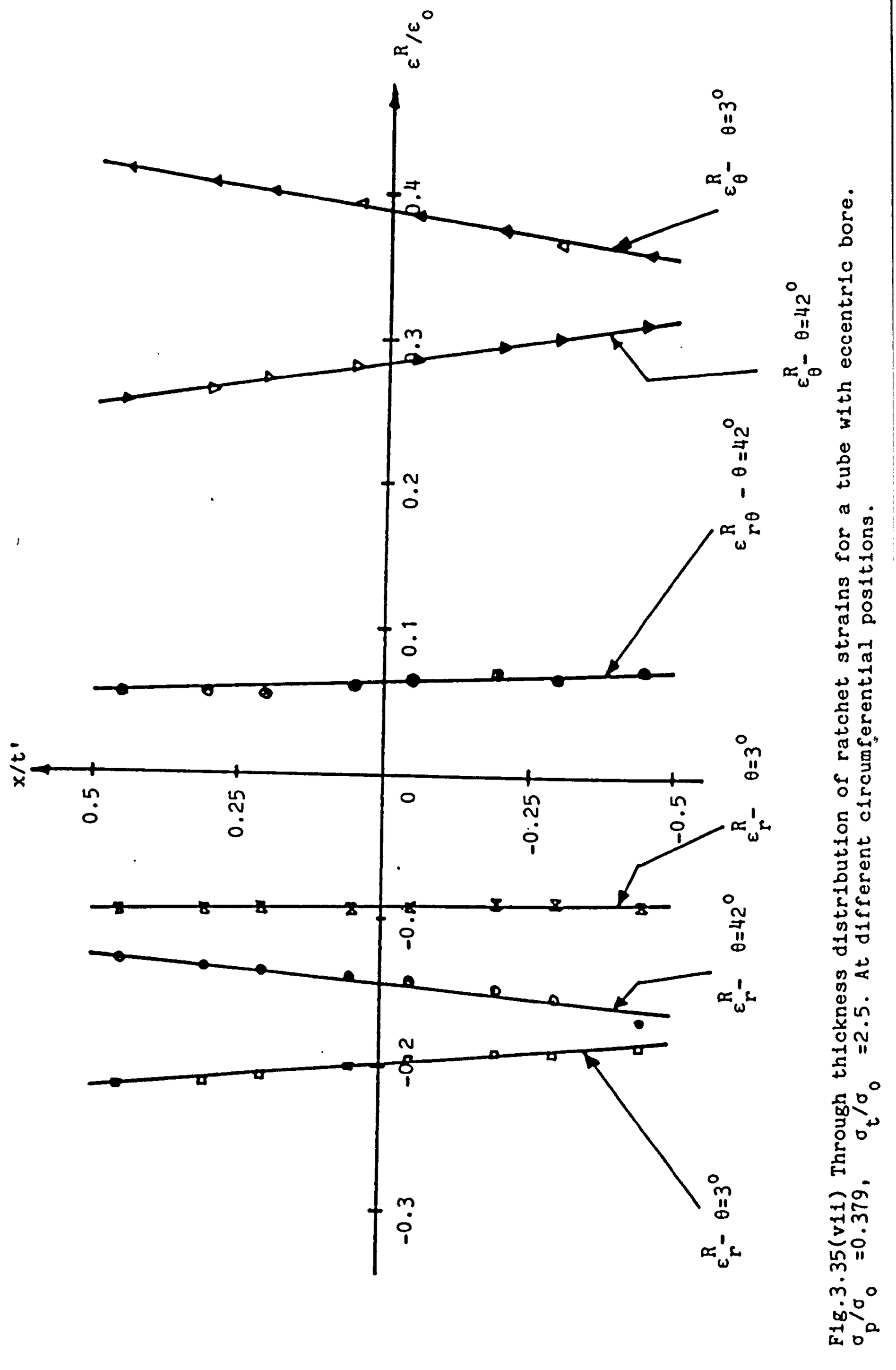

Fig.3.35(v11) Through thickness distribution of ratchet strains for a tube with eccentric bore. σ_p/σ_o =0.379, σ_t/σ_o =2.5. At different circumferential positions.

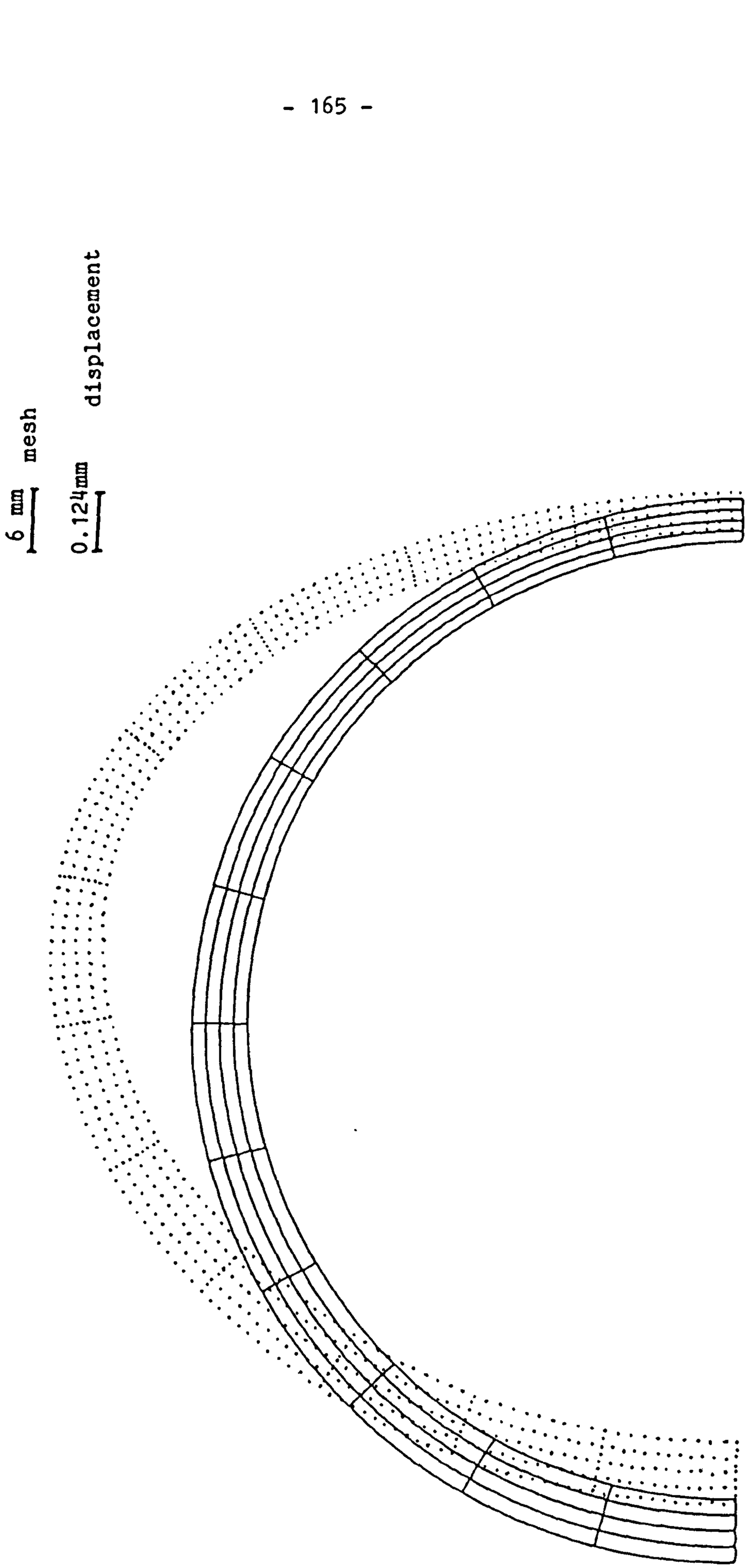

Fig.3.36(i) Displacement at the 10th cycle. σ_p/σ_o =0.379, σ_t/σ_o =2.5

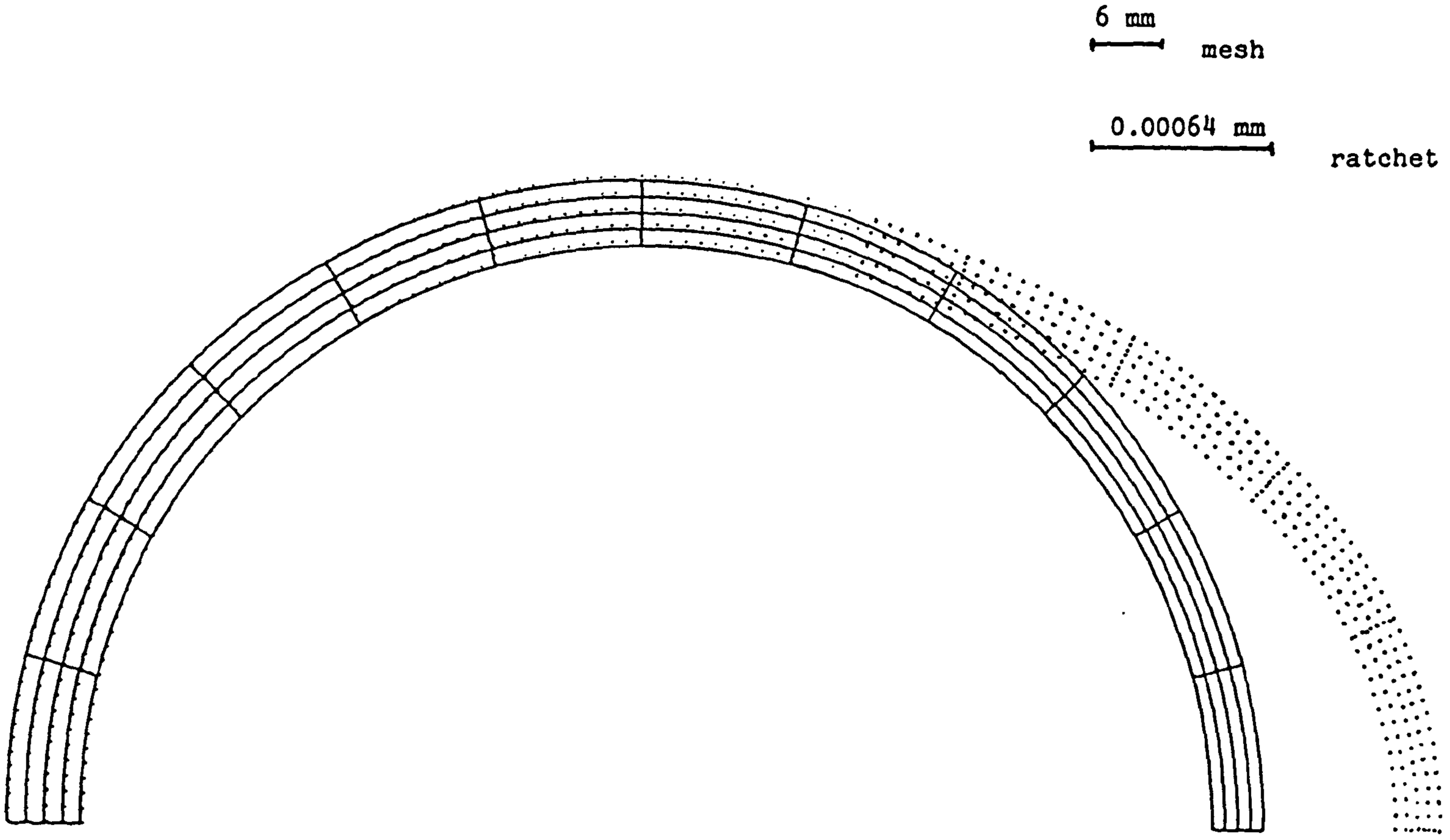

Fig.3.36(ii) Ratchet displacement. σ_p/σ_o =0.379, σ_t/σ_o =2.5

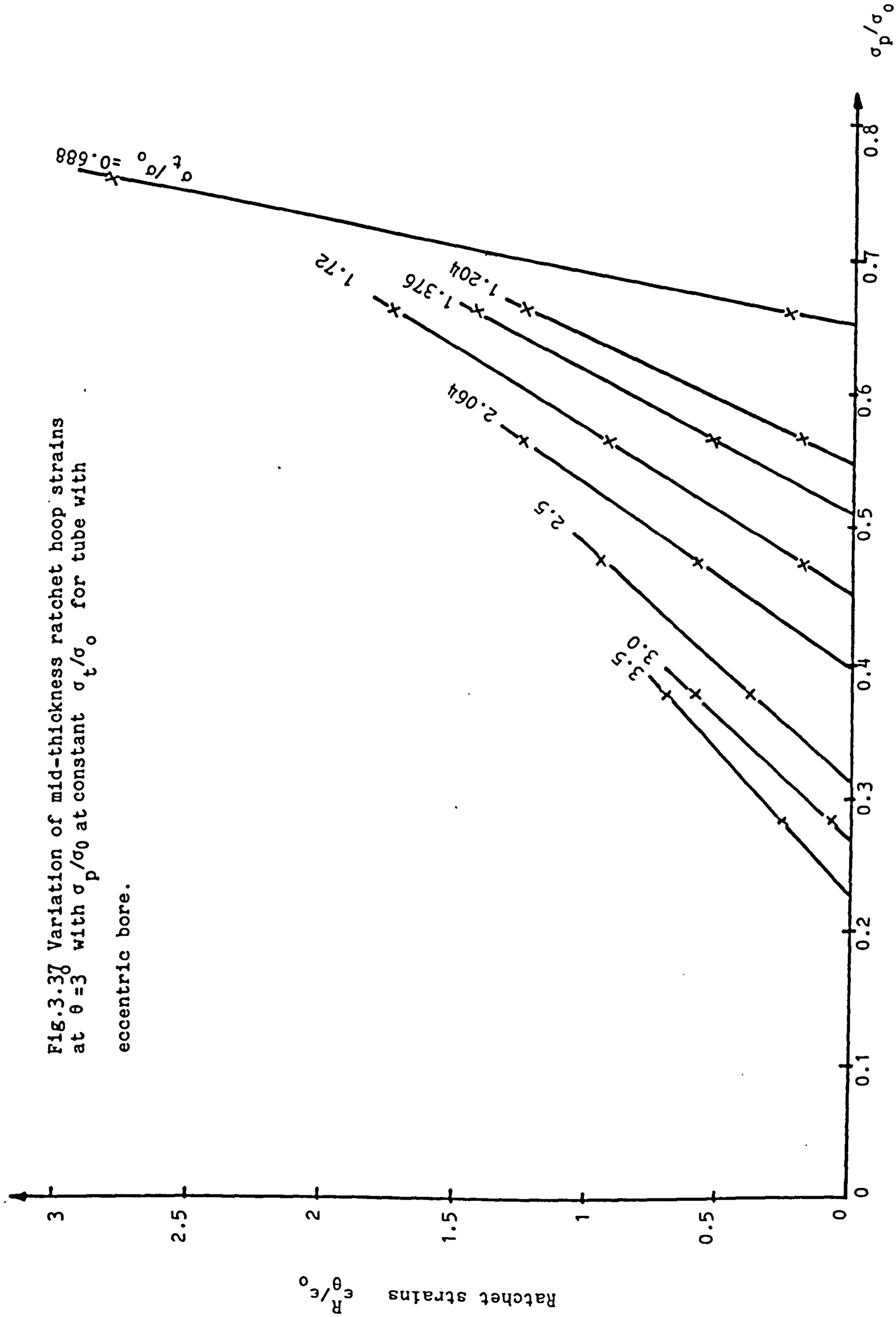

Fig.3.37 Variation of mid-thickness ratchet hoop strains at $\theta = 3^\delta$ with σ_p/σ_0 at constant σ_t/σ_o for tube with eccentric bore.

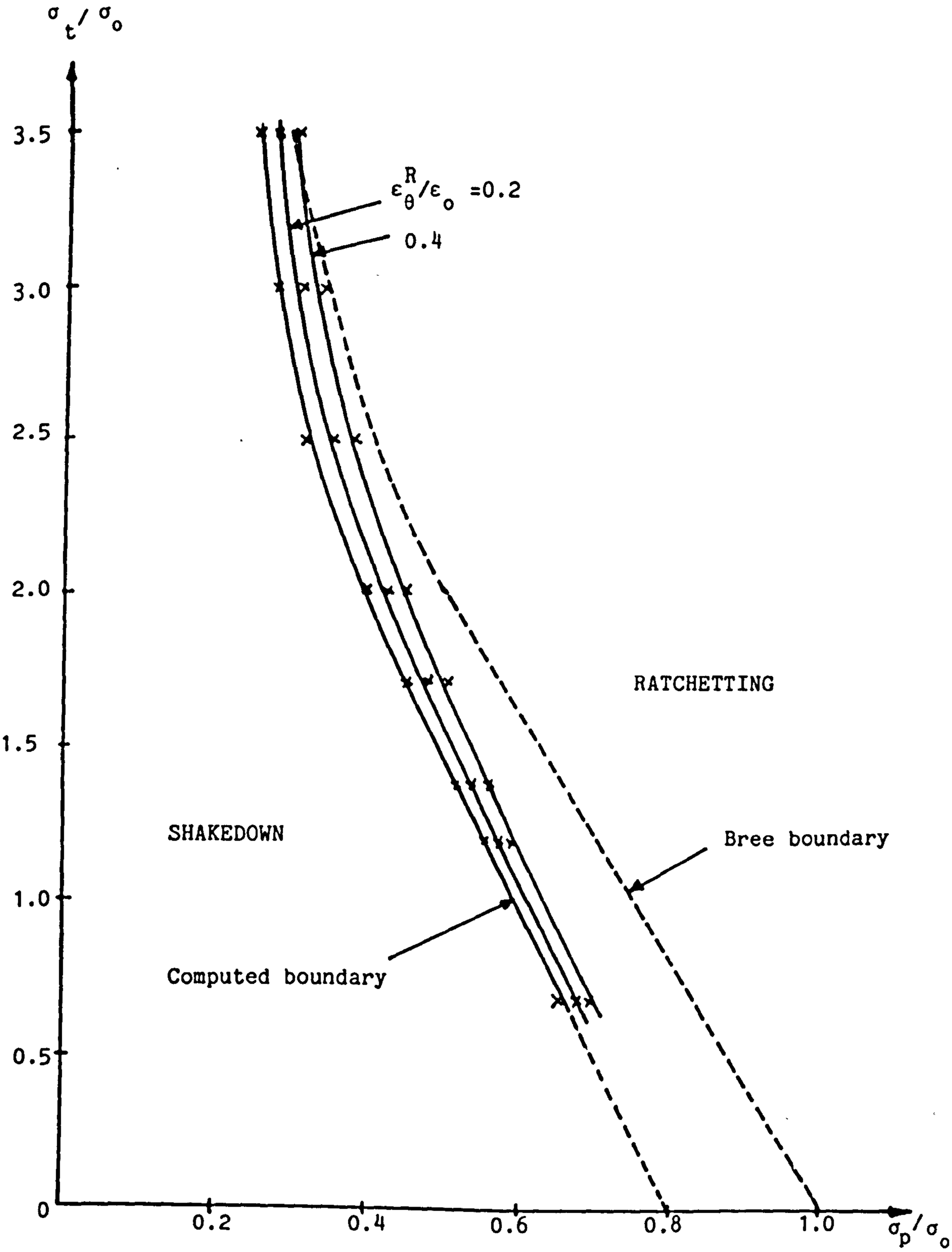

Fig.3.38 Shakedown/ratchetting boundary for a tube with eccentric bore. $\sigma_p = PR_i/h$, $\sigma_t = E\alpha\Delta T/2$

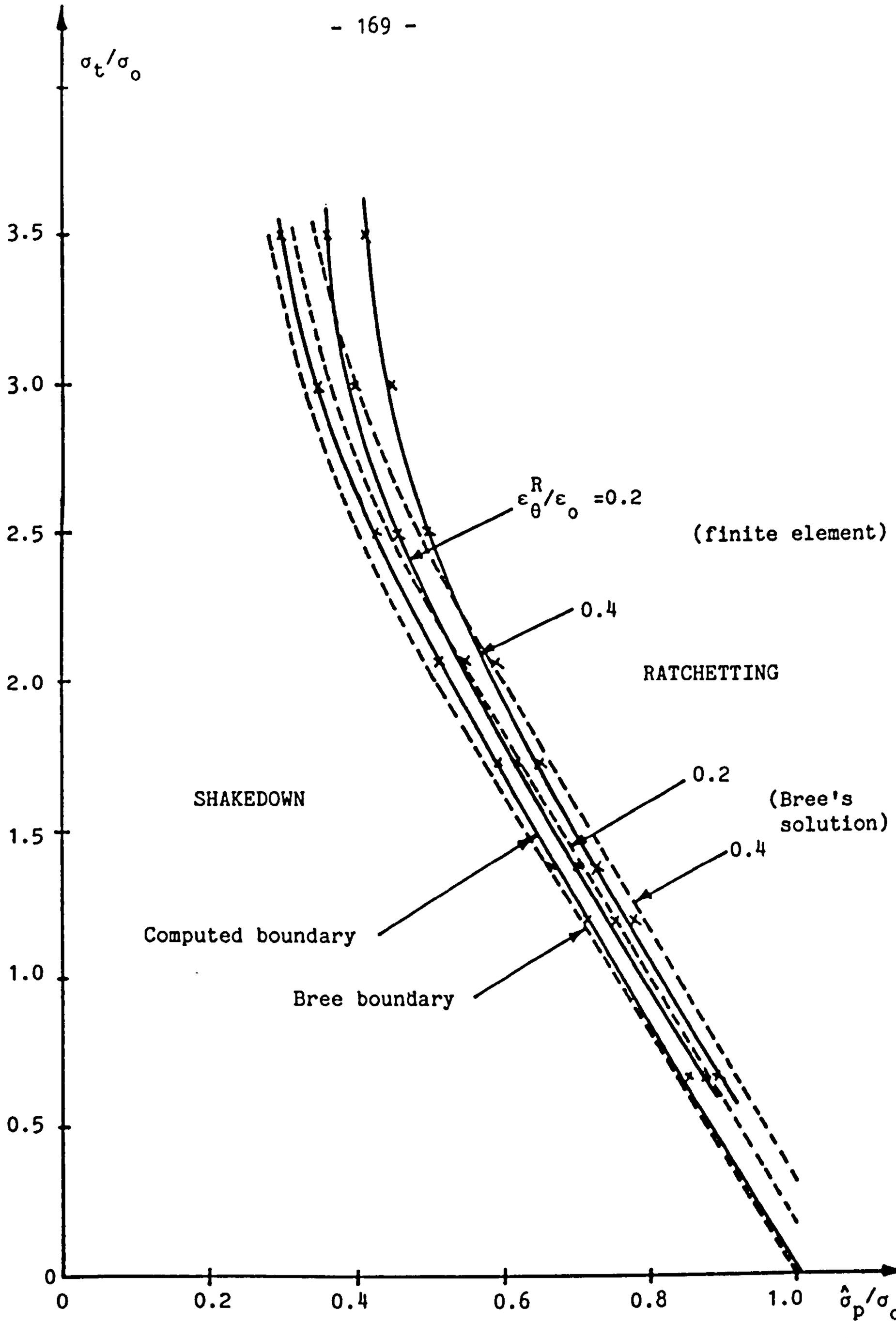

Fig.3.39 Shakedown/ratchetting boundary for a tube with eccentric bore. Correlation with Bree's solution(8).

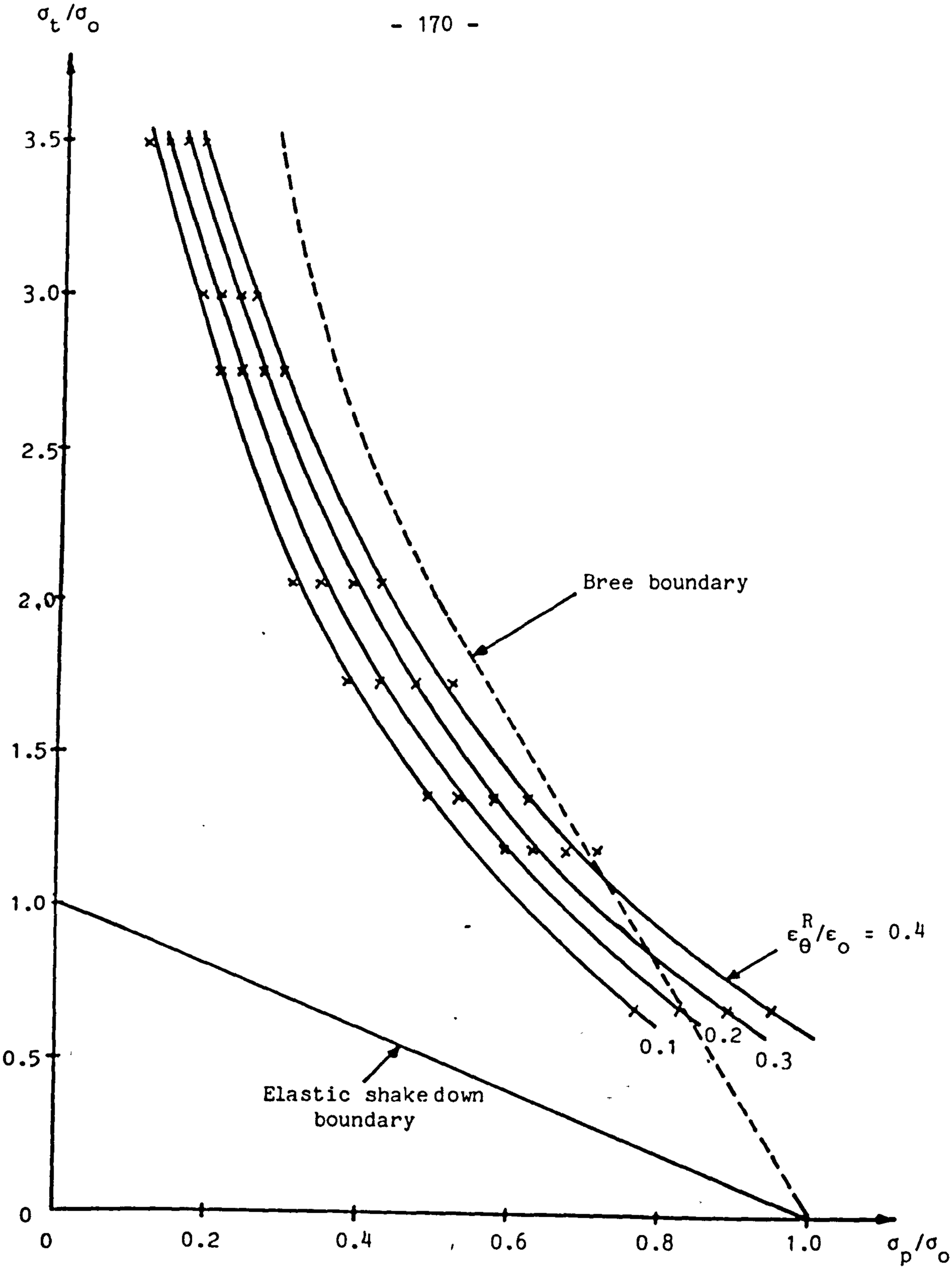

Fig. 3.40 (i) Contours of 1st cycle ratchet hoop strains for a tube with uniform thickness with zero axial stress

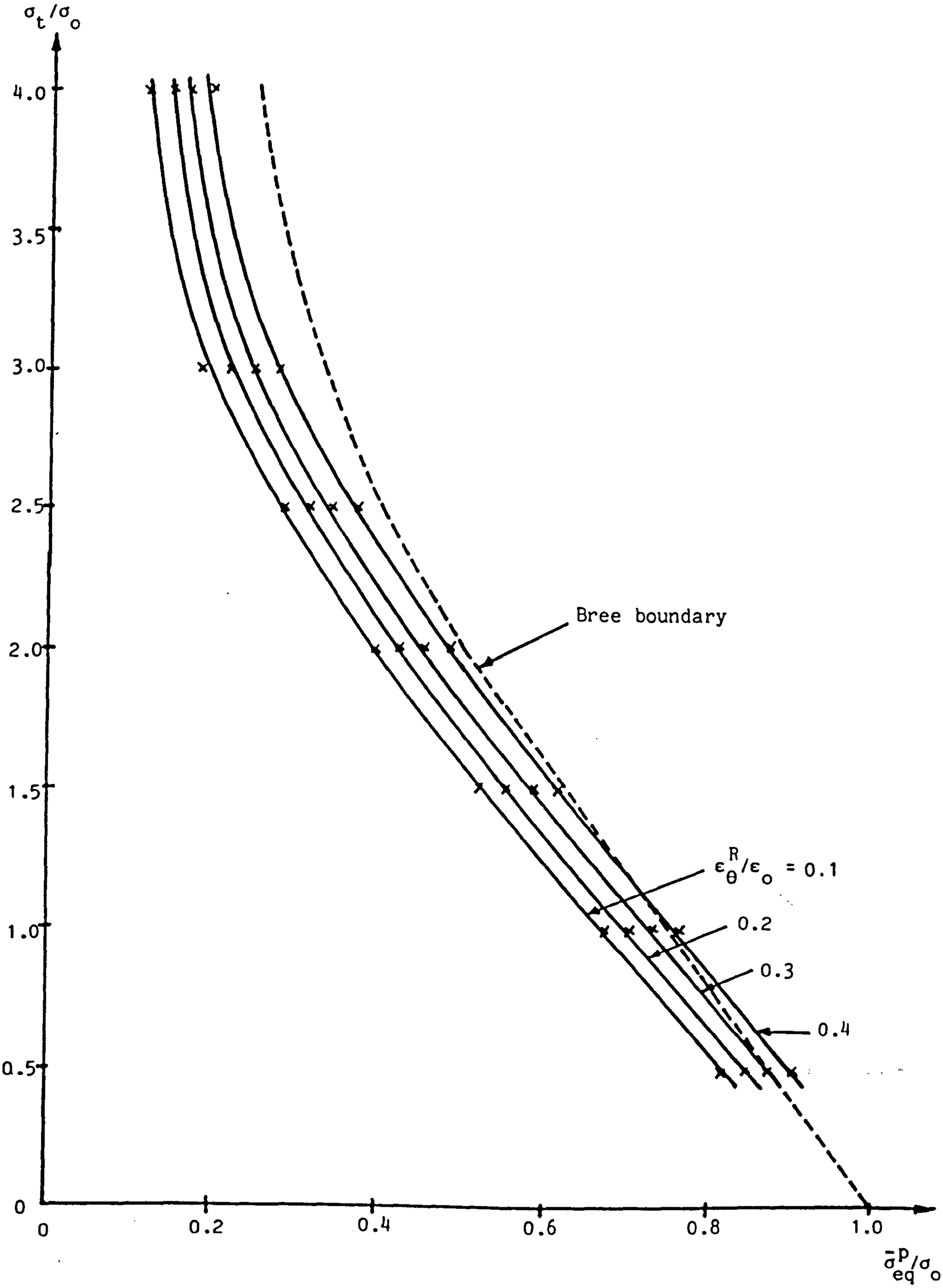

Fig. 3.40(ii) Contours of 1st cycle ratchet hoop strains for pressurised closed ends tube

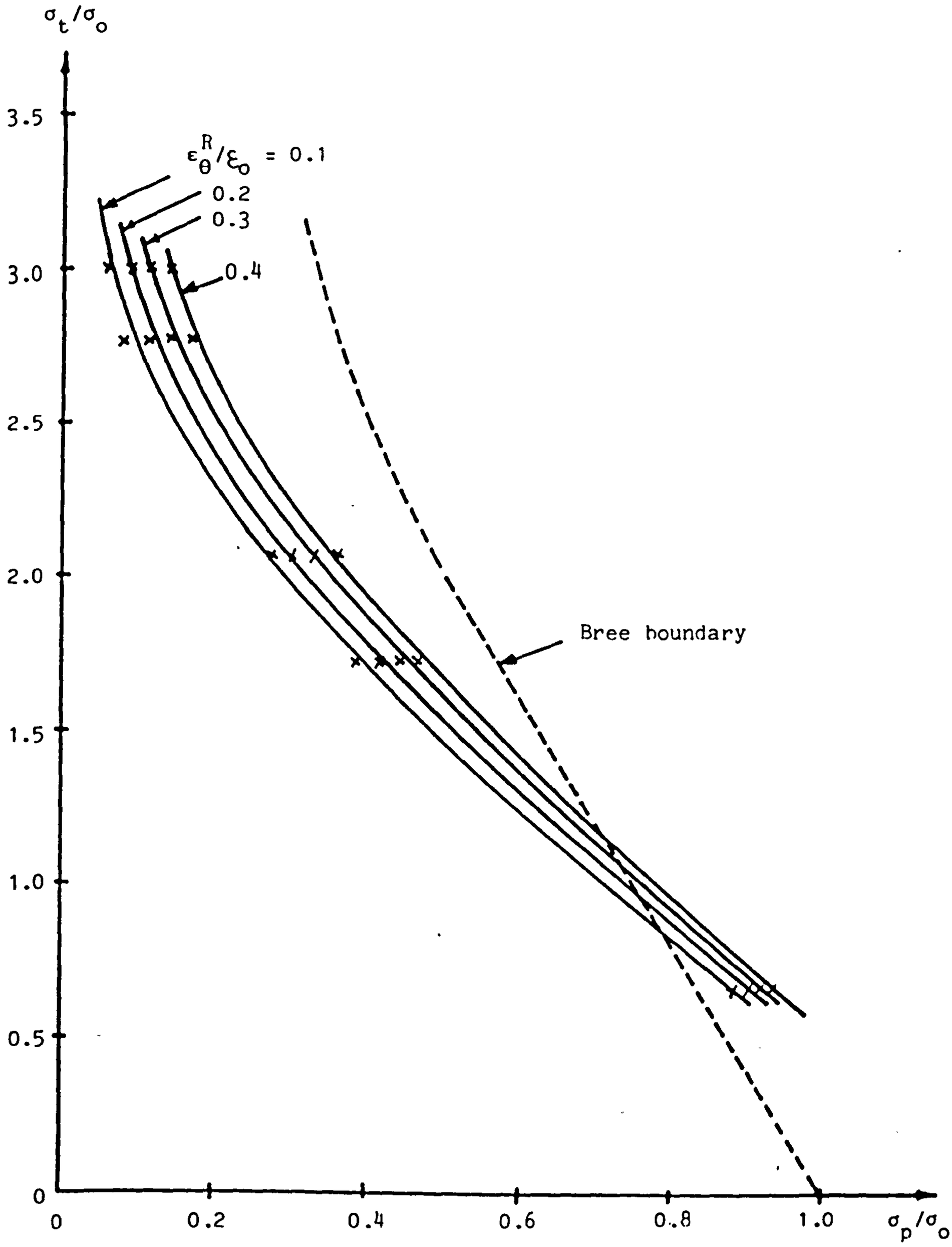

Fig. 3.40(iii) Contours of 1st cycle ratchet hoop strains for a tube with axial restraint

Text cut off in original

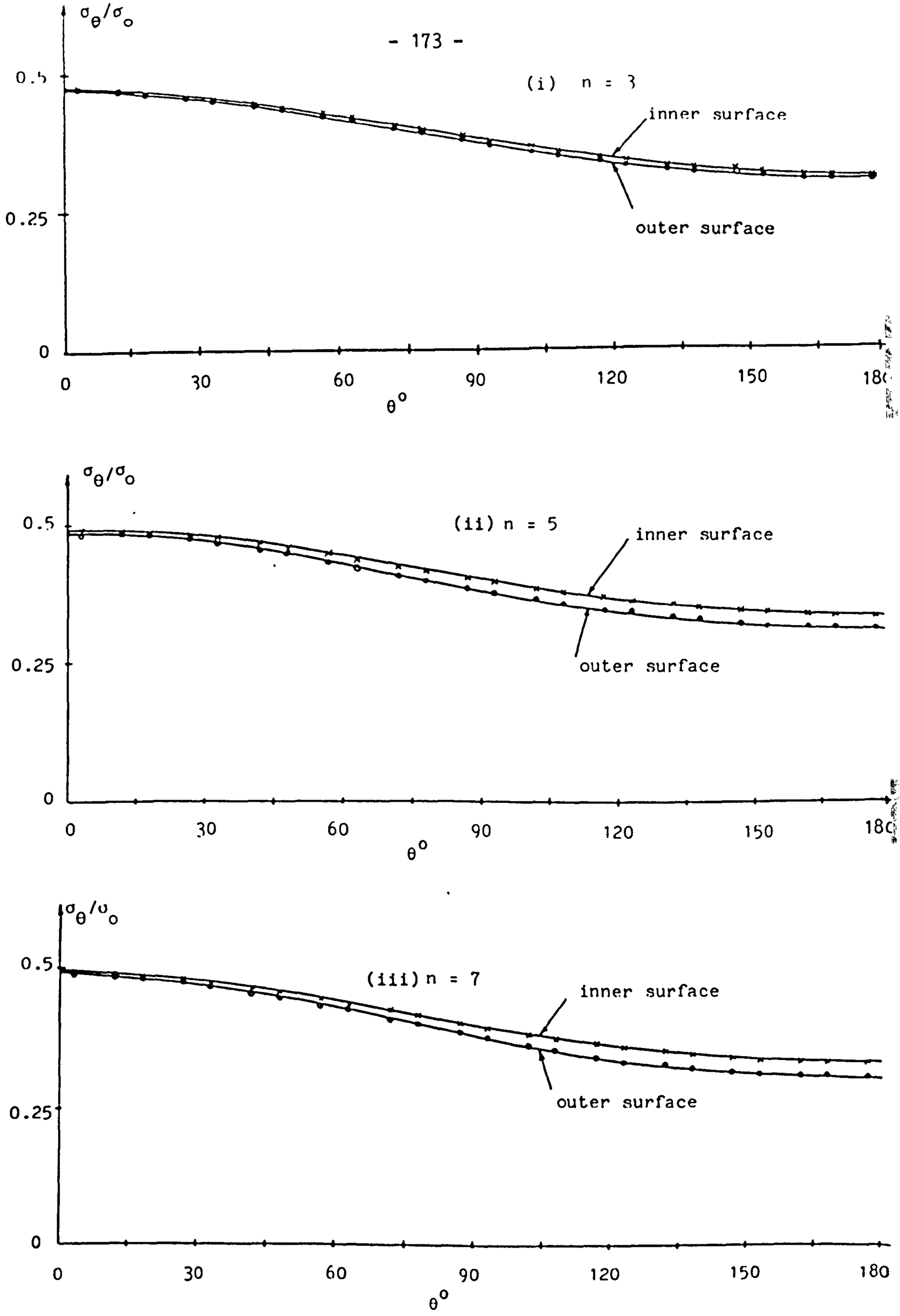

Fig. 3.41 Variation of hoop stress with θ at the complete redistribution state. Tube with an eccentric bore $\sigma_p/\sigma_o = 0.379$, $\sigma_t/\sigma_o = 1.376$

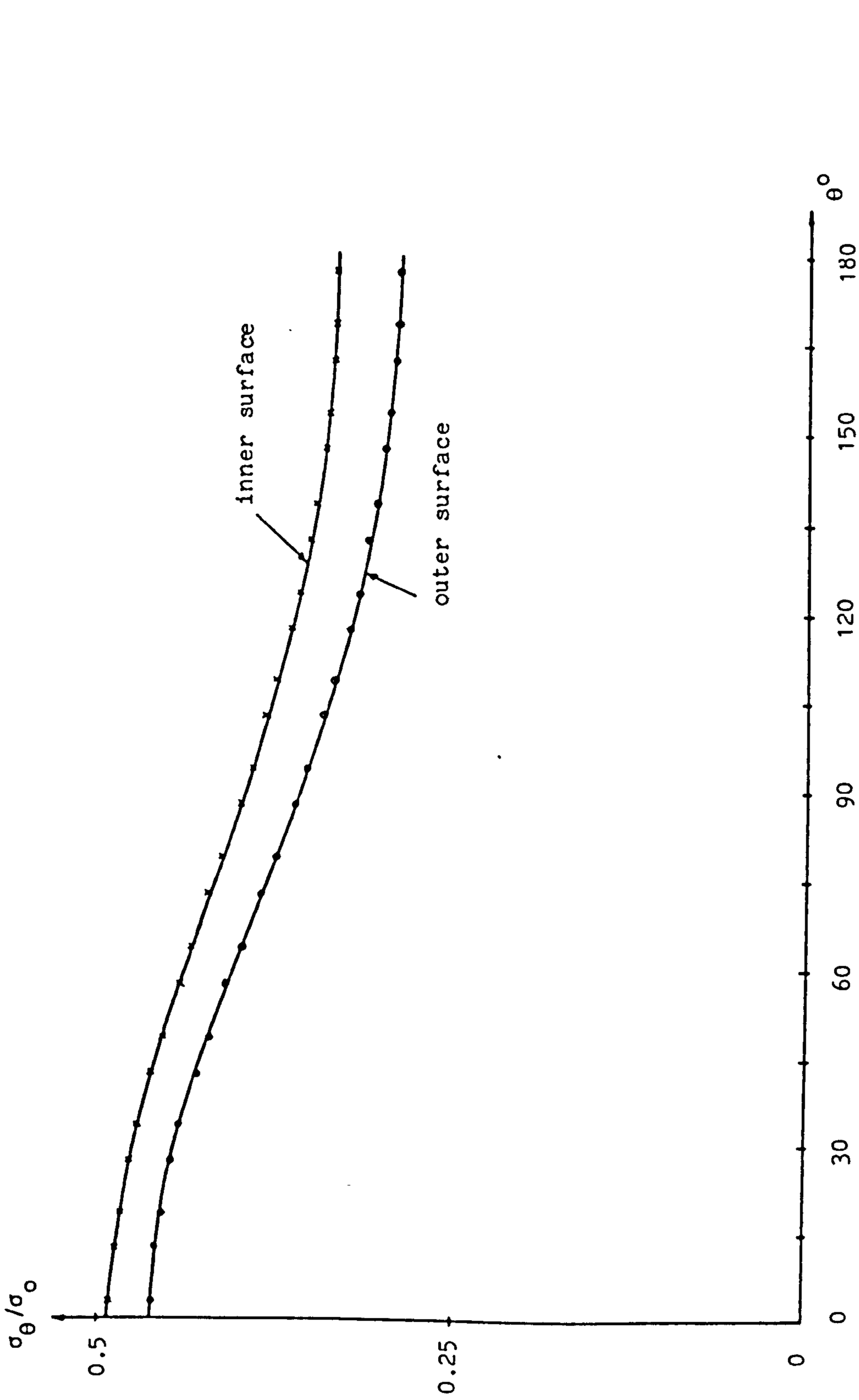

Fig. 3.42 Variation of hoop stress with for a tube with an eccentric bore at $\sigma_p/\sigma_o = 0.379$

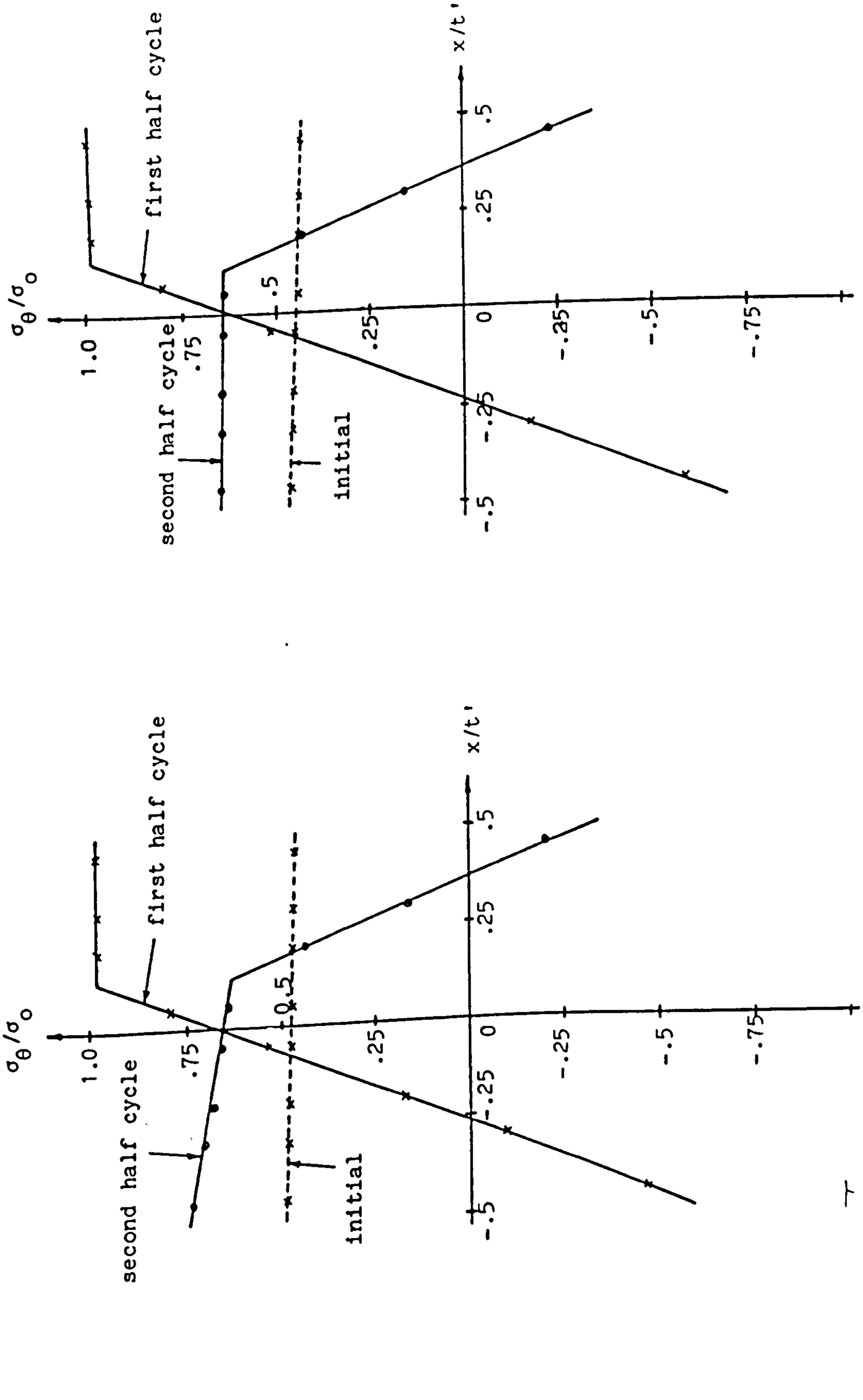

Fig. 3.43 Through thickness distribution of hoop stress at $\theta = 3^o$ and $\theta = 42^o$ for a tube with an eccentric hore $\sigma_p/\sigma_o = 0.379$, $\sigma_t/\sigma_o = 1.376$. No creep case

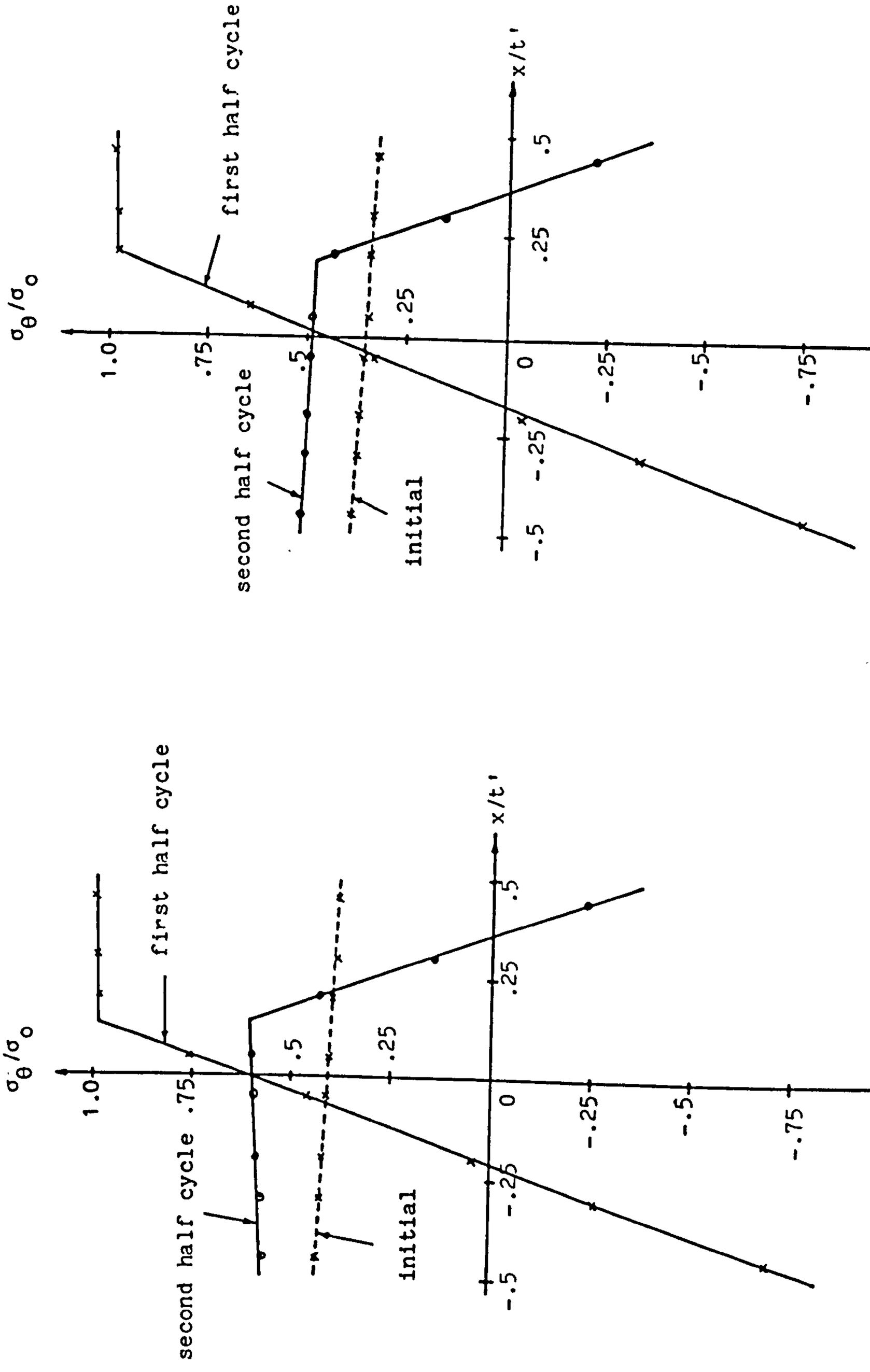

Fig. 3.43 Through thickness distribution of hoop stress at $\theta = 72^o$ and $\theta = 108^o$ for a tube with an eccentric bore $\sigma_p/\sigma_o = 0.379$, $\sigma_t/\sigma_o = 1.376$. No-creep case

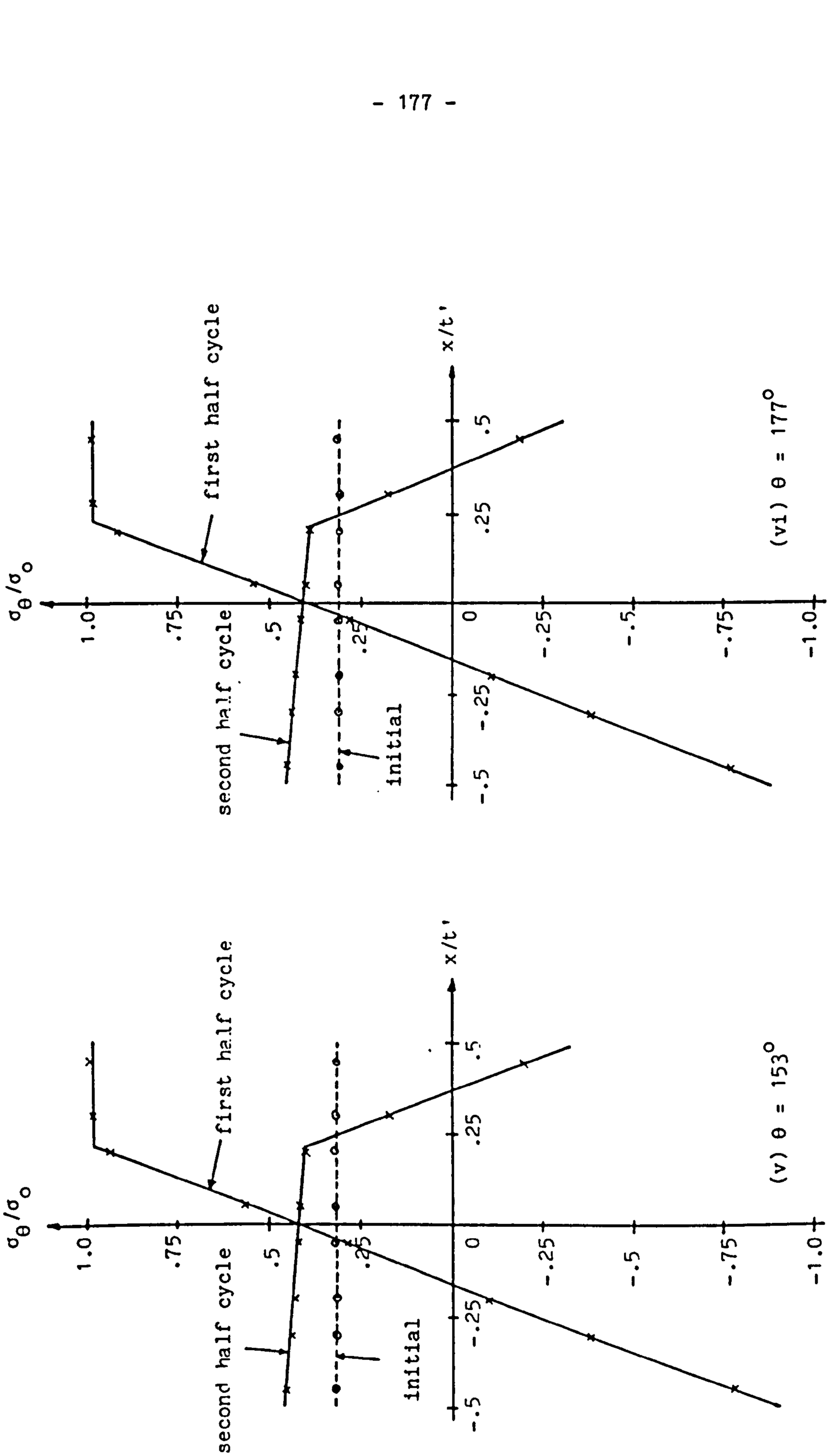

Through thickness distribution of hoop stress at $\theta = 153^o$ and $\theta = 177^o$ for a an eccentric bore $\sigma_p/\sigma_o = 0.379$ $\sigma_t/\sigma_o = 1.376$. No creep case

FIG. 3.43

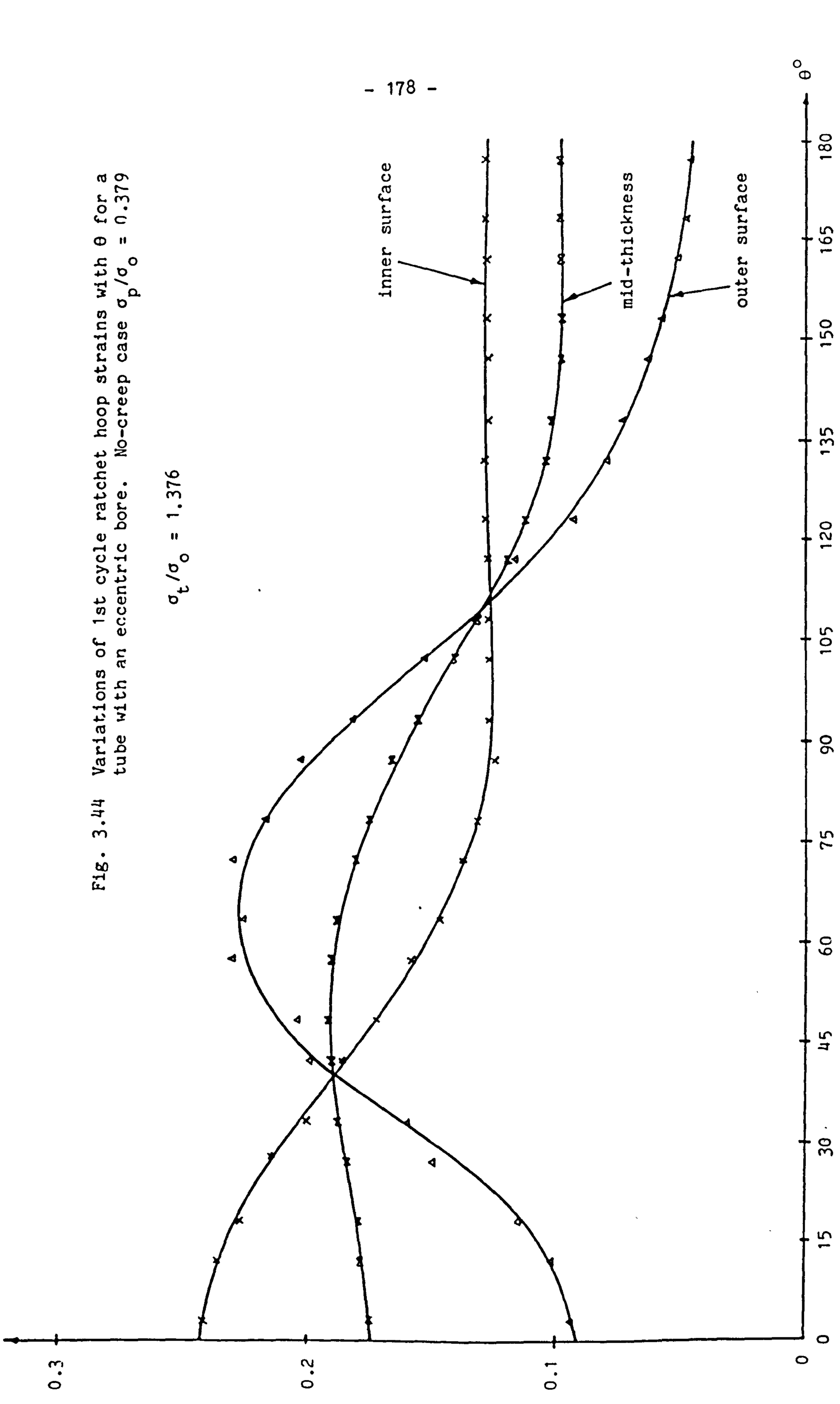

Fig. 3.44 Variations of 1st cycle ratchet hoop strains with θ for a tube with an eccentric bore. No-creep case σ_p/σ_o = 0.379

σ_t/σ_o = 1.376

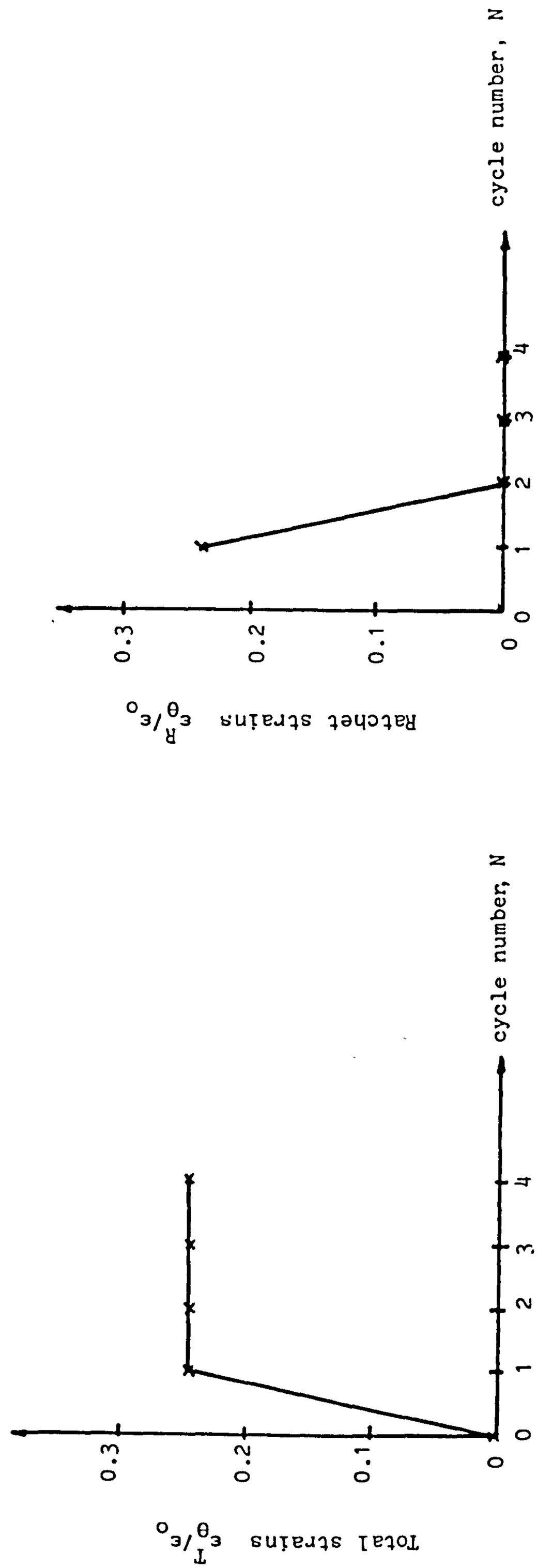

Fig. 3.45 Variation of maximum total and ratchet hoop strains with cycle number for a tube with an eccentric bore under no-creep conditions $\sigma_p/\sigma_o = 0.379$, $\sigma_t/\sigma_o = 1.376$

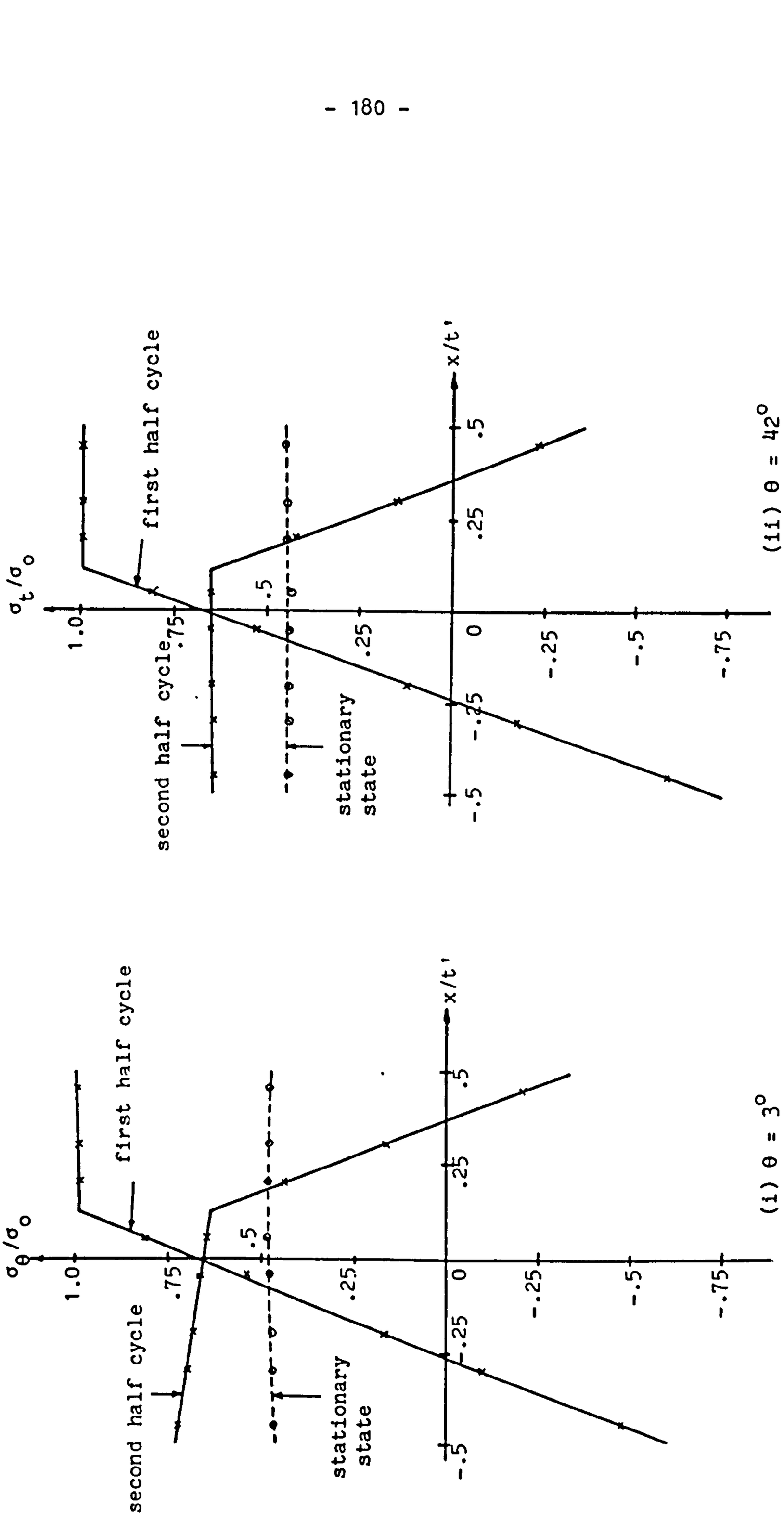

Through thickness distribution of hoop stress for a tube with an eccentric bore
σ_p/σ_o = 0.379, σ_t/σ_o = 1.376. n = 3

Fig. 3.46

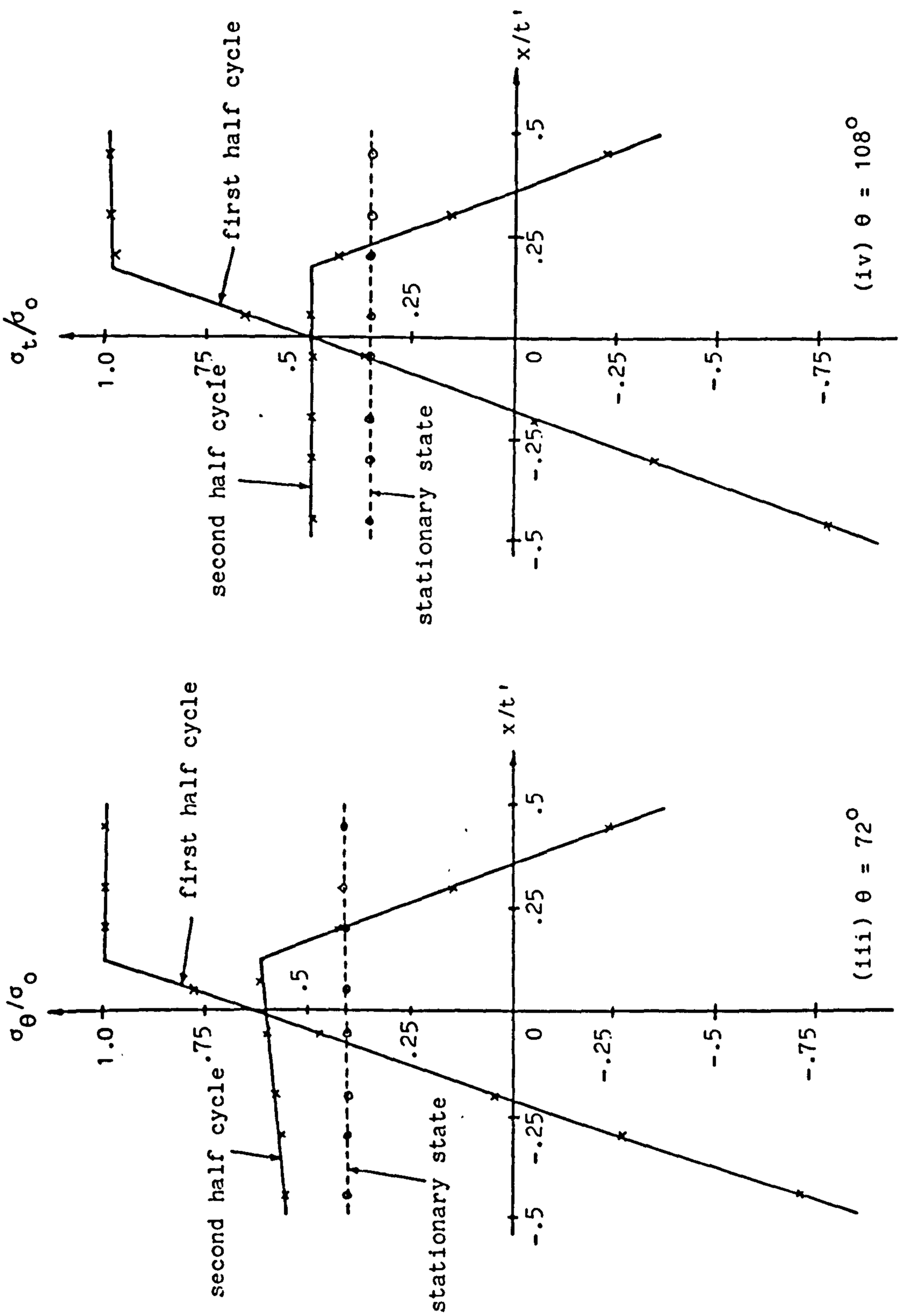

Fig. 3.46 Through thickness distribution of hoop stress for a tube with an eccentric bore
σ_p/σ_o = 0.379, σ_t/σ_o = 1.376 n = 3

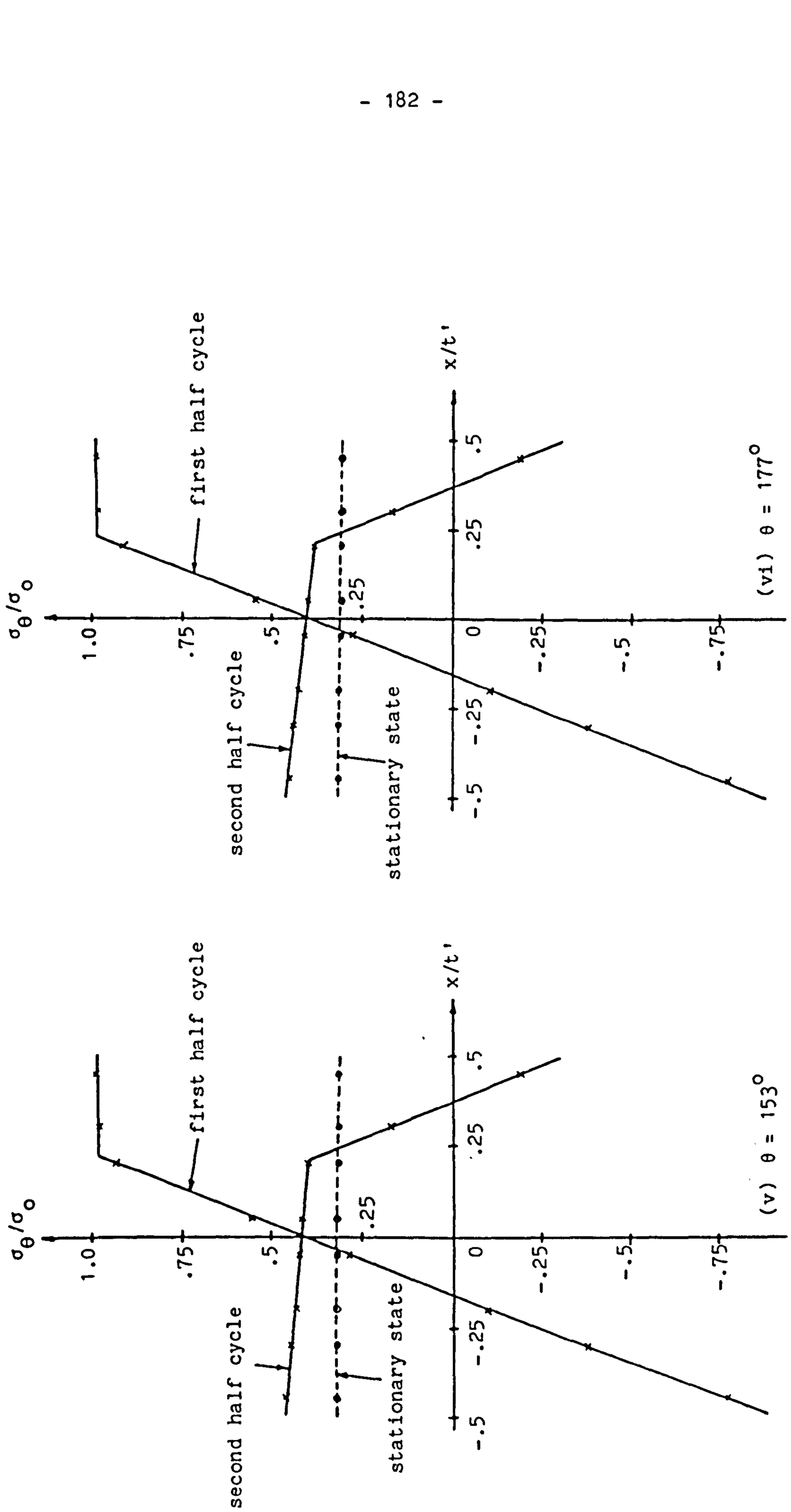

Fig. 3.46 Through thickness distributions of hoop stress for a tube with an eccentric bore. $\sigma_p/\sigma_o = 0.379$, $\sigma_t/\sigma_o = 1.376$. n = 3

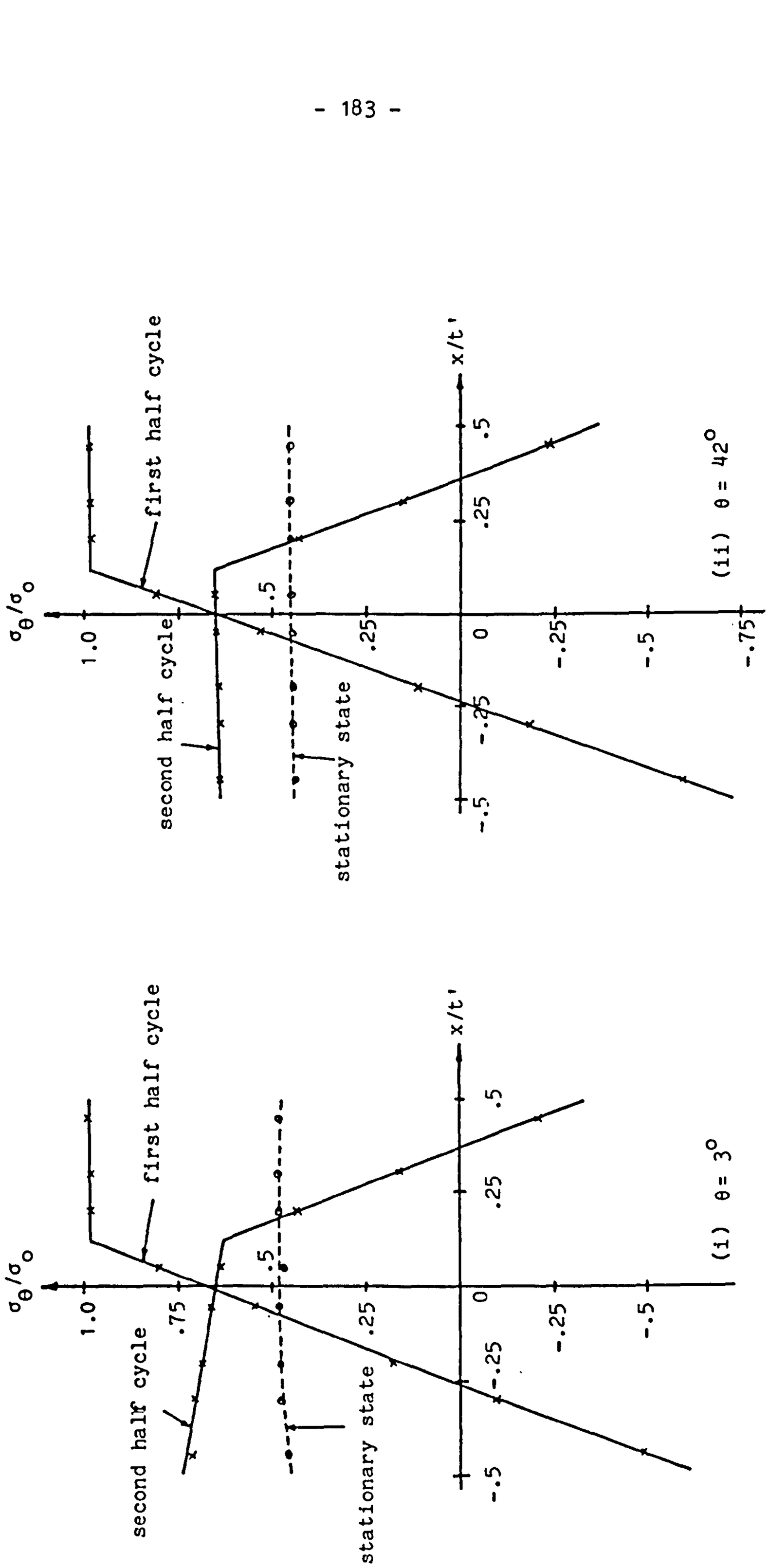

Fig. 3.47 Through thickness distribution of hoop stress for a tube with an eccentric bore $\sigma_p/\sigma_o = 0.379$, $\sigma_t/\sigma_o = 1.376$. n = 5

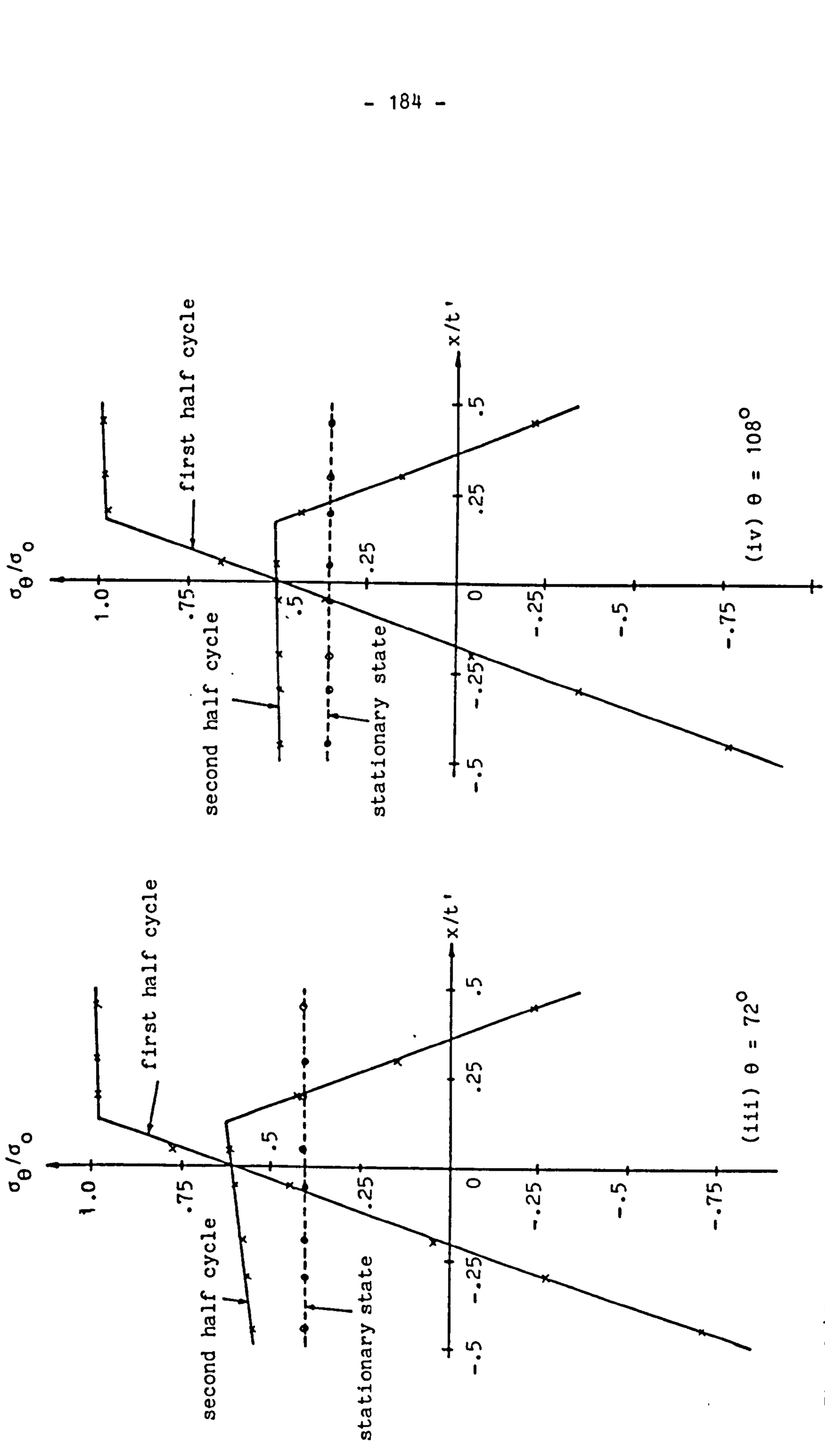

Fig. 3.47 Through thickness distribution of hoop stress for a tube with an eccentric bore
$\sigma_p/\sigma_o = 0.379$, $\sigma_t/\sigma_o = 1.376$. n = 5

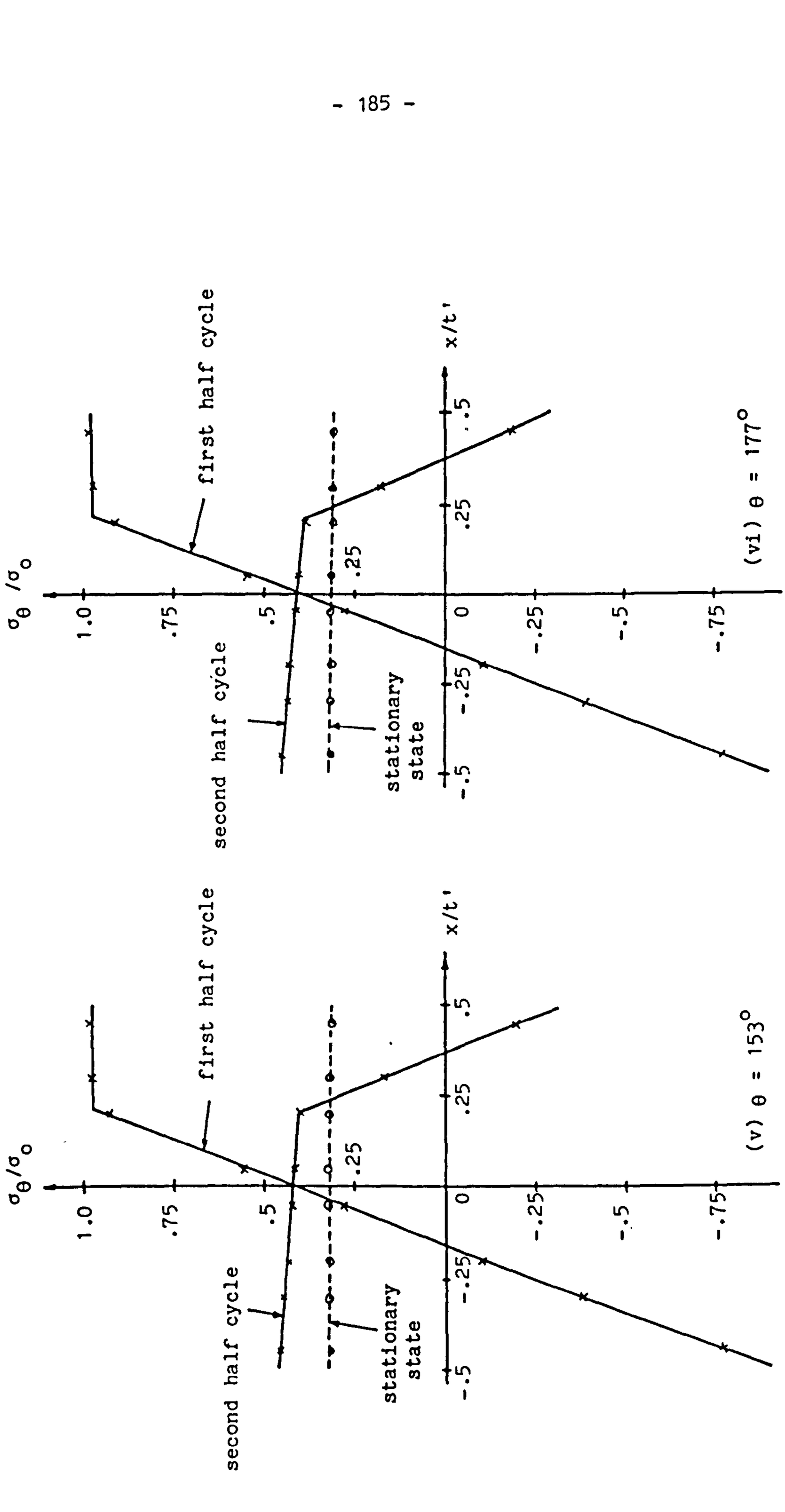

Fig. 3.47 Through thickness distribution of hoop stress for a tube with an eccentric bore $\sigma_p/\sigma_o = 0.379$, $\sigma_t/\sigma_o = 1.376$. n = 5

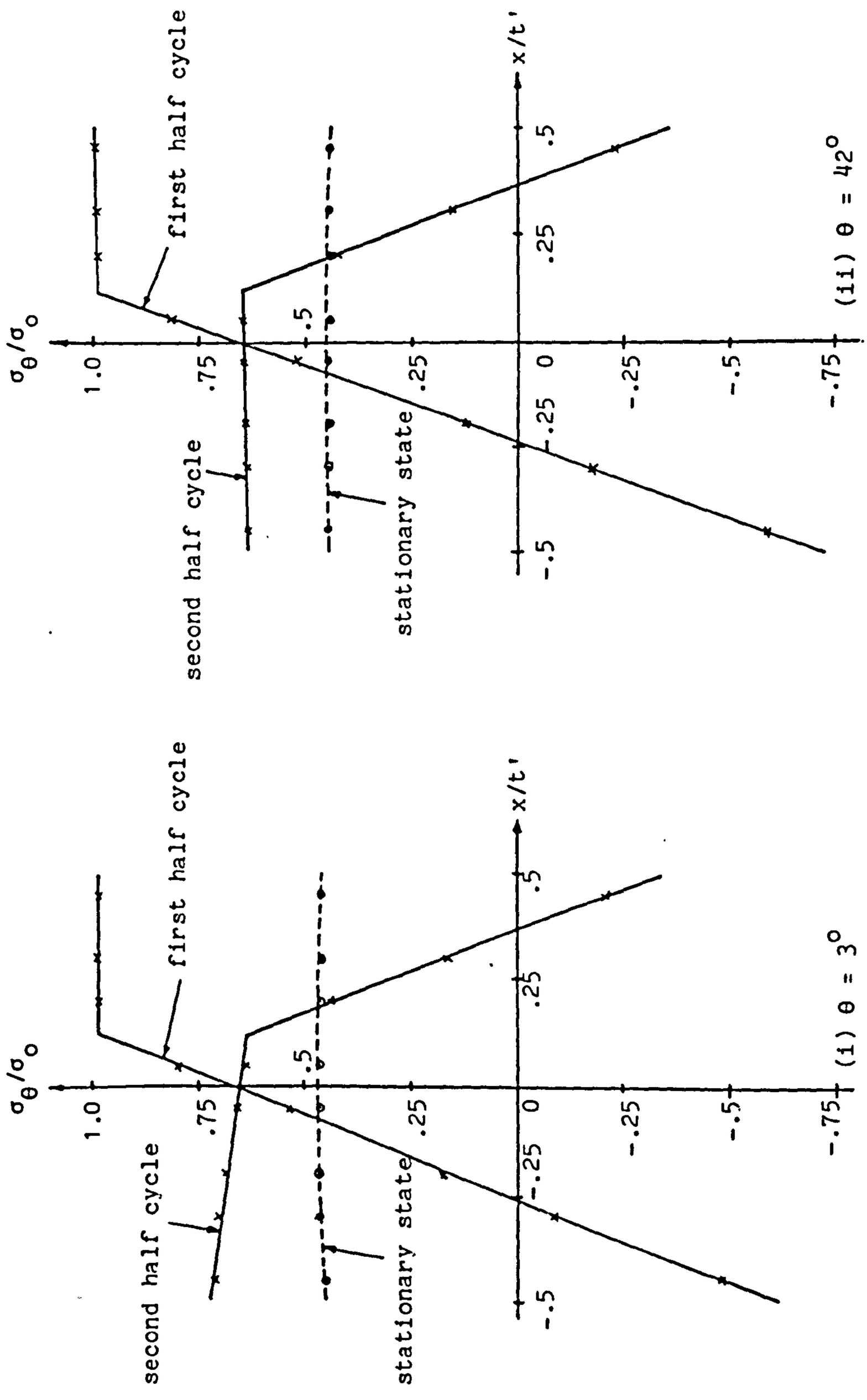

Fig. 3.48 Through thickness distribution of hoop stress for a tube with an eccentric bore
σ_p/σ_o = 0.379, σ_t/σ_o = 1.376. n = 7

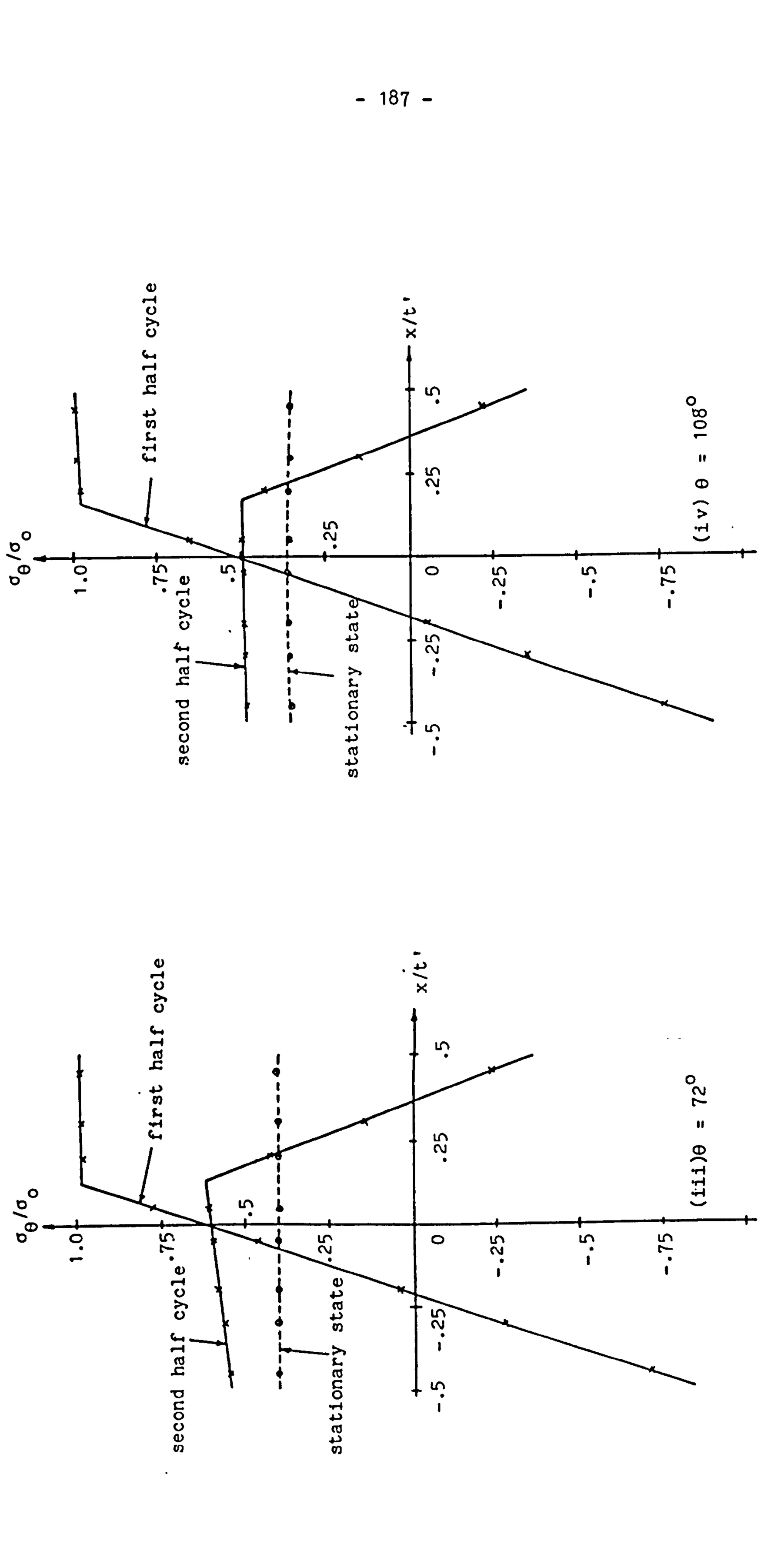

Fig. 3.48 Through thickness distribution of hoop stress for a tube with an eccentric bore σ_p/σ_o = 0.379, σ_t/σ_o = 1.376. n = 7

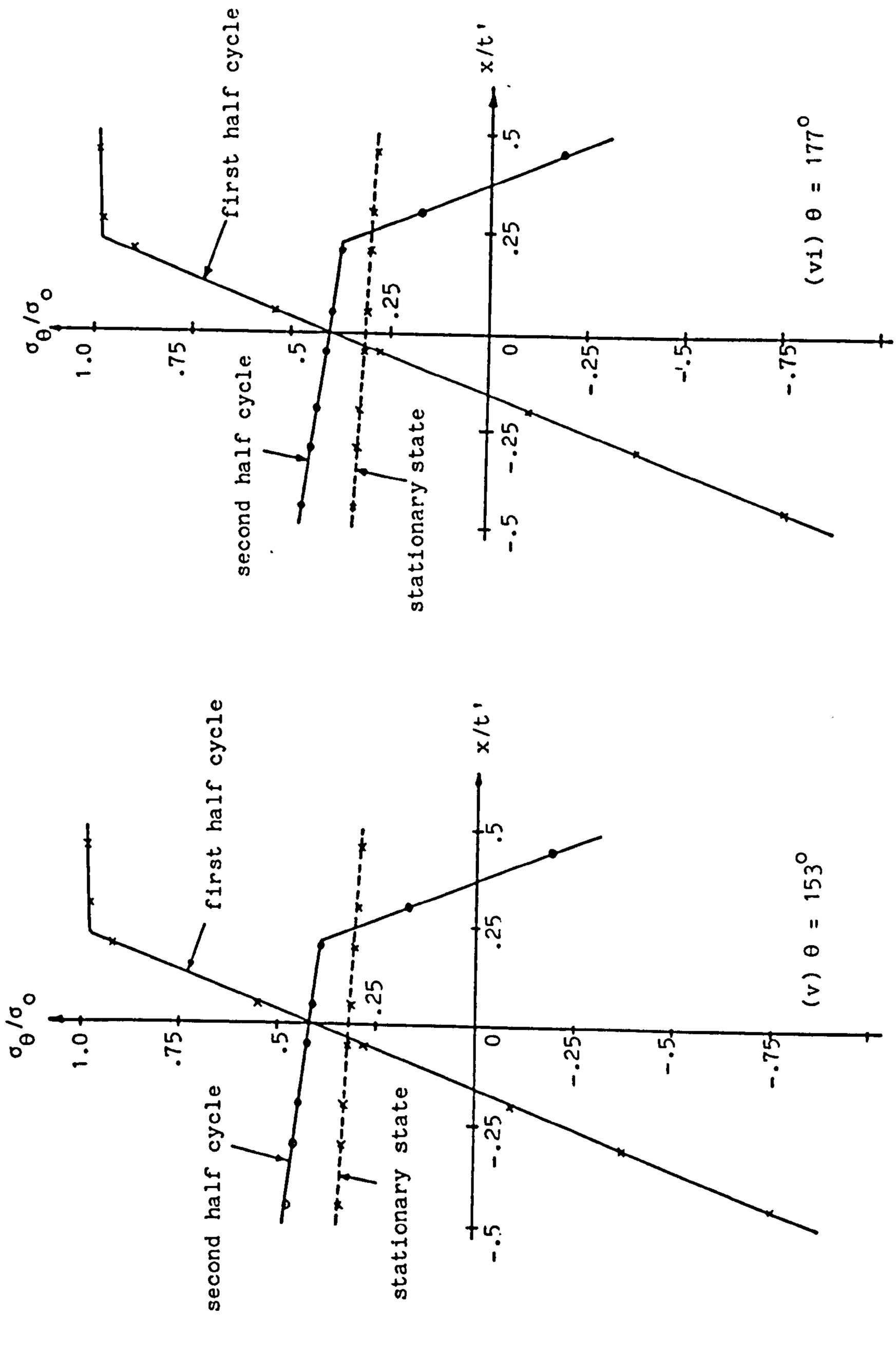

Through thickness distribution of hoop stress for a tube with an eccentric bore
$\sigma_p/\sigma_o = 0.379$, $\sigma_t/\sigma_o = 1.376$. n = 7

FIG. 3.48

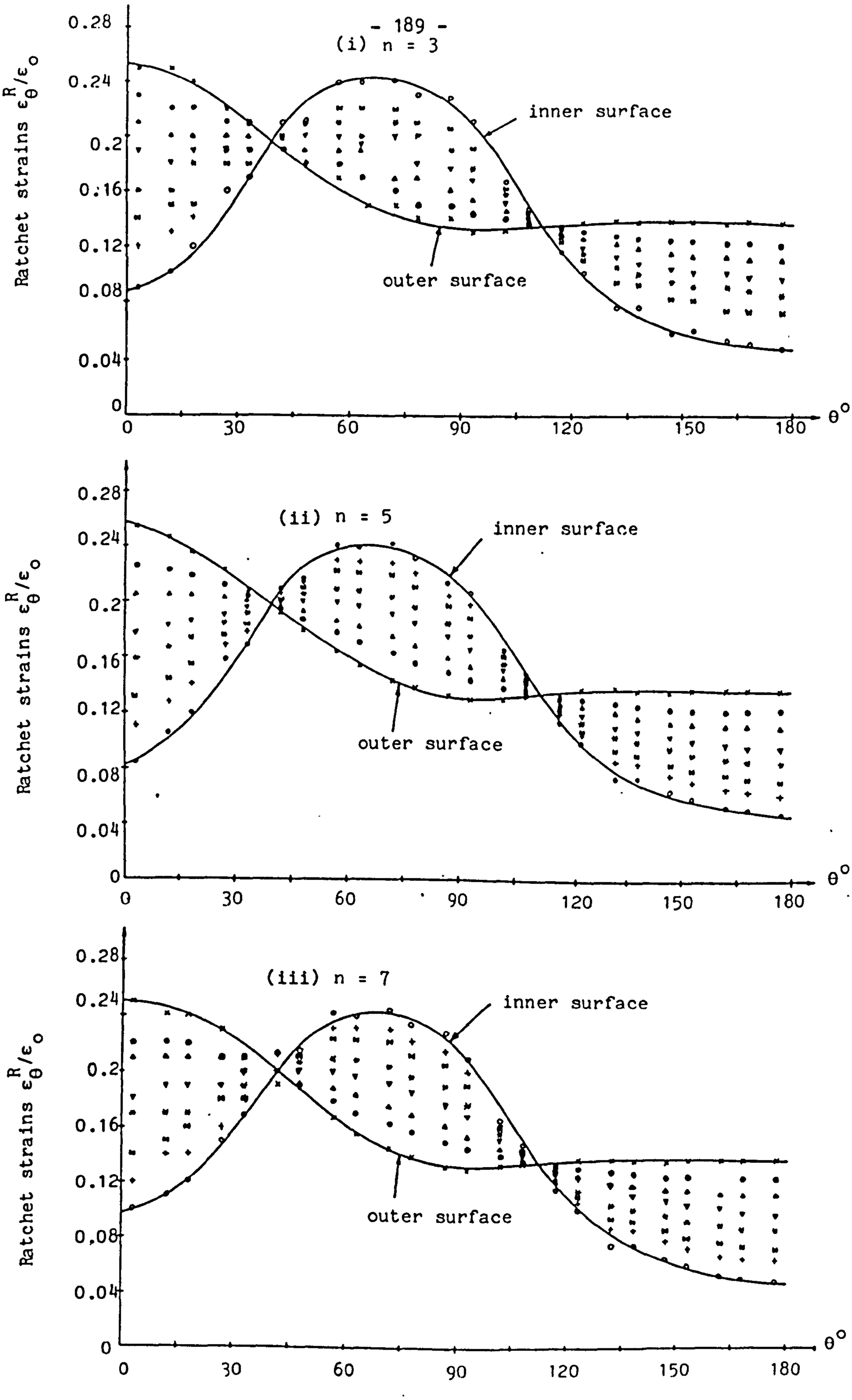

Fig. 3.49 Variation of ratchet hoop strains with θ for n = 3, 5 and 7

CHAPTER 4.

RATCHETTING OF A CIRCULAR PLATE.

4.1 Introduction.

In Chapter 3, the ratchetting behaviour of thin tubes subjected to a steady internal pressure and cyclic through thickness temperature variations was investigated. The analysis included deviations from the classical Bree's analysis (8), which are relevant in practical situations. The deviations caused complications to the stress distributions e.g. the tube with variable thickness had circumferential, as well as radial, stress variations. The mechanisms of ratchetting, however were all found to be similar and could be related to the simple Bree analysis (8). The mechanism of ratchetting in tubes is well understood and a uniaxial simplification can be used to obtain relevant solutions.

Other components, e.g. pressure vessel end closures or plate type structures, do not have the same ratchetting mechanisms as tubes. Also, there are practical situations where this type of structure is used under conditions in which ratchetting could occur, e.g. the above core plate like structures of LMFBR's. Although these structures do not have severe geometrical discontinuities, complicated stress distributions can be created due to self-weight, pressure and non-uniform temperature distributions. The behaviour of plates under some combinations of steady and cyclic, mechanical and thermal loads

is not fully understood, although some work on this type of component has been performed. The behaviour of a simply supported circular plate subjected to steady transverse pressure and cyclic linear radial temperature gradient has been investigated by Goodman and Goodall (18) and Ponter (7). In particular, Ponter (7) suggested that two types of ratchetting mechanisms exist, depending on the magnitudes of the applied mechanical and thermal loads. Hyde (15) and Hardy (16) have investigated the behaviour of a circular plate with a radially movable, direction fixed edge, subjected to combinations of steady membrane stress, transverse pressures and cyclic linear through thickness temperature gradients. With through thickness temperature gradients, the mechanism is different from that produced with radial temperature gradients as investigated by Ponter (7).

In this chapter, the behaviour of a clamped circular plate subjected to a steady transverse pressure and cyclic, linear radial temperature gradient is investigated. The ratchetting mechanism for this component is not the same as the 'Bree mechanism (8)' and therefore the problem cannot be approximated by a simple uniaxial model. The essential features of practical components such as the above core plate like structure of a nuclear reactor and pressure vessel end closures are contained in the present plate component and loading. The effects of complete stress redistribution due to creep are also investigated.

The elastic-perfectly-plastic material properties used in the analyses were based on 316 Stainless Steel properties at 550°C. These properties are given in Table 3.1 and are the same as those used in the tube ratchetting investigation described in Chapter 3. The creep behaviour was modelled by a Norton-Bailey Creep Law (30). Since only the effect of complete stress redistribution on ratchetting behaviour was investigated, the stress indices, n, used in the analyses are the only creep constants of importance, n-values of 3,5 and 7 were used. As in the tube analyses, all material properties were assumed to be temperature independent. Also, the multi-axial plasticity and creep behaviours were related to the uniaxial behaviours using the von-Mises effective stress criterion and the Prandtl-Reuss flow rule.

4.2 Geometry and Loading.

A plate with a radius, R, to thickness, h, ratio of 20 was chosen for the investigation. The finite element mesh, which consists of 40, eight noded, axisymmetric, isoparametric elements is shown in Fig.4.1. The nodes at the edge of the plate were constrained so as not to move radially. Several different methods were used to restrain the edge of the plate, these are described in detail in Appendix II. The most suitable method, for the present purposes was found to be the boundary condition C (Appendix II), in which a uniform shear stress distribution through the thickness was imposed at the outer edge.

The mechanical loading consists of a uniform pressure, P, applied to one surface of the plate; for the purpose of simplifying the subsequent description of the results, this surface is called the top surface. With the plate starting off at a uniform temperature, T, thermal loading consisted of incrementally increasing the temperature of the centre by ΔT whilst maintaining the edge at temperature T, with linear variation of temperature with radius being maintained throughout, i.e. at the end of the thermal loading, the temperature, T(r), at any radius, r, is given by

$$T(r) = T + \Delta T(1-r/R) \qquad 4.1$$

Thermal unloading consisted of incrementally reducing the temperature at the centre of the plate from $T+\Delta T$ back to T, whilst continuing to hold the edge at a constant temperature T. Again, a linear variation of temperature with radius was maintained throughout.

Dwell periods, during which creep occurred, were only allowed during isothermal conditions, i.e. between complete thermal cycles. No creep was allowed to occur during each of the thermal loading cycles. Since complete stress redistribution was allowed between each thermal shock, in the calculation with dwell periods, the stress distributions before each thermal shock were identical. Hence the predicted ratchet strains and deflections were identical for the second and all subsequent thermal cycles.

4.3 Preliminary Analysis.

Details of the elastic and elastic-plastic analytical and approximate solutions for the mechanical and thermal loading of the plate are given in Appendix I.

The finite element and analytical predictions for the variations of surface hoop and radial stresses, and shear stress at the plate centre plane, in the elastic range are shown in Figs.4.2(i) and (ii) respectively. It can be seen that there is good agreement between the finite element and theoretical results. The variation of the transverse deflection is shown in Fig.4.3. A maximum value is obtained at the plate centre. The variation of the deflection at the centre with $PR^2/\sigma_o h^2$ is shown in Fig.4.4. At low pressure, i.e. when no yielding occurs, the variation of the central deflection follows closely the expected elastic variation. When the pressure is increased further, yielding occurs and the deflection increases sharply with $PR^2/\sigma_o h^2$. Close to collapse, convergence problems occur with the elastic-plastic finite element calculations. The maximum value of the pressure achievable by using the finite element method, therefore, depends on the magnitude of the load increments. With very small load increments used for the plate calculations ($1.25 \times 10^{-5} PR^2/\sigma_o h^2$) a maximum $PR^2/\sigma_o h^2$ of 3.25 was achieved. This value which will be very close to the collapse value, corresponds closely to the theoretical value of

3.125 (see Appendix I). The difference is most likely to be due to the neglect of the shear and pressure stresses in the theoretical analysis. The growth of the plastic zones with increasing pressure are shown in Fig.4.5. Yielding starts to occur at a pressure of $PR^2/\sigma_o h^2$ =2.0. Yielding first occurs at C and D at the plate edge and then at points A and B at the plate centre (see Fig.4.5 for the position of A,B,C and D). From these positions, the plastic zones expand through the plate thickness and along the surface. The extent of the plastic zone is symmetric about the centre-plane of the plate with compressive yielding occurring in the plate region around B and D and tensile yielding around A and C. At a pressure of $PR^2/\sigma_o h^2$ = 3.125, which is the theoretical collapse pressure based on von-Mises yield criterion (see Appendix I), the plastic zone is shown in Fig.4.5. The centre plane of the plate remains elastic. The plastic zone at $PR^2/\sigma_o h^2$ = 3.25 are also shown in Fig.4.5.

In the subsequent descriptions of the behaviour of the plate, the pressure loading is normalized with respect to the analytically determined collapse pressure i.e. $P_L = 3.125\sigma_o h^2/R^2$.

The thermo-elastic hoop stress, σ_θ^T, and radial stress, σ_r^T, for a clamped circular plate subjected to a radial temperature distribution (equation 4.1) are given by:-

$$\sigma_\theta^T = -\sigma_t\left(1-\frac{2(1-\nu)r}{(2-\nu)R}\right) \qquad 4.2$$

$$\sigma_r^T = -\sigma_t\left(1 - \frac{(1-\nu)r}{(2-\nu)R}\right) \qquad 4.3$$

where $\sigma_t = \frac{(2-\nu)E\alpha\Delta T}{3(1-\nu)}$ 4.4

σ_t represents the maximum elastic thermal stress in the plate which occurs at the plate centre; it is not dependent upon plate thickness. σ_t has been used as the loading parameter for the thermal load.

For the present plate geometry and loading, failure due to thermal buckling is possible. From reference 82, for a circular plate subjected to an in-plane load per unit length acting on the circumference, F, the plate buckles when

$$F = \frac{14.68D}{R^2} \qquad 4.5$$

where D is the plate stiffness = $\frac{Eh^3}{12(1-\nu^2)}$ 4.6

Due to the load F, the plate is subjected to an equibiaxial compressive stress. For the clamped circular plate subjected to a temperature distribution given by Equation 4.1, a biaxial compressive state of stress occurs. Although equation 4.5 cannot be applied directly to the present problem, it can

be used to give some measure of the value of σ_t/σ_o which is likely to cause buckling. This is carried out as follows. Due to the load F, the radial and hoop stresses σ_r^F and σ_θ^F repectively, are given by:-

$$\left|\sigma_r^F\right| = \left|\sigma_\theta^F\right| = F/h$$

$$= \frac{14.68D}{hR^2} \qquad 4.7$$

or

$$\frac{\sigma_r^F}{\sigma_o} = \left(\frac{E}{\sigma_o}\right)\left(\frac{h}{R}\right)^2 \frac{14.68}{12(1-\nu^2)} \qquad 4.8$$

The lower values of σ_t/σ_o to cause buckling can be obtained by equating Equations 4.2 at r/R=0 and Equation 4.8. This gives

$$\sigma_t/\sigma_o = 3.36 \qquad 4.9$$

for the present plate geometry and material data. The thermal loads σ_t/σ_o for which the finite element results obtained were well below the value given by Equation 4.9 . Table 4.1 gives the load combinations for which the finite element results were obtained.

4.4 Results.

4.4.1 Ratchetting Mechanisms.

The results of the finite element analyses of the plates when subjected to steady transverse pressure loading and cyclic thermal loading indicated that two types of ratchetting mechanisms exist. Results for one load combination within each of these two ratchetting regimes will be presented in detail to describe the mechanisms. The load combinations chosen are:-

(i) P/P_L = 0.832 and σ_t/σ_o=1.5, i.e. a high mechanical load and a low thermal load; and

(ii) P/P_L= 0.104 and σ_t/σ_o=2.3, i.e. a low mechanical load and a high thermal load.

(a) Mechanism of Ratchetting for P/P_L=0.832 and $\frac{\sigma}{\sigma_o}t$ =1.5.

The radial distribution of hoop stress (σ_θ) and radial stress (σ_r) at the plate surfaces and the shear stress (τ_{rz}) at the plate centre-plane when a pressure of P/P_L= 0.832, is applied are shown in Fig.4.6. Some material in the plate has become plastic at this pressure. The plastic zones for P/P_L = 0.832 are shown in Fig.4.7. Also the distributions of the hoop and radial stresses at the top surface are practically equal but opposite in sign to the distributions at the bottom surface. The radial distribution of hoop and radial stresses at the top and bottom surfaces at the end of the first and second half

cycles are shown in Figs.4.8(i) and 4.8(ii) respectively. At the end of the first cycle, yield occurs in the plate. The growth of plastic zone in the plate for the first two cycles is shown in Fig.4.9(i). A small increase in plastic zone occurs at the end of each half cycle until a steady cyclic state is obtained; this was reached after 10 cycles of thermal loading. At the steady cyclic state, the growth of the plastic zones, which are created during each cycle, are shown in Figs.4.9(ii) and (iii). Fig.4.9(ii) shows the growth during the first half of each thermal load cycle. Plastic straining starts to occur at r/R = 0.62 (at the top surface), 0.78 (at the bottom surface) and 0.98 (at the botom surface). From these positions, the plastic zones grow and at the end of each of the first half cycles, the zones are as shown in Fig.4.9(ii). During the second half of each cycle, the growth is shown in Fig.4.9(iii). Yielding starts at the same radial position as that of the first half of each cycle except that the position across the thickness is reversed. The overall plastic zone created during a complete thermal cycle, at the steady cyclic state, is shown in Fig.4.9(iv). The behaviour is symmetrical about the plate centre-plane.

During a complete cycle, it can be seen that, at every radial position, tensile (or compressive) yielding occurs through half of the plate thickness (during each of the first half cycles) and compressive (or tensile) yielding occurs through the other half of the plate thickness (during each of the second half cycles). This type of behaviour is analogous to the plastic hinge which can be created when a mechanical bending load is

applied to a beam, i.e. tensile yielding occurs over half the depth of the beam while compressive yielding occurs over the other half. When a plastic hinge of this type is created due to mechanical loading, unrestrained deformation occurs. However, in the present plate analysis, the yielding occurs over the top and bottom halves of the plate thickness at different times during the cycle. Hence the amount of deformation which can occur is limited by the elastic and thermal deformations which occur in the unyielded half of the plate thickness. Under these conditions, incremental deformation, as opposed to unrestrained deformation in a mechanical loading situation, occurs and there can be said to be an 'incremental plastic hinge' present. When a plastic hinge is created, there is a discontinuity in the stresses at the interface between the tensile and compressive yielding zones. Similarly, with an 'incremental plastic hinge' there are discontinuties in the stresses at the interface between the tensile and compressive yielding zones. This can be clearly seen from the through-thickness variation of the radial and hoop stresses at various radial positions as shown in Fig.4.10(i) to (vi) for each of the first half cycles (during heating) and each of the second half cycles (cooling). It can be seen that a discontinuity in the stress occurs at the plate centre plane (z/h=0) which indicates that an incremental plastic hinge is developed at all radii. Heating and cooling of the plate induces compression and tensile loadings, respectively, which occurs both in the radial and hoop directions. The superposition of the compressive and tensile thermal loads on the mechanical bending of the plate due to the

pressure gives rise to the increments of bending strains in the plate. The through-thickness ratchet hoop and radial strains distribution at various radial positions are shown in Figs.4.11(i) to (vi). In all cases, the ratchet strains vary linearly through the thickness. The magnitudes, however, are different for different radial positions. From these results it can be concluded that a bending type of mechanism exists.

The deflections of the plate at the 10th cycle are shown in Fig.4.12; the maximum deflection is at the centre of the plate (i.e. r/R = 0). The variation of the total accumulated ratchet deflection at plate centre and the corresponding ratchet deflection with cycle number are shown in Figs.4.13(i) and (ii) respectively. A steady ratchet state occurs after 10 cycles of thermal loading were applied. At the steady ratchet state, the variation of ratchet deflection with radius is shown in Fig.4.14. It can be seen that ratchetting occurs throughout the structure with the maximum ratchet deflection occurring at the plate centre. The variation of the steady state hoop and radial ratchet strains with radius, at z/h=-0.4472 (near the top surface) and at z/h=.4472 (near the bottom surface) are shown in Fig.4.15(i) and (ii).The ratchet hoop strain and ratchet radial strain are equal at the plate centre because at this position, an equibiaxial bending occurs. The hoop ratchet strain, at the top surface, reduces from a maximum negative value at the plate centre to zero at the plate edge. However, the radial ratchet strain increases in magnitude rapidly near the plate edge. This indicates that a plastic hinge occurs at the edge of the plate; no matter how fine a mesh was used at

the edge, it would not adequately model a hinge because it is confined to such a small radial width of the plate. However, its effect on the overall behaviour is insignificant. The variation of the steady state ratchet hoop and radial strain with radius at the top surface is equal in magnitude but opposite in sign to that at the bottom surface. The radial variation of the shear ratchet strain is shown in Fig.4.15(iii). The magnitude is considerably less than the magnitude of the hoop and radial ratchet strain. The effect of shear on the overall deformation and hence on the ratchetting mechanism is negligible.

(b) Mechanism of Ratchetting for P/P_L = 0.104 and σ_t/σ_o=2.3.

The load combination represents a low mechanical load and high thermal load which is characteristic of the loading conditions applicable to LMFBR power plant components. Due to the pressure loading of P/P_L = 0.104, an initially elastic behaviour is obtained. The variation of the hoop and radial stresses at the bottom and top surfaces with radius are shown in Fig.4.16. Also, the distribution of the hoop and radial stresses at the top surface are practically equal in magnitude but opposite in sign to the distribution of the stresses at the bottom surface. The radial distribution of the hoop and radial stresses at the top and bottom surfaces at the end of the first and second half cycles are shown in Fig.4.17. In this case, the stresses at the top surface and the stresses at the bottom surface are not symmetrical about the plate centre plane. This is because, the thermal stresses, which are uniform through the

thickness are the dominant stresses compared to the stresses due to pressure. Hence, the combined thermal and pressure stresses will tend to be uniform through the thickness. During thermal loading, a significant amount of material in the plate become plastic. The growth of plastic zone in the plate during the first half cycle of the thermal load is shown in Fig.4.18(i). At the end of the first half cycle, the extent of plastic zone is also shown in Fig.4.18(i) where a large amount of material has become plastic. During the second half cycle, the growth of plastic zone is shown in Fig.4.18(ii) and at the end of the second half cycle, the plastic zone is confined to a smaller volume of the plate. After this, the increment of the plastic zone during each cycle is insignificant. At the steady ratchet state, which is achieved after the third cycle of loading, the extent of plastic zone at the end of each half cycle is similar to that shown in Fig.4.18(ii). Also, at the steady ratchet state, yielding starts at $r/R = 0$ (through the entire plate thickness) and spreads radially to $r/R = 0.2$ for the present thermal load. For higher thermal loads, the plastic zone would extend to larger radii. It is also noted that the plastic zone is confined to a small volume of material which is highly thermally stressed, in this case near the plate centre.

The through thickness distributions of the hoop and radial stresses at various radial positions, at the end of each half cycle, in the steady ratchet state, are shown in Figs.4.19(i) to (vi). The radial and hoop stresses are practically uniform through the thickness. However, for $r/R<0.2$, the radial and

hoop stresses are practically equal in magnitude at the end of each half cycle but for r/R>0.2, the magnitude of the radial and hoop stresses, at the end of the second half cycle, are not equal. It can be seen that in the region r/R<0.2, the material is in plastic compression during each half cycle and in plastic tension during the other half cycle. The stress strain behaviour at r/R = 0.0211 and z/h = -0.447, shown in Fig.4.20, shows that the material near the plate centre is a region of cyclic plasticity. The distribution of the ratchet, radial and hoop, strains in the steady ratchet state, through the thickness, at various radial positions, are shown in Fig.4.21(i) to (v). At r/R<0.1, a bending type of deformation is not apparent. Even though the ratchet hoop strain at r/R=0.0788 is almost linear through the thickness, the ratchet strain in the radial direction is not linear through the thickness. The through thickness distribution of radial ratchet strain indicated that for r/R<0.0788, there is flow of material in the radial direction. Again this could only occur incrementally since the deformation is associated with the development of plastic zone during thermal cycles. At r/R = 0.1789, however, the ratchet radial strain is linear through the thickness (see Fig.4.21(iv)) and is associated with bending in the radial direction. The hoop ratchet strain is negligible at r/R=0.1789 and at r/R>0.2; all the ratchet hoop and radial strains are zero.

The variation of ratchet hoop, radial and shear strains with radius, at the steady ratchet state are shown in Fig.4.22. Ratchet strains are only obtained in the zones in which cyclic

plasticity occurs. The variation of ratchet deflection with radius, at the steady ratchet state, is shown in Fig.4.23. Again maximum ratchet deflections occur at the plate centre. The variation of total accummulation of ratchet deflection and ratchet deflection at the plate centre with cycle number are shown in Figs 4.24(i) and (ii) respectively. Fig.4.12 shows the 'exaggerated' deflection of the plate at the 10th. cycle and maximum deflection, again, occurs at the plate centre.

4.4.2 Effect of Load Combination on Ratchetting.

The results for the ratchet deflection at the plate centre for the load combinations of Table 4.1 are given in Table 4.2 and 4.3. In all cases, except where indicated, a steady ratchet state has been achieved. From these results, the shakedown/ratchetting boundary for a clamped circular plate subjected to a steady transverse pressure and a cyclic linear radial temperature variation was constructed. A linear extrapolation procedure illustrated in Figs 4.25(i) and (ii) was used for this purpose. The shakedown/ratchetting boundary is shown in Fig.4.26. Also shown in Fig.4.26 are the lines of constant ratchet deflection, interpolated from the straight line fits in Figs.4.25(i) and (ii).

It was also observed that, in all cases, steady ratchet deflections were achieved after a number of cycles. However, during this process, a considerable amount of deflection was accummulated. The total accummulated ratchet deflection at the first, fifth, tenth, twentieth and thirtieth cycles are given in Table 4.4.

The total equivalent strains at the plate centre for the first, fifth, tenth, twentieth and thirtieth cycles are given in Table 4.7. At these positions, the radial ratchet strains are practically equal to the hoop ratchet strains. For the case in which low mechanical and high thermal loads were present, these values represent the maximum value obtained. But for high mechanical and low thermal loads the maximum occurs at the plate edge. However, it should be noted that although the behaviour at the edge of the plate does not have a significant effect on overall deformations, the strains at these positions may be in error because a relatively coarse mesh was used. The total accummulated ratchet strains and the ratchet strains at various cycle numbers are given in Tables 4.8 and 4.9 respectively.

The shakedown/ratchetting boundary obtained is compared in Fig.4.26 with that obtained from the Upper Bound Shakedown Theorem; this comparison will be discussed later. The boundary obtained in this manner is derived in Appendix I sections A1.2.4.1 and A1.2.4.2.

4.4.3 Comparison Between Finite Element and Theoretical Shakedown/Ratchetting Boundaries.

Based on the Upper Bound Shakedown Theorem proposed by Koiter (12) and extended by Ponter (7), to include cyclic loading, the shakedown/ratchetting boundary for the circular plate subjected to a steady transverse pressure and a cyclic linear radial temperature distribution has been obtained. The

derivation is given in Appendix 1. Fig.4.26 compares the two boundaries. For $\sigma_t/\sigma_o < 2.0$, the finite element boundary falls within the theoretical boundary. However, for $\sigma_t/\sigma_o > 2.0$, the shakedown/ratchetting boundary obtained by using the finite element method, is outside the theoretical boundary.

4.4.4 Effect of Complete Stress Redistribution Due to Creep.

When stress redistribution due to creep occurs between each thermal loading, ratchetting may occur in the 'no-creep' shakedown region. The effect of creep on ratchetting can be bounded by the no-creep and complete redistribution situations. In the present analysis, only the effect of complete stress redistribution, between each thermal loading cycle, is investigated. For some components, e.g. a tube with uniform thickness under steady internal pressure, the stationary stress distribution is independent of the creep stress index, n. For the present plate component, however, the stationary stress distributions are not independent of n. To illustrate the behaviour of the clamped plate subjected to steady transverse pressure, P, and cyclic linear radial temperature distribution, a load combination in the 'no-creep' shakedown region was chosen; the loads used were $P/P_L = 0.416$ and $\sigma_t/\sigma_o = 1.275$, with n-values of 3,5 and 7.

Under 'no-creep' conditions, the stress distribution when a pressure of $P/P_L = 0.416$ is applied is as shown in Fig.4.27. Under this pressure, the initial deformation is entirely elastic. When the thermal load is applied, plastic deformation

occurs; the plastic zone produced in the first cycle of thermal load is shown in Fig.4.28. A large plastic zone occurs in the first cycle but the behaviour is elastic (i.e. shakedown occurs) after 4 cycles. The variation of the total and ratchet deflections at the plate centre with cycle number are shown in Figs.4.29(i) and (ii) respectively.

When complete redistribution due to creep is allowed, the stress distribution is different from that shown in Fig.4.27. The completely redistributed stress distributions for n=3,5 and 7 are shown in Fig.4.30(i),4.30(ii) and 4.30(iii) respectively. The stationary stress distributions are different for different n. For each value of n, the stress distributions is symmetrical about the centre-plane of the plate. The through thickness variation of the radial and hoop stresses at the stationary stress state at various radial positions are shown in Figs.4.31, 4.32 and 4.33 for n=3,5 and 7 respectively. Generally, the magnitude of the surface stationary state stress at the plate centre is higher for lower values of n. When the thermal load is applied, plastic deformation is produced. The extent of plastic zones during the thermal cycles is shown in Figs.4.34(i),(ii) and (iii) for n=3,5 and 7 respectively. The positions of the zones are similar for all n values but the volume of material in which the plastic zones occur is different in each case. The amount of ratchet deflection depends on the amount of plasticity in the plate material. The variation of the ratchet deflection with radius is shown in Fig.4.35 for the values of n considered. Also shown in Fig.4.35 is the first cycle ratchet deflection under the

'no-creep' conditions. The maximum ratchet deflection occurs at the plate centre. Table 4.10 gives the maximum ratchet deflection for all values of n considered and also for the first cycle 'no-creep' ratchet deflection. The maximum ratchet strains are also given in Table 4.10. Overall the ratchet deflection and the maximum ratchet equivalent plastic strains decrease with increasing values of n. The variation of maximum ratchet deflection with n is shown in Fig.4.36. The maximum ratchet deflection reduces approximately linearly with n for this particular case. It is interesting to note that the extrapolated values, at n=1, of this linear relationship gives the first cycle 'no-creep' ratchet deflection, as shown in Fig.4.36. Even though the result is for a particular load combination, the implication is that when creep occurs, ratchetting occurs in the 'no-creep' shakedown region and the maximum possible ratchet deflection is given by the first cycle 'no-creep' ratchet deflection. This observation can be generalized, i.e. the elastic/shakedown boundary becomes the shakedown/ratchetting boundary when complete redistribution due to creep occurs.

4.5 Discussion.

The ratchetting mechanisms of the plate has been investigated. Due to the pressure, the radial, hoop and shear stresses do not only vary through the thickness but also in the radial direction. The resulting hoop and radial stresses due to thermal loading only vary radially but are uniform through thickness. Ratchetting can occur when two load combinations

are imposed simultaneously. R_1 and R_2 regimes of ratchetting, observed in the tube components, cannot be identified for the plate. More importantly, shakedown with cyclic plasticity does not occur. The results also indicate that two distinct modes of behaviour are obtained, depending on the magnitudes of the applied loads. At low mechanical load and high thermal load, ratchetting is confined to a small volume of material which exhibits cyclic plasticity and at high mechanical load and low thermal load, incremental deformation occurs over the entire plate. In both cases, maximum ratchet deflection occurs at the plate centre. This type of behaviour is different from the behaviour of thin tubes described in Chapter 3, and also different from that analysed in reference 15,7,16 and 18. In particular a shear type of mechanism, as proposed by Ponter (7) for simply supported circular plates subjected to the same loading as the present plate, does not occur for the present plate.

The results also indicate that, increasing the magnitude of the applied load (mechanical or thermal) has the effect of increasing the ratchet deflection i.e. worsening the situation. For load combinations close to the shakedown/ratchetting boundary, it was found that the ratchet deflection is practically linearly related to the applied load (for e.g. at constant value of $\sigma_t/\sigma_o = 1.5$, shown in Fig.4.25(ii), the three points are practically colinear). Hence a linear extrapolation can be used to determine the shakedown/ratchetting boundary (i.e. the load at which the ratchet deflection is zero). This method is used to determine

the shakedown/ratchetting boundary of the plate shown in Fig.4.26. The boundary obtained in this manner, lies within the boundary obtained using the Upper Bound Shakedown Theorem for σ_t/σ_o <2.0. For σ_t/σ_o >2.0, the boundary is above that obtained from the method given in Appendix I. The differences could be attributed to the finite element mesh used being coarse.

The results are normalized with respect to the plate dimension and material properties and therefore are applicable to any thin plate with similar geometry and loading.

σ_t/σ_o	P/P_L
0.5	0.884,0.936,0.988
1.275	0.728,0.832
1.5	0.676,0.728,0.832
2.1	0.416
2.3	0.104, 0.416
2.4	0.104

Table 4.1 Load combinations for which finite element results were obtained.

σ_t/σ_o	P/P_L	Normalised ratchet deflections u^R/h	P/P_L for $u^R/h=0$ (constructed boundary)
0.5	0.884	0.0	0.920
	0.936	0.0116 (1)	
	0.988	0.090 (1)	
1.275	0.728	0.028	0.707
	0.832	0.1588	
1.5	0.676	0.037 (2)	
	0.728	0.102	0.653
	0.832	0.261	

Table 4.2 Normalised steady state ratchet deflection for σ_t/σ_o<2.0

P/P_L	σ_t/σ_o	Normalised ratchet deflection u^R/h	σ_t/σ_o for $u^R/h=0$
0.104	2.2	$0.14X10^{-4}$	2.196
	2.3	$0.84X10^{-4}$	
	2.4	2.00×10^{-4}	
0.416	2.1	0.00084	2.096
	2.3	0.0466	

Table 4.3 Normalised ratchet deflection for σ_t<2.0 σ_o

(1) Values at 30 cycles

(2) Values at 50 cycles

σ_t/σ_o	P/P_L	Total deflection at Nth cycle u^T/h				
		N=1	N=5	N=10	N=20	N=30
0.5	0.884	0.406	0.553	0.611	0.631	-
	0.936	0.518	0.788	0.970	1.197	1.352
	0.988	0.739	1.275	1.825	2.813	3.729
1.275	0.728	0.409	0.745	1.034	1.493	1.870
	0.832	0.586	1.351	2.203	3.813	-
1.5	0.676	0.425	0.790	1.122	1.639	2.055
	0.728	0.491	1.054	1.644	2.752	3.775
	0.832	0.682	1.813	3.148	-	-
2.1	0.416	0.342	0.489	0.562	0.623	0.648
2.3	0.104	0.0559	0.0563	0.0568	-	-
	0.416	0.401	0.670	0.986	1.497	1.977
2.4	0.104	0.0586	0.0597	0.0608	-	-

Table 4.4 Total deflection at plate centre at various number of cycles for a clamped circular plate subjected to a steady transverse pressure and cyclic linear radial temperature gradient.

σ_t/σ_o	P/P_L	Total accumulated ratchet deflection u^R/h				
		N=1	N=5	N=10	N=20	N=30
0.5	0.884	0.112	0.259	0.317	0.336	-
	0.936	0.152	0.422	0.604	0.831	0.985
	0.988	0.223	0.759	1.309	2.297	3.213
1.275	0.728	0.241	0.577	0.866	1.325	1.702
	0.832	0.355	1.119	1.971	3.581	-
1.5	0.676	0.274	0.640	0.972	1.488	1.904
	0.728	0.323	0.886	1.476	2.584	3.607
	0.832	0.451	1.582	2.917	-	-
2.1	0.416	0.2523	0.399	0.472	0.533	0.5583
2.3	0.104	0.0334	0.0339	0.0343	-	-
	0.416	0.3109	0.6098	0.897	1.407	1.887
2.4	0.104	0.0362	0.0373	0.0383	-	-

Table 4.5 Total accumulated ratchet deflection at the plate centre for the clamped circular plate.

σ_t/σ_o	P/P_L	Ratchet deflection at the Nth cycle u^R/h				
		N=1	N=5	N=10	N=20	N=30
0.5	0.884	0.112	0.02476	0.0049	0.00076	0
	0.936	0.152	0.0530	0.0294	0.0190	0.01156
	0.988	0.223	0.120	0.105	0.0946	0.0898
1.275	0.728	0.241	0.0698	0.0512	0.04	0.0363
	0.832	0.355	0.178	0.166	0.159	-
1.5	0.676	0.274	0.0746	0.061	0.0444	0.0386
	0.728	0.323	0.128	0.115	0.108	0.102
	0.832	0.451	0.274	0.263	-	-
2.1	0.416	0.2523	0.0229	0.0108	0.00376	0.00188
2.3	0.104	0.0334	0.000096	0.000088	-	-
	0.416	0.3109	0.0634	0.0547	0.0492	0.0472
2.4	0.104	0.03619	0.000172	0.000212	-	-

Table 4.6 Ratchet deflection at plate centre at various number of cycles for the clamped circular plate.

σ_t/σ_o	P/P_L	Total equivalent strain at r/R=0.02, z/h=-0.447 at the Nth cycles , $\varepsilon^T_{eq}/\varepsilon_o$				
		N=1	N=5	N=10	N=20	N=30
0.5	0.884	3.983	5.817	6.525	6.685	-
	0.936	5.190	8.444	10.680	13.430	15.340
	0.988	7.696	14.20	20.820	32.620	43.580
1.275	0.728	4.949	8.892	12.00	16.82	20.84
	0.832	5.180	13.670	23.10	40.65	-
1.5	0.676	5.478	10.02	13.46	18.729	23.018
	0.728	6.011	12.43	18.53	30.06	40.73
	0.832	7.796	20.24	34.80	-	-
2.1	0.416	7.354	9.314	11.18	14.94	18.92
2.3	0.104	6.584	14.14	23.637	-	-
	0.416	8.418	14.870	23.280	40.540	57.86
2.4	0.104	7.255	17.790	30.98	-	-

Table 4.7 Total equivalent strain at r/R=0.02 and z/h= -0.447 at various cycle number for the clamped circular plate.

σ_t/σ_o	P/P_L	Total accumulated ratchet strain, $\epsilon^R_{eq}/\epsilon_o$ at r/R=0.02 and z/h= -0.447, and Nth cycle.				
		N=1	N=5	N=10	N=20	N=30
0.5	0.884	1.693	3.527	4.235	4.453	-
	0.936	2.105	5.359	7.590	10.34	12.25
	0.988	2.826	9.33	15.950	27.75	38.71
1.275	0.728	3.886	7.829	10.94	15.76	19.78
	0.832	4.190	12.68	22.11	39.66	-
1.5	0.676	4.542	9.084	12.523	17.793	22.082
	0.728	4.948	11.37	17.470	29.0	39.67
	0.832	6.155	18.60	33.160	-	-
2.1	0.416	6.788	8.748	10.61	14.37	18.35
2.3	0.104	6.442	13.998	23.496	-	-
	0.416	7.852	14.304	22.714	39.97	57.29
2.4	0.104	7.113	17.65	30.84	-	-

Table 4.8 Values of total accumulated equivalent ratchet strains at r/R=0.02 and z/h=-0.447 for the clamped circular plate.

σ_t/σ_o	P/P_L	Ratchet strains at r/R=0.02, z/h=-0.447, $\epsilon^R_{eq}/\epsilon_o$ at the Nth cycles.				
		N=1	N=5	N=10	N=20	N=30
0.5	0.884	1.693	0.288	0.064	0.001	0
	0.936	2.105	0.606	0.350	0.230	0.140
	0.988	2.826	1.450	1.270	1.140	1.070
1.275	0.728	3.886	0.766	0.530	0.440	0.390
	0.832	4.190	2.00	1.820	1.730	-
1.5	0.676	4.542	0.846	0.626	0.454	0.399
	0.728	4.948	1.350	1.190	1.120	1.050
	0.832	6.155	2.970	2.870	-	-
2.1	0.416	6.788	0.351	0.380	0.380	0.40
2.3	0.104	6.442	1.891	1.900	-	-
	0.416	7.852	1.640	1.70	1.740	1.720
2.4	0.104	7.113	2.640	2.640	-	-

Table 4.9 Values of ratchet equivalent strains at r/R=0.02, z/h=-0.447 for the clamped circular plate.

values of n	normalised ratchet deflection at plate centre u_c^R/h	normalised ratchet equivalent strain at r/R=0.02, z/h=-0.447 $\varepsilon_{eq}^R/\varepsilon_o$	normalised ratchet equivalent plastic strains at r/R=0.02, z/h=-0.447 $\varepsilon_{eq}^p/\varepsilon_o$
3	0.0644	2.61	2.808
5	0.062	2.52	2.70
7	0.0592	2.34	2.533
first cycle 'no-creep'	0.0671	3.075	2.8849

Table 4.10 Maximum ratchet deflaetion and strain for the clamped circular plate. Completė stress redistribution

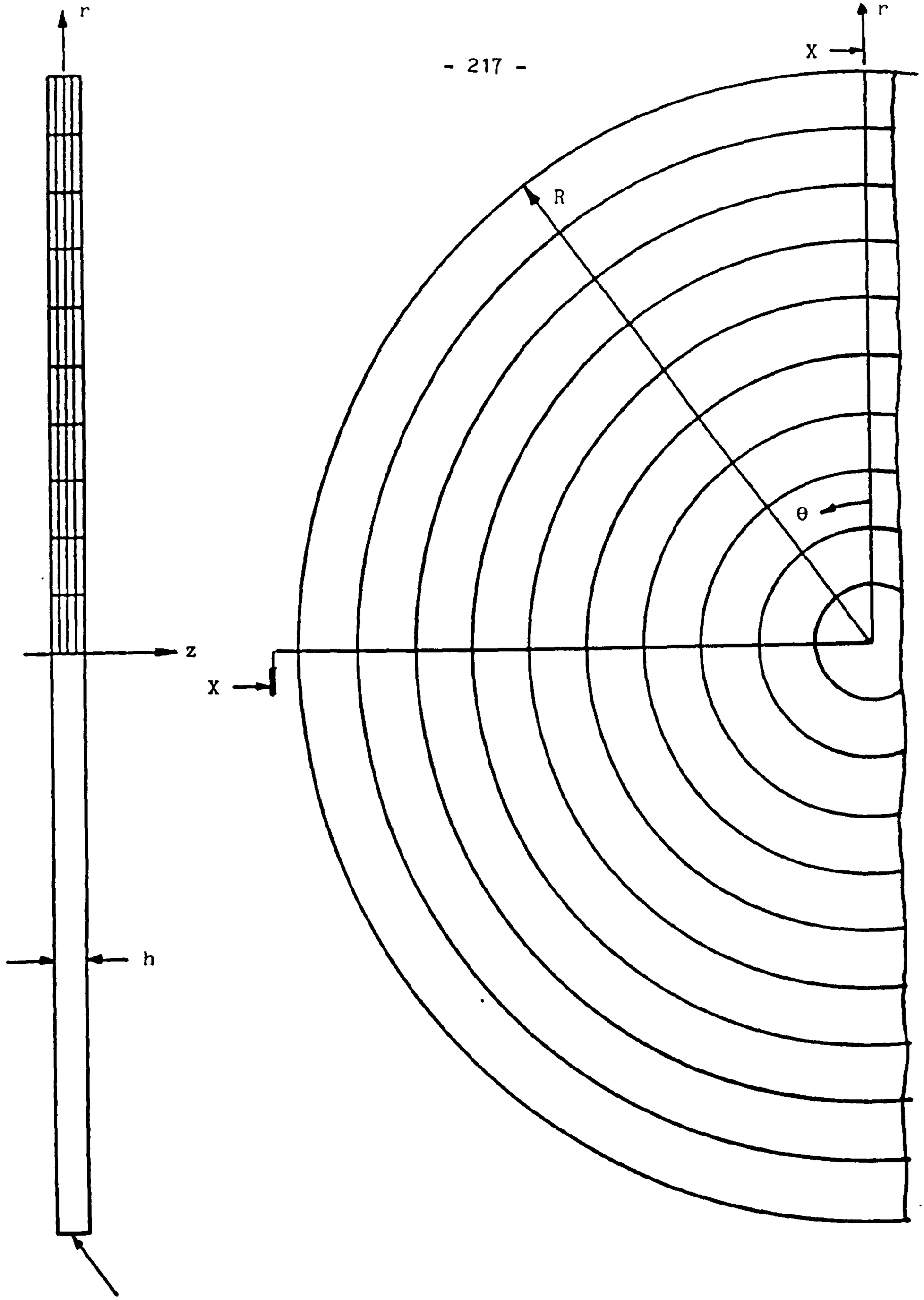

Fig. 4.1 The circular plate and finite element mesh

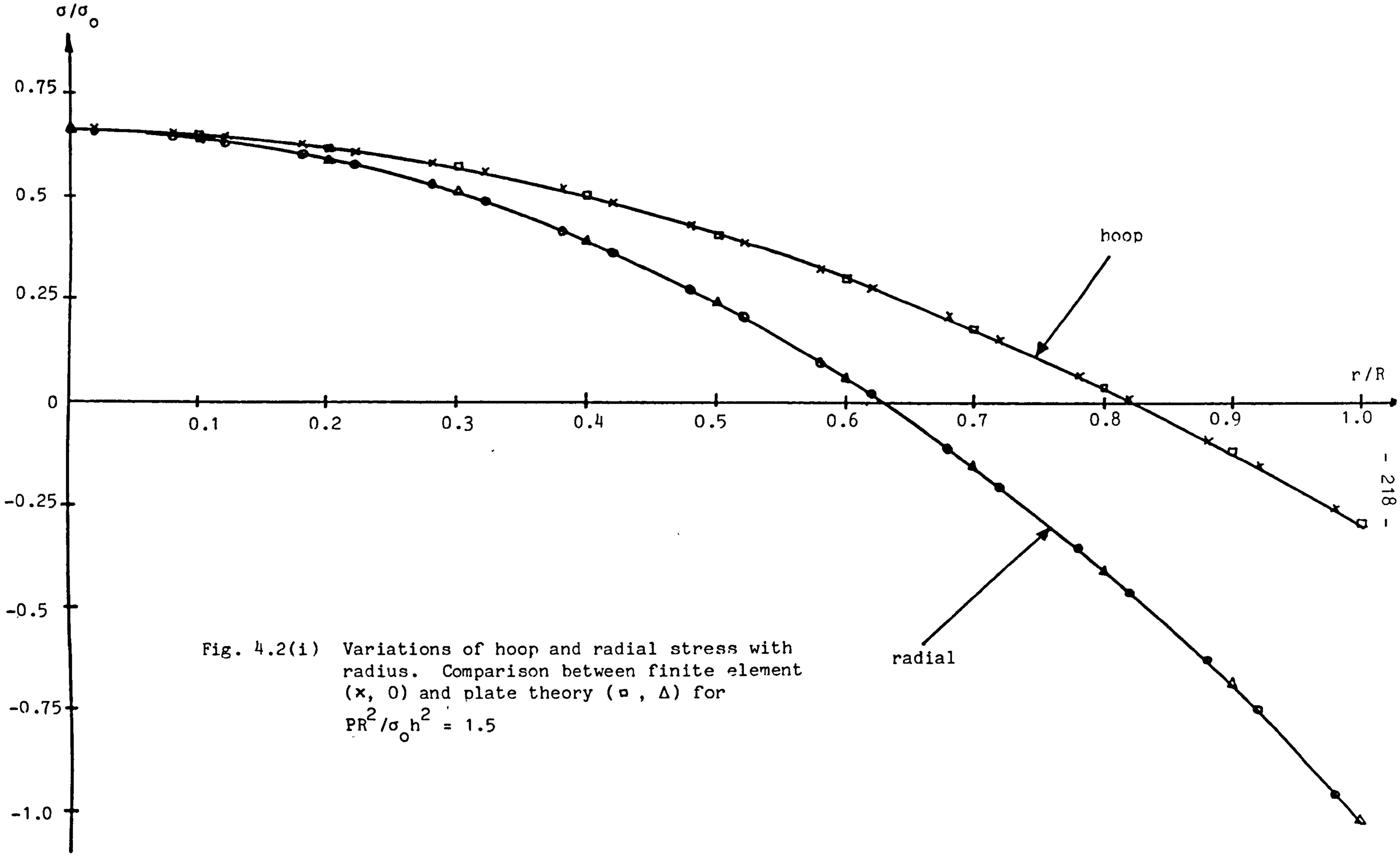

Fig. 4.2(i) Variations of hoop and radial stress with radius. Comparison between finite element (×, 0) and plate theory (□ , Δ) for $PR^2/\sigma_o h^2 = 1.5$

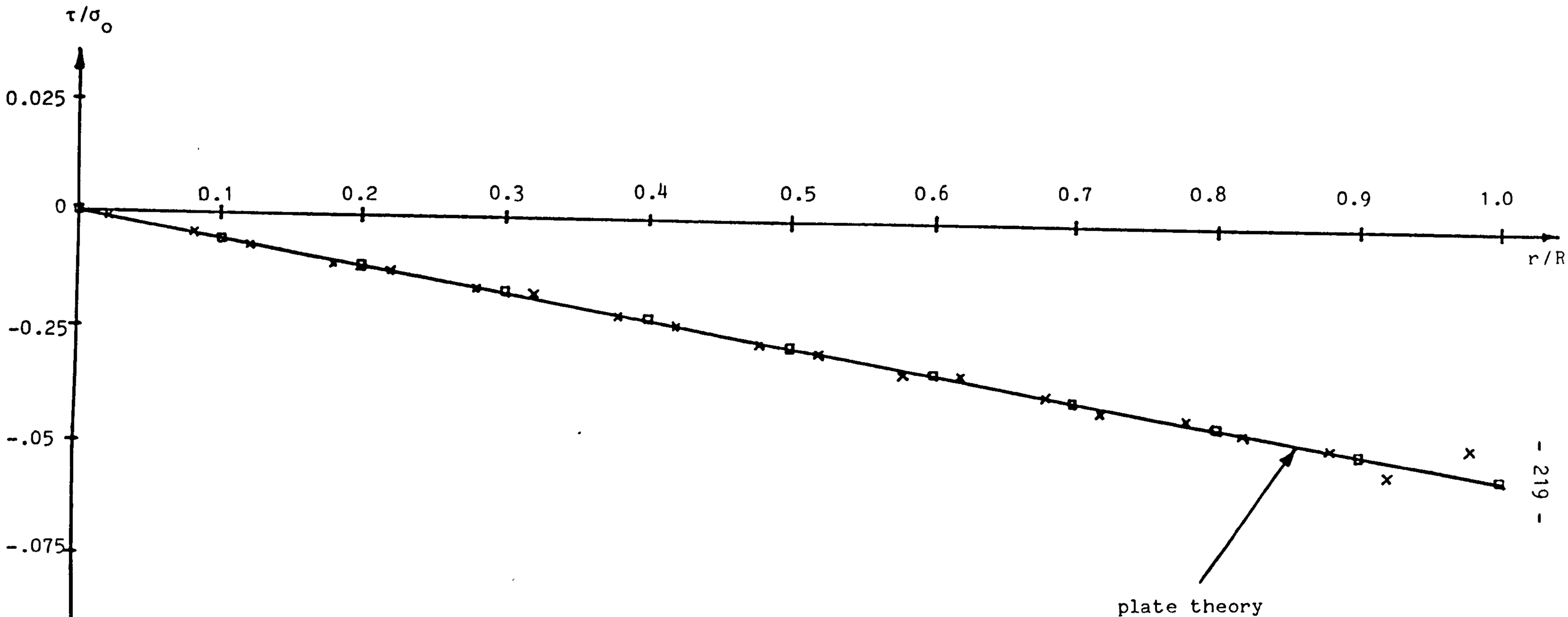

Fig. 4.2(ii) Variations of shear stress with radius
Comparison between finite element (×) with plate theory (—□—) $PR^2/\sigma_o h^2 = 1.5$

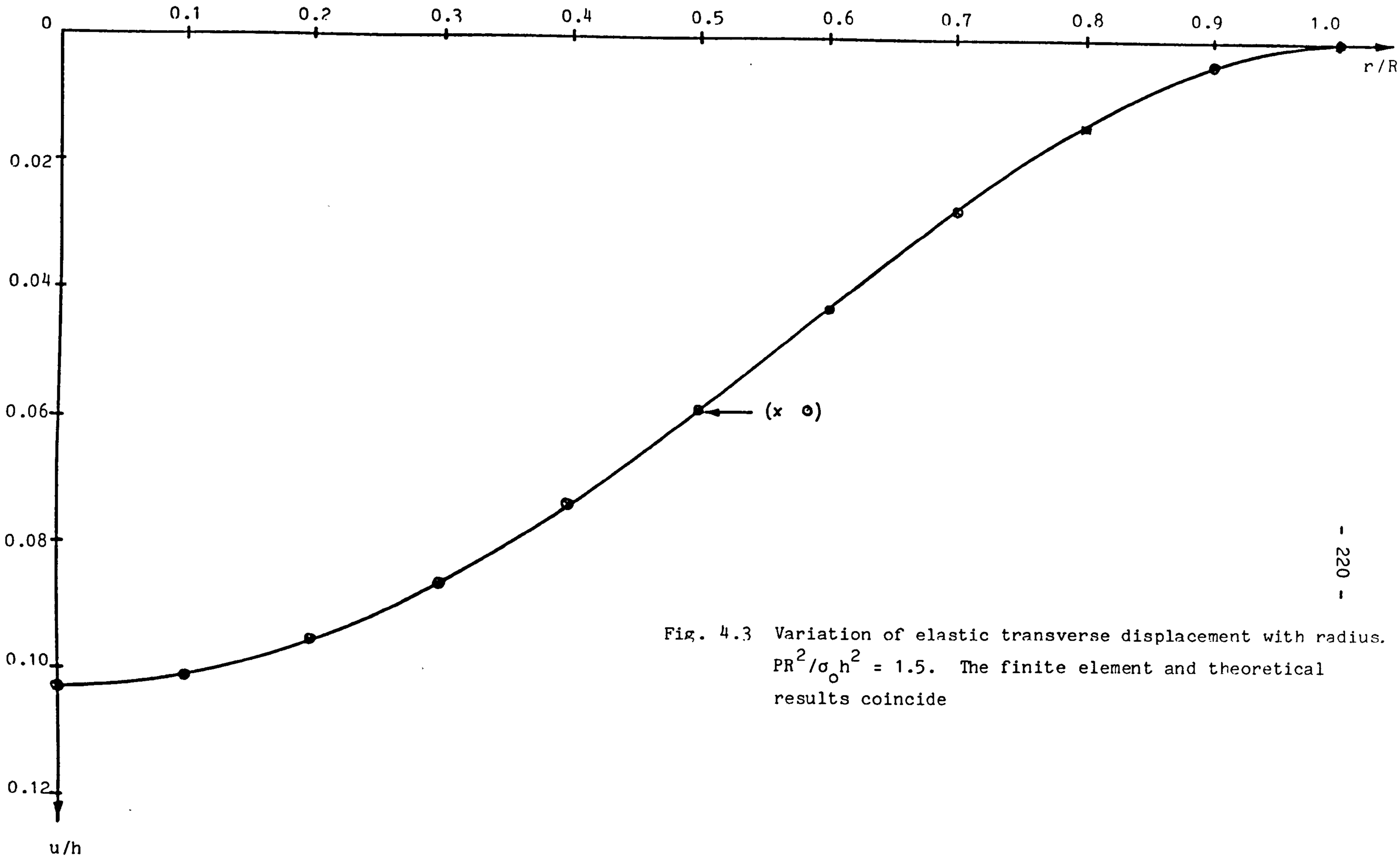

Fig. 4.3 Variation of elastic transverse displacement with radius. $PR^2/\sigma_o h^2 = 1.5$. The finite element and theoretical results coincide

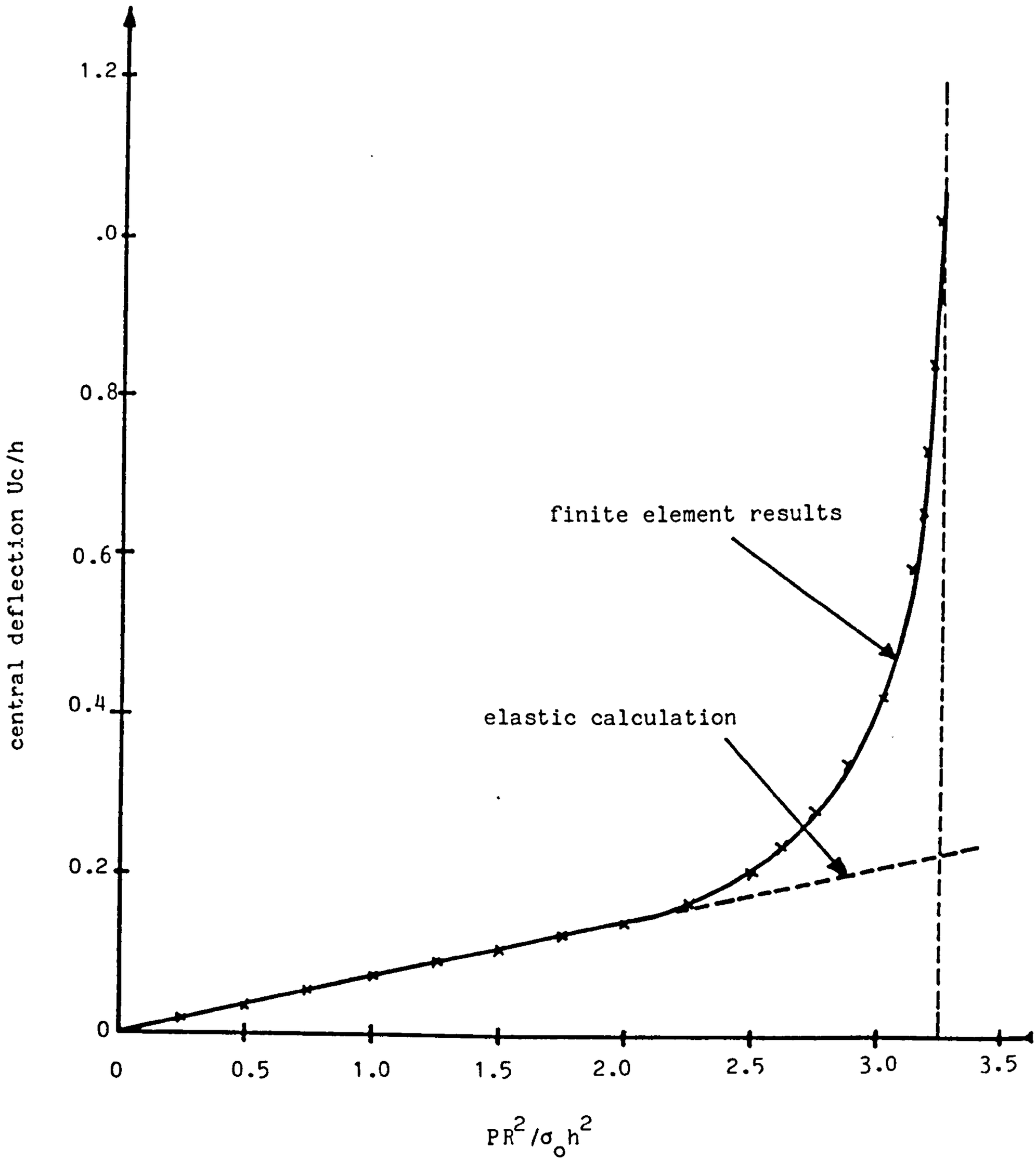

Fig. 4.4 Variation of deflection at the plate centre with pressure

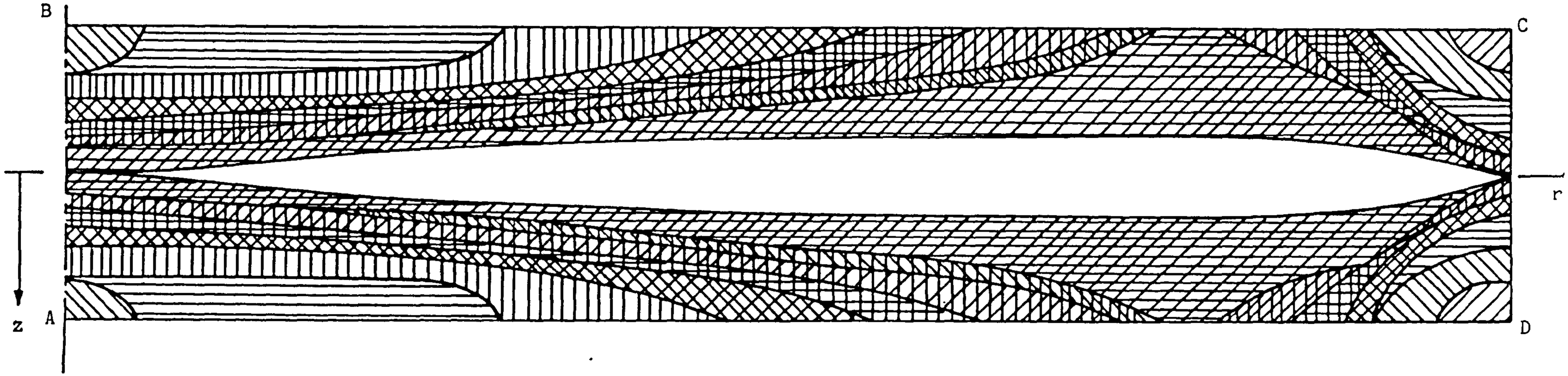

$PR^2/\sigma_o h^2$		$PR^2/\sigma_o h^2$		$PR^2/\sigma_o h^2$	
	2.0		2.75		3.0625
	2.25		2.875		3.125
	2.5		2.9625		3.25

Fig. 4.5 Development of plastic zone with increasing pressure. (Note: the thickness of plate is exaggerated).

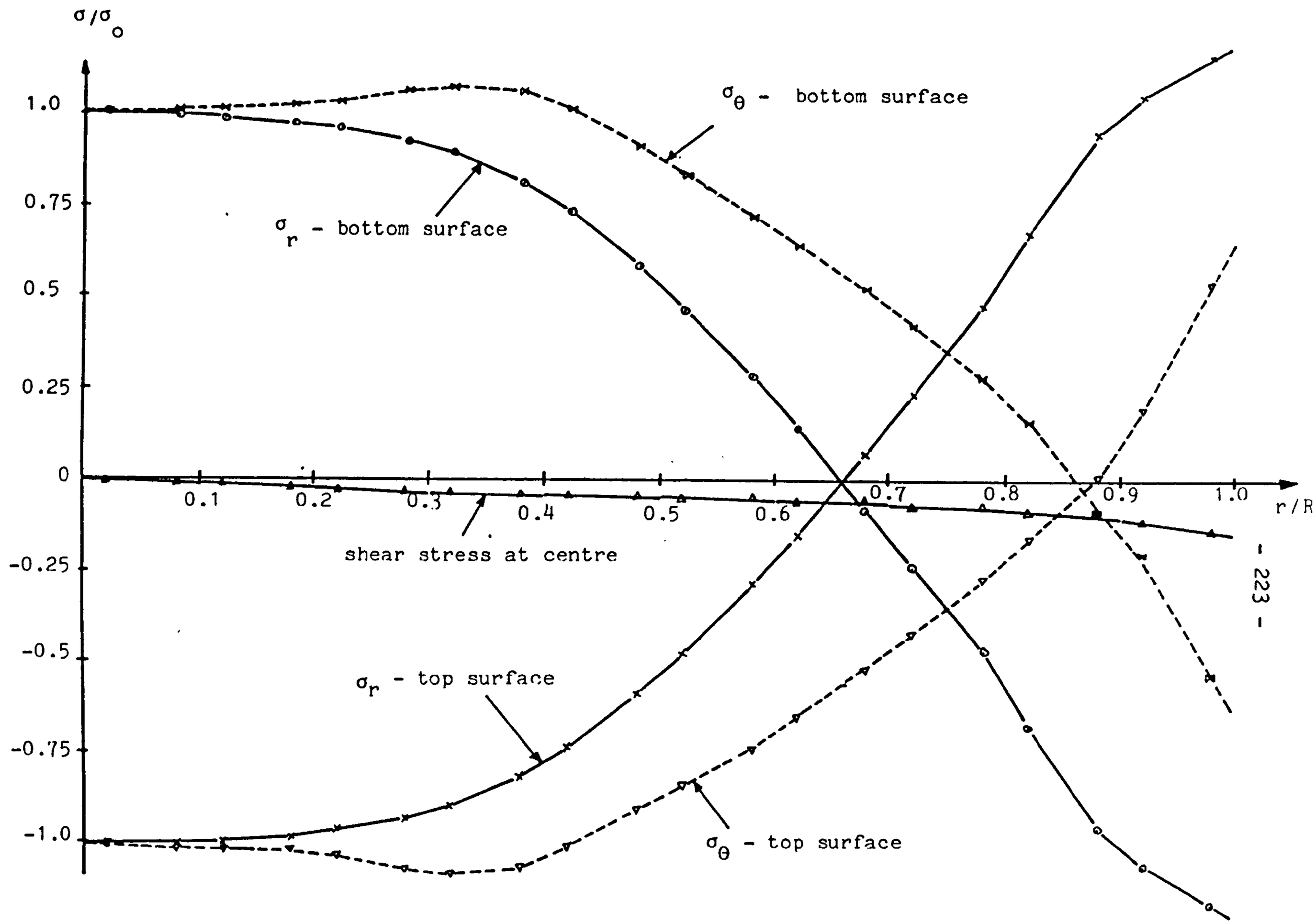

Fig. 4.6 Variations of stresses with radius for $P/P_L = 0.832$

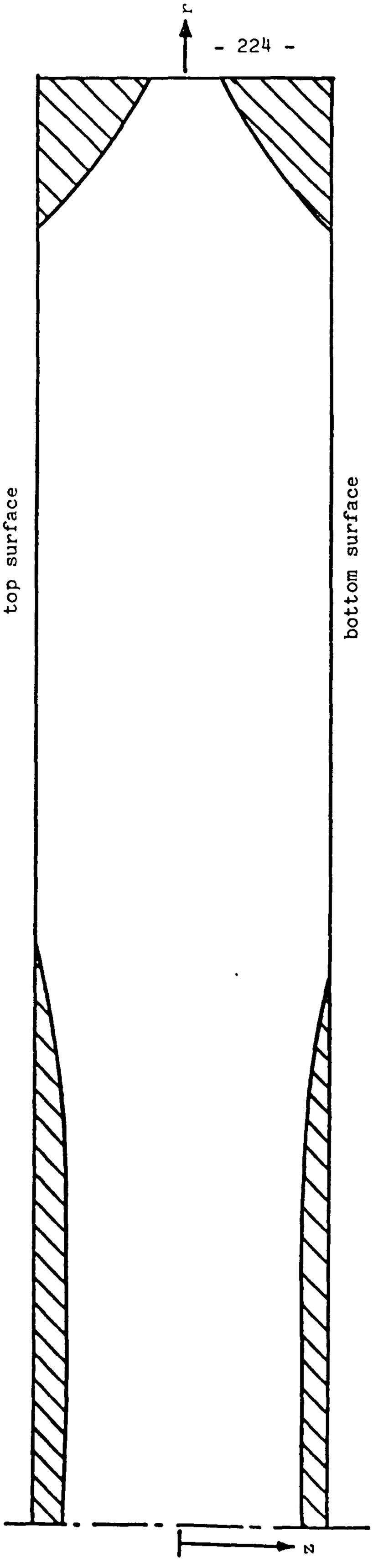

Fig. 4.7 Extent of plastic zone at $P/P_L = 0.832$. (Thickness is exaggerated).

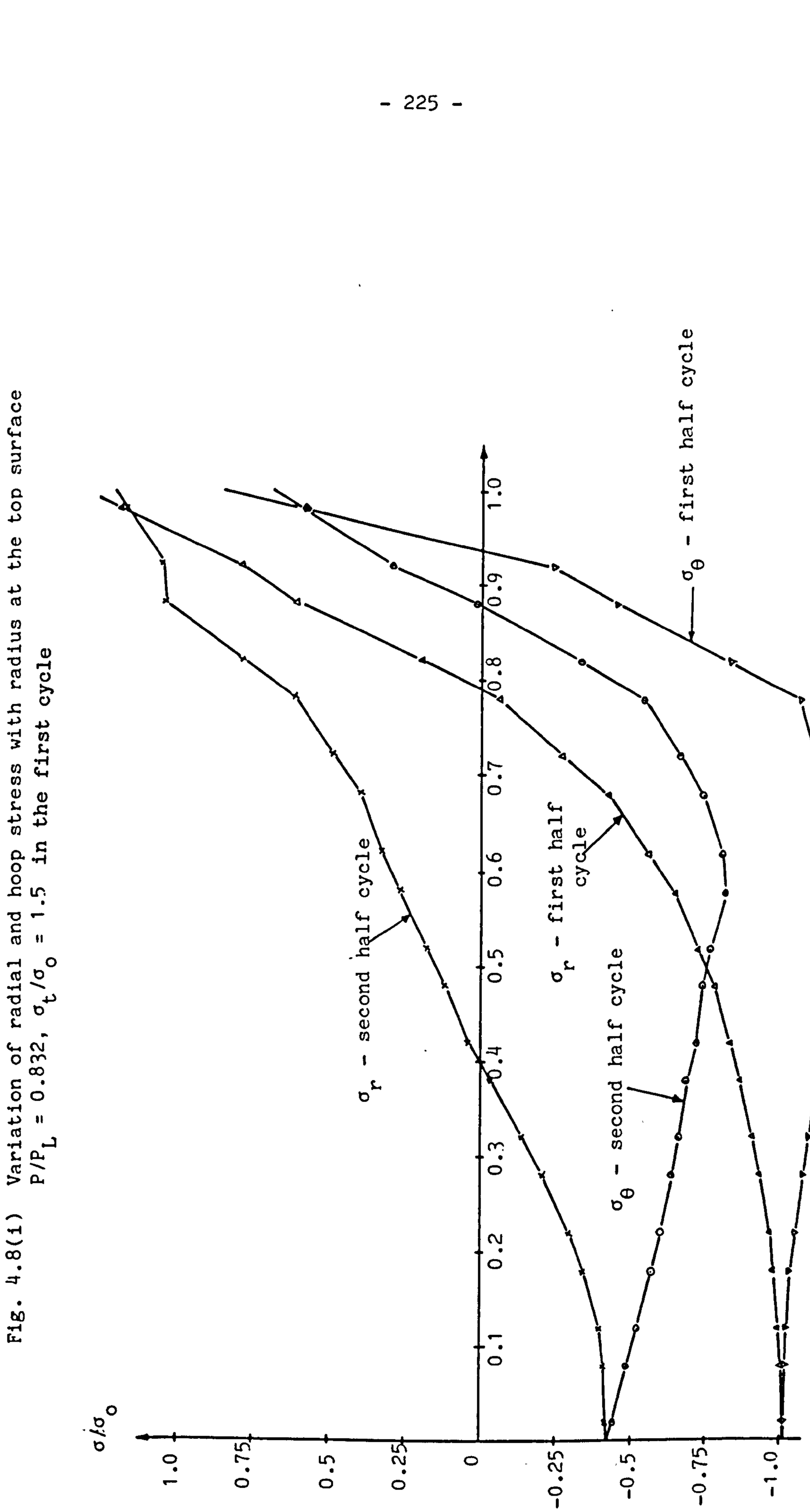

Fig. 4.8(i) Variation of radial and hoop stress with radius at the top surface
$P/P_L = 0.832$, $\sigma_t/\sigma_o = 1.5$ in the first cycle

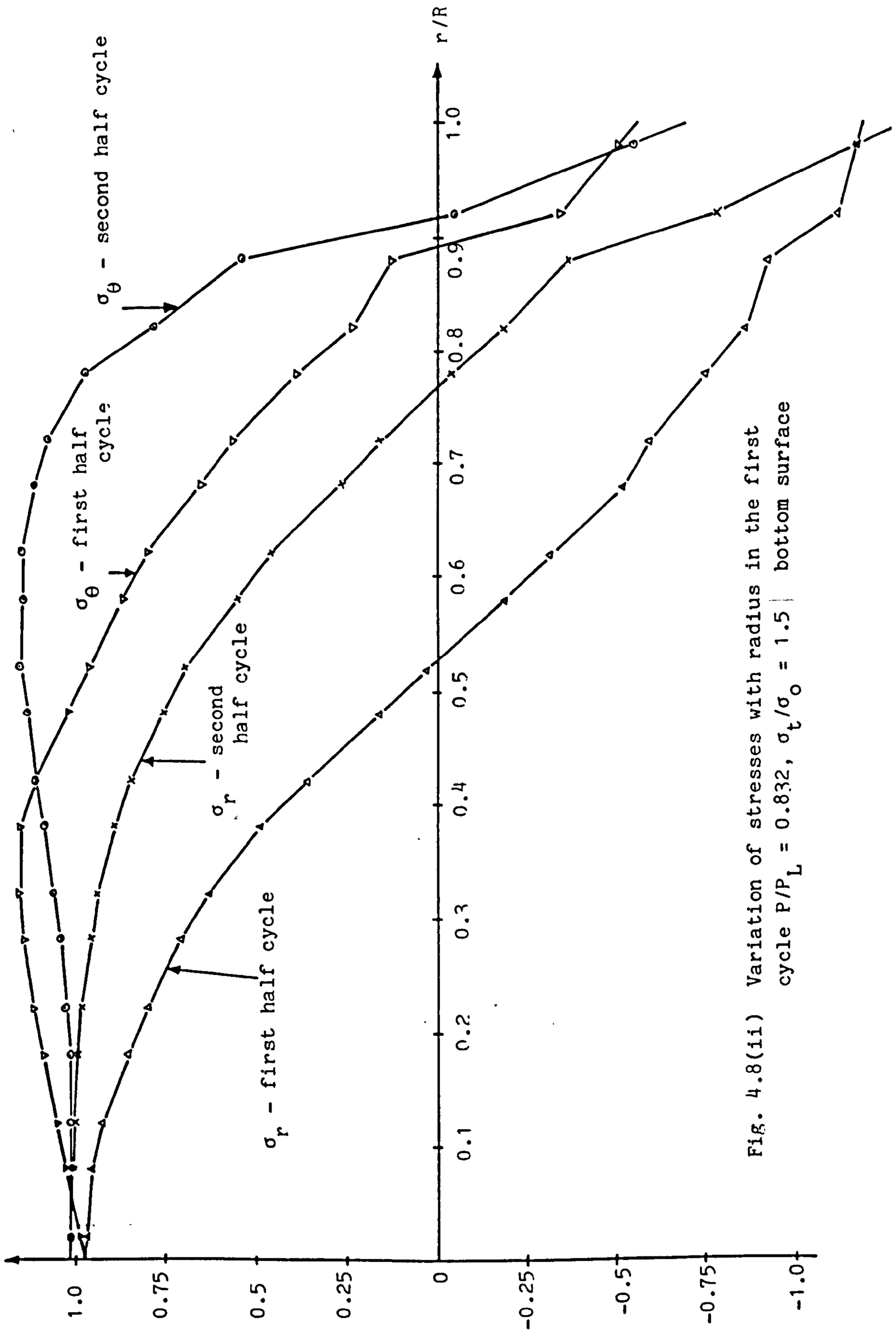

Fig. 4.8(ii) Variation of stresses with radius in the first cycle $P/P_L = 0.832$, $\sigma_t/\sigma_o = 1.5$ | bottom surface

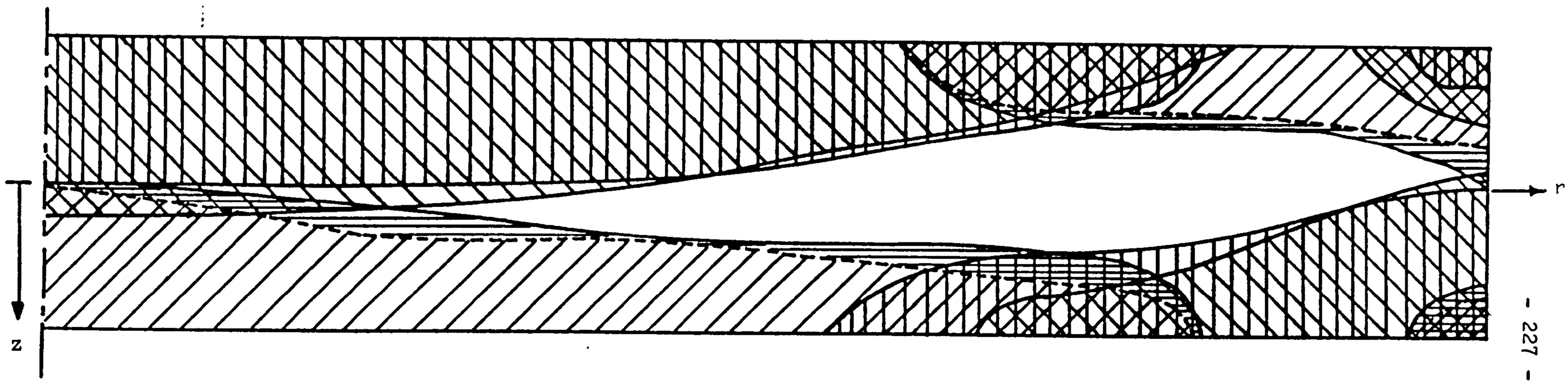

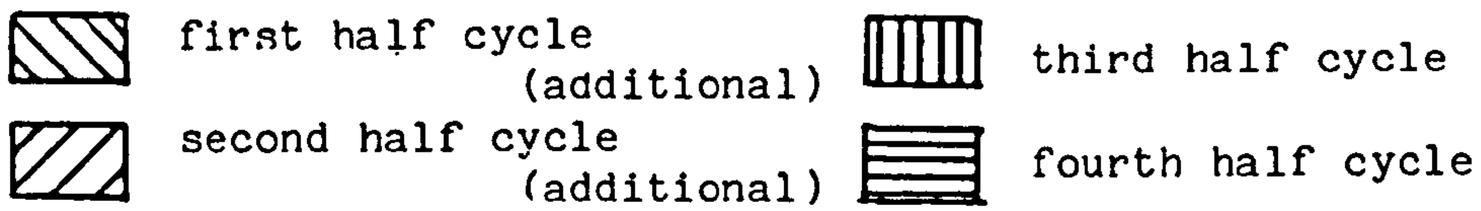

Fig. 4.9(i) Plastic zones for $P/P_L = 0.832$, $\sigma_t/\sigma_o = 1.5$. (Plate thickness is exaggeraged)

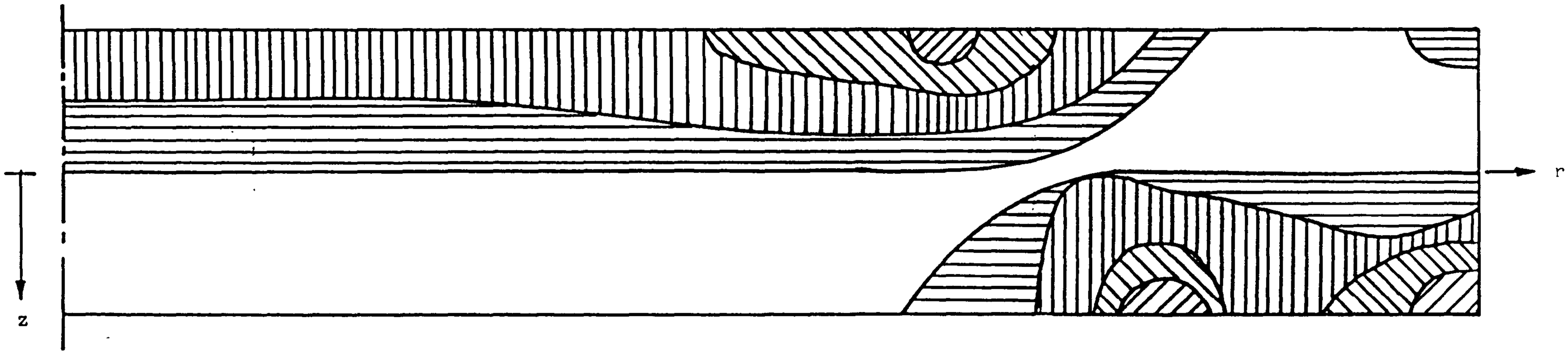

$\sigma_t/4$

$\sigma_t/2$ (additional)

$3\sigma_t/4$ (additional)

σ_t (additional)

Fig. 4.9(ii) Growth of plastic zone during heating in the steady ratchet state. $P/P_L = 0.832$, $\sigma_t/\sigma_o = 1.5$ (Plate thickness is exaggerated)

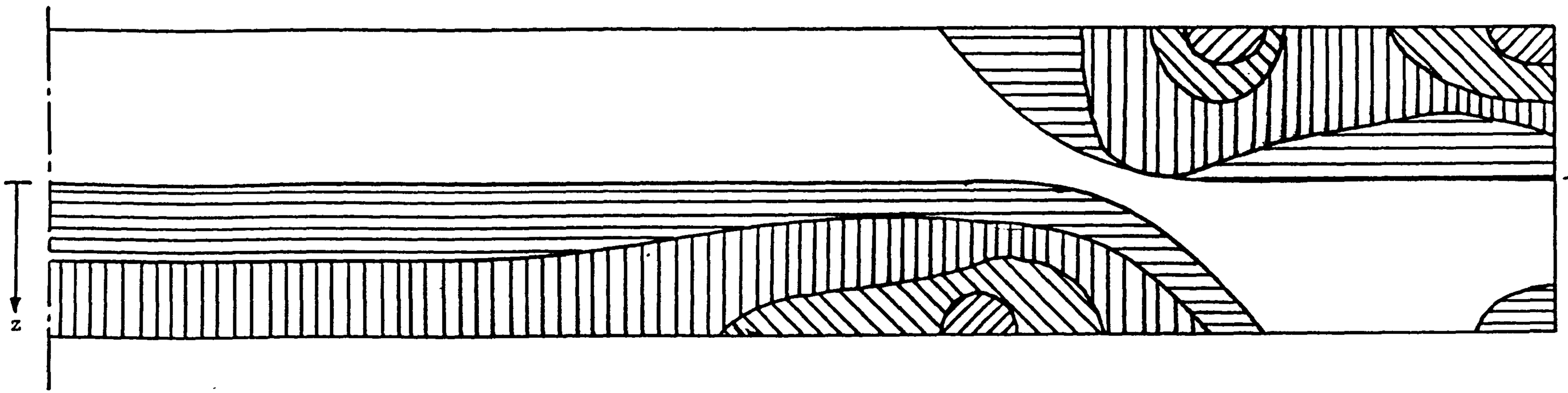

$\sigma_t/4$

$\sigma_t/2$ (additional)

$3\sigma_t/4$ (additional)

σ_t (additional)

Fig. 4.9(iii) Growth of plastic zone during cooling in the steady ratchet state $P/P_L = 0.832$, $\sigma_t/\sigma_o = 1.5$ (Plate thickness is exaggerated).

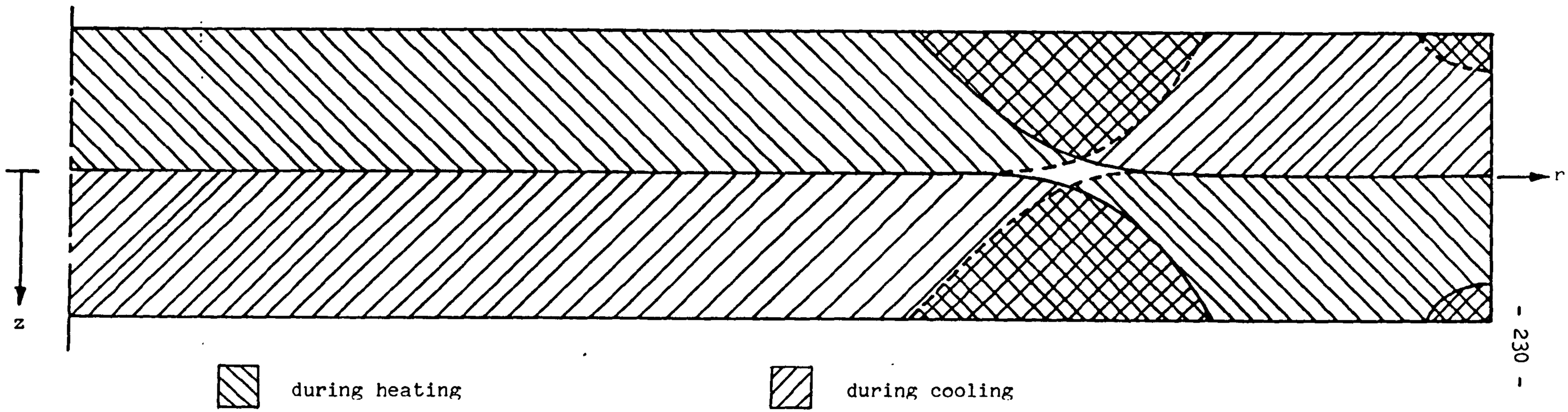

Fig. 4.9(iv) Plastic zone at the steady ratchet state for $P/P_L = 0.832$, $\sigma_t/\sigma_o = 1.5$ (Plate thickness is exaggerated).

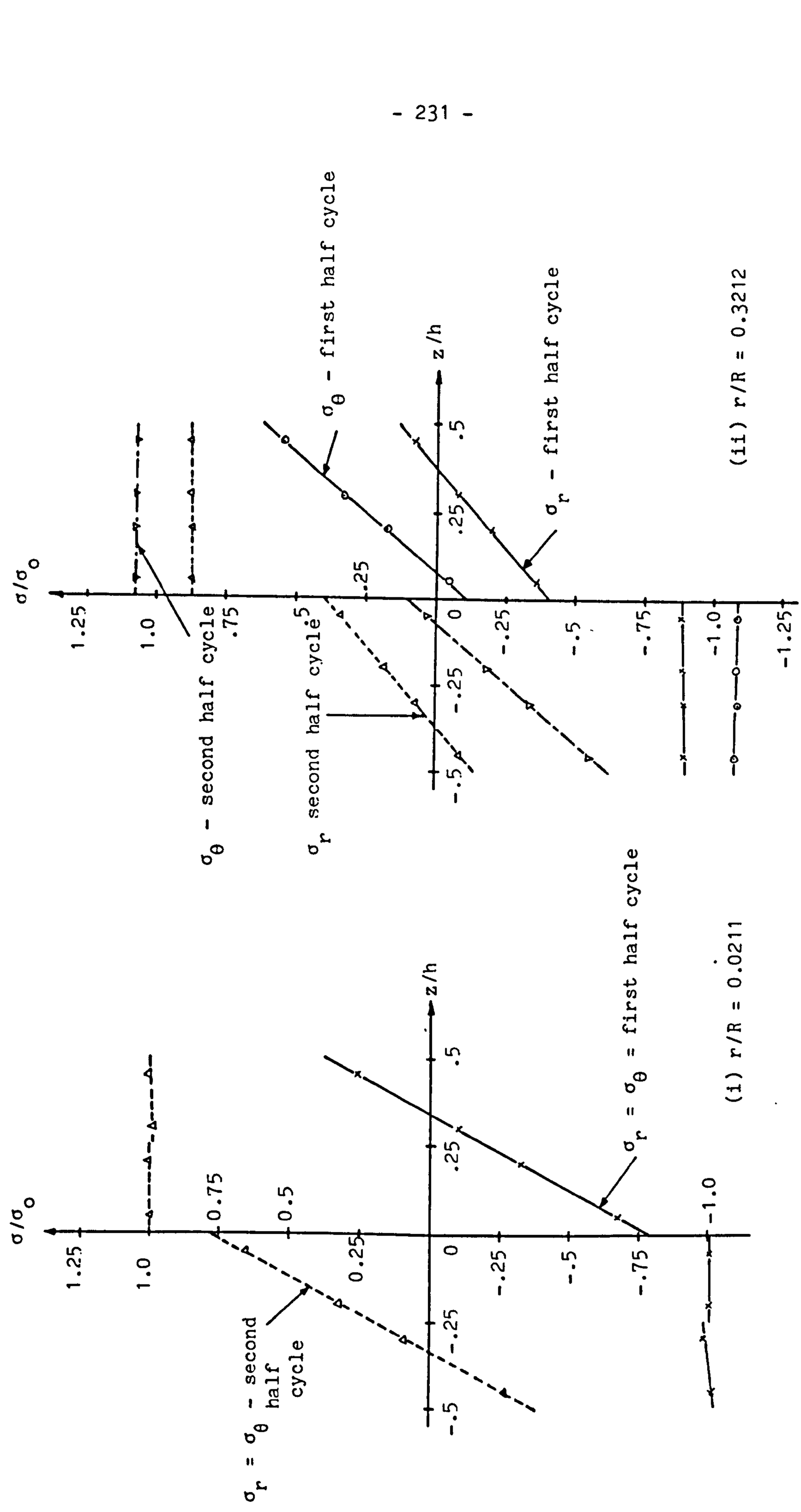

Fig. 4.10 Through thickness variations of steady state stresses. $P/P_L = 0.832$, $\sigma_t/\sigma_o = 1.5$

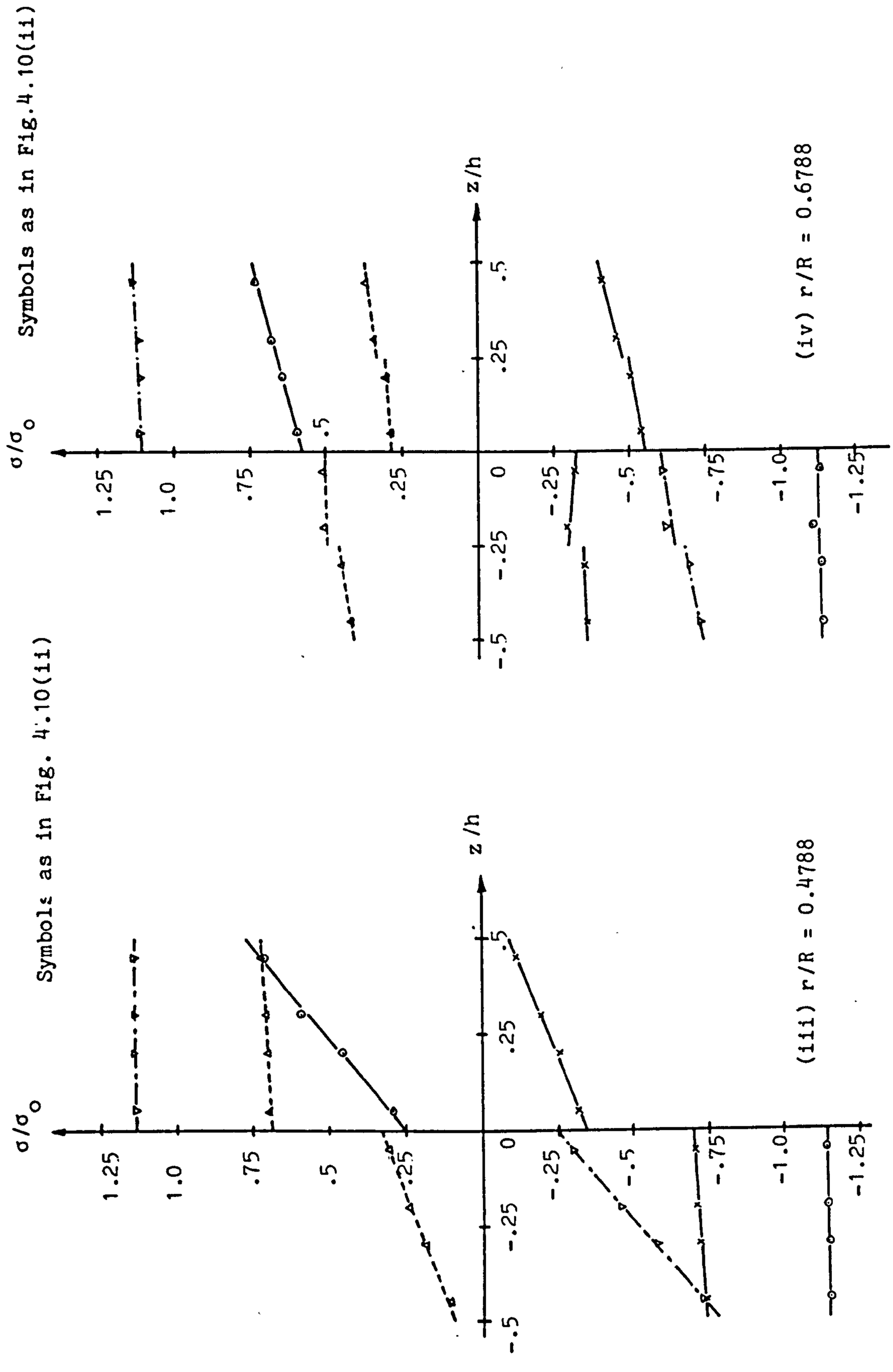

Fig. 4.10 Through thickness variation of steady state stresses. P/P_L = 0.832, σ_t/σ_o = 1.5 Symbols as in Fig. 4.10(ii) Symbols as in Fig.4.10(ii)

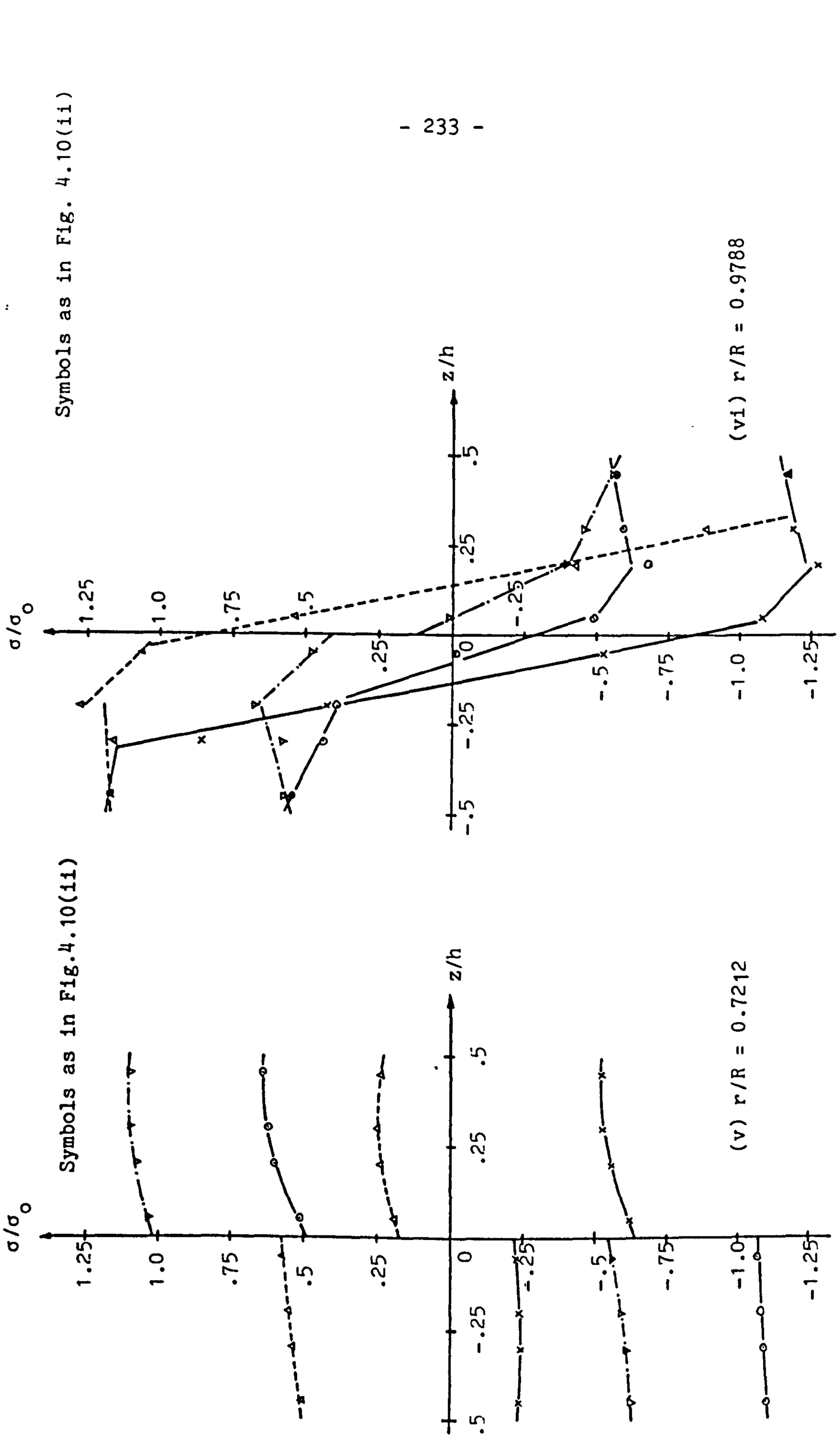

Fig. 4.10 Through thickness variation of steady state stresses $P/P_L = 0.832$, $\sigma_t/\sigma_o = 1.5$

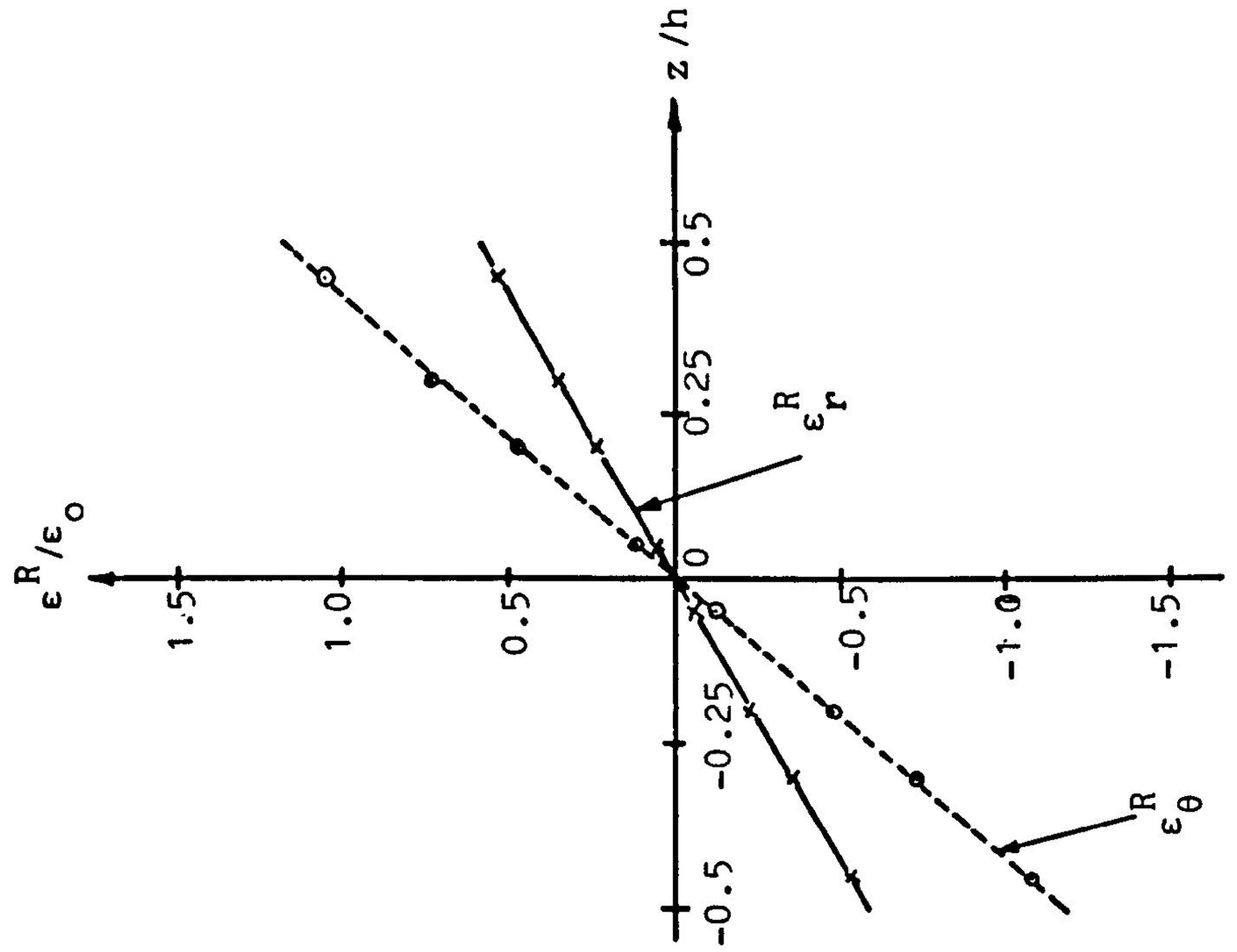

Fig. 4.11 Through thickness variation of steady state ratchet strain P/P_L = 0.832,

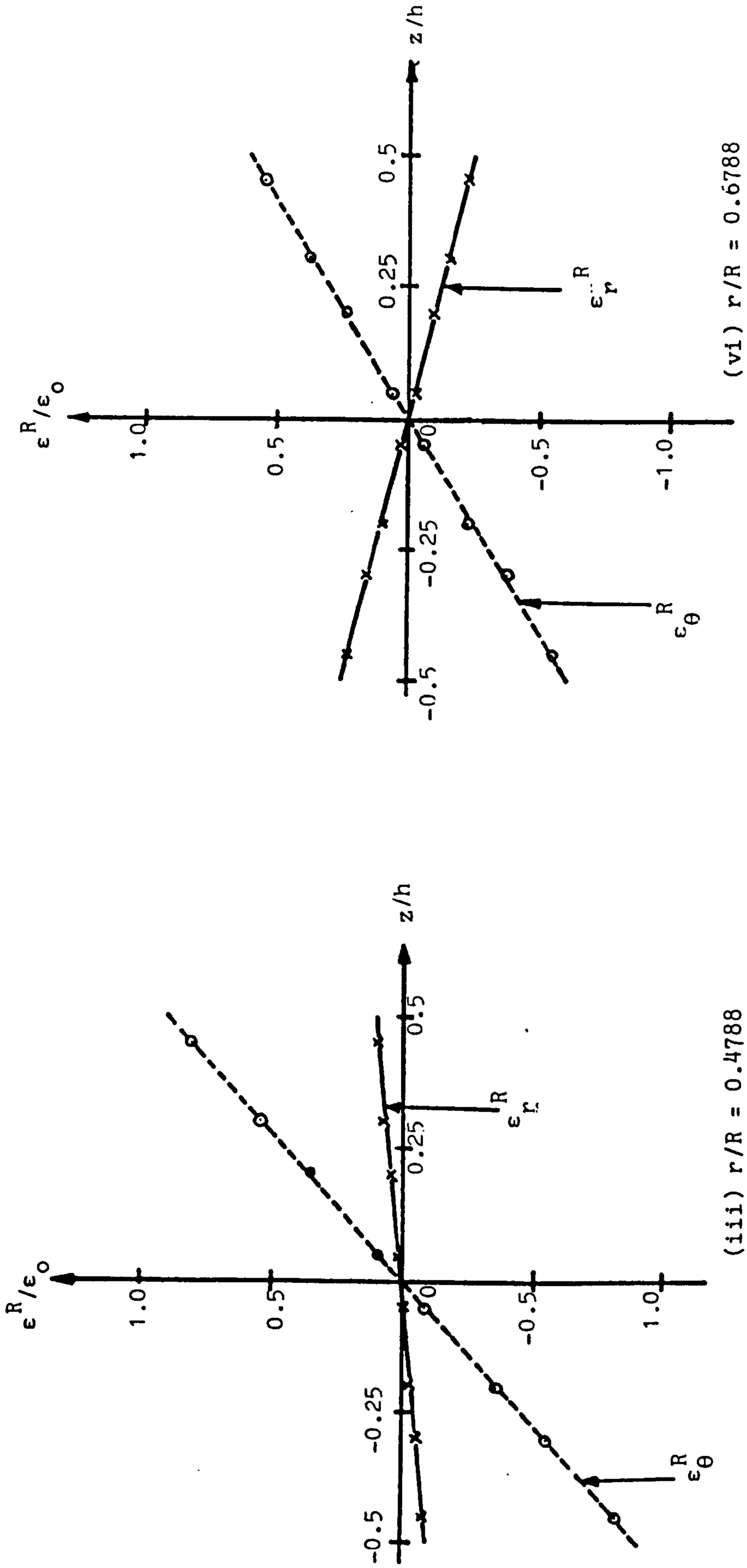

Fig. 4.11 Through thickness variation of steady state ratchet strains. $P/P_L = 0.832$, $\sigma_t/\sigma_o = 1.5$

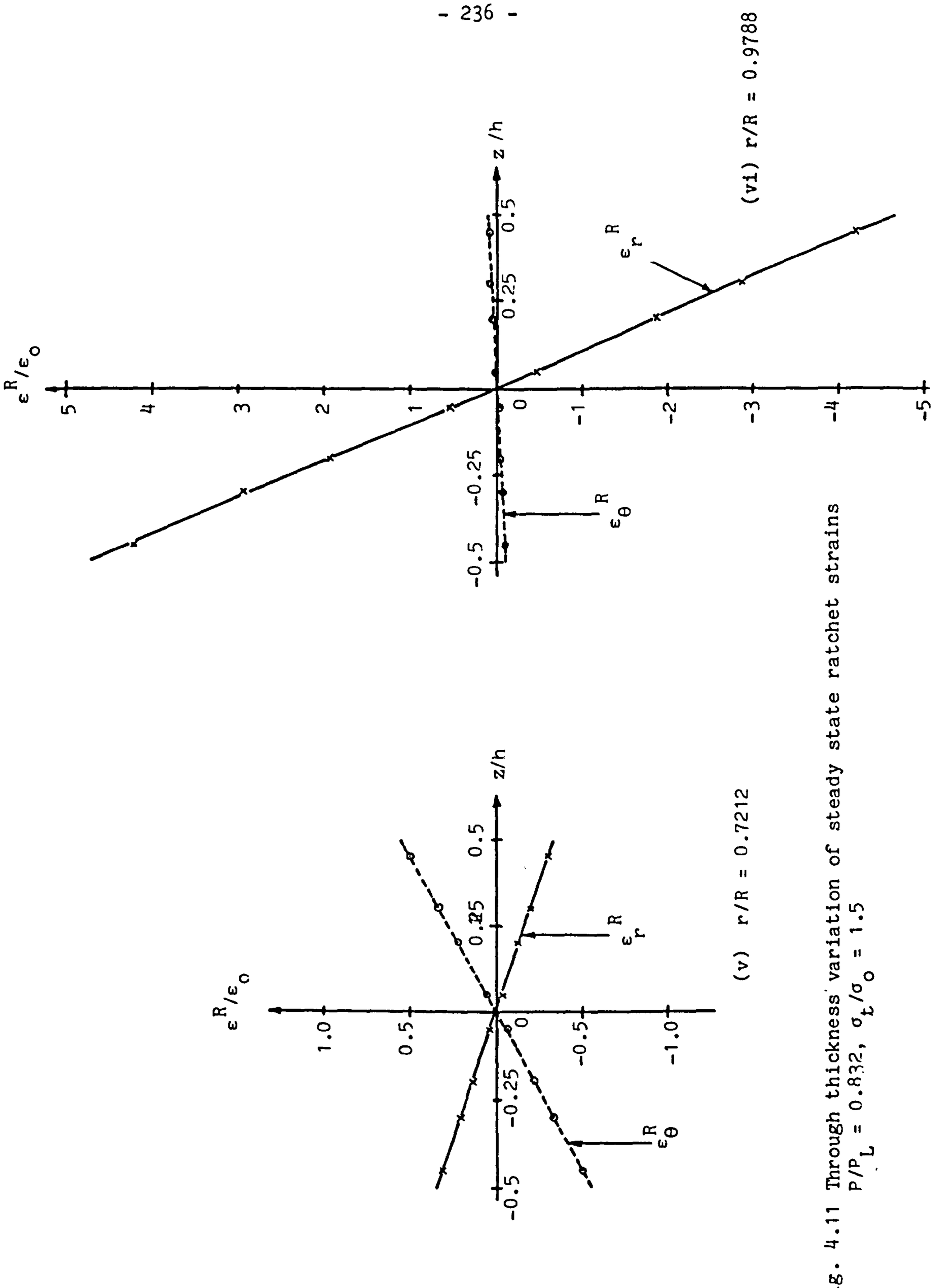

Fig. 4.11 Through thickness variation of steady state ratchet strains
$P/P_L = 0.832$, $\sigma_t/\sigma_o = 1.5$

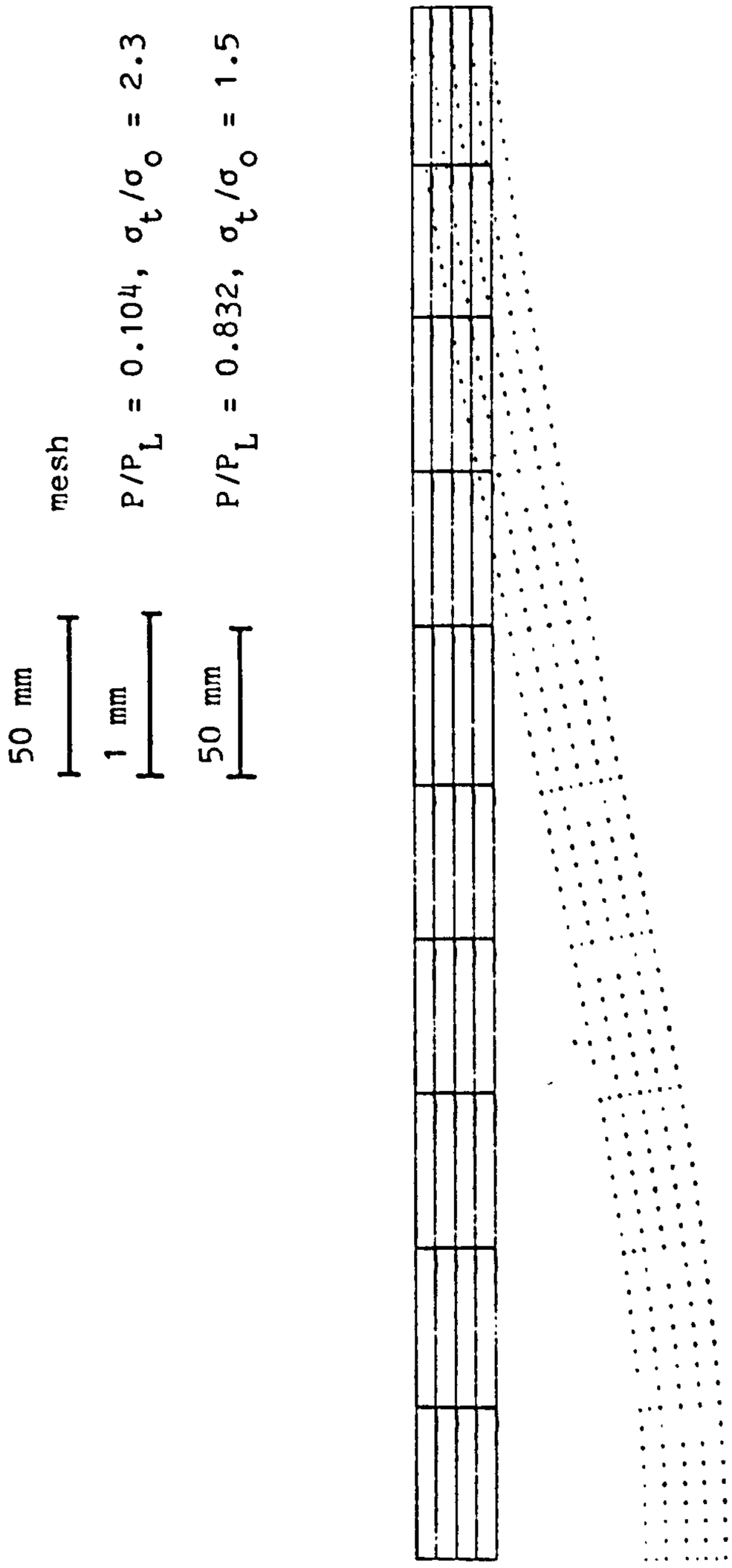

Deflection at the 10th cycle
P/P_L = 0.832, σ_t/σ_o = 1.5 and P/P_1 = 0.104, σ_t/σ_o = 2.3

Fig. 4.12

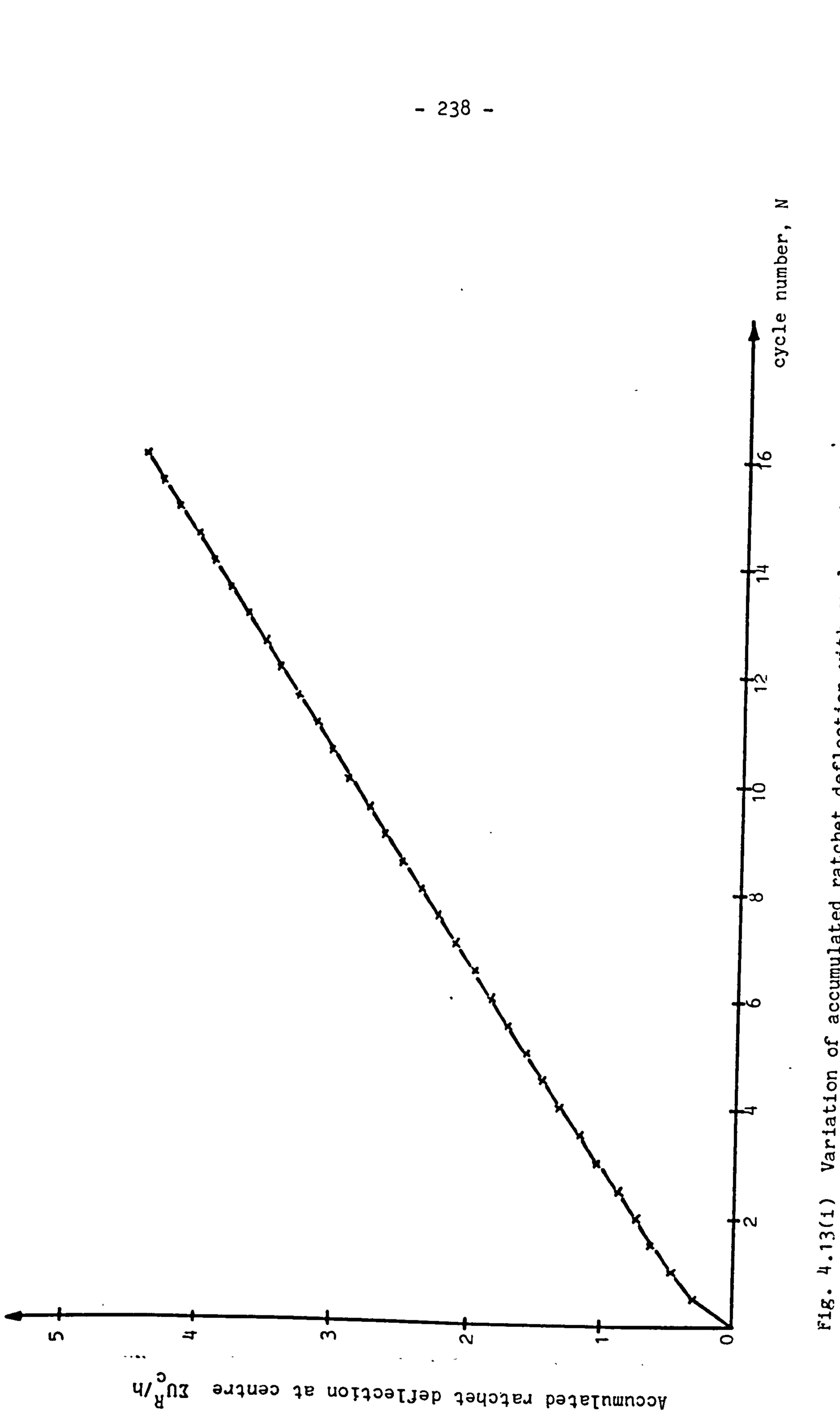
Accumulated ratchet deflection at centre $\Sigma U_c^R/h$
0
1
2
3
4
5
Variation of accumulated ratchet deflection with cycle number P/P_L = 0.832, σ_t/σ_o = 1.5
cycle number, N
2
4
6
8
10
12
14
16

Fig. 4.13(1)

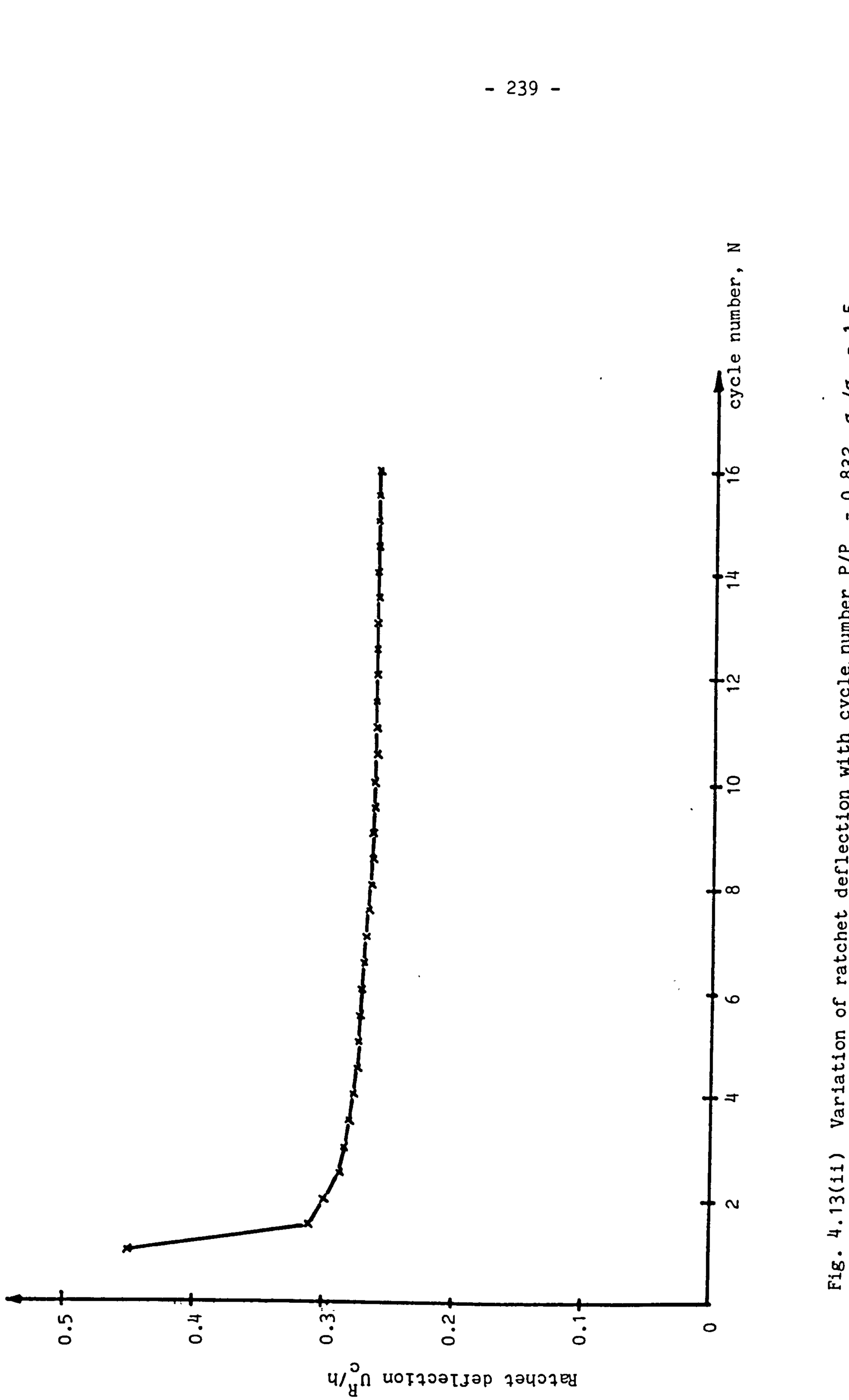

Fig. 4.13(ii) Variation of ratchet deflection with cycle number $P/P_L = 0.832$, $\sigma_t/\sigma_o = 1.5$

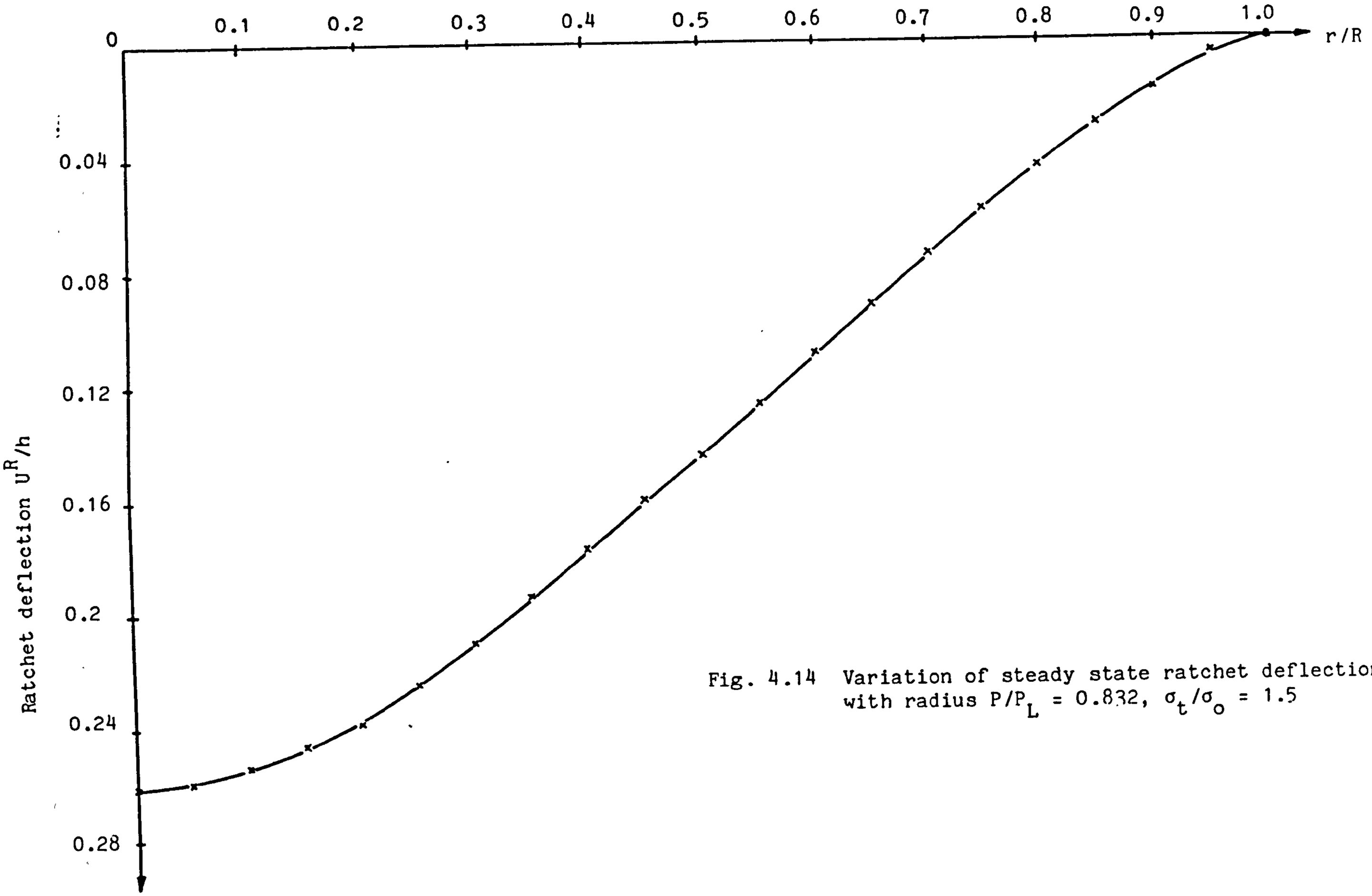

Fig. 4.14 Variation of steady state ratchet deflection with radius $P/P_L = 0.832$, $\sigma_t/\sigma_o = 1.5$

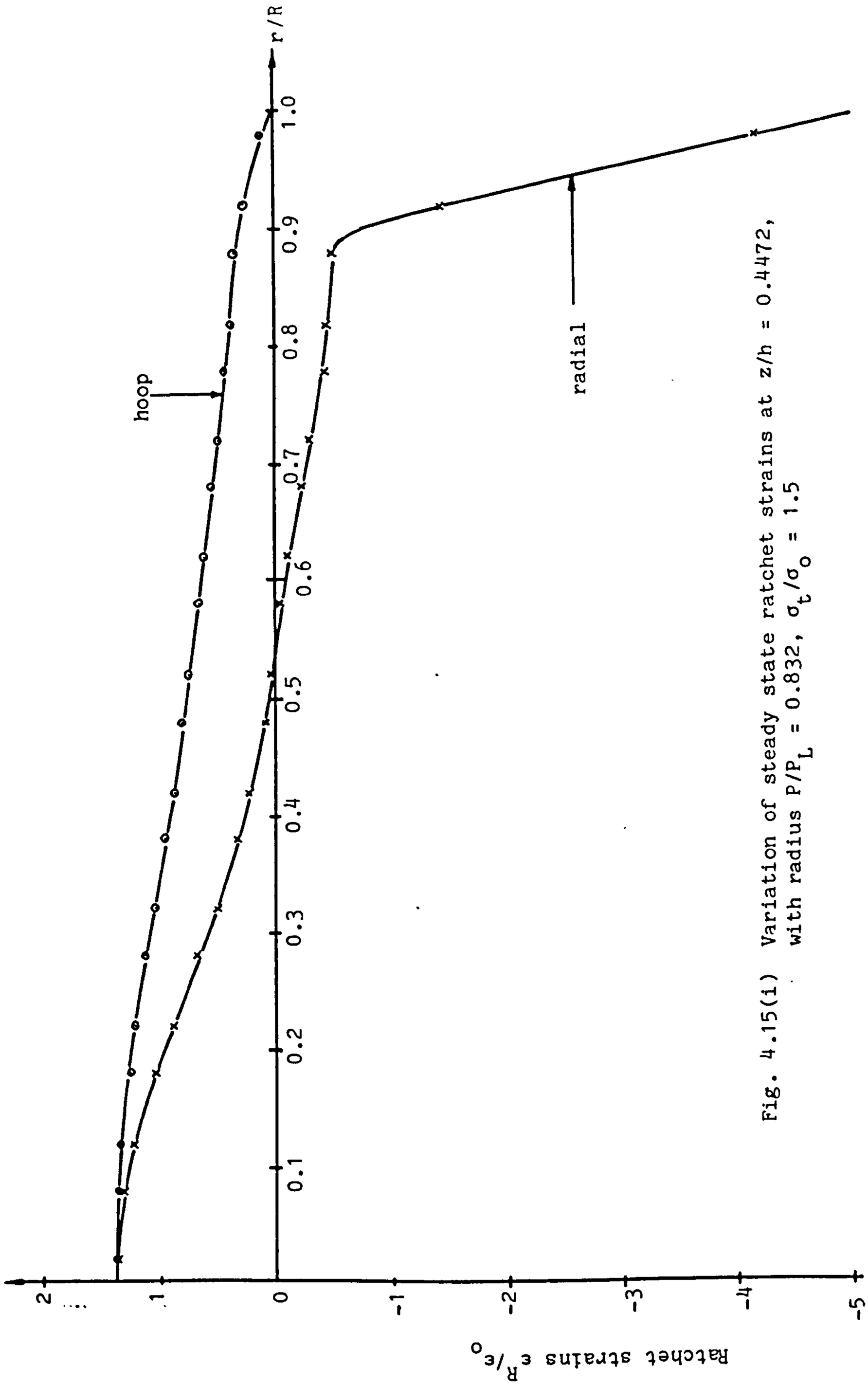

Fig. 4.15(i) Variation of steady state ratchet strains at z/h = 0.4472, with radius P/P_L = 0.832, σ_t/σ_o = 1.5

Fig. 4.15(ii) Variation of steady state ratchet strains at z/h = -0.4412 with radius. $P/P_L = 0.832$, $\sigma_t/\sigma_o = 1.5$

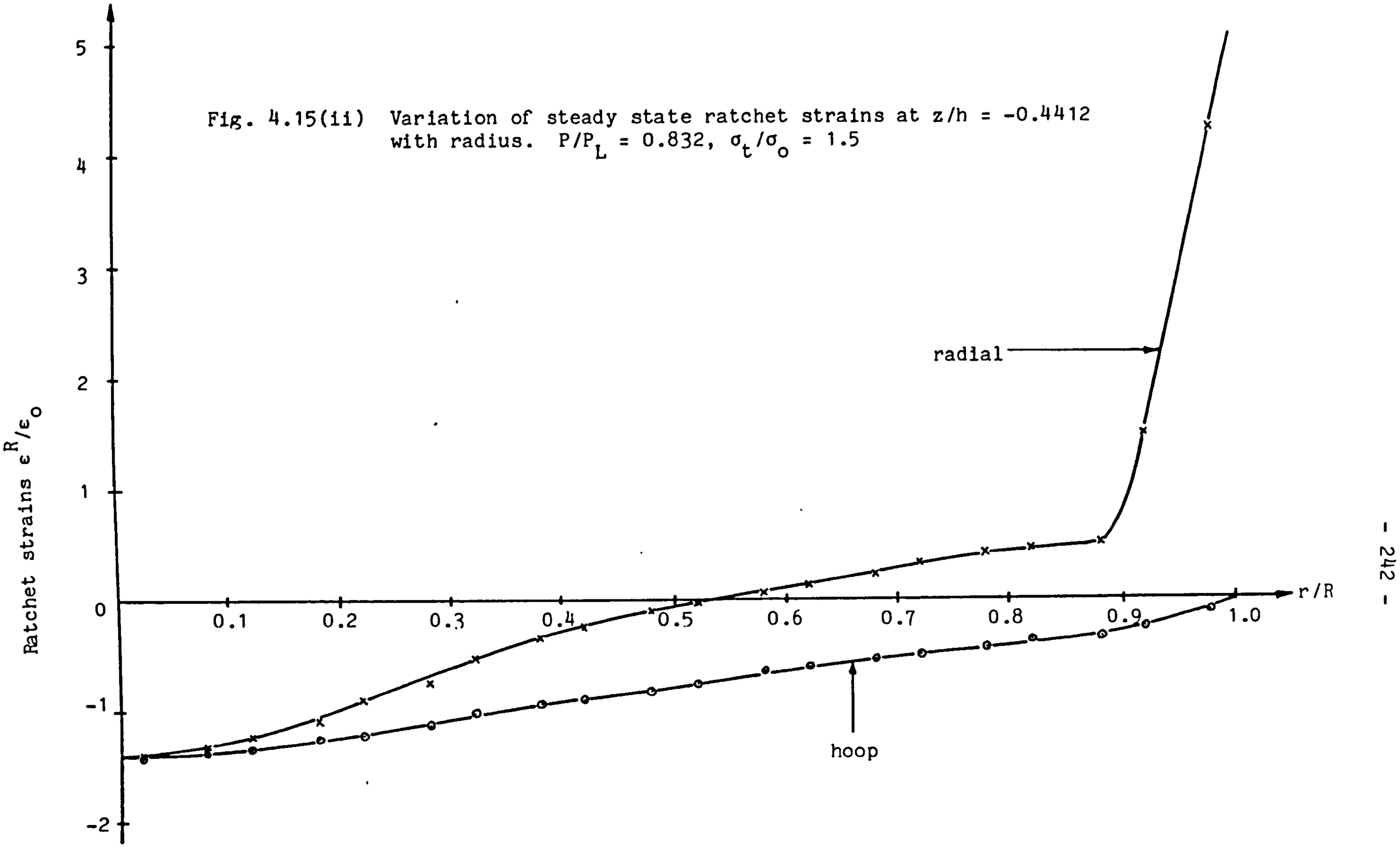

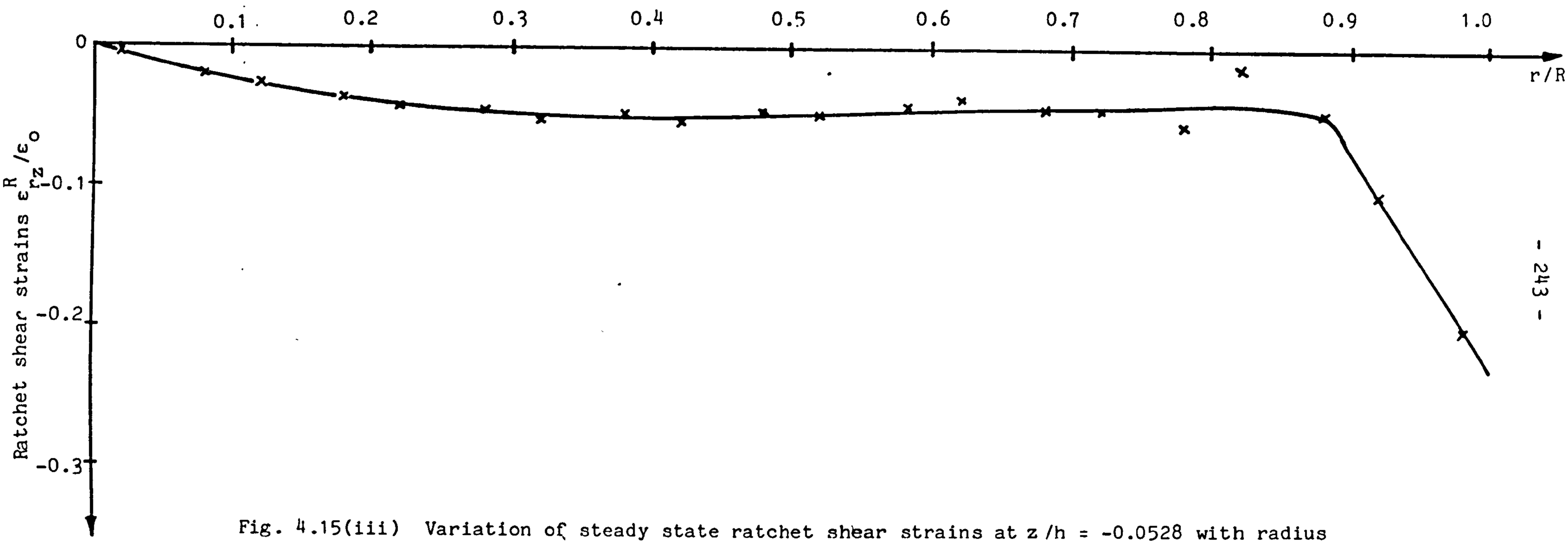

Fig. 4.15(iii) Variation of steady state ratchet shear strains at z/h = -0.0528 with radius $P/P_L = 0.832$, $\sigma_t/\sigma_o = 1.5$

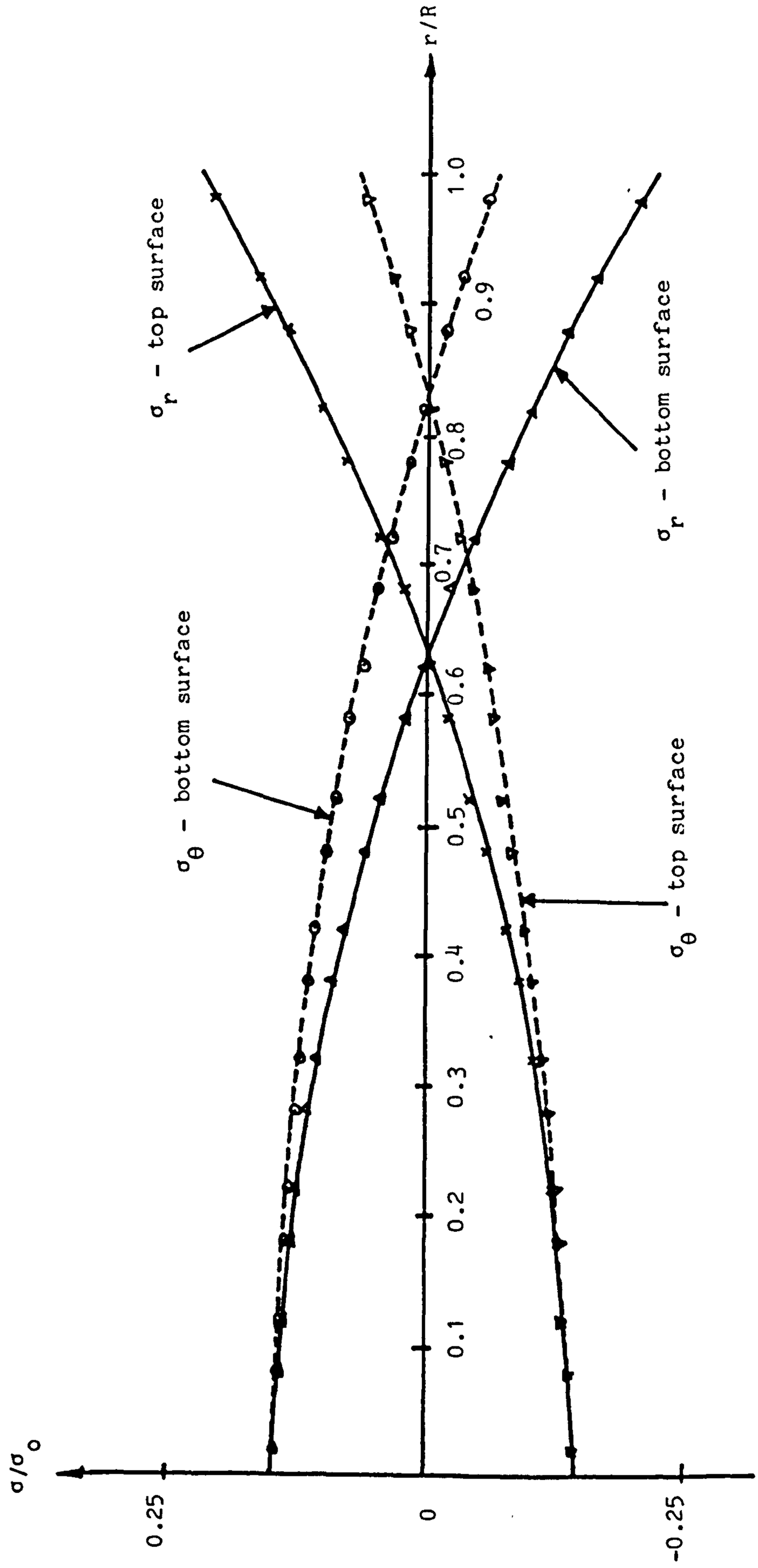

Fig. 4.16 Variation of stresses with radius for $P/P_L = 0.104$

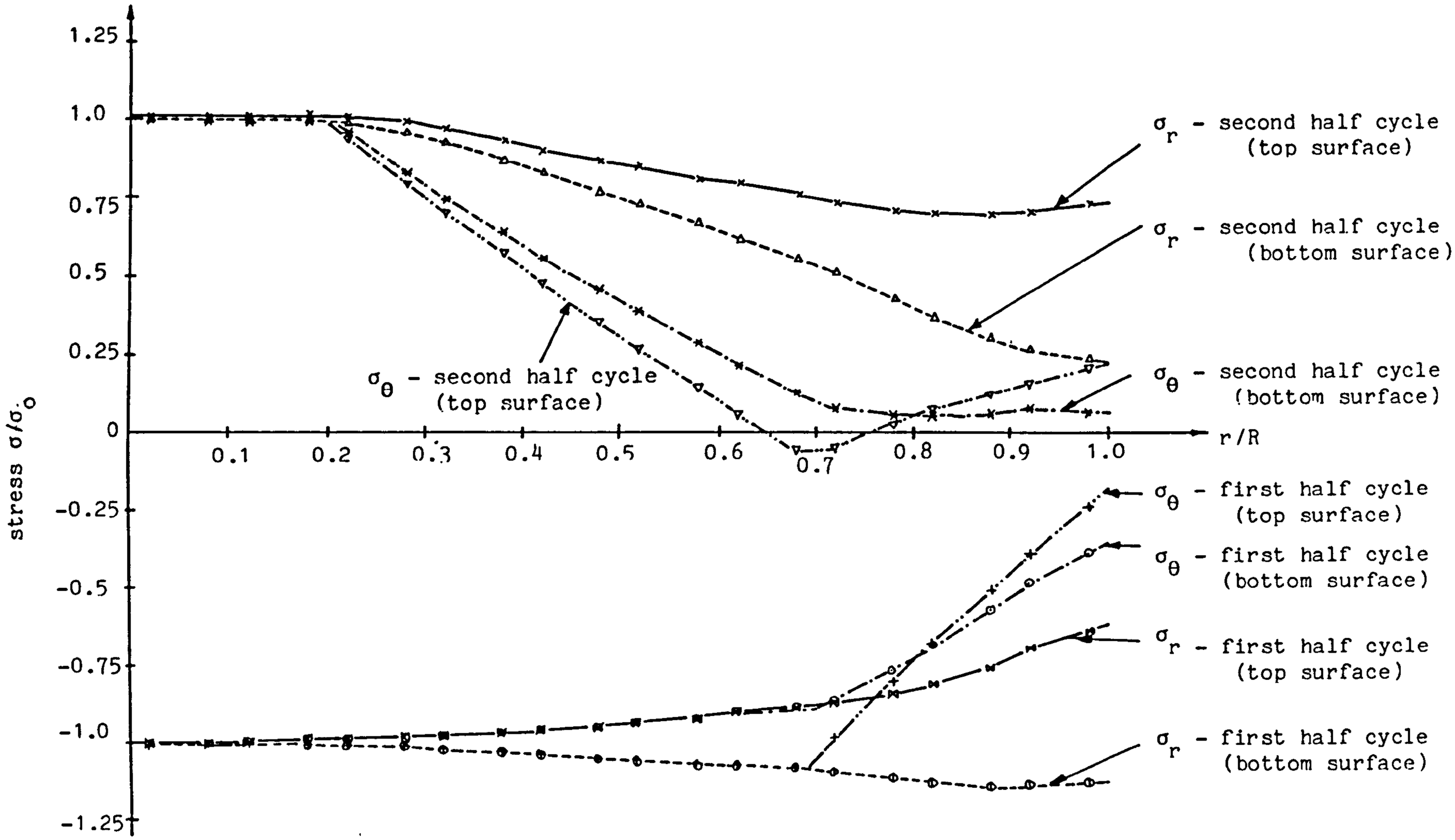

Fig. 4.17 Variation of stresses with radius

$P/P_L = 0.104$, $\sigma_t/\sigma_o = 2.3$

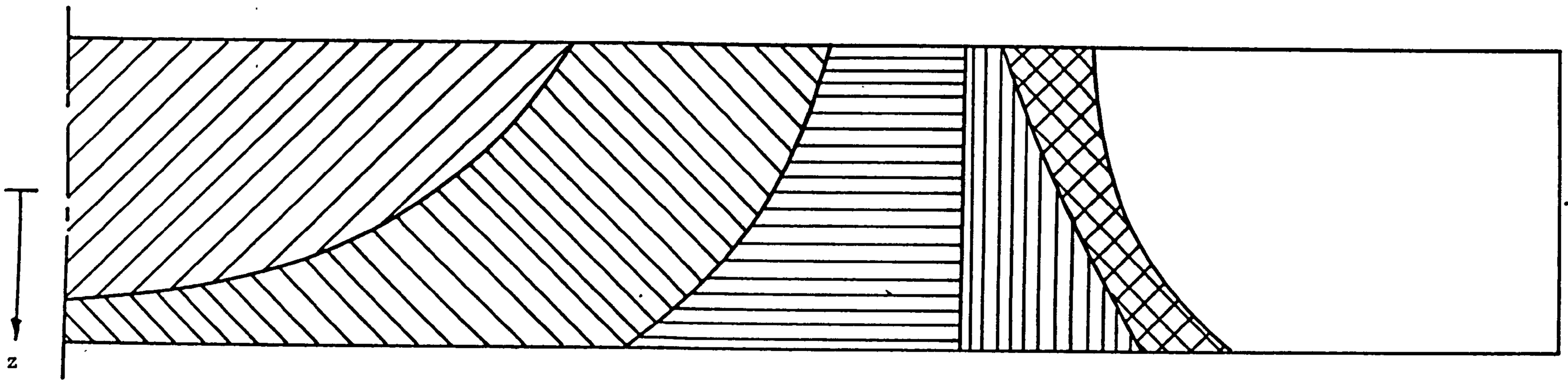

12/32 σ_t (elastic)

16/32 σ_t

20/32 σ_t (additional)

24/22 σ_t (additional)

28/32 σ_t (additional)

32/32 σ_t (additional)

Fig. 4.18(i) Growth of plastic zone during heating at the first cycle for $P/P_L = 0.104$ $\sigma_t/\sigma_o = 2.3$, (plate thickness is exaggerated).

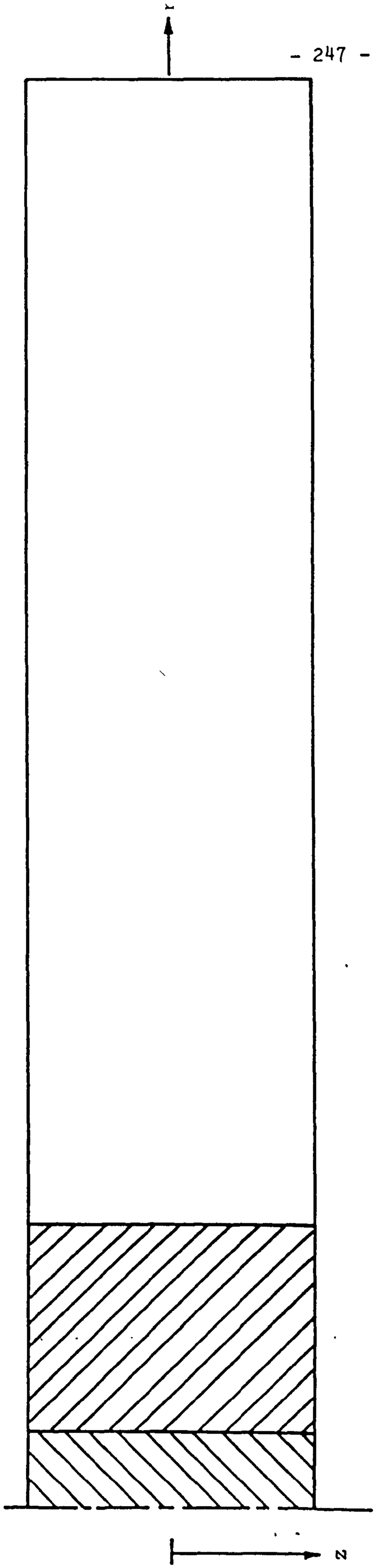

Fig. 4.18(ii) Growth of plastic zone during cooling in the first cycle and at the subsequent cycles for $P/P_L = 0.104$; $\sigma_t/\sigma_o = 2.3$ (plate thickness is exaggerated)

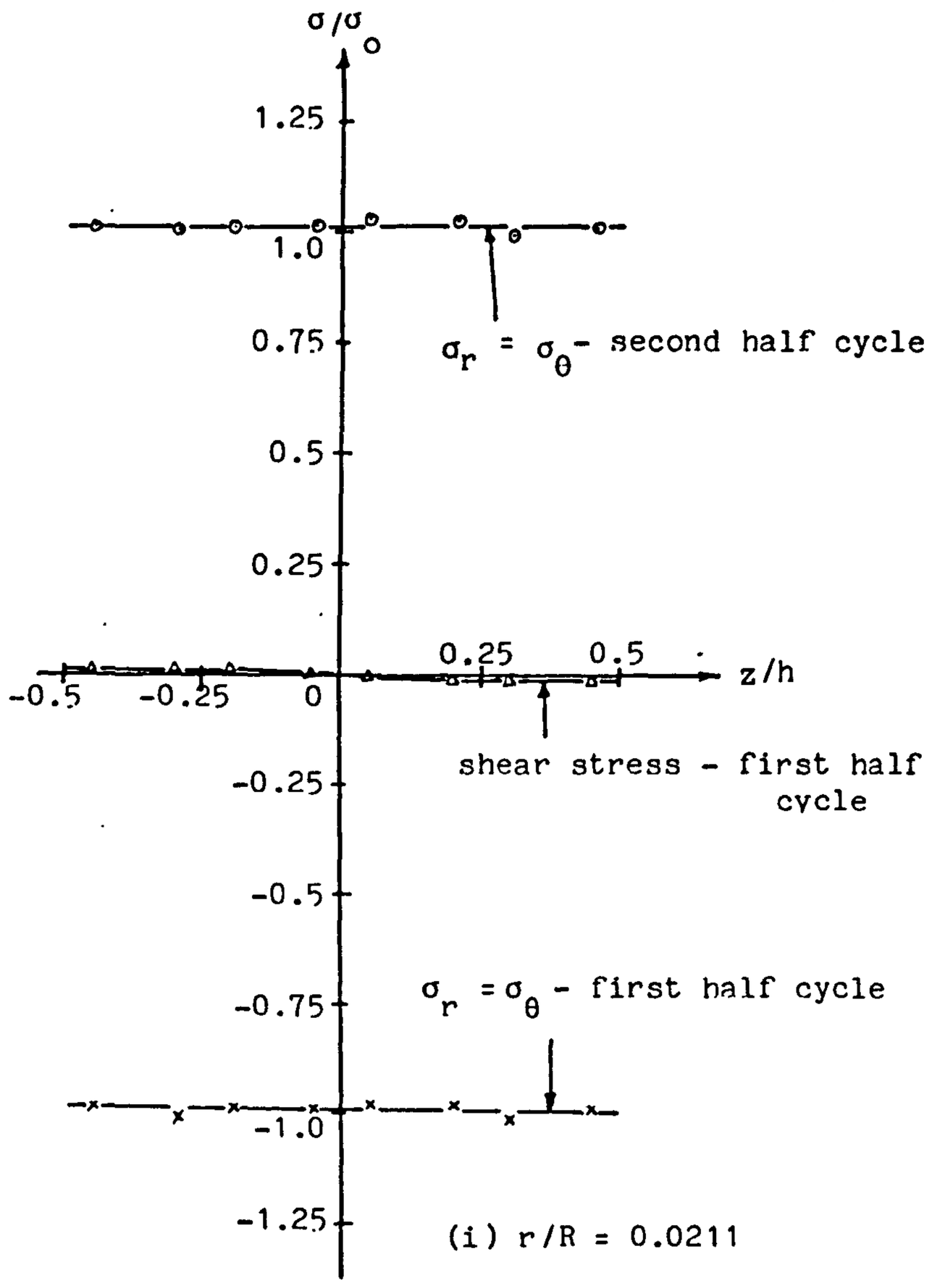

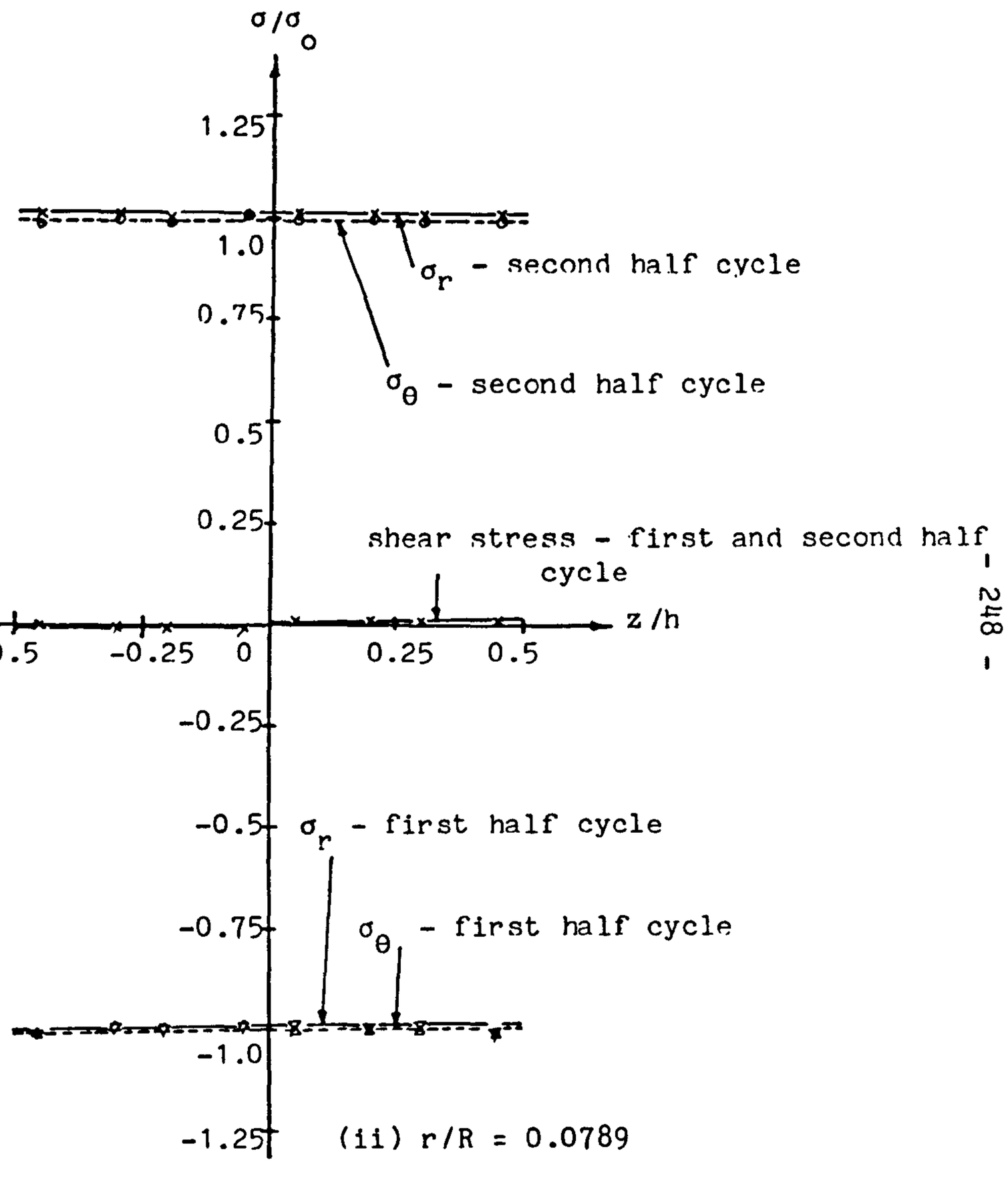

Fig. 4.19 Through thickness variation of stresses. $P/P_L = 0.104$, $\sigma_t/\sigma_o = 2.3$

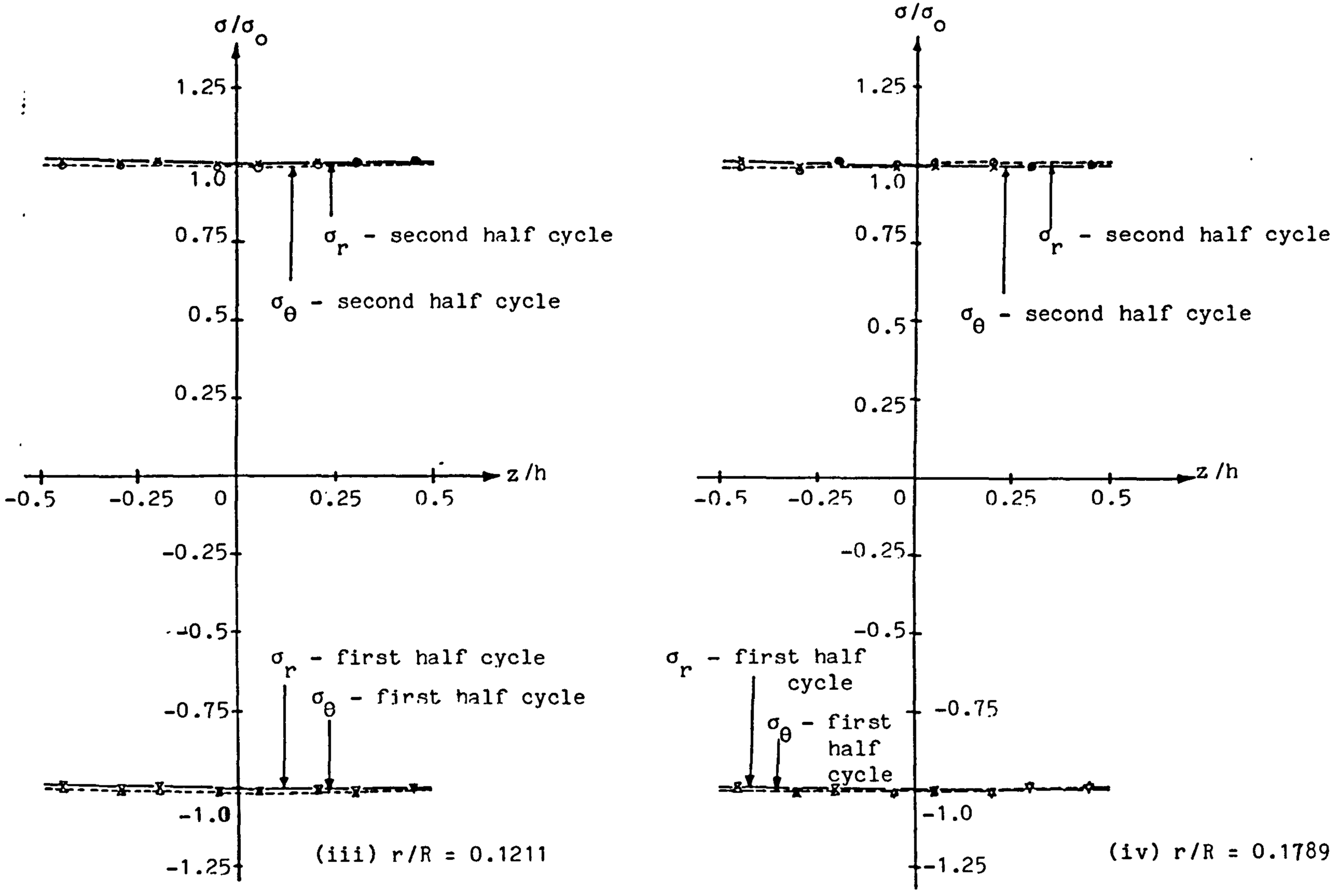

Fig. 4.19 Through thickness variation of stresses. $P/P_L = 0.104$, $\sigma_t/\sigma_o = 2.3$

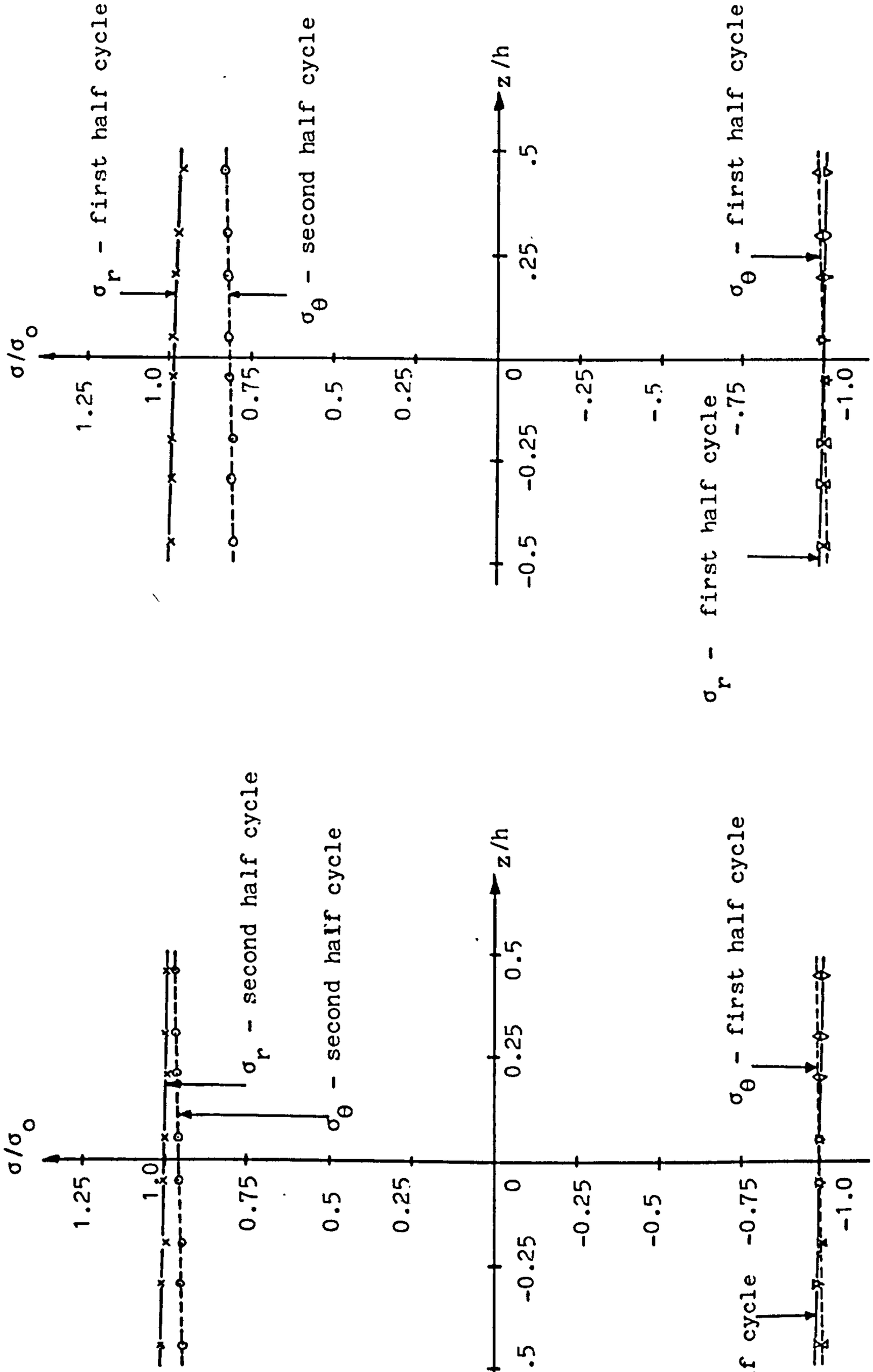

Fig. 4.19 Through thickness variation of stresses. $P/P_L = 0.104$, $\sigma_t/\sigma_o = 2.3$

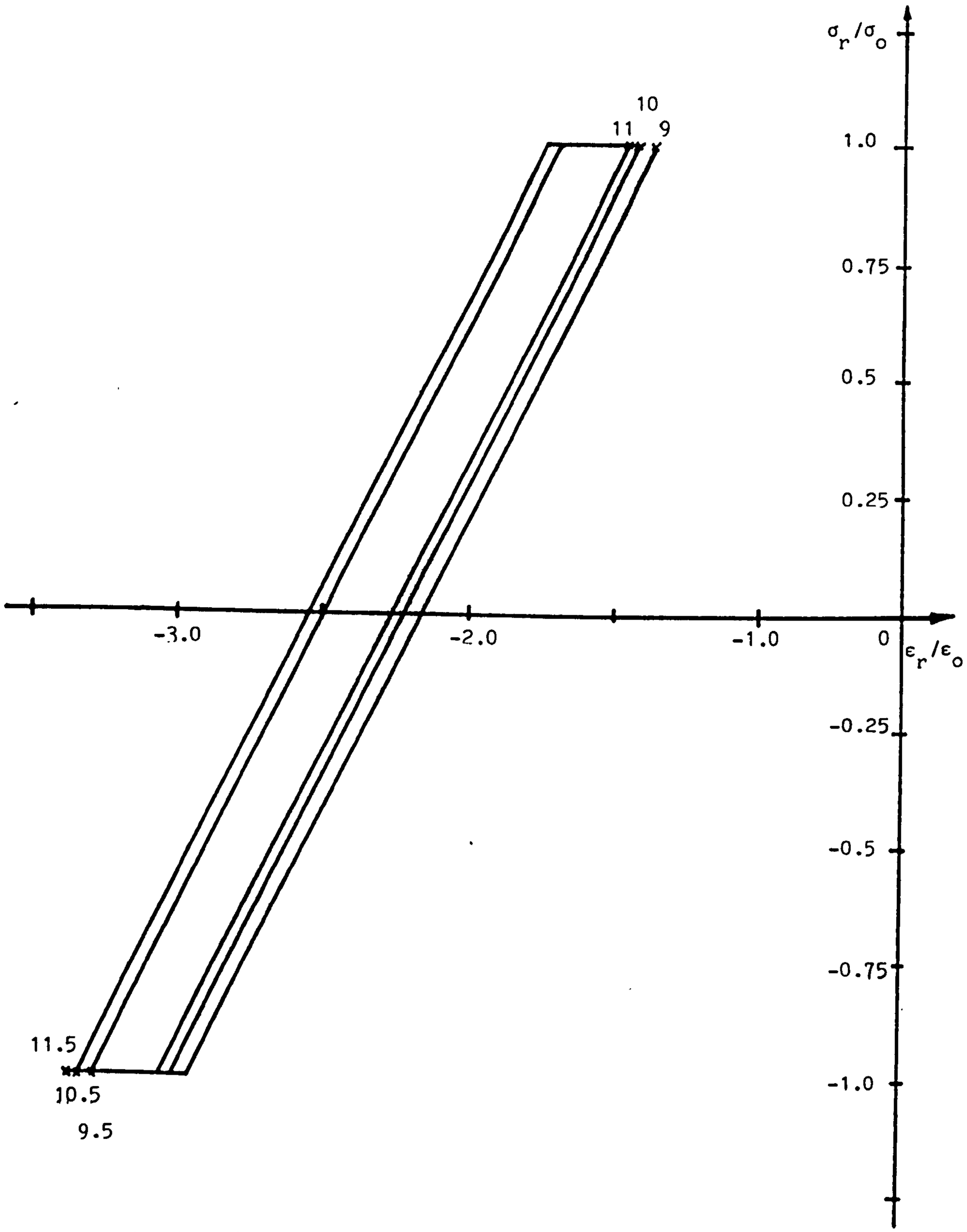

Fig. 4.20 Stress strain history at the plate centre and z/h = -0.447, P/P_L = 0.104, σ_t/σ_o = 2.3 showing a cyclic plasticity

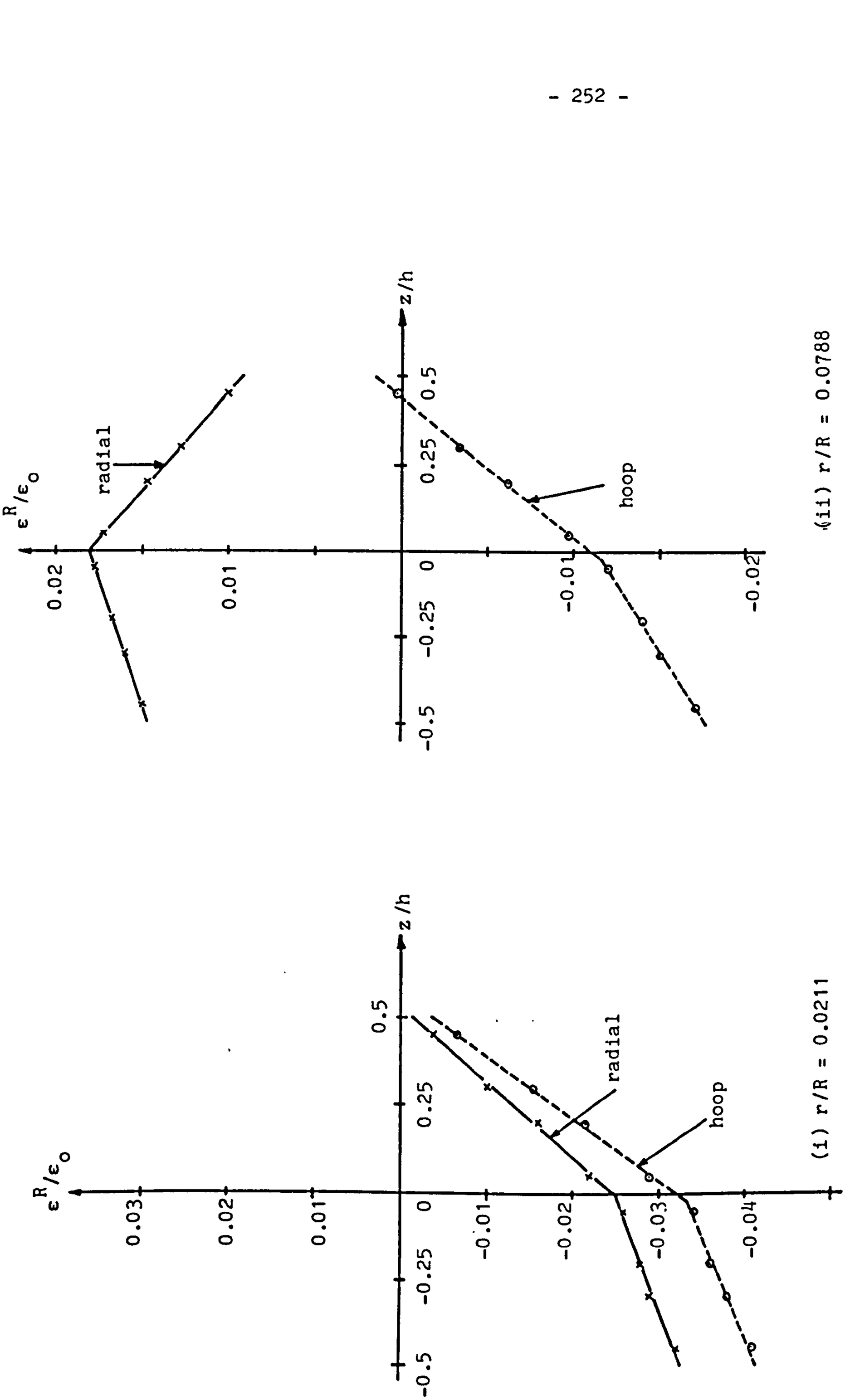

Fig. 4.21 Through thickness distribution of steady state ratchet strains for $P/P_L = 0.104$, $\sigma_t/\sigma_o = 2.3$

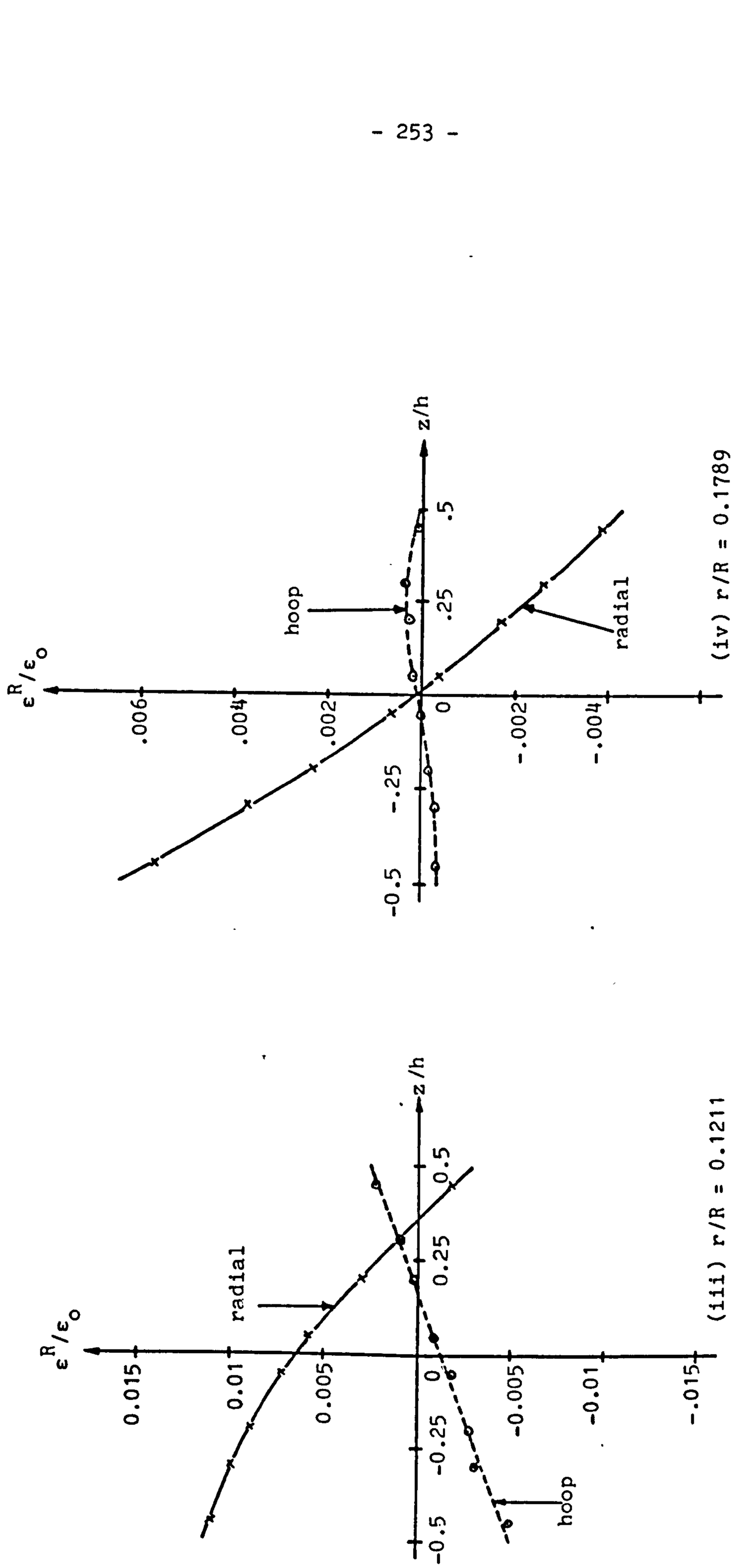

Fig. 4.21 Through thickness variation of steady state ratchet strains for $P/P_L = 0.104$, $\sigma_t/\sigma_o = 2.3$

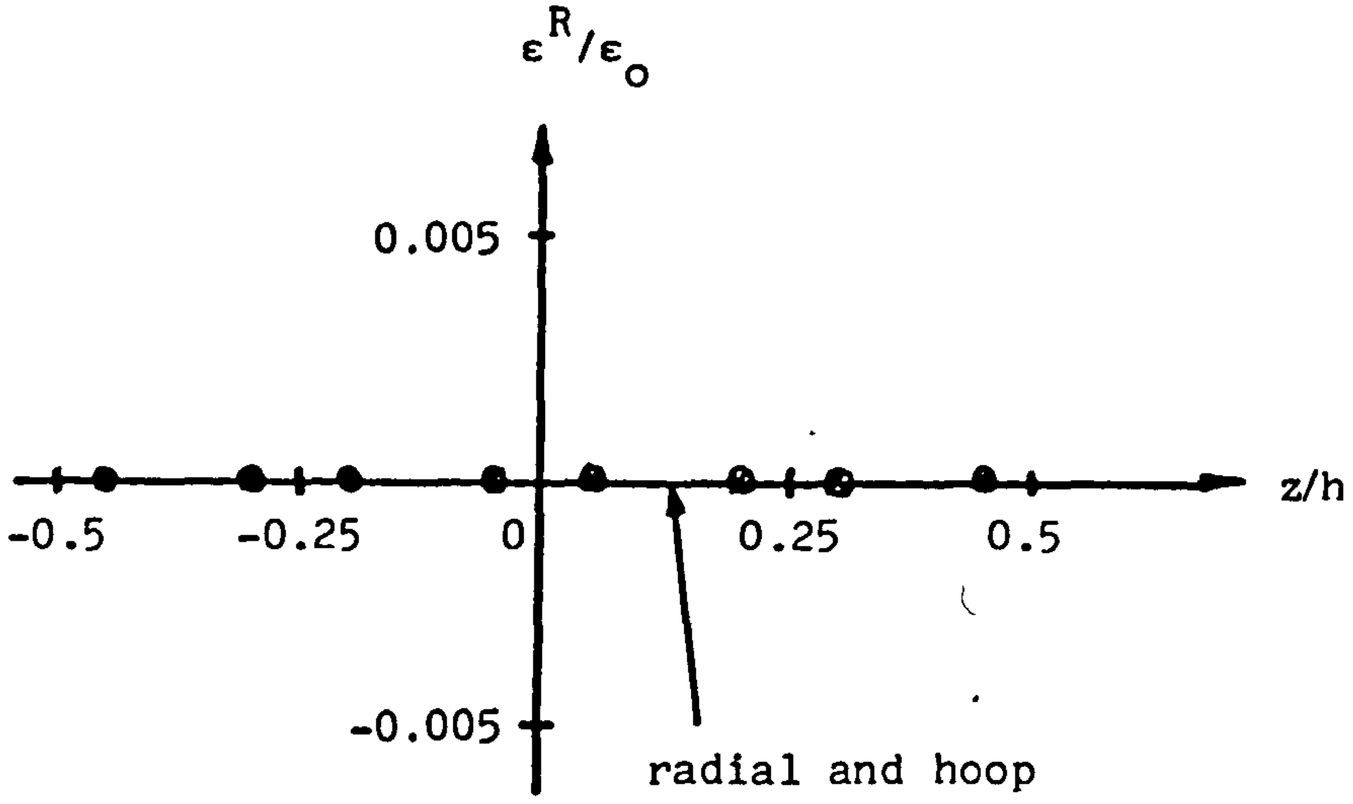

(v) r/R = 0.2212

Fig. 4.21 Through thickness variation of steady state ratchet strains $P/P_L = 0.104$, $\sigma_t/\sigma_o = 2.3$

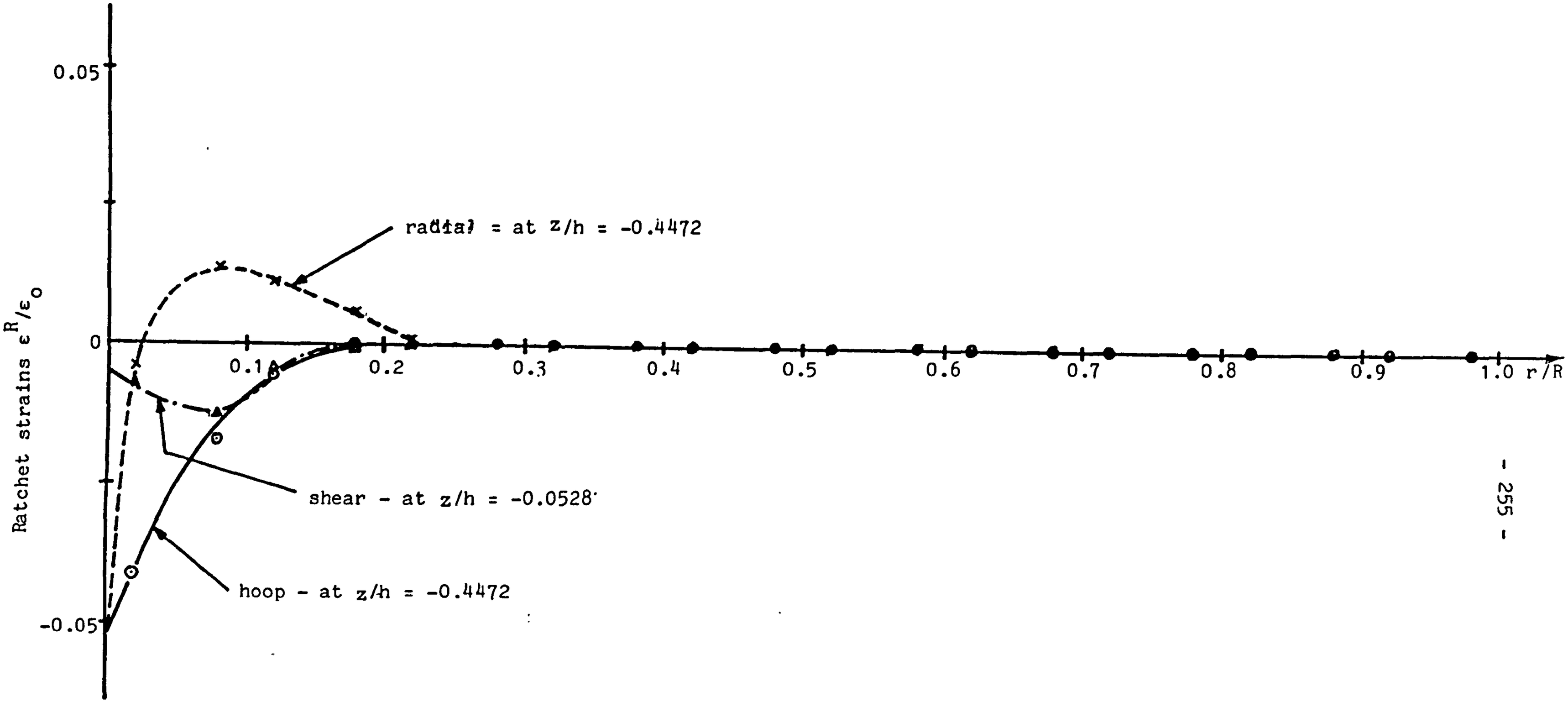

Fig. 4.22 Variation of steady state ratchet strains with radius $P/P_L = 0.104$, $\sigma_t/\sigma_o = 2.3$

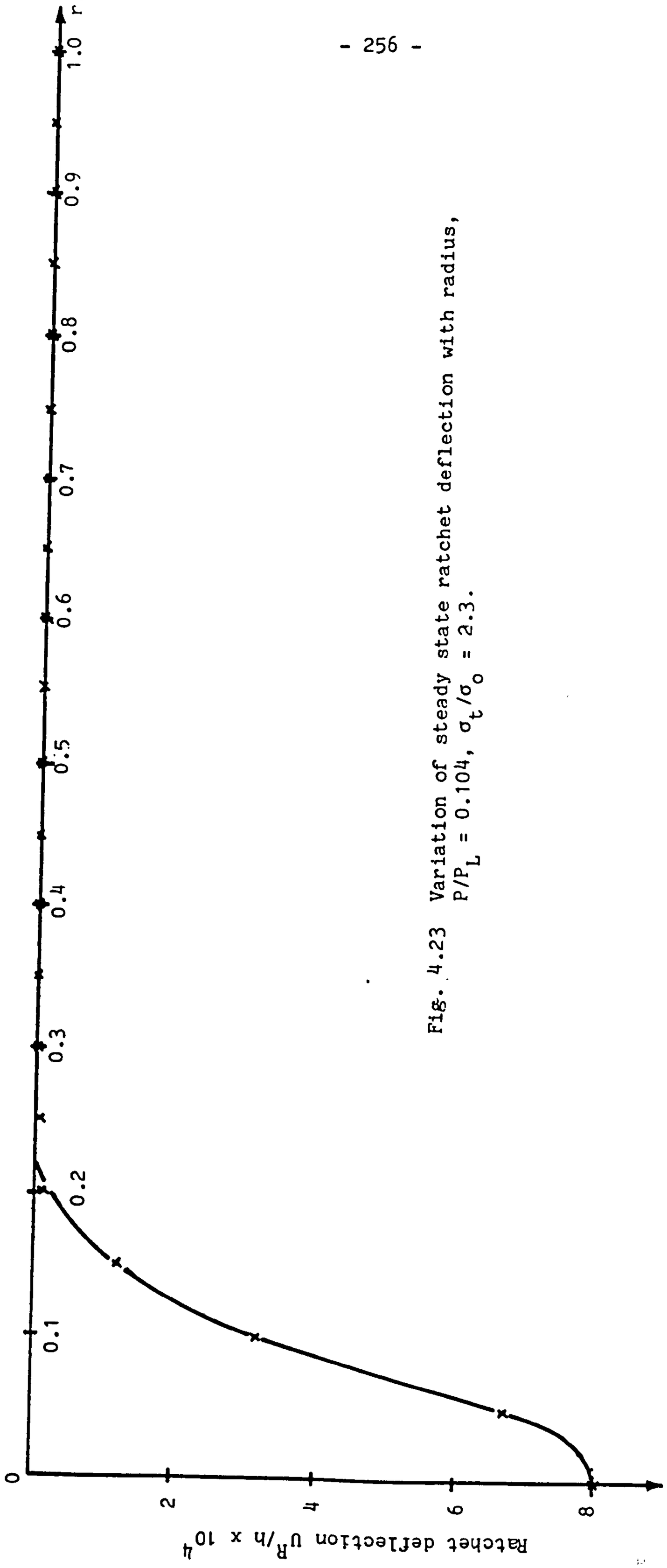

Fig. 4.23 Variation of steady state ratchet deflection with radius, $P/P_L = 0.104$, $\sigma_t/\sigma_o = 2.3$.

Fig. 4.24(i) Variation of accumulated ratchet deflection with cycle number $P/P_L = 0.104$, $\sigma_t/\sigma_o = 2.3$

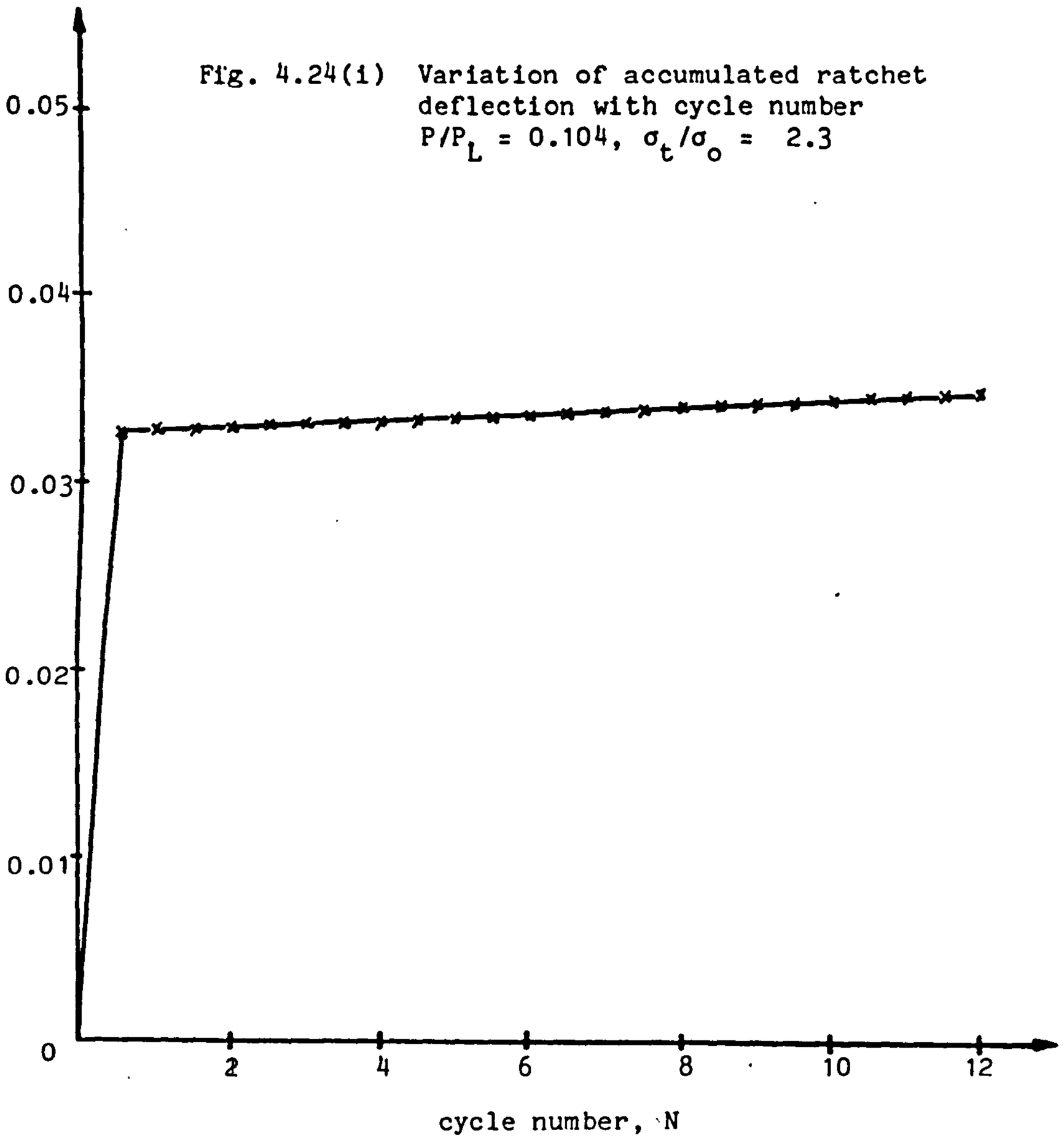

Fig. 4.24(ii) Variation of ratchet deflection with cycle number, $P/P_L = 0.104$, $\sigma_t/\sigma_o = 2.3$

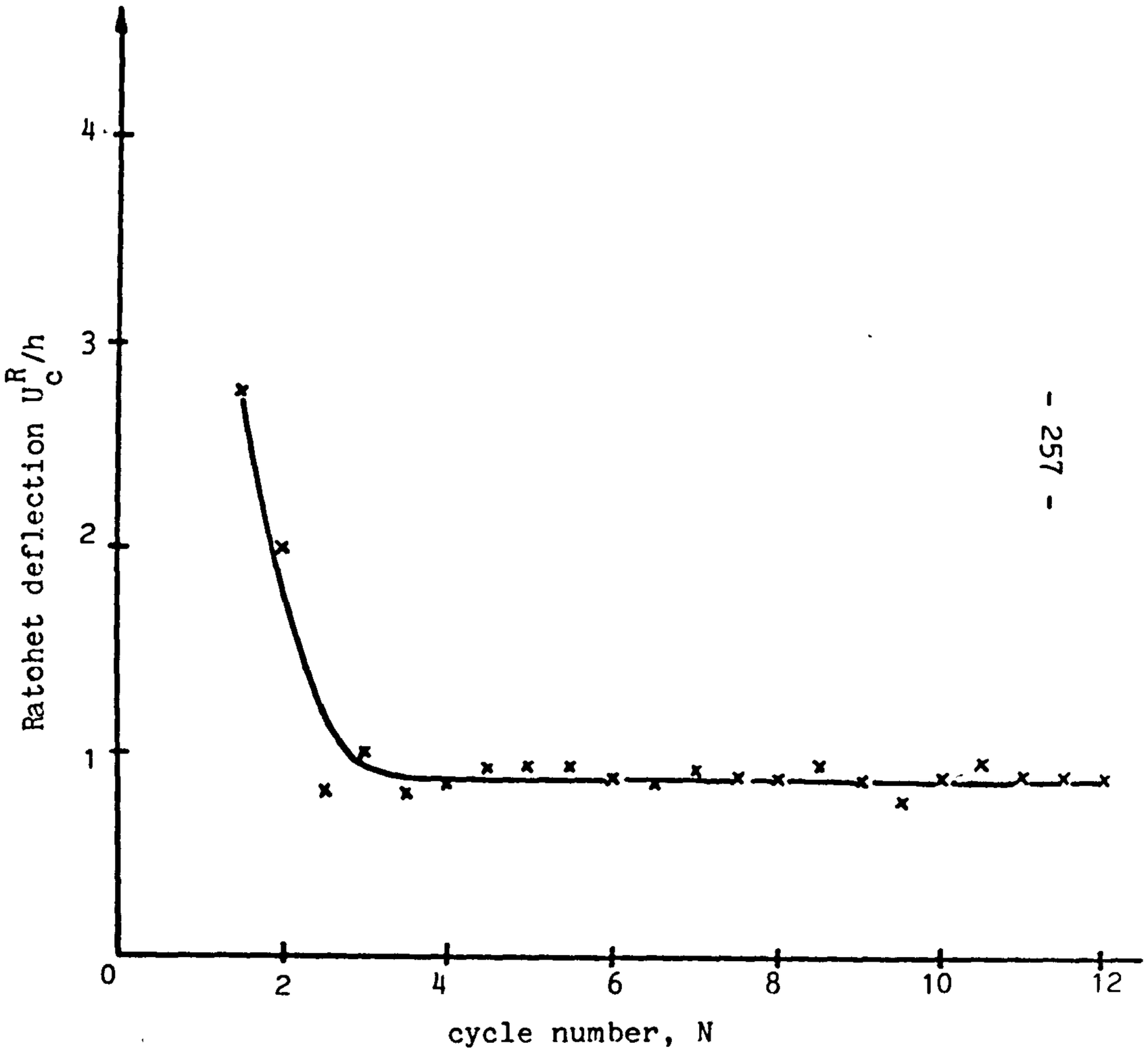

Fig. 4.25(i) Variation of ratchet deflection with σ_t/σ_o at constant P/P_L

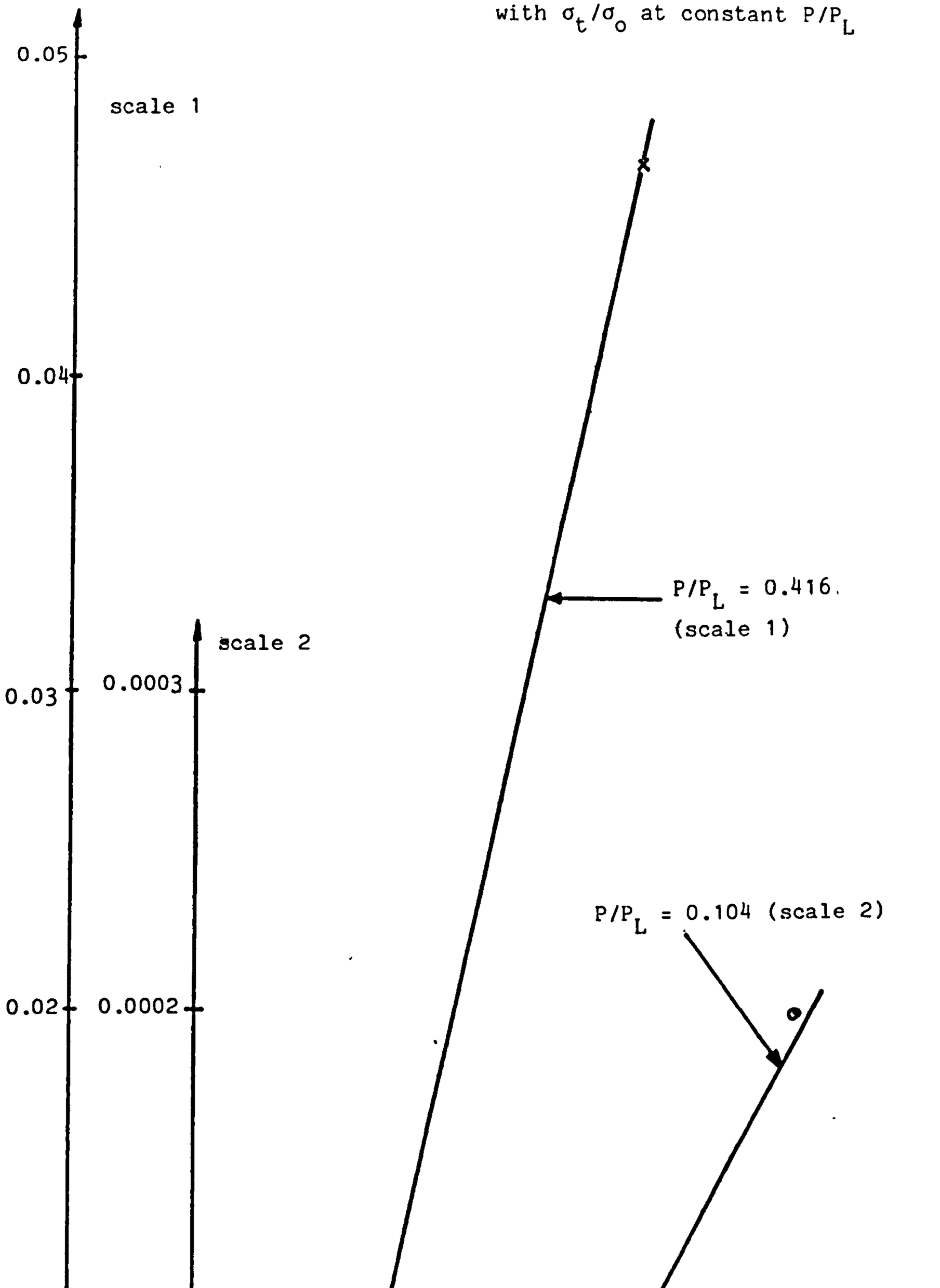

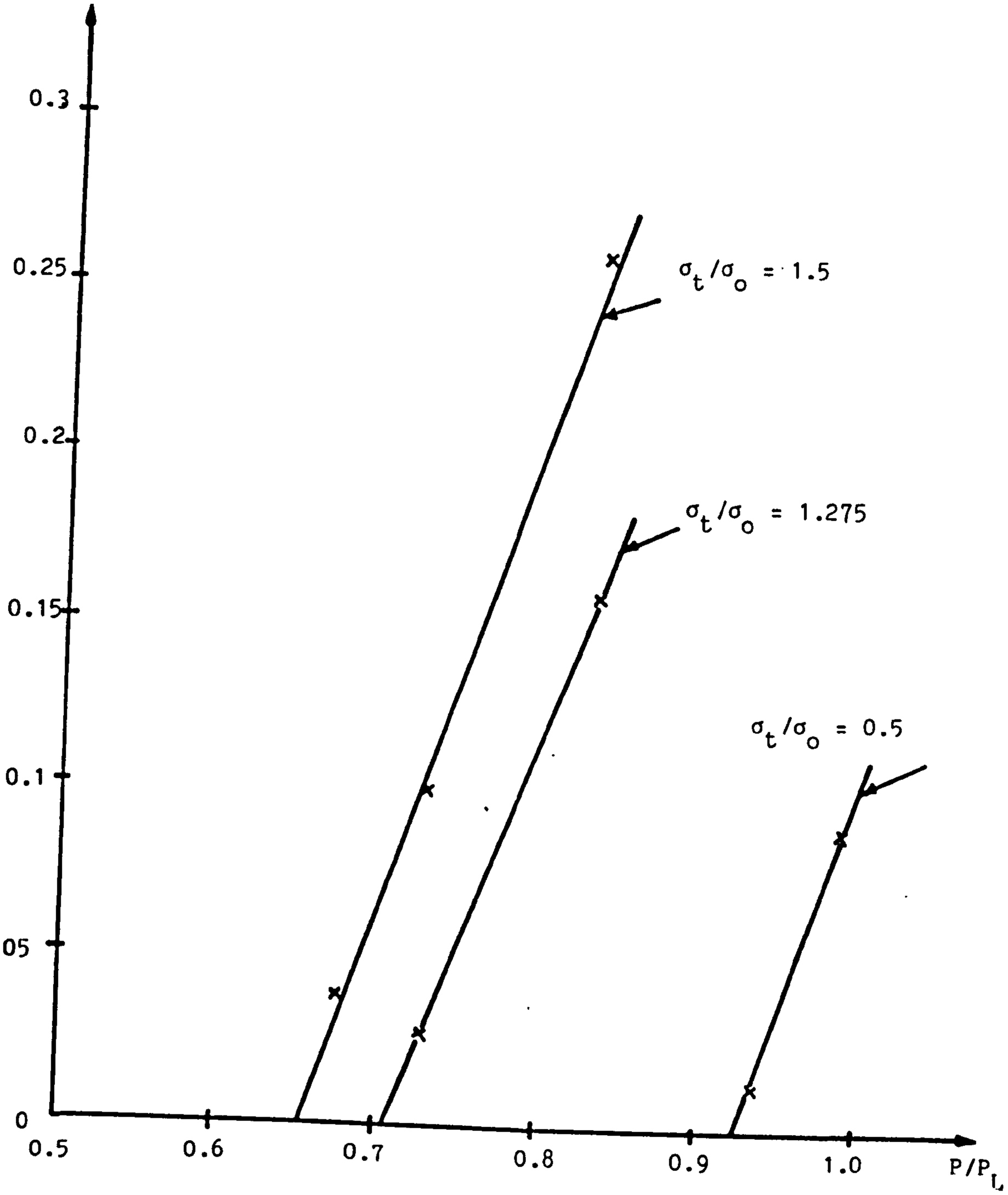

Fig. 4.25(ii) Variation of ratchet deflection with P/P_L constant at σ_t/σ_o

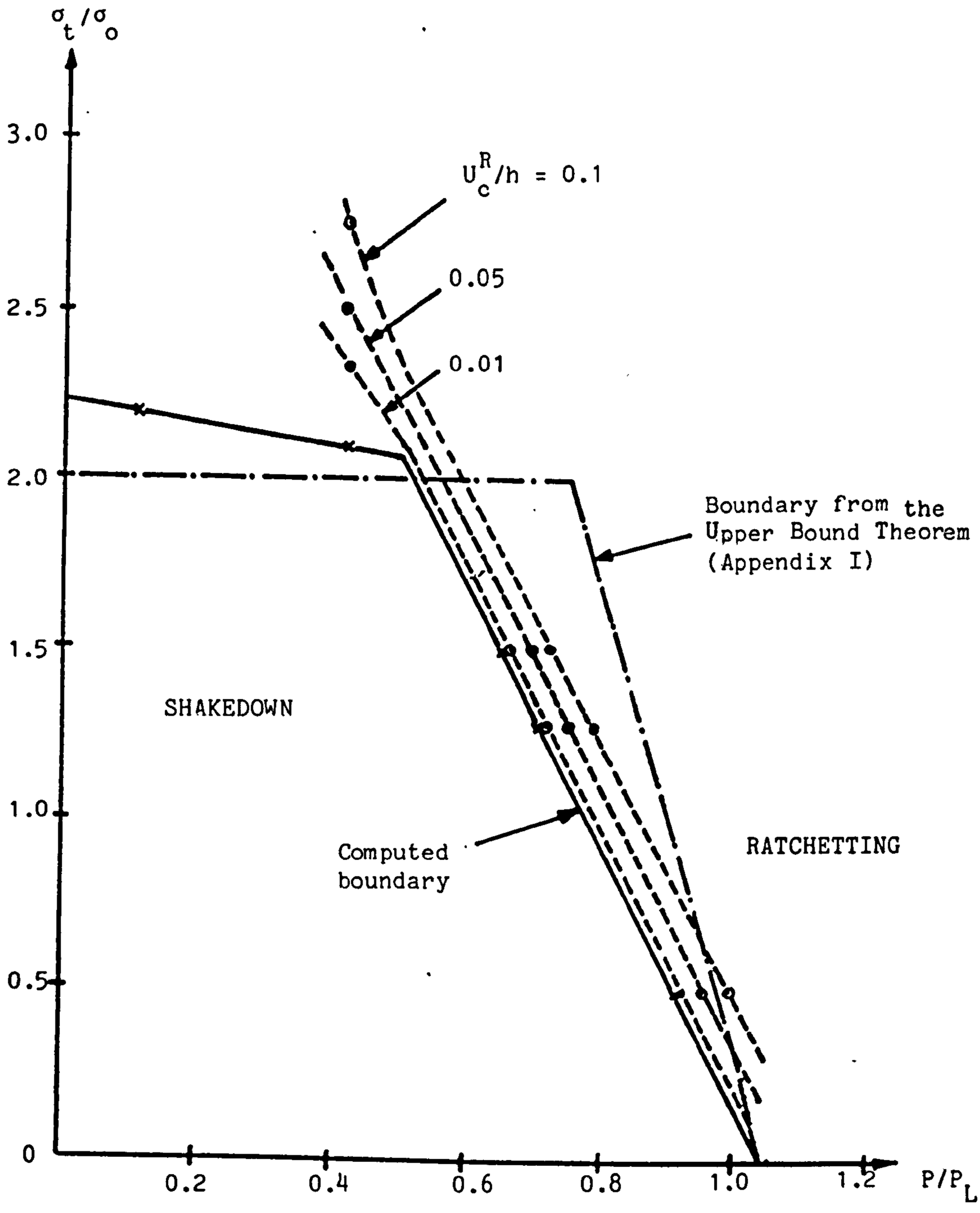

Fig. 4.26 Shakedown/ratchetting boundary and contours of constant ratchet deflection for a clamped circular plate.

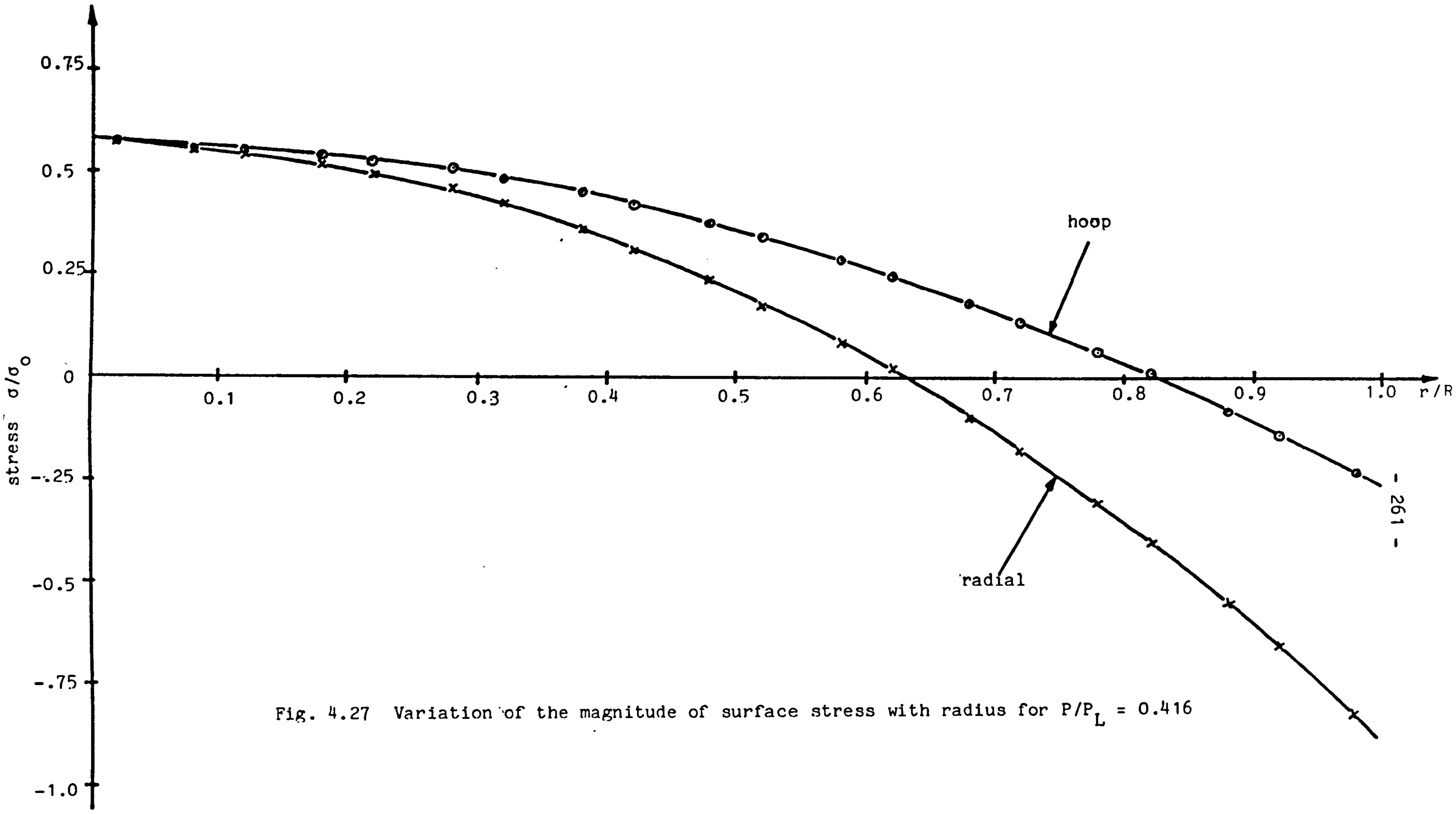

Fig. 4.27 Variation of the magnitude of surface stress with radius for $P/P_L = 0.416$

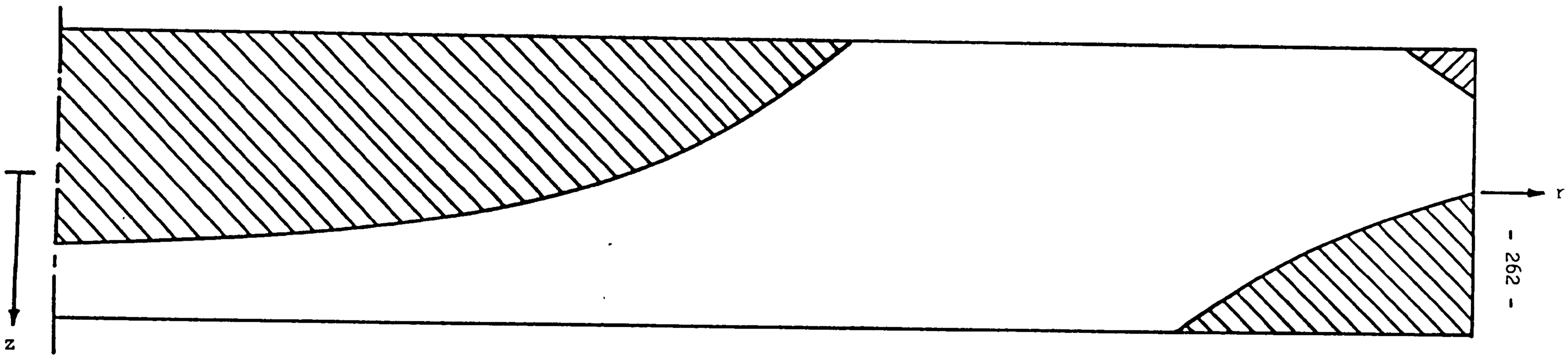

first half cycle

second half cycle

Fig. 4.28 Extent of plastic zone during the first cycle for $P/P_L = 0.416$, $\sigma_t/\sigma_o = 1.275$, (Plate thickness is exaggerated).

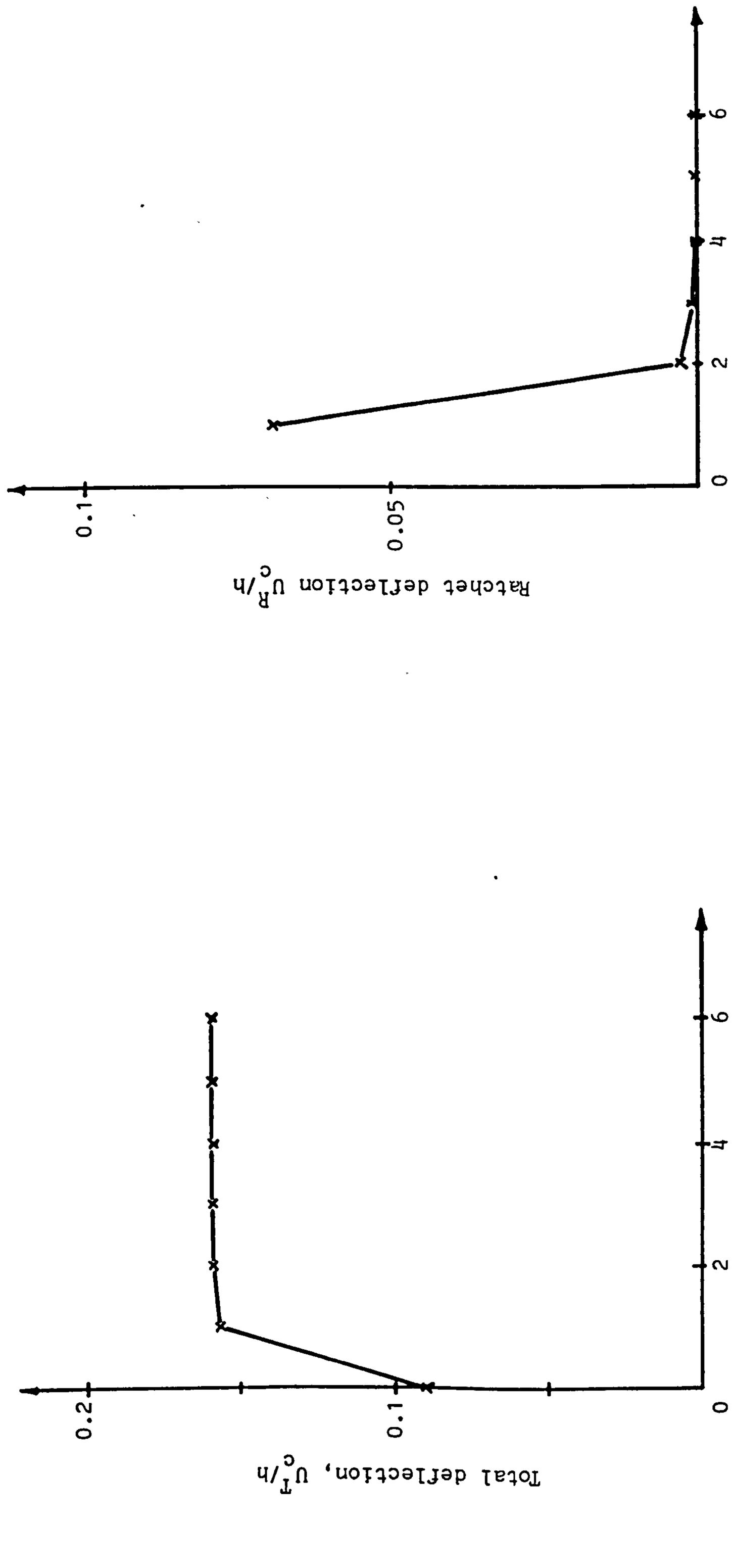

Fig. 4.29 Variation of total deflection and ratchet deflection with cycle number for $P/P_L = 0.416$, $\sigma_t/\sigma_o = 1.275$

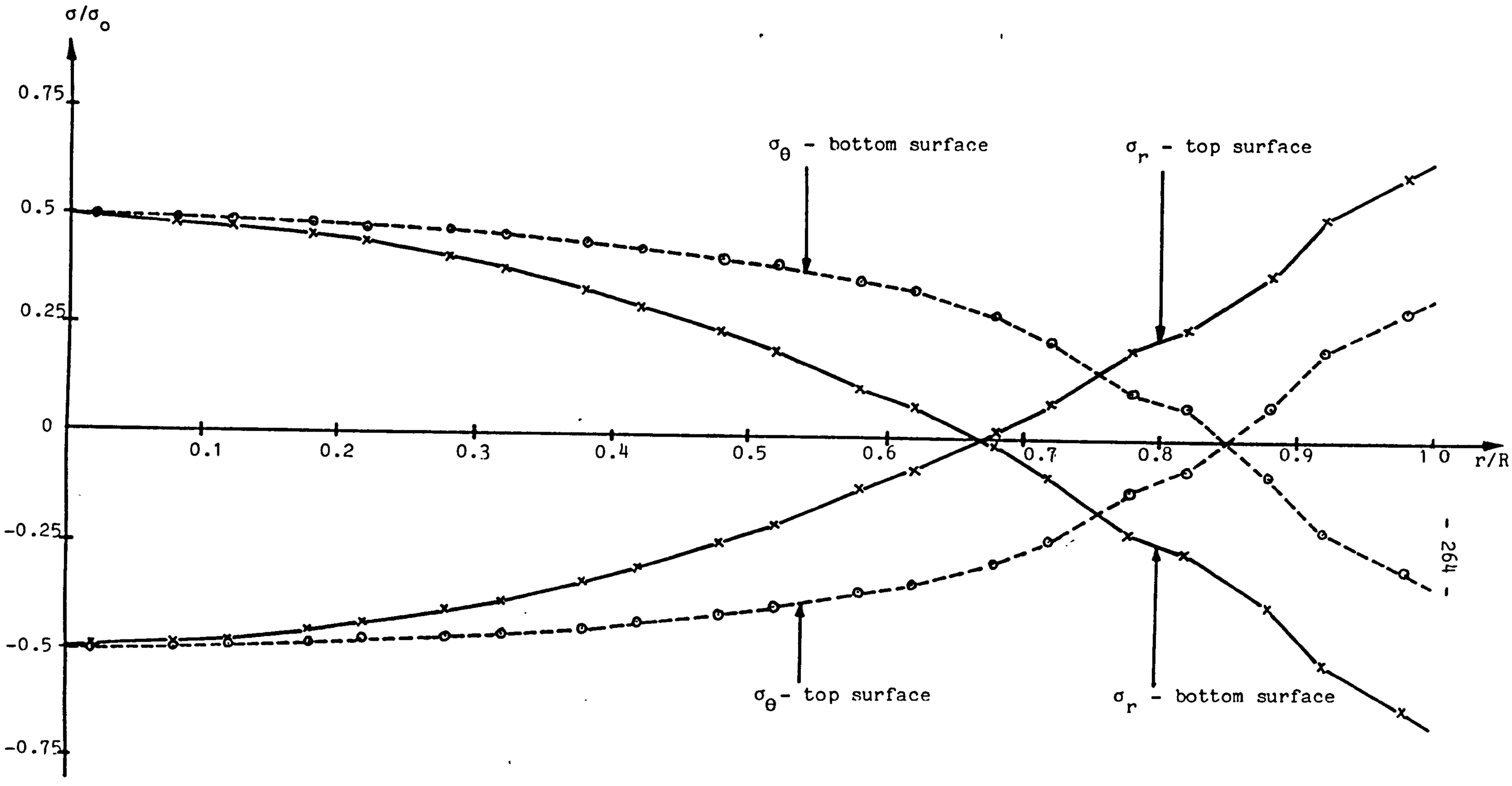

Fig. 4.30(i) Variation of stationary stress with radius for $P/P_L = 0.416$, $\sigma_t/\sigma_o = 1.275$, $n = 3$.

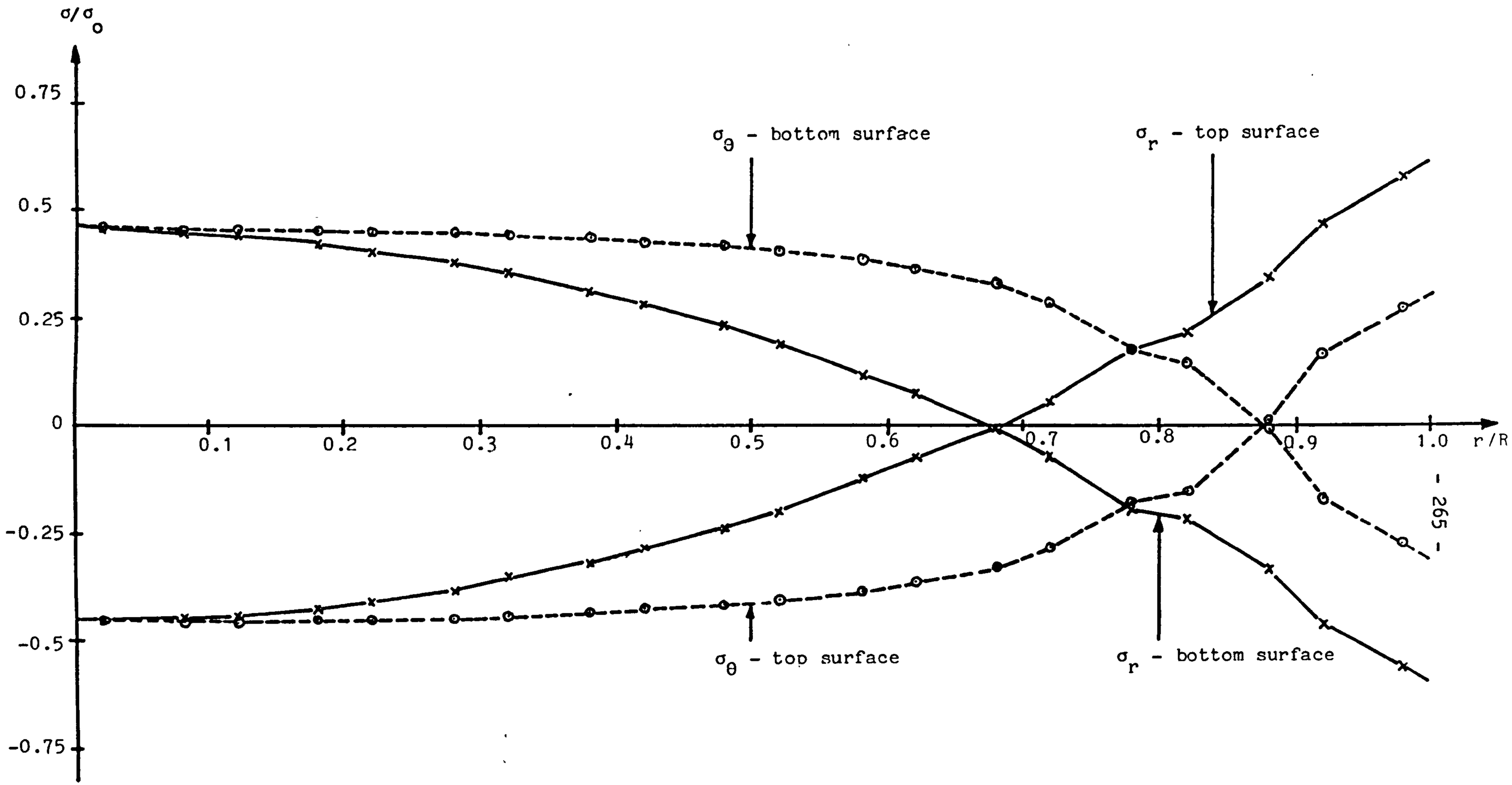

Fig. 4.30(ii) Variation of stationary stress with radius for $P/P_L = 0.416$, $\sigma_t/\sigma_o = 1.275$, n = 5.

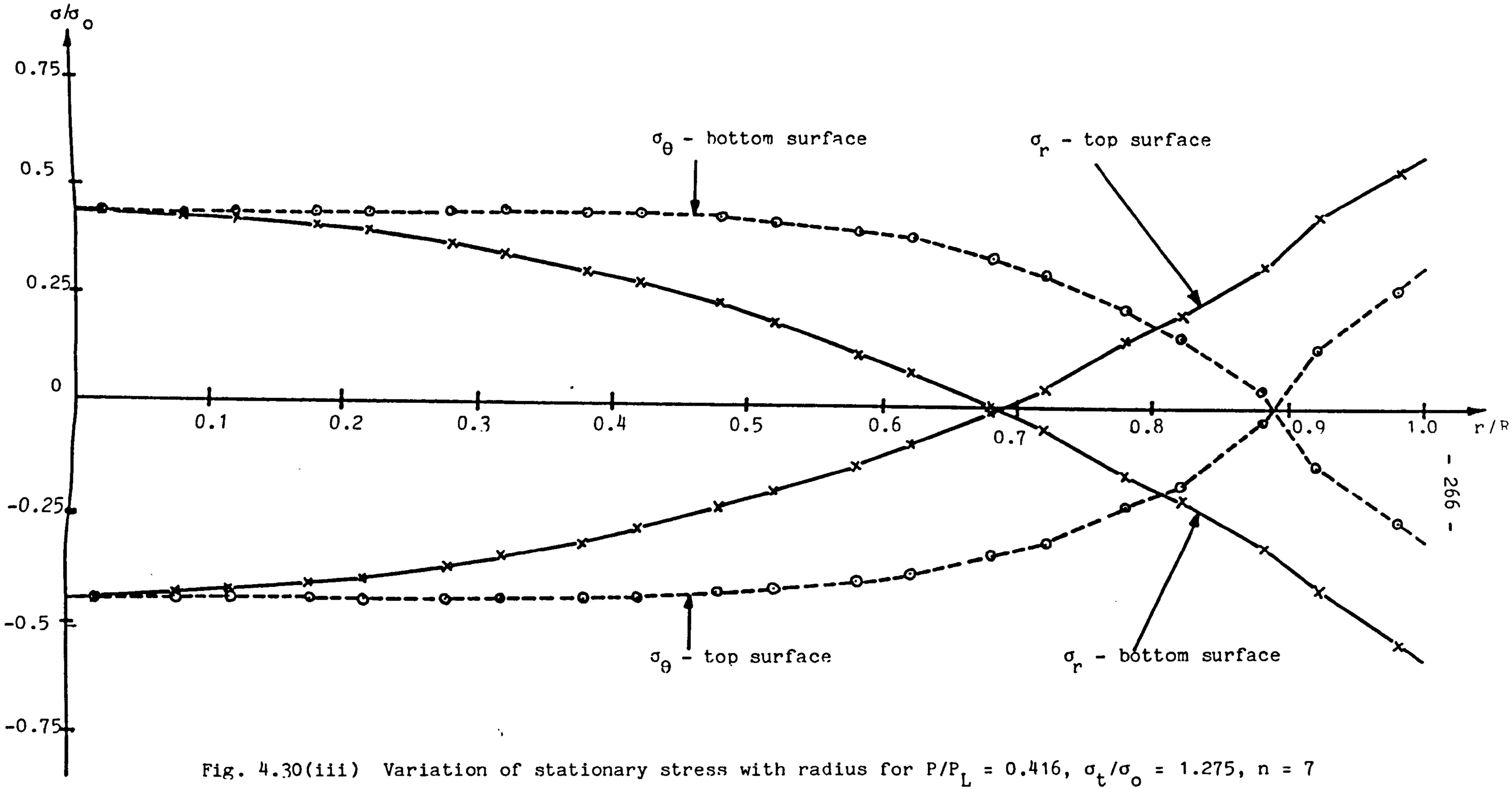

Fig. 4.30(iii) Variation of stationary stress with radius for $P/P_L = 0.416$, $\sigma_t/\sigma_o = 1.275$, n = 7

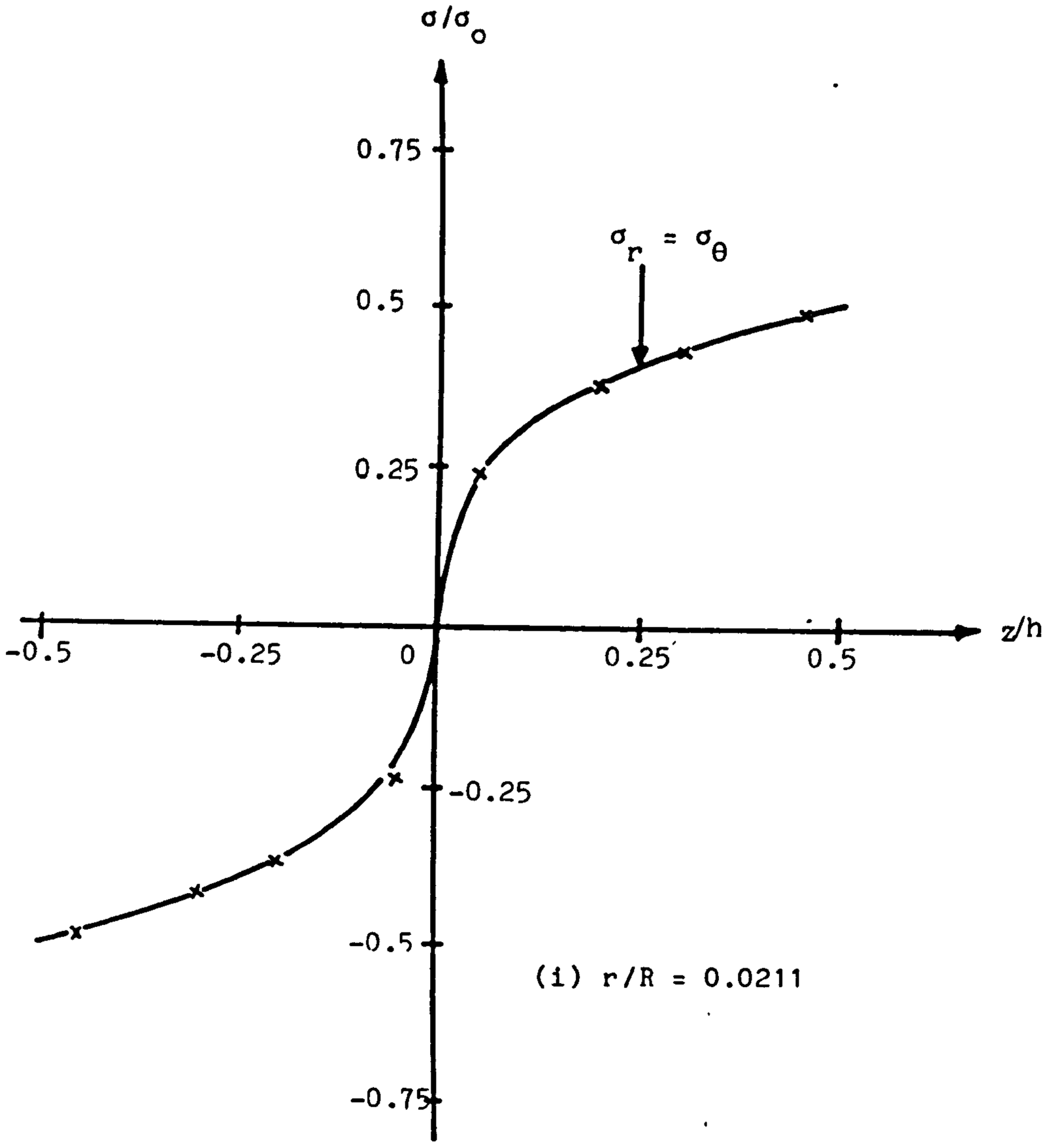

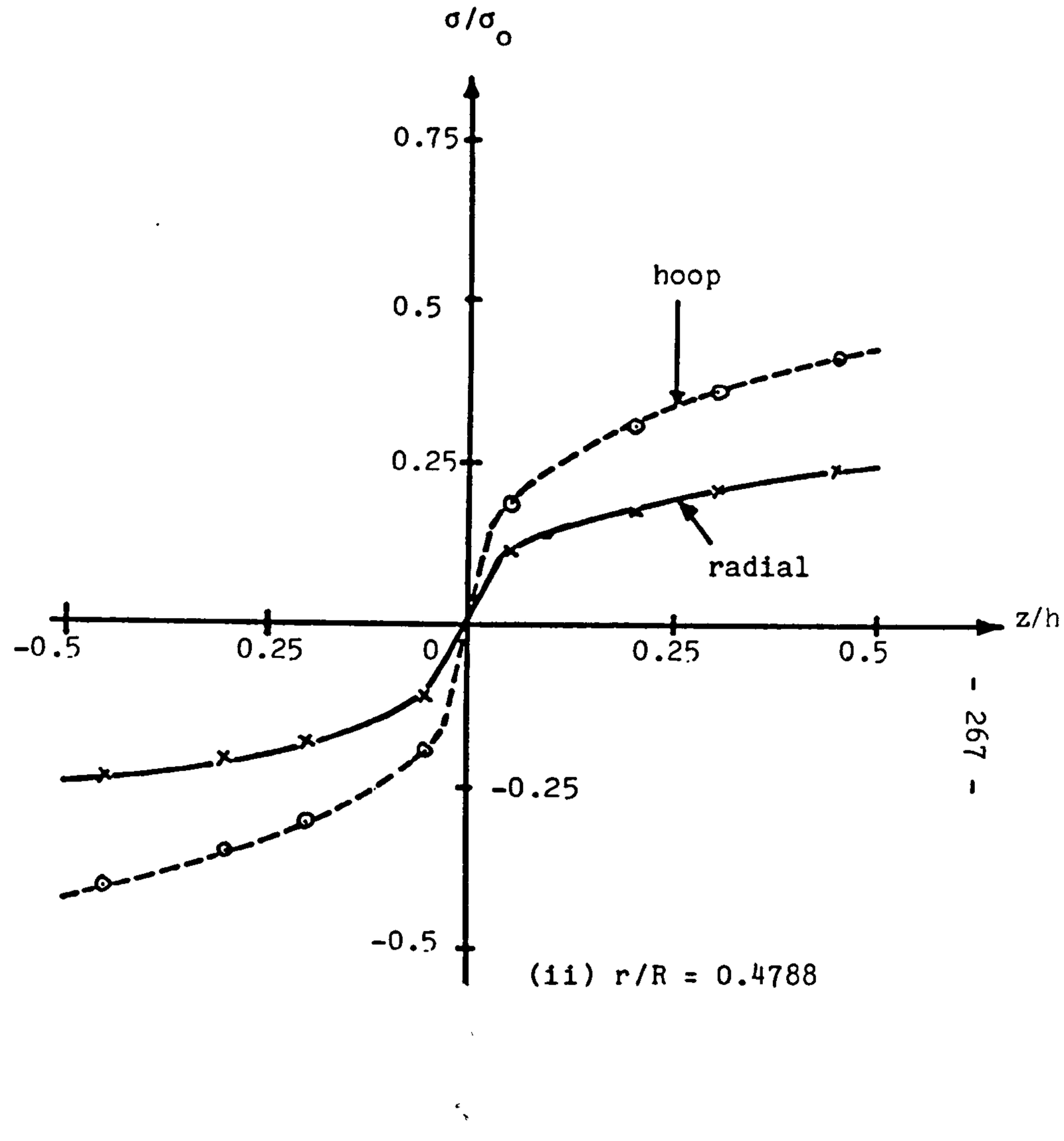

Fig. 4.31 Through thickness variation of stresses at the stationary stress state. $P/P_L = 0.416$, $\sigma_t/\sigma_o = 1.275$, $n = 3$

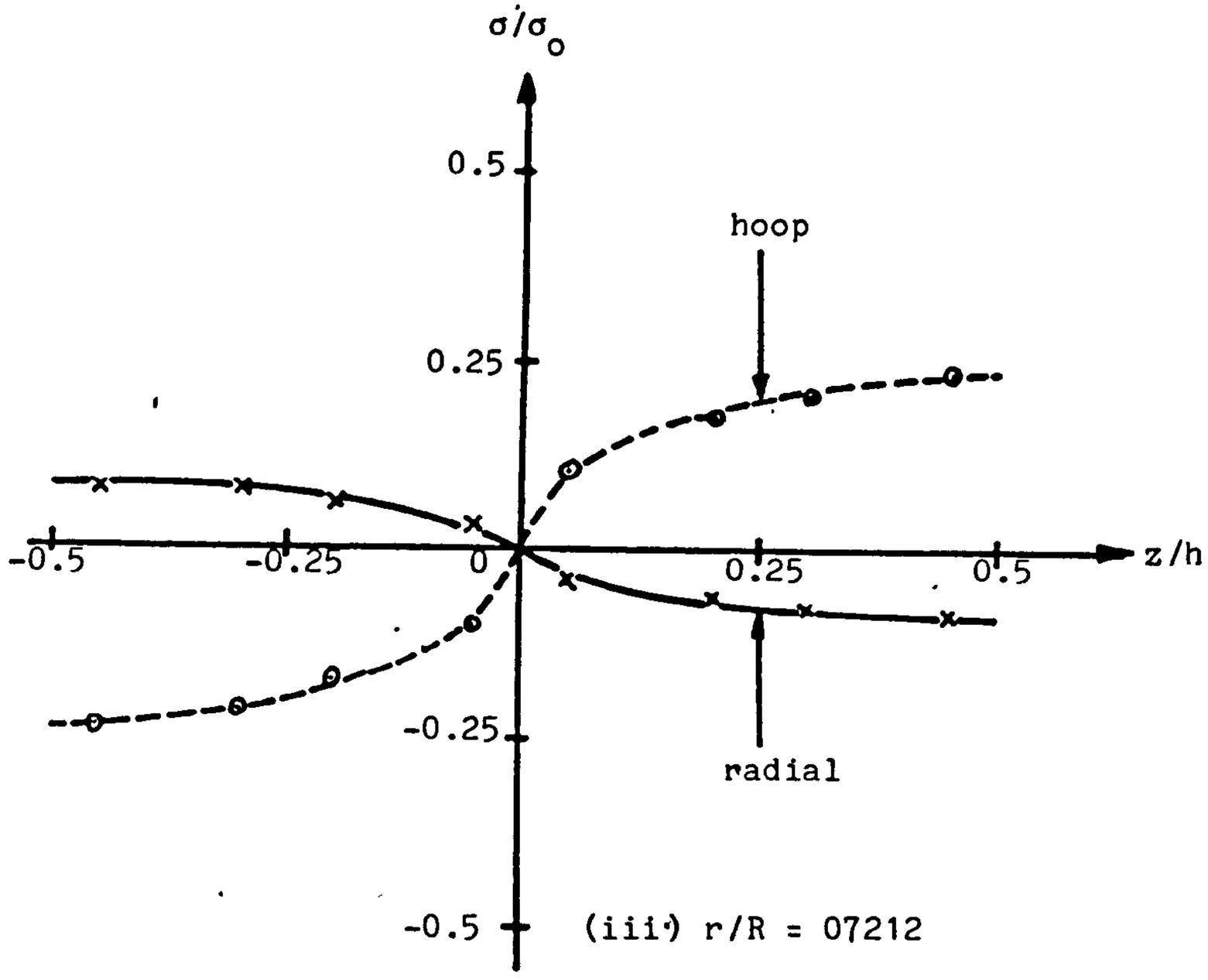

(iii) r/R = 07212

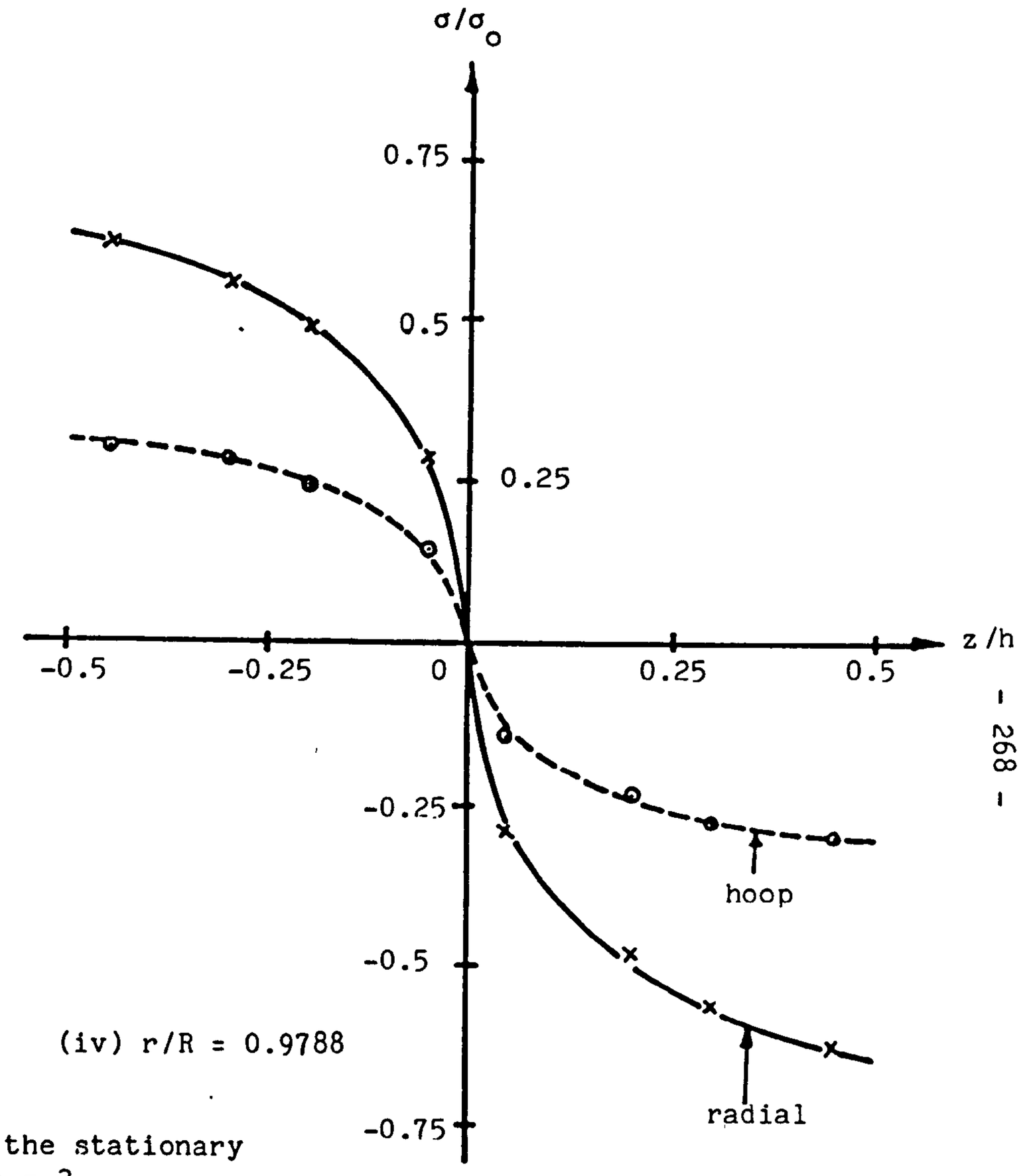

(iv) r/R = 0.9788

Fig. 4.31 Through thickness variation of stresses at the stationary stress state $P/P_L^{\cdot} = 0.416$, $\sigma_t/\sigma_o = 1.275$, $n = 3$.

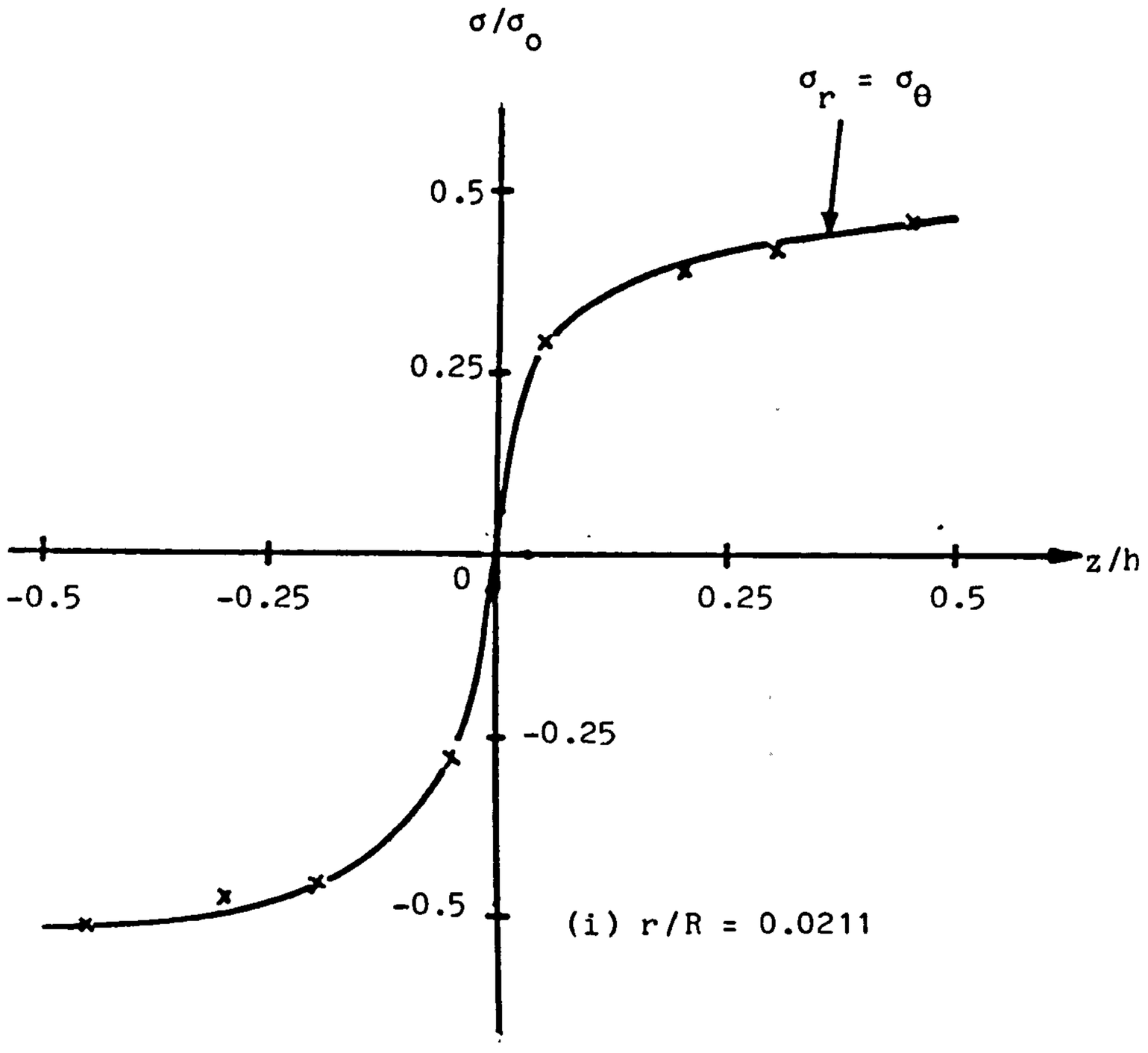

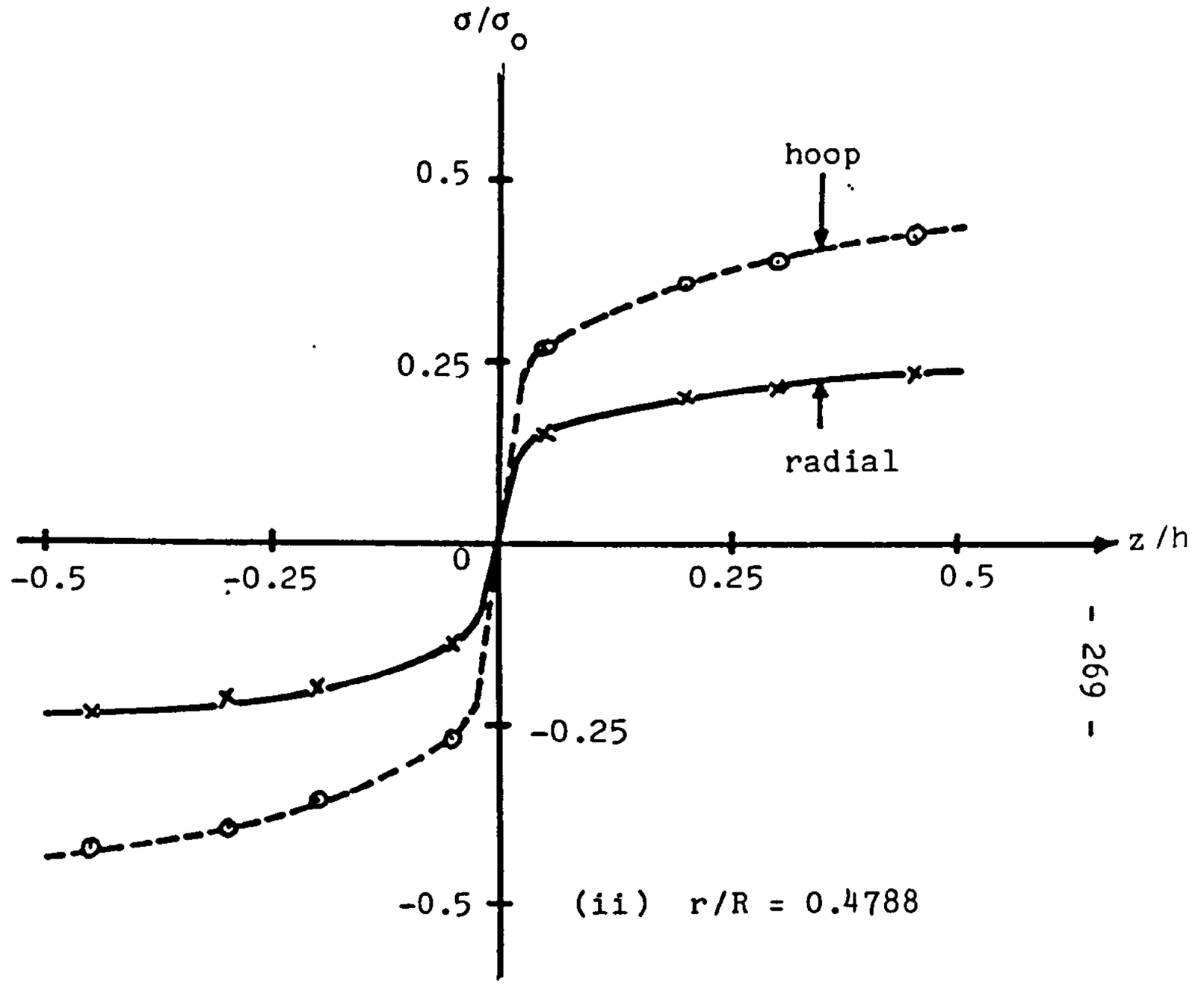

Fig. 4.32 Through thickness variations of stress at the stationary stress state.
$P/P_L = 0.416 \quad \sigma_t/\sigma_o = 1.275$, $n = 5$.

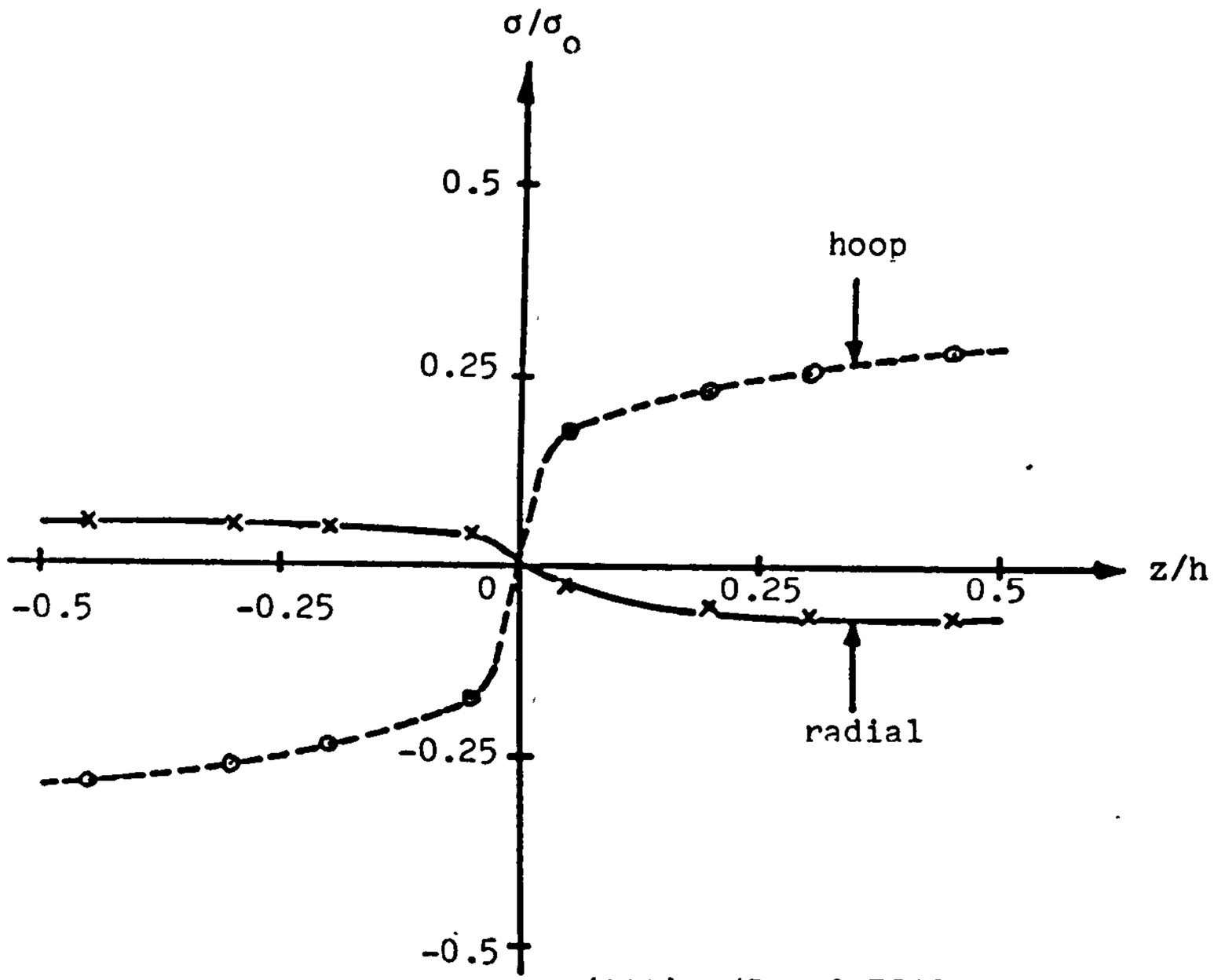

(iii) r/R = 0.7212

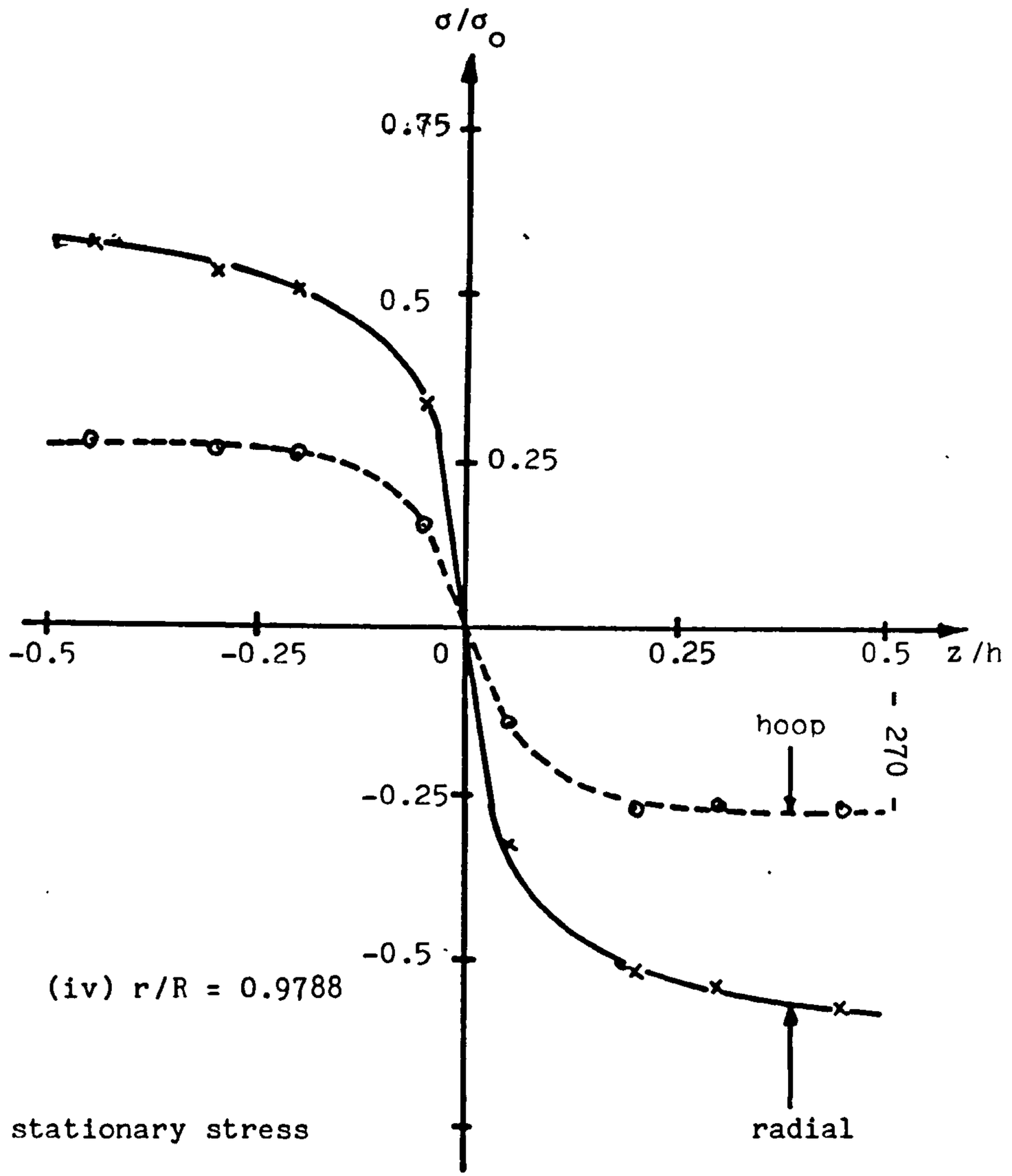

(iv) r/R = 0.9788

Fig. 4.32 Through thickness variation of stresses at the stationary stress state. $P/P_L = 0.416$, $\sigma_t/\sigma_o = 1.275$, $n = 5$

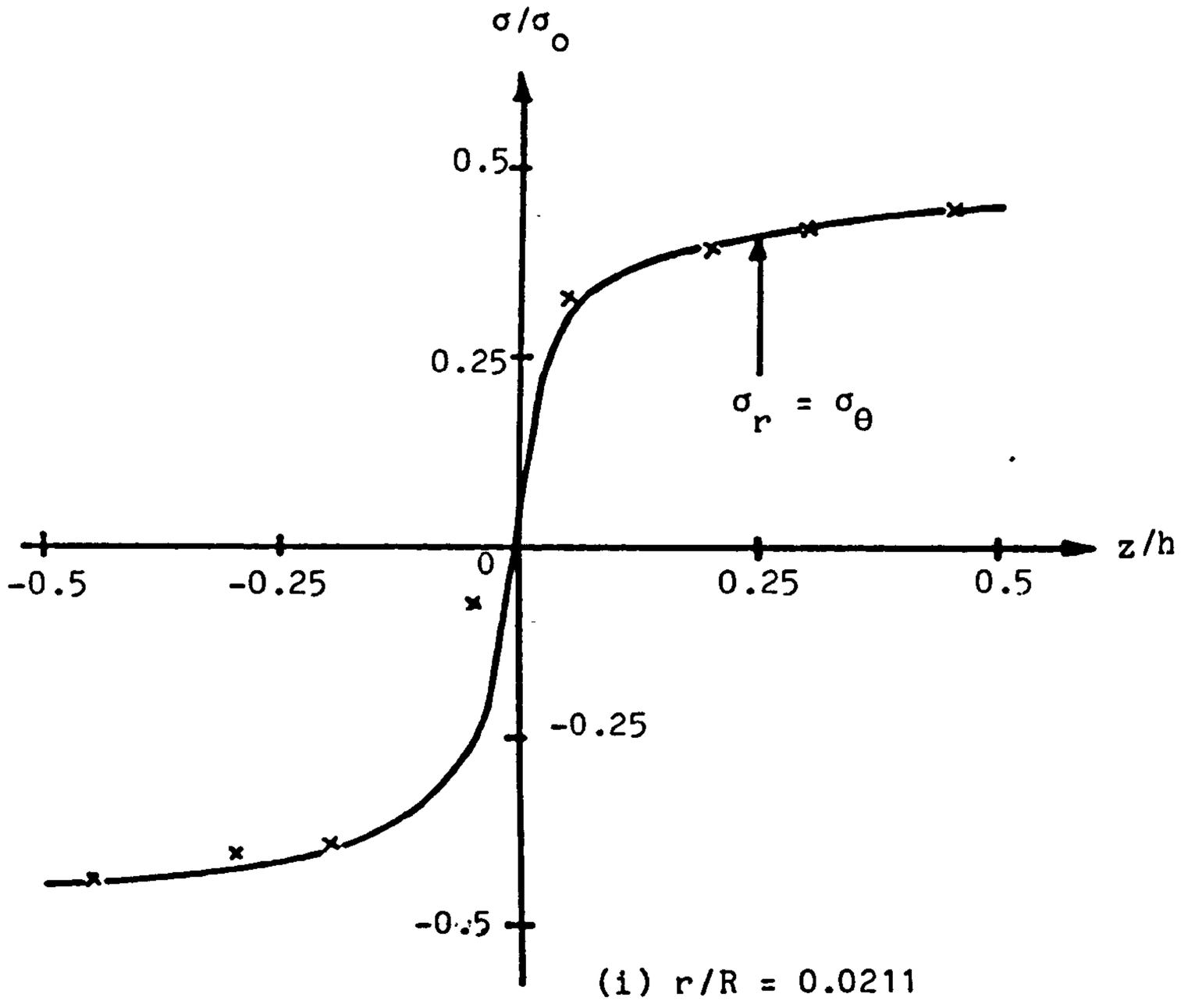

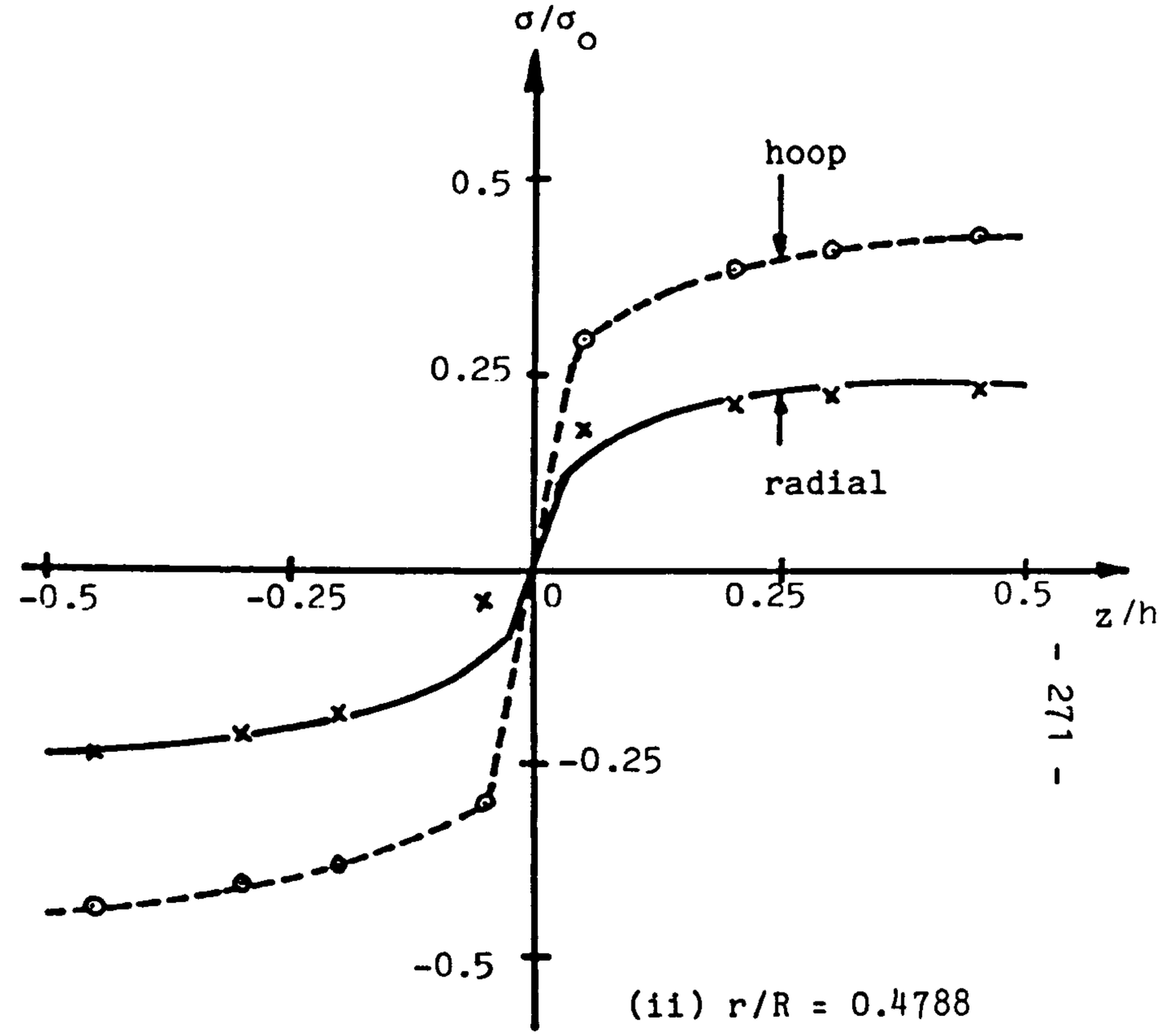

Fig. 4.33 Through thickness variation of stresses at the stationary stress state.
$P/P_L = 0.416$, $\sigma_t/\sigma_o = 1.275$, $n = 7$

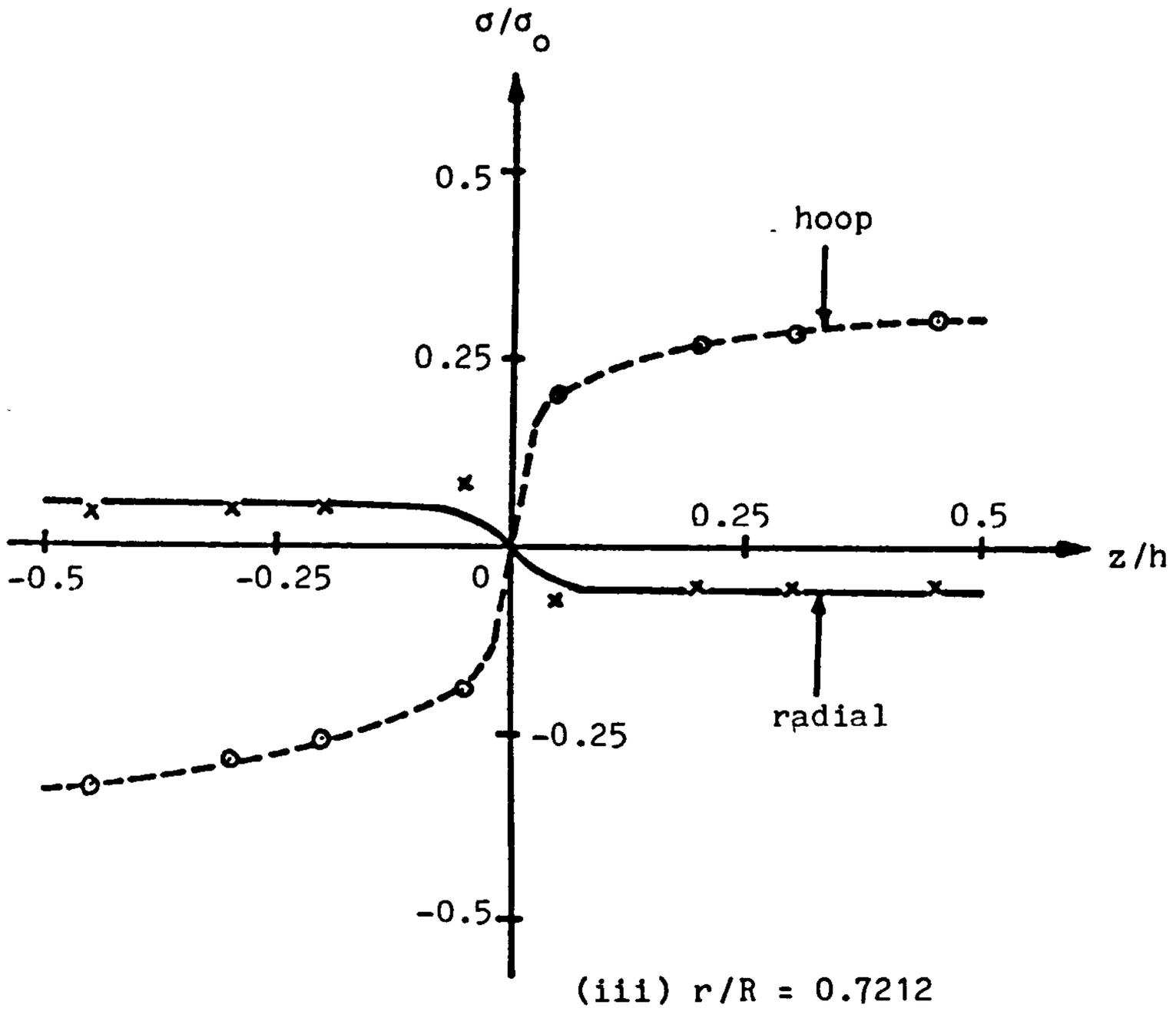

(iii) r/R = 0.7212

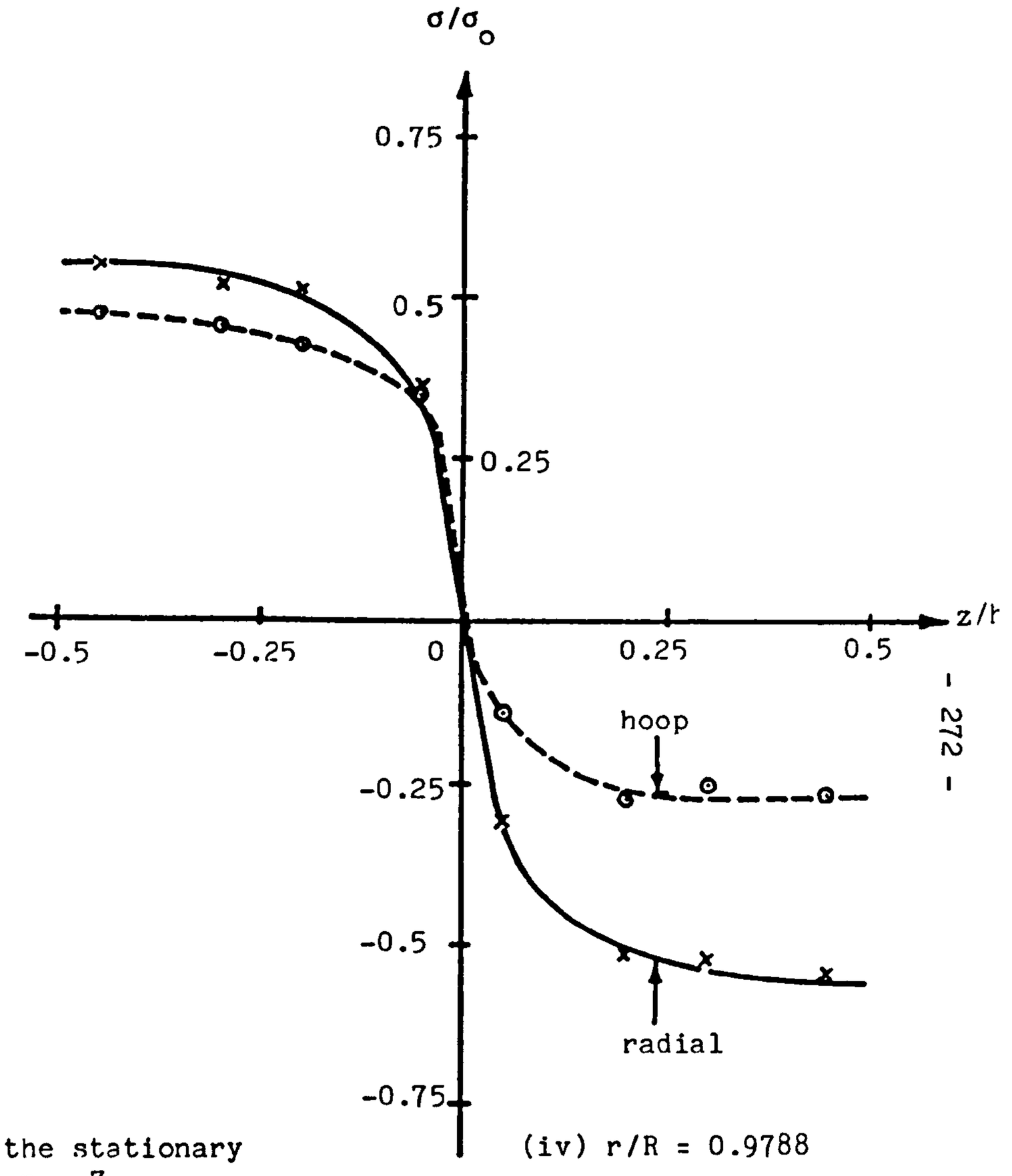

(iv) r/R = 0.9788

Fig. 4.33 Through thickness variation of stresses at the stationary stress state. $P/P_L = 0.416$, $\sigma_t/\sigma_o = 1.275$, n = 7

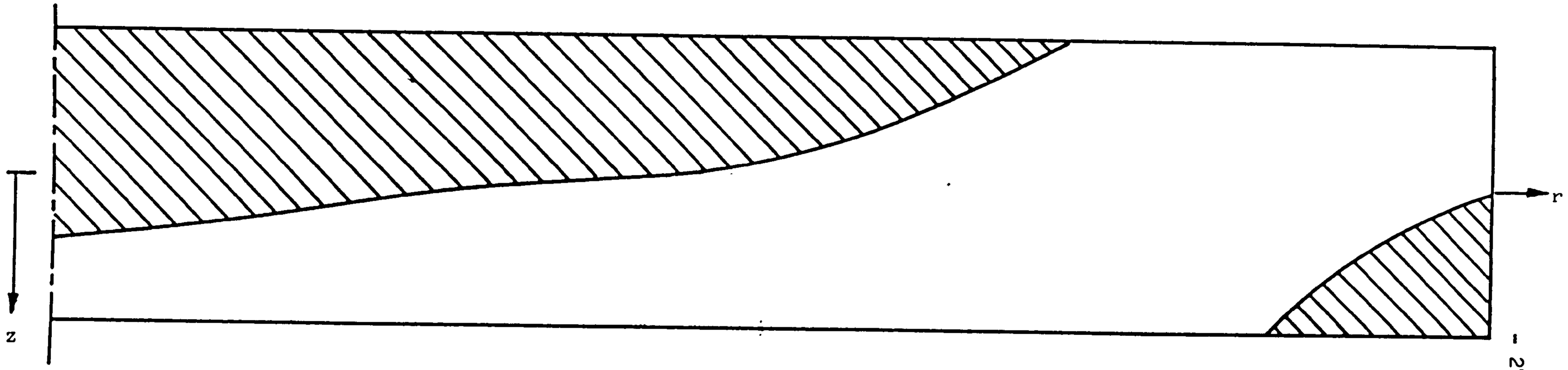

first half cycle. Elastic in the second half

Fig. 4.34(i) Extent of plastic zone during thermal cycle
$P/P_L = 0.416$, σ_t/σ_o, $n = 3$. (Plate thickness is exaggerated).

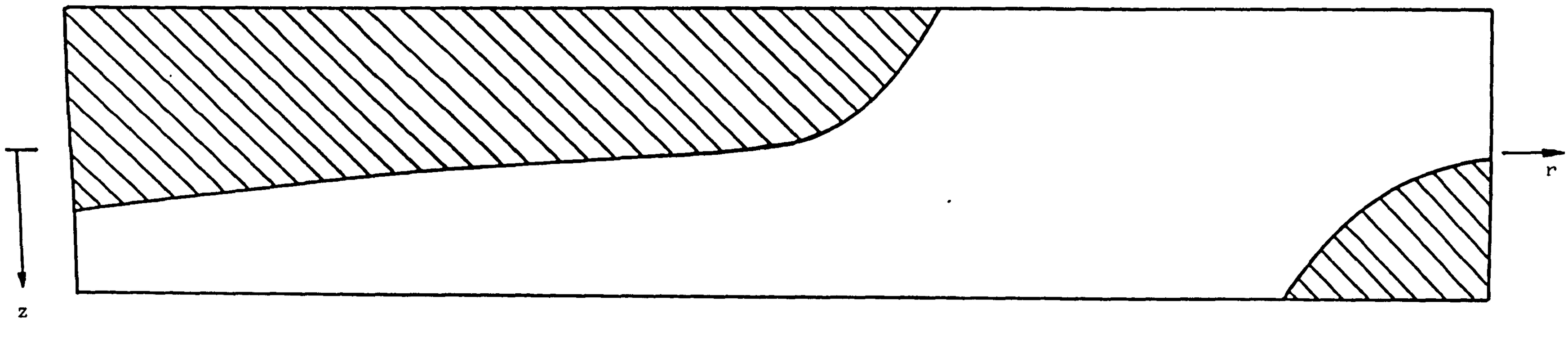

first half cycle. Elastic in the second half cycle

Fig. 4.34(ii) Extent of plastic zone during thermal cycle
$P/P_L = 0.416$, $\sigma_t/\sigma_o = 1.275$, n = 5. (Plate thickness is exaggerated)

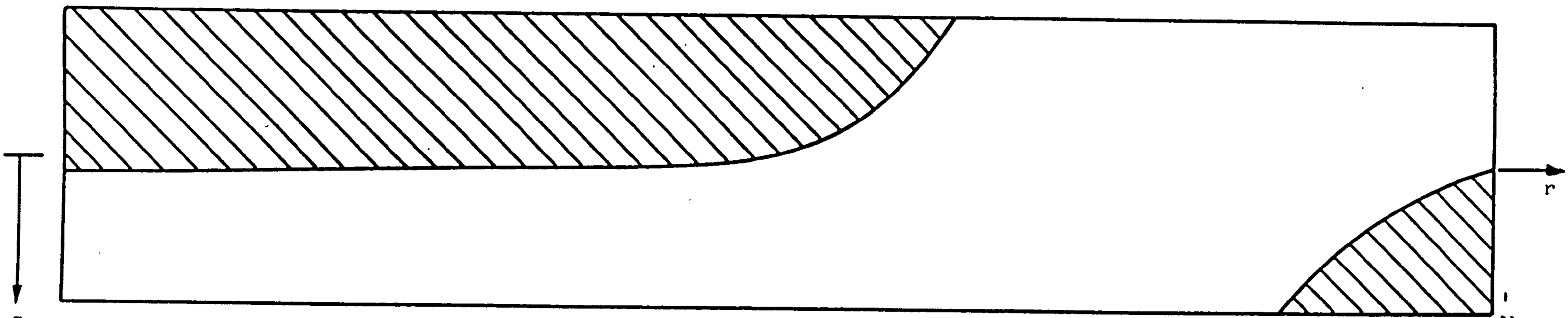

first half cycle. · Elastic in the second half cycle

Fig. 4.34(iii) Extent of plastic zone during thermal cycle $P/P_L = 0.416$, $\sigma_t/\sigma_o = 1.275$, n = 7. (Plate thickness is exaggerated)

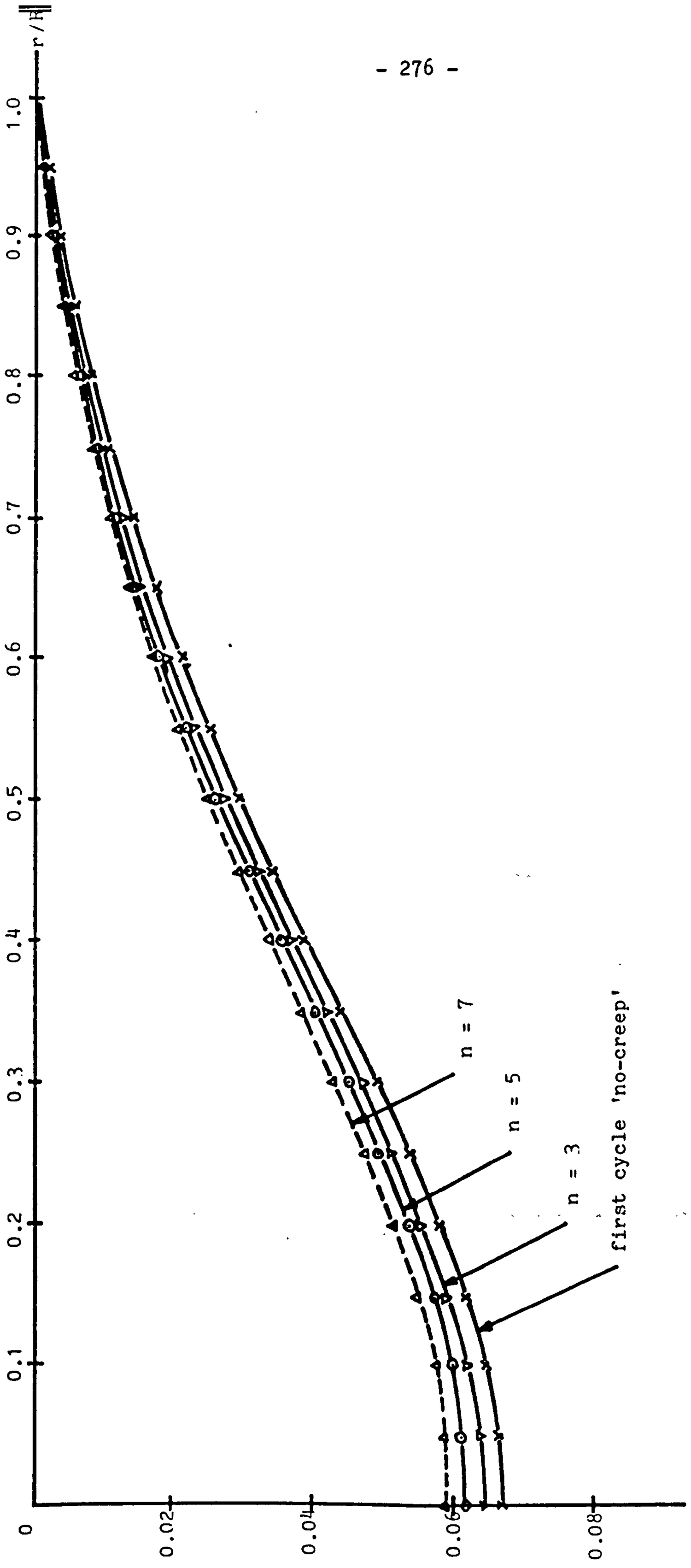

Fig. 4.35 Variation of ratchet deflection with radius for $P/P_L = 0.416$, $\sigma_t/\sigma_o = 1.275$. Complete stress redistribution case.

Fig. 4.36 Variations of ratchet deflection at plate centre with creep stress index n

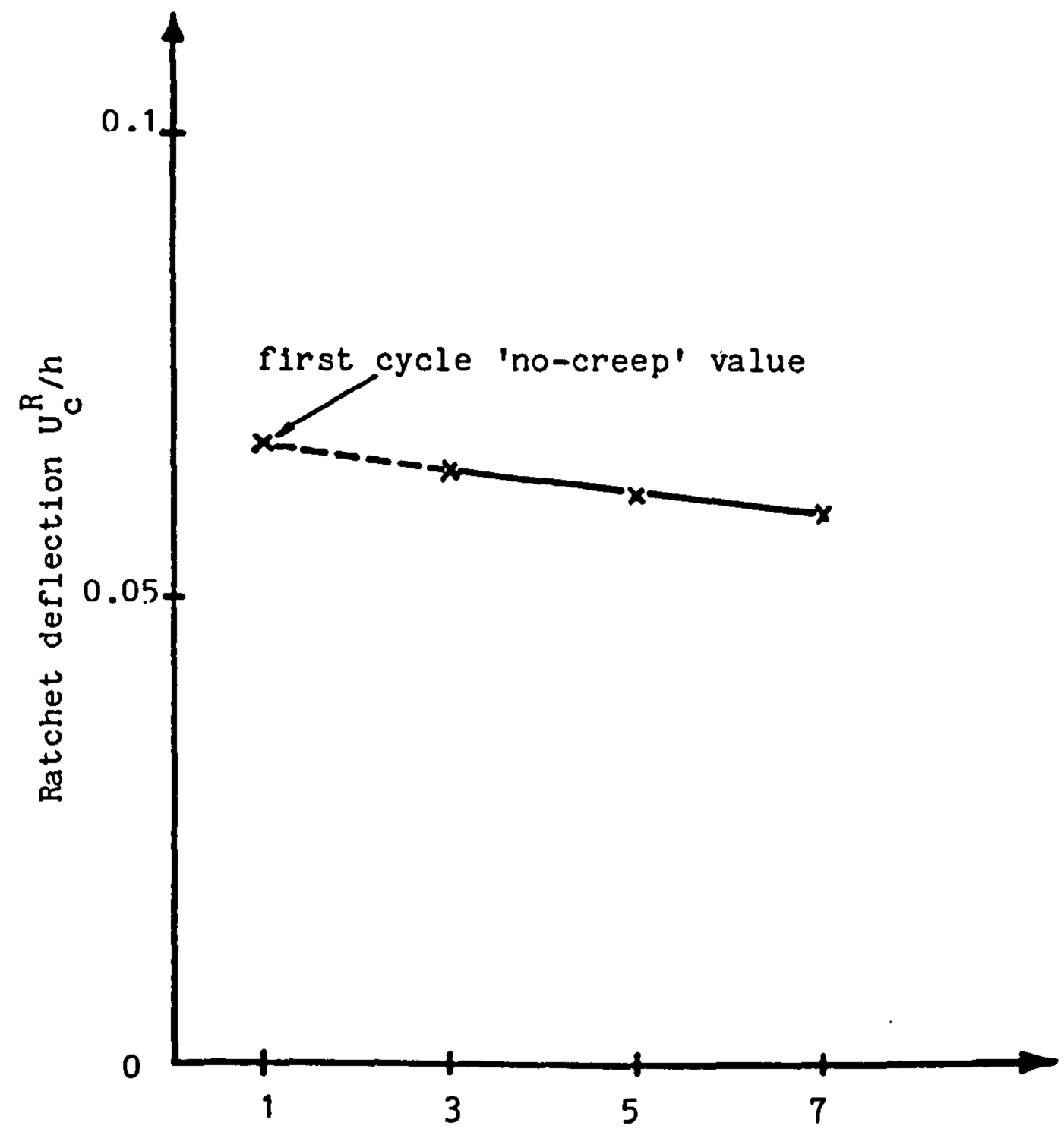

CHAPTER 5.

THE EFFECT OF MATERIAL RATCHETTING.

5.1 Introduction.

In Chapters 3 and 4, the ratchetting of components made of elastic-perfectly-plastic materials was investigated. It was found that with some combinations of steady mechanical and cyclic thermal loads, ratchetting occurred. With an elastic-pefectly-plastic material, this form of ratchetting is termed 'structural ratchetting'. However, the behaviour of real materials is much more complex and phenomena such as strain hardening, material ratchetting (sometimes called cyclic creep), cyclic relaxation, cyclic hardening and cyclic softening occur; see Chapter 2 for details.

The effect of strain hardening has been assessed by using an isotropic or kinematic hardening material behaviour model (e.g. 6,16,61,75). Use of both of these material behaviour models results in predictions of ratchet strains (or deformations) which monotonically reduce to zero after a finite number of cycles. However, experimental data (e.g.55,74,75,4,3) show that ratchetting continues for many more cycles than is predicted and may even continue until failure occurs. This indicates that the inclusion of strain hardening in the material behaviour model is not sufficient to give accurate predictions. Material ratchetting, cyclic relaxation etc. also need to be included.

Hardy et al (75) used experimental results, obtained from tests of lead alloy beams subjected to steady axial load and cyclic bending loads, to assess the accuracy of predictions based upon kinematic and isotropic hardening material behaviour models. The poor predictions obtained were attributed to the fact that material ratchetting was not included in the models. In section 5.2 of this chapter, the results of calculations similar to those of Hardy et al (75) are described. However, a much more complex material behaviour model capable of predicting material ratchetting and cyclic relaxation was used. The predictions are compared with the experimental results in order to assess the accuracy of the material ratchetting model.

In section 5.3 of this chapter, the effect of material ratchetting in 316 Stainless Steel on the behaviour of a beam which is constrained to remain straight and is subjected to a steady axial mechanical load and a cyclic linear through-depth temperature distribution is assessed. This is, in fact, the equivalent uniaxial model used by Bree for the problem of ratchetting of a thin cylinder. The results given in section 5.3 also show that the finite element coding, written for the material ratchetting model, works correctly with thermal loading as well as mechanical loading.

5.2 Assessment of the Goodman and Goodall (18) Material Ratchetting Model, Using Experimental Ratchetting Data from Lead Alloy Beams.

5.2.1 Material Behaviour.

5.2.1.1 Experimental.

In its as-cast condition, a large amount of scatter was obtained in the uniaxial, montonic, stress-strain behaviour for the lead alloy (nominal alloy composition: 2.55%Sb, 0.14%As), see Ref.3. However, when the uniaxial specimens were subjected to a normalising heat treatment of 100°C for 144h before testing, the scatter was greatly reduced (3). The scatter band associated with the monotonic stress-strain behaviour, at $20^{o}C \pm \frac{1^{o}}{2}C$ with a strain-rate of $2 \times 10^{-5}/s$, from all tests, is shown in Fig.5.1. Also shown in Fig.5.1 is the mean stress-strain curve.

Under cyclic loading between $+\varepsilon$ and $-\varepsilon$, for ε in the range $0.1\% < \varepsilon < 1\%$, it was found (3) that no significant cyclic hardening or softening occurred; see Fig.5.2 for example. However, when uniaxial specimens were subjected to cyclic loading between fixed stress levels, with a non-zero mean stress, 'material ratchetting' was found to occur (3); see Fig.5.3 for example. The material ratchet strains were found to reduce during the first three to four cycles, after which an approximately constant ratchet strain was obtained. The average ratchet strains per cycle for each of the four tests

performed are included in Table 5.1 together with the mean stresses and stress ranges associated with each test. The experimental data used in the comparison was obtained by Yahiaoui (3).

5.2.1.2 Material Model Data.

Since the component to be analysed (a beam) is subjected to uniaxial states of stress only, the formulation of the material model relevant to the present analysis is the uniaxial formulation described in detail in Chapter 2. However, the material model is capable of being generalized for use with multi-axial stress states and non-proportional loading. The formulation for multi-axial stress states is described in Appendix III; this multi-axial formulation has been incorporated into the finite element programs.

Because of the scatter in the results obtained from the 'material ratchetting' tests (see Table 5.1), it was decided to obtain three sets of constants for the 'material ratchetting' model. The constants were chosen to give ratchet strains equal to those obtained in tests U1, U3 and U4 in Table 5.1. For each of the models the yield stress, σ_o, and saturation stress, σ_s, were the same, the values used were

$$\sigma_o = 14.0 \text{ MNm}^{-2}$$

and

$$\sigma_s = 29.2 \text{ MNm}^{-2}$$

The other three constants (q, r and t) were obtained iteratively; the iterative procedure used to obtain the constants q , r and t is also described in detail in Appendix III. The constants were determined such that a reasonable fit to the mean, monotonic stress-strain curve of Fig.5.1 was obtained. Also a good prediction on the average experimental ratchet strains from stress controlled cycling test such as that shown in Fig.5.3 was obtained. The resulting constants are given in Table 5.2.

As a comparison, Fig.5.4 shows the resulting stress strain curve under cyclic loading between fixed stress levels; the constants corresponding to material model A were used based on the ratchet strains obtained from Fig.5.3. The discrepancies between the experimental stress strain curve (Fig.5.3) and the prediction (Fig.5.4) can be attributed to a combination of the inherent scatter in material behaviour and the simplifying assumption made for the material model. It is worth noting that, although the monotonic stress strain curve and the ratchet strain were well predicted, the fit to the subsequent stress strain curve may not be as good as the fit to the monotonic stress strain curve.

The fit to the mean, monotonic, stress strain curve is good in all cases (see Fig.5.1). The ratchet strains predicted, by the three models, for each of the 'material ratchetting' experiments are given in Table 5.1. From Table 5.1 it can be seen that material model A generally underestimates the ratchet strains obtained in the experiments (except for test U4 from

which the constants for model A were derived). The effect of the material constants q,r and t on ratchet strains, for a range of mean stresses and stress ranges, is conveniently illustrated by presenting the data in the form of carpet plots, as shown in Fig.5.5. It can be seen that model A gives significantly lower material ratchet strains than both models B and C. The material ratchet strains for model C are slightly greater than those for model B. When compared with the experimental results, material models B and C both give reasonable predictions; material model B appears to be slightly better than model C but there is little to choose between them. Other relevant material constants are given in Table 5.3.

5.2.2 Loading.

5.2.2.1 Experimental.

In the experiments, which were carried out by Yahiaoui (3), the axial load and bending loads were applied using dead-weights. The curvature induced by the bending loads caused the axial load to be offset with respect to the beam centre line. As a result, although constant bending loads were applied to the ends of the beams, the actual maximum bending moments at the centre of the beam, where the strains were measured, were found to vary during the first five cycles. After the first five cycles, the maximum eccentricities caused by the bending loads were found to be constant. Hence the bending moments were constant after the fifth cycle. The actual bending moments at

the centre of the beam are given in Table 5.4. Details of the 'beam rig' together with all the experimental results are described in references (3,74). However, the experimental results relevant to the present analysis are included in Figs.5.6(i),(ii) and (iii) and 5.7(i),(ii) and (iii). In Figs.5.6 and 5.7, the first tensile (FT) surface i.e. z/d=0.5 is defined as the surface which experiences a tensile stress for the first application of moment in the first cycle. The first compressive (FC) surface, i.e. at z/d=-0.5, is the opposite surface which would have a compressive stress for the first application of moment during the first cycle, with zero mean load.

Top and bottom surface strains were measured at the centre of the beam using electrical resistance strain gauges.

5.2.2.2 Finite Element.

The uniform beam, which has a breadth, b, of 10mm and a depth, d, of 25mm was modelled using a uniform mesh of 10 elements through the depth and one element along the length; 8-noded, isoparametric, plane stress elements were used. The loads were applied via an 'effectively rigid' block identical in size to the beam except that it is 100 times thicker. The purpose of the 'rigid' block is to ensure that the face CD remain plane during deformation (see Fig.5.8 for notation and coordinate convention). The axial load and bending moments are applied to the rigid block. The face AB is constrained from displacement in the x-direction and the node at X is also constrained from

displacement in the z-direction. Nodal displacements in the x-direction of face CD are identical to the corresponding nodal displacement along the face FG. In the computation, a 2x2 array of 'gauss integration' points was used.

Firstly, the required axial load was applied. The moment was then applied in increments until the maximum required value was obtained (the moments are given in Table 5.4). The moments were then reduced, incrementally to zero and then applied in the opposite direction to the required maximum value (these moments are also given in Table 5.4). The moments were then reduced incrementally to zero. This process of applying the bending load was repeated for the required number of cycles. Very small load increments (typically 200 increments to cover the full moment range) were used to ensure that accurate solutions were obtained. When the magnitude of the load increments were reduced by a factor of 2, the accumulated strains after 15 cycles increased by a factor of about 1.025. This discrepancy was considered to be acceptable for the present purposes.

5.2.3 Finite Element Results.

5.2.3.1 General Behaviour.

To illustrate the general behaviour of the beam, the finite element results for the load combinations associated with test B2 (Table 5.4) and material model C will be used. Fig.5.9(i) shows the through-thickness stress distributions associated

with the application of the axial load, when the maximum moment is applied during the first cycle and when the maximum reverse moment is applied during the first cycle. It can be seen that tensile yielding occurs through more than half of the depth of the beam at each extreme of moment application. There are also significant regions, near the outside surfaces where reverse plasticity occurs; the cyclic plasticity regions occupy about one-third of the volume of the beam. As cycling proceeds, the maximum stress and the mean stress, during a cycle, near the surfaces of the beam reduce, see Fig.5.9(ii). This is accompanied by a reduction in the width of the stress strain loops at these positions (see Fig..5.10(i) and 5.10(ii)) At the same time, the region of the beam experiencing tensile yielding during the application of each moment and reverse moment is reducing to one-half of the beam depth. The +M and -M stress distributions tend towards a situation in which they are mirror images of each other, (see Fig.5.9(ii)). At positions near the centre-line of the beam, no cyclic plasticity occurs and only small elastic stress reversals are obtained (see Fig.5.10(iii)). At intermediate positions, large elastic stress reversal occurs (e.g. see Fig.5.10(iv) for z/d=-0.22) or cyclic plasticity, with loops narrower than those near the surfaces, occurs (e.g. see Fig.5.10(v) for z/d=-0.28). The zero moment stress distributions, which are in equilibrium with the axial load, redistribute as cycling continues. In the central region, the stress increases. At the same time, the mean stress during a cycle in regions adjacent to the surfaces of the beam reduce and will eventually become zero. At this stage, equal and opposite plastic strains will occur with each

moment reversal and the stress at the centre-line remain constant. Regions between these will experience purely elastic strain variations.

5.2.3.2 Effect of Material Constants.

Figs.5.11(i),5.11(ii),5.12(i) and 5.12.(ii) show the finite element results obtained with the three models for loads corresponding to test B2 (see Table 5.4). As may be expected, Figs.5.11 show that the material models which give the greater material ratchetting lead to the largest strain accumulations in the beams. However, it is interesting to note that the differences are small during the first five cycles. In fact the model which gives the smaller material ratchet strains gives the largest strain accumulation in the first two to three cycles. The finite element predictions, of strains accumulated in 15 cycles, for loads corresponding to all three tests, are presented in Table 5.5 for the three material models used. The experimental results are also given in Table 5.5. It can be seen that the behaviour indicated in Figs.5.11, for load condition B2, is also observed with load conditions B1 and B3. Thus it can be concluded that the material constants which result in the largest material ratchetting will produce the largest strain accumulation in the beams. Also, although there is relatively little difference between the results predicted with models B and C, the predictions based on model C are marginally better when compared with the experimental results. This correlates with the marginally better overall fit to the uniaxial material ratchetting experiments (Table 5.1) obtained with model C.

5.2.3.3 Effect of Axial Load.

Although the moment ranges corresponding to tests B2 and B3 are not identical ($2.13M_o$ and $1.99\ M_o$, respectively, for the 5th to 15th cycles), they are close enough to allow assessment of the effect of axial loading to be made. Fig.5.13 shows the predicted variations of ratchet strains for the surfaces of the beams, plotted against cycle number, for material model B. It can be seen that increasing the axial load from $0.5P_o$ to $0.7P_o$ causes an approximate doubling of the ratchet strains for the 5th to 15th cycles. Although the ratchet strains are reducing with cycle number for both axial loads, the ratio of the ratchet strains does not appear to be changing significantly. Hence it may be expected that the asymptotic strain accumulations will have a ratio of about two. This effect of mean load is similar to that predicted using simpler material behaviour models (75) and to that obtained by Bree (8). Using Bree's solutions (8), taking $\sigma_{0.2}$ as an equivalent yield stress of an equivalent elastic-perfectly-plastic material model, a ratio slightly less than two is obtained. However, it should be noted that the predictions based on the Bree's analysis are much too large; this will be discussed further in section 5.2.6.

5.2.4 Comparisons of Finite Element Predictions with Experimental Results.

It is clear from Table 5.1 that material model A does not fit the overall experimental data accurately. Models B and C give

similar results and both appear to fit the data (Table 5.1) reasonably well. Detailed comparisons between experimental and finite element results are therefore only presented for material model C; model B gives very similar results (see Table 5.5).

The variations in FT and FC surface strains with moment, during the first complete cycle for test B2 are compared with the 'model C' finite element results in Figs.5.14(i) and (ii). It can be seen that for the first quarter cycle (i.e. the first moment application), the predictions are extremely good. This reflects the accurate fit to the monotonic stress-strain curve which has been achieved. During the rest of the first cycle, the predictions for one surface are good, whereas the strains on the other surface are underpredicted. This is probably because the transient behaviour exhibited by the material, i.e. larger material ratchet strains are obtained during the first two to three cycles (see Fig.5.3 for example), is not included in the material model. However, the quality of these predictions is much better than that obtained with simpler material behaviour models (75).

The accumulation of surface strains, with cycle number, in experiments B1, B2 and B3 are compared with the corresponding finite element predictions using material model C in Figs.5.6(i)-(iii) respectively. The corresponding ratchet strains are shown plotted against cycle number in Figs.5.7(i)-(iii). In tests B1 and B2, apart from the first two or three cycles of loading, the predictions of strain

accumulations and ratchet strains are good. Previous analyses (75) based on kinematic or isotropic hardening resulted in shakedown in about four to five cycles. The variations of the total strains and ratchet strains obtained by Hardy (16) using elastic-perfectly-plastic, linear isotropic hardening and linear kinematic hardening and loading condition B2 are shown in Figs.5.15(i) to (iii) and Figs.5.16(i) to (iii) respectively together with the predictions from the present analysis. This very marked improvement is due to the inclusion of material ratchetting in the material behaviour model, together with improved modelling of the 'knee' of the stress strain curve.

The strain accumulations and ratchet strains predicted for test B3 are not as good as those for tests B1 and B2; strains are underpredicted. However, the results are still a significant improvement over previous predictions (16,75). The relatively poor predictions are attributed to the creep occurring during the experiments. For test B3 a mean stress level of 15.05 N/mm^2, which is greater than the yield stress of 14 N/mm^2, was applied. For tests B1 and B2, significantly lower mean stresses (6.45 N/mm^2 and 10.75 N/mm^2, respectively) were applied. Also, the predicted centre-line stresses which are practically constant (there is actually a slight increase) during a cycle, are greater for test B3 than for tests B1 and B2. For example, the centre-line stresses, obtained for the 15th cycle in the finite element analyses, using material model C, were found to be 24.4 N/mm^2, 22.5 N/mm^2 and 26.2 N/mm^2 for load conditions B1, B2 and B3 respectively. The higher stress

levels in test B3 results in significant creep strains occurring whereas the relatively low stresses for tests B1 and B2 do not cause significant creep strains to occur. Apart from the increases in experimental strains which can be directly attributed to creep, the stress redistribution which occurs will increase the structural ratchetting. Also, plasticity/creep interaction tests for a similar lead alloy (33) have shown that plastic straining causes increased creep straining for high creep stress levels. The opposite was found to be true for low creep stress levels. This effect may also be contributing to the relatively poor predictions for test B3.

5.2.5 Effect of Refining the Finite Element Mesh.

To assess the accuracy of the result with respect to the element size, a second finite element mesh with 24 elements was used. The mesh is shown in Fig.5.17. The constraints are identical to the mesh of Fig.5.8. Only results for load conditions B2 (see Table 5.4) and material model C (see Table 5.2) were obtained. The stress distribution at the end of $\frac{1}{4}$, $\frac{3}{4}$, $9\frac{1}{4}$ and $9\frac{3}{4}$ cycles for the two meshes are shown in Figs.5.18(i) and (ii) respectively. It is obvious that there is no significant difference between the two sets of results. The variation of ratchet strain with cycle number is shown in Fig.5.19. Practically, no improvement on the prediction was obtained when the number of elements was increased. It can be concluded that the analysis performed using the 10 element mesh was sufficiently accurate.

5.2.6 Discussion.

For the purpose of simplifying the analysis of components, the exact details of material behaviour are often ignored. It is common to assume that the real material can be represented by an elastic-perfectly-plastic model; the 0.2% proof stress, $\sigma_{0.2}$, is commonly used as the yield stress for the elastic-perfectly-plastic model. Using the curvature range obtained during the 15th cycle of the finite element analyses, equivalent stresses were obtained (see Bree (8) for details). These equivalent thermal stresses and the mean stresses were used to determine the ratchet strains, using the 0.2% proof stress as the yield stress; Bree's (8) analysis was used. The resulting predictions are compared with the finite element predictions in Table 5.6. In all cases, the predictions based on Bree's (8) analysis grossly overestimates the ratchet strains; all of the predictions were about an order of magnitude too large.

The behaviour of the lead alloy is simpler than that of some steels (e.g. 18), i.e. cyclic hardening seems to be relatively insignificant in the lead alloy. Hence it may be concluded that for material which cyclically harden, predictions based on a Bree-type analysis, using $\sigma_{0.2}$, are likely to be even more inaccurate than those obtained for the lead alloy (see Table 5.6). It may be possible to choose an 'equivalent yield stress' other than $\sigma_{0.2}$ and get better predictions in some cases. However, as yet, there is no fundamental basis upon which to determine the appropriate 'equivalent yield stress'.

Also, it is possible to determine an equivalent yield stress for Bree-type analysis which gives the same incremental strains as those obtained from the finite element analysis for the material ratchetting model. The yield stresses calculated in this way, for the 15th cycle, are given in Table 5.7. It can be seen that the stresses obtained for the three loading conditions are different. For load case B1, the resulting yield stress is even larger than the UTS for the lead alloy. Hence some doubt must be cast on this type of approach. It must therefore be concluded that more realistic material behaviour models and more rigorous analysis techniques are required if realistic predictions of incremental growth of components is to be achieved.

It is apparent from the comparisons between the finite element results and the experimental data for test B3 that creep effects become significant with high mean loads and high stresses. The inclusion of creep in the analysis would be necessary to improve the predictions. However, the interactions between plastic and creep strains cannot yet be adequately modelled by constitutive equations. This is true of all metals, not only the lead alloy.

5.3 Assessment of the Effect of Material Ratchetting on the behaviour of a 316 Stainless Steel Component.

The comparisons of the experimental results and the finite element predictions, presented in section 5.2 for lead alloy beams indicate that the inclusion of material ratchetting can

have a significant effect on the quality of predictions for components made from some materials. In this section the significance of material ratchetting in 316 Stainless Steel is assessed. The constants used for the material ratchetting model are given by Goodman and Goodall (18) for 316 Stainless Steel at 600°C. Apart from calculations based on the material ratchetting model, results were also obtained for a linear kinematic hardening model fitted to the 316 Stainless Steel stress strain curve. A comparison of the two sets of results thus allows the effect of material ratchetting to be assessed. The monotonic stress strain curve obtained by using the material constants given by Goodman and Goodall (18) is shown in Fig.5.20.

5.3.1 Material Data.

5.3.1.1 Linear Kinematic Hardening.

The monotonic stress strain curve was approximated by a bilinear stress strain curve, which passes through the stress strain curve at the 0.2% proof stress, as shown in Fig.5.20; the resulting material constants are given in Table 5.8. The material constants were assumed to be independent of temperature.

5.3.1.2 Goodman and Goodall (18) Material Ratchetting Model.

The relevant material constant at 600°C for the cast of 316 Stainless Steel used by Goodman and Goodall (18) are given in Table 5.9.

It was assumed that these material constants were independent of temperature and in the present computations, the cyclic hardening which occurs in 316 Stainless Steel was ignored. The results obtained, which were for the strains accumulated during the first few cycles of loading are not likely to be significantly different if cyclic hardening was included. For large numbers of load cycles, cyclic hardening is significant and would need to be included if accurate predictions were required.

The values of Young's modulus (E), Poisson's ratio (ν) and coefficient of expansion (α) were the same as those used for the ratchetting analyses of thin tubes and circular plate described in Chapters 3 and 4 respectively. The values of the yield stress (σ_o) and 0.2% proof stress ($\sigma_{0.2}$) are different from those used in Chapters 3 and 4.

5.3.1.3 Loading.

A uniform beam of depth, d, and thickness, h, was modelled using 10 equal sized 8-noded isoparametric elements which were subjected to a steady axial load and a cyclic linear through-the-depth temperature gradient. The axial load only causes elastic strains and, hence, was applied in a single load increment. The temperature was applied and removed in not less than 400 increments per cycle to ensure accurate results. The convergence criterion is within 0.1% in all cases (see Appendix III, section AIII.4.1 for definition of convergence criterion). The load combinations used in the analyses are included in Table 5.10.

5.3.2 Results.

5.3.2.1 Linear Kinematic Hardening Model.

The general behaviour for all the load combinations analysed was found to be the same. Therefore, the results obtained for one load combination only is described in detail, to illustrate the behaviour. The load combination chosen is $\sigma_p/\sigma_{0.2}$=0.4571 and $\sigma_t/\sigma_{0.2}$=2.8.

The variation of stress through the depth, in the first cycle, is shown in Fig.5.21(i). Compressive and tensile yielding occurs at the end of each half cycle. The variation of stress through the depth during the tenth cycle is shown in Fig.5.21(ii). Again during this cycle, at the end of each half cycle, yielding occurs near the beam surfaces, remote from the beam centre-line. The variations of total strain with cycle number and the ratchet strain with cycle number are shown in Figs.5.22(V) and (Vi) respectively. For this load combination the total strain monotonically increases with cycle number approaching a maximum value while the ratchet strain reduces monotonically, approaching zero. The ratchet strains in the first and tenth cycles, for different load combinations, are given in Table 5.10. Also shown in Table 5.10 are the total accumulated ratchet strain at the end of 10 cycle of loading. Figs.5.23(i) and (ii) show the results in the form of 'carpet plot'. Figs.5.22(i) to (vi) show the results for all the load combinations obtained.

5.3.2.2 Goodman and Goodall Material Ratchetting Model (18).

The stress distributions, through the depth, obtained at the ends of the first and second halves of the first cycle are shown in Fig.5.24(i) for $\sigma_p/\sigma_{0.2}$=0.4571 and $\sigma_t/\sigma_{0.2}$=2.8. Compressive and tensile yielding occurs during each half cycle. The corresponding stress distributions for the tenth cycle are shown in Fig.5.24(ii). Figs.5.25(i) to (iv) show the stress strain behaviour at various depths through the beam. At the surfaces, cyclic plasticity with a large strain range occurs. Near the beam centre-line, monotonic loading occurs. At other positions, either cyclic plasticity with a smaller strain range or monotonic plastic straining, with elastic strain reversals, occur. For this particular load combination, over 10 cycles, the effect of structural rather than material ratchetting appears to dominate. From the above discussion, it can be concluded that the behaviour is very similar to that of a uniform beam subjected to a steady axial load and a cyclic, fully reversed, bending moment described in detail in Section 5.2.3 above. It can also be concluded that the program can be used for thermal stress analyses.

Figs.5.26 to 5.28 show the total strains plotted against cycle number and ratchet strains plotted against cycle number for the load combinations considered. The ratchet strain reduces with number of cycles.

The results for the accumulated ratchet strains, first cycle ratchet strains and 10th cycle ratchet strains are shown as a

'carpet plot' in Figs.5.29(i) and (ii) for various mean and thermal load combinations. The overall results are also shown in Table 5.10.

5.3.3 Comparison between the prediction using the Linear Kinematic Hardening and Goodman and Goodall models and discussion.

The results for both the kinematic hardening and Goodman and Goodall (18) models are summarised in Tables 5.10. The results are also presented as 'carpet plots' in Figs.5.23 and 5.29.

By comparing Figs.5.23(i) and 5.29(i), it can be seen that there is very little difference between the predictions of first cycle ratchet strains obtained with the two material behaviour models. In all cases the predicted first cycle ratchet strains were found to be larger when the Goodman and Goodall model was used rather than the kinematic hardening model. This is mainly due to the differences in the stress-strain relationships in the vicinity of the 'knee' of the stress strain 'curve'. It can also be seen from Figs.5.23(i) and 5.29(i) that with the lower mechanical loads the predictions of tenth cycle ratchet strains based upon the Goodman and Goodall model were greater than those based on the kinematic hardening model. The opposite was found to be the case with higher mechanical loads. At the higher mechanical loads the accumulated plastic strains are relatively large, see Figs.5.23(ii) and 5.29(ii). At these relatively large values of plastic strains, the kinematic hardening stress-strain

'curve', is below the Goodman and Goodall stress-strain 'curve', see Fig.5.20. Hence the greater accumulation of ratchet strain for strains in excess of about 0.3% may be expected with the kinematic hardening model. It would, therefore, appear that for the range of loads considered, the effect of material ratchetting in 316 Stainless Steel is not significant. A suitably chosen kinematic hardening model would give sufficiently accurate predictions.

Material Ratchetting test number	Stress (Nmm^{-2})		ε^{R}_{ave} με			
	Mean σ	Range σ	Exp.	Model A	Model B	Model C
U1	4.6	35.2	150	33	150	174
U2	2.5	40.0	250	94	360	403
U3	4.76	38.9	625	137	545	625
U4	3.5	43	300	300	1132	1263

Table 5.1 Comparison of the results of the material ratchetting experiments with those predicted by material models A, B and C

Model	q	r	t
A	2.898	0.241	0.085
B	2.520	0.161	0.333
C	2.451	0.147	0.379

Table 5.2 Material constants

Properties	Values
Young's modulus, E	23.2 GNm^{-2}
Poisson's ratio ν	0.44
0.2 % proof stress, $\sigma_{0.2}$	21.5 MNm^{-2}

Table 5.3 Relevant material constants

		M/M_0 (3)		
	Test No.	B1	B2	B3
Cycle No.	P/P_0 (2) / (1) Moment	0.3	0.5	0.7
1	+M	1.35	1.03	0.97
	0	-0.96	-0.66	-0.47
	-M	-1.44	-1.11	-1.09
	0	0.05	0.01	0.05
2	+M	1.37	1.03	0.97
	0	-0.09	-0.04	-0.06
	-M	-1.38	-1.08	-1.06
	0	0.06	0.02	0.05
3	+M	1.38	1.06	0.98
	0	-0.09	-0.02	-0.03
	-M	-1.38	-1.06	-1.02
	0	0.06	0.26	0.03
4	+M	1.37	1.07	0.98
	0	-0.09	-0.01	-0.04
	-M	-1.38	-1.06	-1.03
	0	0.07	0.02	0.17
5 to 15	+M	1.37	1.06	0.97
	0	-0.08	-0.01	-0.05
	-M	-1.38	-1.07	-1.02
	0	0.06	0.04	0.28

Table 5.4 Beam experiment loads

(1) +M, 0 and -M indicate the maximum, zero and minimum applied moment conditions

(2) $P_0 = bd\ \sigma_{0.2}$

(3) $M_0 = bd^2\ \sigma_{0.2} / 6$

Load conditions	Material model	Ratchet strain accumulation in 15 cycles (%)	
		FC surface	FT surface
B1	A	0.662	0.230
	B	0.901	0.434
	C	0.914	0.465
	Experiment	0.947	0.768
B2	A	0.380	0.303
	B	0.462	0.366
	C	0.467	0.375
	Experiment	0.362	0.495
B3	A	1.075	0.757
	B	1.271	0.930
	C	1.297	0.956
	Experiment	2.287	2.386

Table 5.5 Predicted and experimental strain accumulations in 15 cycles

Load conditions	Material model	Predicted 15th cycle centreline ratchet strain (%)	
		Finite element	Bree (using $\sigma_0=\sigma_{0.2}$
B1	A	0.0065	0.1965
	B	0.02086	0.2045
	C	0.02318	0.1901
B2	A	0.0013	0.0585
	B	0.00661	0.0663
	C	0.00758	0.0678
B3	A	0.00208	0.1102
	B	0.01411	0.1287
	C	0.01645	0.1332

Table 5.6 Comparison of finite element and Bree predictions of 15th cycle ratchet strains

Loading conditions	model	Equivalent yield stress (MNm^{-2})
B1	A	30.46
	B	29.52
	C	29.29
B2	A	24.58
	B	24.67
	C	24.69
B3	A	27.03
	B	27.18
	C	27.25

Table 5.7 Equivalent yield stresses required to give correct 15th cycle ratchet strains.

Properties	values
Young's modulus,, E	160.0 GNm^{-2}
yield stress σ_o	131.1 MNm^{-2}
Poisson's ratio, ν	0.3
Plastic modulus, E^p	4.352 MNm^{-2}
$\beta=E^p/E$	0.0272
Coefficient of expansion, α	20 X 10^{-6} K^{-1}

Table 5.8 Materials data for linear kinematic hardening model

Properties		values
Young's modulus, E		160 GNm^{-2}
yield stress, σ_o		100 MNm^{-2}
Poisson's ratio, ν		0.3
0.2% proof stress $\sigma_{0\ 2}$		140 MNm^{-2}
Saturation stress, σ_s		400 MNm^{-2}
Goodman and Goodall constants	r	0.61
	t	0.4
	q_0	2.5
Coefficient of expansion,		20 X 10^{-6} K^{-1}

Table 5.9 Materials data for Goodman and Goodall material ratchetting model.

$\sigma_t/\sigma_{0.2}$	$\sigma_p/\sigma_{0.2}$	Linear kinematic hardening model			Goodman and Goodall(18) model		
		Total accumulated ratchet strains $\Sigma E\varepsilon^R/\sigma_{0.2}$		ratchet strain $\frac{E\varepsilon^R}{\sigma_{0.2}}$	Total accumulated ratchet strains $\Sigma E\varepsilon^R/\sigma_{0.2}$		ratchet strains $E\varepsilon^R/\sigma_{0.2}$
		first cycle	tenth cycle	tenth cycle	first cycle	tenth cycle	tenth cycle
2.2	0.22857	0.2859	0.2859	0.0	0.3082	0.3154	0.00046
	0.34286	0.4348	0.4348	0.0	0.4817	0.5349	0.00233
	0.45714	0.6582	1.5792	0.0598	0.8088	1.6478	0.01883
	0.57143	1.0478	4.4810	0.2131	1.1839	3.7570	0.1056
2.5	0.22857	0.3536	0.3536	0.0	0.3682	0.3765	0.00064
	0.34286	0.5286	0.5286	0.0	0.6187	0.8078	0.00361
	0.45714	0.9299	2.9654	0.1203	1.0105	2.3382	0.03685
	0.57143	1.3734	6.0504	0.2721	1.4424	4.8128	0.1467
2.8	0.22857	0.4244	0.4244	0.0	0.4252	0.4361	0.00087
	0.34286	0.6470	0.9077	0.0181	0.7597	1.1339	0.00795
	0.45714	1.1742	4.0669	0.1418	1.2105	3.0049	0.05381
	0.57143	1.6678	7.3960	0.2958	1.6992	5.8629	0.1870

Table 5.10 Results for a uniform beam subjected to a steady axial load and cyclic linear through the depth temperature distribution.

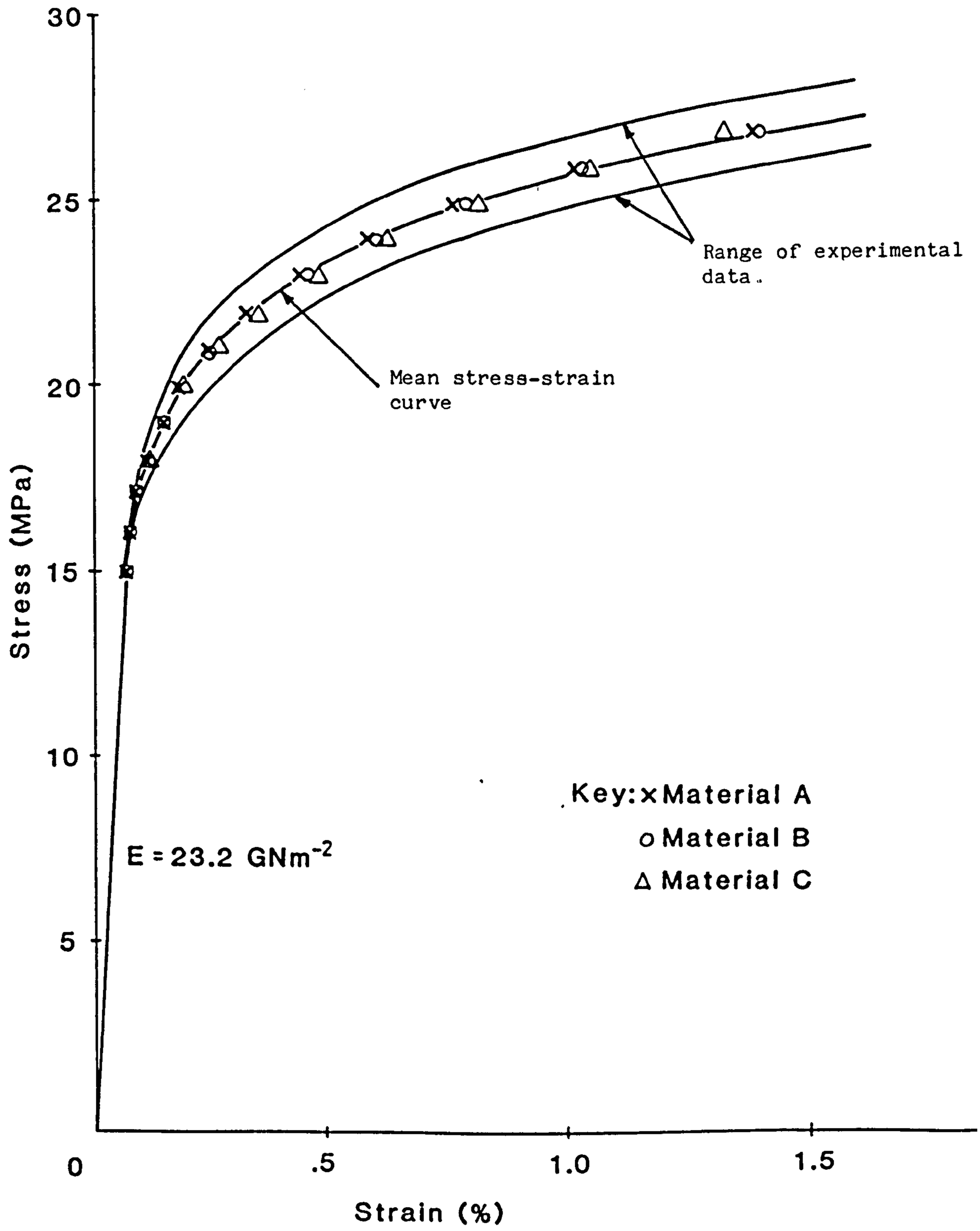

Fig. 5.1 Experimental stress-strain data and fits to the mean data for lead alloy material. (Experimental data obtained from ref. 3.)

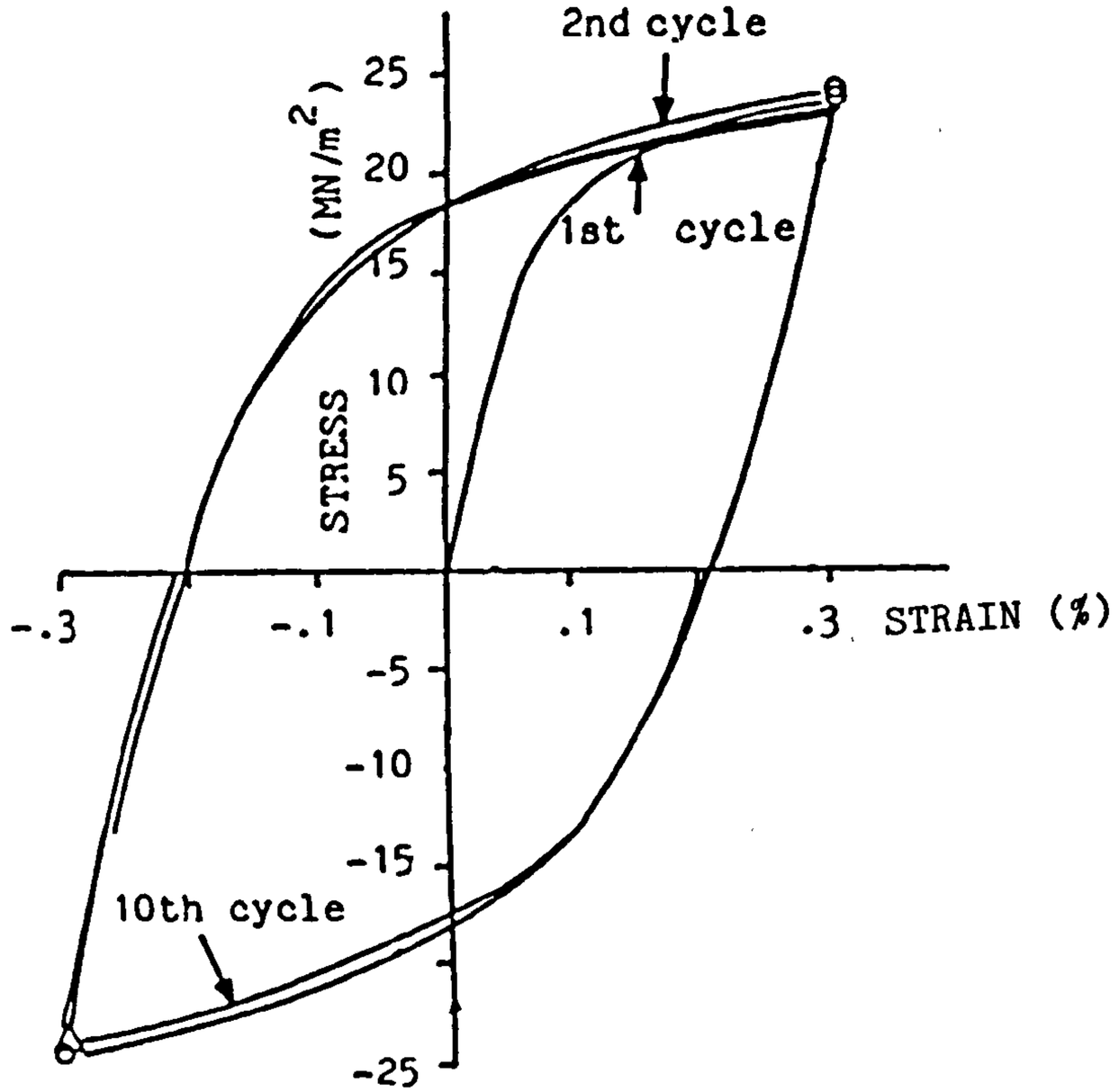

Fig. 5.2 Typical behaviour with fixed strain range cycling (±ε).data obtained from ref. 3.

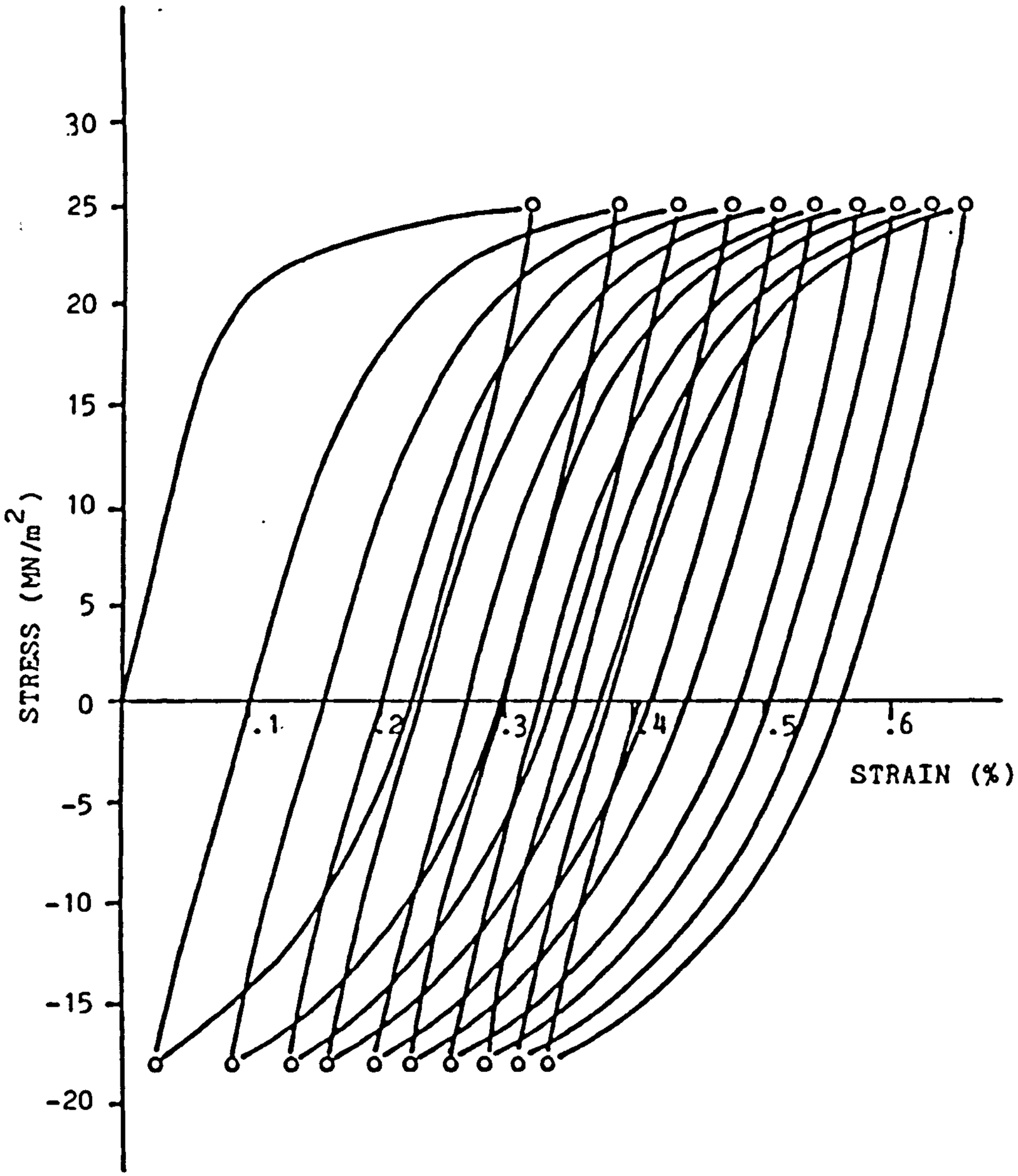

Fig. 5.3 Typical beahaviour with fixed stress range cycling with a non-zero mean stress. Data obtained from ref. 3.

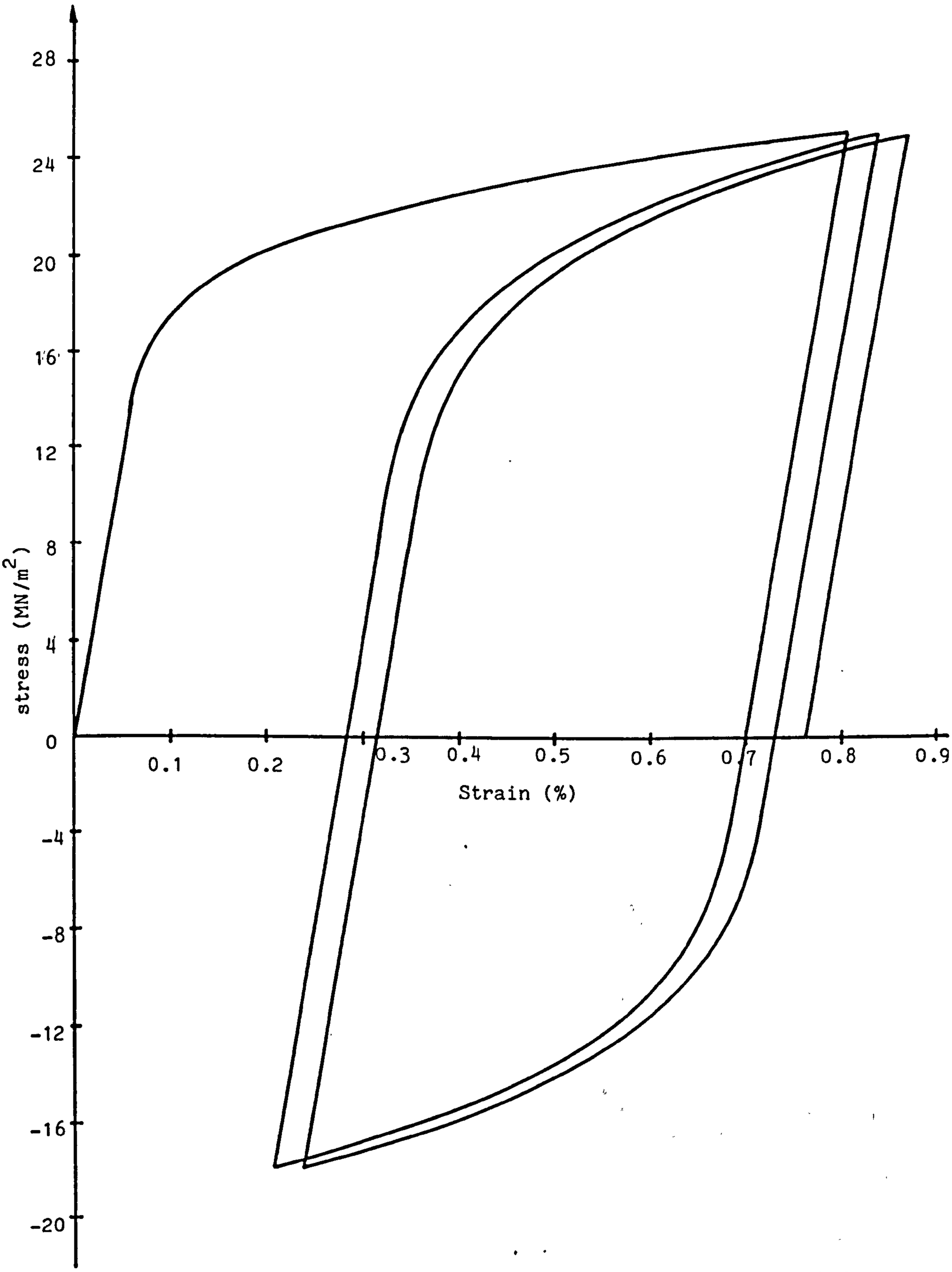

Fig. 5.4 Stress strain behaviour for lead alloy material for fixed stress range cycling with a non-zero mean stress with Goodman and Goodall material model constants A.

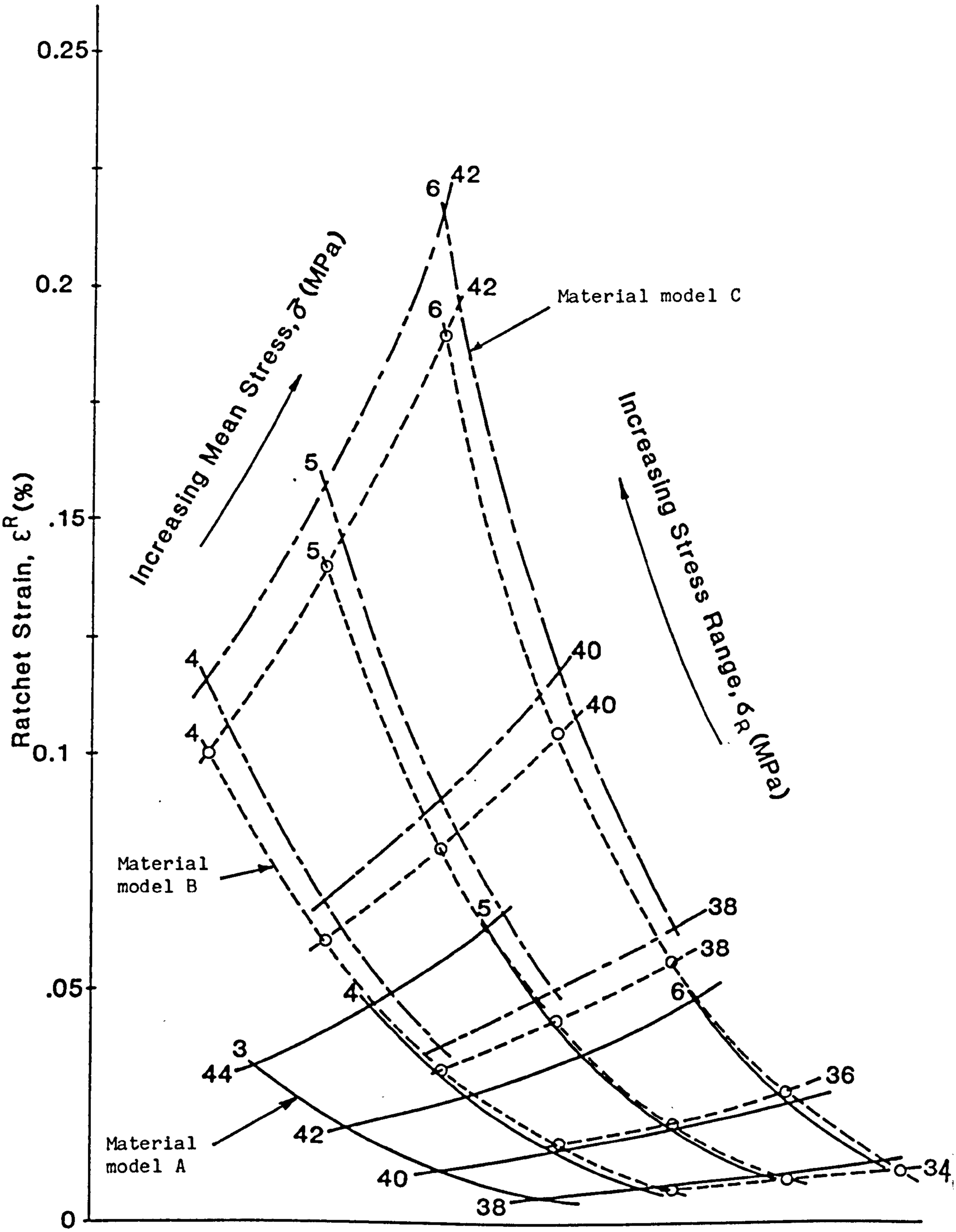

Fig. 5.5 'Carpet plot' showing the variations of ratchet strains which mean stress and stress range for material models A, B and C.

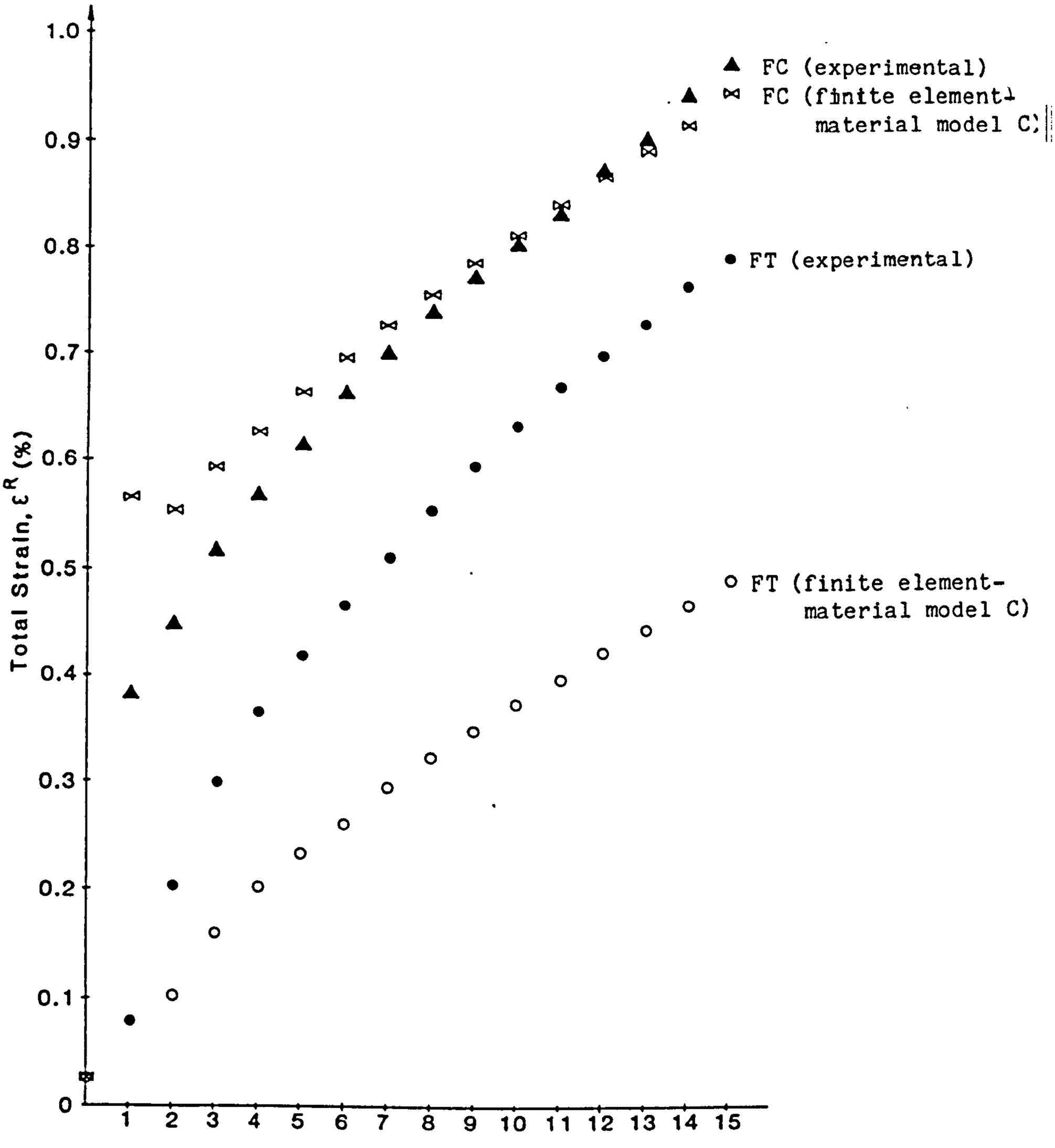

Fig. 5.6(i) Variation of total strain with cycle number for B1 loading conditions (see table 5.4)

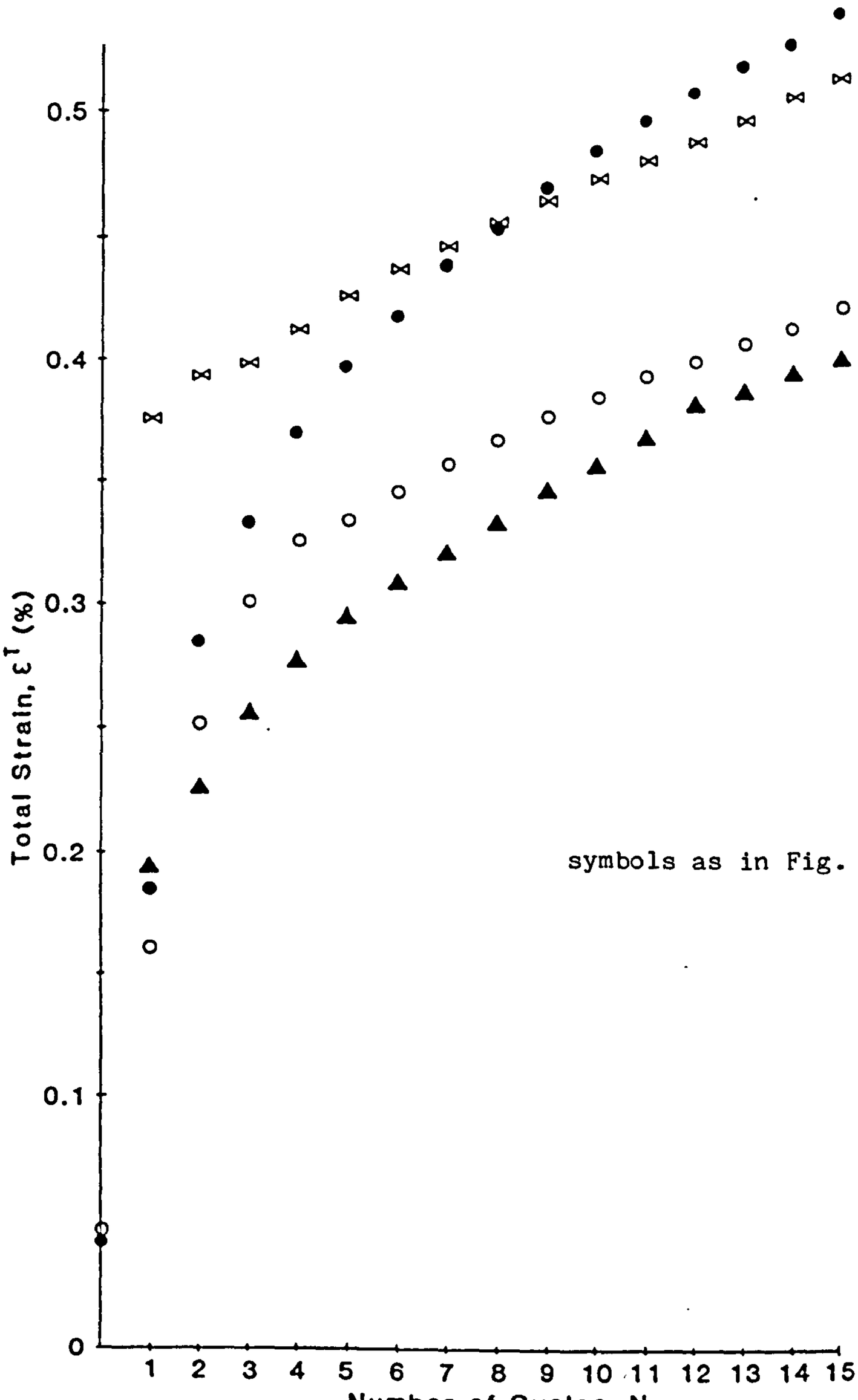

Fig. 5.6(ii) Variation of total strain with cycle number for B2 loading conditions (see table 5.4)

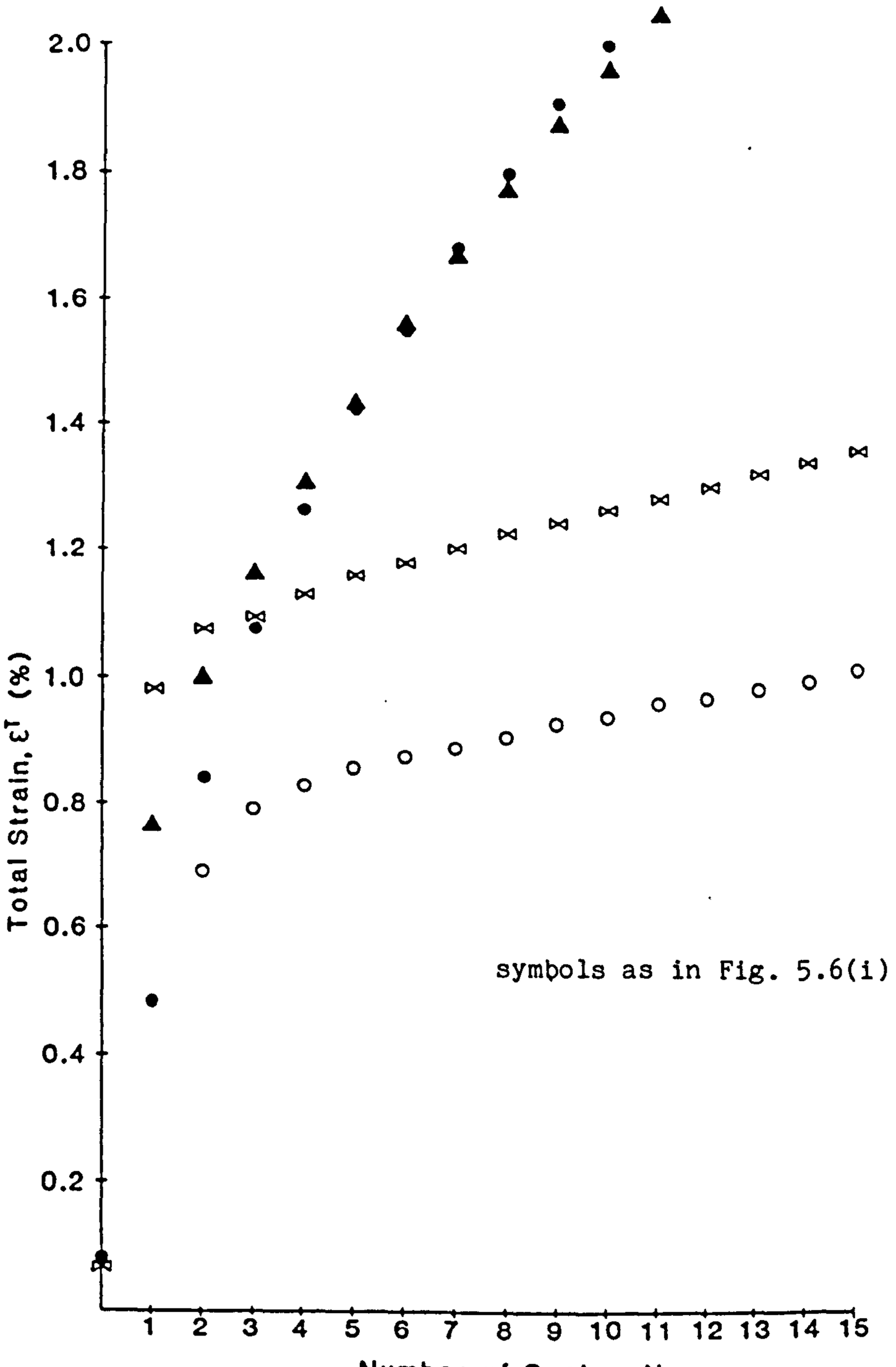

Fig. 5.6(iii) Variation of total strain with cycle number for B3 loading conditions (see table 5.4)

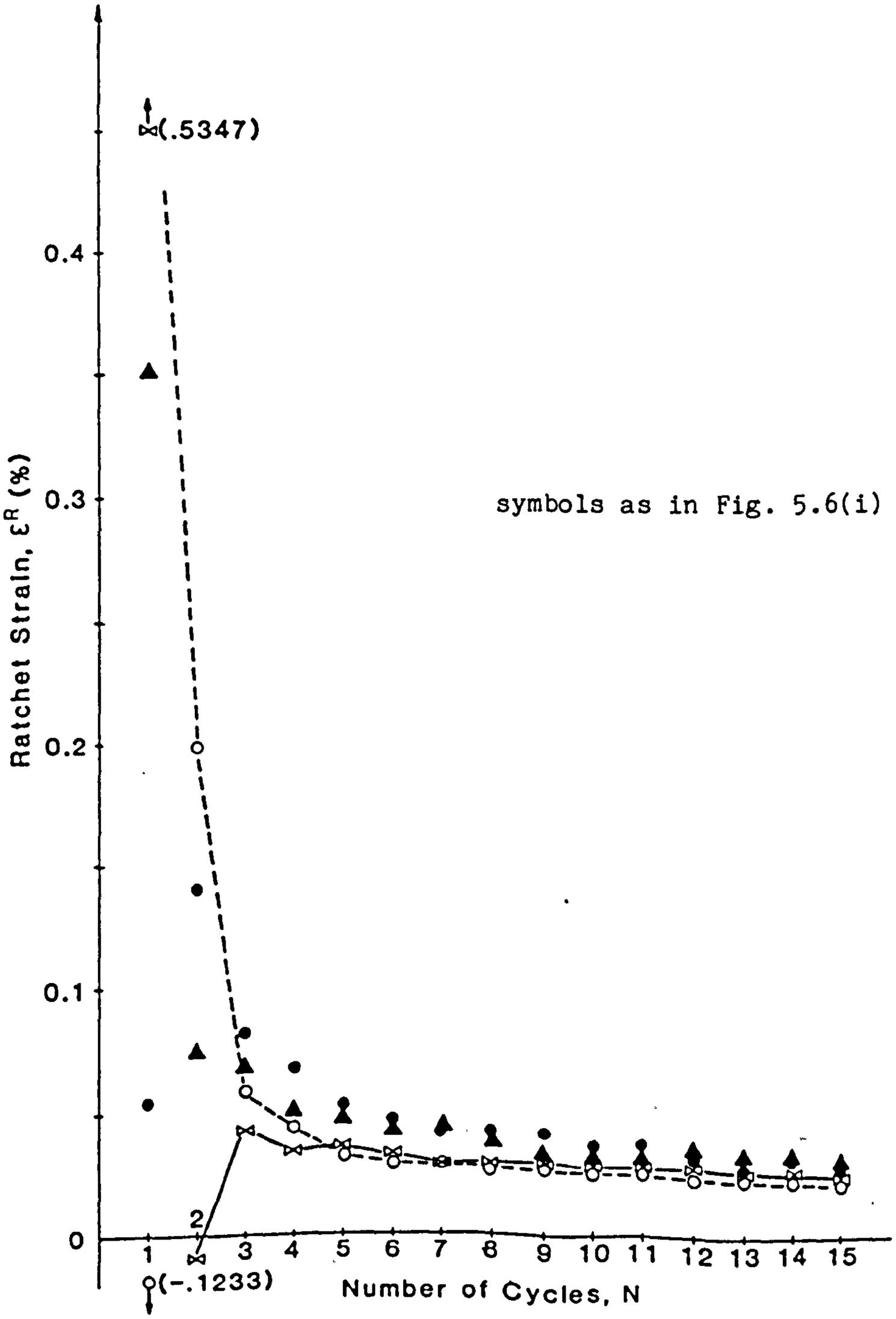

symbols as in Fig. 5.6(i)

Fig. 5.7(i) Variation of ratchet strain with cycle number for B1 loading conditions (see table 5.4)

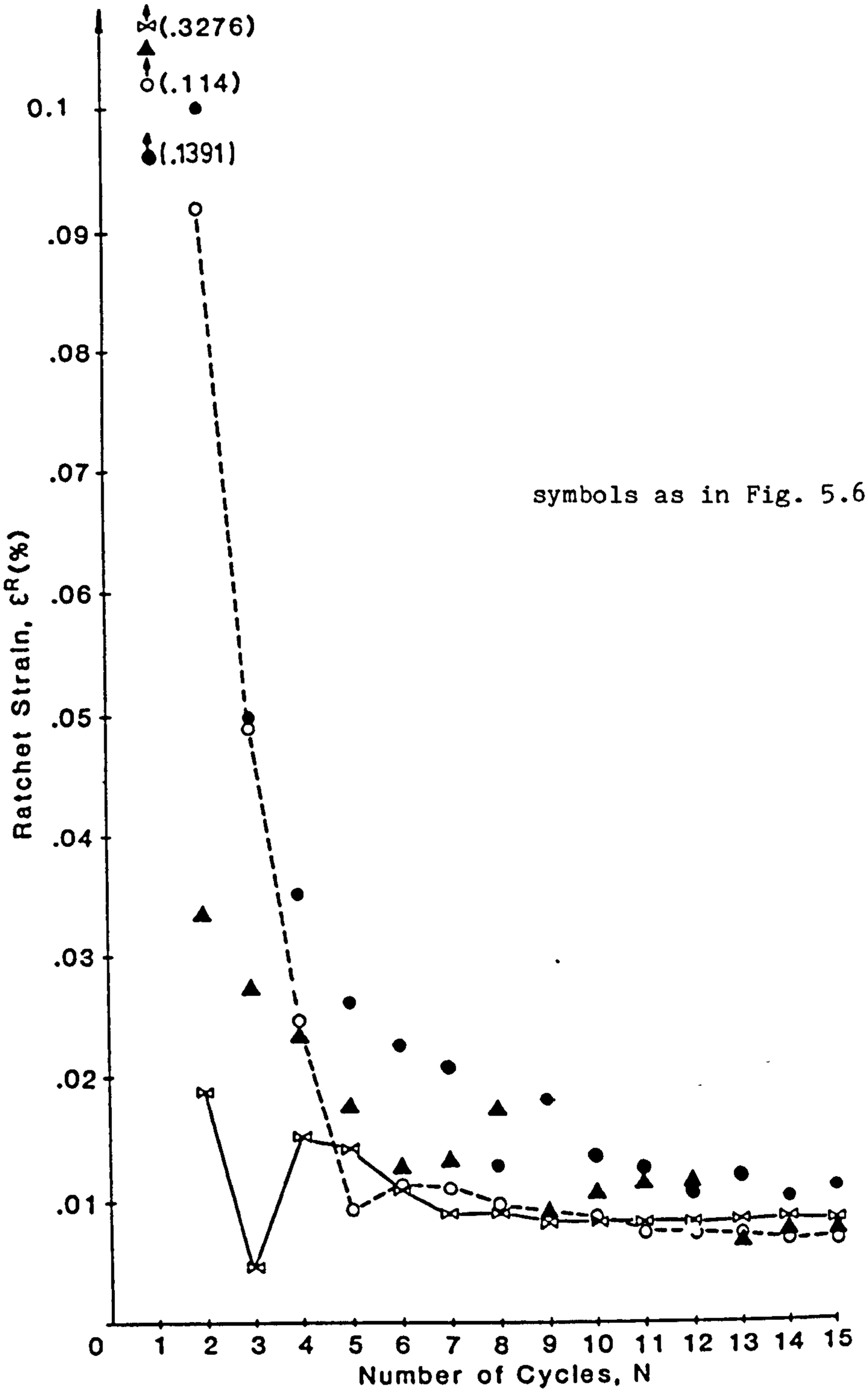

symbols as in Fig. 5.6(i)

Fig. 5.7(ii) Variations of ratchet strain with cycle number for B2 loading conditions (see table 5.4)

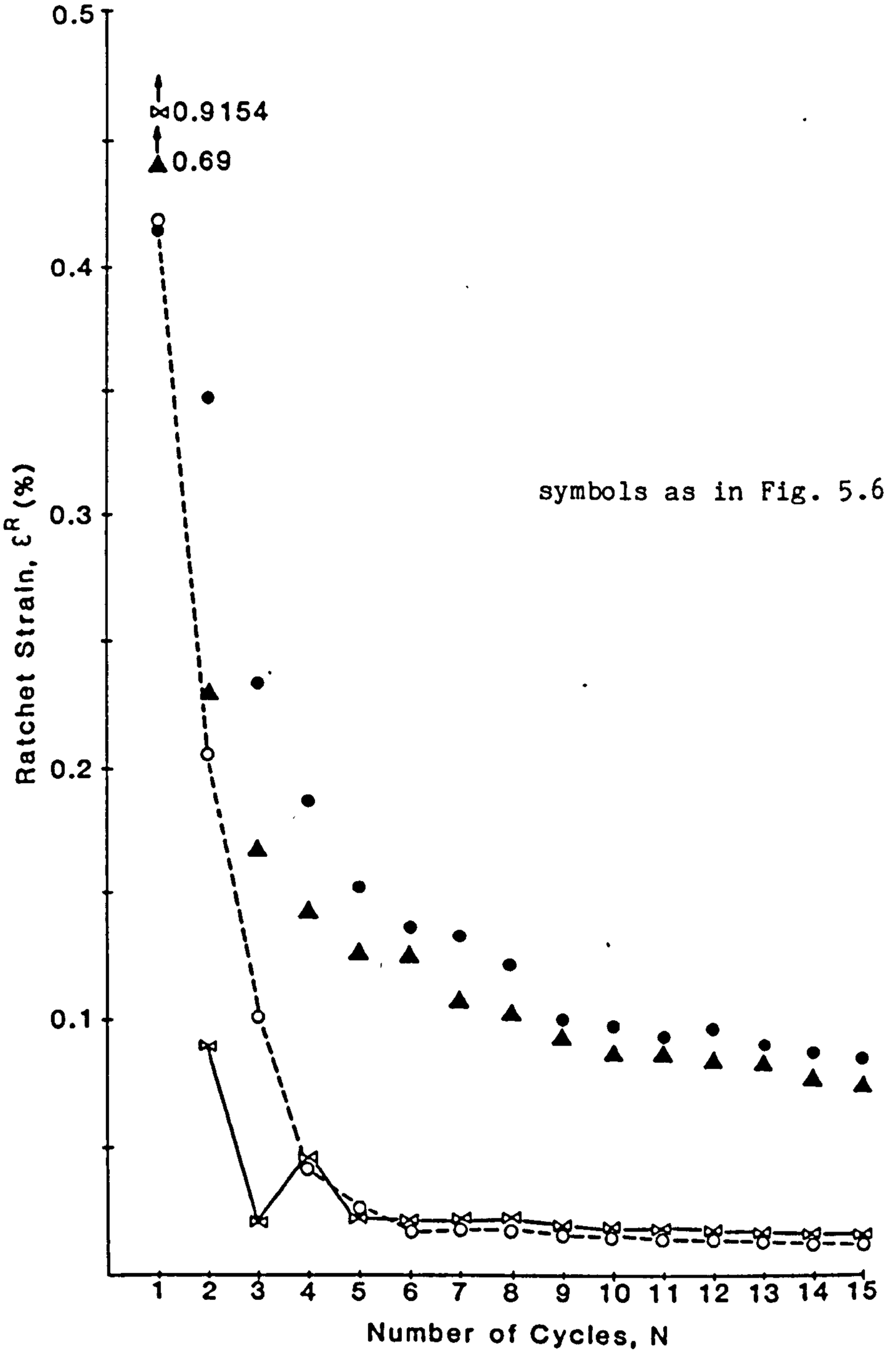

symbols as in Fig. 5.6(i)

Fig. 5.7(iii) Variation of ratchet strain with cycle number for B3 loading conditions (see table 5.4)

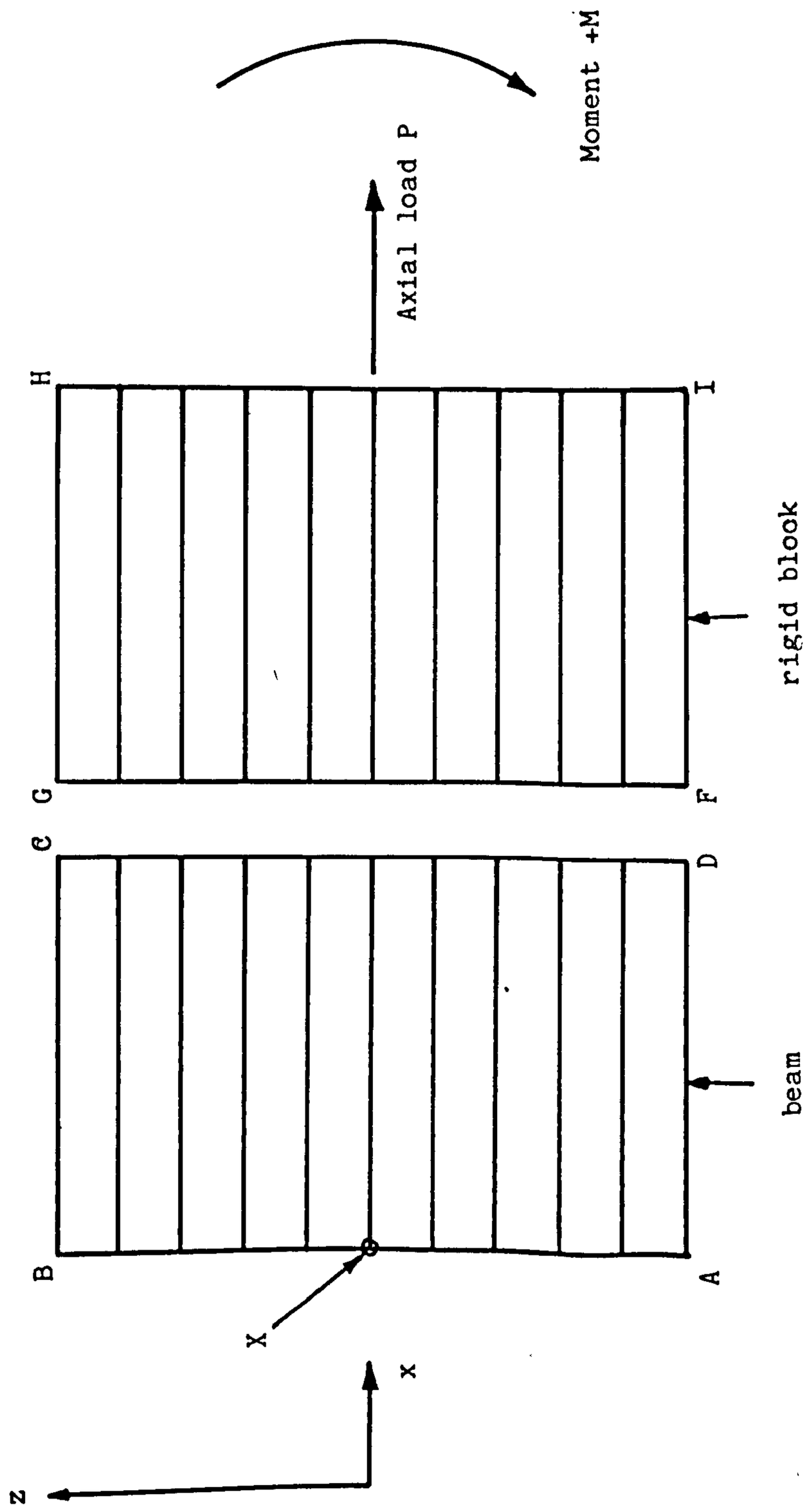

Fig. 5.8 Finite element mesh

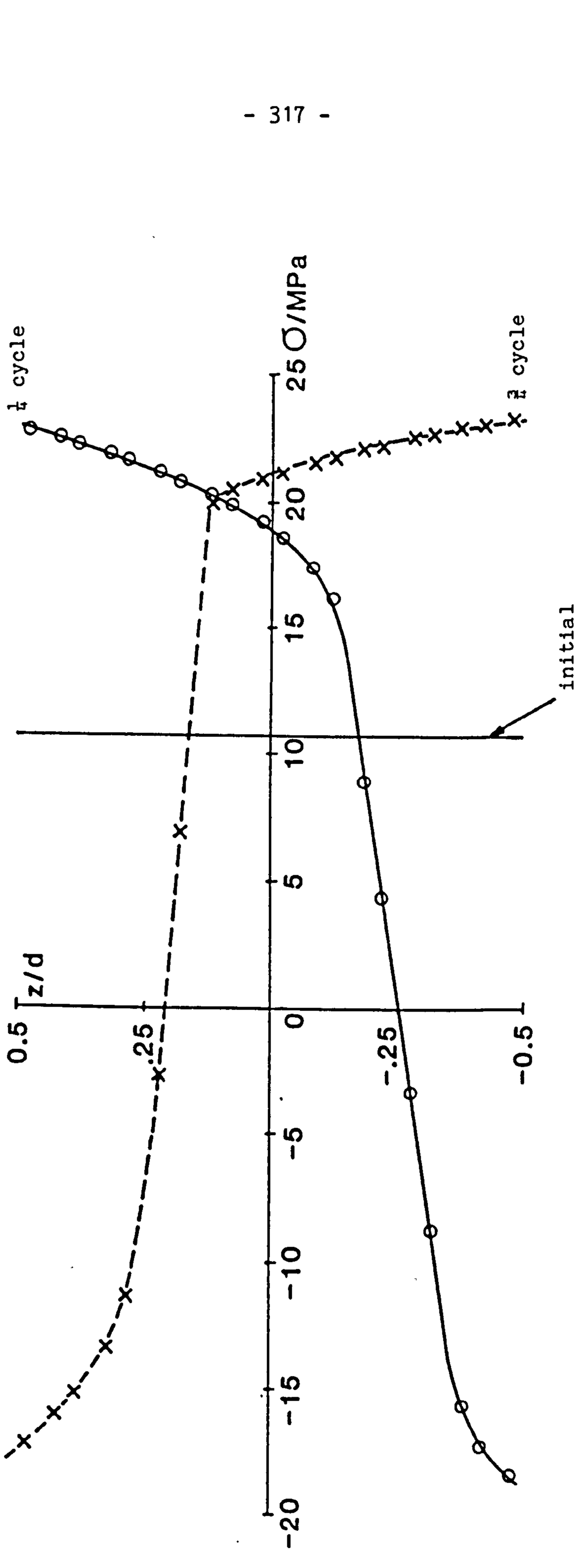

Fig. 5.9(i) Through-thickness stress distributions during the first cycle for B2 loading conditions and material model C

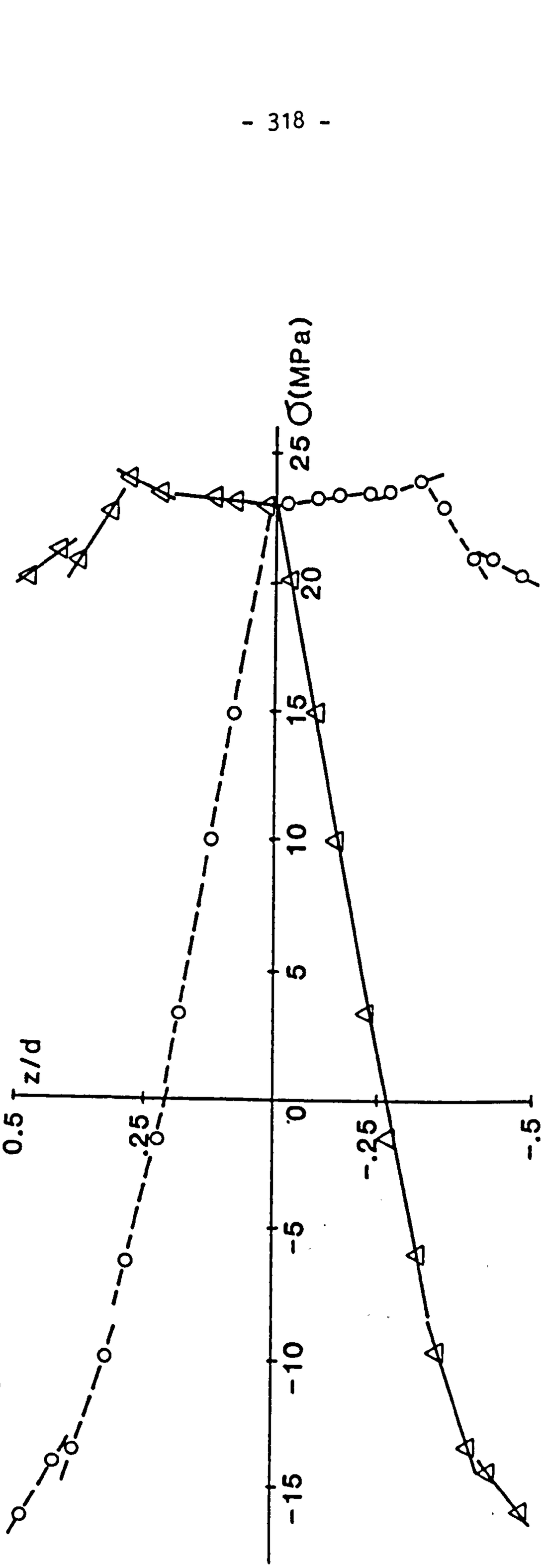

Fig. 5.9(ii) Through thickness stress distributions during the 15th cycle for B2 loading conditions and material model C

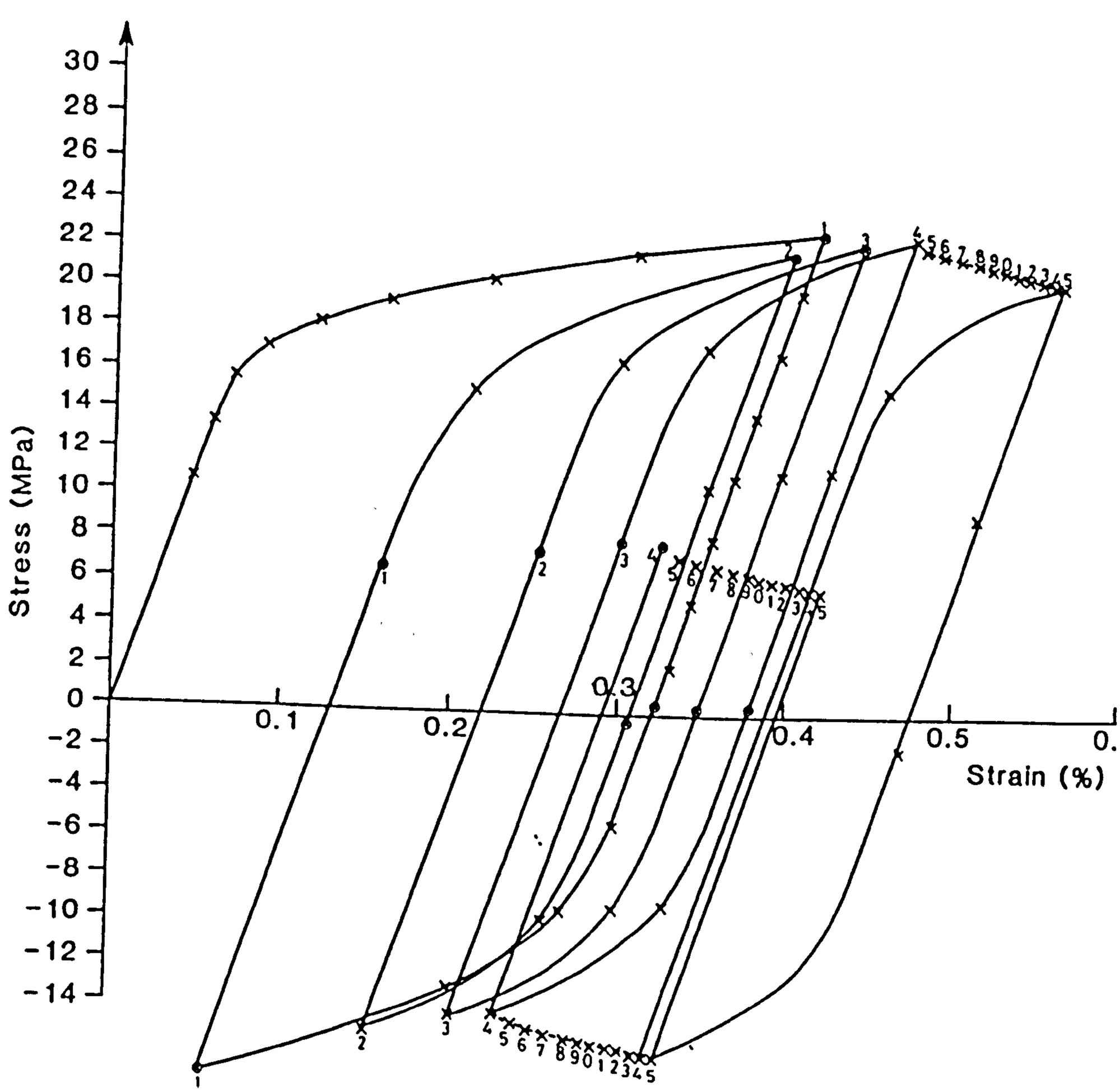

Fig. 5.10(i) Stress-strain histories at z/d = 0.48 for B2 loading conditions and material model C

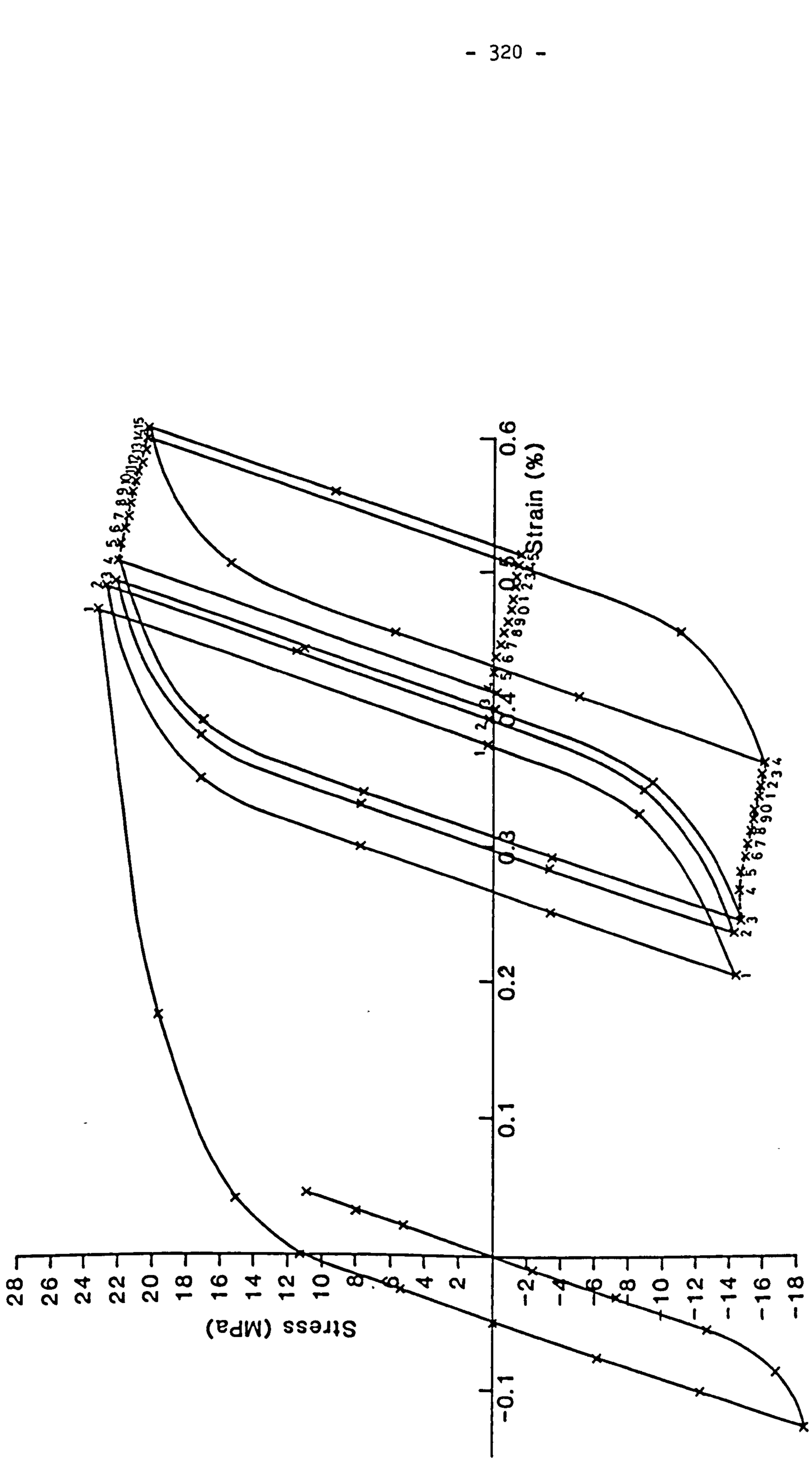

Fig. 5.10(ii) Stress-strain histories at z/d = -0.48 for B2 loading conditions and material model C

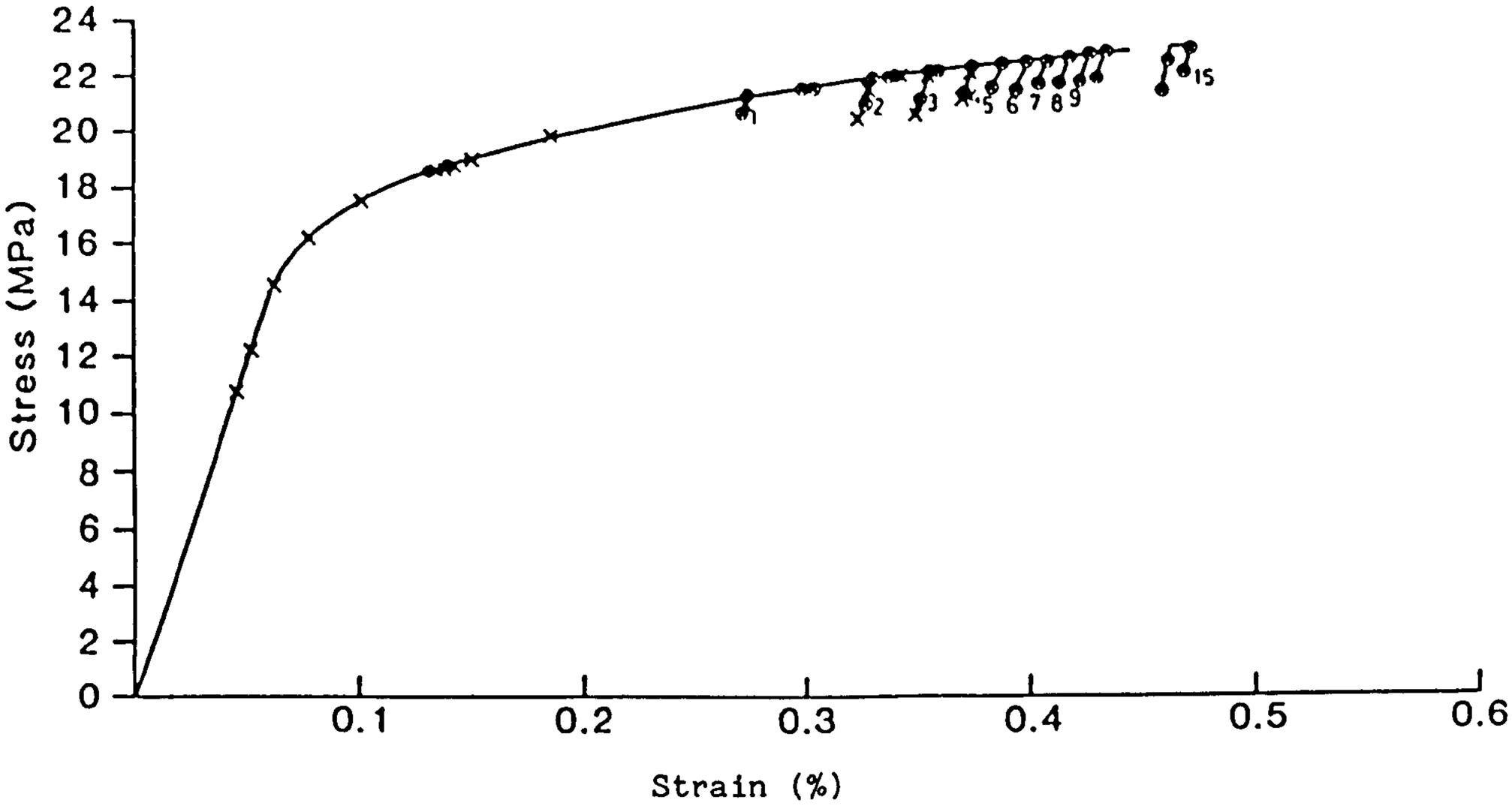

Fig. 5.10(iii) Stress-strain histories at z/d = -0.02 for B2 loading conditions and material model C

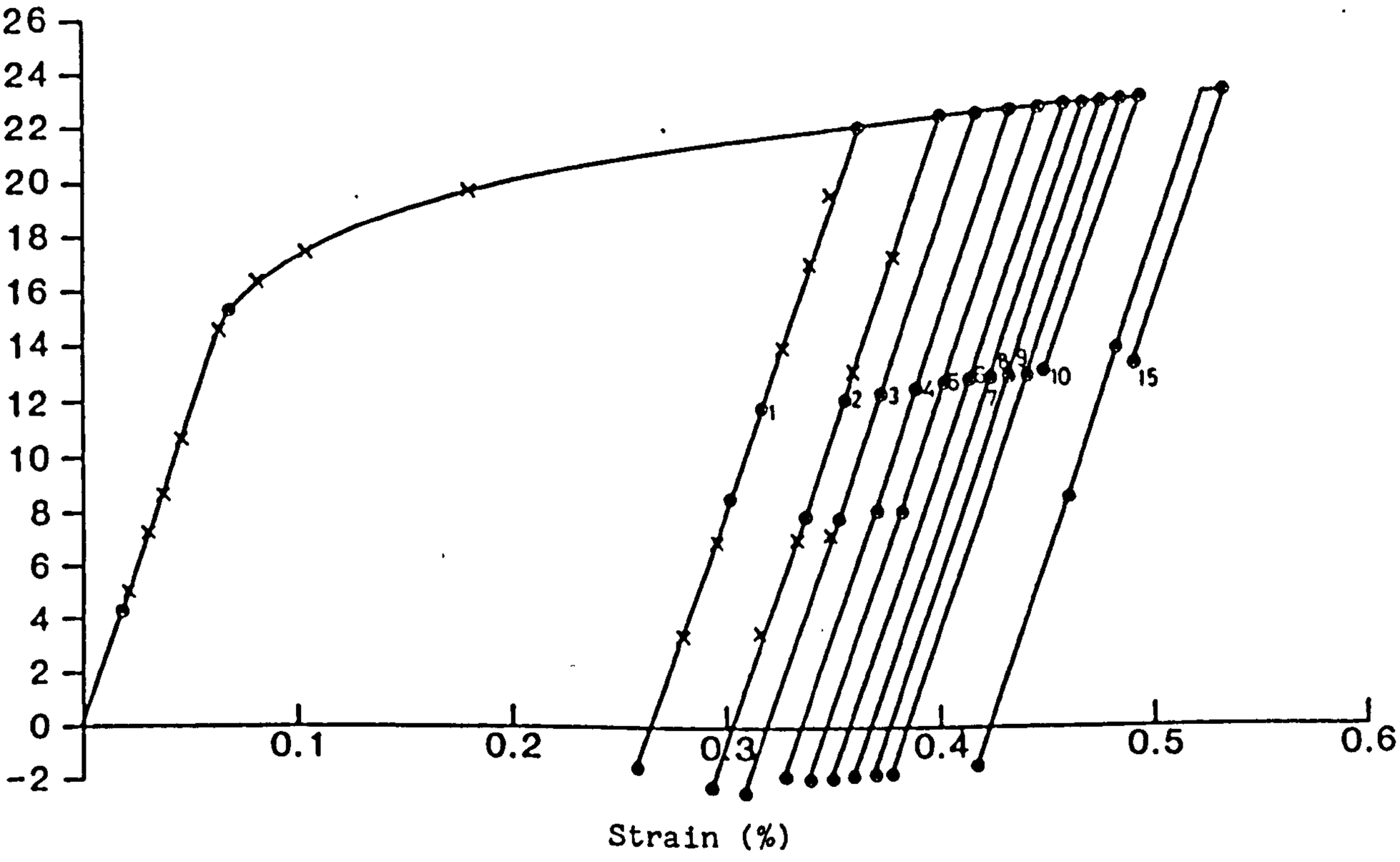

Fig. 5.10(iv) Stress-strain histories at z/d = -0.22 for B2 loading conditions and material model C.

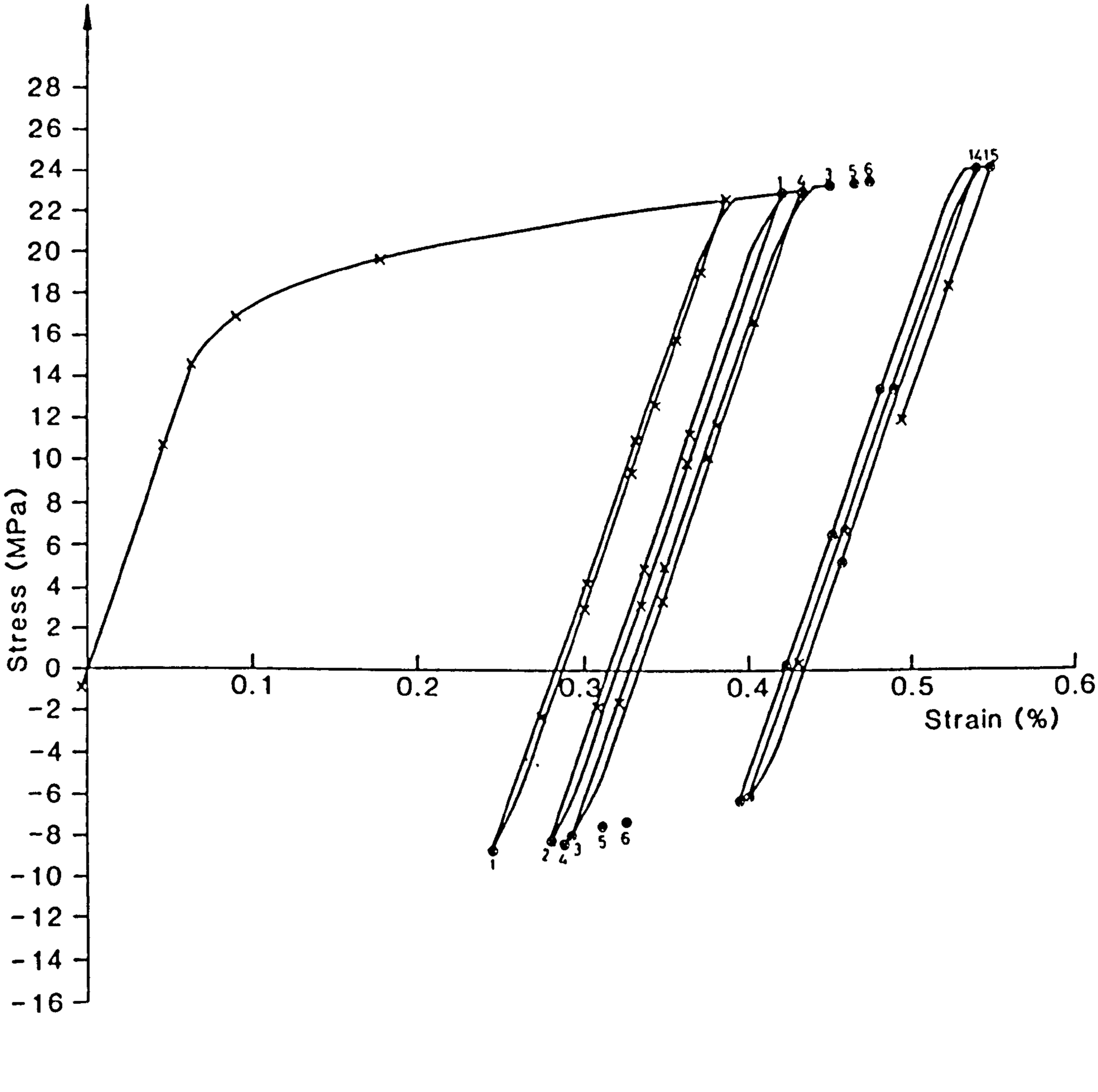

Fig. 5.10(v) Stress-strain histories at z/d = -0.28 for B2 loading conditions and material model C

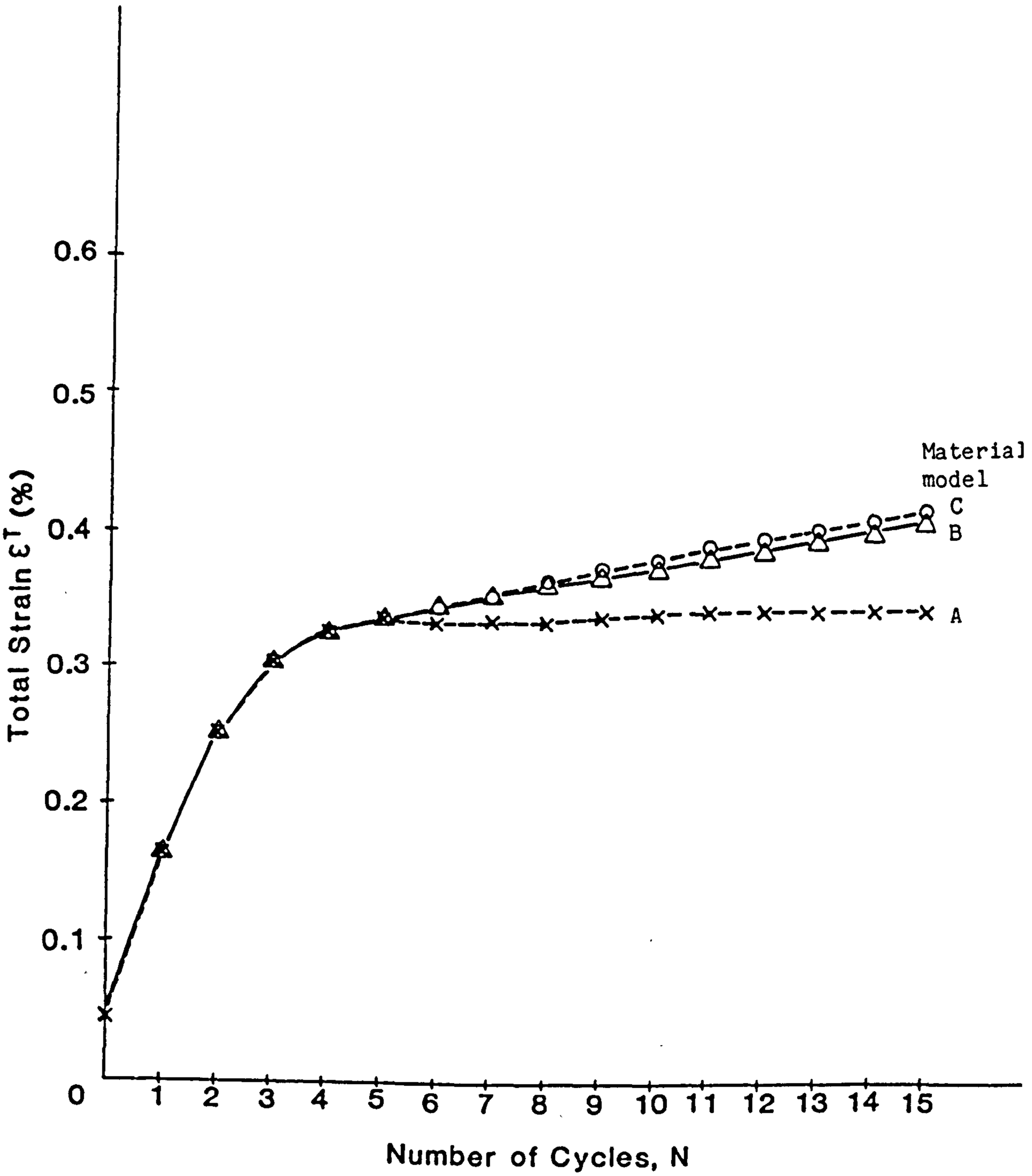

Fig. 5.11(i) Variation of total strains with cycle number for B2 loading conditions, FT surface.

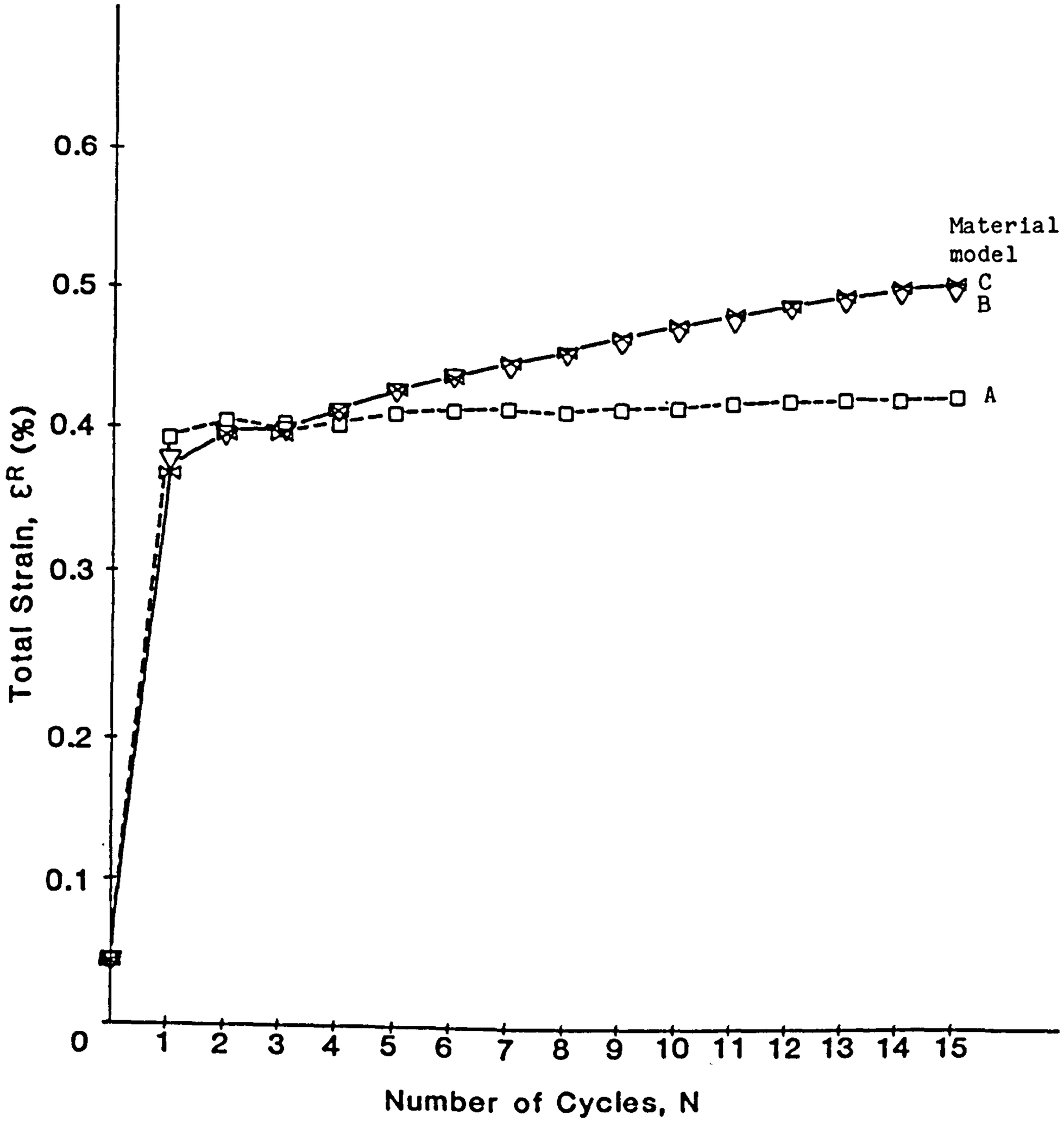

Fig. 5.11(ii) Variation of total strain with cycle number for B2 loading conditions, FC surface.

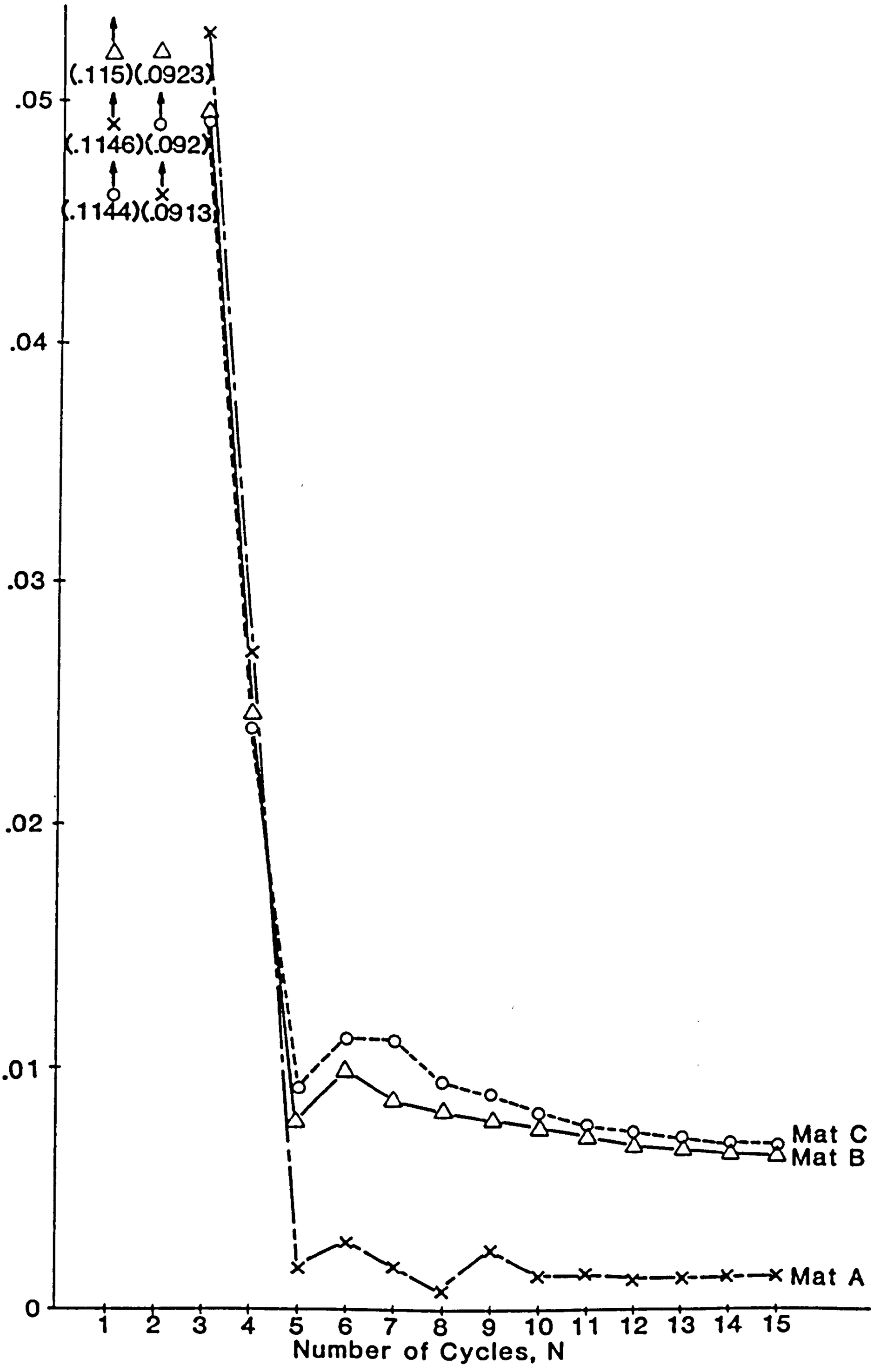

Fig. 5.12(i) Variation of ratchet strain with cycle number for B2 loading conditions, FT surface.

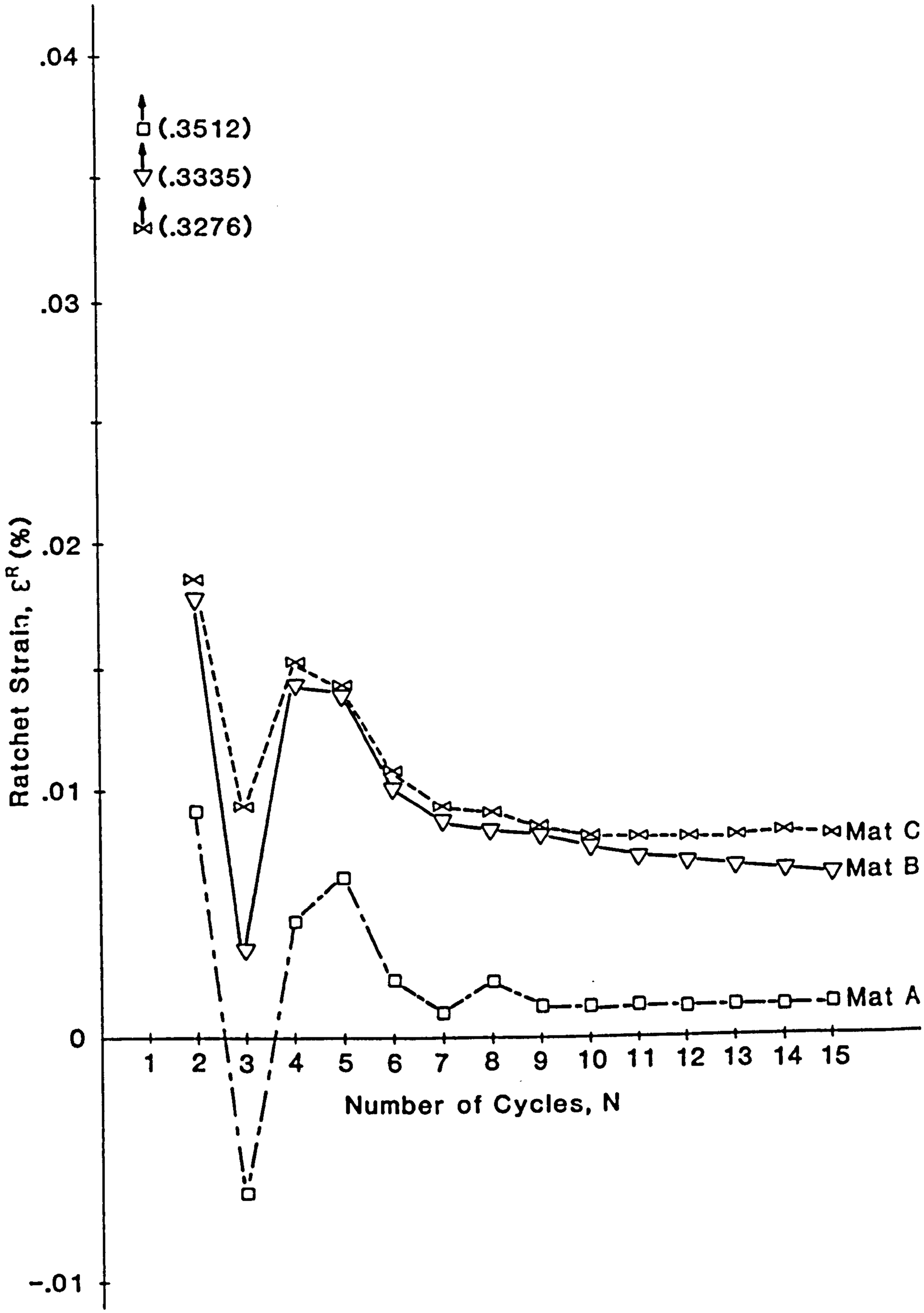

Fig. 5.12(ii) Variation of ratchet strain with cycle number for B2 loading conditions, FT surface

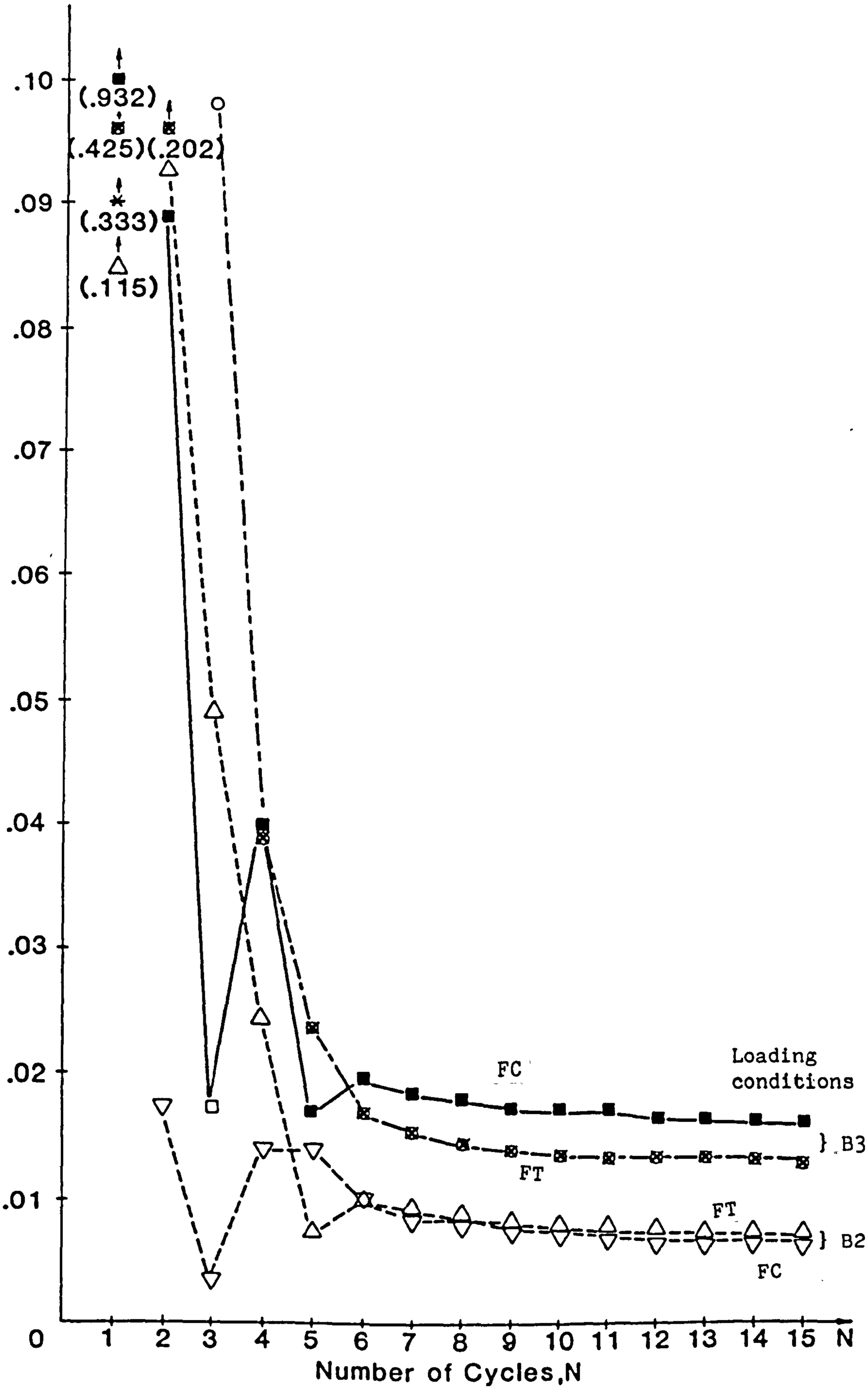

Fig. 5.13 Variations of ratchet strain with cycle number with material model B

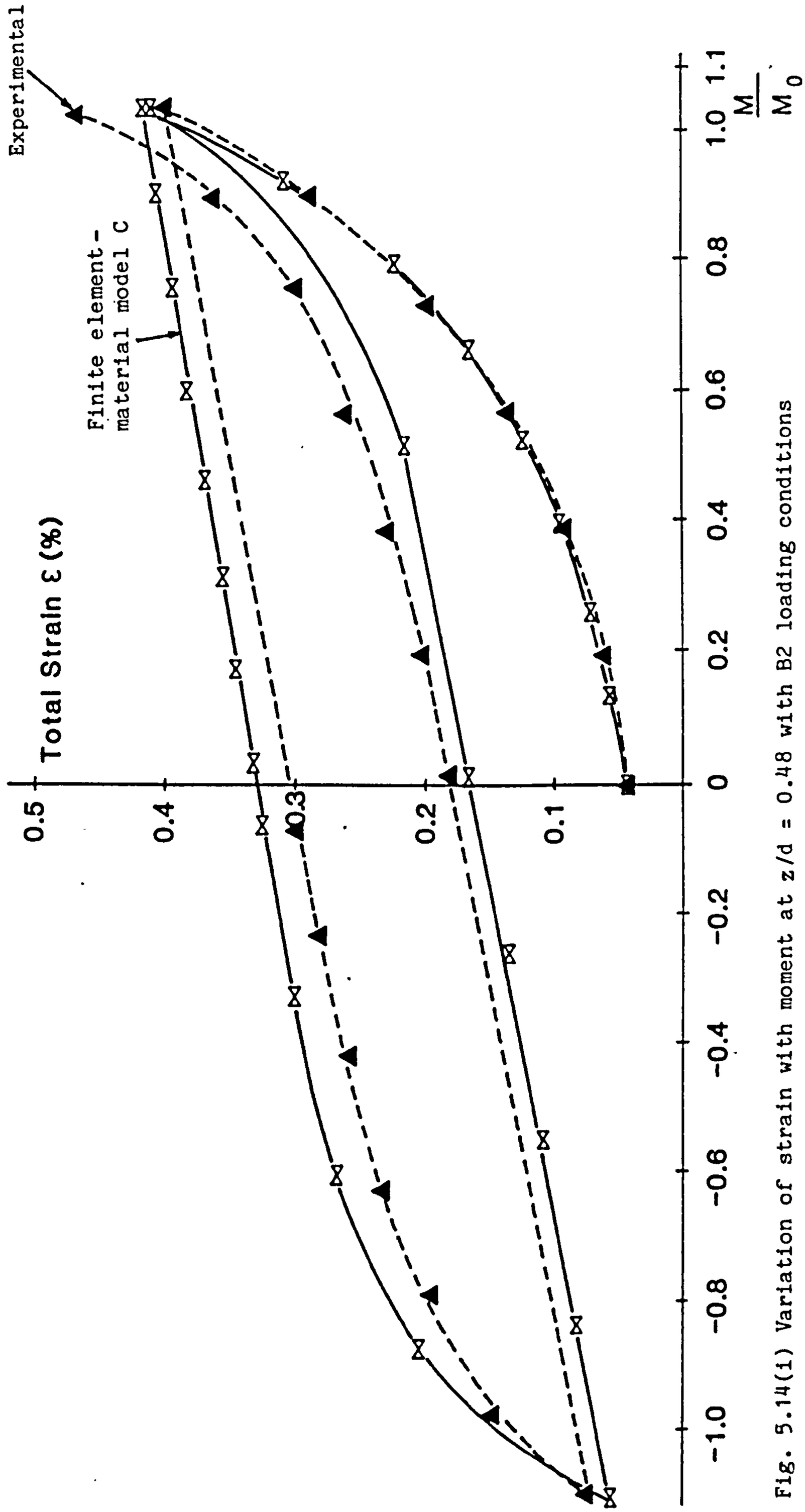

Fig. 5.14(i) Variation of strain with moment at z/d = 0.48 with B2 loading conditions

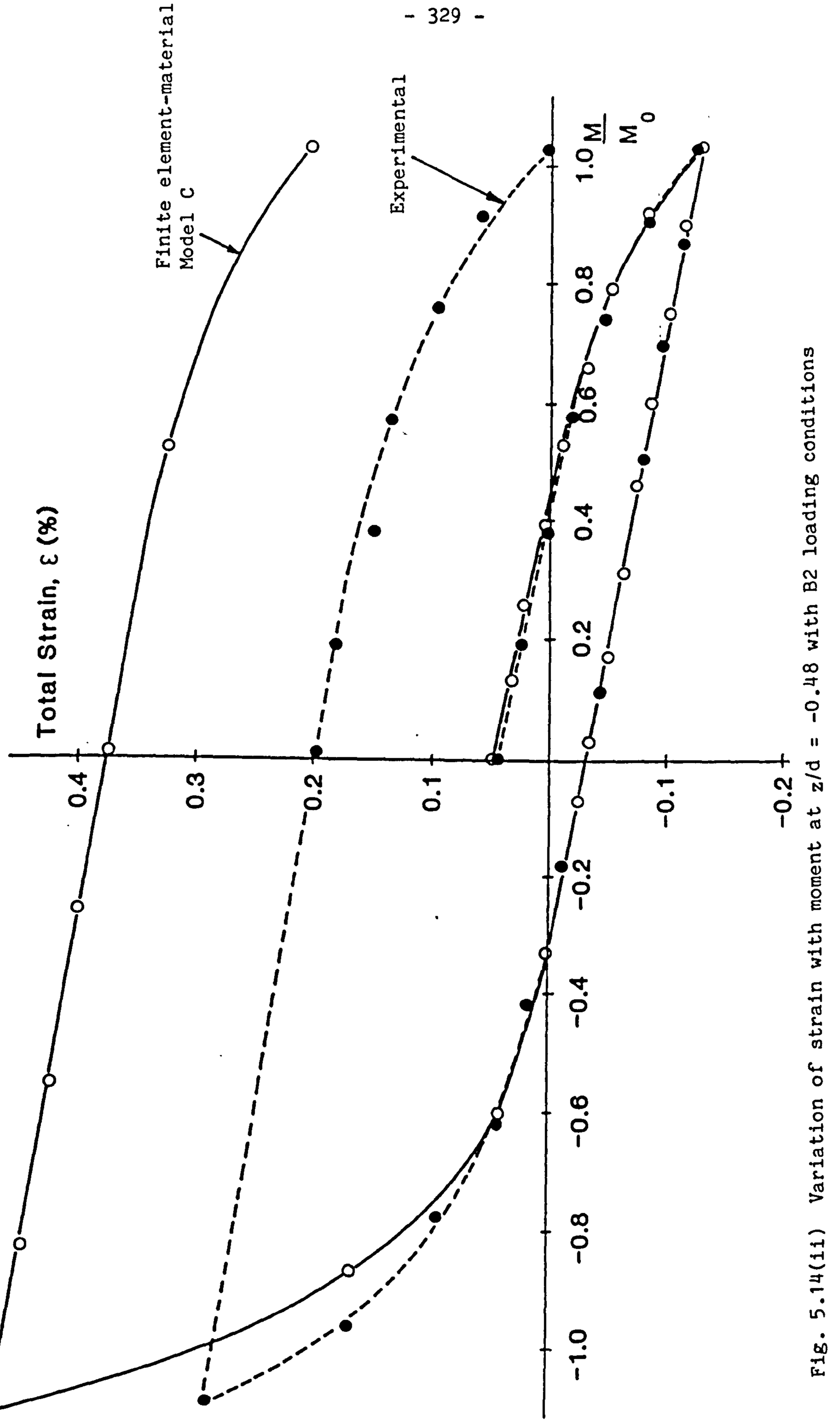

Fig. 5.14(ii) Variation of strain with moment at z/d = -0.48 with B2 loading conditions

Fig. 5.15(i) Comparison between experimental results (3), perfectly plastic model (16) and Goodman and Goodall model C for B2 loading conditions.

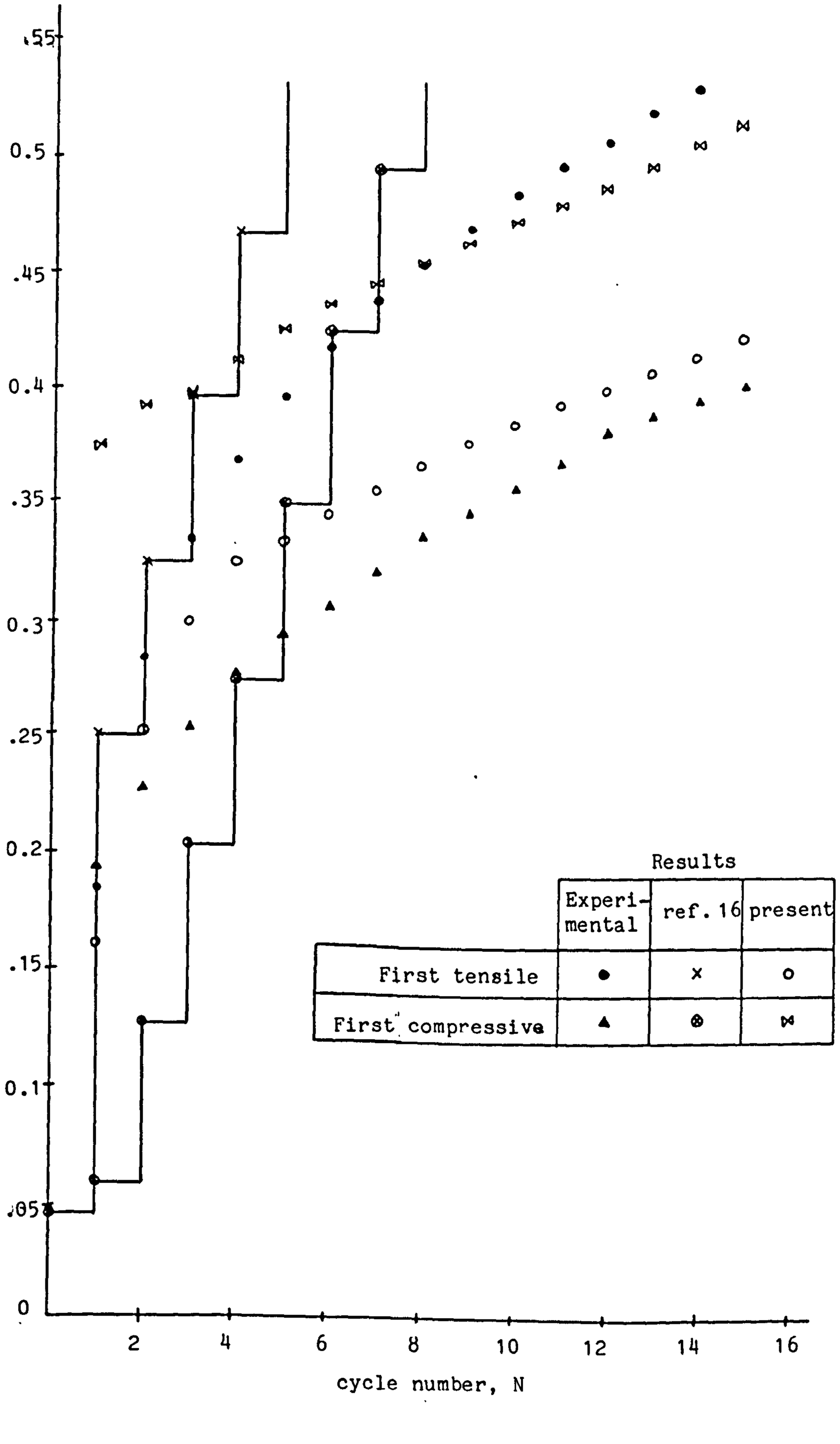

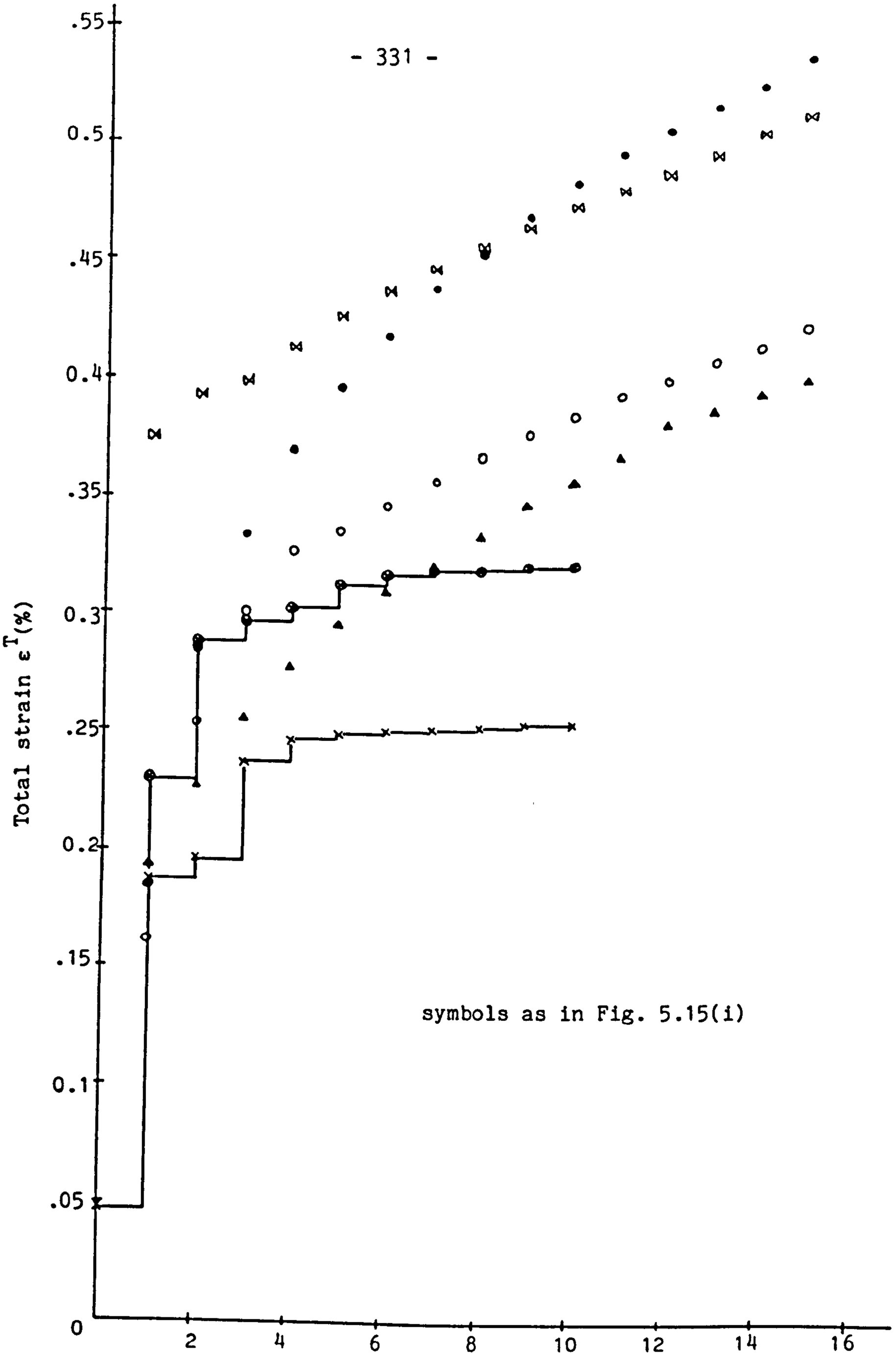

symbols as in Fig. 5.15(i)

Fig. 5.15(ii) Comparison between experimental results (3), linear isotropic hardening model (16) and Goodman and Goodall model C for B2 loading conditions

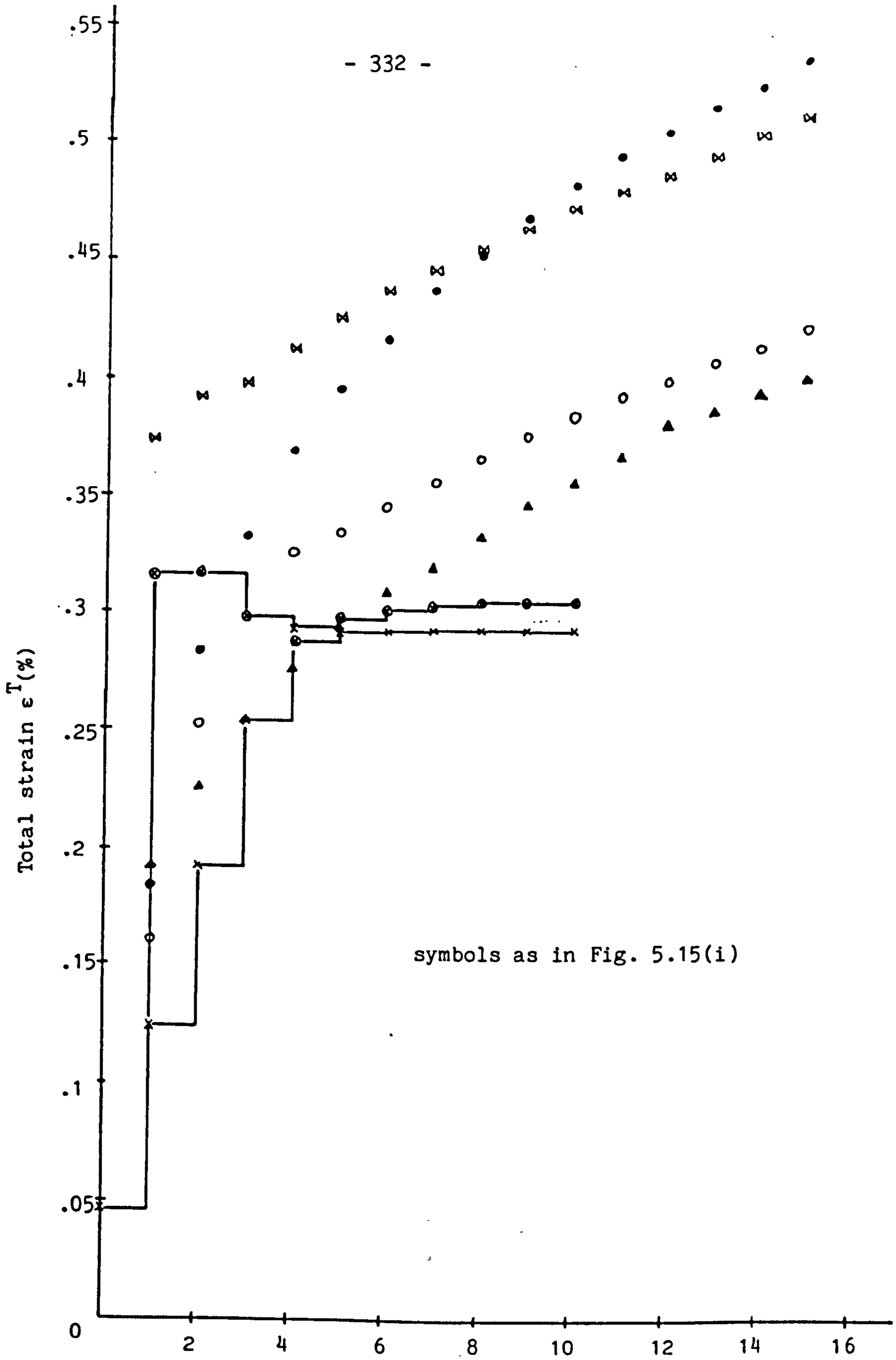

Fig. 5.15(iii) Comparison between experimental results (3), linear kinematic hardening (16) and Goodman and Goodall model C for B2 loading conditions

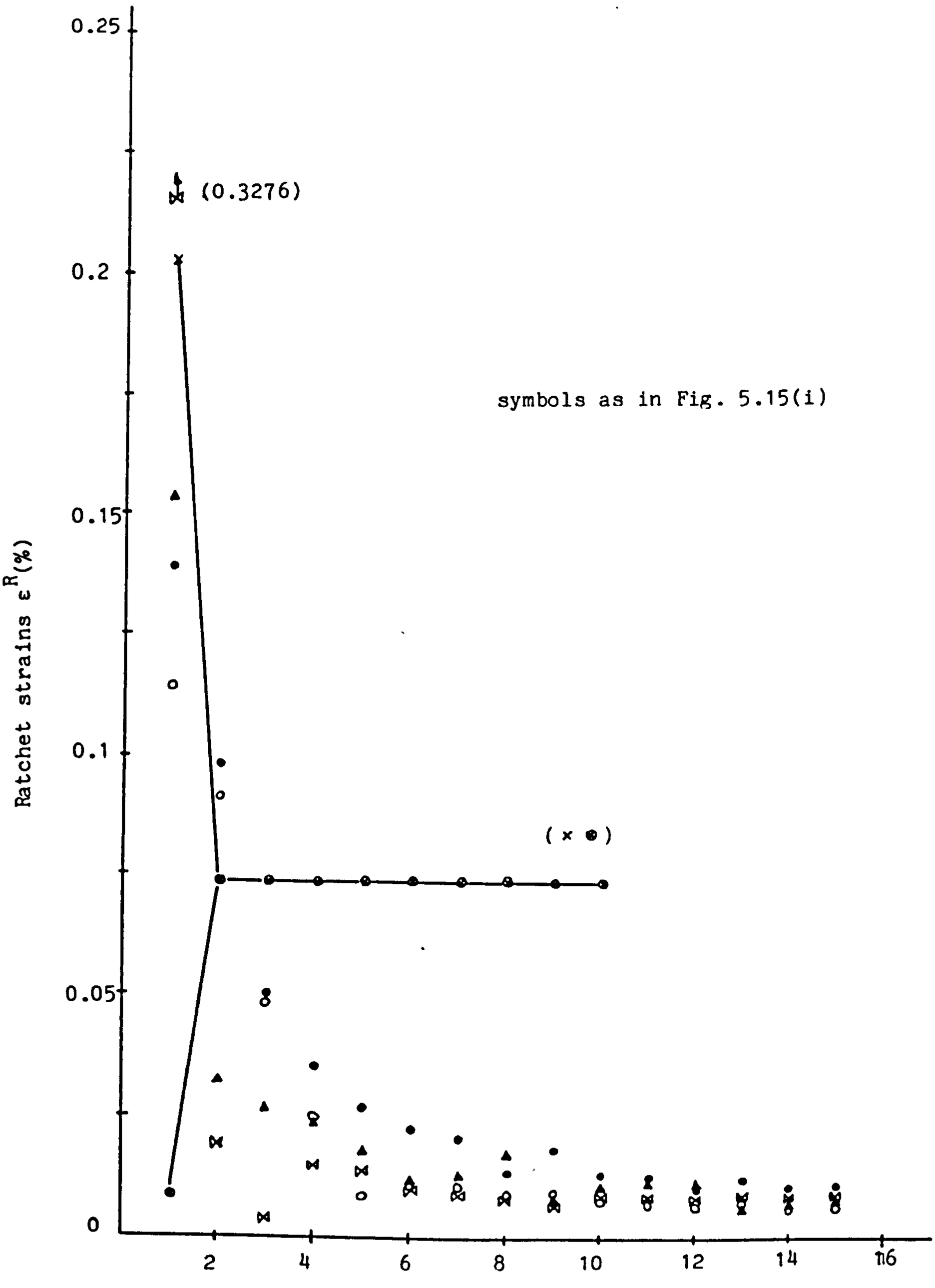

symbols as in Fig. 5.15(i)

Fig. 5.16(i) Comparison between experimental results (3), perfectly-plastic material (16) and Goodman and Goodall model C for B2 loading conditions.

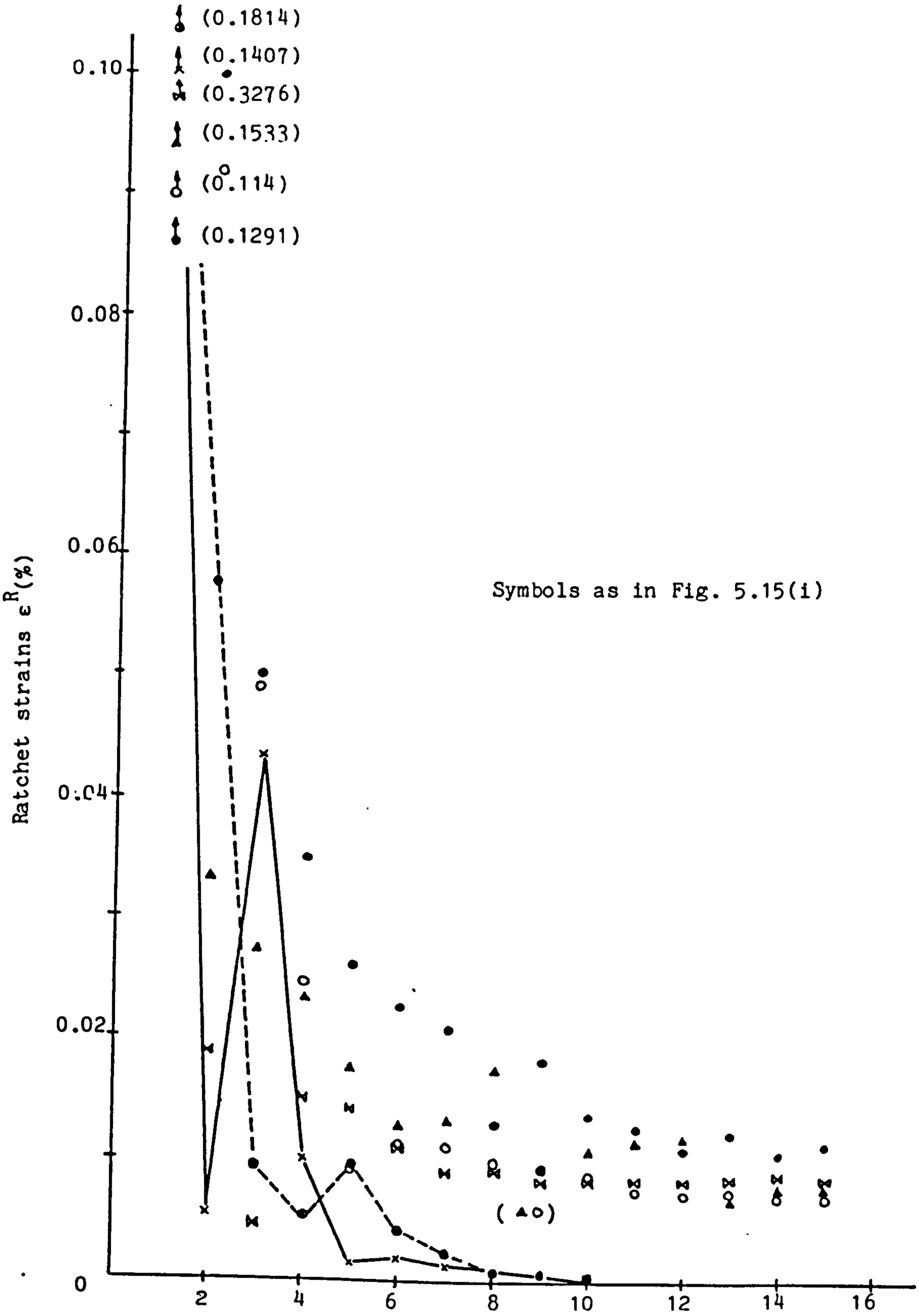

Symbols as in Fig. 5.15(i)

Fig. 5.16(ii) Comparison between experimental results (3), linear isotropic hardening (16) and Goodman and Goodall model C for B2 loading conditions

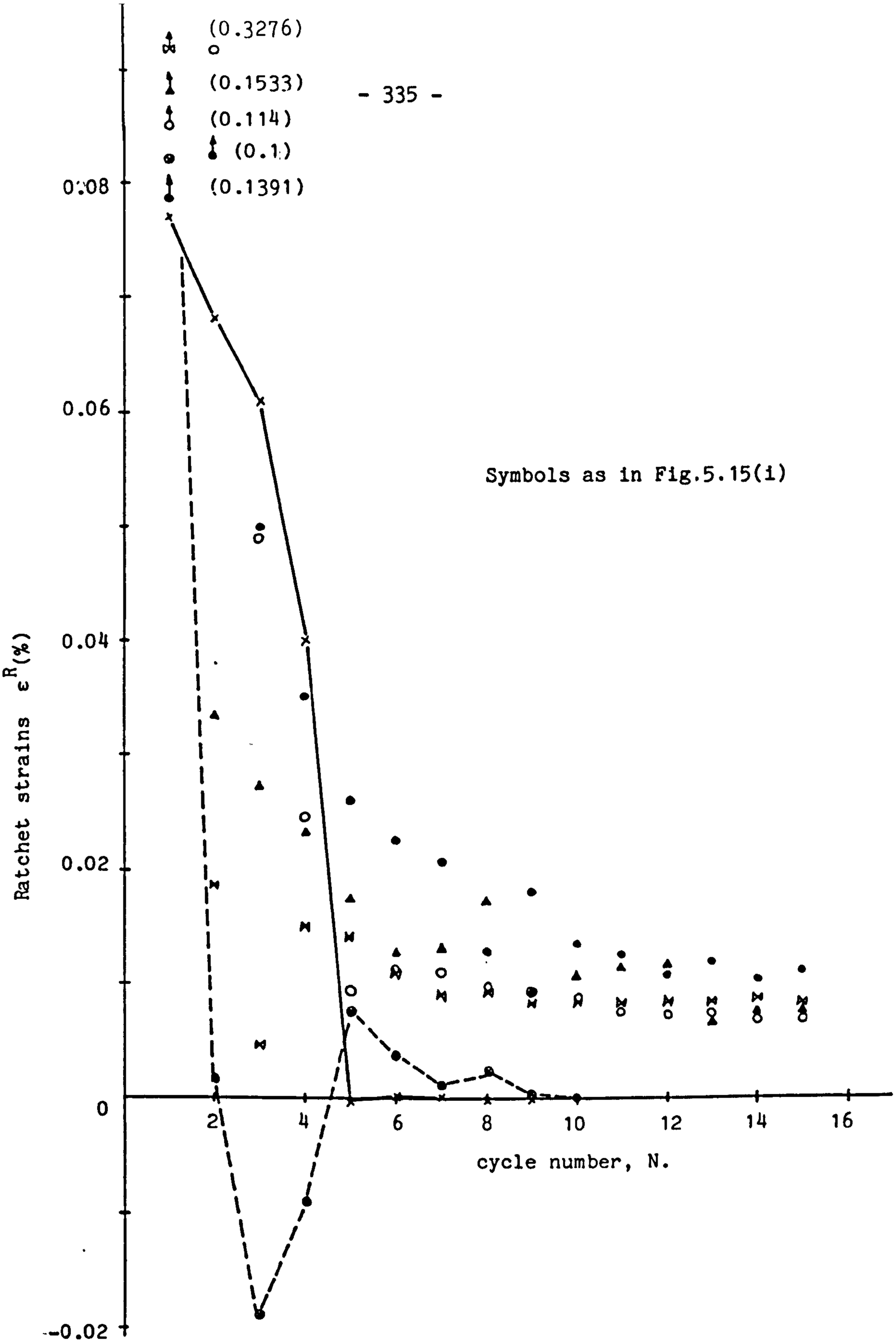

Symbols as in Fig.5.15(i)

Fig.5.16(iii) Comparison between experimental results (3), linear kinematic hardening model (16) and Goodman and Goodall model € for B2 loading conditions

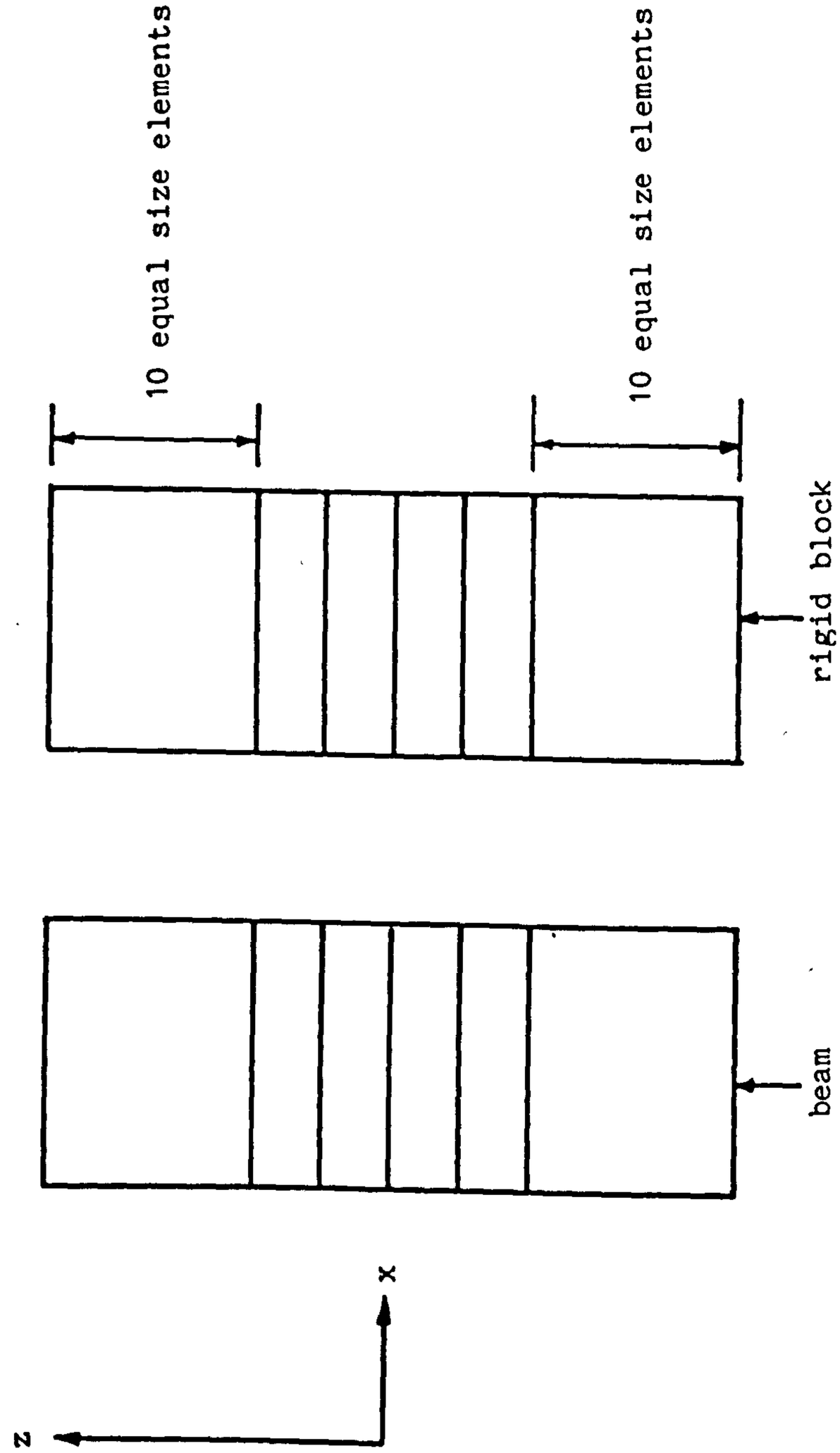

Fig. 5.17 Finer mesh for a uniform beam

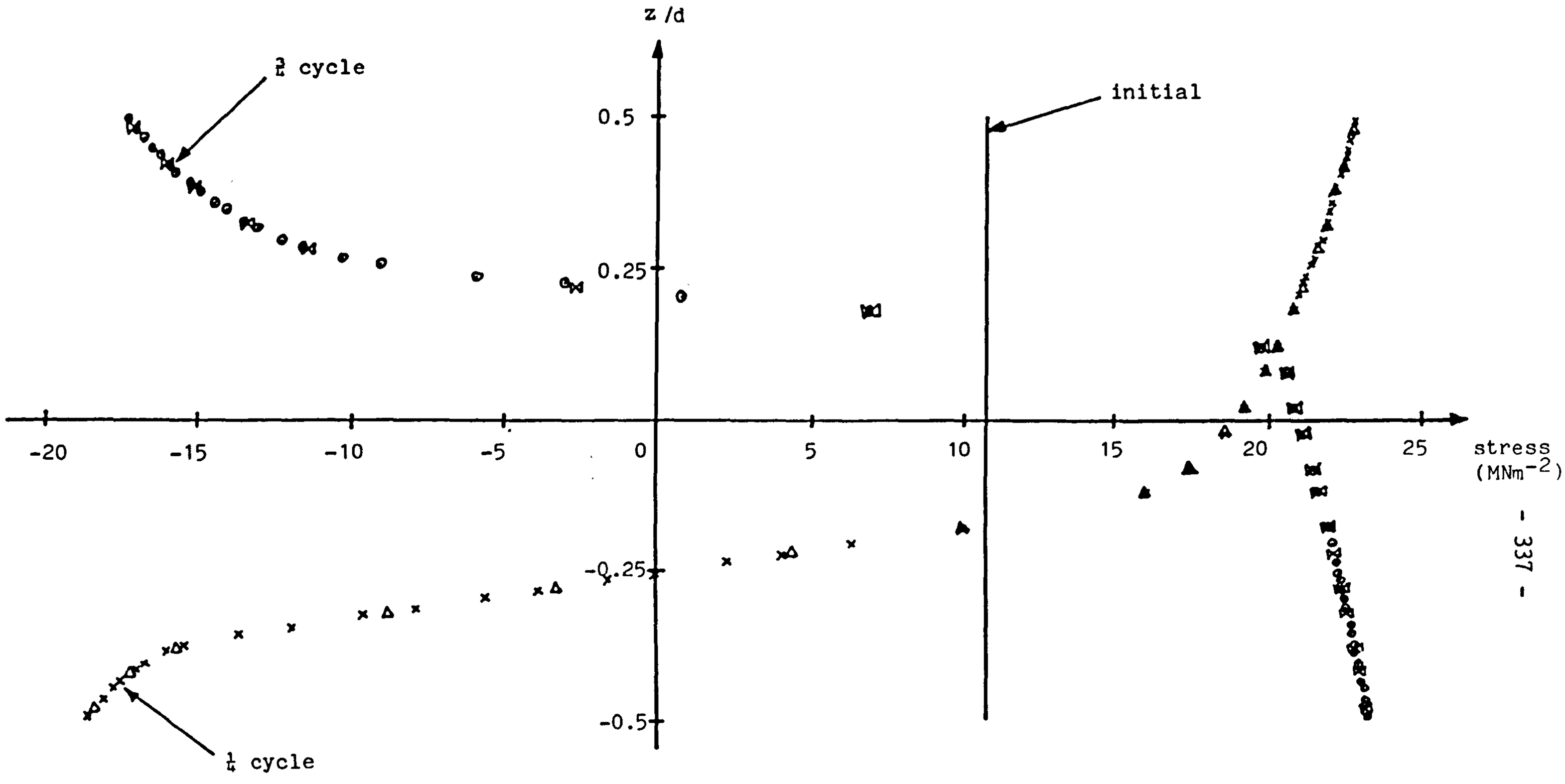

Fig.5.18(i) First cycle through the depth stress distribution. Comparison between coarse mesh in Fig. 5.8 (Δ,$\bowtie$) and finer mesh ($\times$, $\circ$) for B2 loading conditions material model C.

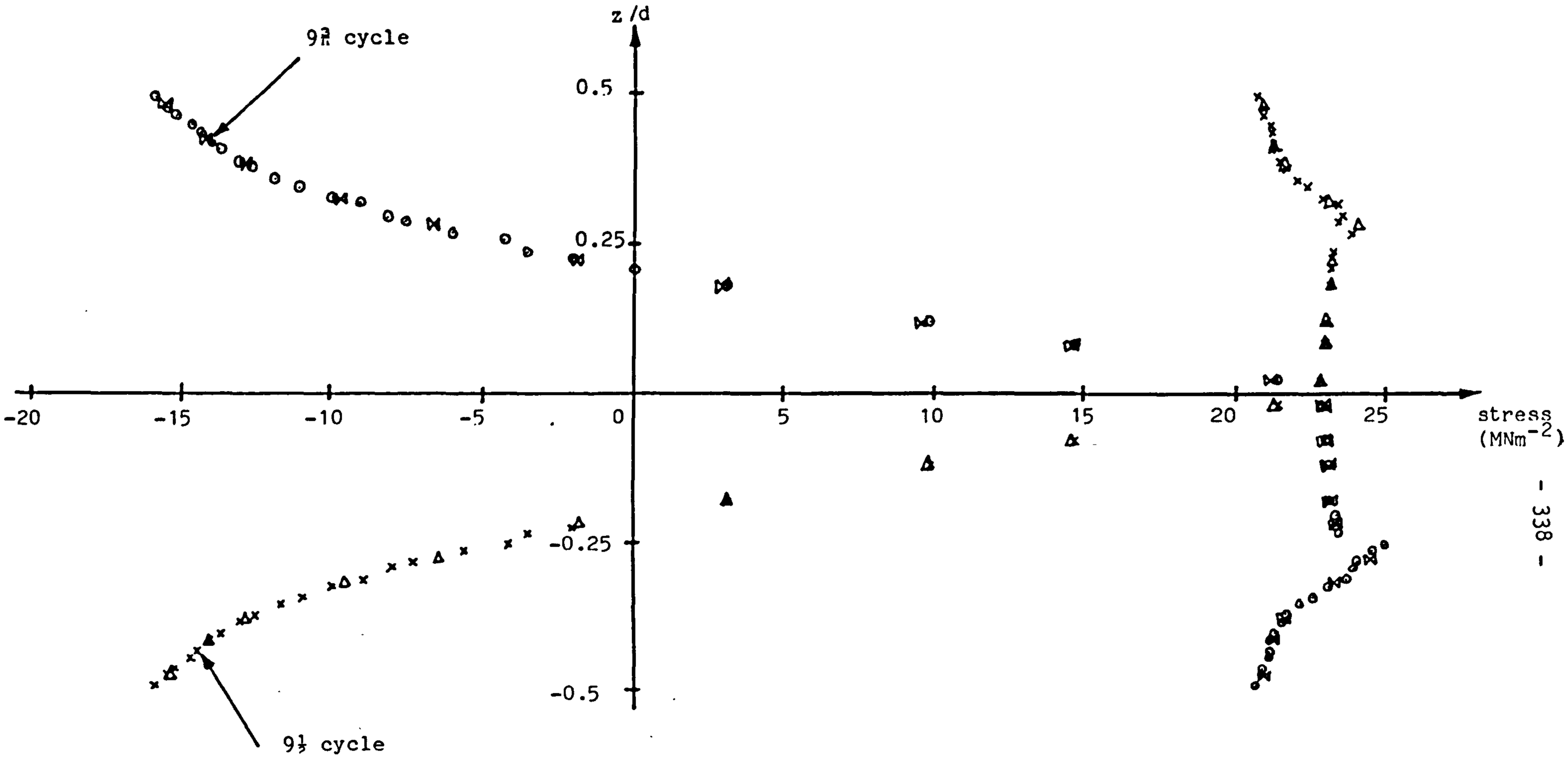

Fig. 5.18(ii) Tenth cycle through the depth stress distribution. Comparison between coarse mesh at Fig. 5.8 (Δ , ⋈) and finer mesh (x, o) for B2 loading conditions material model C

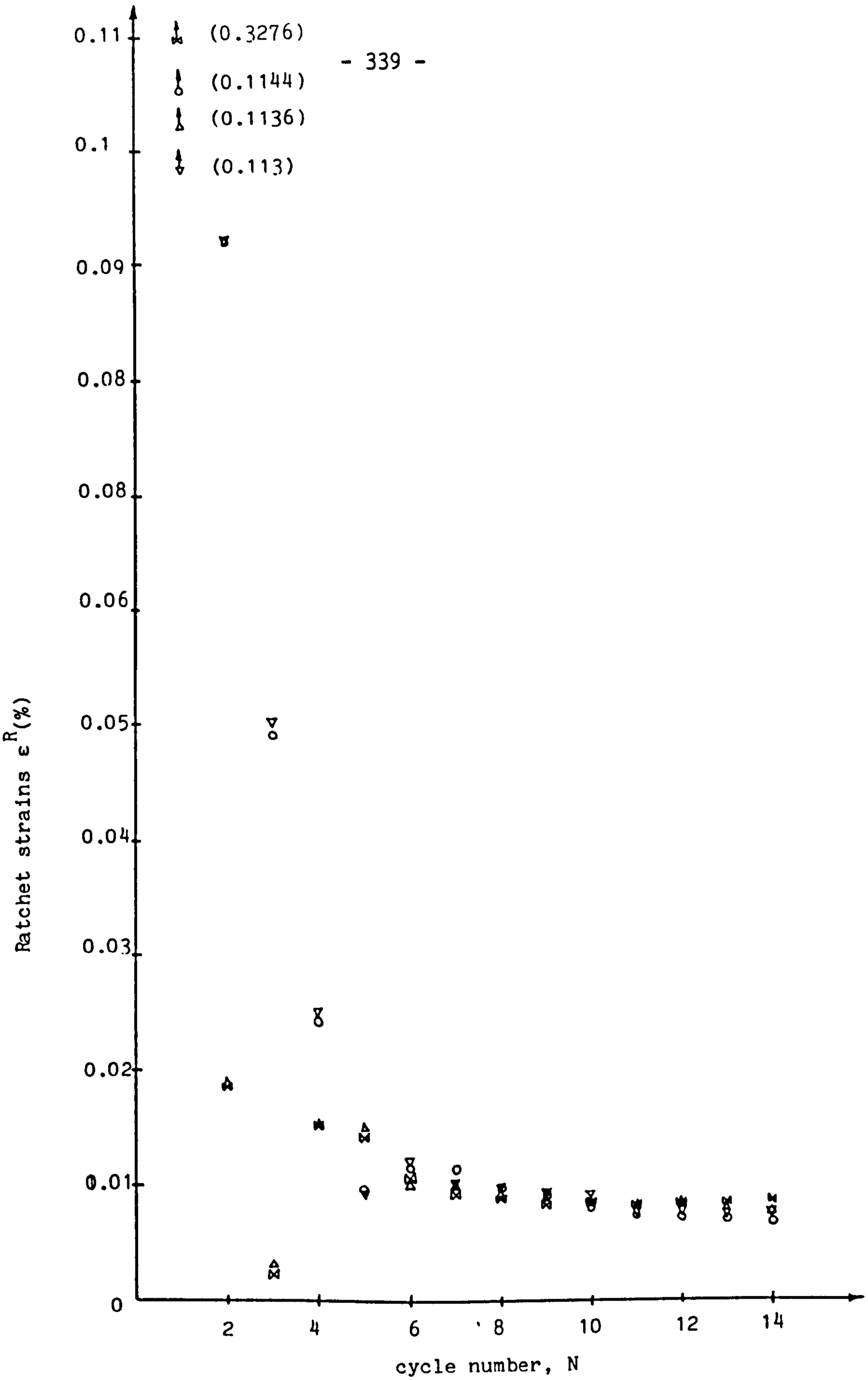

Fig. 5.19 Variation of ratchet strain with cycle number.
Comparison between results for coarse mesh of Fig. 5.8
(o, FT, ⋈, FC) and finer mesh (▽, FT, △, FC)

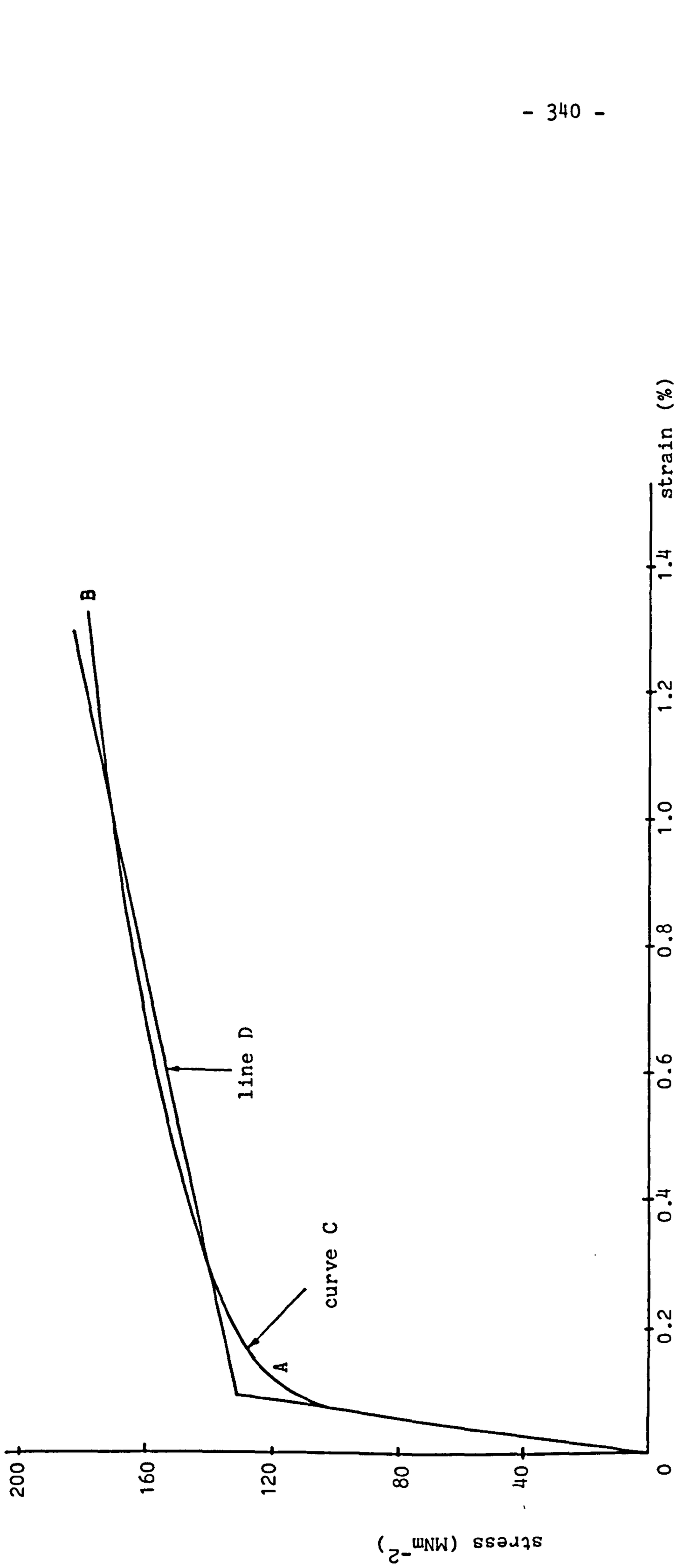

Fig. 5.20 Monotonic stress strain curve for 316 stainless steel using Goodman and Gordon constants of Table 5.9 (curve C) and linear kinematic hardening model idealisation (line D)

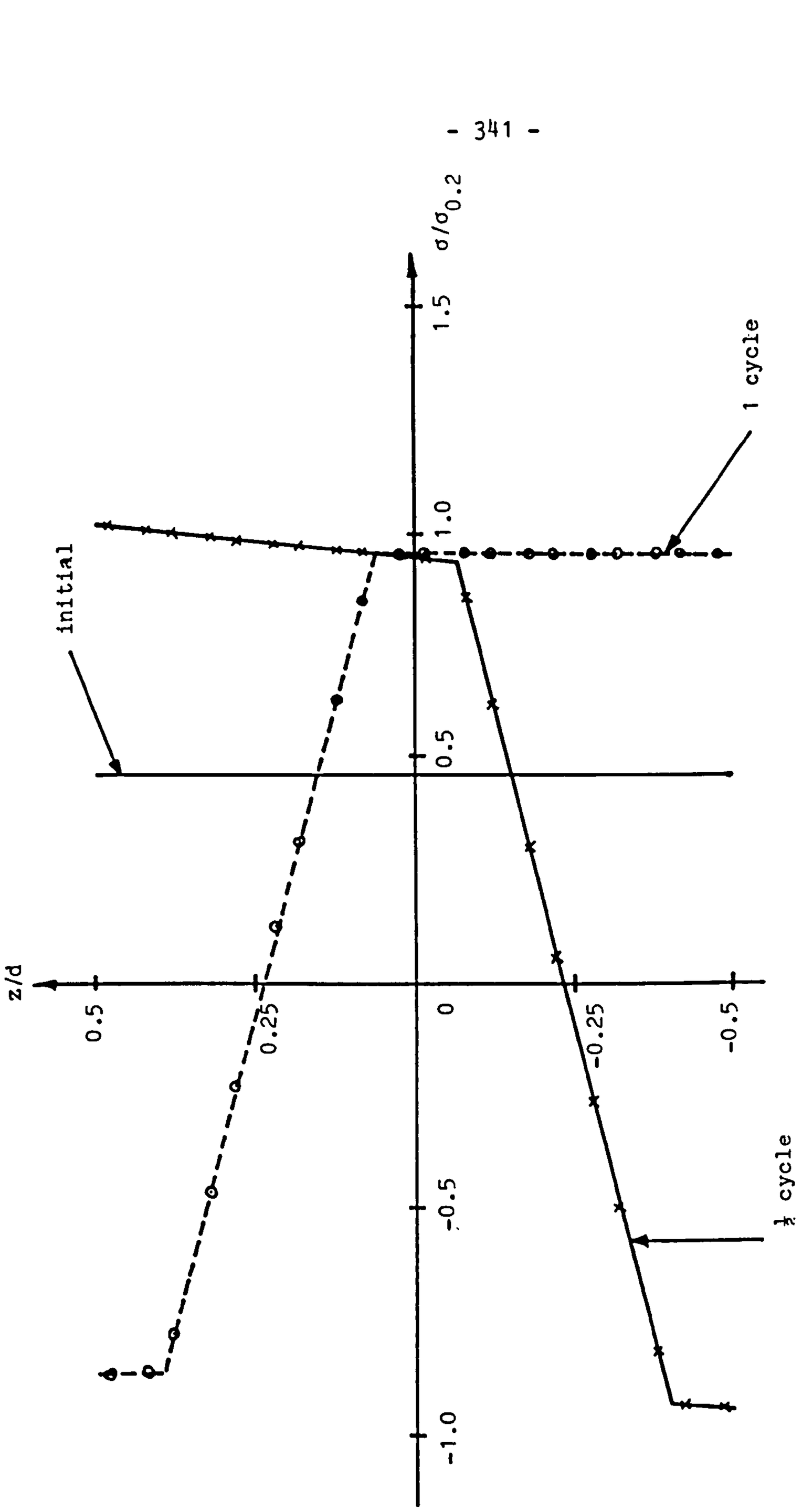

Fig. 5.2(1) First cycle through the depth stress distribution for a beam subjected to a steady axial load and cyclic linear through the depth temperature gradient. Linear kinematic hardening model. $\sigma_p/\sigma_{0.2} = 0.4571$, $\sigma_t/\sigma_{0.2} = 2.8$

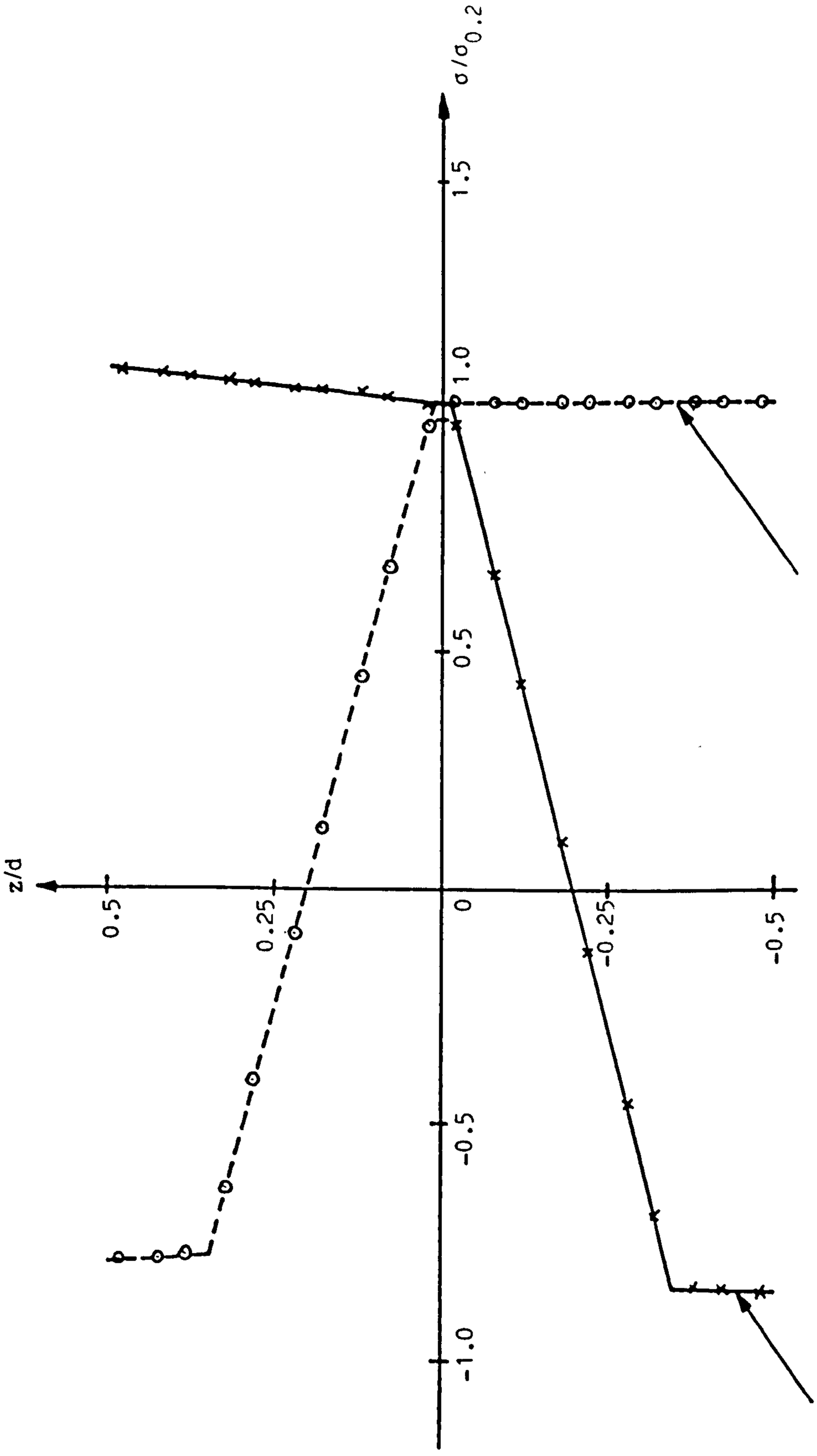

Fig. 5.21(11) Stress distribution for a beam subjected to a steady axial load and cyclic linear through the depth temperature gradient. Linear kinematic hardening model. $\sigma_p/\sigma_{0.2} = 0.4571$, $\sigma_t/\sigma_{0.2} = 2.8$

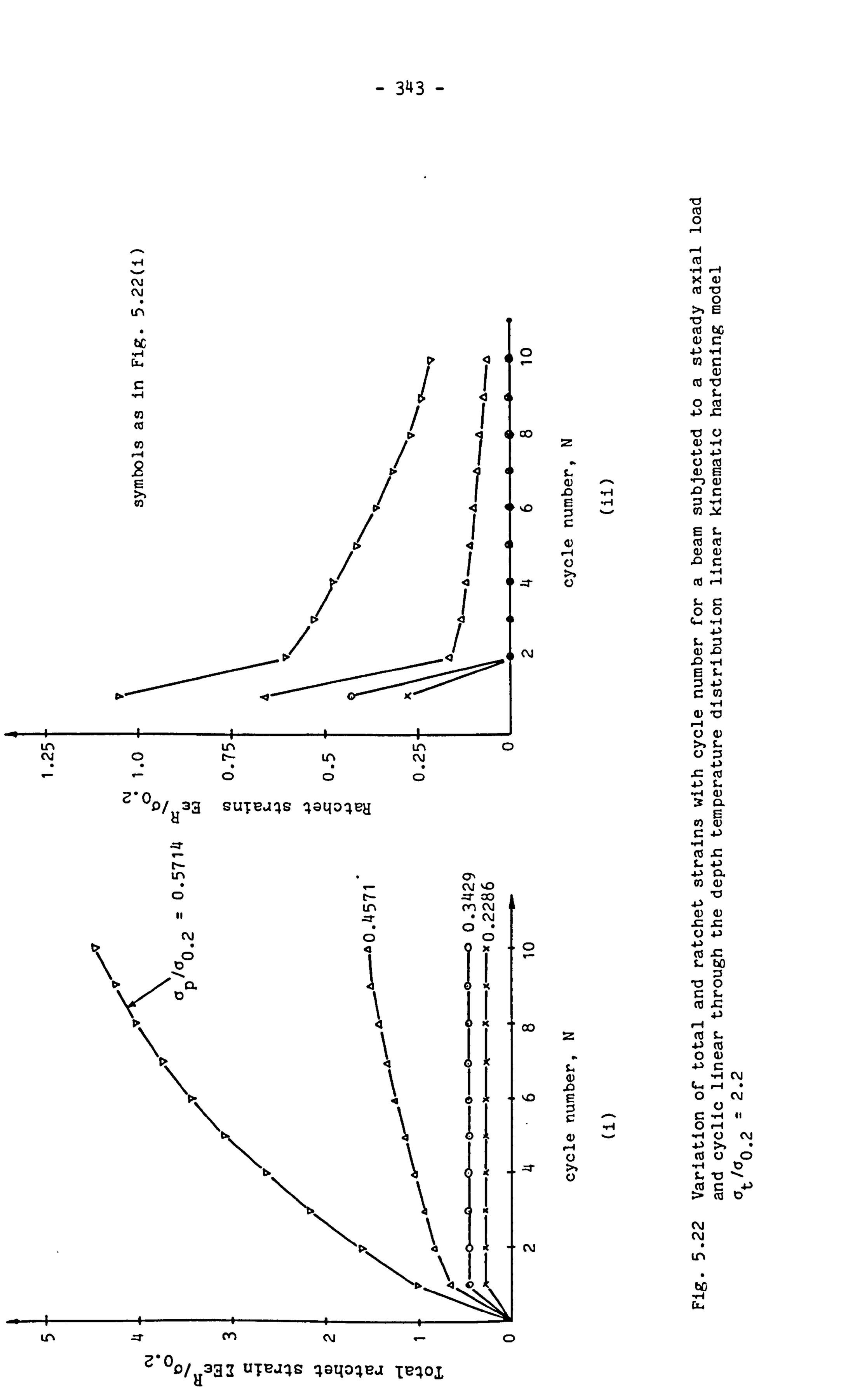

Fig. 5.22 Variation of total and ratchet strains with cycle number for a beam subjected to a steady and cyclic linear through the depth temperature distribution linear kinematic hardening model
$\sigma_t/\sigma_{0.2}$ = 2.2

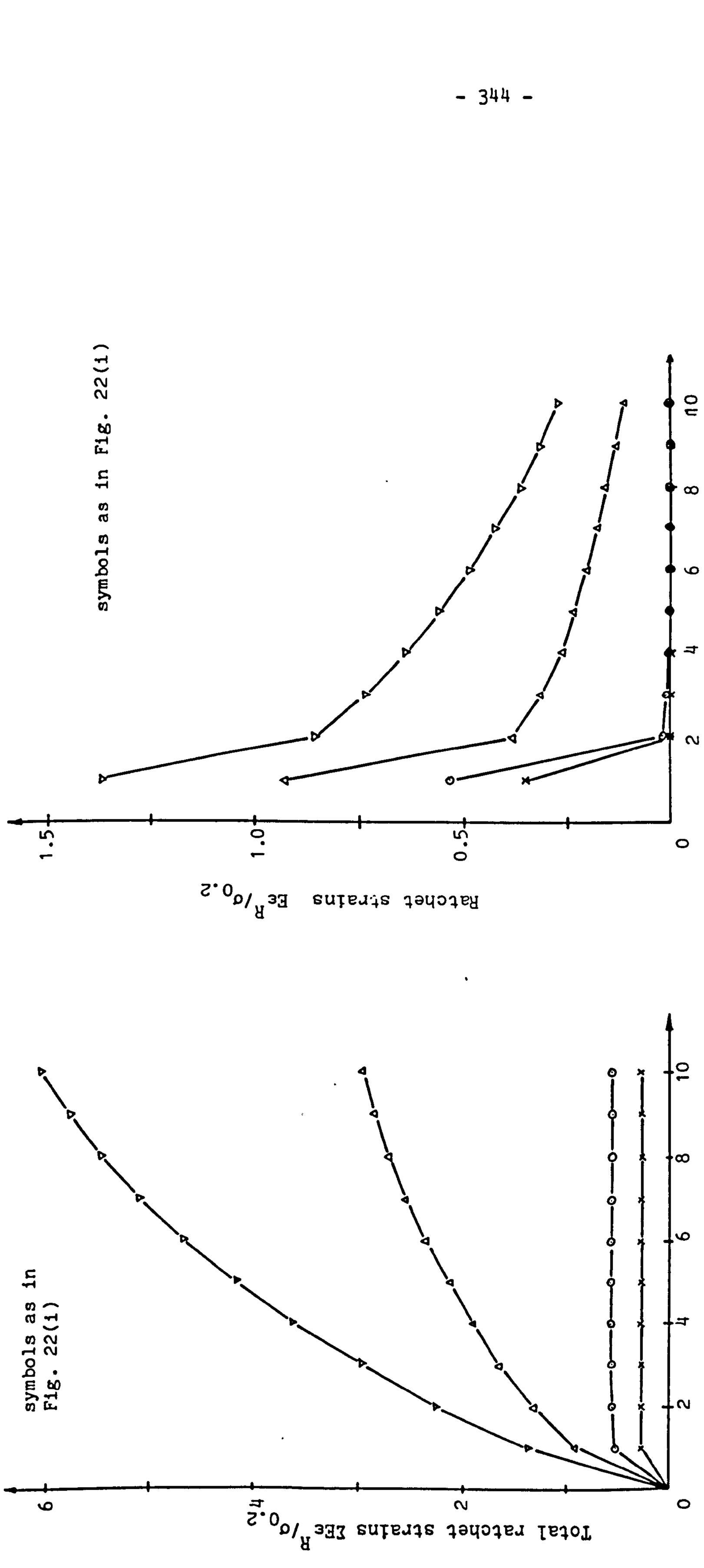

Fig. 5.22 Variation of total and ratchet strains with cycle number for a beam subjected to a steady axial load and cyclic linear through the depth temperature distribution linear kinematic hardening model
$\sigma_t/\sigma_{0.2} = 2.5$

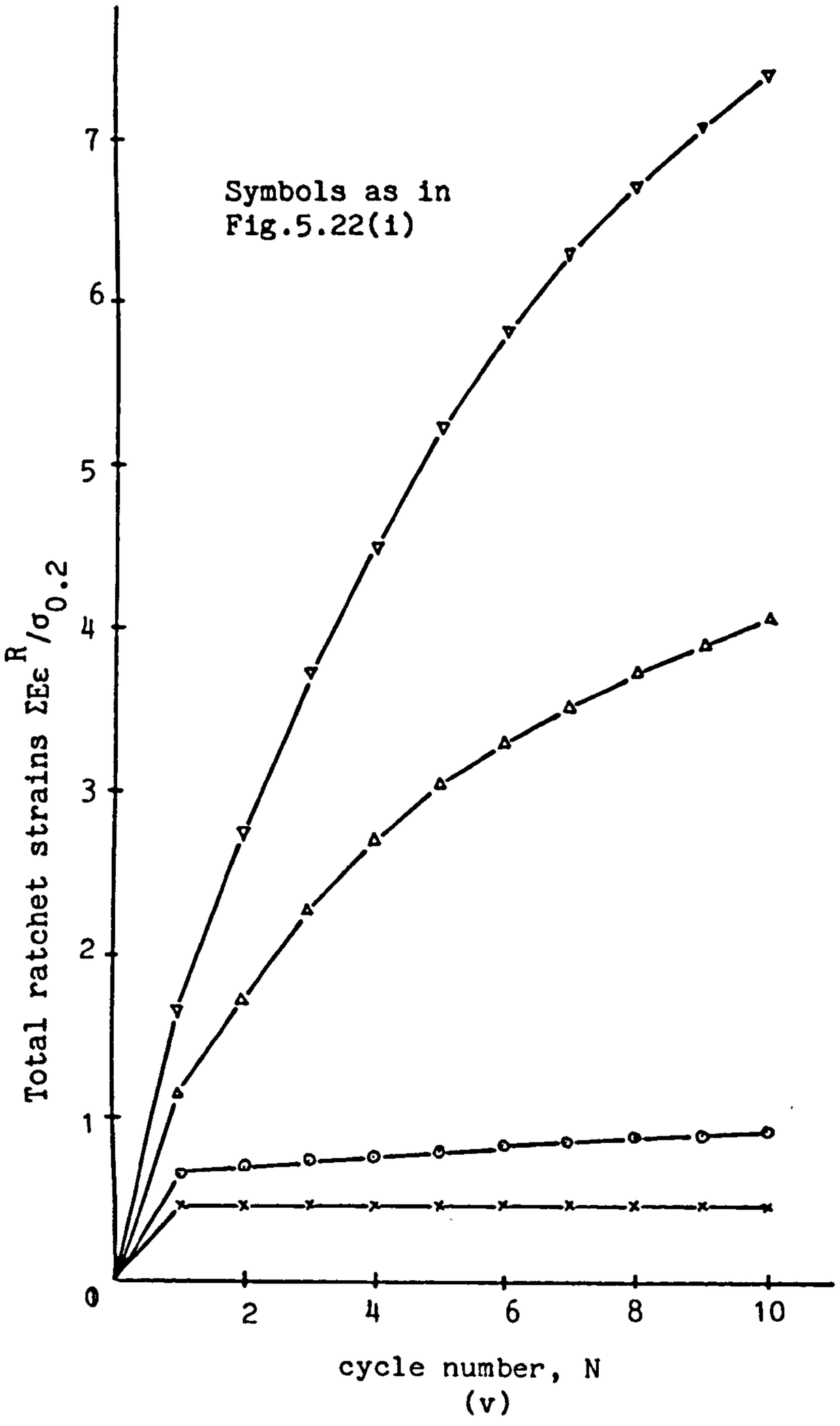

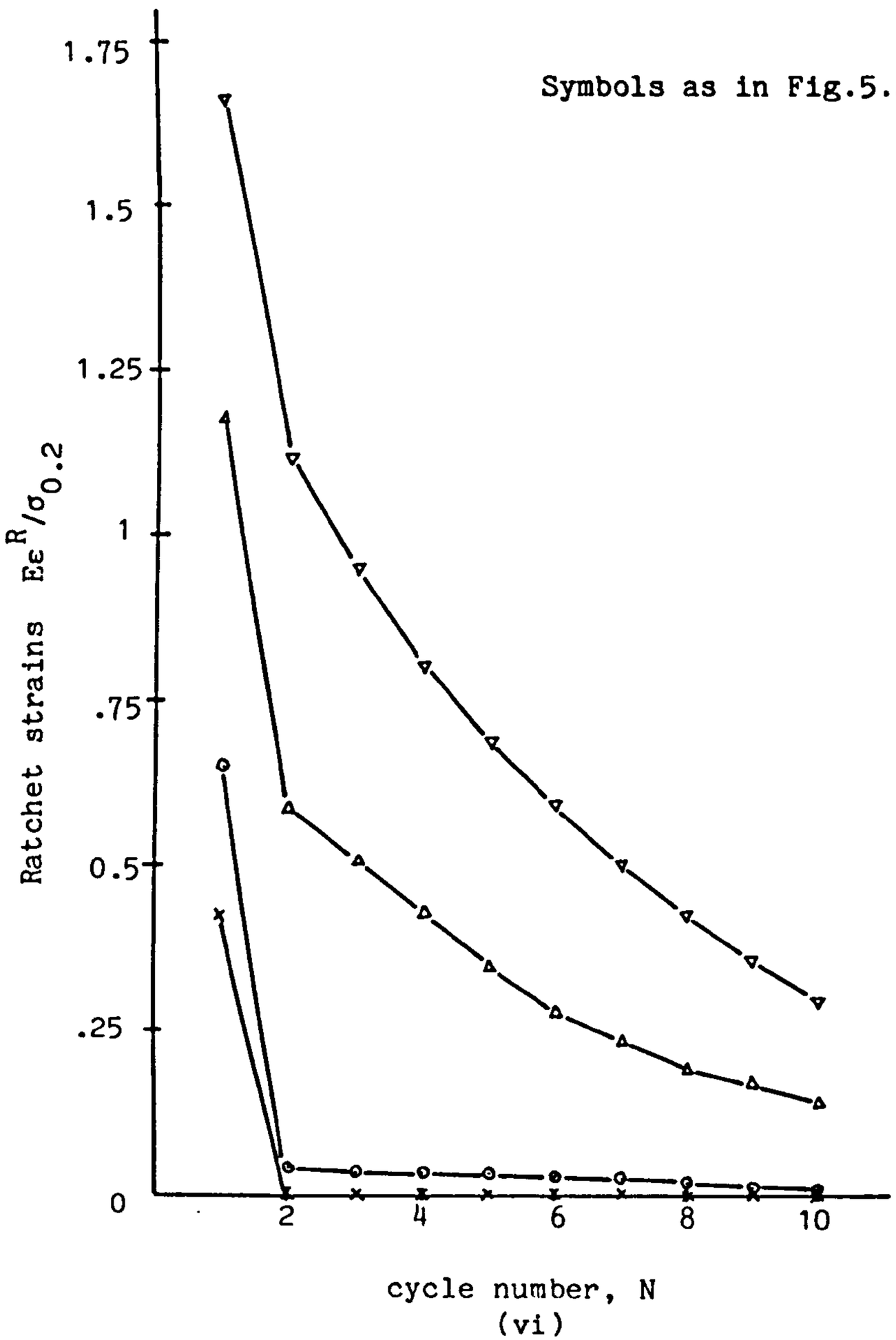

Fig. 5.22 Variation of total and ratchet strains with cycle number for a beam subjected to a steady axial load and cyclic linear through depth temperature distribution linear kinematic hardening model $\sigma_t/\sigma_{0.2} = 2.8$

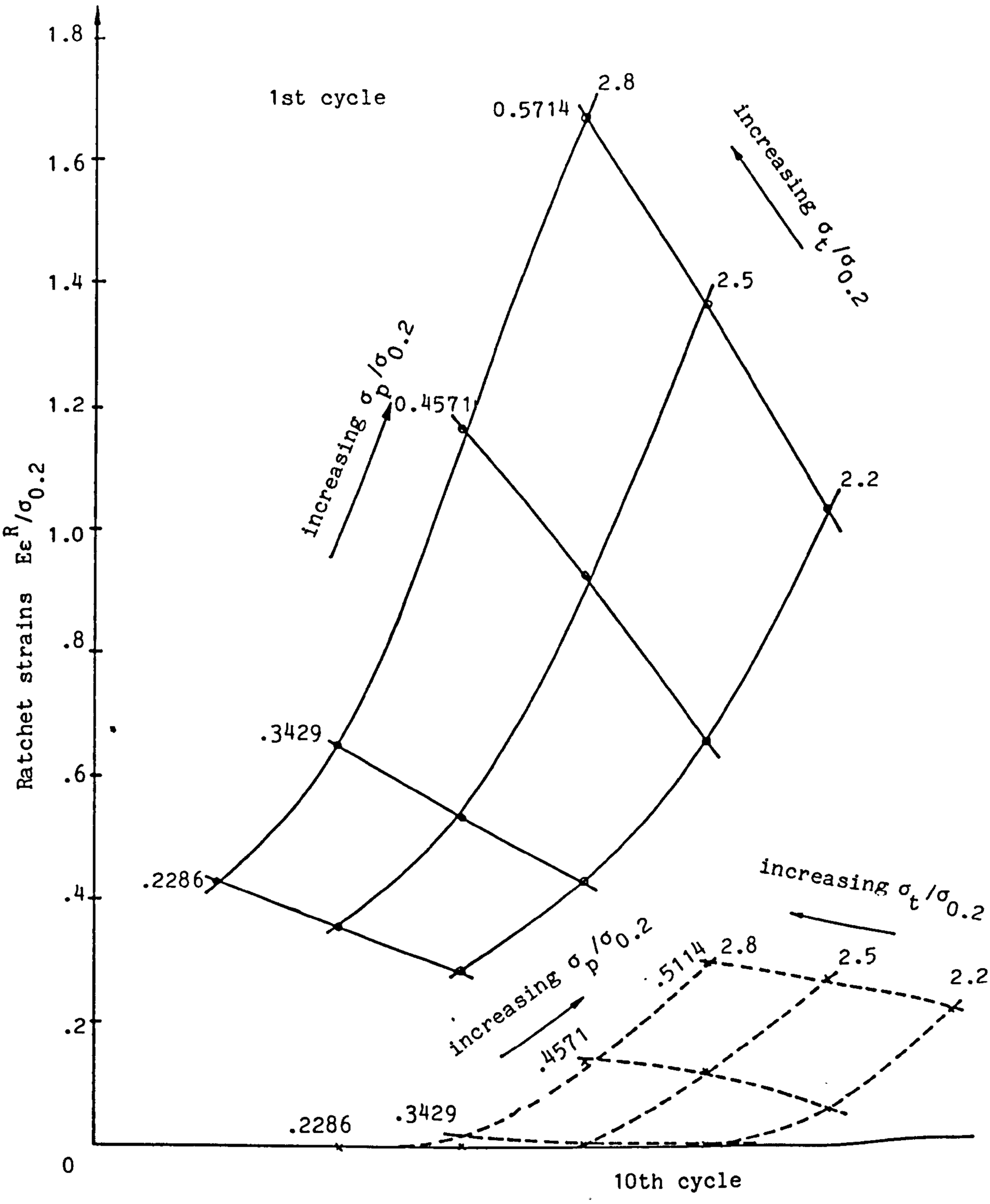

Fig. 5.23(i) 1st and 10th cycle ratchet strains for a beam subjected to a steady axial load and cyclic linera through the depth temperature distribution linear kinematic hardening model $\sigma_{0.2} = 140\ MNm^{-2}$

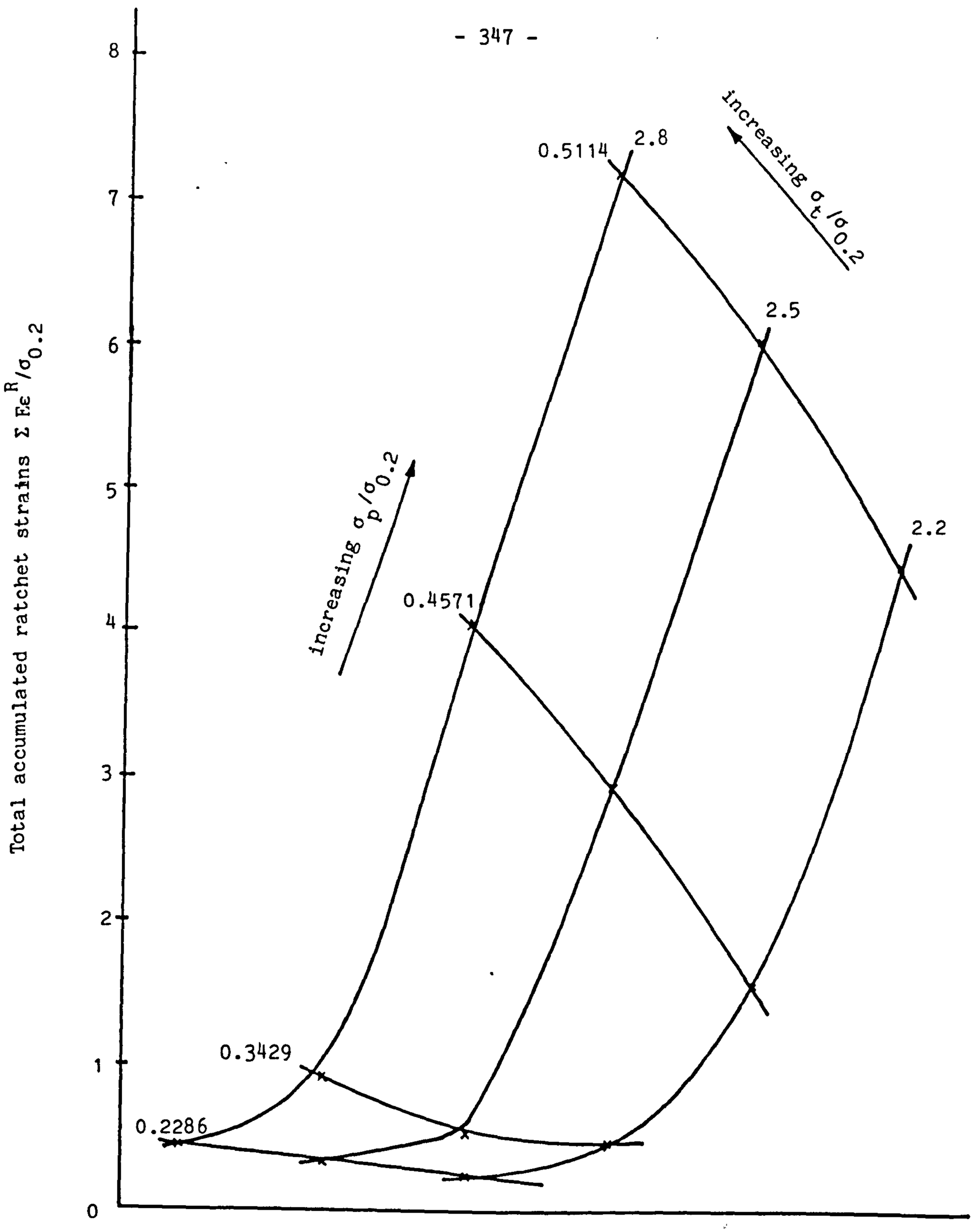

Fig. 5.23(ii) Total accumulated ratchet strains at 10th cycle for a beam subjected to a steady axial load and cyclic linear through the depth temperature gradient linear kinematic hardening model $\sigma_{0.2} = 140\ MNm^{-2}$

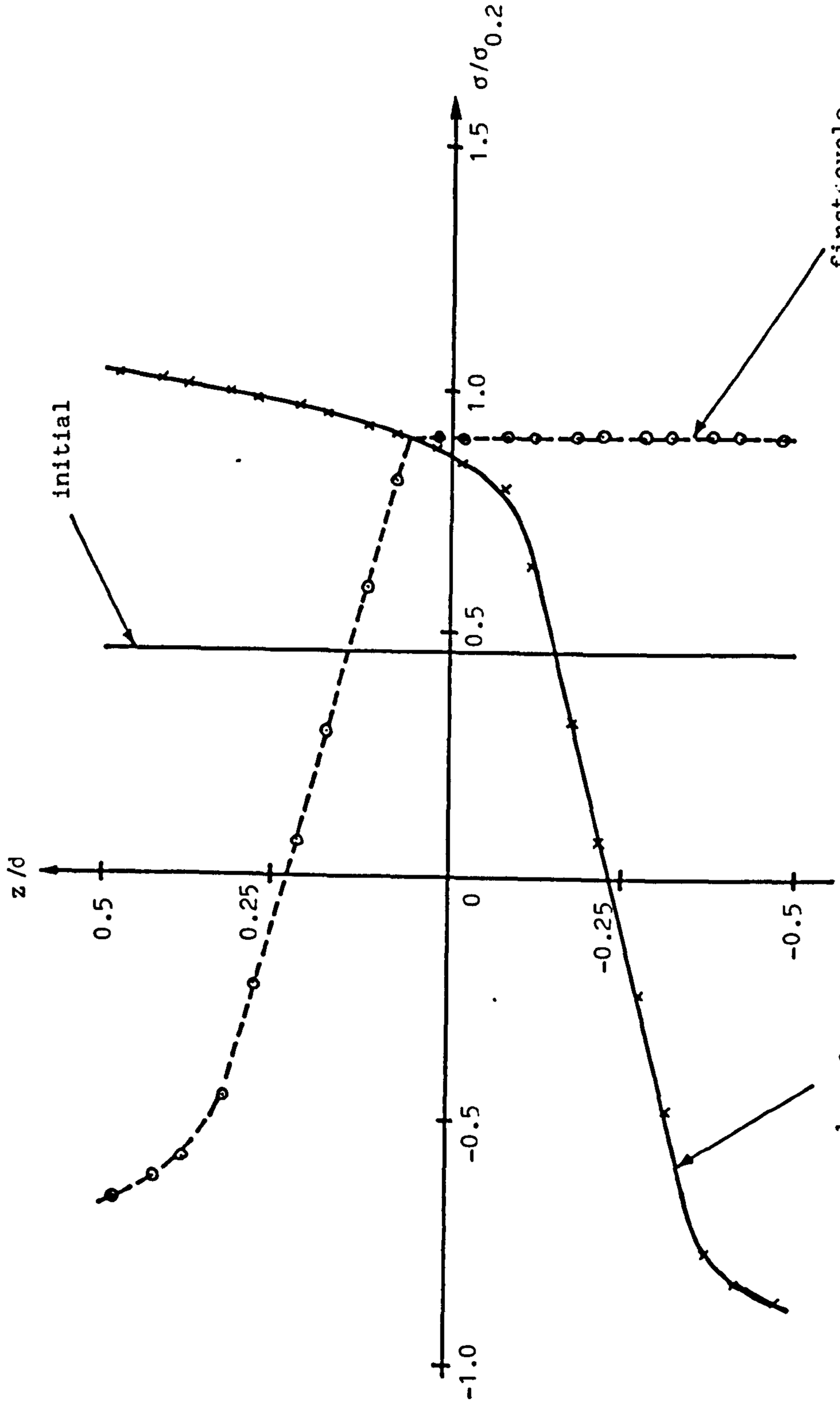

Fig.5.24(i) First cycle through the depth stress distribution for a beam subjected to a steady axial load and cyclic linear through the depth temperature distribution. Goodman and Goodall model. $\sigma_p/\sigma_{0.2} = 0.4571$, $\sigma_t/\sigma_{0.2} = 2.8$

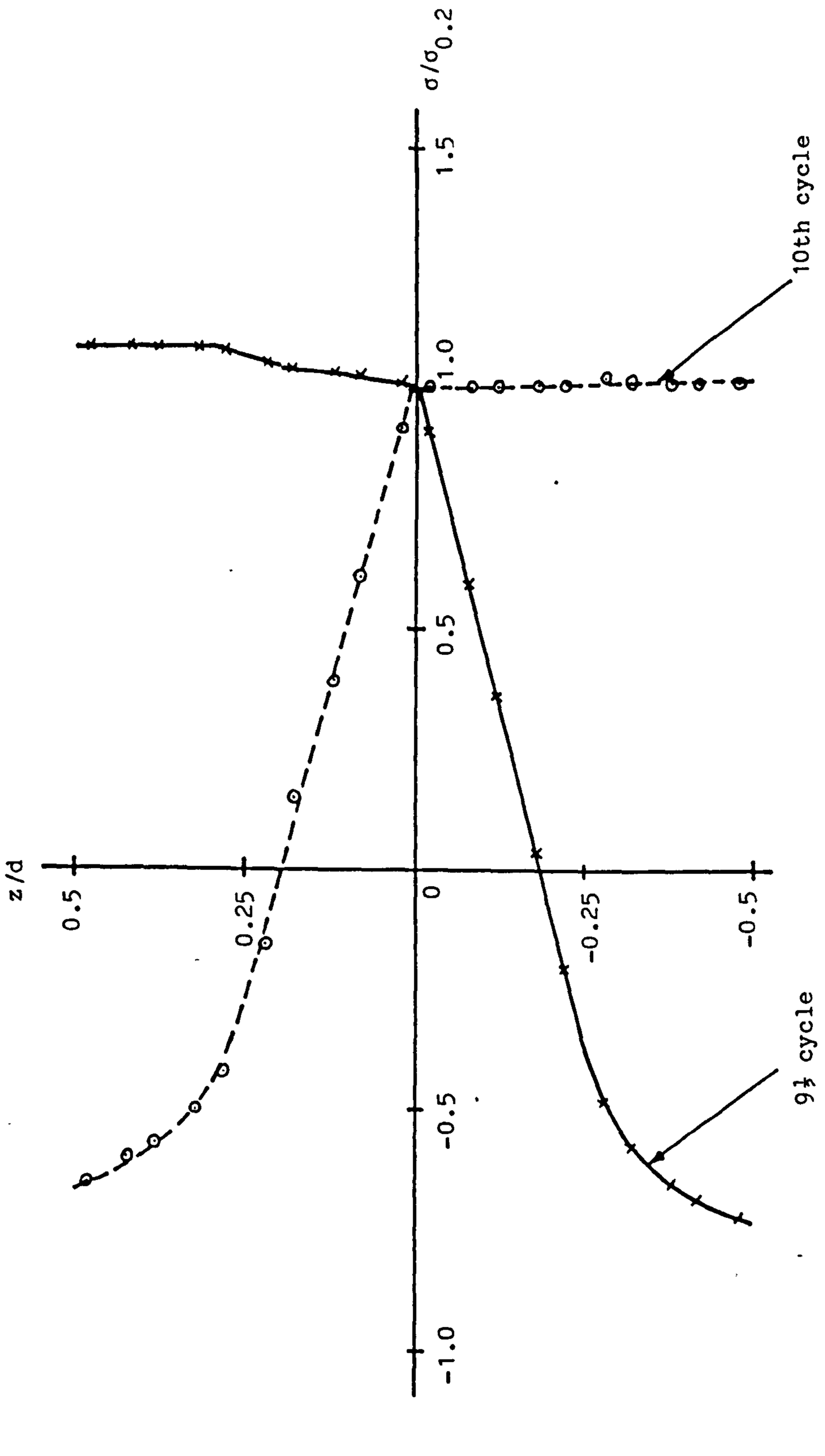

Fig. 5.24(i) 10th cycle through the depth stress distribution for a beam subjected to a steady axial load and cyclic linear through the depth temperature distribution. Goodman and Goodall model. $\sigma_p/\sigma_{0.2} = 0.4571$, $\sigma_t/\sigma_{0.2} = 2.8$

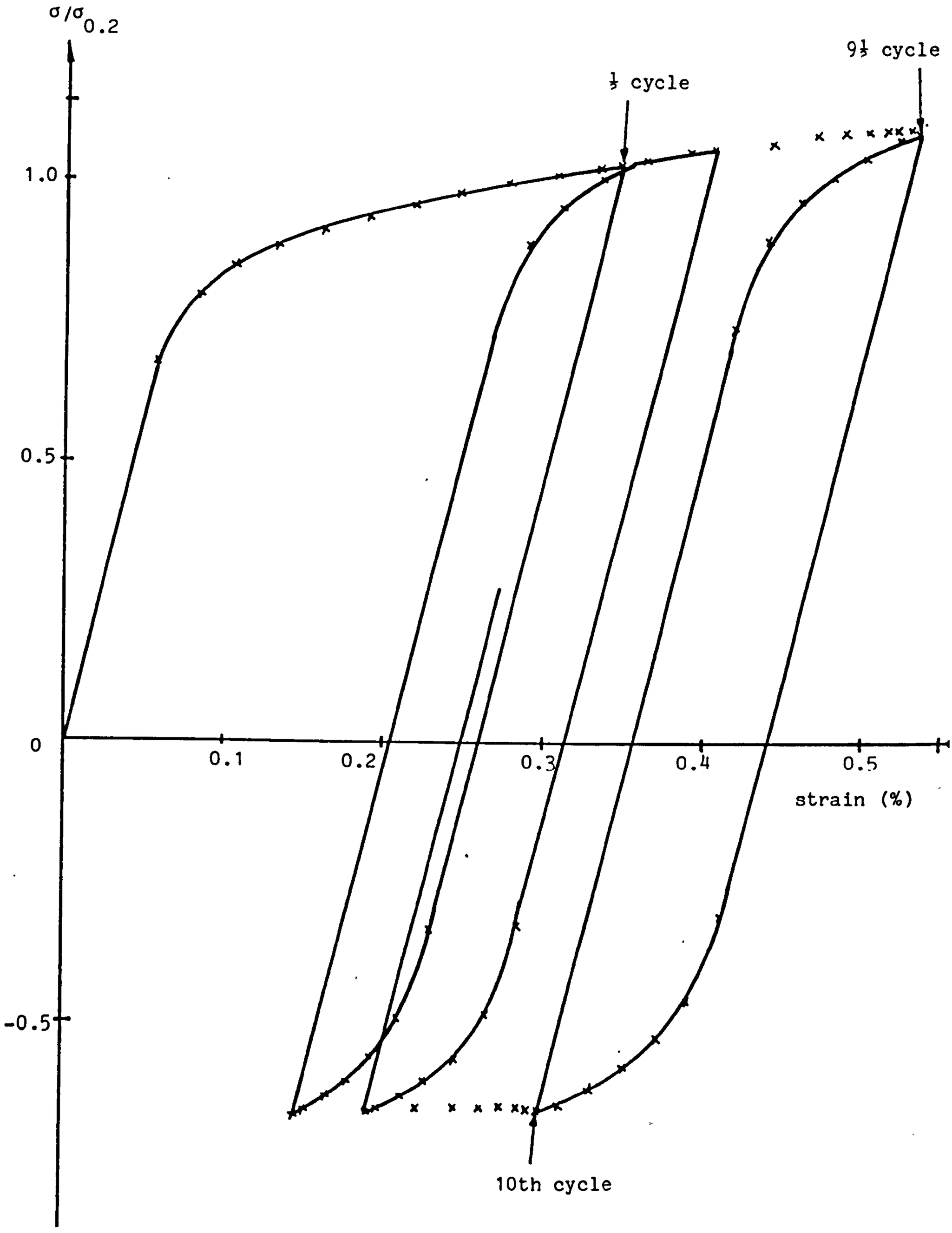

Fig. 5.25(i) Stress strain histories at z/d = 0.447 for a beam subjected axial and thermal loads. Goodman and Goodall model, $\sigma_p/\sigma_{0.2} = 0.4571$, $\sigma_t/\sigma_0 = 2.8$

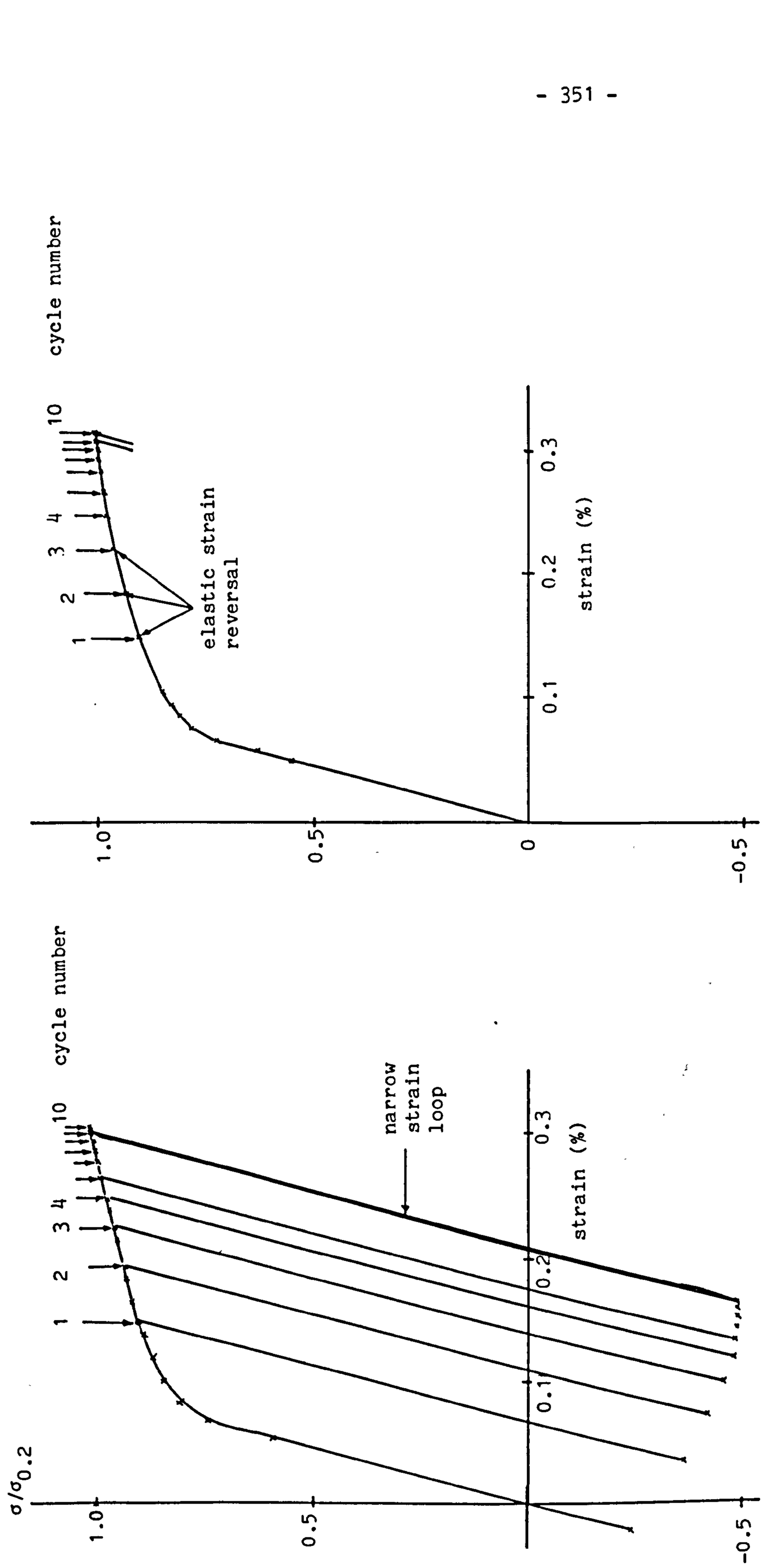

(iii) z/d = 0.021

(ii) z/d = 0.279

Fig. 5.25 Stress strain histories at z/d = 0.279 and 0.021 for a beam subjected axial+thermal loads. Goodman and Goodall model, $\sigma_t/\sigma_{0.2} = 0.4571$, $\sigma_p/\sigma_{0.2} = 2.8$

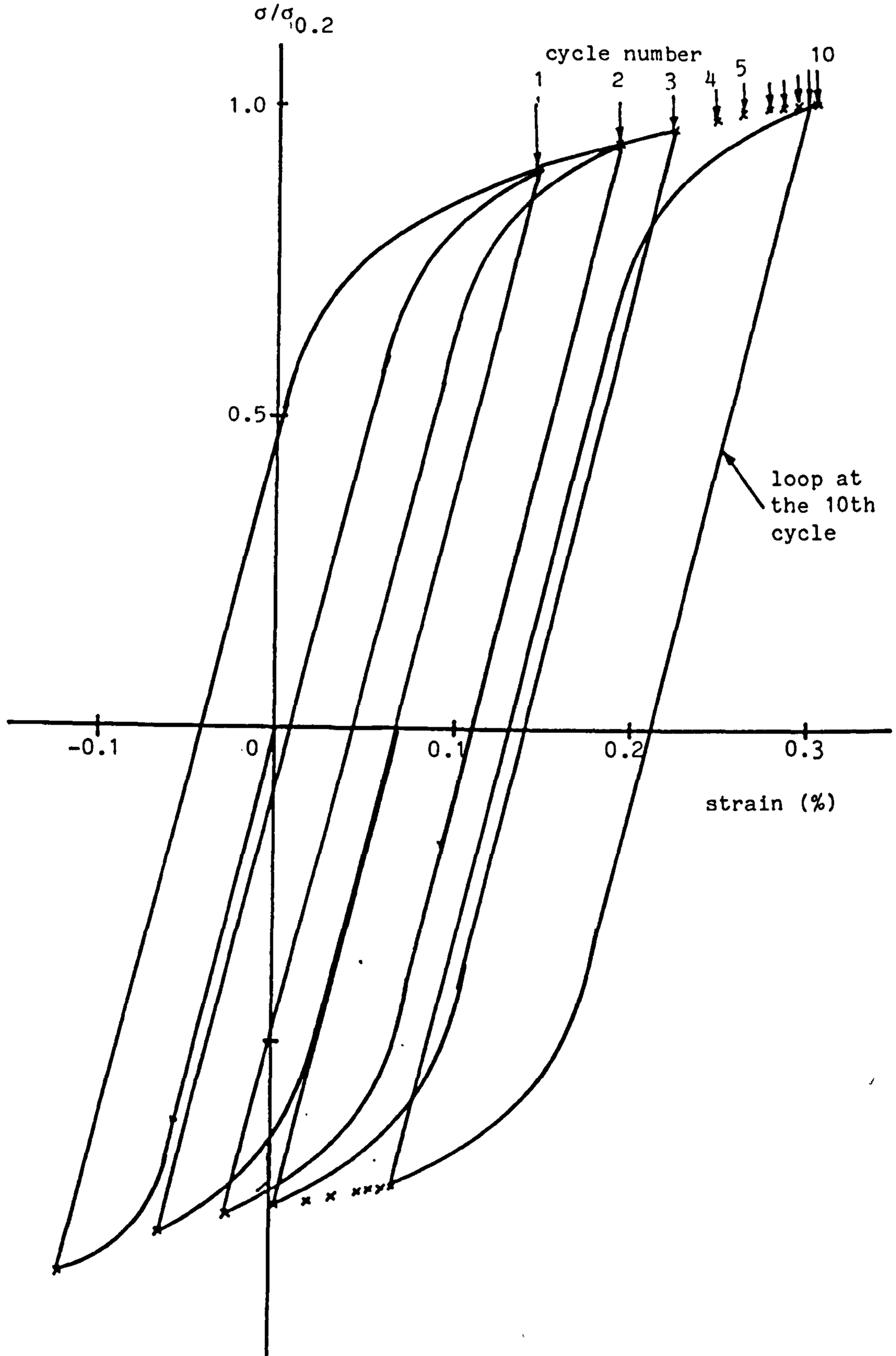

Fig. 5.25(iv) Stress-strain histories at z/d - 0.447 for a beam subjected to axial and thermal load.
Goodman and Goodall model, $\sigma_p/\sigma_{0.2} = 0.4571$, $\sigma_t/\sigma_{0.2} = 2.8$

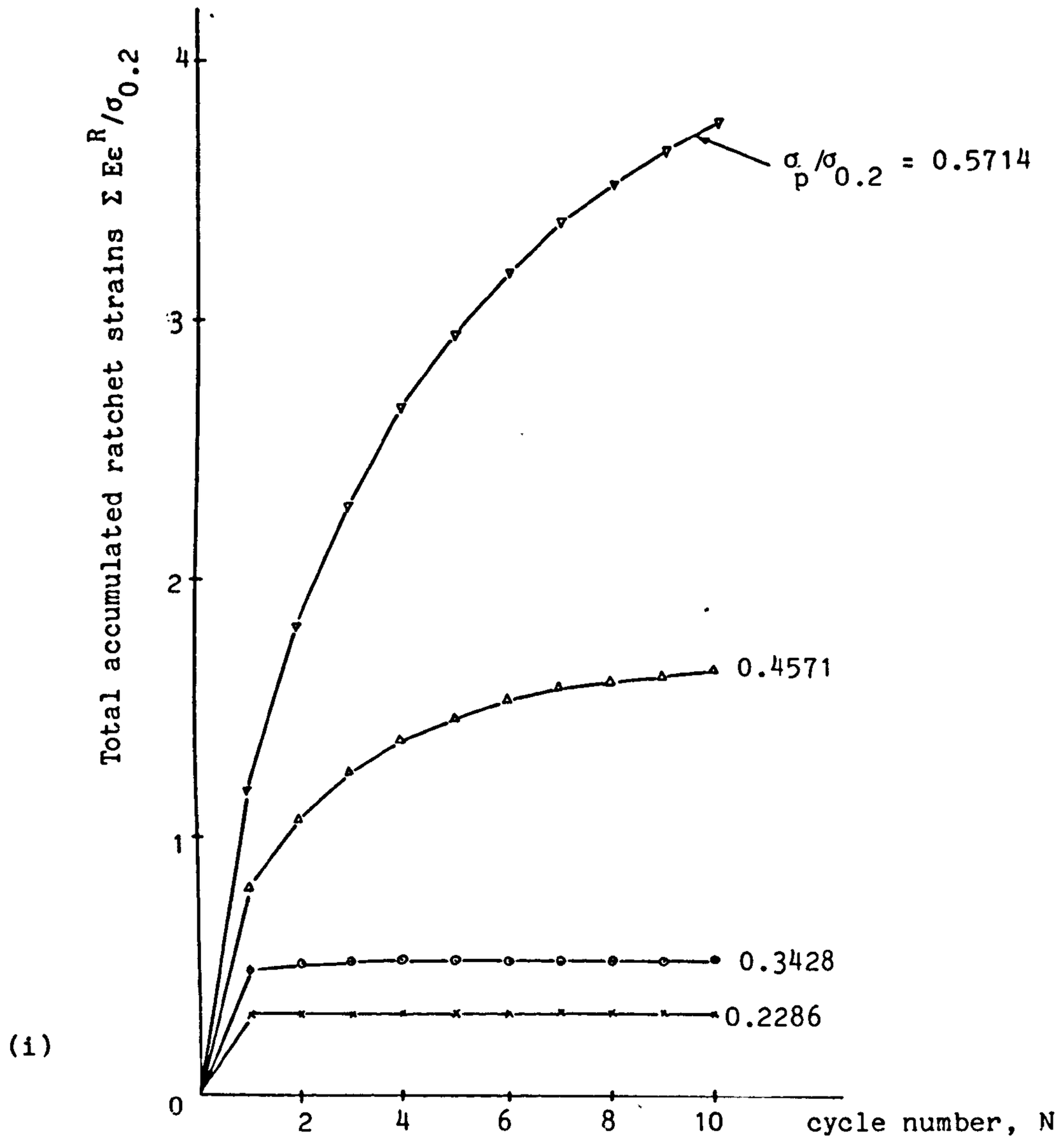

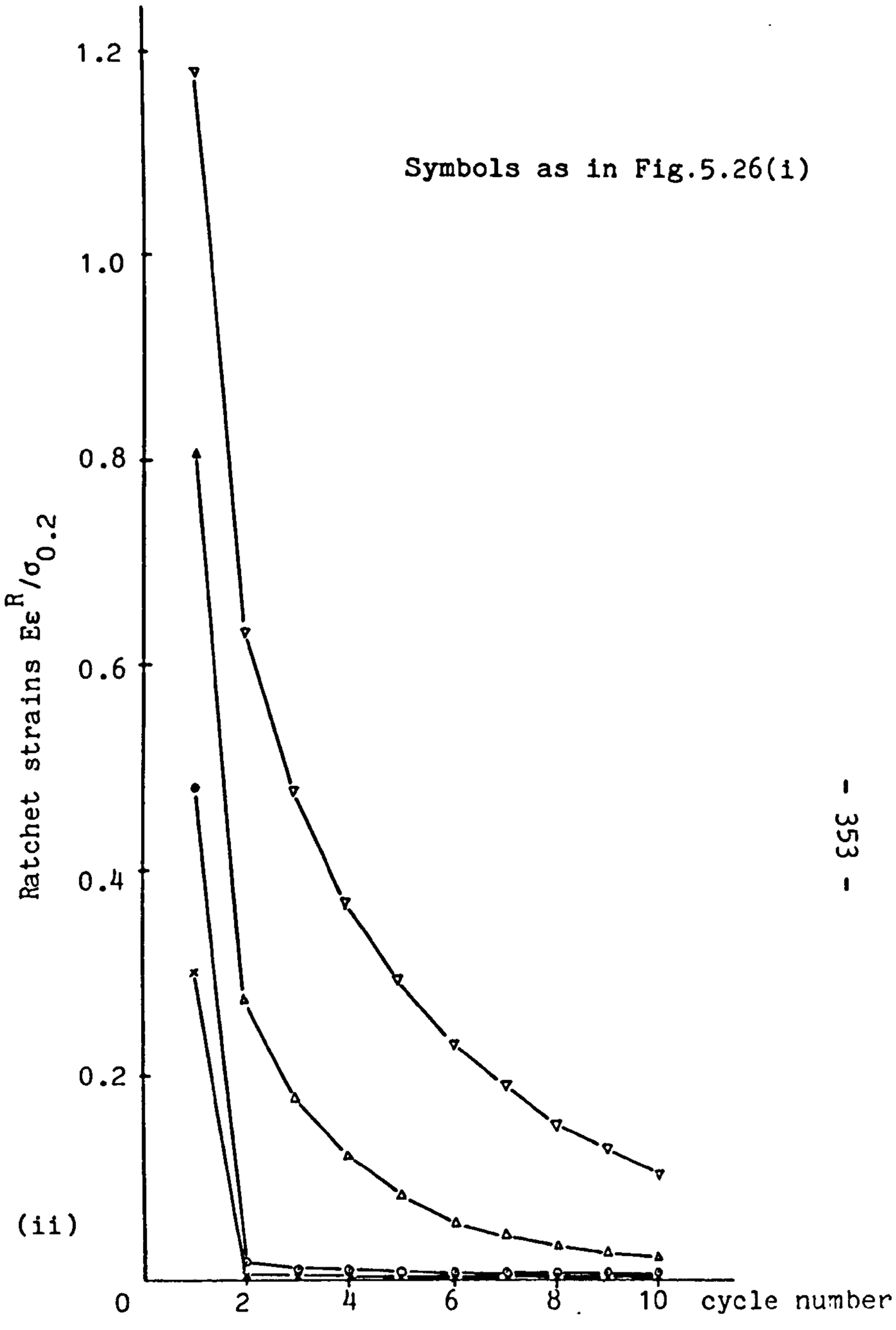

Symbols as in Fig.5.26(i)

Fig. 5.26 Variation of total accumulated ratchet and ratchet strains with cycle number for a beam subjected to axial and thermal loads. Goodman and Goodall model, $\sigma_+/\sigma_{0.2}$ = 2.2

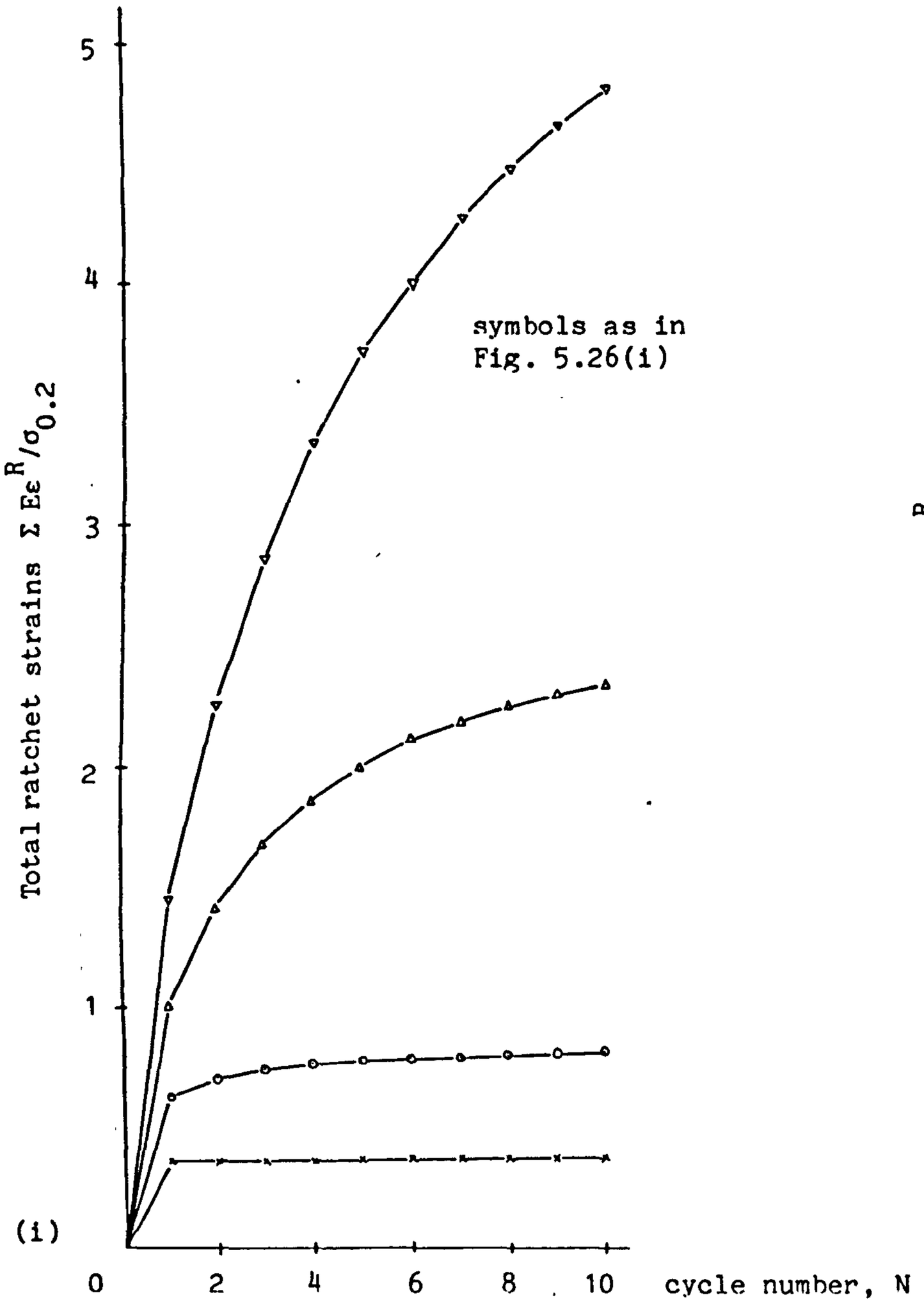

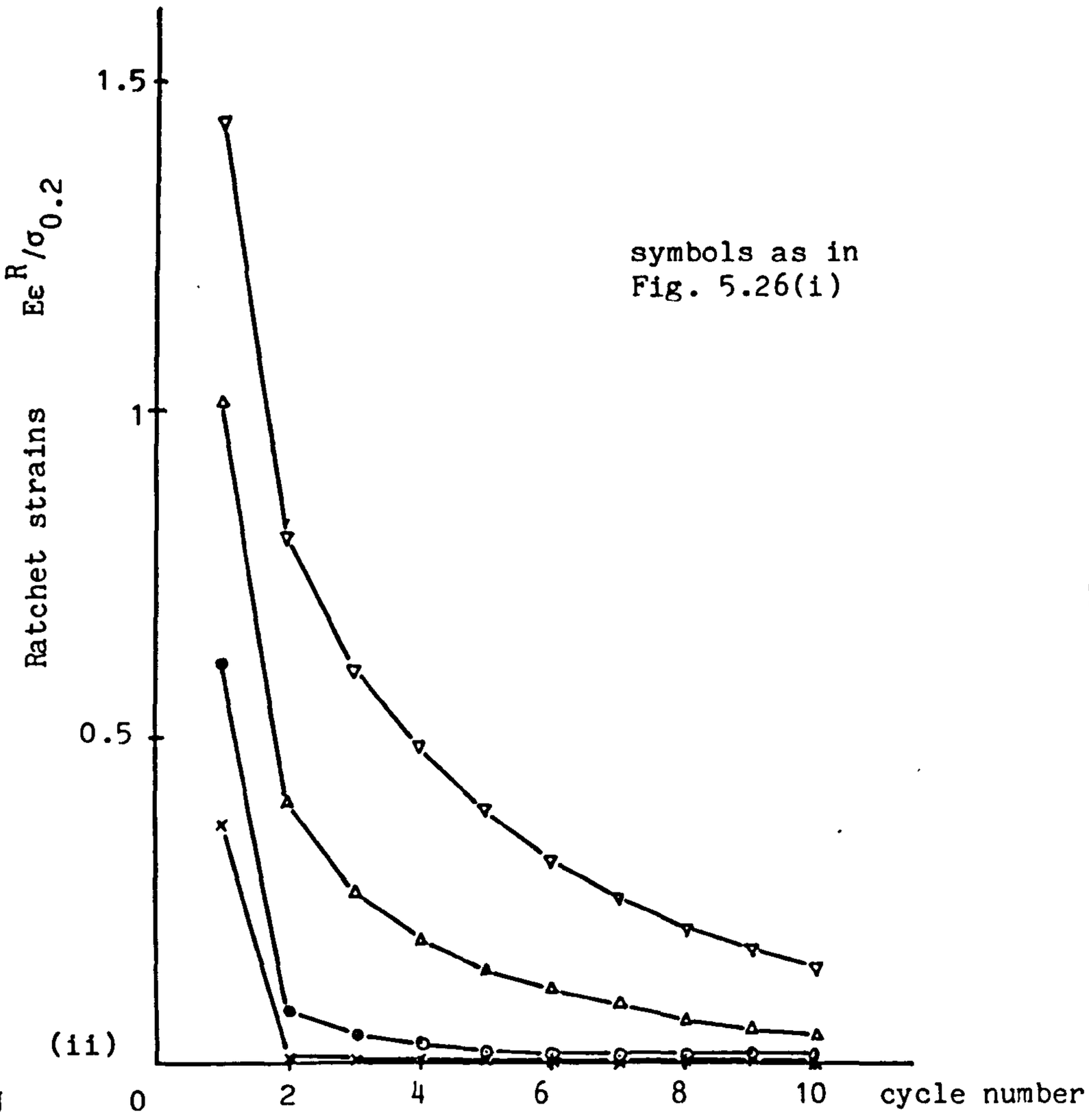

Fig. 5.27 Variation of total ratchet and ratchet strains with cycle number for a beam subjected to axial and thermal loads. Goodman and Goodall model, $\sigma_t/\sigma_{0.2} = 2.5$

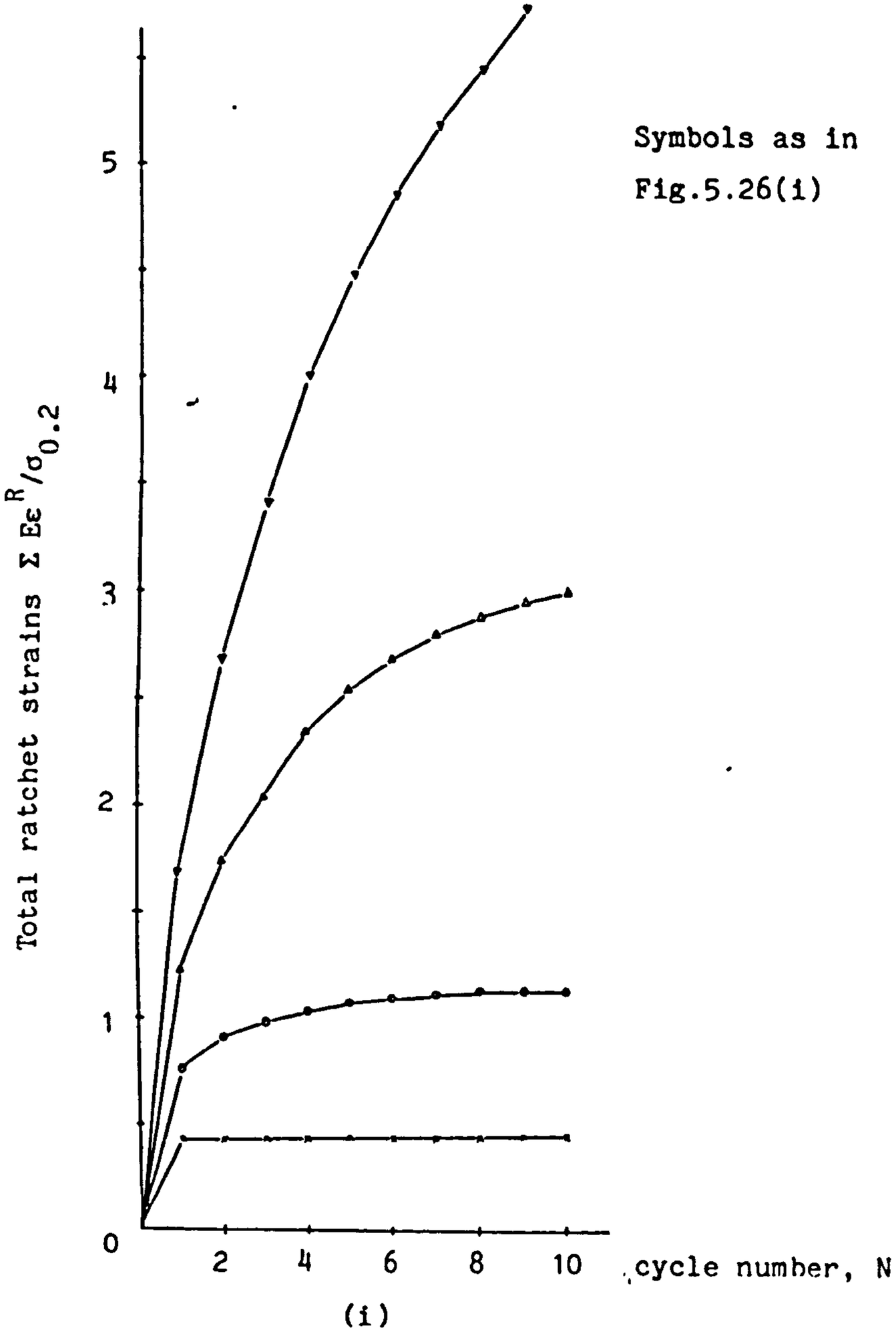

Symbols as in Fig.5.26(i)

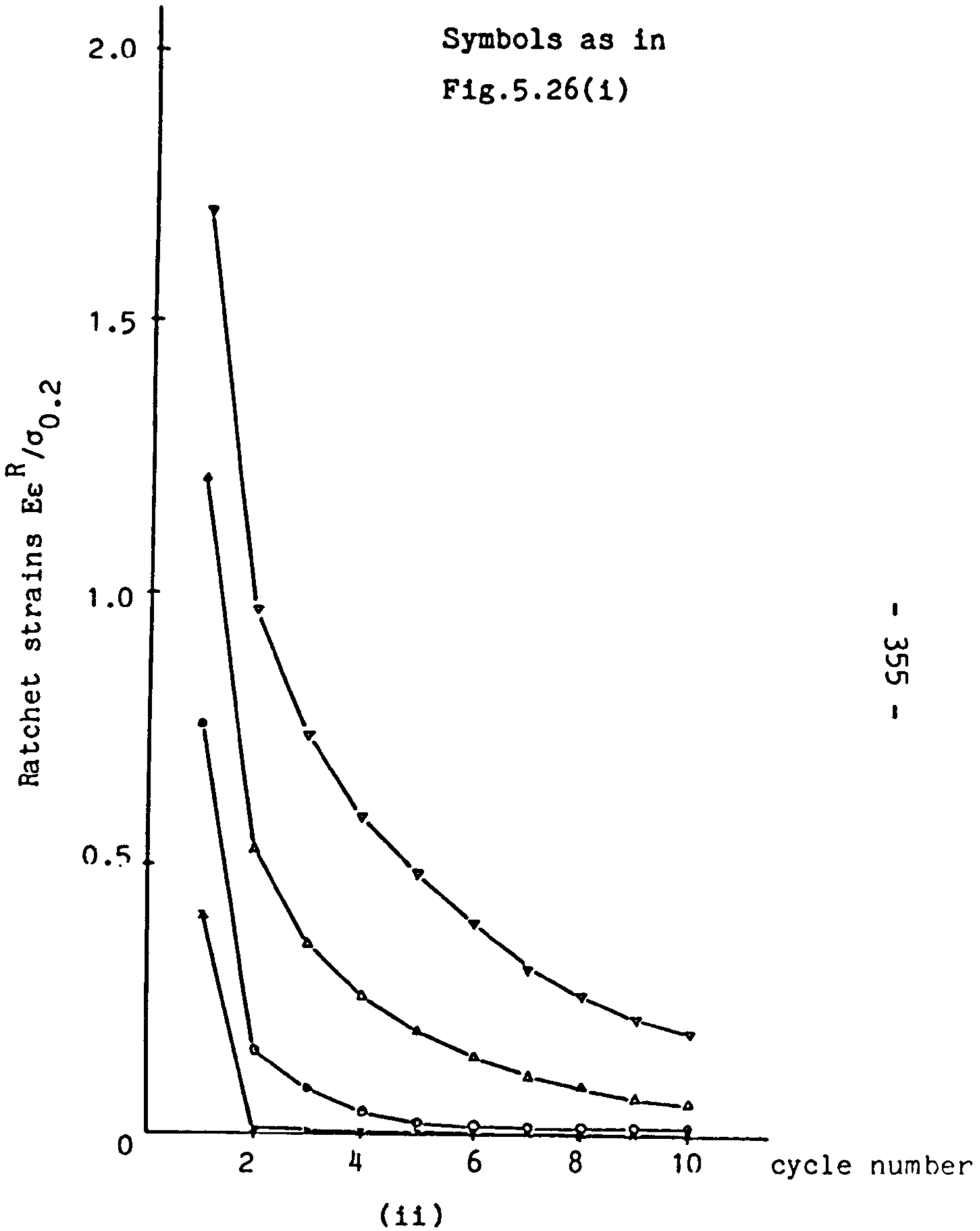

Symbols as in Fig.5.26(i)

Fig. 5.28 Variation of total ratchet and ratchet strains with cycle number for a beam subjected to axial and thermal loads. Goodman and Goodall model, $\sigma_t/\sigma_{0.2} = 2.8$

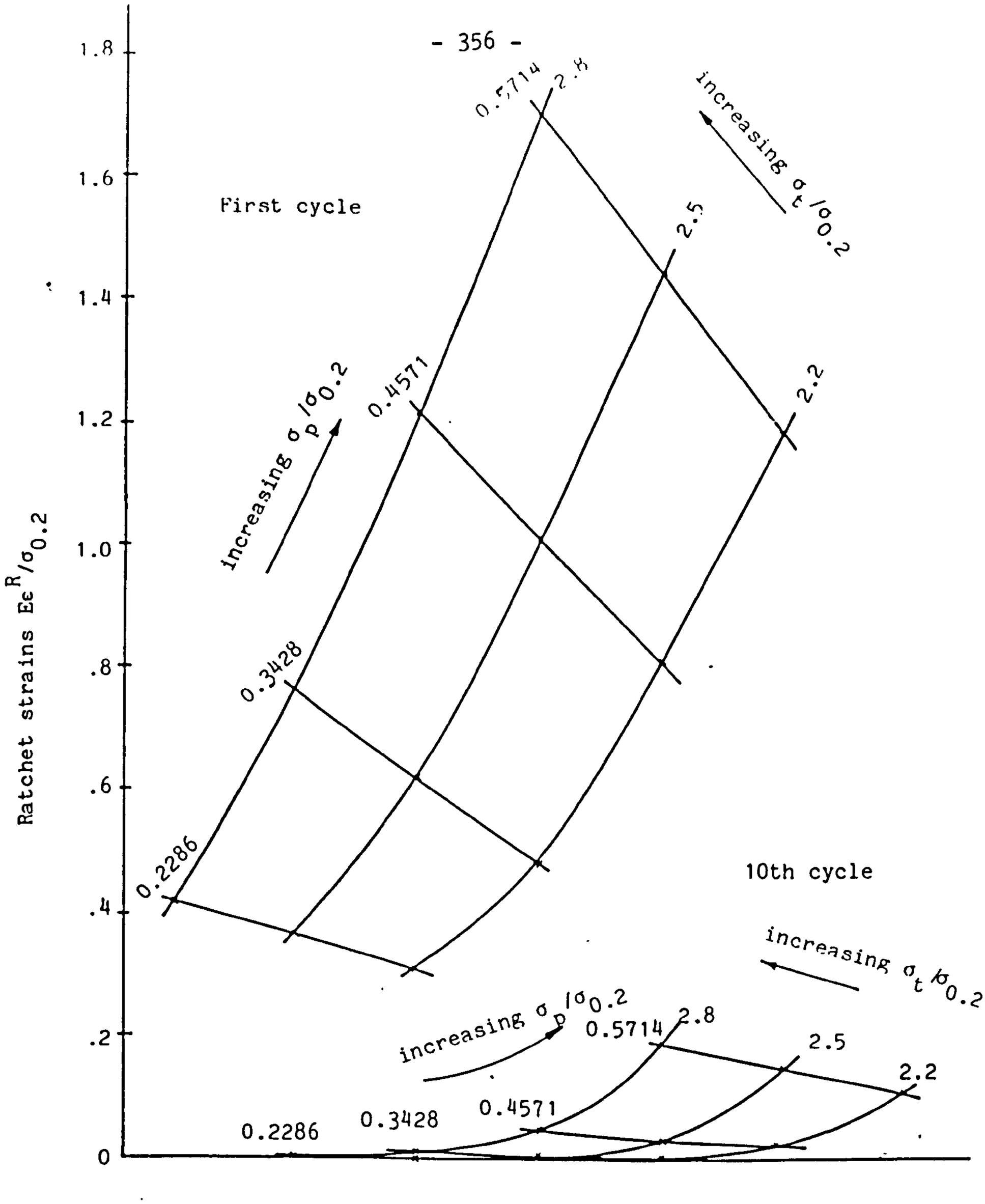

Fig. 5.29(i) Ratchet strains for a beam subjected to a steady axial load and cyclic linear through the depth temperature gradient at the first and 10th cycles. Goodman and Goodall model, $\sigma_{0.2} = 140\ MNm^{-2}$

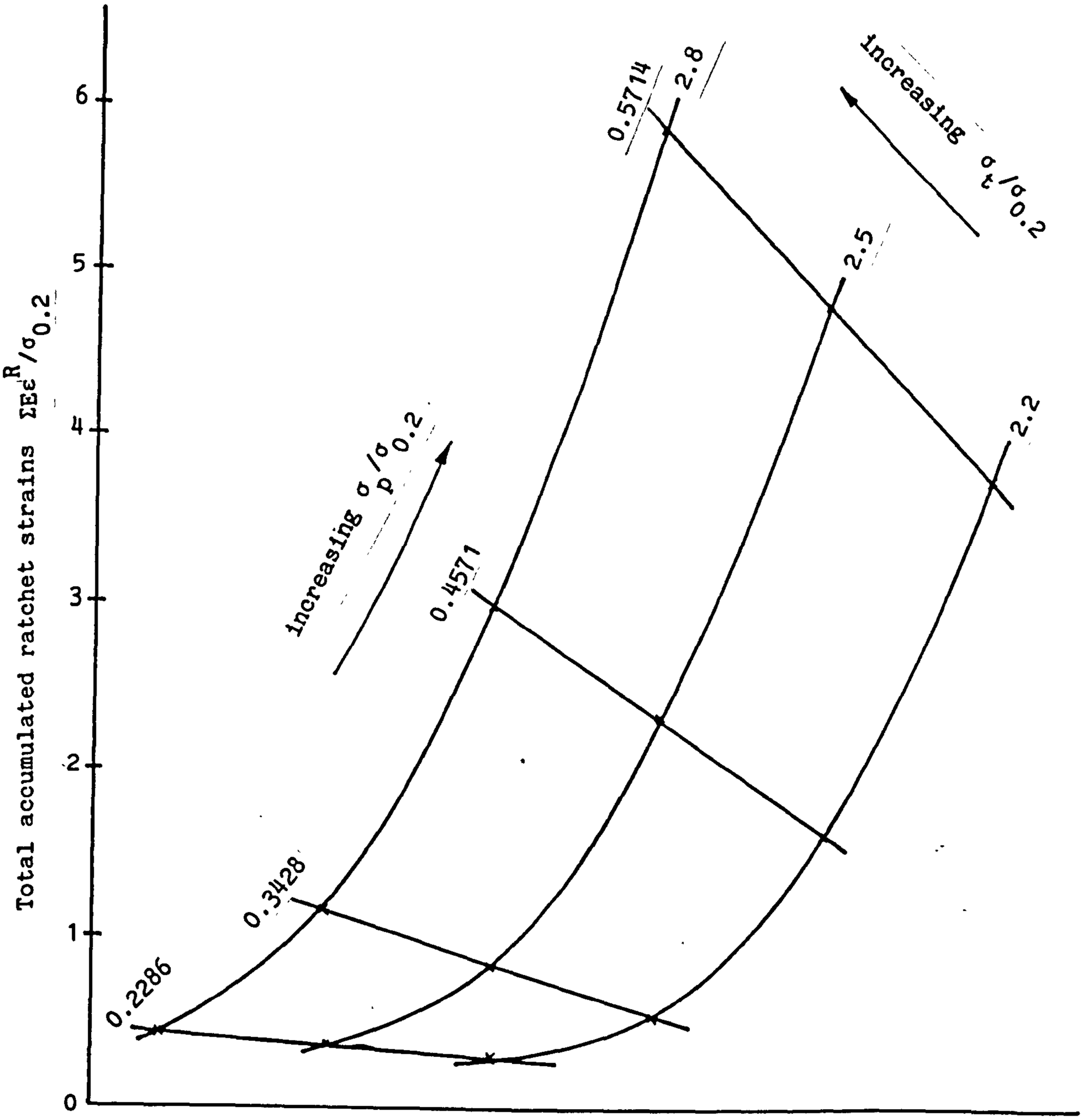

Fig.5.29(ii) Total accumulated ratchet strains at 10th cycle for a uniform beam subjected to a steady axial load and cyclic linear through the depth temperature distribution.

CHAPTER 6.

DISCUSSION.

6.1 Introduction.

Ratchetting has been identified as a potential problem in components operating in conventional and nuclear power plants, chemical plants and aero-engines where components are likely to be subjected to severe loading conditions.

When designing components which would experience severe loading conditions, the load conditions which would cause ratchetting should be determined. The effects of ratchetting on the performance of the components should be assessed.

In particular, the mechanism of ratchetting should be identified. The amount of deformation which would be accumulated over the design life of the component is required. This information is needed, especially at the initial design stage.

To predict the behaviour of component, three methods are available. These are:-

1) Experimental methods,

2) theoretical and approximate methods, and

3) computational methods.

Experiments on actual components or on the prototype under actual loading condition are usually very expensive. The time taken to gather the results is usually long and if high temperatures are involved, measurement of deformation and strains may be difficult. An alternative is to use a model. Even though it is relatively cheap, in some cases data obtained in this manner may not be used directly to predict actual component behaviour. The results are however, useful in assessing the accuracy of theoretical and approximate methods. More importantly, the results are useful in validating the assumptions of the material behaviour model used in the computational methods. The experimental results for the lead alloy beams have been used in this way to validate the Goodman and Goodall model for the lead alloy.

The theoretical methods are usually limited to simple component geometries and also simple material behaviour models. Their advantage is that they can give easily applied closed form solutions.

The third approach, used in this project, is to use computational techniques to predict component behaviour. The finite element method has been used to investigate the various parameters which are likely to influence the ratchetting behaviour of components. The finite element method has also been used to:-

1) investigate the ratchetting behaviour of a number of components subjected to steady mechanical and cyclic thermal loads,

2) identify the mechanisms of ratchetting and to examine the effects of load magnitudes and component geometry on the ratchetting mechanisms,
3) assess the effect of complete stress redistribution due to creep on the behaviour of components and
4) investigate the effect of material ratchetting phenomenon on the finite element prediction of component behaviour.

6.2 Elastic-Plastic Behaviour.

The behaviour of thin tubes and a circular plate subjected to steady mechanical loads and cyclic thermal loads was investigated to identify the effects of geometry and loading on the ratchetting mechanism of components. For these cases a von-Mises elastic-perfectly-plastic material model for 316 Stainless Steel was used. However, the results have been normalized with respect to geometry and material properties so that they could be of more general use.

For all the tubes, the ratio of mean diameter to mean thickness of 19 was used. For all the cases investigated, a Bree type of mechanism was obtained. However, for a tube with zero axial displacement, the R_2 type of behaviour is not clearly identified. Also, for the tube with an eccentric bore, three different types of behaviour (corresponding to ratchetting in the R_1 and R_2 regimes and cyclic plasticity without ratchetting) at various circumferential positions were obtained for one load condition. This is because the hoop stress varies around the circumference. For the value of mean diameter to mean

thickness ratio investigated, there is a through-thickness variation of stresses. The ratchet strains also vary through the thickness as a result of the through thickness variation of the stresses and also the circular compatibility condition. For the tube with zero axial load, the variation is small and the shakedown/ratchetting boundary and the contours of ratchet strains are practically the same as those predicted by Bree's analysis (8). By modifying the mechanical load characteristics, the shakedown/ratchetting boundary for the pressurized closed end and eccentric tubes can be predicted by the simple Bree analysis (8) to a good accuracy. For the tube with zero axial displacement, both the mechanical and thermal load characteristics had to be modified before the shakedown/ratchetting boundary could be correlated. Even so, a good correlation was only obtained for relatively low thermal loads. Except for the uniform tube with zero axial load, the contours of ratchet strains were not well predicted by Bree's analysis (8). This could be due to the effects of the deviations from Bree's analysis (8).

For the circular plate, a diameter to thickness ratio of 40 was used. The results indicated that there are two distinct mechanism of ratchetting depending on the load magnitudes. In this case, the mechanisms of ratchetting are different from the Bree type of mechanism and in particular, shakedown with cyclic plasticity does not exist. The shakedown/ratchetting boundary for low thermal load falls within the boundary obtained from the Upper Bound Theorem. For low thermal load and high mechanical load, the mechanism is very much dominated by the

mechanical load. The mechanical load, which causes bending in the radial and hoop directions, results in the ratchet hoop and radial strains to vary linearly through the thickness at all radii. On the other hand, at high thermal load and low mechanical load, the thermal stresses are the dominant stresses. Since the thermal stresses varies radially such that the maximum occurs at the plate centre, ratchetting only occurs in a region which exhibit cyclic plasticity and is confined to a small radius. Outside this region, elastic shakedown occurs. This type of ratchetting mechanism is different from the ratchetting behaviour of plates investigated by Hyde (15), Hardy (16), Goodman and Goodall (18) and Ponter (7).

The effect of complete redistribution due to creep on the behaviour of the eccentric tube and circular plate was also investigated. In both cases, a 'no-creep' shakedown load was used and ratchetting occurs. For the eccentric tube, the ratchet strains are practically independent of the creep stress index, n, whereas for the circular plate, the ratchet deflection reduces with increasing n values. This is because for the eccentric tube, the hoop stress is dominant and at the complete redistribution, the stress is practically uniform through the thickness. Also for all values of n considered, the stress distribution must be in equilibrium with the same mechanical load. Hence the distribution of stress at the stationary state depends on the mechanical load and is therefore independent of n. This was not the case for the circular plate where the stresses vary radially as well through the thickness. However, in both cases, the ratchet strains obtained when creep

occurs are always lower than the first cycle ratchet strains. Even though the effect of partial redistribution was not investigated, the ratchet strain which would be obtained if the stress is only partially redistributed, would be bounded by the first cycle 'no-creep' ratchet strains and that obtained when complete stress redistribution due to creep occurs.

The above discussion, illustrates that geometry and loading influences the ratchetting mechanism of components subjected to steady and cyclic loads. Structural ratchetting was observed because elastic-perfectly-plastic material was used. To determine if the Goodman and Goodall material ratchetting model give a better prediction, a lead alloy uniform beam subjected to steady axial load and cyclic fully reversed bending moment was used. The material model constants were determined from a uniaxial cyclic plastic test data. The model gave a better representation of the monotonic and cyclic stress-strain curve, in particular, the 'knee' of stress strain curve was accurately modelled. The constants were determined so that an accurate fit to the monotonic stress strain curve and the average ratchet strain for stress controlled cycling were obtained. Cyclic hardening was ignored. For cycling between a non-zero mean stress, the stress strain curve for the initial cycles was not accurately modelled. However, the essential features of the real material behaviour, such as material ratchetting, are contained in this model as opposed to the linear kinematic or the isotropic hardening models. When this model was used to predict the behaviour of the beam, a good agreement between the experimental observation and the finite element predictions was

obtained. When compared to the prediction using either elastic-perfectly-plastic, linear kinematic hardening and linear isotropic hardening models, the Goodman and Goodall model showed a significant improvement. Therefore, the poor prediction using the simpler hardening models is due to neglecting the material ratchetting phenomena. The elastic-perfectly-plastic material model predicts continued ratchetting at a constant ratchet strain after the first cycle. Isotropic hardening model predicts a monotonically reducing ratchet strain and elastic shakedown eventually occurs. Kinematic hardening model predicts ratchetting with monotonically reducing ratchet strains and shakedown with cyclic plasticity finally occurs. The Goodman and Goodall model predicts ratchetting with reducing ratchet strains but ratchetting still occurs even when either the isotropic or kinematic hardening models predicted component shakedown.

The Goodman and Goodall model was also used to predict the behaviour of a uniform beam subjected to a steady axial load and cyclic through the depth temperature distribution. Material constants applicable to 316 Stainless Steel at 600°C were used. The results were compared with that obtained using a linear kinematic hardening model. Initially, when structural ratchetting dominates, there was a slight difference in the predictions for the two models. But later, when material ratchetting dominates, the Goodman and Goodall material model predicted higher ratchet strains compared to the linear kinematic hardening model . Since, the computation was meant to illustrate the phenomena and to test that the program works

for the thermal loading as well, 10 cycles were applied. However, a higher number of cycles could also be applied. This analysis illustrates that material behaviour assumption also influences the component behaviour.

6.3 Classification of Ratchetting Mechanism.

Ponter (7) classified the mechanism of ratchetting into two main categories, namely, kinematically confined and kinematically unconfined types of mechanism. In the present work , both types of mechanisms were observed and are described below.

(a) Kinematically Confined.

In this category, ratchetting occurs such that at any instant, during the cycle, no volume of material which is yielding, contains a kinematically admissible deformation mechanism. As an example, let us look at the Bree type of mechanism. For a volume of material containing an admissible deformation mechanism to be present, yielding would have to occur through the whole thickness; the deformation mechanism would be a continued extension. This never happens in the Bree problem where, at any instant, there is always some elastic material through the thickness which restricts the amount of extension. Thus, a Bree type of mechanism, as observed in the ratchetting of tubes, is a kinematically confined type of ratchetting. For Bree type problems at high thermal load, values of low mechanical load exist for which cyclic

plasticity may occur without ratchetting. Also when ratchetting occurs, the whole section suffers incremental strain . For strain hardening materials, the ratchet strain reduces to zero.

(b) Kinematically Unconfined.

In this category, at some instant, there exists a volume of material which is yielding and contains a kinematically admissible deformation mechanism. The behaviour of the circular plate is an example. At high thermal and low mechanical loads, the centre of the plate, which is high thermally stressed region, yielding occurs through the whole thickness. Transverse and radial deformation can occur. For this case, ratchetting occurs whenever there is a volume of material which exhibits cyclic plasticity. Hence, load combinations which would cause cyclic plasticity without ratchetting do not exist. It is thought that material ratchetting and cyclic hardening would govern the ratchet rate.

6.4 Effects of Uniform and Non-uniform Loading on the Ratchetting Behaviour of Structures.

The effects of loads on the stress distribution in a structure depends on the geometry. For structures with uniform geometry (e.g.tube and plate with uniform thickness) subjected to a uniform loading (e.g.pressure) the stressing of the structure is said to be uniform. On the other hand, a non-uniform loading is said to occur if either the geometry or the stressing is not

uniform such as the eccentric tube subjected to an internal pressure.

Two types of structural behaviour were observed in the present work. Firstly, if the stressing is uniform, then the whole structure suffers incremental strains. The tube with uniform thickness and uniform beams are examples of ratchetting behaviour whereby every part of the structure experienced incremental strains. For the circular plate subjected to high mechanical and low thermal loads, incremental deflection is obtained at all radii. Secondly, for non-uniform stressing, ratchetting could be confined to some part of the structure leaving the rest of the structure shaking down. Some examples are the behaviour of the tube with an eccentric bore and the circular plate subjected to a high thermal and low mechanical loads. In the eccentric tube, the non-uniform stressing results from the variation in the tube thickness. Ratchetting is then confined to the thinnest section of the tube which is highly mechanically stressed, whereas the other part of the tube shakes down. In the case of the circular plate, the non-uniform stressing is due to the variation of the thermal stress. In this case ratchetting is only confined to the plate centre which is highly thermally stressed. The first type of effect is called the global effect as opposed to the local effect. If it is known that a particular stressing results in a local effect, then the shakedown/ratchetting boundary can be determined by considering only the localised ratchetting region. This could prove to be useful in simplifying the analysis. To illustrate this point, to determine the

shakedown/ratchetting boundary for the eccentric tube, only the thinnest section need to be considered.

6.5 Suggestion for Further Work.

It is the author's desire that the investigations into ratchetting of components using the finite element method should be continued. This section gives some suggestions of further work that followed from the present work.

i) Component Analysis.

Data on the ratchetting behaviour of components subjected to combinations of steady and cyclic loading are still scarce. It is suggested that more component analysis should be carried out to provide a general design data base. In particular, the effects of partial redistribution due to creep on the behaviour of components should be investigated. More importantly, analysis of components with material ratchetting should be pursued. More cyclic plastic material data, in particular for 316 Stainless Steel at elevated temperature, should be obtained so that the existing program with material ratchetting and cyclic hardening could be used to investigate the behaviour of stainless steel components. An equally important work is to incorporate the existing data from finite element analysis into the design codes for high temperature plant. Also, the finite element results could be used to investigate the accuracy of the approximate methods.

ii) Creep-plasticity Interaction Model.

Although good agreement between experimental and finite element results for the beam for low mean load, was obtained when material ratchetting was included, the result at high mean load where creep is likely to occur, is still underpredicted. This suggests that there is an interaction between creep and plasticity that should be investigated. Development of creep/plasticity interaction model equations and incorporate them into the finite element scheme should be pursued.

iii) Improvement on the Present Program.

Improvement on the present program in terms of efficiency and speed of convergence is worth pursuing so that the computing time could be reduced.

CHAPTER 7.

CONCLUSIONS.

The following conclusions have been obtained from the present study:-

1. The detailed study of the ratchetting of thin tubes indicated that:-

(i) For thin tubes with uniform thickness, in the absence of axial loading, the shakedown/ratchetting boundary and contours of constant ratchet strain can be accurately predicted by Bree's simplified uniaxial analysis (8). The variation of stress through the thickness has little effect on the shakedown/ratchetting boundary. In the presence of axial loading, with the ratio of mean hoop to axial stress of 2:1, the pressure to cause ratchetting is higher than that necessary for tubes without axial load. However, if the equivalent stress, due to pressure, at the mid-thickness is used to characterise the mechanical load parameter, the shakedown/ratchetting boundary can again be correlated with the Bree boundary (8) for practically all the load combinations considered. For these two cases, ratchetting in both R_1 and R_2 regimes can be identified and the existence of the 'plastic core' is required for ratchetting to occur.

(ii) For thin tube with axial restraint, the behaviour is different from that described above. For this case, R_1 and R_2 ratchetting regimes cannot be clearly identified and the shakedown/ratchetting boundary cannot be

correlated with Bree's simplified uniaxial solution. If the equivalent stress due to pressure at the outer surface ($\overset{\vee}{\sigma}^{p}_{eq}$) and the maximum elastic equivalent thermal stress ($\hat{\sigma}^{T}_{eq}$) are used to characterise the mechanical and thermal load parameters respectively, the shakedown/ratchetting boundary obtained using the simplified analysis is conservative for $\hat{\sigma}^{T}_{eq}/\sigma_{o}<3.35$ and for $\hat{\sigma}^{T}_{eq}/\sigma_{o}>3.35$ the boundary is unsafe.

(iii) For a thin tube with an eccentric bore, without axial loading, ratchetting is most pronounced in the vicinity of the thinnest section. At each circumferential position, the ratchetting mechanism is similar to that of a uniform tube without an axial load. The shakedown/ratchetting boundary can be accurately predicted from Bree's simplified analysis, if it is applied to the thinnest section. For any particular value of applied pressure and thermal load, it is possible that ratchetting in R_1 and R_2 regions and shakedown with cyclic plasticity occur simultaneously, depending on the circumferential position.

(iv) For all the components investigated, there is an increase in ratchet strains with an increase in the magnitude of the loads. For loads close to the shakedown/ratchetting boundary, it was found that the ratchet strains varies linearly with the load.

(v) It was found that creep which occurs between thermal

cycles affects the behaviour of the tube. When complete stress redistribution due to creep occurs, ratchetting can occur in the 'no-creep', shakedown regime. For the tube with uniform thickness, the ratchet strain for each thermal cycle will not vary with creep stress index, n.

For tube with eccentric bore, the ratchet strains obtained, for each thermal cycle, seemed to vary slightly with n.

2. From the analysis of the clamped circular plate, a relatively simple mesh was found to be adequate when the conditions at the plate edge were accurately modelled. The type of behaviour of the plate under combined transverse pressure and cyclic linear radial temperature gradients, was found to depend upon the magnitudes of both the mechanical and thermal loads. For high mechanical loads, incremental deflection, in the direction of the applied pressure, occurs at all radii. For high thermal loads and low mechanical loads, incremental deflection only occurs in the volume of material which undergoes cyclic plasticity. This volume of material is confined to the central region of the plate. The radial extent of this volume of material depends upon the magnitude of the thermal loading. The shakedown/ratchetting boundary, when a high mechanical load and low thermal load is applied, falls within the boundary obtained using the Upper Bound Shakedown Theorem. At low mechanical load and high thermal load, the shakedown/ratchetting boundary obtained was above the theoretical boundary. This is because with thermal loads close to the boundary, the material in which cyclic plasticity occurs

only occupies a small volume, hence accuracy depends upon the closeness of the nearest 'Gauss' point to the centre of the plate. With the mesh used, the boundary predicted is as good as would be expected.

Creep which occurs between thermal cycles was found to affect the behaviour of the plate. When complete stress redistribution due to creep occurs, ratchetting was obtained for load combinationS within the 'no-creep' shakedown regime. The ratchet deflection obtained was found to be dependent upon the creep stress index, n. Under complete redistribution conditions, the ratchet deflection was found to decrease with increasing n. The first cycle 'no-creep' ratchet deflection corresponds to the n=1 case.

In all cases, the ratchet deflection increased with increasing load magnitudes and close to the shakedown/ratchetting boundary, the ratchet deflections were found to vary linearly with the load magnitude.

3. Comparisons of experimental results and finite element predictions, for a uniform beam subjected to steady axial loading and cyclic fully reversed bending mements, indicate that when material ratchetting is included good correlations are obtained. The relatively poor predictions obtained with a high axial load, is due to the effects of creep, which were not included in the finite element calculations. The improvement, with Goodman and Goodall material ratchetting model, compared to predictions obtained with elastic-perfectly-plastic, linear

isotropic hardening and linear kinematic hardening material models, is very significant.

4. Results for a uniform beam, subjected to a steady axial load and cyclic, linear, through the depth, temperature distribution were also obtained; a linear kinematic hardening model and a Goodman and Goodall material ratchetting model (with material constants appropriate to 316 Stainless Steel at 600^{o}C) were used. For the load magnitudes considered and the accumulated strains obtained, no significant difference was apparent.

5. For components which operates at high mean loads at which creep and plasticity are likely to occur, it is essential that a more appropriate material behaviour model, which is capable of describing creep-plasticity interactions is developed if improvements in the accuracy of predictions are to be obtained.

6. The following parameters have been found to influence the elastic-plastic ratchetting behaviour:-

(i) Structural geometry and loading conditions,

(ii) Creep and

(iii) Material behaviour.

Acknowledgements.

The author wishes to thank the following:-

1. His supervisors, Dr. J. J. Webster and Dr. T. H. Hyde for their invaluable help, guidance, support and encouragement throughout the project.

2. Dr. K. Yahiaoui and Dr. S. J. Hardy for their help and permission to use some of their results for comparison.

3. The Head of Department of Mechanical Engineering for providing the facilities for this research.

4. The in-mates in Research Room 3.

5. Mrs.B. J. Martin for her care and effort in producing the typed thesis.

6. Mrs.J. Kelvey for her patience in typing some of the figures in the thesis.

7. To his wife, Zurina and his family for their understanding and encouragement.

REFERENCES.

1 ASME — Code Case N47-15(1592-15). 'Class 1 components in Elevated Temperature Service', ASME, New York, 1979.

2 AINSWORTH, R.A. — 'An Experimental Study of a Three Bar Structure Subjected to Variable Temperature' Int. Jnl. of Mechanical Sciences, Vol.19, 1977, pp 247-256.

3 YAHIAOUI, K. — Experimental Study of Creep and Ratchetting Using Lead Alloy Model Components', Ph.D. Thesis, 1982, Nottingham University.

4 HYDE, T.H. and YAHIAOUI, K. — 'An Experimental Study of the Ratchetting and Creep of Thick Flanged Tubes Subjected to Steady Axial Mechanical Loading and Transient Thermal Loading' Int. Jnl. Mech. Sci. Vol.26, No.1, pp 47-61, 1984.

5 BURGREEN, D. — 'The Thermal Ratchet Mechanism', Jnl. of Basic Engineering, Vol.90, No.3, 1968, pp 319-324.

6 MEGAHED, M.M. — 'Influence of Hardening Rule on the Elasto Plastic Behaviour of a Simple Structure Under Cyclic Loading', Int. Jnl. of Mech. Sci. Vol.23, 1981, pp 169-182.

7 PONTER, A. R. S. 'Shakedown and Ratchetting Below the Creep Range', Report Contract No.544-79-5 ECI U.K. Dept. Engineering, University of of Leicester 1981.

8 BREE, J. 'Elastic-Plastic Behaviour of Thin Tubes Subjected to Internal Pressure and Intermittent High-heat Fluxes with Application to Fast-Nuclear-Reactor Fuel-Elements', Jnl.of Strain Anal. Vol.2, No.3, 1967 pp 226-238.

9 BURGREEN, D. 'Structural Growth Induced by Thermal Cycling', Jnl. Basic Engineering, Trans. ASME Series D, Vol.90, No.3, 1968, pp 469-475.

10 BURGREEN, D. 'Design Method for Power Plant Structures' First Ed. C.P. Press. New York, 1975.

11 KRAUS, H. 'Creep Analysis' John Wiley & Sons. New York, 1980.

12 KOITER, W. T. 'General Theorem for Elastic-Plastic Solids', Progress in Solid Mechanics, Vol.1 pp 167-221, 1964.

13 GOODALL, I. W. 'Approximate Methods of Inelastic Design' Int.Jnl. Mechanical Science, Vol.24, No.4 pp 251-262, 1982 also in S.S. Gill Conference on Pressure Vessels-Analysis for Design.

14 DAWSON, R. J. 'Finite Element Solution of Elasto Plastic Problems', M.Phil. Thesis, University of Nottingham, 1981.

15 HYDE, T. H. 'The Effect of Transverse Pressure Loading on the Thermal Ratchetting of Circular Plates', Jnl. of Strain Analysis, Vol.15, No.1, 1980.

16 HARDY, S. J. 'Finite Element Analysis of Components Subjected to Ratchetting and Creep', Ph.D. Thesis, Nottingham University, 1983.

17 DWIVEDI, V. S.
FESSLER, H.
HYDE, T. H. and
WEBSTER, J.J. 'Thermal Ratchetting of a Hollow Stepped Cylinder', Non-linear Problems in Stress Analysis. Ed. P. Stanley, 1978, (App. Sc. Publishers London) pp 299-316.

18 GOODMAN, A. M. and
GOODALL, I. W. 'Constitutive Relations for Stainless Steels', Metals Society Conference, Varese, May 1981.

19 GOODMAN, A. M. Private Communications.

20 HYDE, T. H. 'The Uniaxial and Biaxial, Monotonic and Cyclic Plasticity Behaviour of a Lead Alloy Model Material', Jnl. Strain Analysis. Vol.18, No.2, 1983.

21 SWINDEMAN, R. W. 'Representation of the High Temperature Tensile behaviour of Reannealed type 304 Stainless Steel by the Voce Equation' Trans. ASME, Jnl. of Eng. Mat. & Tech. 97, 1975, pp 98-106.

22 MENDELSON, A. 'Plasticity: Theory and Applications', Macmillan Company, New York, 1968.

23 MEGAHED, M. M. PONTER, A. R. S. and MORRISON, C. J. 'An Experimental and Theoretical Investigation into the creep properties of a simple structure of 316 Stainless Steel', Int. Jnl. of Mechanical Sciences, Vol.26, No.3, pp 149-164, 1984.

24 VOCE, E. 'The Relationship between Stress and Strain for Homogeneous Deformation', Jnl. of the Inst. of Metals, Vol.74, 1948, pp 537-562.

25 FESSLER, H. and HYDE, T. H. 'The Uniaxial and Biaxial Creep Properties of a Material for Modelling Creep', in Non-linear Problems in Stress Analysis (Ed. P. Stanley), 1978, (App. Science Publishers, London).

26 BENHAM, P. P. 'Some Observations of Cyclic Strain Induced Creep in Mild Steel at Room Temperature', Int. Jnl. Mechanical Science, Vol.7, pp 81-86, 1965.

27 JHANSALE, H. R. 'A Friction Stress Method for Cyclic Inelastic Behaviour of Metals', Proc. Third. Int. Conf. on Structural Mechanics in Reactor Technology Vol.5, 1975.

28 GOODALL, I. W. HALES, R. and WALTERS, J. 'On Constitutive relations and Failure Criteria of an Austenitic Steel Under Cyclic Loading at Elevated Temperature' IUTAM Symp. on Creep in Structures, Leicester 1980 Creep in Structures (Ed. by A.R.S.Ponter and D.R.Hayhurst), pp 103-117. Springer-Verlag, Berlin, (1981).

29 LAI, J. S. and FINDLEY, W. N. 'Creep of 2618 Aluminium under step stress changes predicted by Viscous-Viscoelastic Model', Jnl. of App. Mechanics, Vol.47, 1980, pp 21-26.

30 PENNY, R. K. and MARRIOTT, D. L. 'Design for Creep' McGraw-Hill Book Co. (UK) Ltd. 1971.

31 FESSLER, H. HYDE, T. H. and WEBSTER, J. J. 'Some Tensile, Creep and Plasticity/Creep Interaction Data for the Lead Alloy which is to be used for the Shouldered Tube Tests' 3rd Progress Report to SRC on Creep and Plasticity Interaction, Dept. of Mechanical Engineering, University of Nottingham.

32 HYDE, T. H. and COOPER, D. 'First proper report Creep/Plasticity Interaction in 316 Stainless Steel, Mechanical Engineering Dept. University of Nottingham.

33 HYDE, T. H. and WEBSTER, J. J. 'Assessment of some methods of predicting Creep Deformations and Life of Components' International Conf. on Engineering Aspects of Creep, 1981, I.Mech.E. pp 73-79.

34 HOPKINS, H. G. and PRAGER, W. 'The Load carrying Capacities of Circular Plates', Jnl. of Mech. & Phys. Solids, Vol.2, 1953, pp 1-13,

35 HOPKINS, H. G. and WANG, A. J. 'Load Carrying Capacities of Perfectly-Plastic Materials with Arbitrary Yield Conditions', Jnl. of Mech. & Phy. Solids, Vol.3, pp 117-129, 1954.

36 PRAGER, W. 'A New Method of Analysing Stresses and Strains in Work-Hardening Plastic Solid', Jnl. of App. Mech. Trans. ASME. 78, 1956, pp 493.

37 ZIEGLER, H. 'A modification of Prager's Hardening Rule' Quart. App.Math, Vol.17, 1959, pp 55-65.

38 MICHNO, M. J. Jnr. and FINDLEY, W. N. 'Subsequent Yield Surfaces for Annealed Mild Steel under Servo Controlled Strain and Load Histories: Ageing, Normality, Convexity, Corners, Bauschinger and Cross Effects', Trans. ASME, Jnl. Eng. Materials & Technology, 97, 1975, pp 25-32.

39 ZIENKIEWICZ, O. C, NAYAK, G. C. and OWEN, D. R. J. 'Composite and Overlay Models in Numerical Analysis of Elasto-Plastic Continua', Symp. on Foundations of Plasticity, Warsaw 1972.

40 MROZ, Z. 'On the Description of Anisotropic Work-Hardening', Jnl. Mech. Phys. Solids. Vol.15 1967, pp 163-175.

41 MROZ, Z. 'An Attempt to Describe the Behaviour of Metals under Cyclic Loads Using a More General Work-Hardening Model' Acta. Mechanica 7, 1969, pp 199-212.

42 MROZ, Z. SHRIVASTAVA, H. P. and DUBEY, R. N. 'A Non-Linear Hardening Model and its Application to Cyclic Loading', Acta. Mechanica 25, 1976, pp 51-61.

43 EISENBERG, M. A. and PHILLIPS, A. 'On Non-Linear Kinematic Hardening', Acta. Mechanica 5, 1 (1968).

44 GREEN, A. E. and NAGHDI, P. M. 'A General Theory of an Elastoc-Plastic Continuum', Arch. Rat. Mech. Anal 18,. 251 (1965).

45 DAFALIAS, Y. F. and POPOV, E. P. 'A Model of Non-Linearly Hardening Materials for Complex Loading', Acta. Mechanica 21, pp 173-192, 1975.

46 JHANSALE, H. R. 'A new parameter for the Hysteretic Stress-Strain Behaviour of Metals', Trans. of the ASME, Jnl. of Eng. Mat. & Tech. Vol.97, No.1, 1975, pp 33-38.

47 DAFALIAS, Y. F. 'A novel bounding surface Constitutive Law for Monotonic and Cyclic Hardening Response of Metals', 6th Int. Conf. on Material Modelling of Inelastic Behaviour of Materials and Structures. Vol. L. Paris, pp 17-21, Aug.1981, North Holland Publishing Co.

48 LIU, M. C. M. KREMPL, E, and NAIRN, D. C. 'An Exponential Law for Cyclic Plasticity', Trans. ASME, Jnl. of Eng. Mat. & Tech. 98, 1976, pp 322-329.

49 MILLER, A. 'An Inelastic Constitutive Model for Monotonic Cyclic and Creep Deformation. Part I-Equations Development and Analytical Procedures', Trans. ASME, Jnl. of Eng. Mat. & Tech. 98, 1976, pp 97-105.

50 MILLER, A. 'An Inelastic Constitutive Model for Monotonic, Cyclic and Creep Deformation:- Part II-Application to type 304 Stainless Steel' Trans. ASME, Jnl. of Mat. & Tech. 98, 1976, pp 106-113.

51 KREMPL, E. 'Cyclic Creep -An Interpretive Literature Survey', Welding Research Council Bulletin, Vol. 195, June 1974, pp 63-123.

52 KREMPL, E. 'An Inelastic Stress-Strain Law for Elevated Temperature and Slowly Time Varying Loads', Int. Jnl. Fracture Mechanics, Vol.8, 1972, pp 365-382.

53 TIMOSHENKO, S. and WAINOWSKY-KRIEGER, S. 'Theory of Plates and Shells', Mc Graw Hill, New York. (1959).

54 JOHNS, D. J. 'Thermal Stress Analyses', Permagon Press, Oxford, First Ed. 1965.

55 MEGAHED, M. PONTER, A. R. S. and MORRISON, C. J. 'A Theoretical and Experimental Investigation of Material Ratchetting Rates in a Bree Beam Element', Int. Jnl. Mech. Science, Vol.25, No.12, 1983, pp 917-933.

56 PARKES, E. W. 'Incremental Collapse due to Thermal Stresses' Aircraft Engineering, Vol.28, No.333, 1956, pp 395-396.

57 PARKES, E. W. 'Effects of Repeated Thermal Loading', Aircraft Engineering, Vol.32, 1960, pp 222-229.

58 MULCAHY, T. M. 'An Assessment of Kinematic Hardening Thermal Ratchetting', Jnl. Eng. Mat. & Tech. Trans ASME, Vol.96, 1974, pp 214-221.

59 MILLER, D. R. 'Thermal-Stress Ratchet Mechanism in Pressure Vessels', Jnl. of Basic Eng. Vol.81, No.2, 1959, pp 190-196.

60 EDMUNDS, H. G. and BEER, F. J. 'Notes on Incremental Collapse in Pressure Vessels', Jnl. of Mech. Eng. Sciences, Vol.3, No.3, 1961, pp 187-199.

61 DAWSON, R. J. FESSLER, H. HYDE, T. H. and WEBSTER, J. J. 'Elasto-Plastic and Creep Behaviour of Axially loaded shouldered Tubes', Jnl. of Strain Analysis, Vol.15, 1980, pp 21-29.

62 CORUM, J. M. YOUNG, H. C. and GRINDELL, A. G. 'Thermal Ratchetting in Pipes Subjected to Intermittent Thermal Downshocks at Elevated Temperatures', Pressure Vessels and Piping, ASME, New York, 1975. pp 79-98.

63 YAMAMOTO, S.
KANO, J. and
YOSHITOSHI, A.
'Thermal Ratchetting experiments of type 304 Stainless Steel pipes under alternating cold and hot thermal shocks with varying axial loads', Elevated Temperature Design Symp. ASME, New York, 1976, pp 25-32.

64 GOODMAN, A. M.
'Incremental Plastic Deformation of a Cylinder Subjected to Cyclic Thermal Loading', Non-Linear Problems in Stress Analysis, Ed. P. Stanley, App. Science Publishers Ltd., London 1978, pp 317-344.

65 HYDE, T. H.
WEBSTER, J. J. and
FESSLER, H.
'Thermal Ratchetting of Axially Loaded Tubes Operating in the Creep Range', Jnl. of Strain Anal. Vol.17, No.4 1982, pp 243-251.

66 HYDE, T. H. and
WEBSTER, J. J.
'Experimental thermal ratchetting data for a component with a stress concentration', Jnl. of Strain Anal. Vol.17,4 1982, pp 253-261.

67 HYDE, T. H. and
WEBSTER, J. J.
'Predicting the thermal ratchetting and creep behaviour of a component with a stress concentration', Jnl. of Strain Anal. Vol.17,4. 1982, pp 263-268.

68 MULCAHY, T. M.
'Thermal Ratchetting of a Beam Element Having an Idealized Bauschinger Effect', Jnl. of Eng. Materials & Technology, Trans, ASME, Vol.98, 1976, pp 264-271.

69 PONTER, A. R. S. and WALTER, M. H. 'A Theoretical & Experimental Investigation of Creep Problems with Variable Temperature' Jnl. of App. Mech. Trans ASME, Vol.43, 1976, pp 639-644.

70 COUSSERAN, P. LEBEY, J. MOULIN, D. ROCHE, R. and CLEMENT, G. 'Ratchetting-experimental tests and practical method of analysis', Int. Conf. on Eng. Aspects of Creep (Vol.II) University of Sheffield, Sept. 1980, pp 143-151.

71 MEGAHED, M. M. and PONTER, A. R. S. 'Creep and Plastic ratchetting in a Simple Structure', Dept. of Eng. Leicester University, Report. No. 79-9, 1979.

72 MELAN, E. 'Der Spannungszustand eines' Hencky-Mises' 'schen' Kontinuums bei versender licher Belastung'; Sitzungsberichte der Akademic der Wissenschaften in Wien, Vol.147, 1938, pp 73-87.

73 SYMONDS, P. S. 'Shakedown in Continuous Media', Jnl. of App. Mechanics, Trans. ASME, Vol. 73. March 1951, pp 85-89.

74 FESSLER, H. and HYDE, T. H. 'Ratchetting Tests of a Stepped Beam Under Constant Tensions and Cyclic Bending'. Submitted to the Jnl. of Strain Analysis.

75 HARDY, S. J.
HYDE, T. H. and
WEBSTER, J. J.
'Mechanical Ratchetting of a Stepped Beam; Comparison of finite element predictions with experimental results', Submitted to the Jnl. of Strain Analysis.

76 AINSWORTH, R. A.
'Bounding Solutions for Creeping Structures Subjected to Load Variations above the Shakedown Limit', Int. Jnl. Solids Strs. Vol.13, 1977, pp 971-980.

77 AINSWORTH, R. A.
'Application of Bounds for Creeping Structures Subjected to Load Variations above the Shakedown Limit', Int. Jnl. Solids Str. Vol.13, 1977, pp 981-993.

78 AINSWORTH, R. A.
'A Note on Bounding Solutions for Creeping Structures Subjected to Load Variations above the Shakedown Limit', Int. Jnl. Solids Str. Vol.15, 1979, pp 981-986.

79 O'DONNELL, W. J.
and POROWSKI, J.
'Upper bounds for Accumulated Strain Due to Creep Ratchetting', Welding Research Bulletin, 195, 1974, pp 57-62.

80 LECKIE, F. A.
'A review of Bounding Techniques in Shakedown and Ratchetting at Elevated Temperatures', Welding Research Council Bulletin, 195, 1971, pp 1-56.

81 JEFFREY, G. B. 'Plane Stress and Plane Strain in Bipolar Coordinates', Phil. Trans. Royal Society, London, Serial A, Vol.221, 1921, pp 265-293.

82 TIMOSHENKO, S. 'The Theory of Elastic Stability' Mc Graw Hill. 1936, p 367.

83 HARDY, S. J. "Finite Element Program User Manual', University of Nottingham, Dept. Mech. Eng. Research Report, March 1983.

APPENDIX I.

ANALYTICAL SOLUTIONS FOR CLAMPED CIRCULAR PLATES.

AI.1 Introduction.

The elastic solution for a variety of plates structures subjected to pressure load are available (e.g. 53). Solutions for the limit loads of circular plates, subjected to axisymmetric loading, made of elastic-perfectly-plastic material, which obeys the von-Mises yield conditions, are also available (35). The elastic stresses induced due to a general temperature distribution in plates are given in reference 54. These solutions have been obtained and will not be derived in this appendix; the relevant results will simply be quoted. The results for the elastic stress distribution in a circular plate clamped at its edge with a linear radial temperature distribution will also be quoted. The shakedown/ratchetting boundary for the present plate geometry and loading is derived here by applying the Upper Bound Shakedown Theorem, as extended by Ponter (7). The solutions will be used for comparison with those obtained from the finite element results described in Chapter 4. The component geometry is a circular plate with outer radius, R, and thickness, h, clamped at its outer edge.

AI.2 Elastic Solutions.

AI.2.1 Uniform Transverse Pressure, P.

The transverse deflection u(r) is given by (53):-

$$u(r) = \frac{3(1-\nu^2)PR^4}{16Eh^3}\left[1 - \left(\frac{r}{R}\right)^2\right]^2 \qquad \text{AI.1}$$

The stresses due to pressure P are (52):-

$$\sigma_r^p = \frac{3(1+\nu)}{4}\left(\frac{R}{h}\right)^2\left(\frac{z}{h}\right)P\left[1 - \frac{(3+\nu)}{(1+\nu)}\left(\frac{r}{R}\right)^2\right] \qquad \text{AI.2}$$

and

$$\sigma_\theta^p = \frac{3(1+\nu)}{4}\left(\frac{R}{h}\right)^2\left(\frac{z}{h}\right)P\left[1 - \frac{(3\nu+1)}{(1+\nu)}\left(\frac{r}{R}\right)^2\right] \qquad \text{AI.3}$$

where σ_r^p is the radial stress and σ_θ^p is the hoop stress due to pressure P.

The average through-thickness shear stresses, τ_{rz}, is given by:-

$$\tau_{rz} = -\frac{Pr}{2h} \qquad \text{AI.4}$$

AI.2.2 Thermal Stresses.

The elastic thermal hoop stress (σ_θ^T) and thermal radial stress (σ_r^T) for a clamped circular plate with a radial temperature distribution of:-

$$T(r) = \Delta T(1 - r/R) \qquad \text{AI.5}$$

are given by

$$\sigma_r^T = -\sigma_t\left(1 - \frac{(1-\nu)r}{(2-\nu)R}\right) \qquad \text{AI.6}$$

and

$$\sigma_\theta^T = -\sigma_t\left(1 - \frac{2(1-\nu)r}{(2-\nu)R}\right) \qquad \text{AI.7}$$

where

$$\sigma_t = \frac{(2-\nu)}{3(1-\nu)} E\alpha\Delta T \qquad \text{AI.8}$$

AI.2.3 Limit Pressure.

A complete and detailed analysis of the load carrying capacity of circular plates made of elastic-perfectly-plastic material and obeying the von-Mises yield criterion is given in

reference 35. The analysis is complicated and hence the reader is referred to reference 35 for a complete analysis. The final result for the limit pressure, P_L^V, for a clamped circular plate subjected to a uniform transverse pressure, made from an elastic plastic material obeying the von-Mises yield condition is given by:-

$$P_L^V = 3.125\sigma_o\left(\frac{h}{R}\right)^2 \qquad \text{AI.9}$$

where σ_o is the yield stress of the material. For a material which obeys the Tresca yield criterion the expression for the limit pressure, P_L^T, is given by:-

$$P_L^T = 2.815\sigma_o\left(\frac{h}{R}\right)^2 \qquad \text{AI.10}$$

The limit pressure evaluated from expressions AI.9 and AI.10. will be compared with the value obtained from the finite element analysis. The analysis in references 53 and 35 are based on thin plate theory and the effect of shear and transverse stresses are therefore ignored.

AI.3 Elastic-Plastic Cyclic Solutions.

AI.3.1 Shakedown/Ratchetting Boundary for $\sigma_t/\sigma_o < 2.0$

The shakedown/ratchetting boundary determined in this section is based on the Upper Bound Theorem proposed by Koiter (12) and extended, to include the case where cyclic plasticity region exists, for cyclic loading, by Ponter (7). In the present case, the extended theorem is employed. The theorem states that:-

'The body cannot support a given system of external loads if any kinematically admissible strain field $d\varepsilon^c_{ij}$ exists for which the rate of work of the external loads exceeds the rate of plastic energy dissipation'.

Conversely: 'The body can support the given external loads if the rate of plastic energy dissipation is greater than the rate of work done by the external loads'.

The second definition implies that, for a body to support the external loads, the following inequality must be satisfied:-

$$\int_V D(d\varepsilon^c_{ij})dV \geq \int_{S_p} P_i du_i dS_p + \int_V \hat{\sigma}^T_{ij}(\bar{x},t_o)d\varepsilon^c_{ij}dV \qquad \text{AI.11}$$

where P_i is a boundary traction acting on S_p ,

V is the volume ,

$d\varepsilon^c_{ij}$ is a compatible strain field,

du^c_i is a displacement field which satisfies the boundary conditions,

σ^c_{ij} is a state of stress on the yield surface and

$D(d\varepsilon^c_{ij})$ is the energy dissipation function given by

$$D(d\varepsilon^{c}_{ij}) = \sigma^{c}_{ij} d\varepsilon^{c}_{ij}$$

For $\sigma_t/\sigma_o<2.0$ where σ_t is given by equation AI.8 the mechanism of collapse, shown in Fig.AI.1 may be assumed. For this case, the displacement field u is simply

$$u = U_o(1 - r/R) \qquad \text{AI.12}$$

where U_o is the displacement at the plate centre. For this deformed shape, the curvatures in the hoop direction, K_θ, and in the radial direction, K_r, are given by

$$K_\theta = -\frac{1}{r}\frac{du}{dr} = \frac{U_o}{Rr} \qquad \text{AI.13}$$

and

$$K_r = -\frac{d^2u}{dr^2} = 0 \qquad \text{AI.14}$$

Hence the strain field $d\varepsilon^{c}_{ij}$ consists of

$$\varepsilon_\theta = K_\theta . z = \frac{U_o z}{Rr} \qquad \text{AI.15}$$

only and

$$\varepsilon_r = K_r z = 0 \qquad \text{AI.16}$$

Assuming small deformations, the angular displacement at the clamped edge ϕ is given by

$$\phi = \frac{U_o}{R} \qquad \text{AI.17}$$

The thermal stresses are given by equations AI.6 and AI.7, which, together with AI.8, give the results:-

$$\sigma_r = -\sigma_t\left(1 - \frac{(1-\nu)r}{(2-\nu)R}\right) \qquad \text{AI.18}$$

$$\sigma_\theta = -\sigma_t\left(1 - \frac{2(1-\nu)r}{(2-\nu)R}\right) \qquad \text{AI.19}$$

Now, the terms in inequality AI.11 will be evaluated separately.

External Work.

Due to pressure, P

$$\int_{S_p} P_i du_i dS_p = \text{volume of cone X pressure}$$

$$= \frac{1}{3}\pi R^2 U_o P \qquad \text{AI.20}$$

The term $\int_V \hat{\sigma}^T_{ij}(\bar{x},t_o)d\varepsilon^c_{ij}dV$ involves an instant t_o during the thermal cycle. The value of $\hat{\sigma}^T_{ij}(\bar{x},t_o)$ is found by translating the thermal stress history using rigid body translation to the point on the yield surface which has the compatible strain field. The point which touches the yield surface during the translation is the required value. This is

carried out for the present history at each point in the structure. Fig.AI.2 shows the yield surface and the thermal load history AB. The stress history OA is the thermal load at the plate centre and OB is the thermal load at the plate edge.

By the method outlined above and for the thermal cycle shown in Fig.AI.3 and period $2t_1$, it was found that

for $z > 0$, $t_o = 2nt_1$, where $n = 0, 1, 2$ etc. and

for $z < 0$, $t_o = nt_1$, where $n = 1, 2, 3$ etc.

Hence

$$\hat{\sigma}^T_{ij}(\bar{x},t_o) = 0 \text{ for } z > 0$$

and for $z<0$, the components of $\hat{\sigma}^T_{ij}(\bar{x},t_o)$ are given by Equations AI.18 and AI.19.

$$\therefore \int_V \hat{\sigma}^T_{ij}(\bar{x},t\ )d\varepsilon^c_{ij}dV = \int_{-\frac{h}{2}}^{0}\int_0^R \sigma^T_r.\varepsilon_r.2\pi r dr dz$$

$$+ \int_{-\frac{h}{2}}^{0}\int_0^R \sigma^T_\theta.\varepsilon_\theta.2\pi r dr dz$$

Evaluating the integrals give

$$\int_V \hat{\sigma}^T_{ij}(\bar{x},t\ )d\varepsilon^c_{ij}dV = \frac{\pi\sigma_t U_o h^2}{4(2-\nu)} \qquad \text{AI.21}$$

Plastic Energy Dissipation. $\int D(d\varepsilon_{ij}^{c})dV$

Now, $D(d\varepsilon_{ij}^{c})$ consists of 2 parts. Firstly the energy dissipated in the hoop bending which occurs at all radii and secondly, the energy dissipated due to the formation of a plastic hinge at the edge.

Hence

$$\int_V D(d\varepsilon_{ij}^{c})dV = \int_{-\frac{h}{2}}^{\frac{h}{2}}\int_0^R \frac{2}{\sqrt{3}}\sigma_o\varepsilon_\theta 2\pi r dr dz + (M_o\phi)_{\text{at the edge}} \qquad \text{AI.22}$$

Where M_o is the plastic moment

Now
$$M_o\phi = \frac{U_o\sigma_o h^2}{2} \qquad \text{AI.23}$$

and
$$\int_{-\frac{h}{2}}^{\frac{h}{2}}\int_0^R \frac{4}{\sqrt{3}}\sigma_o\frac{U_o z}{R}.\pi dr dz = \frac{8U_o\pi\sigma_o}{\sqrt{3}R}\left|\frac{z^2}{2}\right|_0^{\frac{h}{2}}\left|r\right|_0^R$$

$$= \frac{U_o\pi\sigma_o h^2}{\sqrt{3}} \qquad \text{AI.24}$$

Collecting terms and substituting into equation AI.11 gives the following equation.

$$\pi U_o\sigma_o h^2\left(\frac{1}{2}+\frac{1}{\sqrt{3}}\right) = \frac{\pi R^2 U_o P}{3} + \frac{\pi U_o h^2\sigma_t}{4(2-\nu)} \qquad \text{AI.25}$$

Normalizing with respect to $3.125PR^2/\sigma_o h^2$

gives

$$\frac{3X1.0774\sigma_o(\frac{h}{R})^2}{3.125\sigma_o(\frac{h}{R})^2} = \frac{P}{P_L^V} + \frac{\frac{3}{4(2-\nu)}(\frac{h}{R})^2\sigma_t}{3.125\sigma_o(\frac{h}{R})^2}$$

$$\text{i.e.} \quad 1.0343 = \frac{P}{P_L^V} + \frac{0.24\sigma_t}{(2-\nu)\sigma_o} \qquad \text{AI.26}$$

putting $\nu=0.3$, the bound become

$$1.0343 = \frac{P}{P_L^V} + 0.1412\frac{\sigma_t}{\sigma_o} \qquad \text{AI.27}$$

The bound is given in Fig.AI.4.

AI.3.2 Boundary for $\sigma_t/\sigma_o > 2.0$

For this load condition, the volume of material can be divided into 2 parts. The first part, is a region where the material exhibits cyclic plasticity, in which case the elastically calculated thermal stress history cannot be translated into the yield surface by rigid body translation. The second part, is the region in the plate where the thermal stress history can be translated into the yield surface in which shakedown occurs. In the region where there is cyclic plasticity, ratchetting occurs. For low mechanical loads, which are considered here, the thermal load dominates. Under these conditions, the problem becomes that of determining the volume of material which exhibits cyclic plasticity and to determine the bound to avoid ratchetting. Referring to Fig.AI.5 AB represent the thermal load history for the plate at the hot state. OA is the

stress history at the plate centre and OB is the stress history at the plate edge etc. The surface I is the yield surface. For convenience, another surface, II, is also defined. By rigid body translation, the history CB can be translated into the yield surface whereas AC cannot. Therefore cyclic plasticity occurs at the position in the plate which has the stress histories AC. The cyclic plasticity zone extends from the plate centre, with thermal stress history OA, to a radius $r=R_1$, with stress history OC. The problem is to determine the radius R_1. Now, the equation of line AB is given by

$$\sigma_\theta - 2\sigma_r = \sigma_t$$

or

$$\sigma_\theta = 2\sigma_r + \sigma_t \qquad \text{AI.28}$$

The equation of the yield surface (surface I) is

$$\sigma_r^2 + \sigma_\theta^2 - \sigma_r\sigma_\theta = \sigma_o^2 \qquad \text{AI.29}$$

and the equation of surface II is

$$\sigma_r^2 + \sigma_\theta^2 - \sigma_r\sigma_\theta = 4\sigma_o^2 \qquad \text{AI.30}$$

substituting equation AI.28 into AI.30 gives

$$\sigma_r^2 + (2\sigma_r+\sigma_t)^2 - \sigma_r(2\sigma_r+\sigma_t)^2 = 4\sigma_o^2$$

$$3\sigma_r^2 + 3\sigma_r\sigma_t + \sigma_t^2 - 4\sigma_o^2 = 0$$

which simplifies to

$$\sigma_r = -\frac{\sigma_t}{2} \pm \frac{\sigma_t}{6}\sqrt{48\left(\frac{\sigma_o}{\sigma_t}\right)^2 - 3}$$

The negative root is required here for $\sigma_r < 0$

$$\therefore \qquad \sigma_r = -\frac{\sigma_t}{2} - \frac{\sigma_t}{6}\sqrt{48\left(\frac{\sigma_o}{\sigma_t}\right)^2 - 3} \qquad \text{AI.32}$$

This is the value of σ_r at $r=R_1$

substituting AI.32 into equation AI.18 and putting $r=R_1$ gives

$$-\frac{\sigma_t}{2} - \frac{\sigma_t}{6}\sqrt{48\left(\frac{\sigma_o}{\sigma_t}\right)^2 - 3} = -\sigma_t\left(1 - \frac{(1-\nu)R_1}{(2-\nu)R}\right)$$

$$1 - \frac{(1-\nu)R_1}{(2-\nu)R} = \frac{1}{2} + \frac{1}{6}\sqrt{48\left(\frac{\sigma_o}{\sigma_t}\right)^2 - 3} \qquad \text{AI.33}$$

and hence

$$\frac{R_1}{R} = \frac{(2-\nu)}{(1-\nu)}\left[\frac{1}{2} - \frac{1}{6}\sqrt{48\left(\frac{\sigma_o}{\sigma_t}\right)^2 - 3}\right]$$

$$= \frac{(2-\nu)}{6(1-\nu)}\left[3 - \sqrt{48\left(\frac{\sigma_o}{\sigma_t}\right)^2 - 3}\right] \qquad \text{AI.34}$$

for $\nu=0.3$

$$\frac{R_1}{R} = 0.4048\left[3 - \sqrt{48\left(\frac{\sigma_o}{\sigma_t}\right)^2 - 3}\right] \qquad \text{AI.35}$$

Since ratchetting occurs in the region $0<r<R_1$, in order to avoid ratchetting, it is necessary to have $R_1=0$. That is σ_t must not exceed $2\sigma_o$.

Hence for $\sigma_t/\sigma_o > 2$, the shakedown boundary become $\sigma_t/\sigma_o = 2.0$.

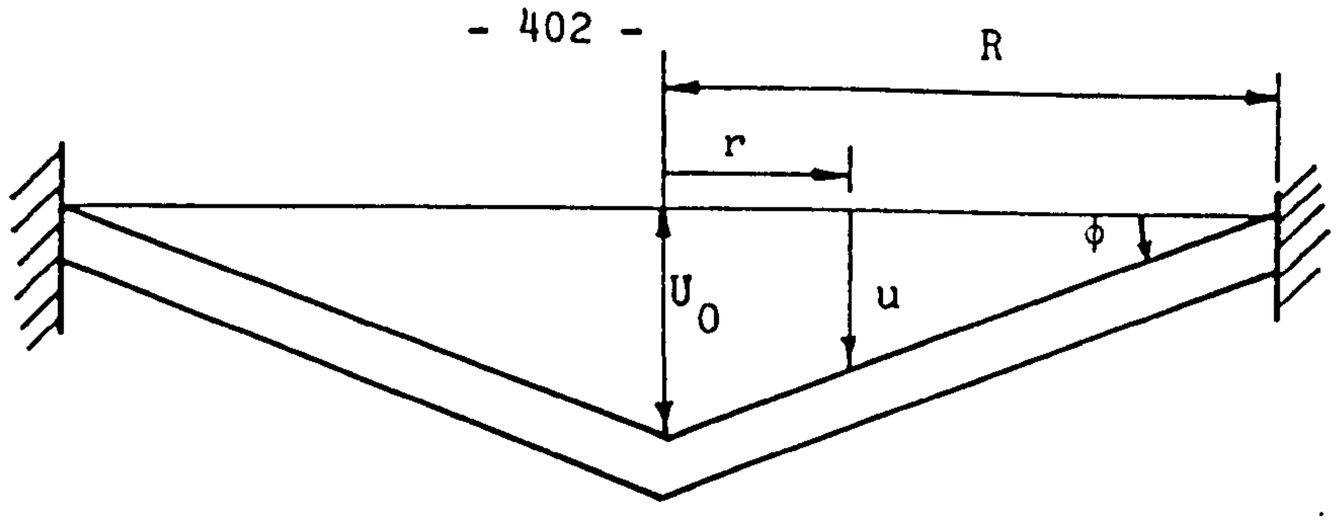

Fig.AI.1 Assumed collapse mechanism for $\sigma_t/\sigma_o < 2$

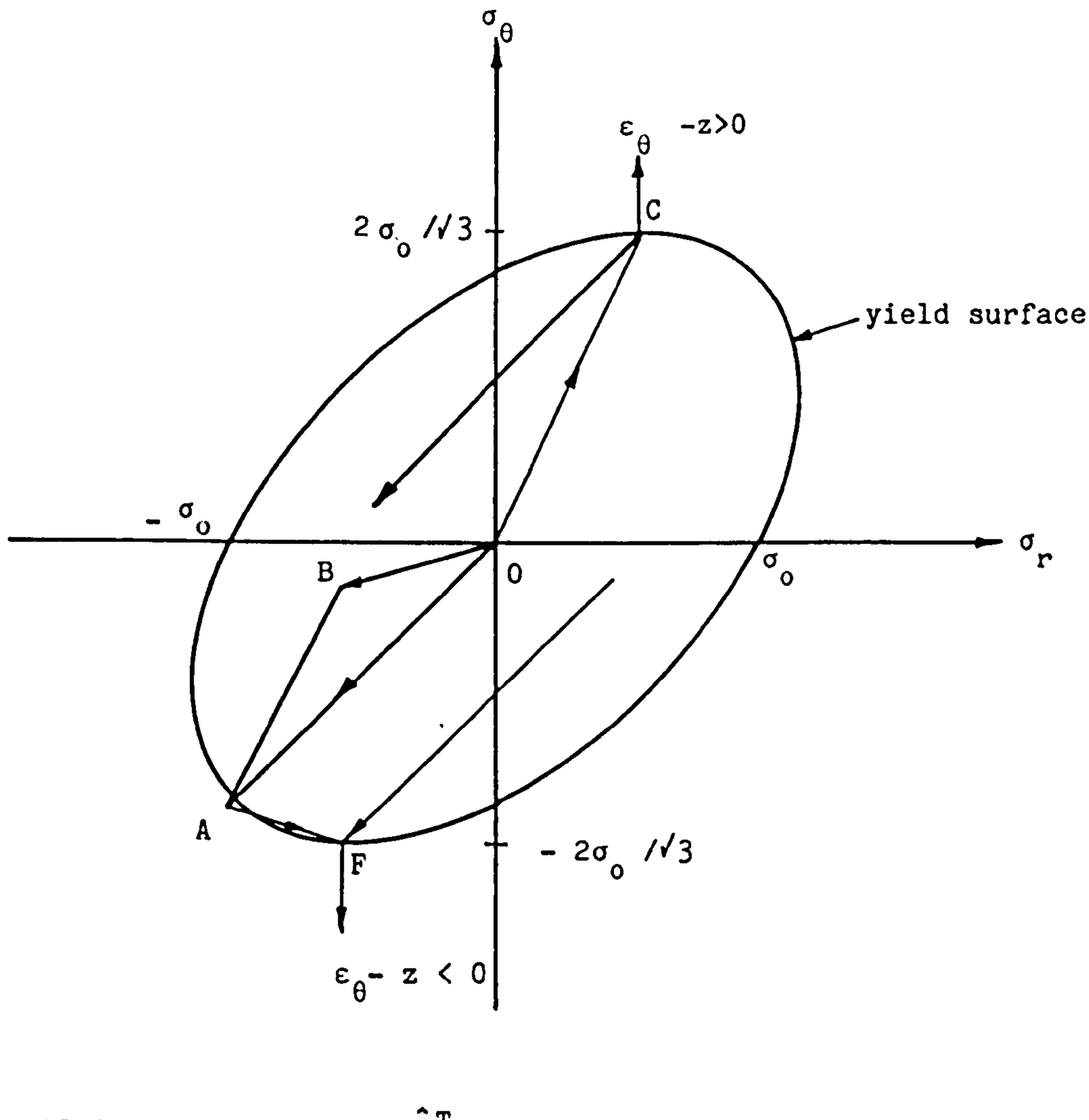

Fig.AI.2 Determination of $\hat{\sigma}^T_{ij}(\bar{x},t_o)$. Translation of stress history OA in the direction OC gives $\hat{\sigma}^T_{ij}(\bar{x},t_o)= 0$ whereas translation in the direction AF gives $\hat{\sigma}^T_{ij}(\bar{x},t_o) = \sigma_t$.

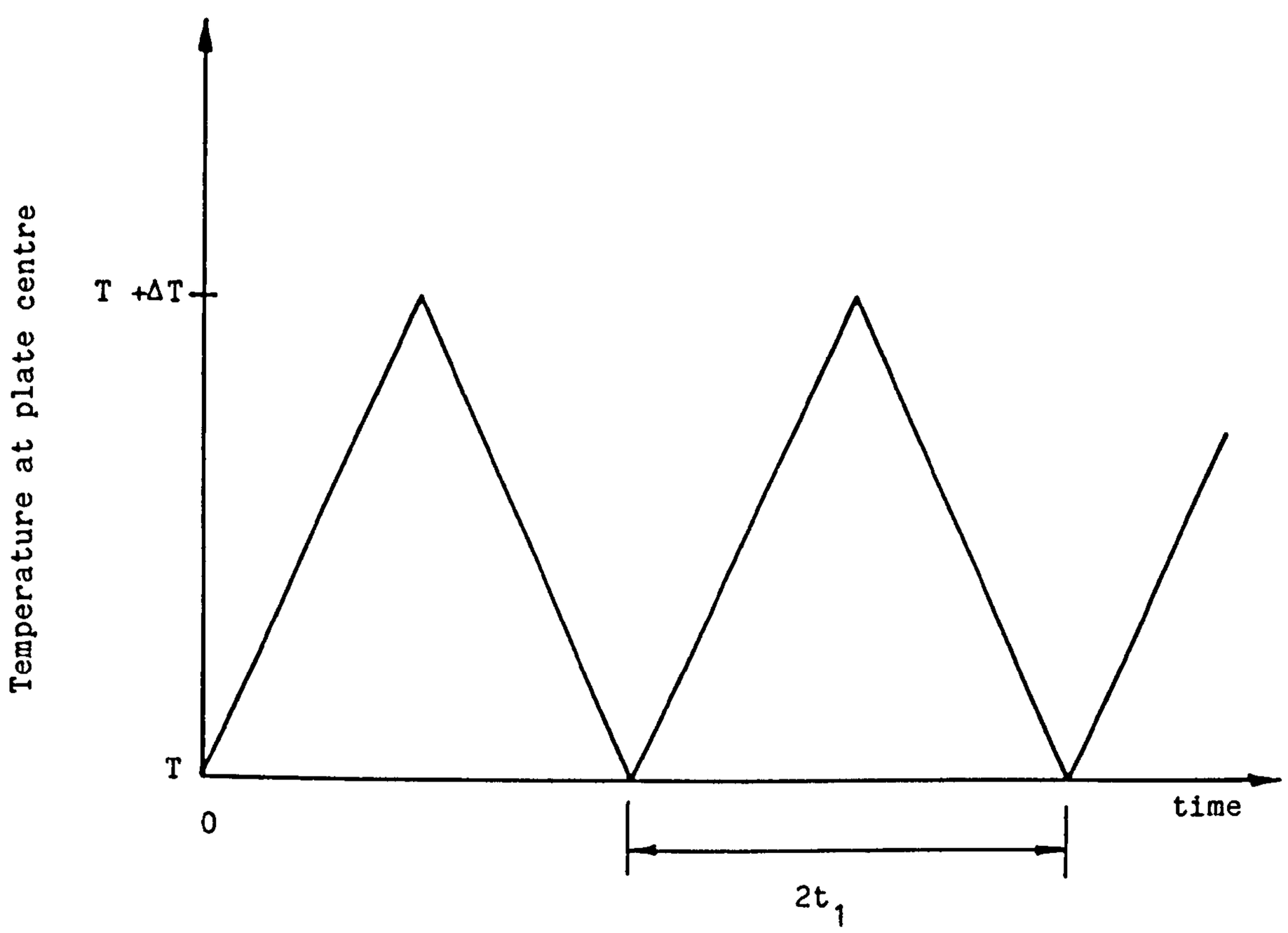

Fig.AI.3 Temperature-time history for the clamped circular plate

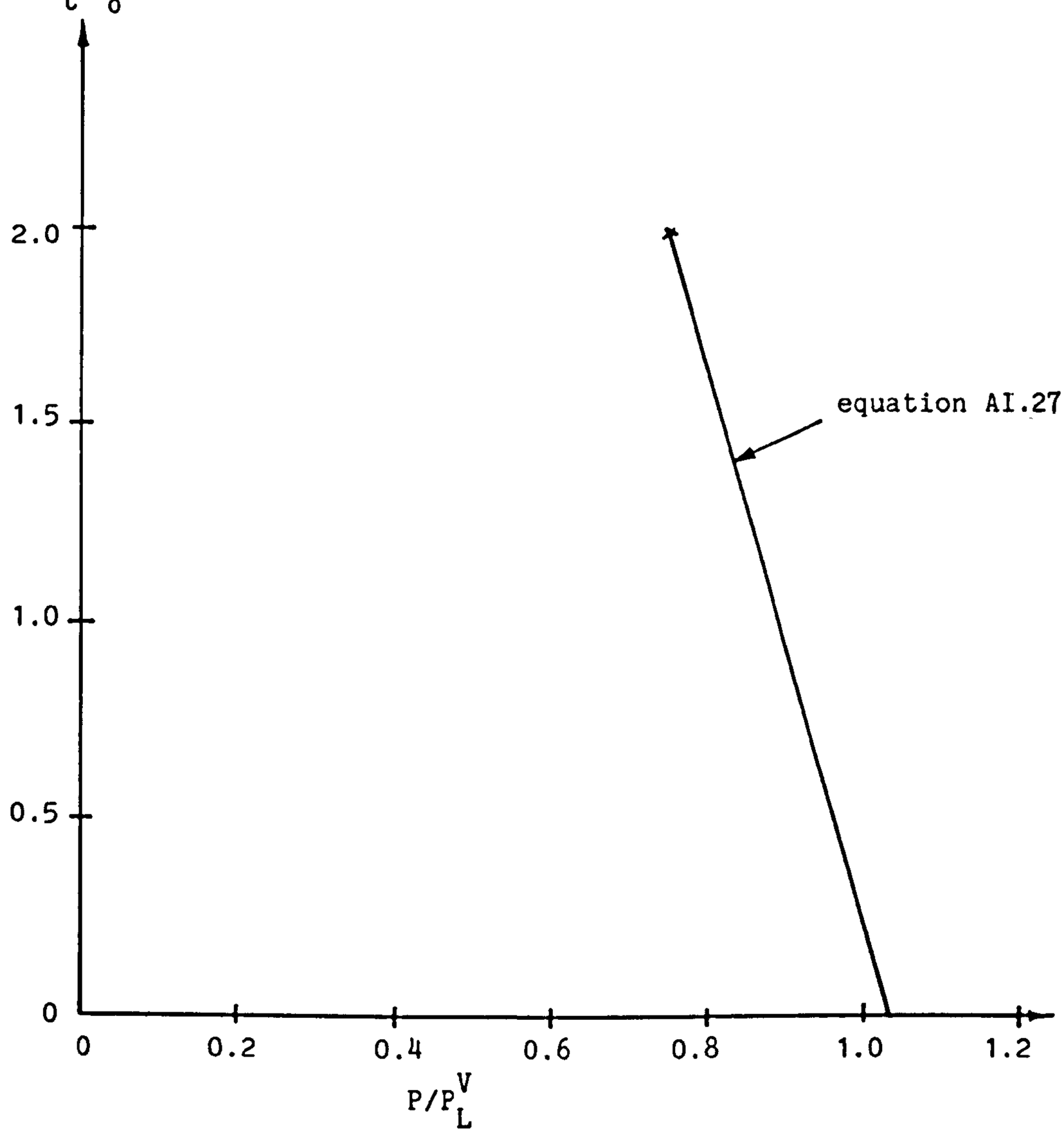

Fig.AI.4 Shakedown/ratchetting boundary for $\sigma_t < 2\sigma_o$

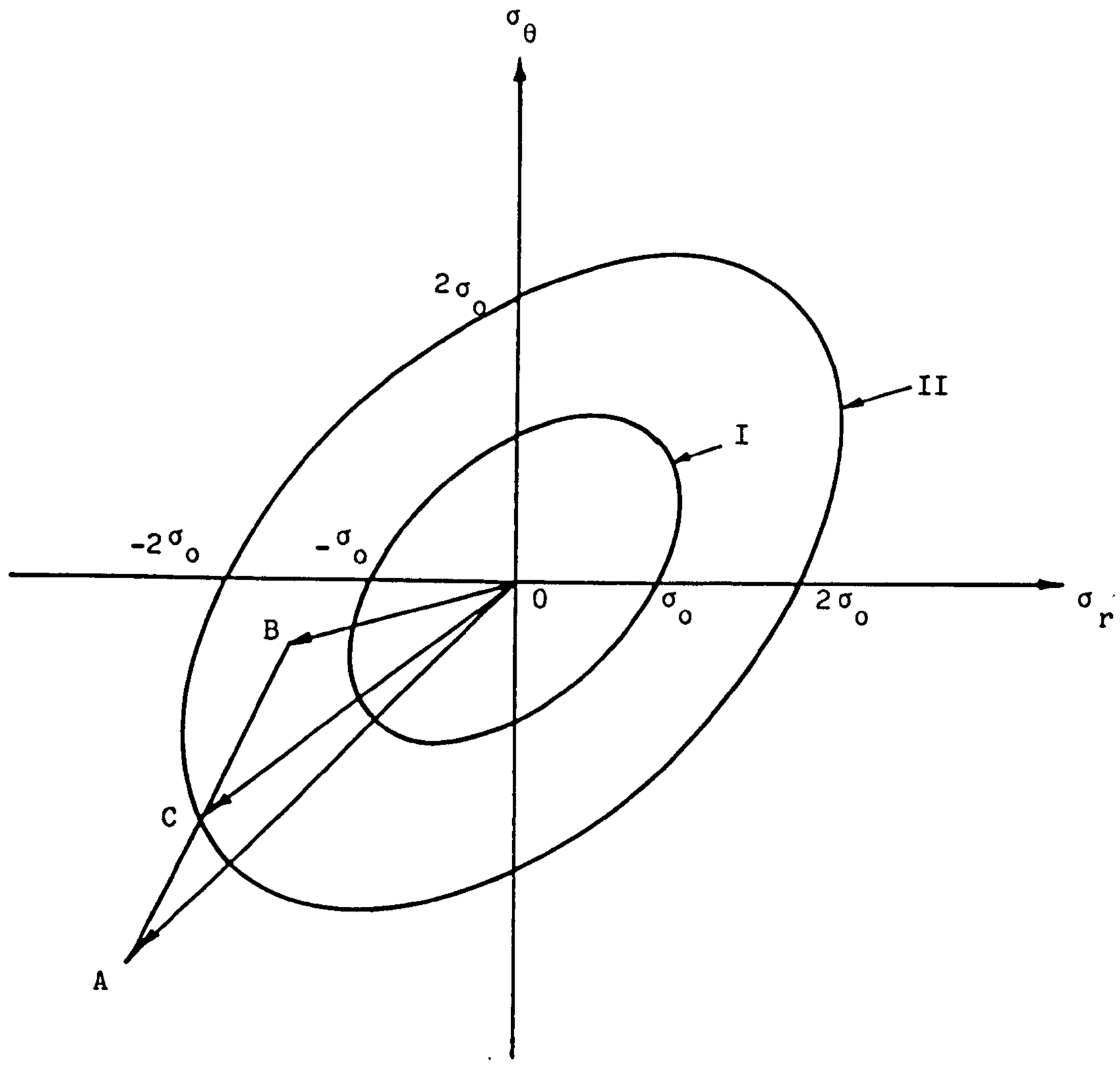

Fig.AI.5 Determination of volume which exhibit cyclic plasticity for $\sigma_t > 2\sigma_o$

APPENDIX II

VALIDATION OF THE FINITE ELEMENT MESH FOR THE CLAMPED CIRCULAR PLATE.

AII.1 Introduction.

In this appendix, the validation of the finite element mesh for a clamped circular plate subjected to a uniform transverse pressure is described. The results will be compared to theoretical values whenever possible.

AII.2 Finite Element Model.

The plate is 25mm thick and 1m diameter made of an elastic-perfectly-plastic material with Young's modulus 160 GNm^{-2}, yield stress 160 MNm^{-2} and a Poisson's ratio of 0.3. The plate was modelled using 40 x 8 noded isoparametric elements, 4 elements through the thickness and 10 elements in the radial direction as shown in Fig.AII.1. The mesh is similar to that used by Hyde (15) and Hardy (16). A theoretical solution for the stresses due to the applied transverse pressure is available (53). The elastic solution due to a linear radial temperature gradient is given elsewhere (54). The collapse pressure for the plate made of an elastic-perfectly-plastic material which obeys a Tresca yield criterion has been solved by Hopkins and Prager (34) whereas Hopkins and Wang (35) have determined the collapse pressure by assuming the von-Mises yield condition. The finite element results are compared with the theoretical values from the above sources.

AII.3 Edge Conditions.

Results for three different edge conditions were obtained in order to determine suitable conditions for the analysis. The edge conditions tested were:-

A) All the nodes at the clamped edge CF of Fig.AII.1 were constrained from any displacement in either the radial or transverse directions.

B) All nodes at the clamped edge are constrained from radial displacement and the node at F_1, is also constrained from transverse displacement.

C) As in B above except that transverse nodal forces which results in a uniform shear stress distribution were applied to 'balance' the applied pressure as shown in Fig.AII.2.

In all cases, the nodes at the plate centre, i.e. across AB of Fig.AII.1, were constrained in the radial direction to maintain symmetry.

AII.4 Results.

The finite element results for the plate with edge conditions A,B and C are presented here. Fig.AII.3 shows the variation of the elastic transverse deflection with the radius. The theoretical values from the simple plate theory (53) are also

shown. There is good agreement between the finite element results and the theoretical values.

Fig.AII.4 shows the variation of the elastic radial and hoop surface stresses with radius. All the results for the edge conditions A,B and C agree with the theoretical values. The variation of the shear stresses at the centre plane of the plate with radius are shown in Fig.AII.5. The comparison between the plate theory and finite element results for the plate edge conditions A,B and C shows that better agreement is obtained for the edge condition C.

The variation of the central deflection with transverse pressure are shown in Fig.AII.6. In the elastic range, where deflections are small compared to the plate thickness, the results obtained with edge conditions A,B and C all agree with the plate theory. For larger deflections, however, the results differ. From Fig.AII.6, the collapse pressure for the plate can be obtained since the deflections become very large at pressures close to the collapse pressure. The values, thus determined for the collapse pressure from Fig.AII.6 are given in Table AII.1. Also given in Table AII.1 are the values of the collapse pressures for an elastic-perfectly-plastic material obeying the Tresca criterion obtained by Hopkins and Prager (34), P_L^T, and the value for plate made of elastic-perfectly-plastic material obeying the von-Mises yield condition, P_L^V, from Hopkins and Wang (35). In the finite element analysis, a von-Mises yield criterion was used. The results for the collapse pressure for the plate with edge

conditions B and C are closer to that obtained in (35) than the collapse pressure for a plate with edge condition A. With edge conditions B and C, higher values of collapse pressure were obtained by comparison with that obtained by Hopkins and Wang (35). From the close agreement obtained with both the elastic-plastic results it was concluded that the mesh together with edge condition C were suitable for use in the cyclic thermal loading analyses.

Thermal Loading.

Fig.AII.7 shows the variation of elastic radial and hoop stresses with radius when a linear radial temperature gradient was imposed. The theoretical elastic solutions given by equations AI.6 and AI.7 are also given in AII.7. Good agreement between finite element and theoretical solutions was again obtained.

Edge conditions	Collapse pressure P_L / MNm^{-2}
A	1.46
B	1.30
C	1.31
P_L^T	1.13
P_L^V	1.25

Table AII.1 Values of collapse pressures for different edge conditions and theretical.

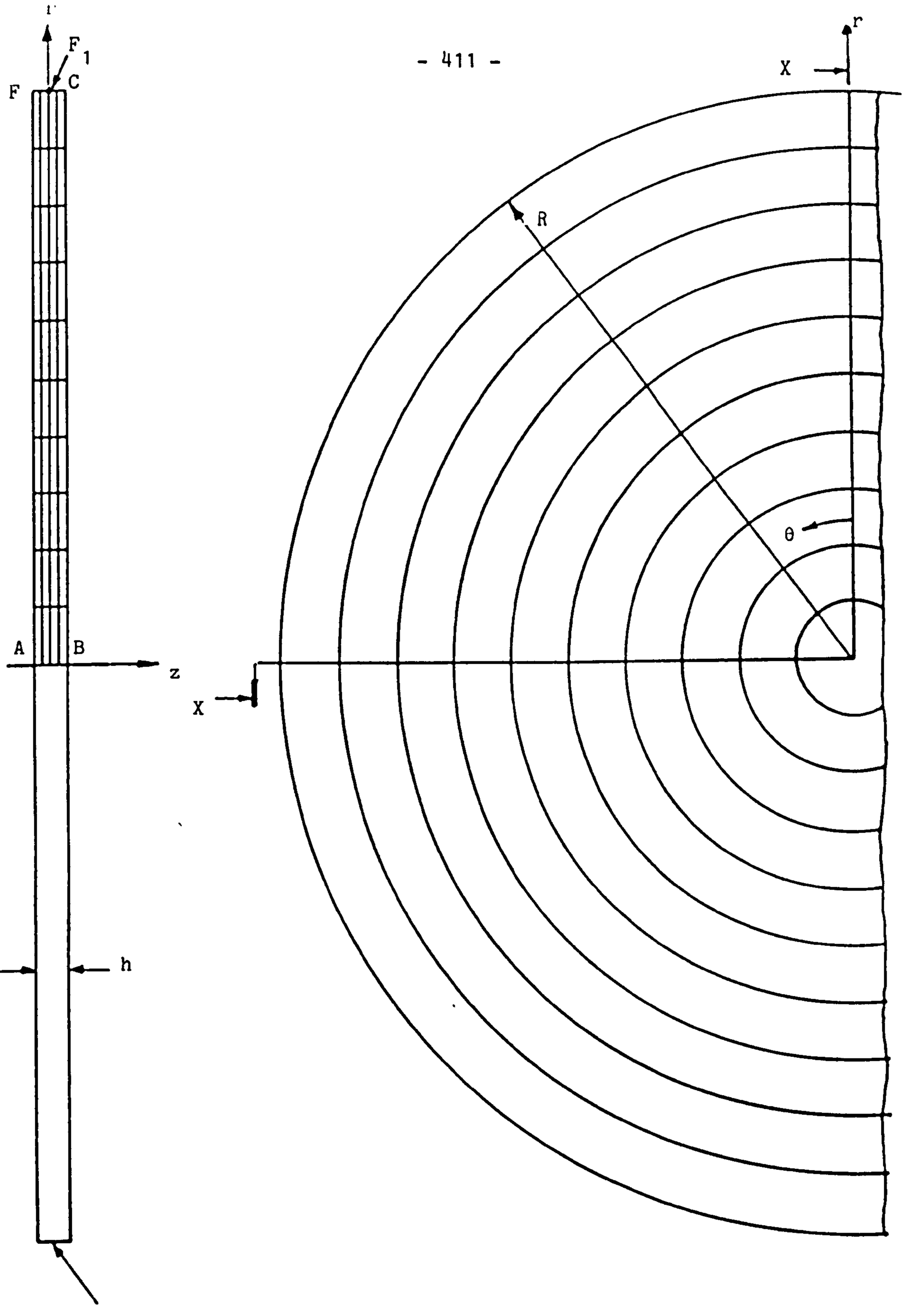

Fig.AII.1 Clamped circular plate and finite element mesh

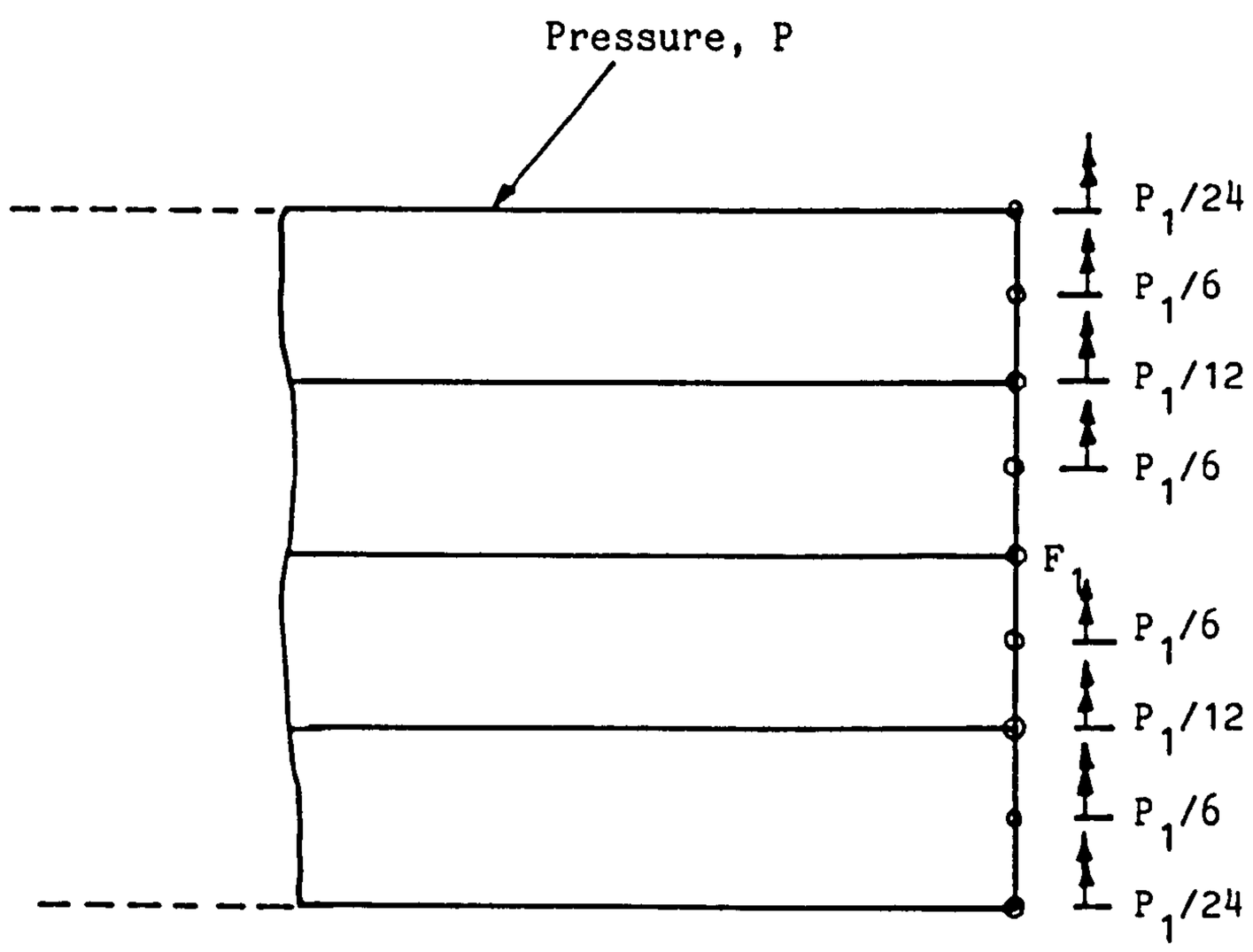

Fig.AII.2 Distribution of nodal forces at the clamped edge for condition C.

$P_1 = P/8$

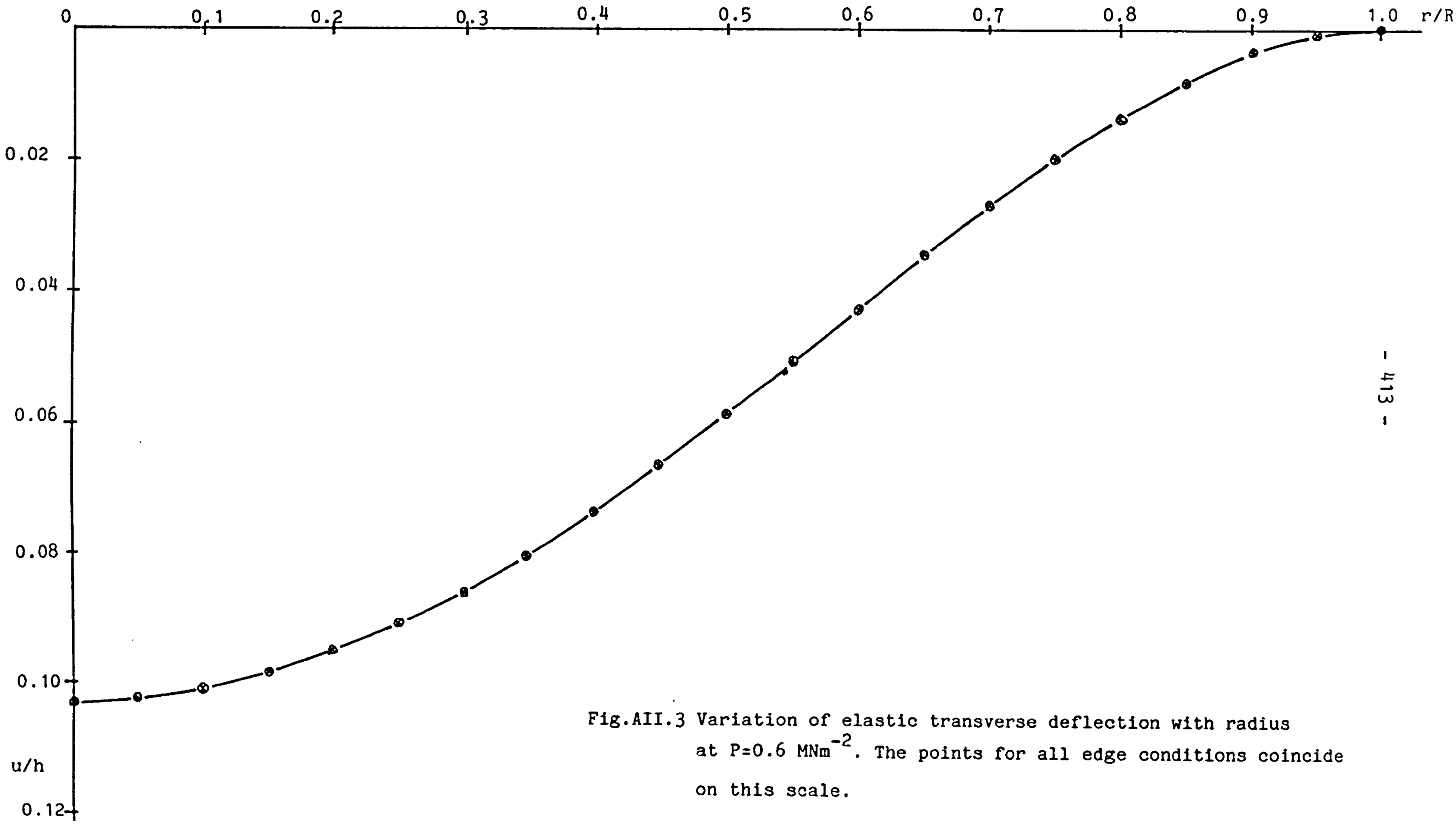

Fig.AII.3 Variation of elastic transverse deflection with radius at P=0.6 MNm^{-2}. The points for all edge conditions coincide on this scale.

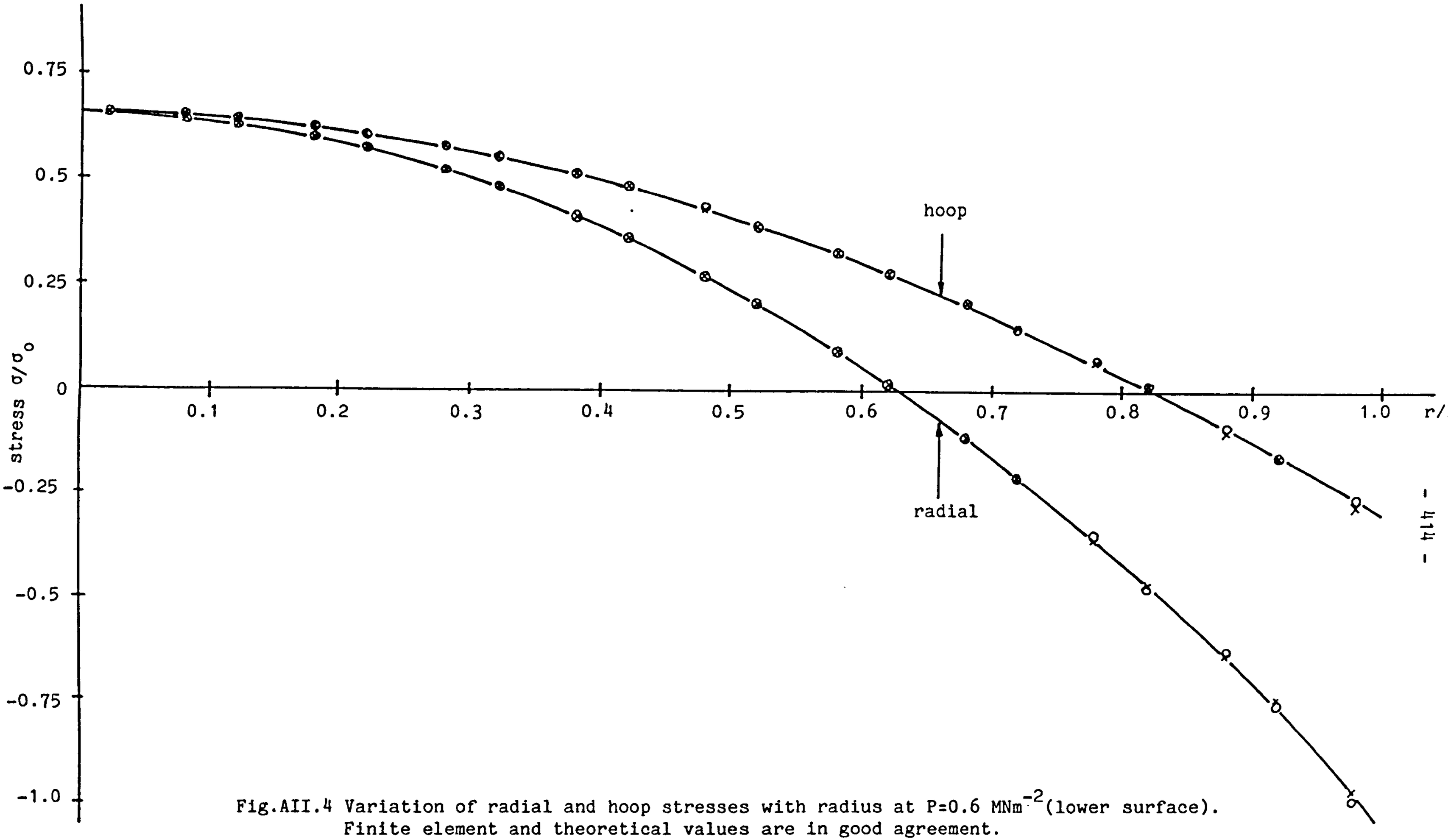

Fig.AII.4 Variation of radial and hoop stresses with radius at P=0.6 MNm^{-2}(lower surface). Finite element and theoretical values are in good agreement.

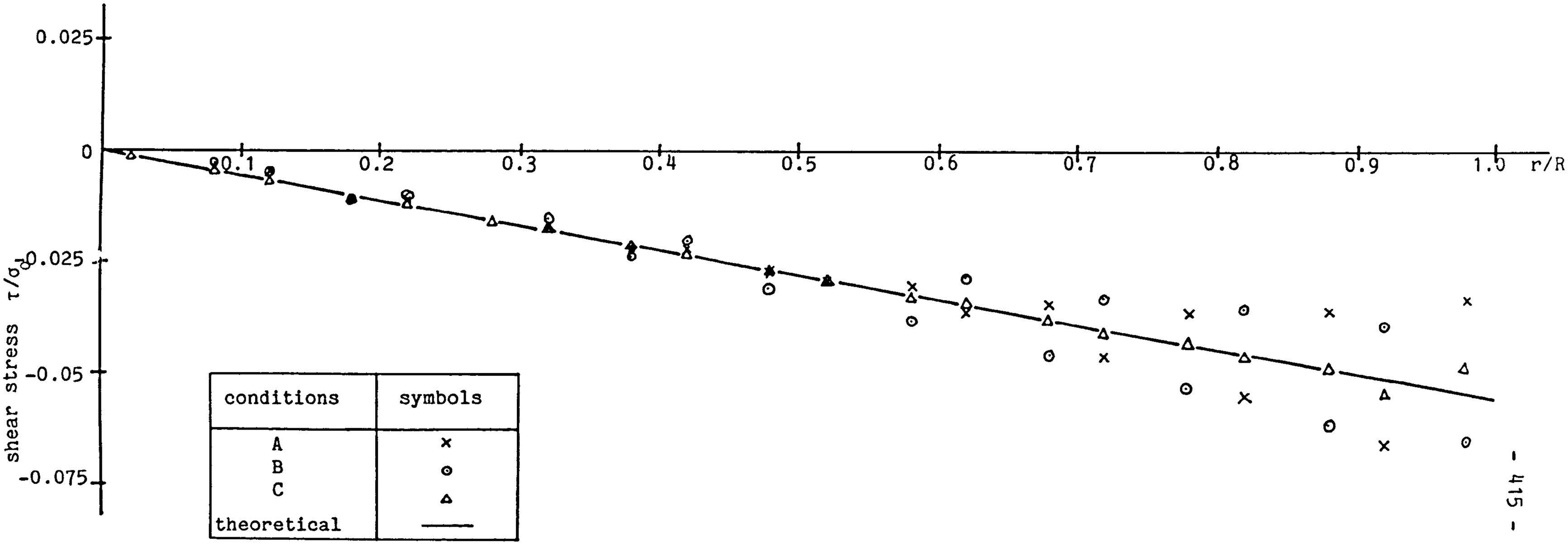

conditions	symbols
A	×
B	⊙
C	△
theoretical	——

Fig.AII.5 Variation of shear stress with radius at P=0.6 MNm^{-2}. (Shear stress at centre plane)

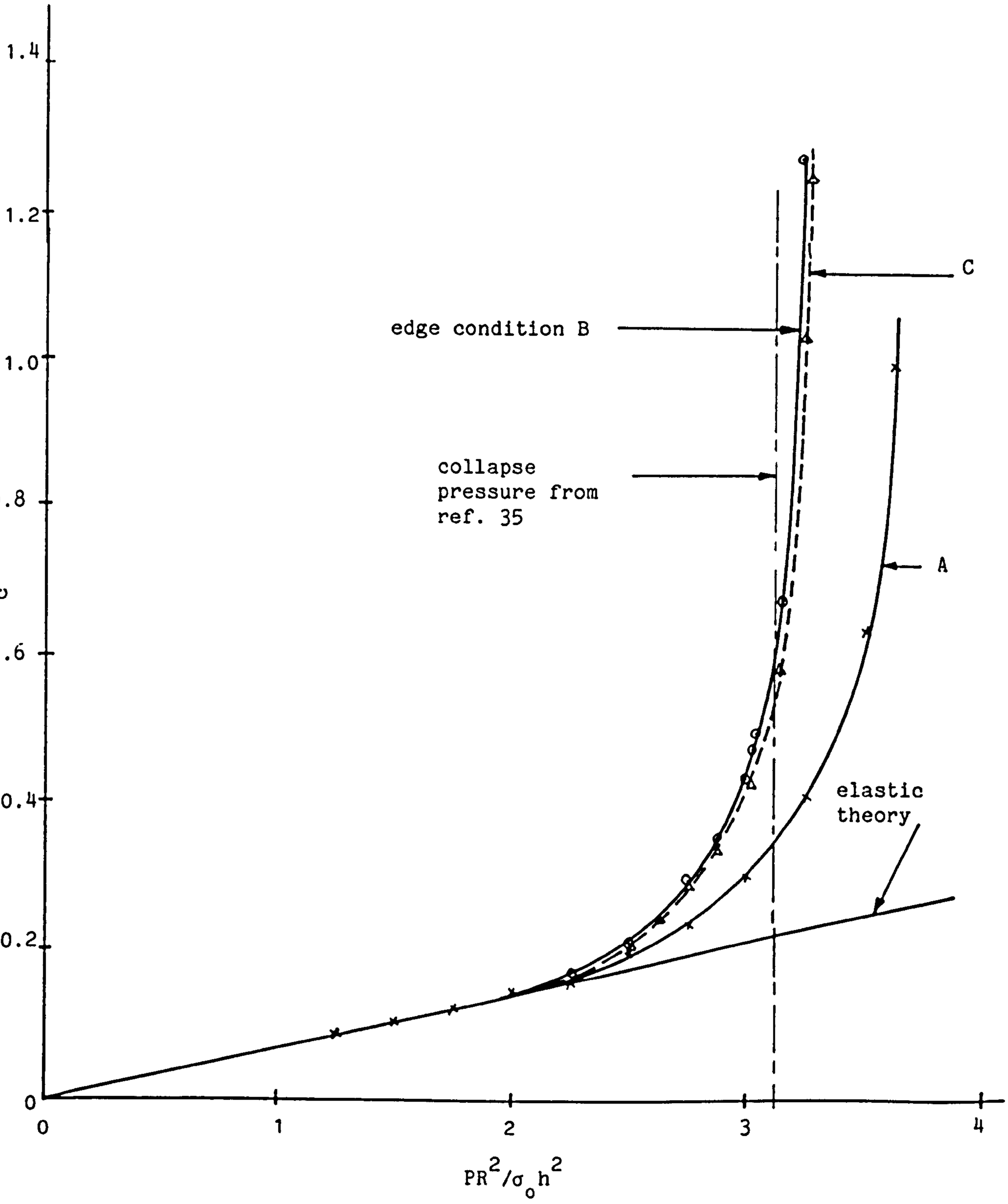

Fig.AII.6 Variation of central deflection with pressure for the plate with different edge conditions and comparison with the theoretical values.

Fig.AII.7 Thermal stress distribution at σ_t/σ_o = 0.81. Comparison between finite element (×,o) and theoretical (——)

APPENDIX III

AIII.1 MULTI-AXIAL FORMULATION OF THE GOODMAN AND GOODALL MODEL.

In the multi-axial formulation of the Goodman and Goodall model (18,19), the von-Mises yield criterion is used. The effective stress is derived from the second invariant of the stress deviator tensor where

$$\sigma_{eq} = \sqrt{1.5 S_{ij} S_{ij}} \qquad \text{AIII.1}$$

and the initial yield is given by:-

$$\sigma_{eq} > \sigma_o \qquad \text{AIII.2}$$

In plasticity, the associated flow rule is used to determine the individual plastic strain increments. It is assumed that previous plastic flow influences subsequent plasticity. The influence is stored in an internal tensor α_{ij}. In the kinematic hardening model used here, α_{ij} represents the position of the centre of the yield surface. Further yielding therefore occurs when

$$f = \left[1.5(S_{ij}-\alpha'_{ij})(S_{ij}-\alpha'_{ij})\right]^{1/2} \geqslant \sigma_o \qquad \text{AIII.3}$$

where $\alpha'_{ij} = \alpha_{ij} - \frac{1}{3}\alpha_{kk}\delta_{ij}$

In the π -plane, f is a circle with a fixed radius σ_o and centre α_{ij}. The associated flow rule can now be written as

and $$d\varepsilon^p_{ij} = \lambda \frac{\partial f}{\partial S_{ij}} \qquad \text{AIII.4}$$

$$d\varepsilon_p = \sqrt{\frac{2}{3} d\varepsilon^p_{ij} d\varepsilon^p_{ij}} \qquad \text{AIII.5}$$

The surface equivalent to the saturation stress in the uniaxial case, is the surface f_s defined by:

$$f_s = \sqrt{1.5 S_{ij} S_{ij}} - \sigma_s = 0 \qquad \text{AIII.6}$$

In the π-plane f_s is a circle with radius σ_s and centred at the origin. Similarly, σ_m is equivalent to a surface f_m defined as

$$f_m = \sqrt{1.5 S_{ij} S_{ij}} - \sigma_m = 0 \qquad \text{AIII.7}$$

For convenience, the maximum equivalent stress reached during the previous loading history is denoted by σ^m_{eq}.

It is convenient at this stage to define some terms commonly used in describing cyclic behaviour. When the current equivalent stress σ_{eq} is either greater than σ^m_{eq} (or greater than f^{max}_m the last value of f_m), then loading occurs along the monotonic 'stress-strain curve' otherwise the loading is not monotonic. For the movement of the surfaces f, f_m and f_s, a rule similar to that adopted by Mroz (40) is used here. In general, the surface can either touch or slide against one another but they are not allowed to intersect. It is important to note here that f_s is normally well above the operational stress level. It is assumed that neither surface f nor f_m will touch surface f_s. If f touches f_m and monotonic loading occurs, then f_m expands isotropically. But if f touches f_m and the loading is not monotonic, f will slide so as to prevent f from

intersecting f_m. Initially f and f_m coincide. If sliding does not occur, the instantaneous translation of f is in the same direction as the plastic straining.

Now consider the application of a monotonically increasing tensile load from O to B. Referring to Fig.AIII.1, elastic deformation takes place from O to A. Further loading from A to B produces some plastic deformation. Surface f translates kinematically such that the centre of f initially at O moves to O_1. Since f can only touch f_m, i.e. f and f_m cannot intersect, then in the process of moving from O to O_1, f_m expands isotropcally from f_{m0} to f_{m1}. Unloading is always elastic until yield occurs as defined in equation AIII.3 , after which plastic loading occurs and f will translate within f_{m1} so long as f and f_{m1} do not touch one another. OO_1, is denoted by the tensor α_{ij} . The surface f_m is only updated (in this case expands) whenever the loading is monotonic.

Suppose from the point B, the material is unloaded elastically to C and loaded again in the direction CDFG as shown in Fig.AIII.2. Along the loading path BCD, elastic changes occur. Along DF, plastic deformation takes place. The loading, however, is not monotonic. Therefore surface f_m remains at f_{m1}. Since f (now denoted by f_1) is not allowed to intersect but always touches surface f_{m1}, surface f must slide within f_{m1}. The increment of plastic strain is normal to the yield surface. In this case in the direction O_1D as shown. The instantaneous translation of f_1 occurs along O_1O_i which is parallel to the tangent of f_{m1} at B. As the stress point moves from D to F, the

centre of f_1 moves along the arc O_1O_2. At O_2, the surface f is denoted by f_2. Along the path FG, monotonic loading occurs. The increment of plastic strain is, again, normal to yield surface (in this case f_2) at F as shown. The instantaneous translation of f is in the direction of plastic strain. As the stress point moves along FG, f_2 moves along O_2O_3. Surface f_m is updated to f_{m2}.

AIII.2 Development of Equations.

A complete constitutive equations for the model described previously is developed in this section. In the elasto-plastic analysis, the load is applied in increments. The plastic strain for a monotonic loading is given, in integral form, as:-

$$\varepsilon^p = (rU^*)^q V^* t \qquad \text{AIII.8}$$

where U* is the equivalent expression of U in the uniaxial case. Similarly V* is the equivalent expression of V (see Chapter 2).

For monotonic loading i.e. $\sigma_{eq} \geqslant f_m$,

$$U^* = \left| \frac{\sigma_{eq} - \sigma_o}{\sigma_s - \sigma_o} \right| \qquad \text{AIII.9}$$

In general,

$$V^* = \left| \frac{\sigma_s - \sigma_o}{\sigma_s - \sigma_{eq}} \right| \qquad \text{AIII.10}$$

The equivalent expression for plastic modulus is:-

$$E^p = \frac{U^*(\sigma_s - \sigma_o)}{(rU^*)^q \, V^{*t}(q+tU^*V^*)} \qquad \text{AIII.11}$$

$$= g(U^*, V^*) \qquad \text{AIII.12}$$

For non-monotonic loading, a rule for updating U* is required. U* is updated to zero for radially reversed yielding. U* is unaltered if forward radial yielding, from an elastic unloading, occurs. U* has an intermediate value for a non-radial yield path. Radial here refers to the surface f . The rule is:-

$$U^*_{new} = \frac{1}{2}(1+\omega)U^*_{old} \qquad \text{AIII.13}$$

where

$$\omega = \frac{\frac{3}{2}\beta_{ij}\beta_{ij}}{\beta_{eqo}\beta_{eq}} \quad , \qquad \text{AIII.14}$$

and

$$\beta_{ij} = S_{ij} - \alpha_{ij} \quad , \qquad \text{AIII.15}$$

$$\beta_{eqo} = \sqrt{\frac{3}{2}\beta_{ijo}\beta_{ijo}} \quad , \qquad \text{AIII.16}$$

$$\beta_{eq} = \sqrt{\frac{3}{2}\beta_{ij}\beta_{ij}} \quad . \qquad \text{AIII.17}$$

In this model, $\beta_{eqo} = \beta_{eq} = \sigma_o$. AIII.18

The quantities α_{ij}, β_{ij}, β_{ijo} are illustrated in Fig.AIII.3, for a loading path BCD.

For any kinematic hardening model, a translation rule is required. For this case two rules are required. One for the case when surface f slides over surface f_m and the other for the no sliding condition.

When sliding does not occur, the surface translates in the direction of the outward normal to the yield surface at the stress point. The rule is given by:-

$$d\alpha_{ij} = \frac{2}{3} g(U^*,V^*)d\epsilon^p_{ij} \qquad \text{AIII.19}$$

together with the associated flow rule AIII.4

The evolution of U* is half as rapid as that for monotonic loading. That is

$$dU^* = \frac{1}{2} \frac{|d\alpha_{eq}|}{(\sigma_s - \sigma_o)} \qquad \text{AIII.20}$$

where $d\alpha_{eq}$ is the change in α_{eq} . V* is given by equation AIII.10 throughout.

When sliding occurs, the surface f translates, instantaneously, in a direction tangential to the f_m surface, at the point where f and f_m touch each other, as described in section AIII.1. The condition for sliding to occur is when

$$\alpha_{eq} + \sigma_o > f_m \quad \text{and} \quad \sigma_{eq} < \sigma^m_{eq} \qquad \text{AIII.21}$$

When the condition AIII.21 is satisfied, the translation rule becomes

$$d\alpha_{ij} = \phi\eta_{o1} \qquad \text{AIII.22}$$

where ϕ is a scalar and η_{o1} is a vector in the direction O_1O_i of Fig.AIII.2.

Now, the position vector of O_1 is defined by α_{ij} from the origin O. The surface f_α is defined by:-

$$f_\alpha = \sqrt{\frac{3}{2}\alpha'_{ij}\,\alpha'_{ij}} = \alpha_{eq} \qquad \text{AIII.23}$$

$$= \left[0.5\ (\alpha_{xx}-\alpha_{yy})^2+(\alpha_{yy}-\alpha_{zz})^2+(\alpha_{zz}-\alpha_{xx})^2+6\alpha_{xy}^2\ \right]^{1/2} \qquad \text{AIII.24}$$

; this is the surface containing O_1. In the π-plane, f_α is a circle of radius α_{eq} and origin at O. The vector normal to f_α at O_1 is given by:-

$$\eta_{\alpha_{ij}} = \frac{\partial f_\alpha}{\partial \alpha'_{ij}} \qquad \text{AIII.25}$$

This vector is denoted by O_1H in Fig.AIII.2.

The vector in the direction normal to the surface at D, $\eta_{\sigma_{ij}}$ is given by:-

$$\eta_{\sigma_{ij}} = \frac{\partial f}{\partial S_{ij}} \qquad \text{AIII.26}$$

Both vectors $\eta_{\alpha_{ij}}$ and $\eta_{\sigma_{ij}}$ are required to uniquely define the vector in the direction O_1O_i, η_{o1}. The magnitudes of $\eta_{\alpha_{ij}}$, $\eta_{\sigma_{ij}}$ and η_{o1} are not relevant.

The vector η_{o1} is evaluated via an intermediate vector η_2 which is perpendicular to both $\eta_{\alpha_{ij}}$ and $\eta_{\sigma_{ij}}$.

Hence $$\eta_2 = \eta_{\sigma_{ij}} \times \eta_{\alpha_{ij}} \qquad \text{AIII.27}$$

where X indicates a vector product.

The required vector, η_{o1} is thus given by:-

$$\eta_{01} = \eta_{\alpha_{ij}} \; X \; \eta_2$$

$$= \frac{\partial f_{\alpha}}{\partial \alpha_{ij}'} \; X \; \frac{\partial f}{\partial S_{ij}} \; X \; \frac{\partial f_{\alpha}}{\partial \alpha_{ij}'} \qquad \text{AIII.28}$$

The condition that the stress point lies on the yield surface is given by:-

$$(d\alpha_{ij} - d\sigma_{ij}) \frac{\partial f}{\partial S_{ij}} = 0 \qquad \text{AIII.29}$$

where $d\sigma_{ij}$ is the increment of stress.

Substituting equations AIII.22 into AIII.29 gives,

$$(\phi \eta_{o1} - d\sigma_{ij}) \frac{\partial f}{\partial S_{ij}} = 0 \qquad \text{AIII.30}$$

which gives

$$\phi = d\sigma_{ij} \frac{\partial f}{\partial S_{ij}} \; / \; \eta_{o1} \frac{\partial f}{\partial S_{kl}} \qquad \text{AIII.31}$$

Hence

$$d\alpha_{ij} = \frac{d\sigma_{ij} \frac{\partial f}{\partial S_{ij}}}{\eta_{o1} \frac{\partial f}{\partial S_{kl}}} \; \eta_{o1} \qquad \text{AIII.32}$$

Now, η_{o1} can be evaluated as

$$\eta_{o1} = \left(\frac{\partial f_\alpha}{\partial \alpha'_{ij}} \cdot \frac{\partial f_\alpha}{\partial \alpha'_{ij}}\right)\frac{\partial f}{\partial S_{ij}} - \left(\frac{\partial f_\alpha}{\partial \alpha'_{ij}} \cdot \frac{\partial f}{\partial S_{ij}}\right)\frac{\partial f_\alpha}{\partial \alpha'_{ij}}$$

$$= \frac{3}{2}\frac{\partial f}{\partial S_{ij}} - \left(\frac{\partial f_\alpha}{\partial \alpha'_{ij}} \cdot \frac{\partial f}{\partial S_{ij}}\right)\frac{\partial f_\alpha}{\partial \alpha'_{ij}} \qquad \text{AIII.33}$$

Since $\frac{2}{3}\frac{\partial f_\alpha}{\partial \alpha'_{ij}} \cdot \frac{\partial f_\alpha}{\partial \alpha'_{ij}} = 1$.

The value of ϕ can be evaluated as follows.

From

$$\phi = \frac{d\sigma_{ij}\frac{\partial f}{\partial S_{ij}}}{\eta_{o1}\frac{\partial f}{\partial S_{kl}}}$$

we have

$$\eta_{o1}\frac{\partial f}{\partial S_{ij}} = \left(\frac{3}{2}\frac{\partial f}{\partial S_{ij}} - \left(\frac{\partial f_\alpha}{\partial \alpha'_{ij}} \cdot \frac{\partial f}{\partial S_{ij}}\right)\frac{\partial f_\alpha}{\partial \alpha'_{ij}}\right)\frac{\partial f}{\partial S_{ij}}$$

$$= \frac{9}{4} - \left(\frac{\partial f_\alpha}{\partial \alpha'_{ij}} \cdot \frac{\partial f}{\partial S_{ij}}\right)^2 \qquad \text{AIII.34}$$

since $\frac{2}{3}\frac{\partial f}{\partial S_{ij}} \cdot \frac{\partial f}{\partial S_{ij}} = 1$.

Substituting the results of AIII.34 into equation AIII.31 gives

$$\phi = \frac{d\sigma_{ij}\frac{\partial f}{\partial S_{ij}}}{\frac{9}{4} - \left(\frac{\partial f_\alpha}{\partial \alpha'_{ij}} \cdot \frac{\partial f_\alpha}{\partial S_{ij}}\right)^2}$$

and hence

$$d\alpha_{ij} = \frac{d\sigma_{ij}\frac{\partial f}{\partial S_{ij}}\left(\frac{3\partial f}{2\partial S_{ij}} - \left(\frac{\partial f_\alpha}{\partial \alpha'_{ij}} \cdot \frac{\partial f}{\partial S_{ij}}\right)\frac{\partial f_\alpha}{\partial \alpha'_{ij}}\right)}{\left(\frac{9}{4} - \left(\frac{\partial f_\alpha}{\partial \alpha'_{ij}} \cdot \frac{\partial f}{\partial S_{ij}}\right)^2\right)} \qquad \text{AIII.35}$$

The vector $d\alpha_{ij}$ can be expressed in terms of plastic strain increment $d\varepsilon^p_{ij}$ so that $d\alpha_{ij}$ can be evaluated within the iterations loop of the finite element program. This is achieved from the Prandtl-Reuss flow rule and the 'stress'-'plastic strain' relationship. From the flow rule,

$$d\varepsilon^p_{ij} = d\varepsilon_p \frac{\partial f}{\partial S_{ij}} \qquad \text{AIII.36}$$

and from the stress strain curve the increment of plastic strain is related to the increment of stress by

$$d\sigma_{eq} = g(U^*, V^*)d\varepsilon_p \quad . \qquad \text{AIII.37}$$

Substituting relationship AIII.36 and AIII.37 into equation AIII.35 gives

$$d\alpha_{ij} =$$

$$\frac{\frac{2}{3}g(U^*,V^*)\left(\frac{d\sigma_{ij}}{d\sigma_{eq}}.\frac{d\varepsilon^p_{ij}}{d\varepsilon_p}\right)}{\left[1-\frac{4}{9}\left(\frac{\partial f_\alpha}{\partial \alpha'_{ij}}.\frac{\partial f}{\partial S_{ij}}\right)^2\right]}\left[d\varepsilon^p_{ij}-\frac{2}{3}\left(\frac{\partial f_\alpha}{\partial \alpha'_{ij}}.d\varepsilon^p_{ij}\right)\frac{\partial f_\alpha}{\partial \alpha'_{ij}}\right]. \quad \text{AIII.38}$$

Equation AIII.38 defines the translation rule.

The equations are now expressed in expanded form:-

The total equivalent stress is given by,

$$\sigma_{eq} = \sqrt{\frac{3}{2}S_{ij}S_{ij}}$$

$$=\left[\frac{1}{2}\left[(\sigma_{xx}-\sigma_{yy})^2+(\sigma_{yy}-\sigma_{zz})^2+(\sigma_{zz}-\sigma_{xx})^2+6\tau^2_{xy}\right]\right]^{1/2} \quad \text{AIII.39}$$

and the yield surface is expressed as:-

$$f = \left[\frac{3}{2}(S_{ij}-\alpha'_{ij})(S_{ij}-\alpha'_{ij})\right]^{1/2}$$

$$=\Big[1.5\Big(\Big(\frac{2\sigma_{xx}-\sigma_{yy}-\sigma_{zz}}{3}-\alpha_{xx}\Big)^2+\Big(\frac{2\sigma_{yy}-\sigma_{zz}-\sigma_{xx}}{3}-\alpha_{yy}\Big)^2+$$

$$\Big(\frac{2\sigma_{zz}-\sigma_{xx}-\sigma_{yy}}{3}-\alpha_{zz}\Big)^2+2(\tau_{xy}-\alpha_{xy}/2)^2\Big)\Big]^{1/2} \quad \text{AIII.40}$$

The components of plastic strain increment are given by:-

$$d\varepsilon^p_{xx} = d\varepsilon_p \frac{(2(\sigma_{xx}-\alpha_{xx}) - (\sigma_{yy}-\alpha_{yy}) - (\sigma_{zz}-\alpha_{zz}))}{2f} \quad \text{(i)}$$

$$d\varepsilon^p_{yy} = d\varepsilon_p \frac{(2(\sigma_{yy}-\alpha_{yy}) - (\sigma_{zz}-\alpha_{zz}) - (\sigma_{xx}-\alpha_{xx}))}{2f} \quad \text{(ii)}$$

$$d\varepsilon^p_{xy} = 3d\varepsilon_p \frac{(\tau_{xy}-\alpha_{xy}/2)}{f} \quad \text{(iii)}$$

$$d\varepsilon^p_{zz} = d\varepsilon_p \frac{(2(\sigma_{zz}-\alpha_{zz}) - (\sigma_{xx}-\alpha_{xx}) - (\sigma_{yy}-\alpha_{yy}))}{2f} \quad \text{(iv)}$$

} AIII.41

Two expressions for the translation rule are required. One for the no-sliding condition and another for the sliding condition.

For no-sliding condition:-

$$d\alpha_{xx} = \frac{2}{3}g(U^*,V^*)d\varepsilon^p_{xx} \quad \text{(i)}$$

$$d\alpha_{yy} = \frac{2}{3}g(U^*,V^*)d\varepsilon^p_{yy} \quad \text{(ii)}$$

$$d\alpha_{xy} = \frac{2}{3}g(U^*,V^*)d\varepsilon^p_{xy} \quad \text{(iii)}$$

$$d\alpha_{zz} = \frac{2}{3}g(U^*,V^*)d\varepsilon^p_{zz} \quad \text{(iv)}$$

} AIII.42

where $g(U^*,V^*)$ is defined by equation AIII.12.

when sliding occurs,

$$d\alpha_{xx} = \Omega(d\varepsilon^{p}_{xx} - \mu d\alpha'_{xx}) \qquad \text{(i)}$$

$$d\alpha_{yy} = \Omega(d\varepsilon^{p}_{yy} - \mu d\alpha'_{yy}) \qquad \text{(ii)}$$

$$d\alpha_{zz} = \Omega(d\varepsilon^{p}_{zz} - \mu d\alpha'_{zz}) \qquad \text{(iii)}$$

$$d\alpha_{xy} = \Omega(d\varepsilon^{p}_{xy} - \mu d\alpha'_{xy}/2) \qquad \text{(iv)}$$

AIII.43

where:-

$$d\alpha'_{xx} = \frac{2\alpha_{xx} - \alpha_{yy} - \alpha_{zz}}{2f_{\alpha}} \qquad \text{(i)}$$

$$d\alpha'_{yy} = \frac{2\alpha_{yy} - \alpha_{zz} - \alpha_{xx}}{2f_{\alpha}} \qquad \text{(ii)}$$

$$d\alpha'_{xy} = \frac{3(\alpha_{xy}/2)}{2f_{\alpha}} \qquad \text{(iii)}$$

$$d\alpha'_{zz} = \frac{2\alpha_{zz} - \alpha_{xx} - \alpha_{yy}}{2f_{\alpha}} \quad , \qquad \text{(iv)}$$

AIII.44

$$f_{\alpha} = \left[((\alpha_{xx}-\alpha_{yy})^2+(\alpha_{yy}-\alpha_{zz})^2+(\alpha_{zz}-\alpha_{xx})^2+6(\alpha_{xy}/2)^2)/2\right]^{1/2} \quad , \qquad \text{AIII.45}$$

$$\mu = \left[d\alpha'_{xx}d\varepsilon^{p}_{xx}+d\alpha'_{yy}d\varepsilon^{p}_{yy}+d\alpha'_{zz}d\varepsilon^{p}_{zz}+2d\alpha'_{xy}d\varepsilon^{p}_{xy}\right]\frac{2}{3} \quad , \qquad \text{AIII.46}$$

$$\Omega = \frac{\frac{2}{3}g(U^{*},V^{*})((\sigma_{xx}-\sigma^{o}_{xx})d\varepsilon^{p}_{xx}+(\sigma_{yy}-\sigma^{o}_{yy})d\varepsilon^{p}_{yy}+(\sigma_{zz}-\sigma^{o}_{zz})d\varepsilon^{p}_{zz}+2(\tau_{xy}-\tau^{o}_{xy})d\varepsilon^{p}_{xy}}{d\varepsilon_{p}(\sigma_{eq}-\sigma^{o}_{eq})(1-\frac{4}{9}\frac{\mu^{2}}{d\varepsilon^{2}_{p}})} \; .$$

AIII.47

In the above expression, $d\varepsilon_{p}$ is the equivalent plastic strain

increment given by:-

$$d\varepsilon_p = \sqrt{\frac{2}{3} d\varepsilon^p_{ij} d\varepsilon^p_{ij}} \qquad \text{AIII.48}$$

the superscript o refers to the value at the last converged solution (see section AIII.4.1). The above formulation has been incorporated into the finite element program.

To include the effect of cyclic hardening, the parameter q increases from q_o . It is a gradual process and a stable cyclic state is reached after a very large number of cycles. It is assumed that q varies as a function of plastic strain path. An empirical relation suggested by Goodman and Goodall (18) is employed here . q varies according to the following relation:-

$$q = q_o \lg(10 + H \lg(1+100p^*)) \qquad \text{AIII.49}$$

H is a constant. p^* is the total cyclic plastic strain path, given by :-

$$p^* = \Sigma \left|\Delta\varepsilon_p\right| - \varepsilon^*_p \qquad \text{AIII.50}$$

$\Delta\varepsilon_p$ is given by equation AIII.48 and

$$\varepsilon^*_p = \sqrt{\frac{2}{3} \varepsilon^p_{ij} \varepsilon^p_{ij}} \qquad \text{AIII.51}$$

Altogether, six constants are needed to describe the model. These are $\sigma_s, \sigma_o, r, t, q_o$ and H. These constants can be determined from uniaxial cyclic stress strain curves.

AIII.3.1 Determination of Material Constants.

Any material model requires a method of determining the necessary constants, preferably, without excessive or complicated material testing. A method for finding the constants r, t, q_o and H are outlined here. The procedure follows closely the method suggested by Goodman and Goodall (18). The method assumes that a montonic stress strain curve and a cyclic plastic stress strain curve are available. The cyclic plastic stress strain curve are obtained from cycling between fixed stress level with stress range σ_R and maximum tensile stress σ^T. The experimental ratchet strain at the hardened state ε^R can be obtained. An iterative procedure described below can then be applied.

1) Estimate σ_s and σ_o.

2) Guess a value of $t=t_o$. It is convenient to put $t_o=0$ to start with.

3) Find r and q_o so that equation AIII.8 fits the monotonic loading curve.

4) From the hardened hysteresis loop find q

to fit

$$\varepsilon_R^T = \sigma_R/E + \int_{\sigma^T-\sigma_R+2\sigma_o}^{\sigma^T} E^p d\sigma \qquad \text{AIII.52}$$

where

$$E^p = \frac{U^*(\sigma_s-\sigma_o)}{(rU^*)^q V^{*t}(q+tU^*V^*)} \qquad \text{AIII.53}$$

$q=q_o$ can be taken as the starting point. ε_R^T is the total strain range for the loop considered.

5) Determine the hardening constant H from equation AIII.49

6) From q obtained in step (4), obtain a new value of t to give the correct ratchet strain

$$\varepsilon^R = \int_{\sigma^T-\sigma_R+2\sigma_o}^{\sigma^T} E^p d\sigma - \int_{\sigma^T-2\sigma_o}^{\sigma^T-\sigma_R} E^p d\sigma \qquad \text{AIII.54}$$

7) Go to step 3 until all values converge.

If cyclic hardening is negligible, steps 4 and 5 can be omitted; this simplifies the procedure considerably. The integration which is necessary in equations AIII.52 and AIII.54 may have to be carried out numerically.

AIII.3.2 Determination of the Constants for the Lead Alloy.

The lead alloy had been shown to exhibit the phenomena of cyclic hardening, cyclic relaxation and material ratchetting (see references 3 and 20). The cyclic stress-strain curves in (3) and (20) also indicate that for cycling between fixed strain limits, a stable loop is obtained after the first cycle, the material does not cyclically harden. For this reason, cyclic hardening is ignored in determining the material constants for the lead alloy, this simplifies the procedure very considerably.

The monotonic stress-strain curve obtained by Yahiaoui (3) for lead alloy is reproduced here in Fig.AIII.4(i). It indicates that there is a scatter in the experimental data. The average stress-strain curve is used here. A typical uniaxial cyclic plastic stress-strain curve for cycling between two fixed stresses is shown in Fig.AIII.4(ii). The ratchet strain per cycle is taken to be the average for the first 10 cycles.

Because of the scatter in the results obtained from 'material ratchetting' tests (see Table AIII.1), it was decided to obtain three sets of constants for the 'material ratchetting' model. The constants were chosen to give ratchet strains equal to those obtained in tests U4,U1 and U3. The resulting sets of constants denoted as material models A,B and C respectively are also shown in Table AIII.1.

Using the material constants obtained, Fig.AIII.4(i) shows the predicted monotonic stress-strain curves; these are compared with the experimental stress-strain curve. The constants for

materials A,B and C all give good prediction of the monotonic stress-strain curve. The predictions of ratchet strain per cycle, however, are not so good. The variation of ratchet strains per cycle with the mean stress and stress range for materials A,B and C are shown in Fig.AIII.5. Material A gives, overall, lower predictions of ratchet strains, compared to materials B and C. For all cases, overall, the lead alloy behaviour was found to be better predicted by the constants for material models B and C. Fig.AIII.6 shows the cyclic plastic stress-strain curve obtained using material model A, constant ratchet strains are obtained after the first cycle because cyclic hardening is ignored.

AIII.4 Program Development.

Full details of the elastic-plastic creep finite element programs, data input system, flow charts etc., which were used as the basis for the present developments, are decribed by Hardy (83). The relevant subroutines used for the inclusion of the Goodman and Goodall model are called PLASTIC and T86010. These subroutines are stored in a file called EAFESLIB.EAXSHCPLEEP?. Both of these subroutines were modified to accommodate the present model. A minor modification was made in PLASTC to retain the restart facility. A separate routine called GOOD2 for the present model was written. A major modification to T86010 was necessary; thus allowing it to call GOOD2 without affecting the existing perfectly-plastic, linear kinematic and linear isotropic models in the routine. Parts of the flow chart for T86010, where modifications were

made, and the flow chart for GOOD2 are shown in Figs.AIII.7 and AIII.8 respectively.

AIII.4.1 Program Detail.

To solve elastic-plastic problem an incremental approach is adopted. The load is increased in small, but finite, steps by increasing the displacement. The total strain is then calculated from the total displacements and the elastic strain is extracted, from which the components of the stresses are calculated. The equivalent stress is then calculated taking into account any shift in the yield surface which may be due to kinematic hardening. If the equivalent stress is above the yield stress, then yielding occurs and the plastic strain must be determined. An iterative precedure described in detail in reference 14 is used. A 'negative gradient' technique is used to speed up the convergence of the iterative solution. This technique is briefly described here. Fig.AIII.9 shows the equivalent stress-equivalent strain curve for a 'gauss' point in the structure. At some stage in the iteration, point A is reached which is not on the stress-strain curve. If the converged solution at the end of the last load step is at B, then CA is the current estimate of the equivalent plastic strain. A 'guess' for the solution on the uniaxial stress strain curve is obtained, i.e. point D, by taking a negative gradient, usually minus the Young's Modulus, from A towards the stress strain curve. The new estimate of the equivalent plastic strain is given by ED. If A is below the stress-strain curve, the same negative gradient is used which would give a

smaller estimate of plastic strain than the previous iteration. The iteration procedure is continued until the stresses at each 'gauss point' within the structure are within X% of the stress-strain curve. X is called the accuracy criterion of the converged solution.

The Goodman and Goodall (18) model is a particular case for which certain approximations to the actual stress-strain curve are made. The stress-strain curve is approximated by a series of short straight lines each with a plastic modulus E^p, given by equation AIII.11, evaluated at the last converged solution. Hence, in Fig.AIII.9 the curve BGD is approximated by a straight line BD which is the tangent of the curve at B with plastic modulus E^p calculated using stress σ_B. The plastic modulus is constant during the iteration. Due to this approximation, the stress-strain curve is always 'above' the actual stress-strain curve. For infinitesimally small stress increments, the generated stress-strain curve would converged to the actual stress-strain curve. More sophisticated techniques for obtaining an appropriate value of E^p could be used but for the present development work, these were not considered to be necessary.

AIII.5 Illustrative Examples.

In this section the results of uniaxial and biaxial calculations obtained with the above model are presented to illustrate the behaviour of the model and to demonstrate that the finite element coding is working correctly. In all but one

case, i.e. the case in which cyclic hardening is included, the constants for the lead alloy material model C of Table AIII.1 were used. For uniaxial loading case, with cyclic hardening, the material constants for 316 Stainless Steel, obtained by Goodman and Goodall (18), were used. The constants for 316 Stainless Steel are given in Table AIII.2. A one element model was used throughout. For convenience, the results for stress controlled cycling were obtained.

AIII.5.1 Uniaxial Loading.

AIII.5.1.1 Without Cyclic Hardening.

Fig.AIII.10 shows the stress-strain curve obtained for stress controlled cycling with a zero mean stress. The curve OAB represents the monotonic loading curve. When the stress is reversed, the curve BCD is generated. On reloading from D, the curve DEB is generated. A closed hysteresis loop BCDEB is obtained and there is no ratchet strain obtained with cycling about a zero mean stress.

When cycling between the stress levels of $25 MNm^{-2}$ and $-18\ MNm^{-2}$, the stress-strain curve shown is Fig.AIII.11(i) was obtained. For convenience, the stress has been plotted against the plastic strain. The curve OAB represents the monotonic loading curve. The results for only $1\frac{1}{2}$ cycles are shown. However, since there is no cyclic hardening, the plastic branch of the curve in the tensile direction in the subsequent cycles will be identical to the curve DEF and similarly for the

compressive branch it will be identical to FGH. The ratchet strain per cycle ε^R is indicated in Fig.AIII.11(i). If cycling between the strain limits at B and D was carried out, for the first cycle, there would be a stress relaxation of $\delta\sigma$ as shown. Subsequent cycling would cause the hysteresis loop to shift downwards, tending towards a loop with zero mean stress.

AIII.5.1.2 With Cyclic Hardening.

The stress-strain curve obtained is shown in Fig.AIII.11(ii). The monotonic loading curve is denoted by OAB. For this part, the hardening index, q , takes a value q_o. On unloading from B, the material undergoes cyclic hardening, i.e. plastic slope of the curve BCD is higher than it would be if cyclic hardening was not included. The hardening index, q , is constant over a loading path until a plastic reversal occurs. For example, q is constant at q_1, for curve BCD, q_2 for DEF, q_3 for FGH etc. where q_1, q_2 , q_3 etc. in general different. The ratchet strain reduces after each cyclic loop until q become approximately uniform when a constant ratchet strain occurs.

AIII.5.2 Biaxial Loading.

AIII.5.2.1 Proportional Loading.

In this case, the element is subjected to stresses in the x and y directions denoted by σ_{xx} and σ_{yy} respectively (see Fig.AIII.12 for the coordinate axes). The loading is such that at any instant the ratio of σ_{xx} to σ_{yy} is constant. As a result, a radial

loading path is obtained. A modified effective stress (σ'_{eff}) and plastic strain ($\varepsilon^{p'}_{eff}$) are used so that the result can be presented in a similar manner to the uniaxial stress-strain curves, where σ'_{eff} and $\varepsilon^{p'}_{eff}$ are given by equation AIII.55(i) and (ii) respectively.

$$\sigma'_{eff} = \text{sgn}(\sigma_{xx})\sqrt{\frac{3}{2}S_{ij}S_{ij}} \qquad \text{(i)}$$

AIII.55

$$\varepsilon^{p'}_{eff} = \text{sgn}(\varepsilon^{p}_{xx})\sqrt{\frac{2}{3}\varepsilon^{p}_{ij}\ \varepsilon^{p}_{ij}} \qquad \text{(ii)}$$

where $\text{sgn}(\sigma_{xx})$ is the sign of σ_{xx} and $\text{sgn}(\varepsilon^{p}_{xx})$ is the sign of ε^{p}_{xx}.

The results for biaxiality ratio of 1:1 (i.e. $\sigma_{xx}:\sigma_{yy}=1:1$) are shown in Fig.AIII.13(i) and for biaxiality ratio of 1:2 are shown in Fig.AIII.13(ii). As would be expected, the curves obtained were found to be identical to those obtained for uniaxial loading, i.e. Fig.AIII.11(i).

AIII.5.2.2 Non-Proportional Loading.

Results were obtained for the following load combinations:-

(a) uniaxial monotonic loading to $\sigma_{yy}=12\text{MNm}^{-2}$ followed by cyclic variations of σ_{xx} between -9MNm^{-2} and 28.74MNm^{-2},

(b) uniaxial monotonic loading to $\sigma_{xx}=4\text{MNm}^{-2}$ followed by cyclic variations of τ_{xy} between -12MNm^{-2} and 12MNm^{-2} and

(c) uniaxial monotonic loading to $\sigma_{xx}=4MNm^{-2}$ followed by cyclic variations of the shear strain between -0.25% and +0.25%.

AIII.5.2.2.1 Results for Load Case (a).

A graph of σ_{xx} against $\varepsilon^{p'}_{eff}$ is shown in Fig.AIII.14(i). The results are somewhat surprising since the effective plastic strain was found to be decreasing with cycle number. The variation of total strain in the y direction, ε^{T}_{yy}, shown in Fig.AIII.14(ii), however, shows that ε^{T}_{yy} is increasing with cycle number. The result is different from either the uniaxial or the proportional loading cases. The movement of the yield surface is denoted by α_{ij}. In the π-plane, the position of α_{ij} during loading is shown in Fig.AIII.14(iii). The curve OA represents the movement of the yield surface during the loading on the virgin material. Subsequent loading in which plastic straining occurs, causes the centre of the yield surface to follow the curve ABCDEFG. Sliding of surfaces f and f_m are denoted by the curves CD and FG. Because the stress increment in the computation is finite, there is a small expansion in the surface f_m. If the stress increments were reduced, point D would be closer to point A, point E would be closer to point B and so on. For infinitesimal small stress increments, point D would be identical to point A and so on.

AIII.5.2.2.2 Results for Load Case (b).

This load case corresponds to that of a thin tube subjected to a steady axial load and a cyclic torsional moment.

Fig.AIII.15(i) shows the shear stress-shear strain behaviour of the element. The curve OAB corresponds to the virgin material. Unloading from B follows the curve BCD with subsequent reloading following the curve DEF. Because it is a stress controlled situation, the shear strain at F is less than that at B; and the loop is not symmetric, with a non-zero mean strain. The loops for the second, third and fourth cycles are also shown in Fig.AIII.15(i). For the third and fourth cycles, the loops almost coincide. The variation of total axial strain with shear stress is shown in Fig.AIII.15(ii) and Fig.AIII.15(iii) shows the variation of total axial strain with cycle number. The axial strain increases for the first few cycles and reaches a constant value at about 4 cycles.

AIII.5.2.2.3 Results for Load Case (c).

This load case corresponds to one commonly used in experimental work. The axial load is held constant while a cyclic torsional moment is applied such that the shear strain is cycled between fixed levels with zero mean shear strain. Fig.AIII.16(i) shows the shear stress-shear strain loop for shear strain cycling between $\pm$ 0.25% with a constant axial stress, σ_{xx}, of 4 MNm^{-2}(i.e.σ_{xx}/σ_o=0.2857). Initially, curve OA is traced which is the virgin material curve followed by curve ABC and so on. At the end of each quarter cycle, the magnitude of the shear stress increases. The increment in the shear stress reduces. The stress-strain loop eventually reaches a stable loop with zero mean stress. The variation of total axial strain with cycle number is shown in Fig.AIII.16(ii). There is an increase

in the total axial strain with cycle number and the increment reduces. The total axial strain finally reaches a steady value. When this happens, a stable stress-strain loop is obtained. This describes qualitatively the behaviour of some metals, e.g. in reference 26.

From these observations, it is concluded that the model is capable of describing commonly observed material behaviour in multi-axial as well as uniaxial loading and that the coding in the program is correct.

Experimental data						Calculated constants		
Material ratchetting test number	Maximum tensile stress σ_T MNm^{-2}	Mean stress σ MNm^{-2}	Stress range σ_R MNm^{-2}	Mean ratchet strain ε^R (%)	Material model number	r	t	q
U4	25	3.5	43	0.03	A	0.241	0.085	2.898
U1	22.2	4.6	35.2	0.015	B	0.161	0.333	2.520
U3	24.2	4.76	38.9	0.0625	C	0.147	0.379	2.451

Table AIII.1 Material ratchetting data and Goodman and Goodall material model for lead alloy material

Taking $\sigma_o = 14.0 \quad MNm^{-2}$

$\sigma_s = 29.2 \quad MNm^{-2}$

Yield stress, σ_o		100.0 MNm^{-2}
Saturation stress, σ_s		400.0 MNm^{-2}
Young's modulus, E		160.0 GNm^{-2}
Poisson's ratio, ν		0.3
Goodman and Goodall (18) constants	r	0.61
	t	0.4
	q_0	2.5
	H	60.0

Table AIII.2 Material constants for 316 Stainless Steel at 500-600°C

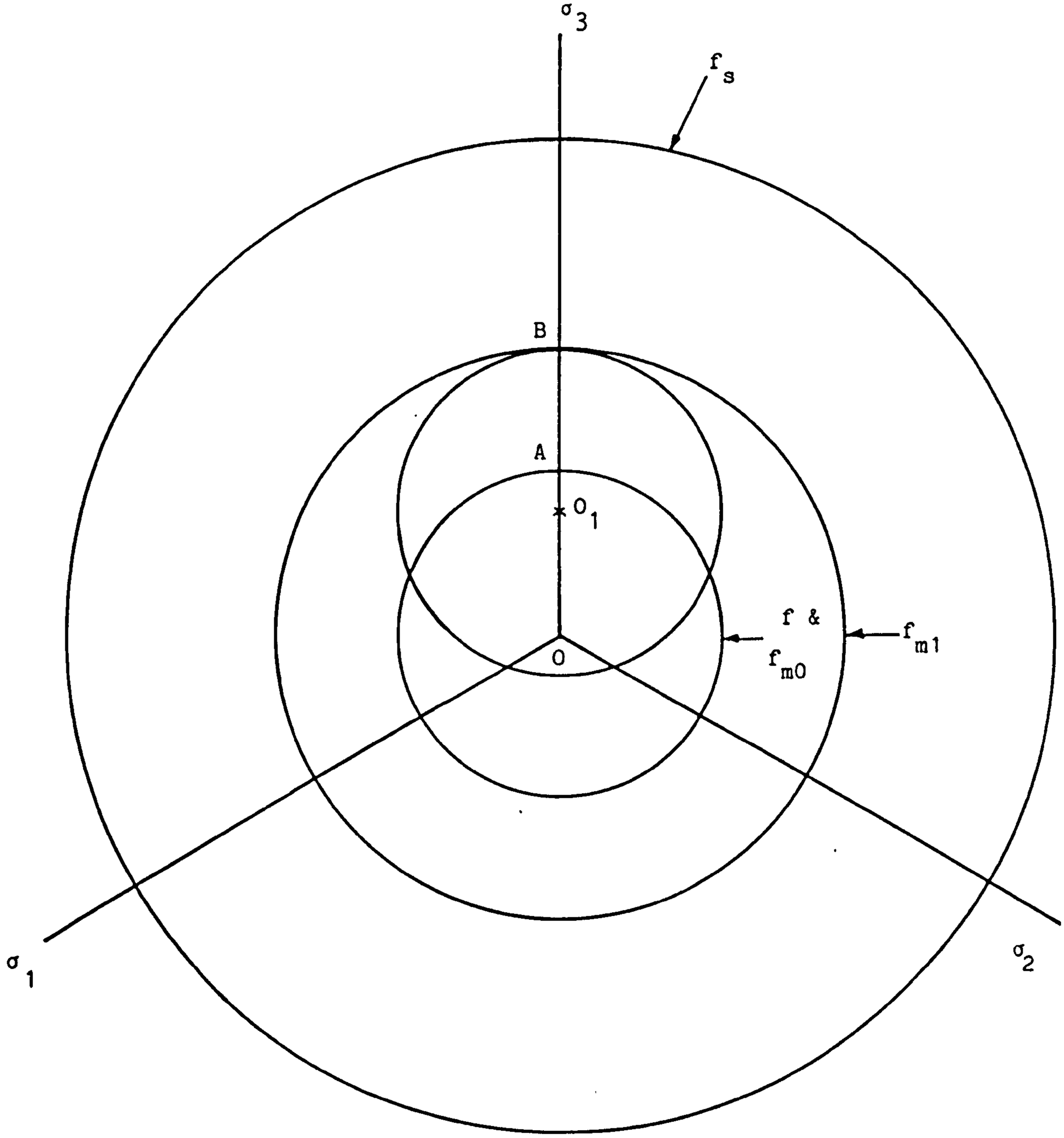

Fig.AIII.1 Multi-axial model.

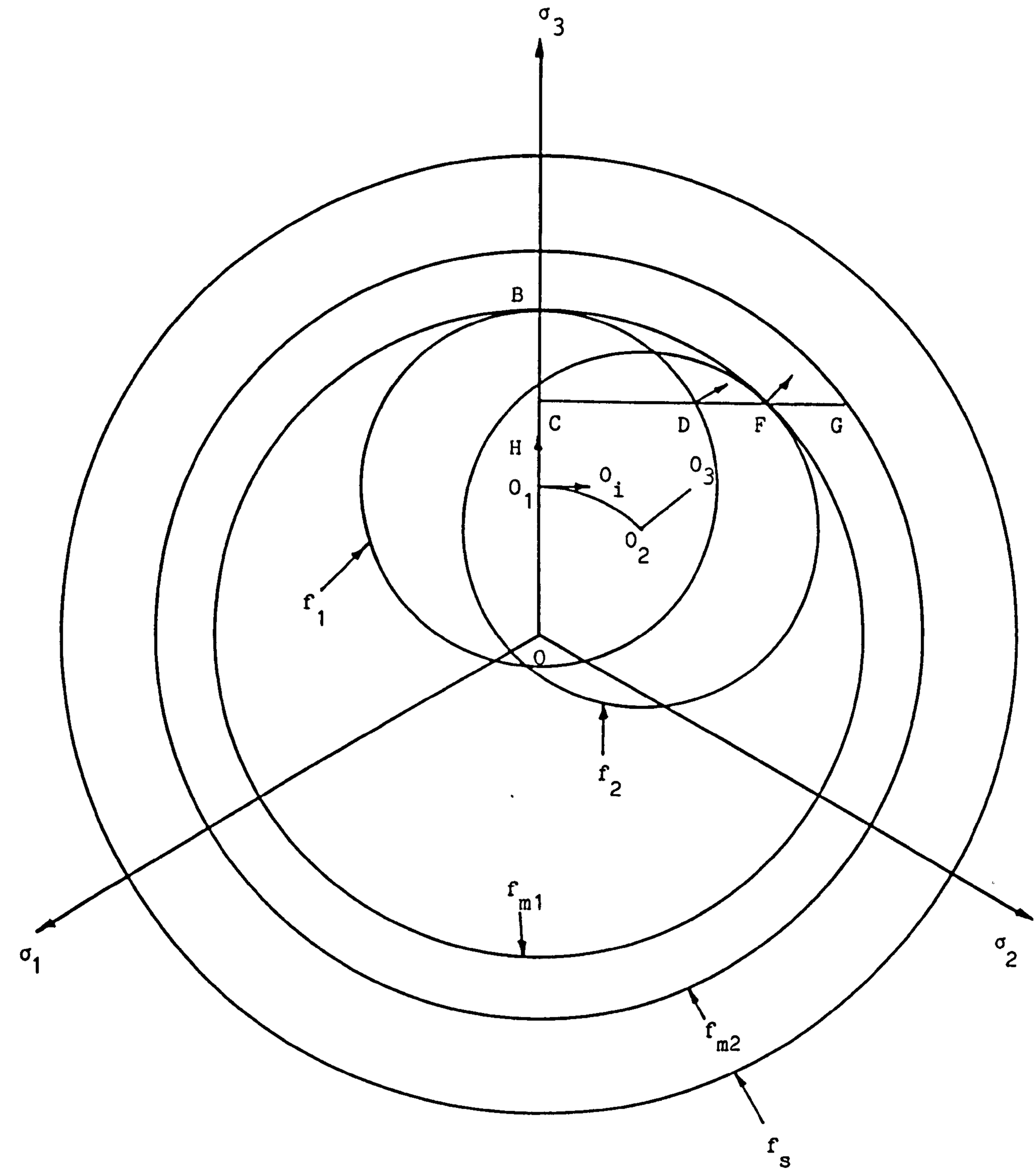

Fig.AIII.2 Multi-axial model. Non-proportional loading.

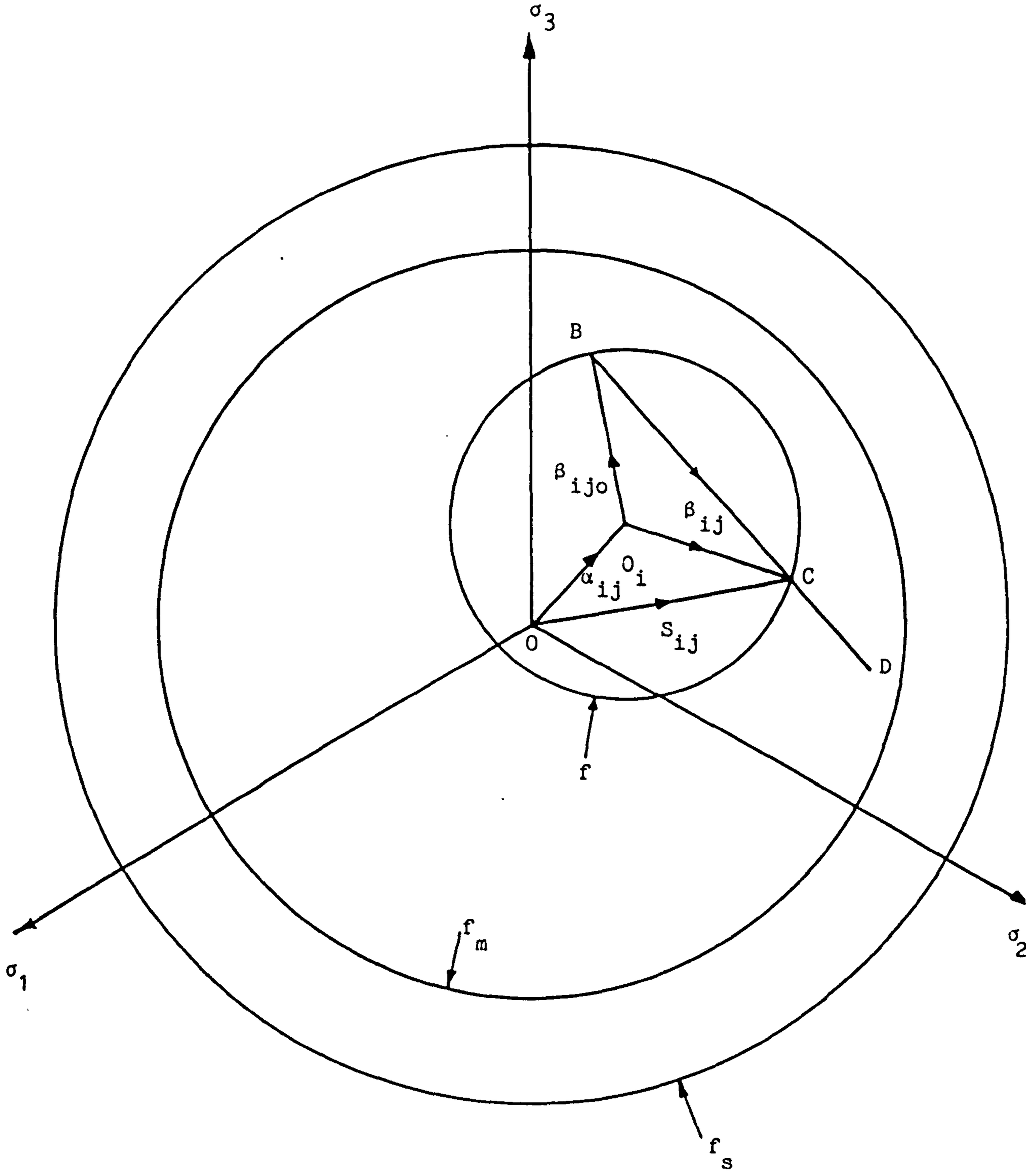

Fig.AIII.3 Definition of parameters for loading path BCD.

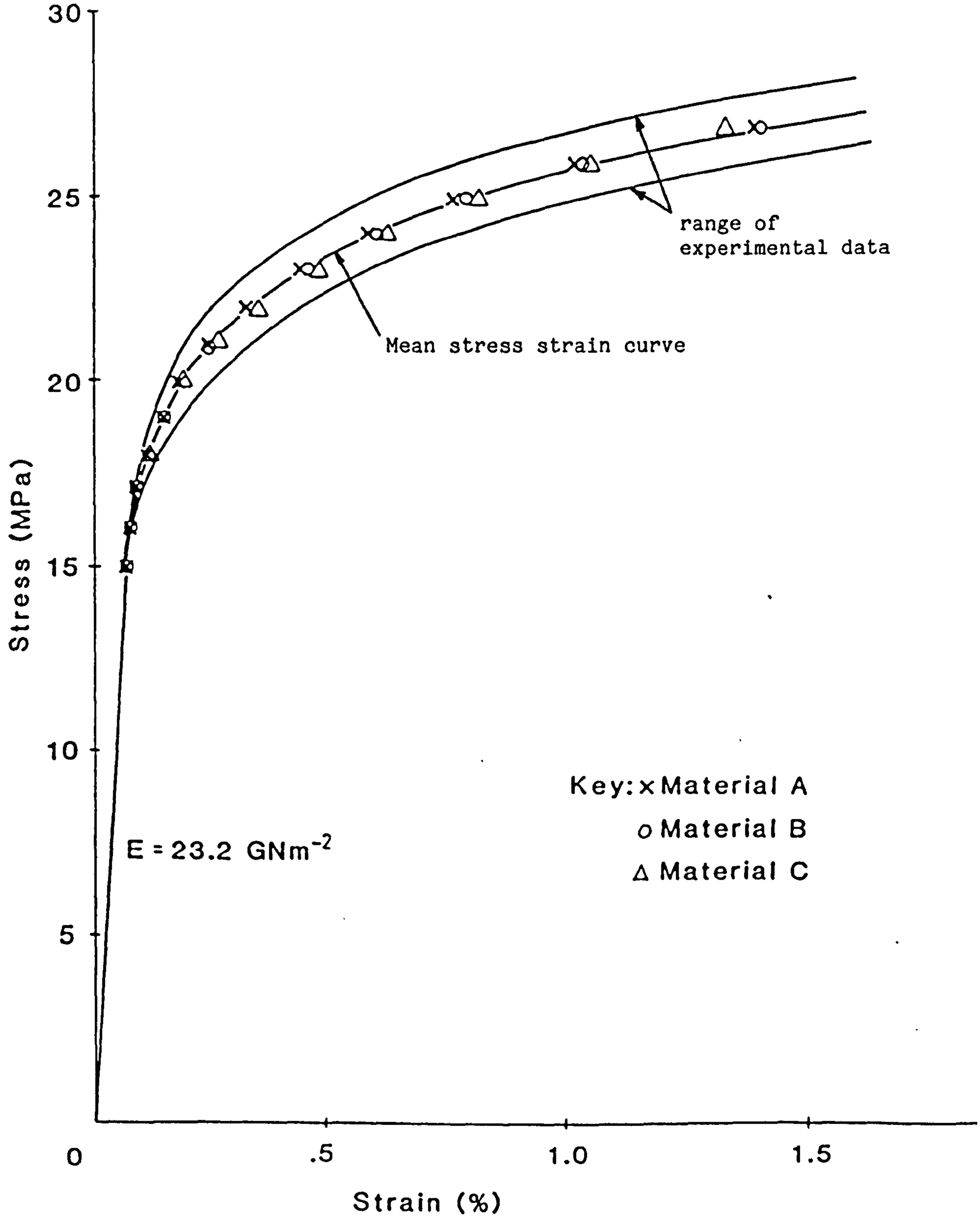

Fig.AIII.4(i) Experimental stress-strain data and fit to the mean data.

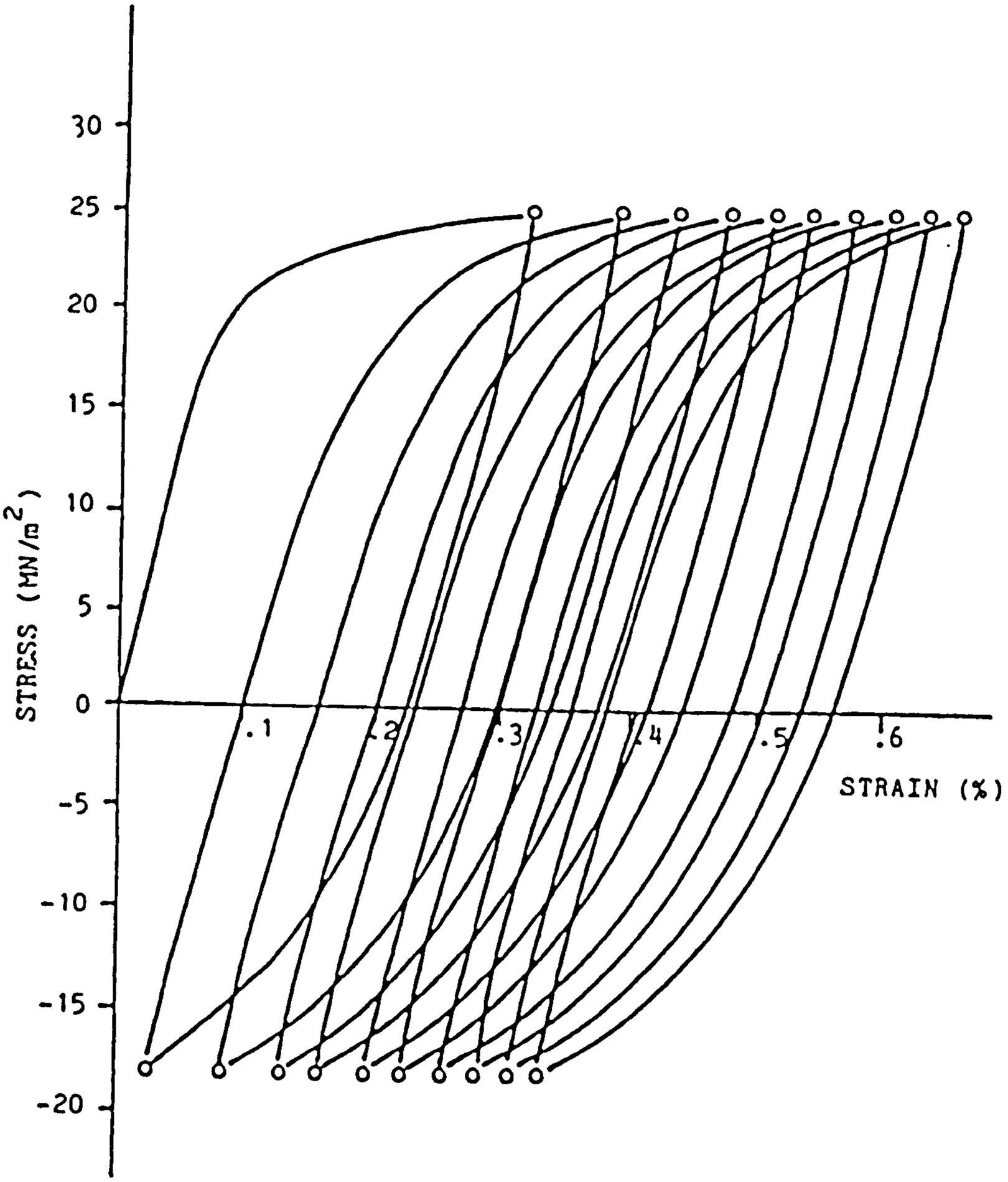

Fig.AIII.4(ii) Typical behaviour with fixed stress range cycling with a non-zero mean stress.

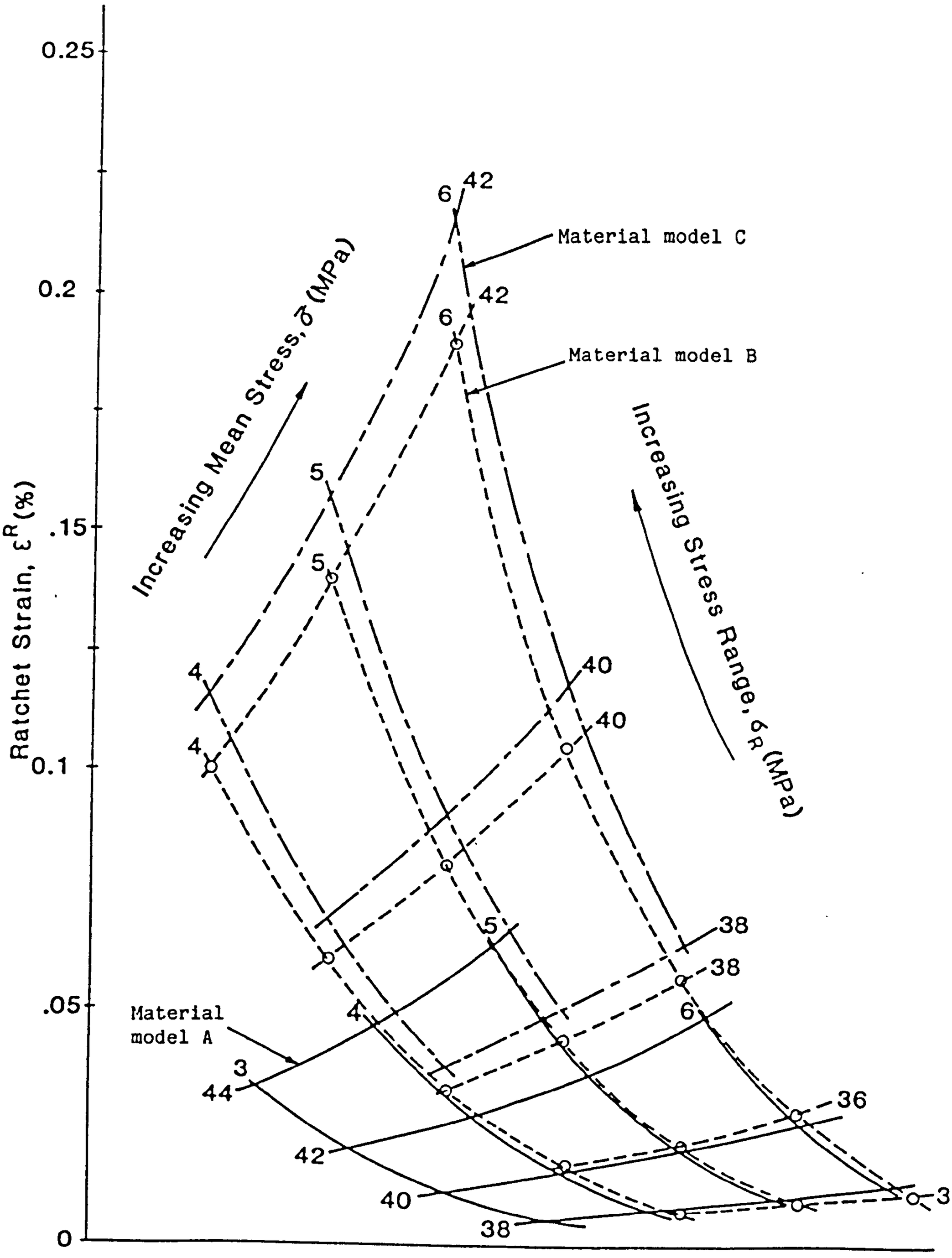

Fig.AIII.5 'Carpet plot' showing the variations of ratchet strains with mean stress and stress range for material models A, B and C.

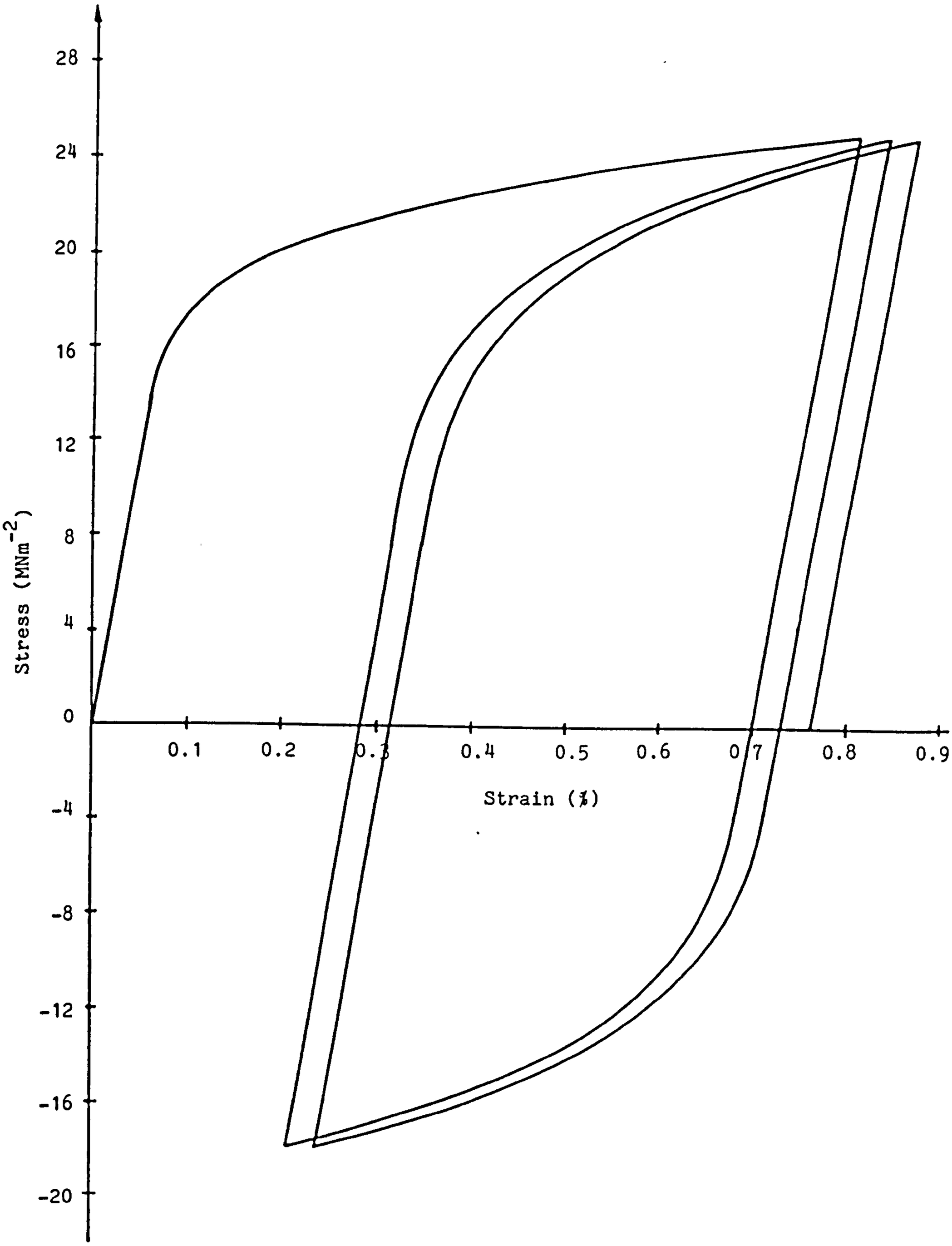

Fig.AIII.6 Stress-strain behaviour for fixed stress cycling for material model A.

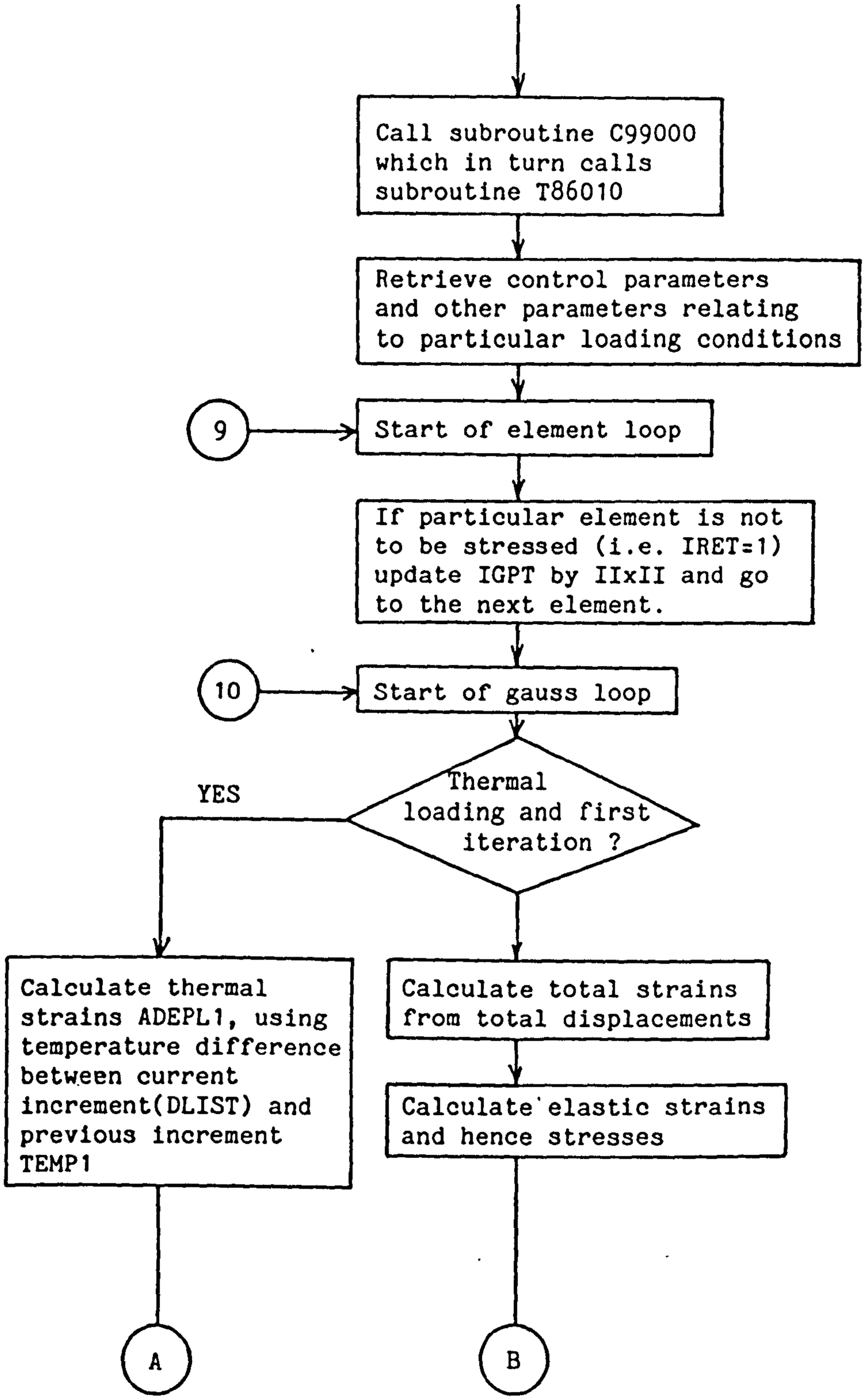

Fig. AIII.7 Program flow chart (part of Subroutine Plastic of reference 83)

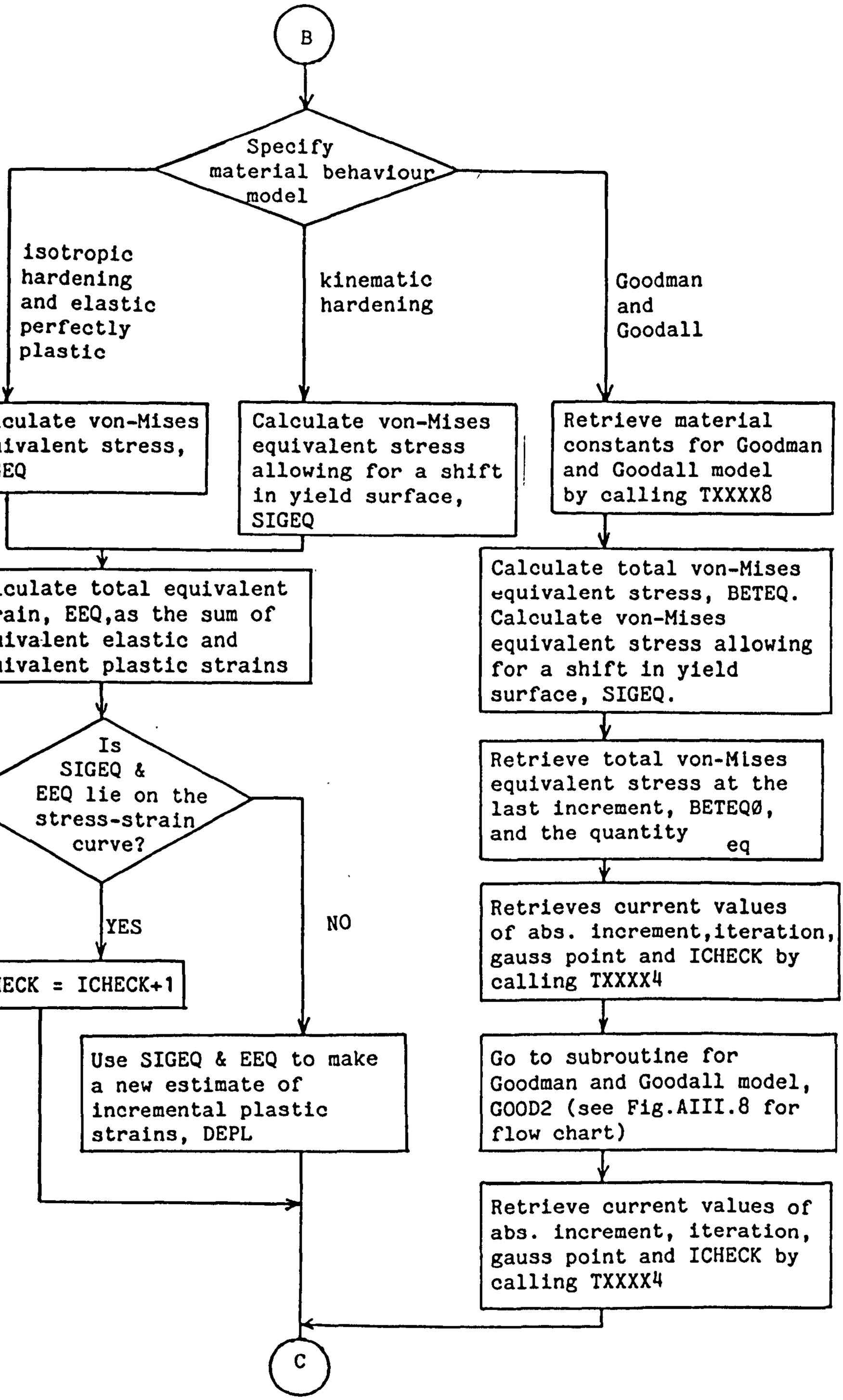

Fig.AIII.7 contd.

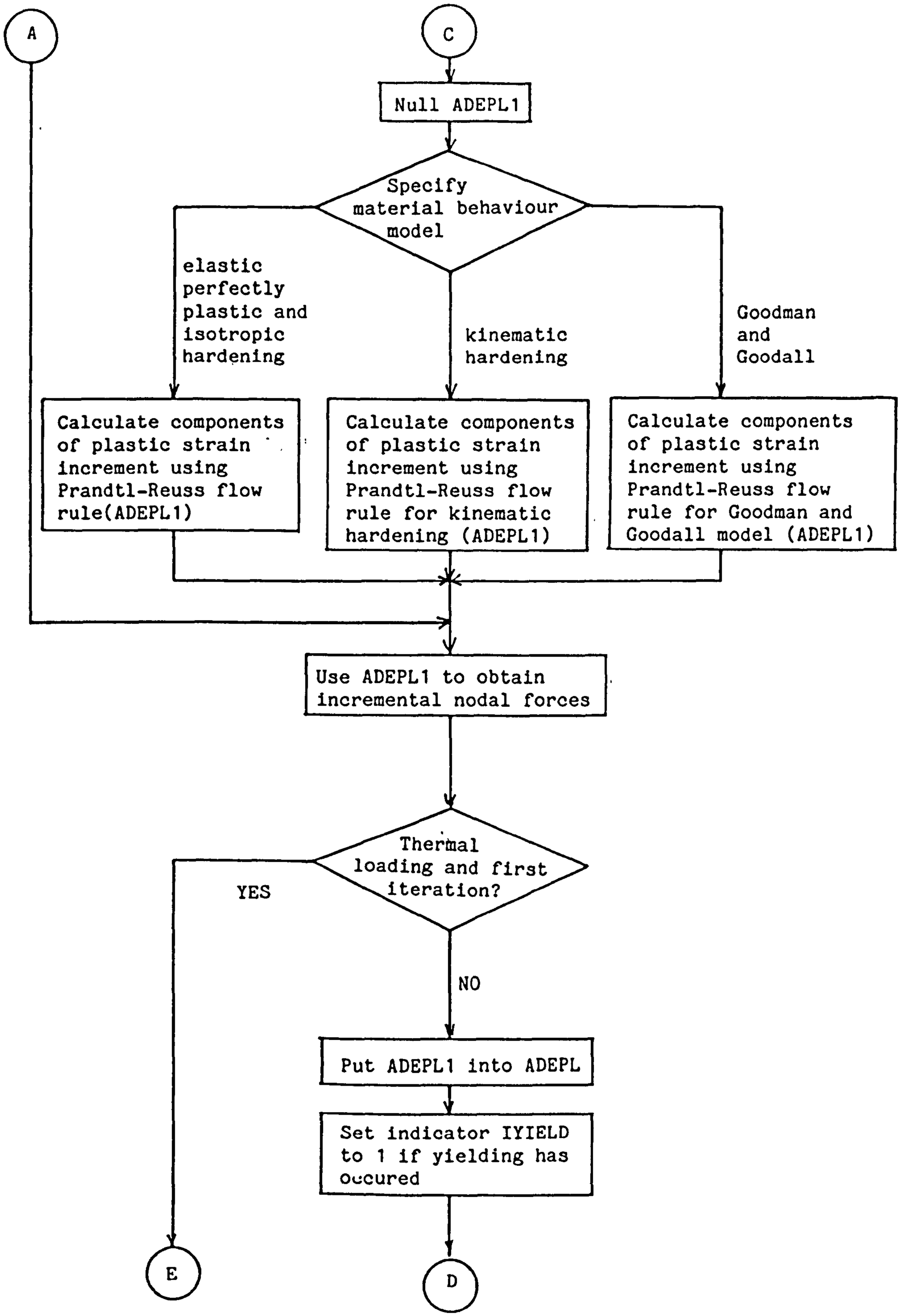

Fig.AIII.7 contd.

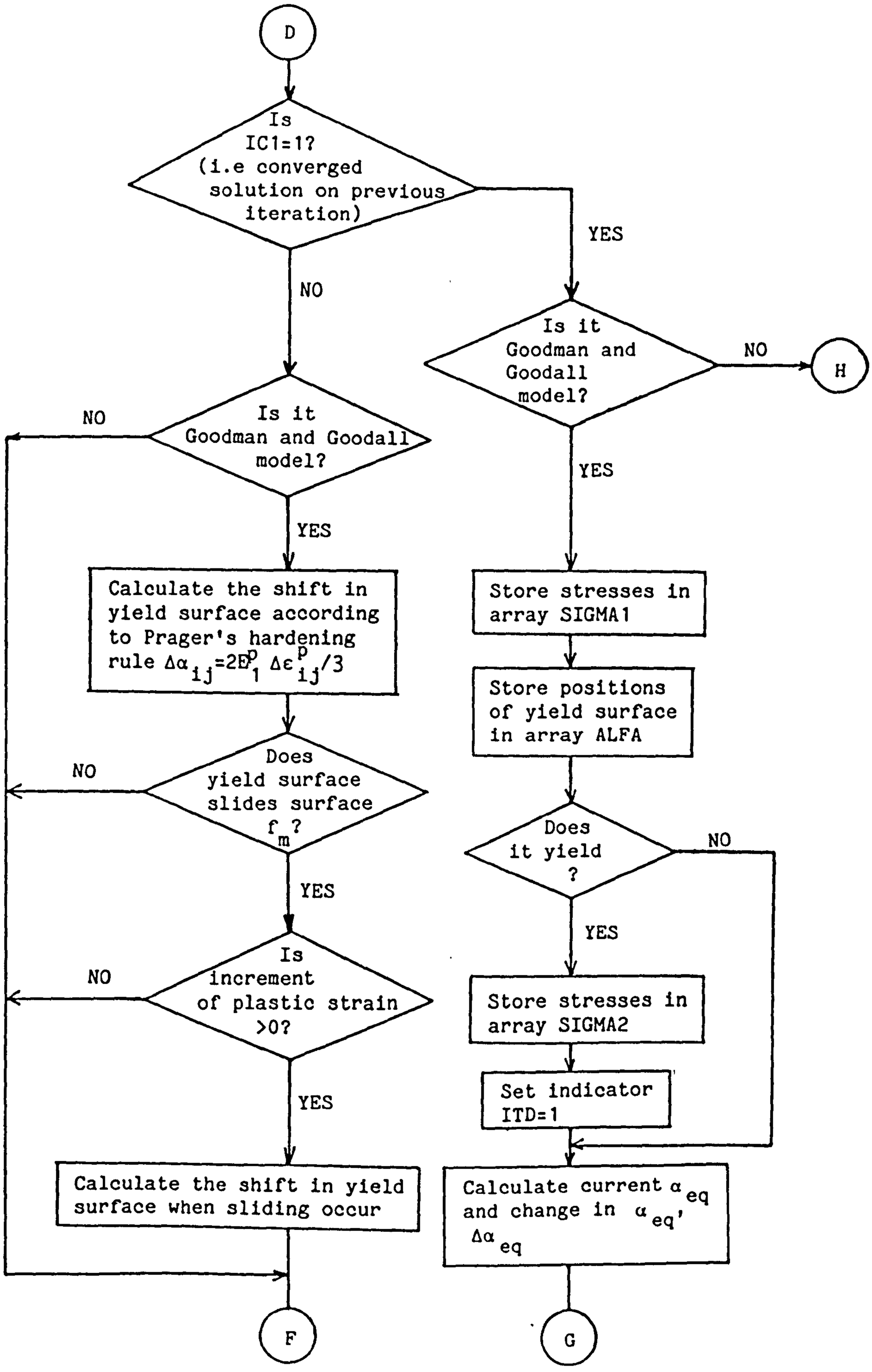

Fig.AIII.7 contd.

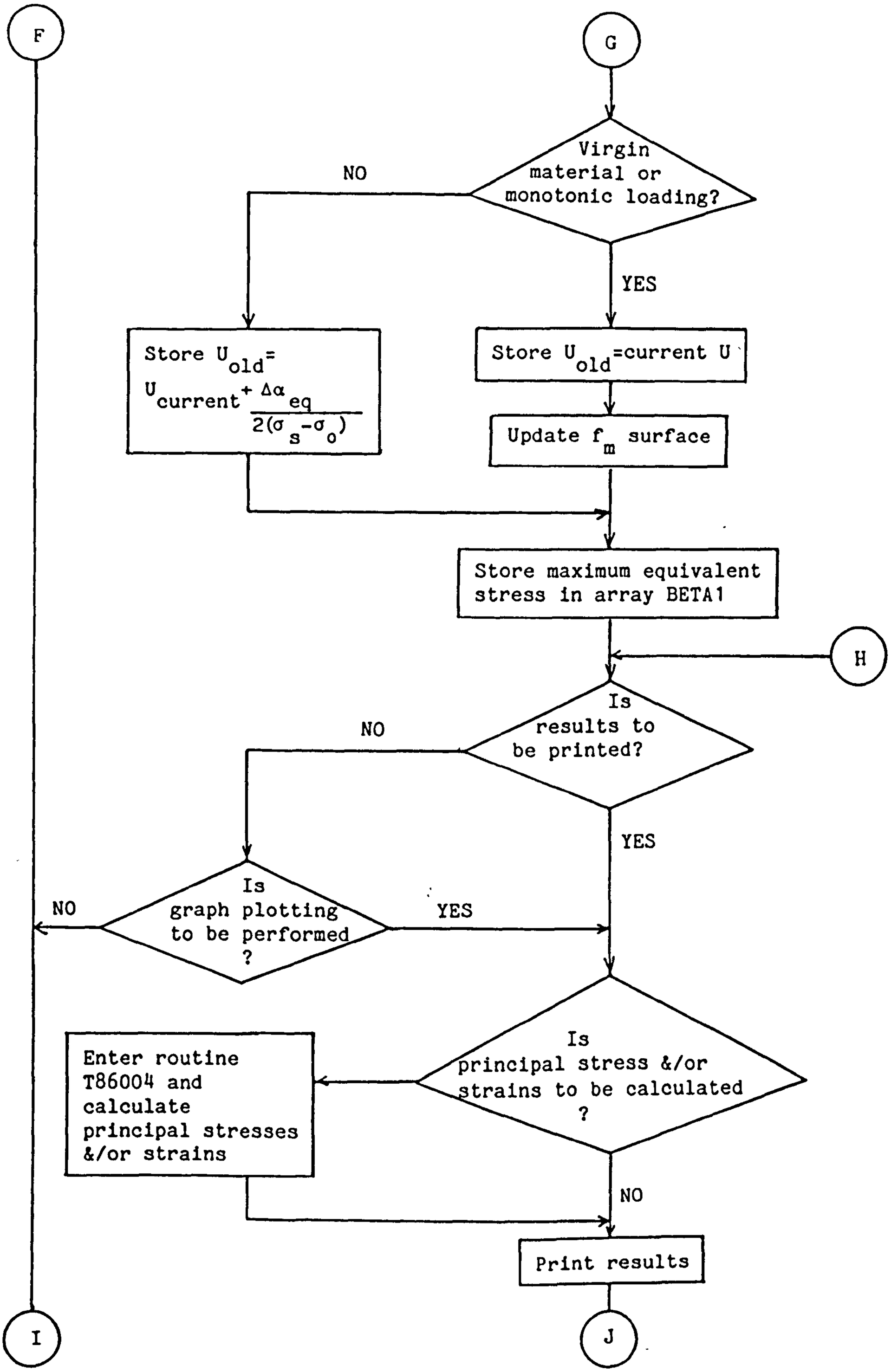

Fig.AIII.7 contd.

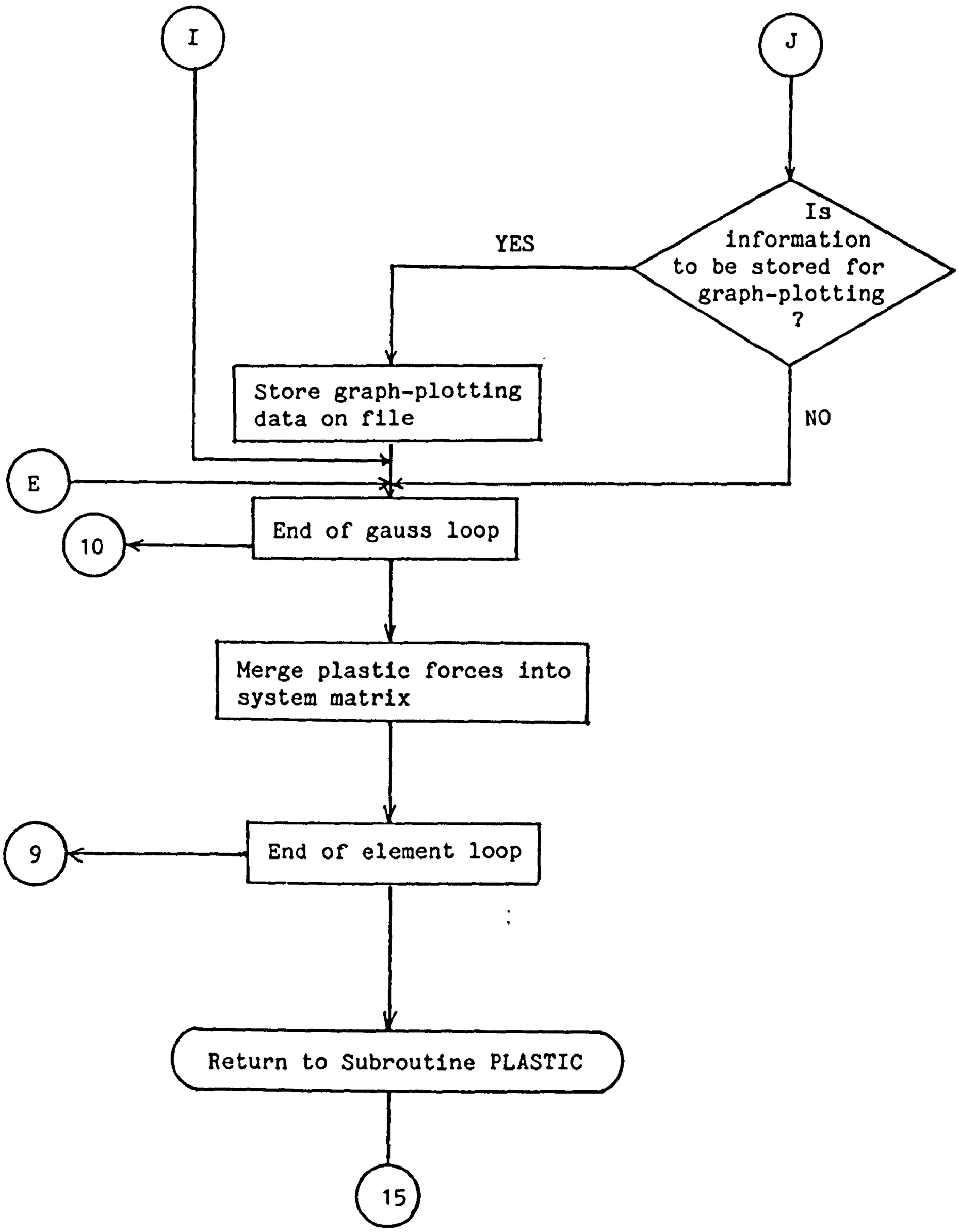

Fig.AIII.7 contd.

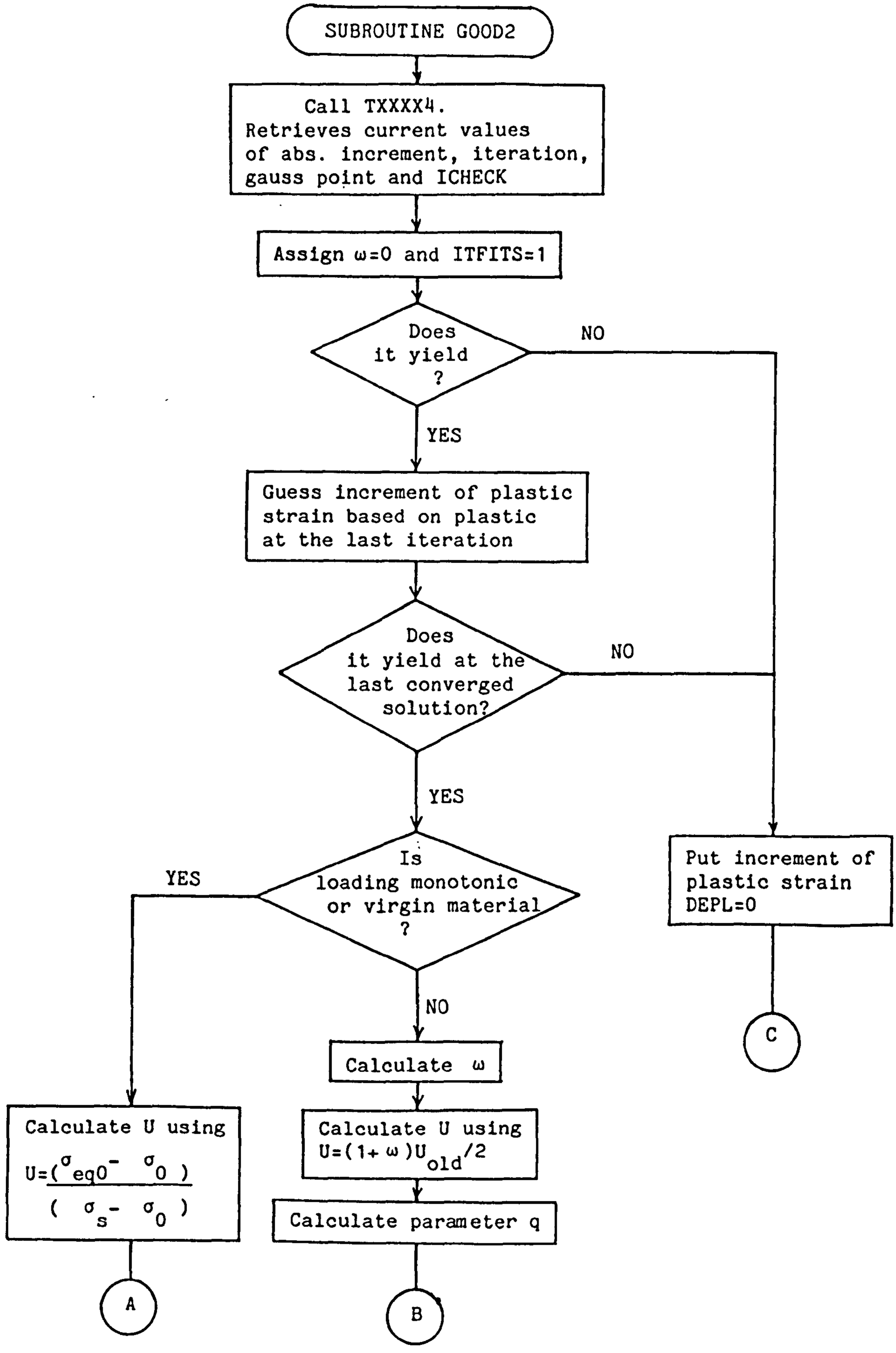

Fig.AIII.8 Flow chart for Goodman and Goodall model

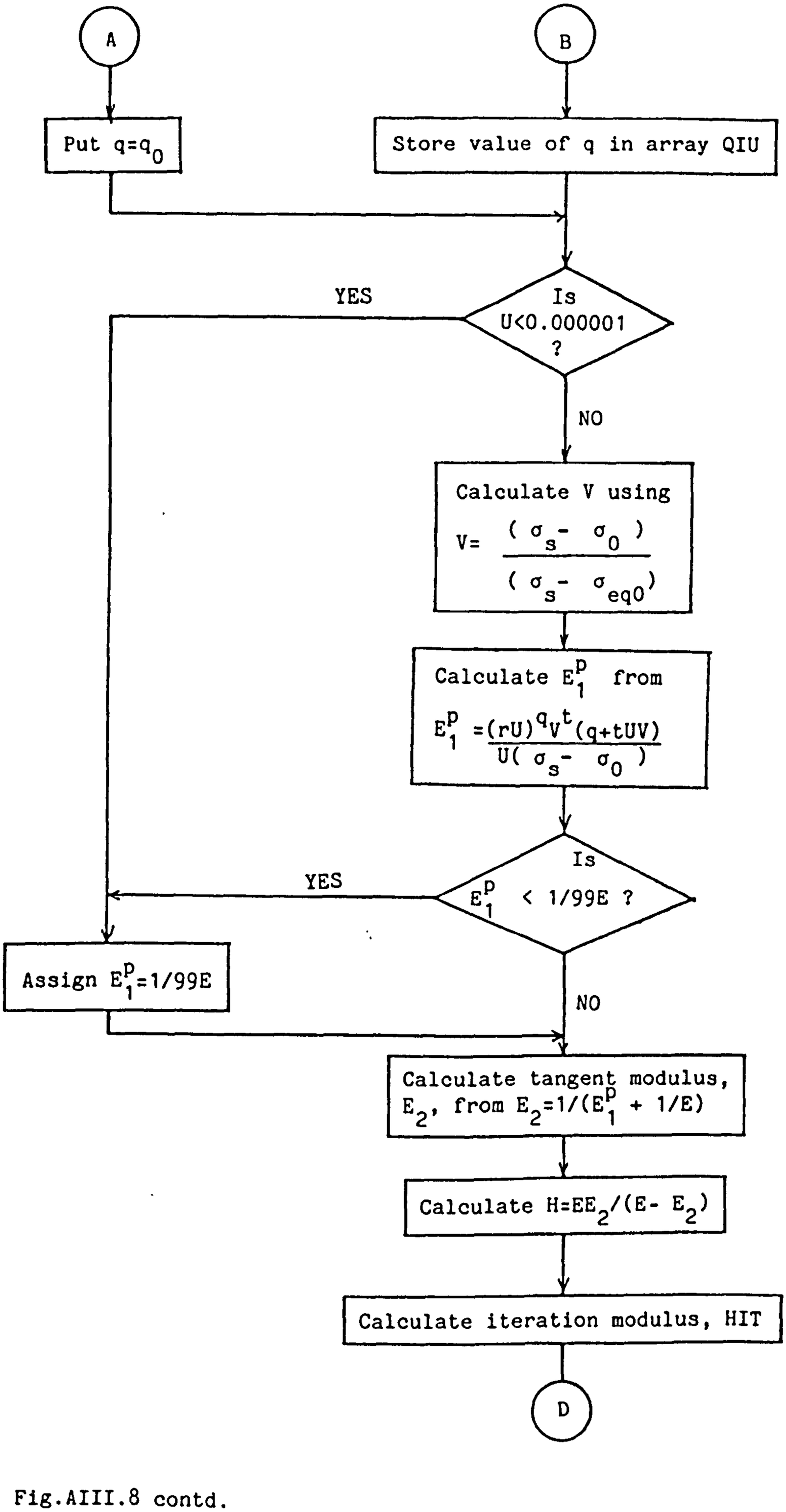

Fig.AIII.8 contd.

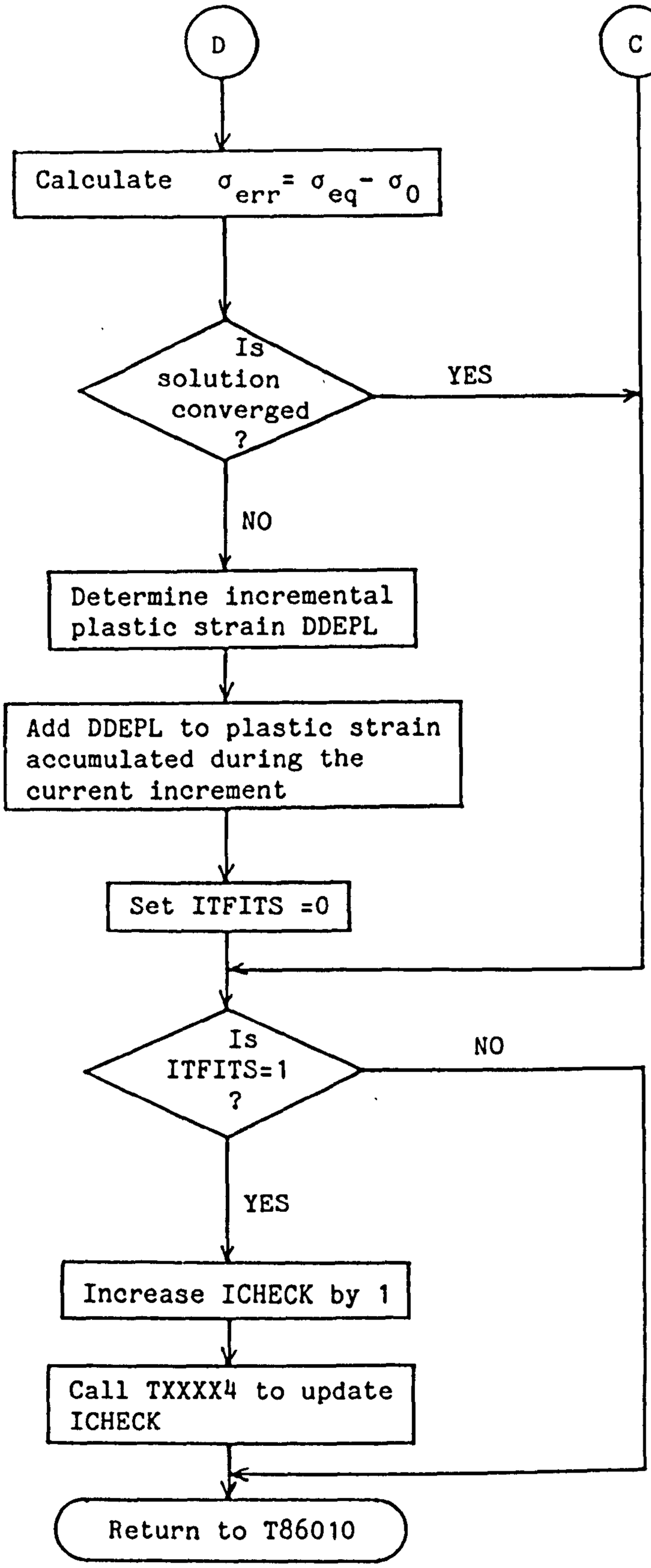

Fig.AIII.8 contd.

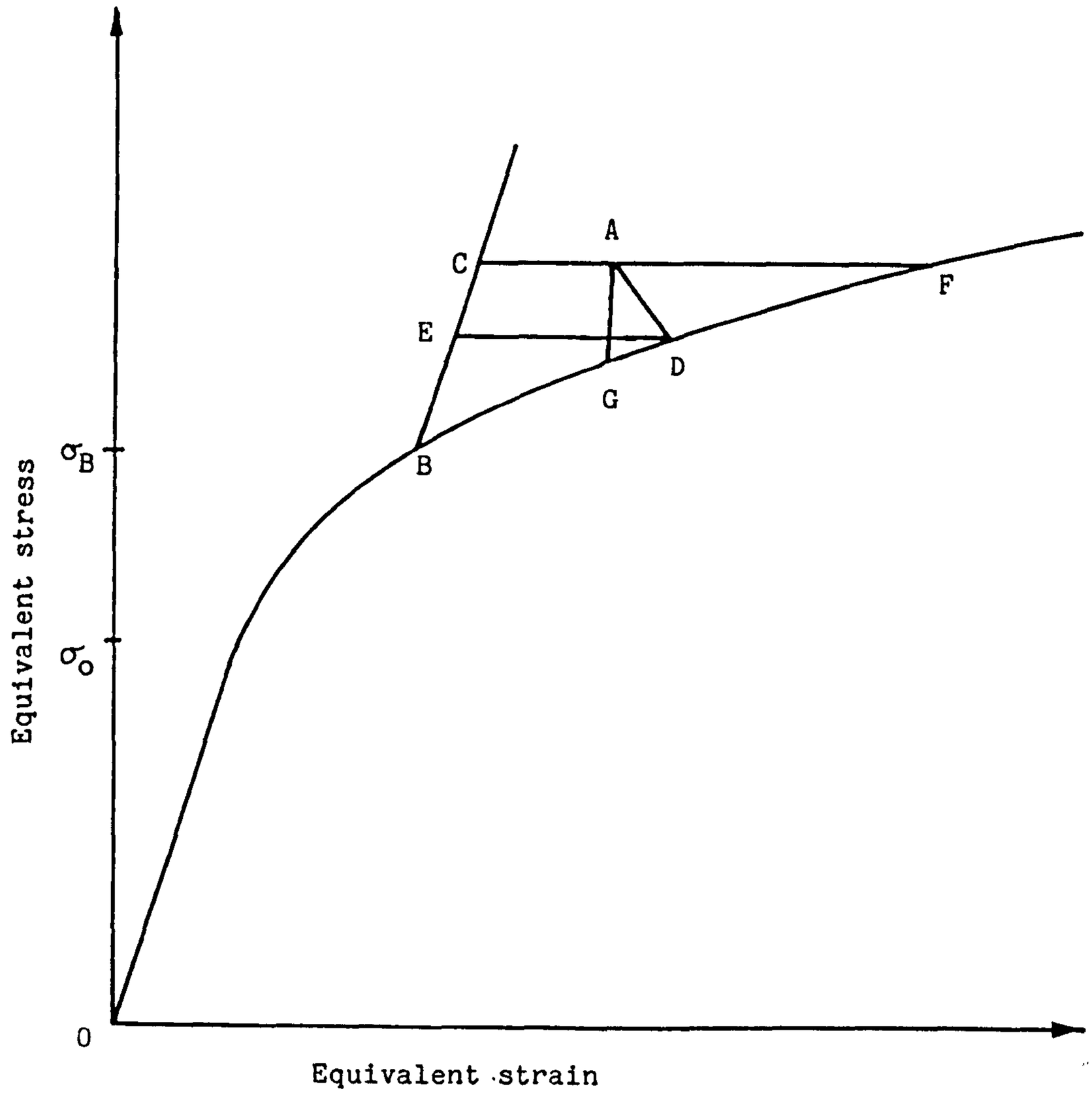

Fig.AIII.9 Equivalent stress-equivalent strain curve showing the method of estimating the equivalent plastic strain increment.

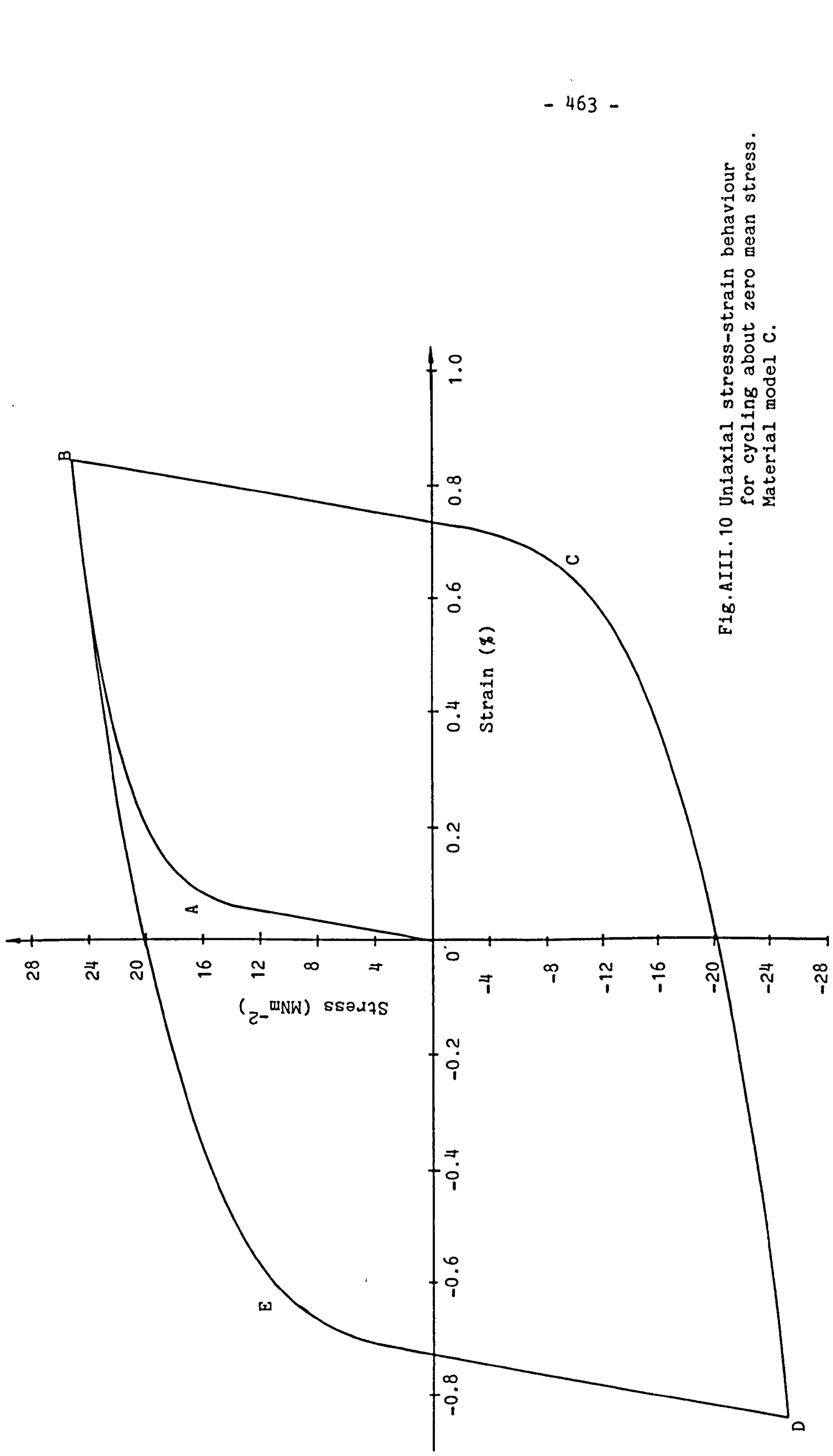

Fig.AIII.10 Uniaxial stress-strain behaviour for cycling about zero mean stress. Material model C.

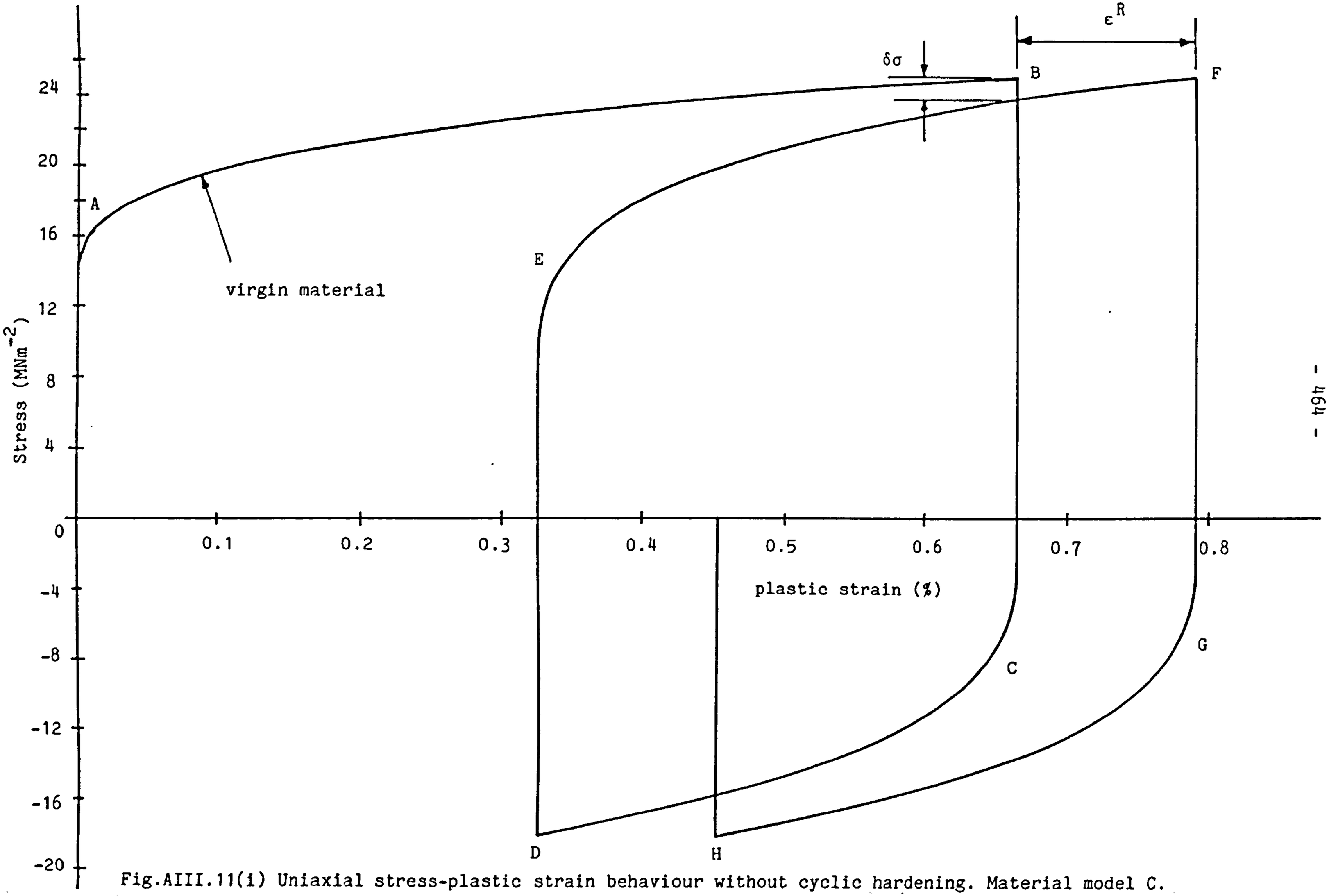

Fig.AIII.11(i) Uniaxial stress-plastic strain behaviour without cyclic hardening. Material model C.

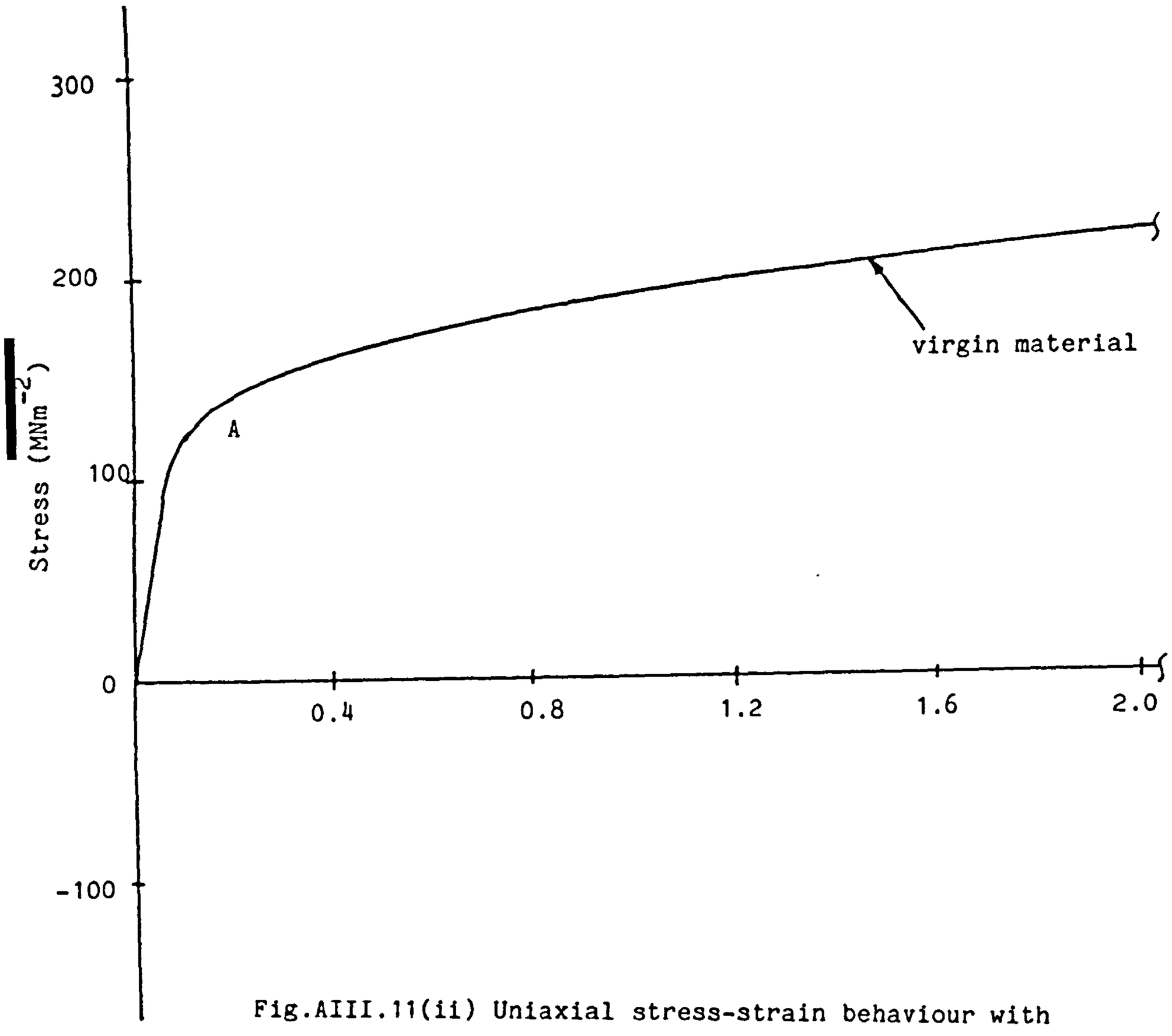

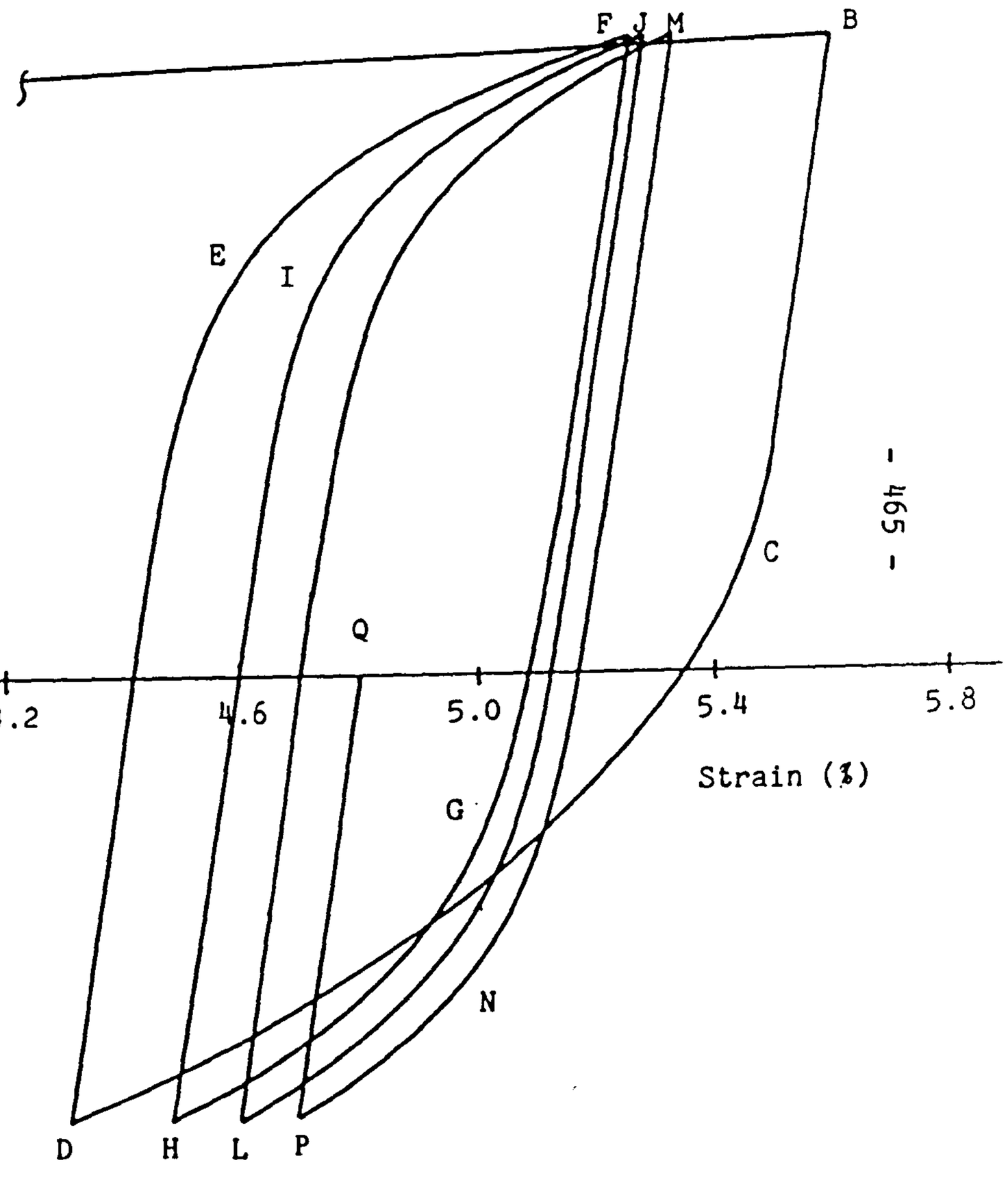

Fig.AIII.11(ii) Uniaxial stress-strain behaviour with cyclic hardening. Material constants of Table AIII.2.

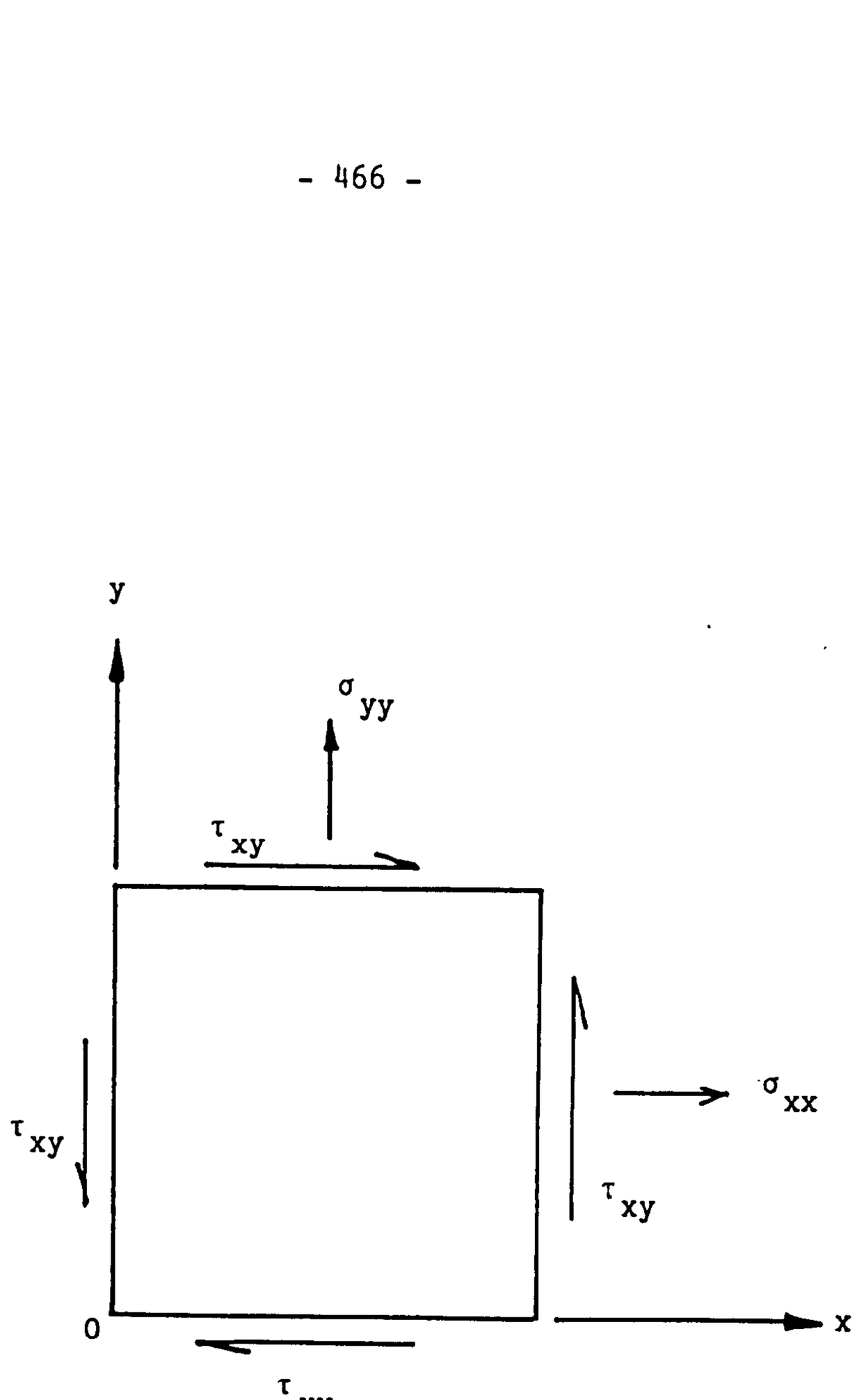

Fig.AIII.12 One element test

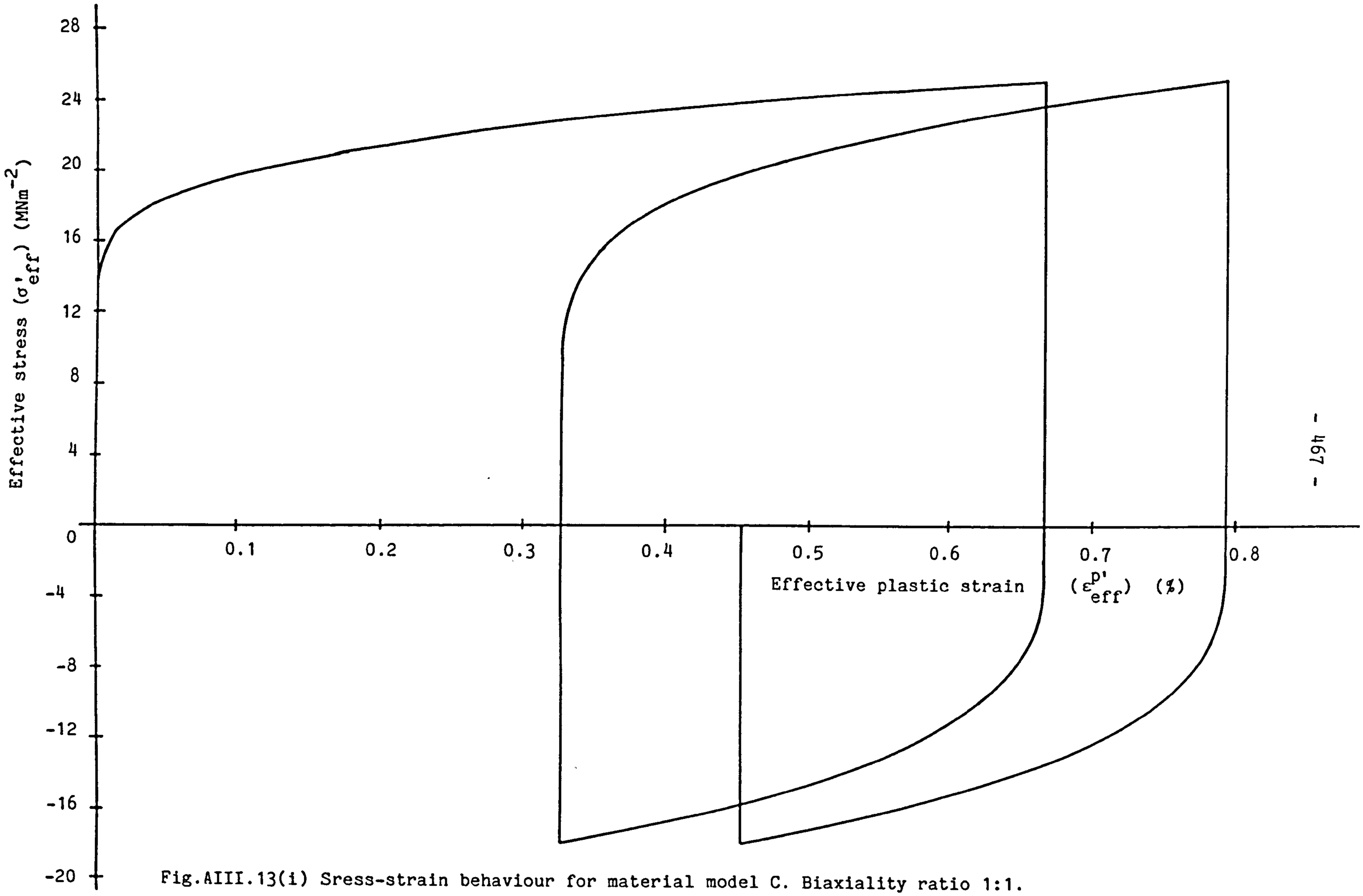

Fig.AIII.13(i) Sress-strain behaviour for material model C. Biaxiality ratio 1:1.

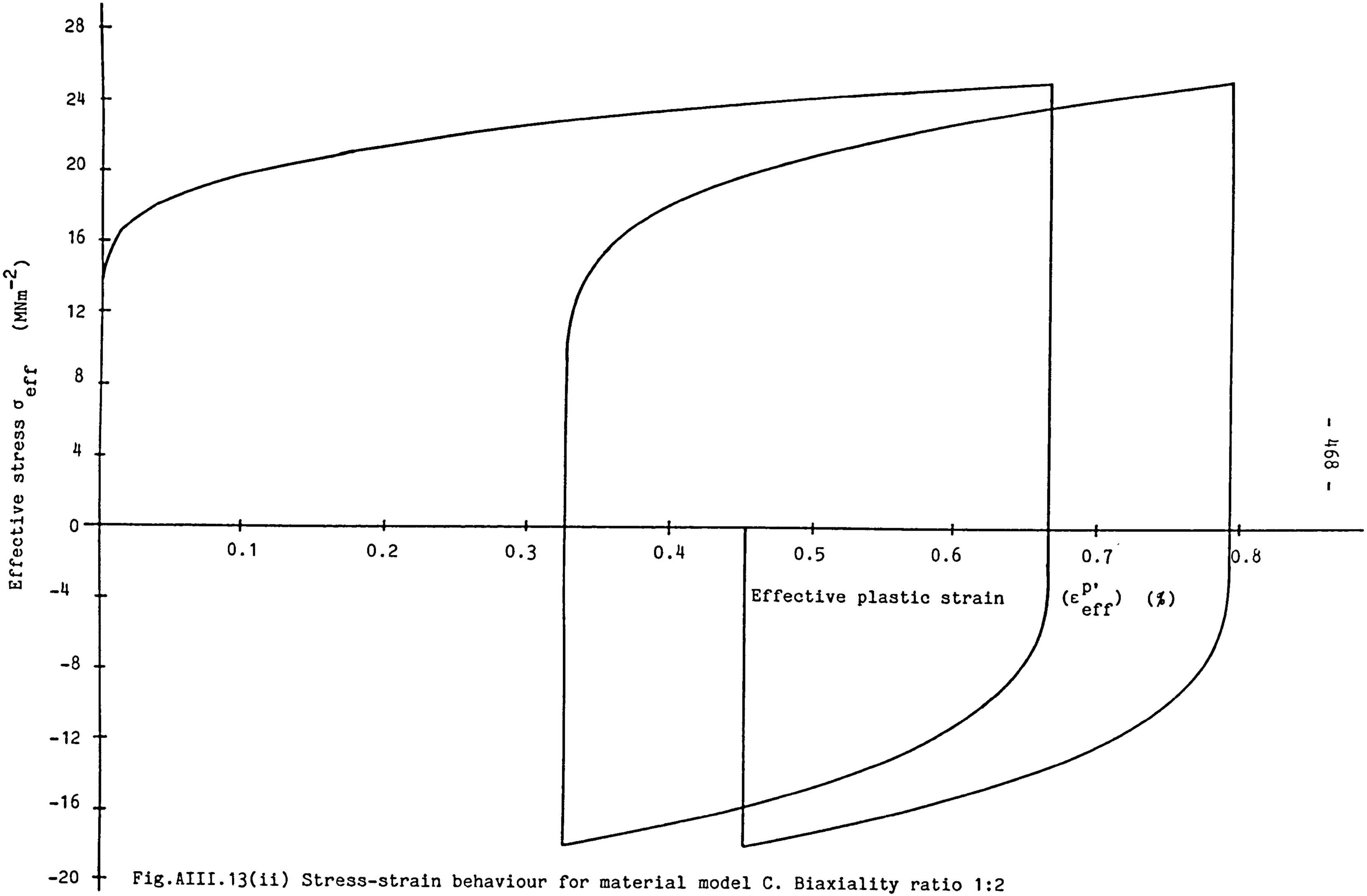

Fig.AIII.13(ii) Stress-strain behaviour for material model C. Biaxiality ratio 1:2

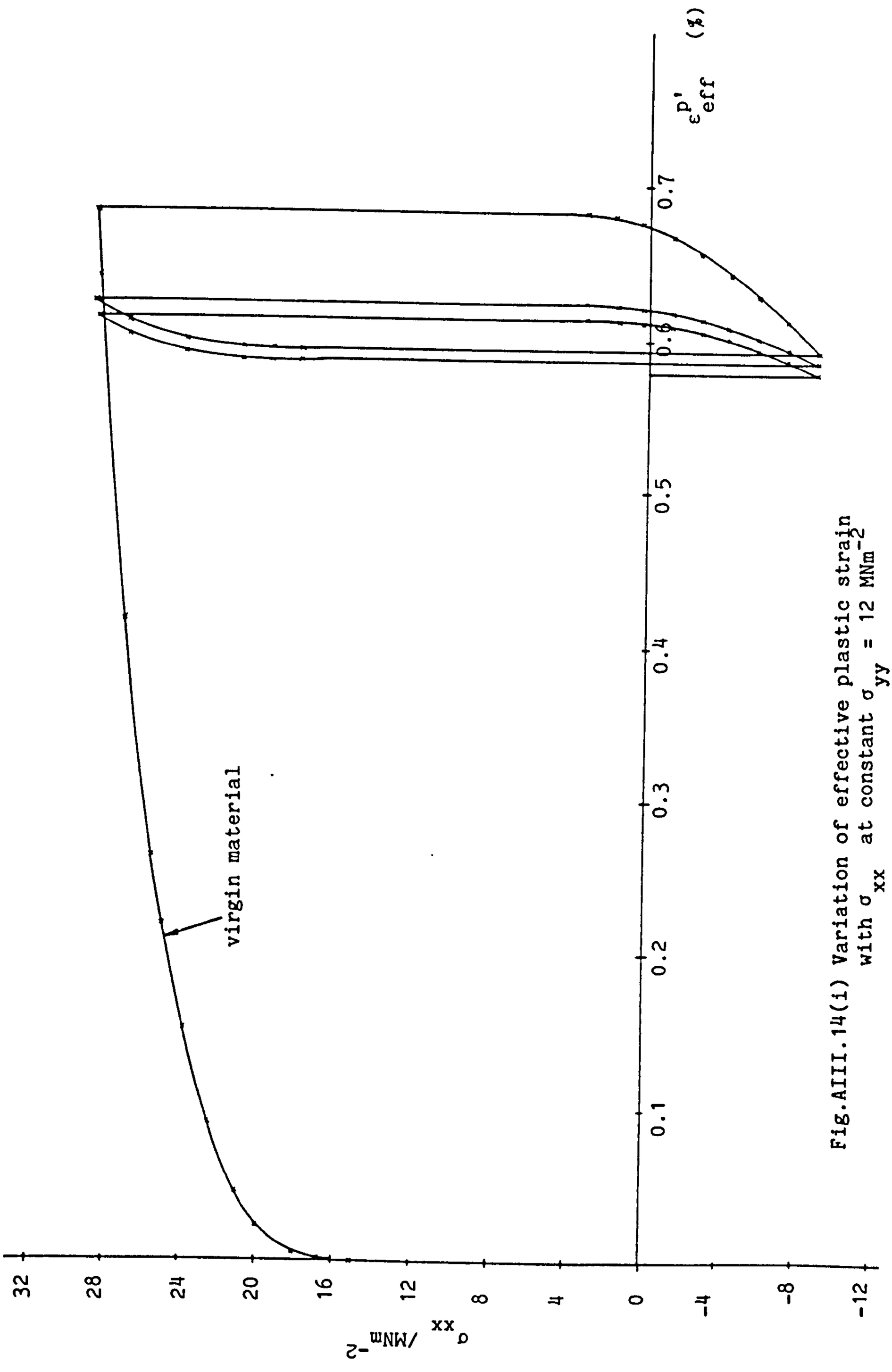

Fig.AIII.14(i) Variation of effective plastic strain with σ_{xx} at constant σ_{yy} = 12 MNm^{-2}

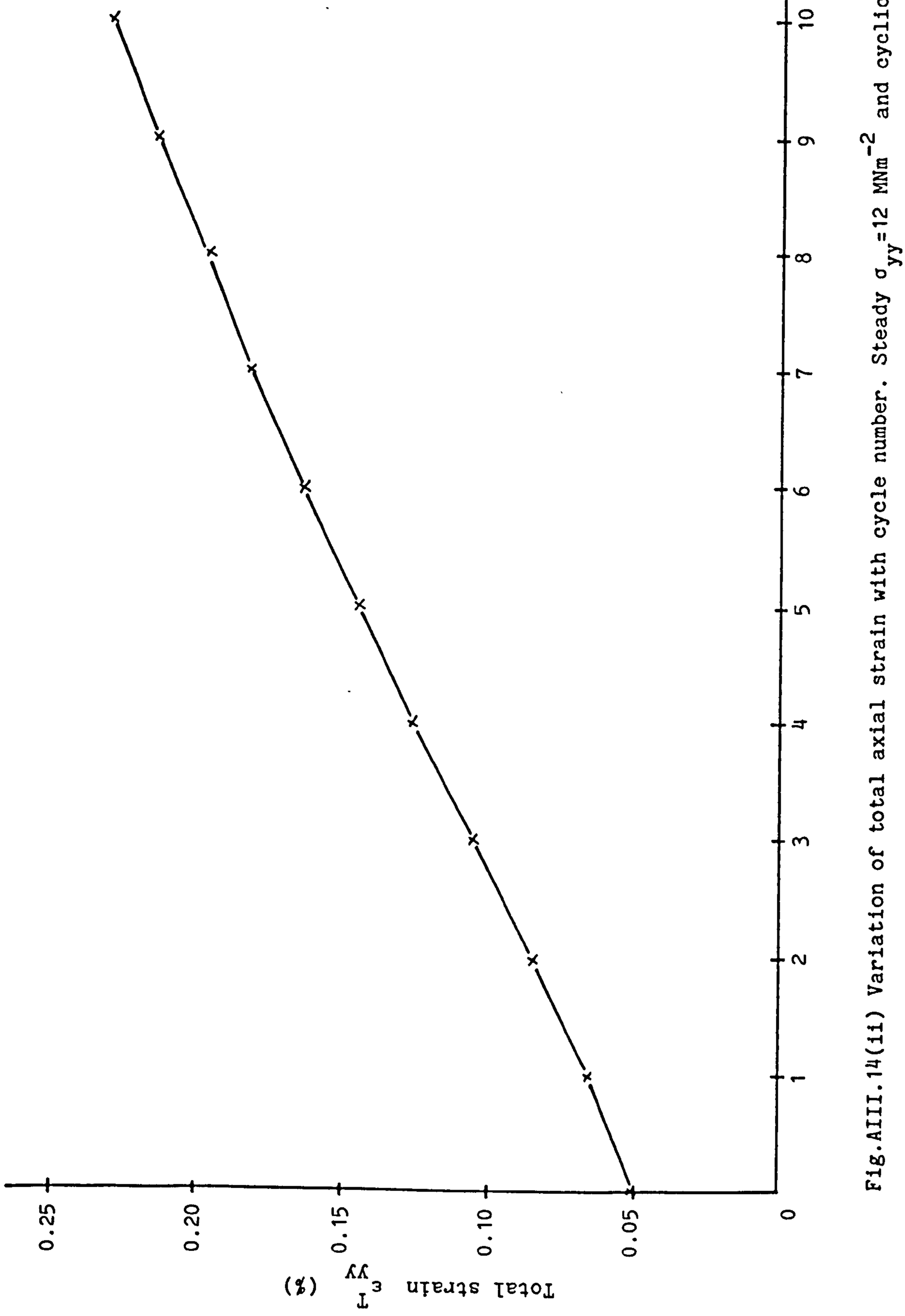

Fig.AIII.14(ii) Variation of total axial strain with cycle number. Steady σ_{yy}=12 MNm^{-2} and cyclic σ_{xx} between + 28.74 MNm^{-2} and - 9.0 MNm^{-2} .

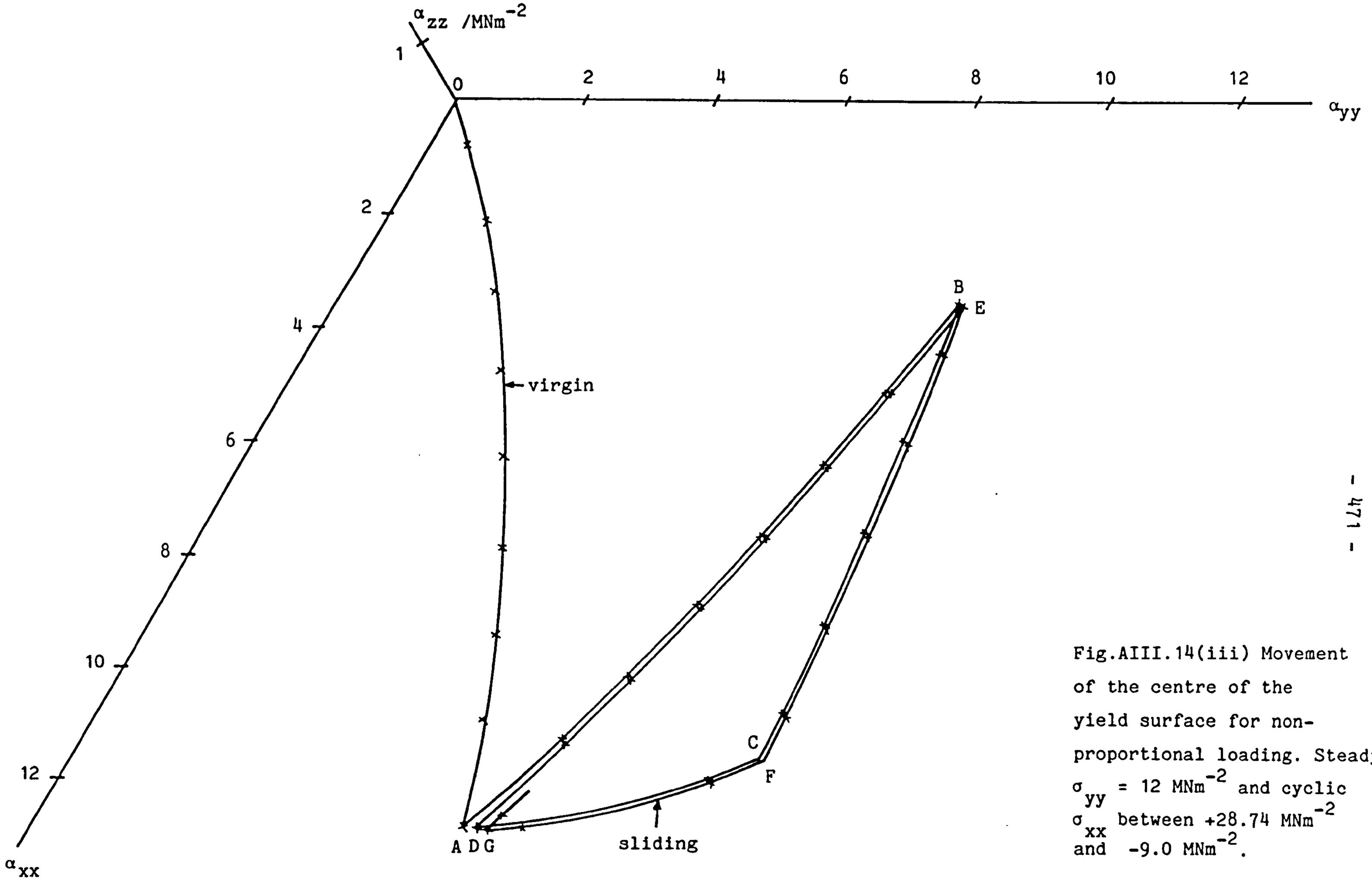

Fig.AIII.14(iii) Movement of the centre of the yield surface for non-proportional loading. Steady σ_{yy} = 12 MNm^{-2} and cyclic σ_{xx} between +28.74 MNm^{-2} and -9.0 MNm^{-2}.

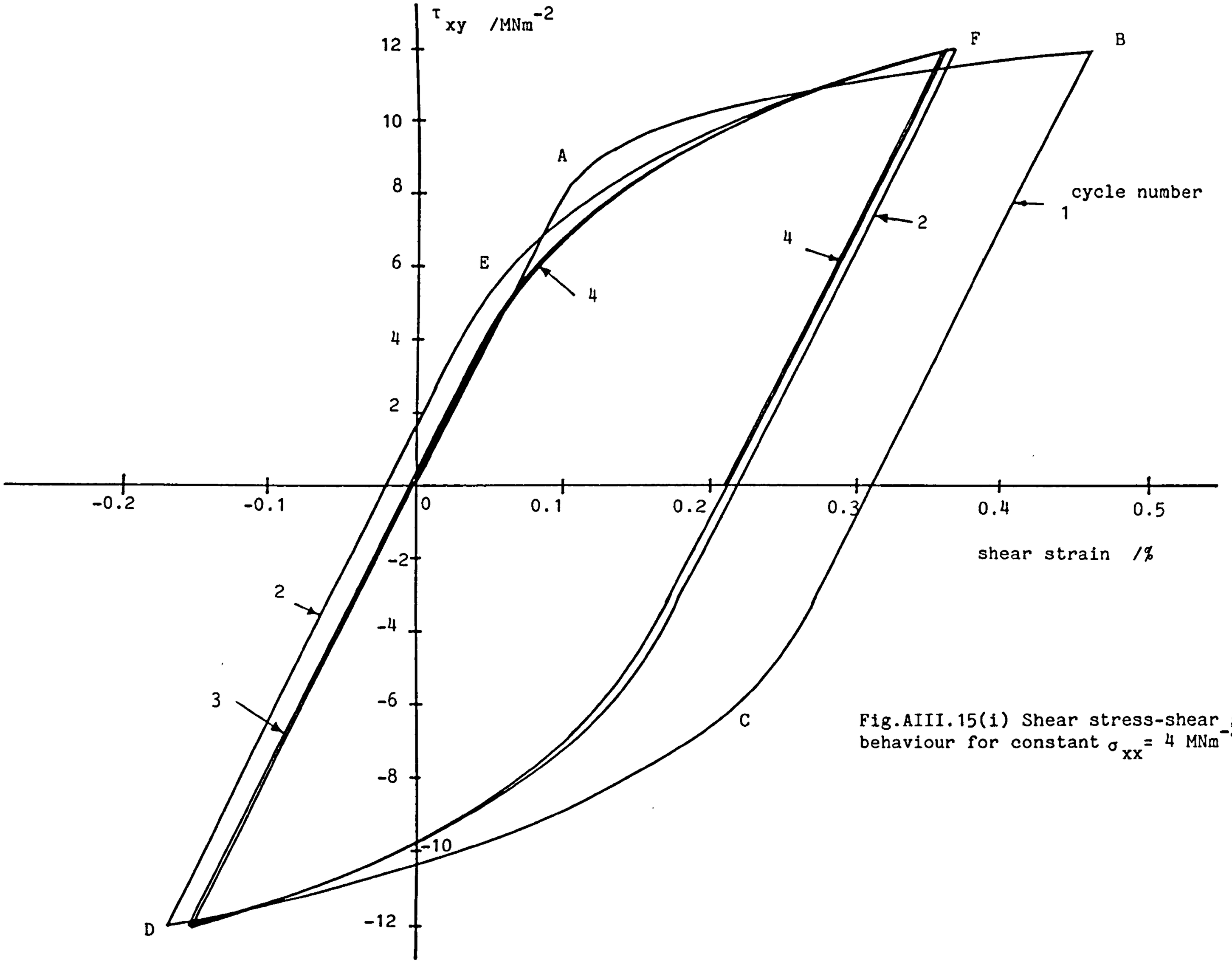

Fig.AIII.15(i) Shear stress-shear strain behaviour for constant σ_{xx} = 4 MNm^{-2}

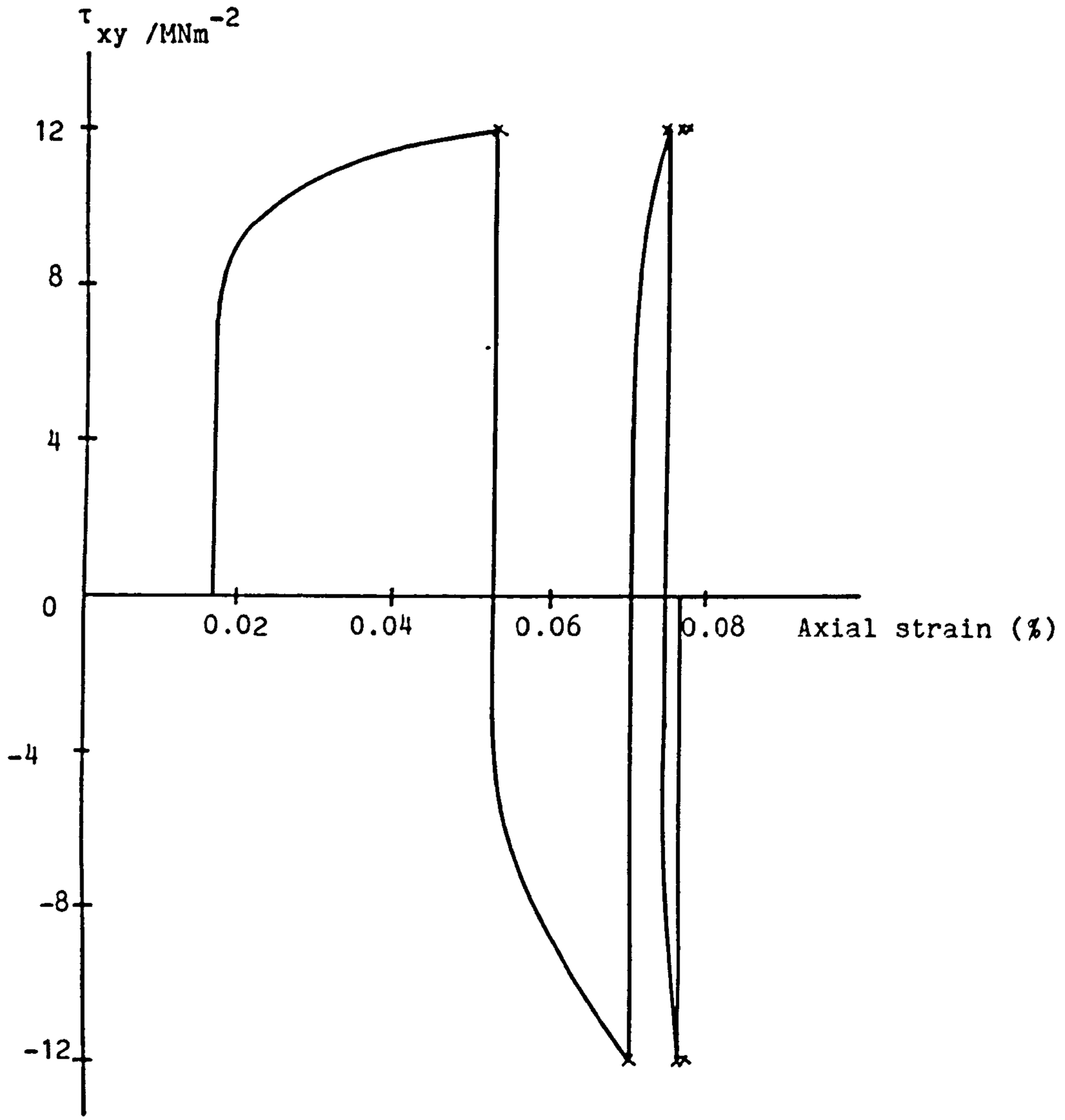

Fig.AIII.15(ii) Variation of axial strain with shear stress for constant σ_{xx} = 4 MNm^{-2}

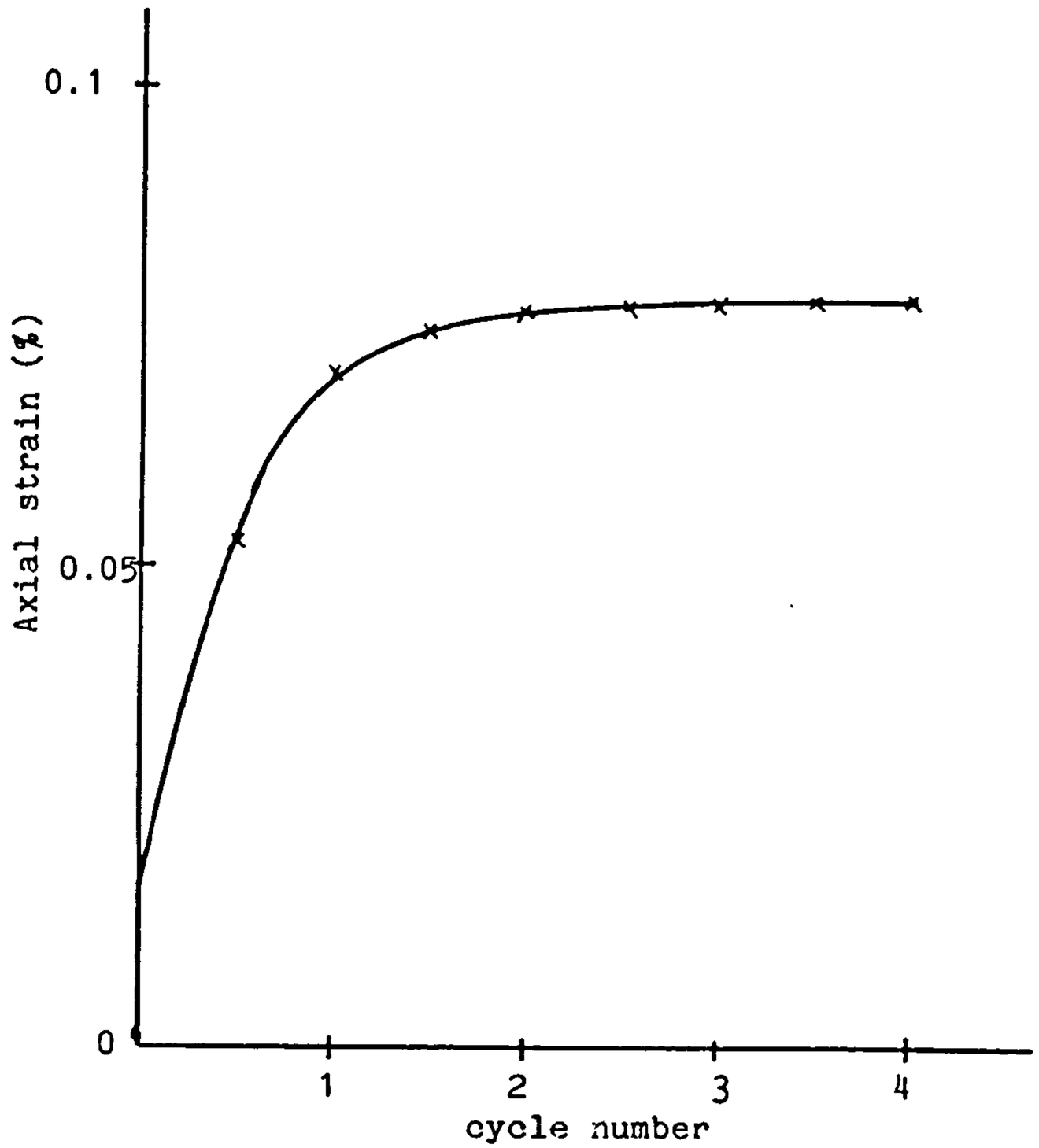

Fig.AIII.15(iii) Variation of axial strain with cycle number for constant σ_{xx} = 4 MNm^{-2} and cyclic shear stress τ_{xy} = ± 12 MNm^{-2}

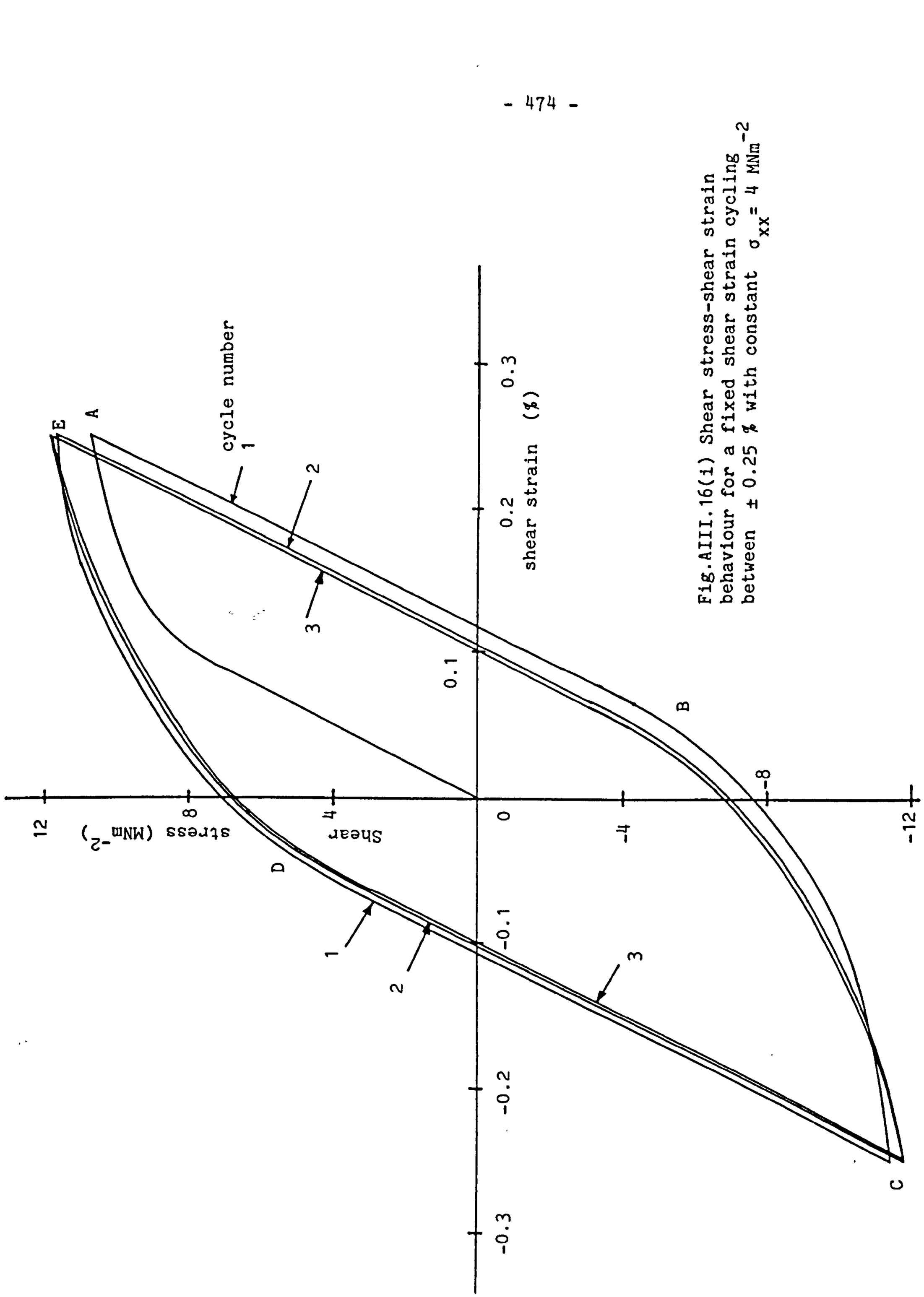

Fig.AIII.16(i) Shear stress-shear strain behaviour for a fixed shear strain cycling between ± 0.25 % with constant σ_{xx}= 4 MNm^{-2}

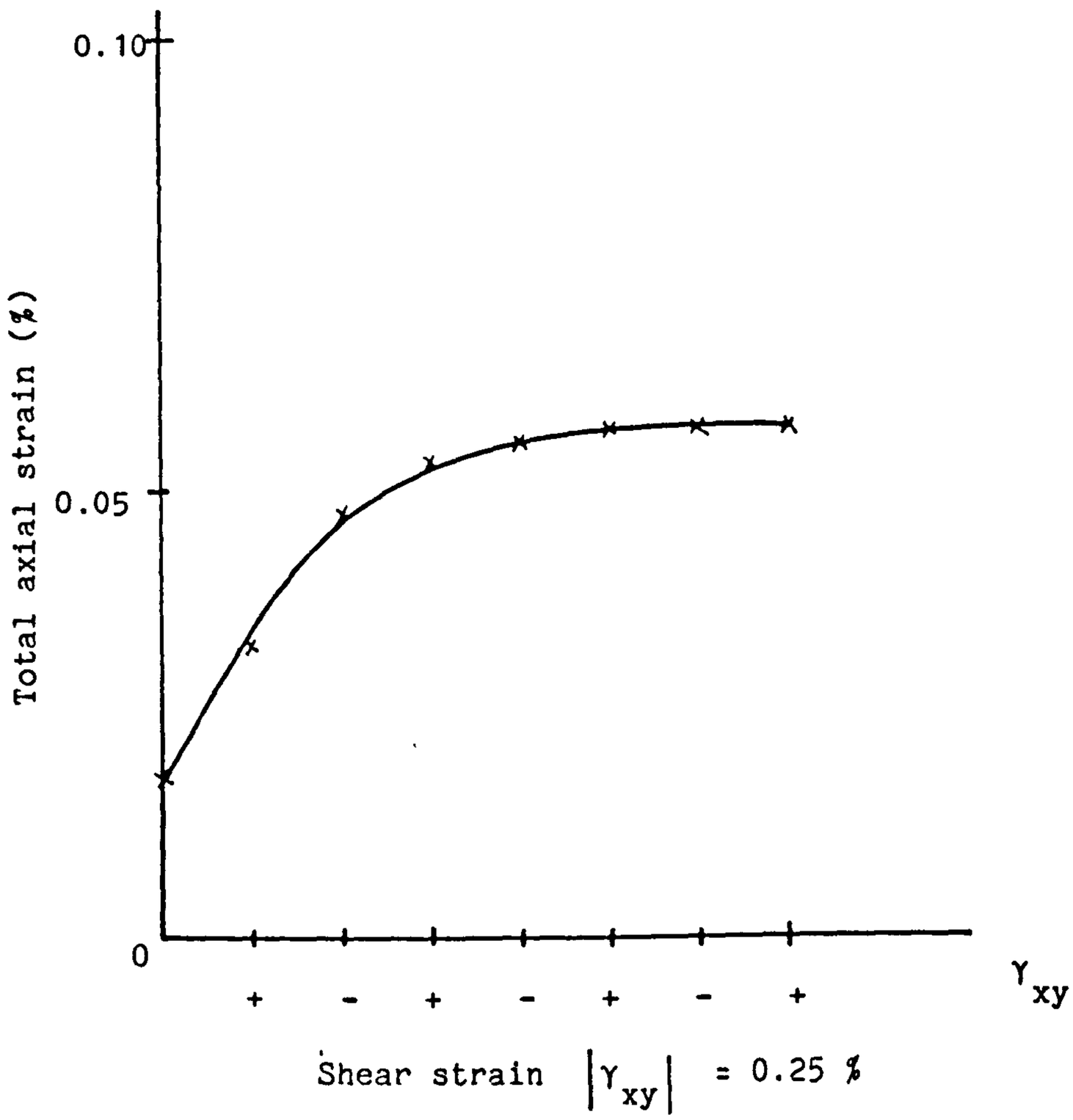

Fig.AIII.16(ii) Variation of total axial strain with shear strain for fixed shear strain cycling of ± 0.25 % and constant $\sigma_{xx} = 4\ MNm^{-2}$